Summer 8-13-2010

ON MACROSCOPIC CONSTITUTIVE RELATIONS AND MICROSTRUCTURE EVOLUTION IN MULTI-SCALE VISCOPLASTIC COMPOSITES

Michalis Agoras
University of Pennsylvania, agoras@seas.upenn.edu

ON MACROSCOPIC CONSTITUTIVE RELATIONS AND MICROSTRUCTURE EVOLUTION IN MULTI-SCALE VISCOPLASTIC COMPOSITES

Abstract
The determination of the effective or macroscopic properties of composite materials from the corresponding local properties of the constituent phases and the underlying sub-structure constitutes the fundamental problem in Mechanics of Composites. This problem is motivated from the remarkable physical observation that the constitutive properties of these materials appear to be homogeneous or uniform at the length scale of practical applications, despite the sharp variation of their local properties at the length scale of the heterogeneity and the fairly complex spatial distribution of their phases. This dissertation is concerned with the macroscopic mechanical properties of "multi-scale" viscoplastic composites, i.e., composite systems with viscoplastic constituents exhibiting heterogeneity at more than one, well-separated length-scales. Semi-crystalline polymers, such as polyethylene, polypropylene, Nylon-6, etc., are prominent examples of two-scale systems, and constitute the largest class of polymers used in technological applications. At the larger length-scale, a semi-crystalline polymer is an aggregate of a large number of randomly distributed grains that, at the smaller length scale, are made up of alternating layers of an amorphous and a crystalline phase, both of which exhibit nonlinear material behavior. During processing, these materials are often subjected to large deformations that may lead to highly anisotropic mechanical properties as a result of the evolution of the underlying sub-structure.

Primarily motivated by applications to semi-crystalline polymers, this work develops general variational methods for the estimation of the effective behavior of multi-scale viscoplastic composites. This general theory is applied to several two-scale material systems with increasing degree of complexity and sophistication. The predictions and some important features of these methods are first investigated in the context of two-dimensional model problems. Then, the general variational methods are used to develop homogenization-based constitutive models for the macroscopic response and texture evolution of semi-crystalline polymers under arbitrary finite-strain loading histories. Finally, the theory is specialized to two-scale polycrystals with granular structures at the meso-scale level and lamellar structures at the micro-scale level. In this context, we model the macroscopic instantaneous plastic anisotropy of -TiAl-based polysynthetically twinned crystals and the rolling textures of (alpha+beta) Ti alloys.

Degree Type
Dissertation

Degree Name
Doctor of Philosophy (PhD)

Graduate Group
Mechanical Engineering & Applied Mechanics

First Advisor
Pedro Ponte Castaneda

Keywords
Multi-scale Composites, Homogenization, Finite Strains, Semi-crystalline Polymers, Fiber-reinforced Composites, Instabilities

Subject Categories
Applied Mechanics

On Macroscopic Constitutive Relations and Microstructure Evolution in Multi-Scale Viscoplastic Composites

Michalis Agoras

A Dissertation

in

MECHANICAL ENGINEERING AND APPLIED MECHANICS

Presented to the Faculties of the University of Pennsylvania
in Partial Fulfillment of the Requirements for the
Degree of Doctor of Philosophy.
2010

Supervisor of Dissertation

Pedro Ponte Castañeda, Professor of
Mechanical Engineering and Applied Mechanics

Graduate Group Chairperson

Jennifer R. Lukes, Associate Professor of
Mechanical Engineering and Applied Mechanics

Dissertation Committee

John L. Bassani, Professor of
Mechanical Engineering and Applied Mechanics

Prashant K. Purohit, Assistant Professor of
Mechanical Engineering and Applied Mechanics

Pedro Ponte Castañeda, Professor of
Mechanical Engineering and Applied Mechanics

To my family

Acknowledgments

I would like to especially thank the advisor of my thesis, Professor Pedro Ponte Castañeda, for his guidance throughout the course of my dissertation and for his valuable research experience and time that he shared with me. It is certainly a privilege working with one of the worlds leading experts in the field of nonlinear homogenization.

I am especially indebted to my undergraduate advisor, Professor Nikolaos Aravas, for introducing me in the fascinating world of research in solid mechanics and for his constant encouragement thereafter. His lectures will always be a source of inspiration for me.

I gratefully thank Professor John Bassani and Professor Prashant Purohit for accepting to be members of my dissertation committee and for their useful comments on my work.

I would also like to thank Dr. Oscar Lopez-Pamies, Dr. Vikranth Racherla and Dr. Ricardo Lebensohn for their help in the research projects I was involved during these years. Special thanks go to Dr. Ricardo Lebensohn for providing his VPSC code which proved particularly useful in the core parts of this thesis.

I would like to express my deep gratitude to my colleague and friend Dr. Konstantinos Danas for helping me in a variety of issues and also for our delightful conversations on political philosophy and other matters. Many thanks go to the Ph.D. candidates and friends in the solid mechanics lab who made my stay in Philadelphia easier and more pleasant.

Finally, let me express my deepest gratitude to my family for their constant support, care and unconditional love.

ABSTRACT

ON MACROSCOPIC CONSTITUTIVE RELATIONS
AND MICROSTRUCTURE EVOLUTION
IN MULTI-SCALE VISCOPLASTIC COMPOSITES

Michalis Agoras

Pedro Ponte Castañeda

The determination of the effective or macroscopic properties of composite materials from the corresponding local properties of the constituent phases and the underlying sub-structure constitutes the fundamental problem in Mechanics of Composites. This problem is motivated from the remarkable physical observation that the constitutive properties of these materials appear to be homogeneous or uniform at the length scale of practical applications, despite the sharp variation of their local properties at the length scale of the heterogeneity and the fairly complex spatial distribution of their phases. This dissertation is concerned with the macroscopic mechanical properties of "*multi-scale*" *viscoplastic* composites, i.e., composite systems with viscoplastic constituents exhibiting heterogeneity at more than one, well-separated length-scales. Semi-crystalline polymers, such as polyethylene, polypropylene, Nylon-6, etc., are prominent examples of two-scale systems, and constitute the largest class of polymers used in technological applications. At the larger length-scale, a semi-crystalline polymer is an aggregate of a large number of randomly distributed grains that, at the smaller length scale, are made up of alternating layers of an amorphous and a crystalline phase, both of which exhibit nonlinear material behavior. During processing, these materials are often subjected to large deformations that may lead to highly anisotropic mechanical properties as a result of the evolution of the underlying sub-structure.

Primarily motivated by applications to semi-crystalline polymers, this work develops *general variational methods* for the estimation of the effective behavior of multi-scale viscoplastic composites. This general theory is applied to several two-scale material systems with increasing degree of complexity and sophistication. The predictions and some important features of these methods are first investigated in the context of two-dimensional model problems. Then, the general variational methods are used to develop homogenization-based constitutive models for the *macroscopic response* and *texture evolution* of *semi-crystalline polymers* under arbitrary finite-strain loading histories. Finally, the theory is specialized to *two-scale polycrystals* with granular structures at the meso-scale level and lamellar structures at the micro-scale level. In this context, we model the macroscopic instantaneous plastic anisotropy of γ-TiAl-based polysynthetically twinned crystals and the rolling textures of $(\alpha + \beta)$ Ti alloys.

Contents

Acknowledgements . . . iii
Abstract . . . iv
List of Tables . . . x
List of Figures . . . xi

1 Introduction **1**

2 Theory **9**
2.1 Sub-structural characterization of granular composites . . . 10
2.1.1 Single-scale systems . . . 11
2.1.2 Two-scale systems . . . 13
2.2 Sub-structural characterization of particulate composites . . . 18
2.2.1 Single-scale systems . . . 18
2.2.2 Two-scale systems . . . 20
2.3 Viscoplastic constitutive behavior . . . 23
2.4 Variational formulations of the homogenization problem . . . 24
2.4.1 Single-scale composites . . . 24
2.4.2 Two-scale composites . . . 26
2.5 Linear comparison composite methods for single-scale composites . . . 29
2.5.1 Secant method . . . 30
2.5.2 Tangent method . . . 33
2.5.3 Generalized-secant method . . . 35
2.5.4 Estimates for single-scale linear thermoelastic composites . . . 39
2.6 Secant method for two-scale composites . . . 42
2.6.1 Direct linearization scheme . . . 42
2.6.2 Sequential linearization scheme . . . 45
2.7 Tangent method for two-scale composites . . . 48
2.7.1 Direct linearization scheme . . . 48
2.7.2 Sequential linearization scheme . . . 51
2.8 Generalized-secant method for two-scale composites . . . 53

2.8.1 Direct linearization scheme . . . 53
2.8.2 Sequential linearization scheme . . . 56
2.9 Concluding remarks . . . 59

3 Applications to 2-D model problems **62**
3.1 Preliminaries . . . 63
3.2 Application to particulate composites—I . . . 65
3.2.1 Secant estimates for P1 . . . 67
3.2.2 Tangent second-order estimates for P1 . . . 68
3.2.3 Generalized-secant second-order estimates for P1 . . . 73
3.2.4 Results and discussion for P1 . . . 78
3.3 Application to particulate composites—II . . . 81
3.3.1 Secant estimates for P2 . . . 82
3.3.2 Tangent second-order estimates for P2 . . . 83
3.3.3 Generalized-secant second-order estimates for P2 . . . 86
3.3.4 Results and discussion for P2 . . . 88
3.4 Application to granular composites . . . 92
3.4.1 Secant estimates for G2 . . . 94
3.4.2 Tangent second-order estimates for G2 . . . 95
3.4.3 Generalized-secant second-order estimates for G2 . . . 96
3.4.4 Results and discussion for G2 . . . 97
3.5 Concluding remarks . . . 100
3.6 Appendix I. Two-phase single-scale linear thermoelastic composites . . . 102
3.7 Appendix II. Some useful relations . . . 104

4 Applications to semi-crystalline polymers **109**
4.1 Idealizations and instantaneous effective behavior . . . 110
4.1.1 Sub-structural characterization . . . 112
4.1.2 Amorphous phase . . . 114
4.1.3 Crystalline phase . . . 117
4.1.4 Effective behavior . . . 119
4.2 Estimates for the instantaneous effective behavior . . . 120
4.3 Estimates for the evolution of the internal variables . . . 124
4.3.1 Morphological texture evolution . . . 124
4.3.2 Lamellar texture evolution . . . 125
4.3.3 Crystallographic texture evolution . . . 126
4.3.4 Macromolecular texture evolution: the back-stress tensor . . . 127
4.3.5 Evolution of the critical resolved shear stresses . . . 127
4.4 Estimates for the linear comparison composite . . . 128

4.4.1 Self-consistent estimates for the granular composite . . . 129
4.4.2 Exact estimates for the lamellar grains . . . 130
4.5 Results and discussion . . . 133
4.5.1 On the choice of the model parameters . . . 134
4.5.2 Uniaxial compression . . . 142
4.5.3 Simple shear . . . 149
4.5.4 Uniaxial tension . . . 158
4.6 Concluding remarks . . . 164
4.7 Appendix I. Numerical aspects . . . 166
4.8 Appendix II. Material frame indifference . . . 170

5 Applications to two-scale polycrystals **174**
5.1 Preliminary definitions . . . 175
5.1.1 Sub-structural characterization . . . 175
5.1.2 Constitutive relations for the single-crystals . . . 178
5.2 Estimates for the instantaneous effective behavior . . . 179
5.3 Estimates for the evolution of the sub-structure . . . 181
5.3.1 Morphological texture evolution . . . 182
5.3.2 Lamellar texture evolution . . . 182
5.3.3 Crystallographic texture evolution . . . 183
5.4 Plastic anisotropy of γ-TiAl-based PST alloys . . . 184
5.5 Texture evolution in $(\alpha + \beta)$ Ti alloys . . . 188
5.6 Concluding remarks . . . 190

6 Closure **192**

A A general hyperelastic model for incompressible fiber-reinforced elastomers **198**
A.1 Introduction . . . 198
A.2 Problem formulation . . . 200
A.2.1 Transverse Isotropy . . . 203
A.3 Second-order homogenization estimates . . . 204
A.3.1 Local and effective properties of the LCC . . . 205
A.3.2 Tangent second-order estimates . . . 206
A.3.3 Generalized second-order estimates . . . 208
A.4 A constitutive model for general loading conditions . . . 210
A.4.1 Comparisons with bounds and other estimates . . . 214
A.5 Results and discussion . . . 215
A.6 Concluding remarks . . . 222

A.7 Appendix. Generalized second-order estimates for incompressible fiber-reinforced rubbers under generalized plane-strain conditions 223

B Onset of macroscopic instabilities in fiber-reinforced elastomers at finite strain 229

B.1 Introduction 229

B.2 Homogenization estimates for fiber-reinforced hyperelastic materials 232

B.2.1 The estimate of Agoras et al. for generalized Neo-Hookean phases 234

B.2.2 The estimate of Agoras et al. for Neo-Hookean phases 236

B.2.3 The estimate of deBotton et al. for Neo-Hookean phases 236

B.3 Onset of macroscopic instabilities 237

B.4 Aligned loadings 241

B.4.1 Axisymmetric shear 241

B.4.2 Pure shear 247

B.4.3 Asymptotic results in the limit of rigid fibers 248

B.4.4 Comparisons with earlier results for laminates under pure shear loading . . 249

B.5 Non-aligned loadings 251

B.5.1 Axisymmetric shear at an angle 251

B.5.2 Pure shear at an angle 253

B.5.3 Simple shear at an angle 255

B.6 General loading conditions 256

B.6.1 A closed-form analytical result for general loadings 256

B.6.2 Transverse uniaxial tension 257

B.7 Concluding remarks 262

B.8 Appendix I. Exact results for the macroscopic behavior of Neo-Hookean laminates 264

B.9 Appendix II. Demonstration of the criticality expressions (B.47), (B.48), and (B.49) 266

Bibliography 267

List of Tables

4.1 The values of the material parameters in the strain-hardening relation (4.77) for the CRSSs $\tau_{0k}^{(r,c)}$ in the slip systems of the crystalline phase used in the calculations of the LCC estimates of this section. The superscript "$*$" indicates quantities determined experimentally by Bartczak et al. [8]. 136

4.2 The values of material parameters defining the hyperelastic model (4.16) (with $M = 3$) for the back-stress tensor (4.15), used in the context of the various LCC estimates of Fig. 4.5. The LCC estimates discussed in subsections 4.5.2, 4.5.3 and 4.5.4 have been computed by using the set of values (c). 137

5.1 The critical resolved shear stresses τ_{0k} in the (matrix and tween) PST crystals, as determined by Lebensohn et al. [79]. 185

List of Figures

1.1 (a) TEM micrograph of "granular" microstructure in polyethylene crystallized at 130 C for 27 days. (b) Optical micrograph of "spherulitic" microstructure in a typical semi-crystalline polymer (PPS). (Taken from Ref. [13].) 2

2.1 A two-scale granular composite with random distributions of ellipsoidal symmetry (dotted ellipses). (a) Macroscopic RVE Ω: composite-grain families (distinguished by color). (b) Mesoscopic RVE of the composite-grain family r: single-crystal orientations. 11

2.2 A two-scale particulate composite with random distributions of ellipsoidal symmetry (dotted ellipses). (a) Macroscopic RVE Ω: composite-inclusion families in a composite-matrix (distinguished by color). (b) Mesoscopic RVE of the composite-inclusion family r: homogeneous-inclusion families in a homogeneous-matrix. 18

3.1 Schematic of rigidly-reinforced *particulate* systems. (a) *Single-scale* composite P0 with rigid-fiber concentration $c^{(f)} = |\Omega^{(f)}|/|\Omega|$. (b) *Two-scale* composite P1 with (meso-scale ℓ_1) composite-fiber concentration $c^{(2)} = |\Omega^{(2)}|/|\Omega|$, (micro-scale ℓ_2) rigid-fiber concentration $c^{(2,2)} = |\Omega^{(2,2)}|/|\Omega^{(2)}|$ and overall rigid-fiber content $c^{(2)}c^{(2,2)} \equiv c^{(f)}$. 66

3.2 Comparison of the secant (SEC) bound (3.20) for a single-scale composite P0 (Fig. 3.1(a)), with rigid-fiber concentration $c^{(f)}$, and the secant (SEC) bound (3.17) for a two-scale composite P1 (Fig. 3.1(b)), with the same overall rigid-fiber content $c^{(f)} = c^{(2)}c^{(2,2)}$. The corresponding normalized effective in-plane yield-stresses $\tilde{\sigma}_0/\sigma_0$ are plotted (a) as a function of the nonlinearity exponent $m = 1/n$ for fixed values of $c^{(f)} = 0.1, 0.25, 0.4$ and (b) as a function of $c^{(f)}$ for fixed values of $m = 0.1, 0.25, 0.5$. 79

3.3 Comparison of SLS (continuous thin lines) and DLS (continuous thick lines) estimates for the two-scale *particulate* composite P1 (Fig. 3.1(b)). Part (a) shows the SLS-GSO estimate (3.54), with (3.51), and the DLS-GSO estimate (3.49) for the normalized effective in-plane yield-stress $\tilde{\sigma}_0/\sigma_0$ as a function of the rate-sensitivity exponent $m = 1/n$ for fixed values of the total rigid-fiber concentration $c^{(f)} = c^{(2)}c^{(2,2)} = 0.1, 0.25, 0.4$ in P1, with $c^{(2)} = c^{(2,2)} = \sqrt{c^{(f)}}$; part (c) shows the same estimates for $\tilde{\sigma}_0/\sigma_0$ as a function of $c^{(f)}$ for the cases $m = 0.1, 0.25, 0.5$. Parts (*b*) and (*d*) present the corresponding predictions of the SLS-TSO estimate (3.44), with (3.39), and the DLS-TSO estimate (3.34), respectively. GSO and TSO results corresponding to the special case $c^{(1)} = 0$ and $c^{(2,2)} = c^{(f)}$, i.e., the case of the single-scale *particulate* composite P0 (Fig. 3.1(a)), have been included in the relevant parts (dotted lines). 80

3.4 Schematic of rigidly-reinforced *particulate* systems. (a) *Single-scale* composite P0 with rigid-fiber concentration $c^{(f)} = |\Omega^{(f)}|/|\Omega|$. (b) *Two-scale* composite P2 with meso-scale ℓ_1 rigid-fiber concentration $c^{(2)} = |\Omega^{(2)}|/|\Omega|$, micro-scale ℓ_2 rigid-fiber concentration $c^{(1,2)} = |\Omega^{(1,2)}|/|\Omega^{(1)}|$ and overall rigid-fiber content $1 - (1 - c^{(2)})(1 - c^{(1,2)}) \equiv c^{(f)}$. 82

3.5 Comparison of the secant (SEC) bound (3.20) for a single-scale composite P0 (Fig. 3.1(a)), with rigid-fiber concentration $c^{(f)}$, and the secant (SEC) bound (3.62) for a two-scale composite P2 (Fig. 3.4(b)), with the same overall rigid-fiber content $c^{(f)} = 1-(1-c^{(2)})(1-c^{(1,2)})$. The corresponding normalized effective in-plane yield-stresses $\tilde{\sigma}_0/\sigma_0$ are plotted (a) as a function of the nonlinearity exponent $m = 1/n$ for fixed values of $c^{(f)} = 0.1, 0.25, 0.4$ and (b) as a function of $c^{(f)}$ for fixed values of $m = 0.1, 0.25, 0.5$. 89

3.6 The effect of the meso-scale ℓ_1 and micro-scale ℓ_2 rigid-fiber contents $c^{(2)}$ and $c^{(1,2)}$, respectively, on the overall response of the two-scale *particulate* composite P2 (Fig. 3.4(b)). Predictions of the (a) DLS-GSO estimate (3.81) and (b) DLS-TSO estimate (3.74) for the normalized effective in-plane yield-stress $\tilde{\sigma}_0/\sigma_0$ are plotted for the fixed values $m = 0.1, 0.25$ of the nonlinearity exponent $m = 1/n$ as functions of the total rigid-fiber concentration $c^{(f)} = 1-(1-c^{(2)})(1-c^{(1,2)})$ for the combinations $c^{(2)} = c^{(1,2)}$, $c^{(2)} = 3c^{(1,2)}$, $c^{(2)} = 10c^{(1,2)}$ (continuous thick lines) and $c^{(1,2)} = 3c^{(2)}$, $c^{(1,2)} = 10c^{(2)}$ (continuous thin lines), as well as for the special case $c^{(2)} = 0$ or $c^{(1,2)} = 0$ (dotted lines), i.e., the case corresponding to the single-scale *particulate* composite P0 (Fig. 3.4(a)). 90

3.7 Comparison of SLS (continuous thin lines) and DLS (continuous thick lines) estimates for the two-scale *particulate* composite P2 (Fig. 3.4(b)). Part (a) shows the SLS-GSO estimate (3.84), with (3.85), and the DLS-GSO estimate (3.81) for the normalized effective in-plane yield-stress $\tilde{\sigma}_0/\sigma_0$ as a function of the rate-sensitivity exponent $m = 1/n$ for fixed values of the total rigid-fiber concentration $c^{(f)} = 0.1, 0.25, 0.4$ in P2, with $c^{(2)} = c^{(1,2)} = 1-\sqrt{1-c^{(f)}}$; part (c) shows the same estimates for $\tilde{\sigma}_0/\sigma_0$ as a function of $c^{(f)}$ for the cases $m = 0.1, 0.25, 0.5$. Parts (*b*) and (*d*) present the corresponding predictions of the SLS-TSO estimate (3.78), with (3.79), and the DLS-TSO estimate (3.74), respectively. GSO and TSO results corresponding to the special case $c^{(2)} = 0$ and $c^{(1,2)} = c^{(f)}$ (or $c^{(1,2)} = 0$ and $c^{(2)} = c^{(f)}$), i.e., the case of the single-scale *particulate* composite P0 (Fig. 3.4(a)), have been included in the relevant parts (dotted lines). 91

3.8 Schematic of rigidly-reinforced *granular* systems. (a) *Single-scale* composite G0 with rigid-phase concentration $c^{(f)} = |\Omega^{(f)}|/|\Omega|$. (b) *Two-scale* composite G2 with meso-scale ℓ_1 rigid-phase concentration $c^{(2)} = |\Omega^{(2)}|/|\Omega|$, micro-scale ℓ_2 rigid-phase concentration $c^{(1,2)} = |\Omega^{(1,2)}|/|\Omega^{(1)}|$ and overall rigid-phase content $1-(1-c^{(2)})(1-c^{(1,2)}) \equiv c^{(f)}$. 93

3.9 The effect of the meso-scale ℓ_1 and micro-scale ℓ_2 rigid-phase contents $c^{(2)}$ and $c^{(1,2)}$, respectively, on the overall in-plane response of the two-scale *granular* composite G2 (Fig. 3.8(b)). Predictions of the (a) DLS-GSO estimate (3.81) and (b) DLS-TSO estimate (3.74) for the normalized effective in-plane yield-stress $\tilde{\sigma}_0/\sigma_0$ are shown for the fixed value $m = 0.25$ of the nonlinearity exponent $m = 1/n$ as functions of the total rigid-phase concentration $c^{(f)} = 1-(1-c^{(2)})(1-c^{(1,2)})$ for the combinations $c^{(2)} = c^{(1,2)}$, $c^{(2)} = 3c^{(1,2)}$, $c^{(2)} = 10c^{(1,2)}$ (continuous thick lines) and $c^{(1,2)} = 3c^{(2)}$, $c^{(1,2)} = 10c^{(2)}$ (continuous thin lines), as well as for the special case $c^{(2)} = 0$ or $c^{(1,2)} = 0$ (dotted lines), i.e., the case corresponding to the single-scale *granular* composite G0 (Fig. 3.8(a)). 98

3.10 Comparison of SLS (continuous thin lines) and DLS (continuous thick lines) estimates for the two-scale *granular* composite G2 (Fig. 3.8(b)). Part (a) shows the SLS-GSO estimate (3.84), with (3.85), and the DLS-GSO estimate (3.81) for the normalized effective in-plane yield-stress $\tilde{\sigma}_0/\sigma_0$ as a function of the rate-sensitivity exponent $m = 1/n$ for fixed values of the total rigid-phase concentration $c^{(f)} = 0.1, 0.25, 0.4$ in G2, with $c^{(2)} = c^{(1,2)} = 1-\sqrt{1-c^{(f)}}$; part (c) shows the same estimates for $\tilde{\sigma}_0/\sigma_0$ as a function of $c^{(f)}$ for the cases $m = 0.1, 0.25, 0.5$. Parts (*b*) and (*d*) present the corresponding predictions of the SLS-TSO estimate (3.78), with (3.79), and the DLS-TSO estimate (3.74), respectively. GSO and TSO results corresponding to the special case $c^{(2)} = 0$ and $c^{(1,2)} = c^{(f)}$ (or $c^{(1,2)} = 0$ and $c^{(2)} = c^{(f)}$), i.e., the case of the single-scale *granular* composite G0 (Fig. 3.8(a)), have been included in the relevant parts (dotted lines). 99

3.11 Comparison of SLS (continuous thin lines) and DLS (continuous thick lines) estimates for the two-scale *granular* composite G2 (Fig. 3.8(b)) in the ideally plastic limit $m = 0$. (a) SLS-GSO and DLS-GSO estimates for the normalized effective in-plane yield-stress $\tilde{\sigma}_0/\sigma_0$ as a function of the total rigid-phase concentration $c^{(f)}$, with $c^{(2)} = c^{(1,2)} = 1 - \sqrt{1 - c^{(f)}}$. (b) Corresponding SLS-TSO and DLS-TSO results. The associated results for the single-scale composite G0 of Fig. 3.8(a) are also shown (dotted lines). In addition, the corresponding secant (SEC) upper bounds for G2 and G0 are included. 100

4.1 Schematic illustration of the mapping of a semi-crystalline polymer from the reference (Parts (a) and (b)) to the current (Parts (c) and (d)) configuration during an arbitrary finite deformation process prescribed through the macroscopic deformation gradient $\overline{\mathbf{F}}(t)$, with t standing for the time variable. At the meso-structural level (Parts (a) and (c)), the material consists of a large number N of grain-families distributed randomly with *isotropic* symmetry in the reference configuration (dotted circles in Part (a)) which evolves into *ellipsoidal* symmetry in the current configuration (dotted ellipses in Part (c)). At the micro-structural level (Parts (b) and (d)), the grains are taken to be lamellar composites consisting of alternating layers of an amorphous and a crystalline phase; both the orientation of the lamellar grains—defined by the vectors $\mathbf{n}^{(r)}$ normal to the layers—and the orientation of the crystals—defined by the associated lattice vectors $\mathbf{a}^{(r)}$, $\mathbf{b}^{(r)}$ and $\mathbf{c}^{(r)}$—evolve in time. 111

4.2 Physical description of the back-stress tensor $\mathbf{T}_d$ in principal stress space, where t_i and λ_i denote the principal values of $\mathbf{T}_d$ and the principal stretches, respectively, and θ_g denotes the glass transition temperature of the polymer. (reproduced from Boyce [14]). 115

4.3 The initial crystallographic and lamellar texture in the 500-grain composite system used in the calculations of the LCC estimates of this section. Parts (a), (b) and (c) show respectively the equal area projections of the (100), (010) and (001) plane poles, i.e., the crystallographic axes $\mathbf{a}^{(r)}$, $\mathbf{b}^{(r)}$ and $\mathbf{c}^{(r)}$, respectively. Part (d) shows the corresponding representation of the lamination orientations $\mathbf{n}^{(r)}$. 135

4.4 Left: Plots of the strain hardening relation (4.77) for the CRSSs $\tau_{0k}^{(r,c)}$ as functions of the deformation measure $\overline{\Gamma}^{(r,c)}$ for the values of the material parameters of Table 4.1. Right: Response of the homogeneous hyperelastic material (4.16) under axisymmetric shear compression—i.e., for $\mathbf{F} = \mathrm{diag}\{\lambda^{-1/2}, \lambda^{-1/2}, \lambda\}$ with $\lambda < 1$—for the three different sets of material parameters (a), (b) and (c) of Table 4.2; the equivalent stress $T_e \equiv \sqrt{3\mathbf{T}_d \cdot \mathbf{T}_d/2}$ is plotted as a function of the equivalent strain $\overline{\varepsilon}_e \equiv \sqrt{2\varepsilon \cdot \varepsilon/3}$, with $\mathbf{T}_d$ and ε defined respectively by (4.15) and (4.110). 138

4.5 Fitting the LCC model to the experimental data of Bartczak et al. [10] for uniaxial compression of HDPE. The dotted curves correspond to constant CRSSs $\tau_{0k}^{(r,c)} = \tau_{0k}$ and the continuous curve corresponds to $\tau_{0k}^{(r,c)}$ given by (4.77), using the relevant material parameters of Table 4.1. The estimates (a), (b) and (c) make use of the respective sets of values (a), (b) and (c) of Table 4.2 for the elastic properties of the amorphous phase and the estimate (d) makes use of the set of values (c) of Table 4.2. 139

4.6 LCC estimates for the macroscopic stress-strain response of HDPE under simple shear and uniaxial tension loadings, corresponding to different values of the material parameters of the phases. The dotted curves correspond to constant CRSSs $\tau_{0k}^{(r,c)} = \tau_{0k}$ and the continuous curve corresponds to $\tau_{0k}^{(r,c)}$ given by (4.77), using the relevant material parameters of Table 4.1. The estimates (b) and (c) make use of the respective sets of values (b) and (c) of Table 4.2 for the elastic properties of the amorphous phase and the estimate (d) makes use of the set of values (c) of Table 4.2. 140

4.7 Macroscopic response of HDPE under uniaxial compression at a constant deformation rate $\overline{D}_{33} = -10^{-3}s^{-1}$. Comparison of the LCC estimate (4.80), the estimate of Lee et al. [80] and the estimate of Nikolov et al. [110] with the corresponding experimental results of Bartczak et al. [10]. The applied equivalent stress measure $\overline{\sigma}_e$ is plotted as a function of the applied equivalent strain measure $\overline{\varepsilon}_e$, with $\overline{\sigma}_e$ and $\overline{\varepsilon}_e$ defined by $(4.112)_1$ and $(4.112)_2$, respectively. 143

4.8 Morphological texture evolution in HDPE under uniaxial compression as predicted by the LCC model. The maximum $w_{\max}$ and minimum $w_{\min}$ aspect ratios of the distributional ellipsoid (4.8), defined respectively by $(4.113)_1$ and $(4.113)_2$, are plotted as functions of the applied equivalent strain $\overline{\varepsilon}_e$. Results are shown both for the 500-grain system of Fig. 4.3 and also for a refined 1000-grain system. For comparison, the aspect ratio $w_{\max} = w_{\min} = \mathrm{Exp}[3\overline{\varepsilon}_e/2]$ corresponding to a perfectly transversely isotropic material is also shown. . . 144

4.9 Lamellar texture evolution in HDPE under uniaxial compression as predicted by the LCC model. Equal area projection figures of the lamination orientations $\mathbf{n}^{(r)}$ are shown at various values of the applied equivalent strain $\overline{\varepsilon}_e$. The direction of compression is along the 3−axis. 145

4.10 Crystallographic texture evolution in HDPE under uniaxial compression as predicted by the LCC model. Equal area projection figures of the (001) plane poles are shown at various values of the applied equivalent strain $\overline{\varepsilon}_e$. The direction of compression is along the 3−axis. 146

4.11 Crystallographic texture evolution in HDPE under uniaxial compression. The equal area projection figures of the (100) and (010) plane poles predicted by the LCC model are compared with the corresponding pole intensity plots measured experimentally by Bartczak et al. [10] at various values of the applied equivalent strain $\overline{\varepsilon}_e$. The direction of compression is along the 3−axis. 148

4.12 Crystallographic texture evolution in HDPE under uniaxial compression. The equal area projection figures of the {110} and {011} plane poles predicted by the LCC model are compared with the corresponding pole intensity plots measured experimentally by Bartczak et al. [10] at various values of the applied equivalent strain $\overline{\varepsilon}_e$. The direction of compression is along the 3−axis. 149

4.13 The effect of the deformation rate $\overline{D}_{33}$ on the LCC estimate (4.80) for the macroscopic response of HDPE under uniaxial compression. The applied equivalent stress $\overline{\sigma}_e$ is plotted as a function of the applied equivalent strain $\overline{\varepsilon}_e$ for $\overline{D}_{33} = -10^{-4}s^{-1}$, $\overline{D}_{33} = -10^{-3}s^{-1}$ and $\overline{D}_{33} = -10^{-2}s^{-1}$. 150

4.14 Macroscopic response of HDPE under simple shear at a constant shear rate $\dot{\overline{\gamma}} = 10^{-3}s^{-1}$. Comparison of the LCC estimate (4.80), the estimate of Lee et al. [80] and the estimate of Nikolov et al. [110] with the corresponding experimental results of Bartczak et al. [9] and Dahoun [24]. The applied equivalent stress measure $\overline{\sigma}_e$ is plotted as a function of the applied equivalent strain measure $\overline{\varepsilon}_e$, with $\overline{\sigma}_e$ and $\overline{\varepsilon}_e$ defined by $(4.114)_1$ and $(4.114)_2$, respectively. 151

4.15 Morphological texture evolution in HDPE under simple shear as predicted by the LCC model. (a) The aspect ratio $w = \overline{\lambda}_{\max}/\overline{\lambda}_{\min}$, with $\overline{\lambda}_{\max}$ and $\overline{\lambda}_{\max}$ being respectively the maximum and minimum applied stretches, is plotted as a function of the applied amount of shear $\overline{\gamma}$. (b) The angle $\overline{\theta}_E = \tan^{-1}(2/\overline{\gamma})/2$ between the major principal axis and the shear direction $\mathbf{e}_2$ is plotted as a function of the applied amount of shear $\overline{\gamma}$. 152

4.16 Lamellar texture evolution in HDPE under simple shear as predicted by the LCC model. Stereographic projection figures of the lamination orientations $\mathbf{n}^{(r)}$ are shown at various values of the applied amount of shear $\overline{\gamma}$. The direction of shear is indicated by the arrows. 153

4.17 Crystallographic texture evolution in HDPE under simple shear. Stereographic projection figures of the (001) and (100) plane poles predicted by the LCC model are compared with corresponding experimental results by Bartczak et al. [9]. The theoretical predictions are presented below the corresponding experimental results. The direction of shear is indicated by the arrows. 155

4.18 Crystallographic texture evolution in HDPE under simple shear. Stereographic projection figures of the (010) and {110} plane poles predicted by the LCC model are compared with corresponding experimental results by Bartczak et al. [9]. The theoretical predictions are presented below the corresponding experimental results. The direction of shear is indicated by the arrows. 156

4.19 The effect of the shear rate $\dot{\overline{\gamma}}$ on the LCC estimate (4.80) for the macroscopic response of HDPE under simple shear. The applied equivalent stress $\overline{\sigma}_e$ is plotted as a function of the applied equivalent strain $\overline{\varepsilon}_e$ for $\dot{\overline{\gamma}} = 10^{-4}s^{-1}$, $\dot{\overline{\gamma}} = 10^{-3}s^{-1}$ and $\dot{\overline{\gamma}} = 10^{-2}s^{-1}$. 157

4.20 Macroscopic response of HDPE under uniaxial tension at a constant deformation rate $\overline{D}_{33} = 10^{-3}s^{-1}$. Comparison of the LCC estimate (4.80), the estimate of Lee et al. [80] and the estimate of Nikolov et al. [110] with the experimental results of G'Sell and Jonas [46] and Hiss et al. [54]. The applied equivalent stress measure $\overline{\sigma}_e$ is plotted as a function of the applied equivalent strain measure $\overline{\varepsilon}_e$, with $\overline{\sigma}_e$ and $\overline{\varepsilon}_e$ defined by $(4.112)_1$ and $(4.112)_2$, respectively. 159

4.21 Morphological texture evolution in HDPE under uniaxial tension as predicted by the LCC model. The maximum $w_{\max}$ and minimum $w_{\min}$ aspect ratios of the distributional ellipsoid (4.8), defined respectively by $(4.116)_1$ and $(4.116)_2$, are plotted as functions of the applied equivalent strain $\overline{\varepsilon}_e$. Results are shown both for the 500-grain system of Fig. 4.3 and also for a refined 1000-grain system. For comparison, the aspect ratio $w_{\max} = w_{\min} = \text{Exp}[3\overline{\varepsilon}_e/2]$ corresponding to a perfectly transversely isotropic material is also shown. 160

4.22 Lamellar texture evolution in HDPE under uniaxial tension as predicted by the LCC model. Stereographic projection figures of the lamination orientations $\mathbf{n}^{(r)}$ are shown at various values of the applied equivalent strain $\overline{\varepsilon}_e$. The direction of tension is along the 3−axis. . 161

4.23 Crystallographic texture evolution in HDPE under uniaxial tension as predicted by the LCC model. Stereographic projection figures of the (001), (100), (010) and {011} plane poles are shown at various values of the applied equivalent strain $\overline{\varepsilon}_e$. The direction of tension is along the 3−axis. 162

4.24 Crystallographic texture in the HDPE specimen used by Li et al. [83] in their uniaxial tension test. The corresponding stereographic projection figures of the (001), (100) and (010) plane poles are shown in the undeformed and deformed to $\overline{\varepsilon}_e = 2.1$ sample, after relaxation. The direction of tension is normal to the plane shown. 163

4.25 The effect of the deformation rate $\overline{D}_{33}$ on the LCC estimate (4.80) for the macroscopic response of HDPE under uniaxial tension. The applied equivalent stress $\overline{\sigma}_e$ is plotted as a function of the applied equivalent strain $\overline{\varepsilon}_e$ for $\overline{D}_{33} = 10^{-4}s^{-1}$, $\overline{D}_{33} = 10^{-3}s^{-1}$ and $\overline{D}_{33} = 10^{-2}s^{-1}$. 164

5.1 Schematic illustration of the mapping of a two-scale polycrystal from the reference (Parts (a) and (b)) to the current (Parts (c) and (d)) configuration during an arbitrary finite deformation process prescribed through the macroscopic deformation gradient $\overline{\mathbf{F}}(t)$, with t standing for the time variable. At the meso-structural level (Parts (a) and (c)), the material consists of a large number N of composite-grain-families distributed randomly with *ellipsoidal* symmetry (dotted ellipses in Parts (a) and (c)), the specific features of which change from the reference to the current configuration. At the micro-structural level (Parts (b) and (d)), the composite-grains have a lamellar structure consisting of alternating layers of two different single-crystal-grains; both the orientation of the lamellar grains—defined by the vectors $\mathbf{n}^{(r)}$ normal to the layers—and the orientation of the crystals evolve in time. 176

5.2 (a) The matrix-twin lamellar structure used to model a γ-TiAl PST crystal. (b) Comparison of the laminate model (Part (a)) predictions for the normalized yield stress $\widetilde{\tau}_\phi/\widetilde{\tau}_{90^o}$, given by 5.40, with the corresponding experimental results for a PST crystal subjected to uniaxial compression as a function of the loading angle ϕ, defined in Part (a). (Reproduced from Lebensohn et al. [79].) 186

5.3 Equal area projection figures of the crystallographic {111} plane poles (Part (a)) and of the lamination orientations $\mathbf{n}^{(r)}$ (Part (b)) in the as-cast sample of the PST polycrystal. . 187

5.4 Instantaneous plastic anisotropy of the textured PST polycrystal (see Fig. 5.3), subjected to compression along an axis forming an angle ϕ with the axis X_3 on the plane $X_2 - X_3$ (see Fig. 5.3). The predictions of the SOE model (5.23) and those of the model of Lebensohn [73] are compared with the corresponding experimental results (Lebensohn [73]). (a) The effective yield stress ratio $\widetilde{\tau}_\phi/\widetilde{\tau}_{90^o}$ is shown as a function of the loading angle ϕ. (b) The corresponding ratios of the macroscopic deformation rate components $\overline{D}_{11}/\overline{D}_{33}$ and $\overline{D}_{22}/\overline{D}_{33}$ are shown as a function of ϕ. 188

5.5 Texture development in the $(\alpha+\beta)$ Ti alloy under rolling, as predicted by the SOE model. Equal area projection figures are shown for the (0001) basal plane poles of the α-phase, the {110} plane poles of the β-phase and the lamination orientations $\mathbf{n}^{(r)}$. In these figures, RD and TD indicate the rolling and the transverse direction, respectively. 189

A.1 The GSO estimate (A.28) for the effective stored-energy $\widehat{\phi}$ of a fiber-reinforced elastomer with compressible Gent phases subjected to an $\overline{\mathbf{F}}$ of the form (A.11), as a function of the loading parameter ℓ, for various values of the invariant $\overline{\psi}_{\overline{\gamma}}$. 211

A.2 The GSO (A.28) and TSO (A.19) estimates for the effective stored-energy $\widehat{\phi}$ of fiber-reinforced elastomers with compressible Gent phases subjected to antiplane combined with axisymmetric shear loadings, as a function of the loading parameter ℓ, for $\kappa^{(1)} = \kappa^{(2)} = 10$ and $\kappa^{(1)} = \kappa^{(2)} = 1000$. The corresponding incompressible TSO estimate (A.26) is also shown. 212

A.3 Second-order estimates (SOE) for the effective response of a fiber-reinforced elastomer with incompressible Neo-Hookean phases under the three different modes of shear. The results are shown as a function of the corresponding amount of shear $\overline{\gamma}_a$,$\overline{\gamma}_p$ and $\overline{\gamma}_n$. (*a*) The energies $\widehat{\Psi}(\overline{\gamma}_a, 0, 0)$, $\widehat{\Psi}(0, \overline{\gamma}_p, 0)$ and $\widehat{\Psi}(0, 0, \overline{\gamma}_n)$, normalized by $\mu^{(1)}$. (*b*) The corresponding (non-zero) normalized stresses $\overline{S}_a(\overline{\gamma}_a, 0, 0)$, $\overline{S}_p(0, \overline{\gamma}_p, 0)$ and $\overline{S}_n(0, 0, \overline{\gamma}_n)$. 217

A.4 Second-order estimates (SOE) for the effective response of a fiber-reinforced elastomer with incompressible Gent phases under the three different modes of shear. The results are shown as a function of the corresponding amount of shear $\overline{\gamma}_a$,$\overline{\gamma}_p$ and $\overline{\gamma}_n$. (*a*) The energies $\widehat{\Psi}(\overline{\gamma}_a, 0, 0)$, $\widehat{\Psi}(0, \overline{\gamma}_p, 0)$ and $\widehat{\Psi}(0, 0, \overline{\gamma}_n)$, normalized by $\mu^{(1)}$. (*b*) The corresponding (non-zero) normalized stresses $\overline{S}_a(\overline{\gamma}_a, 0, 0)$, $\overline{S}_p(0, \overline{\gamma}_p, 0)$ and $\overline{S}_n(0, 0, \overline{\gamma}_n)$. 218

A.5 (a) SOE predictions for the macroscopic stresses $\overline{S}_p(0,\overline{\gamma}_p,0)$ and $\overline{S}_n(0,0,\overline{\gamma}_n)$ of fiber-reinforced elastomers made out of an incompressible Gent matrix and Neo-Hookean fibers, with various values of $\mu^{(2)}$, as functions of the amounts of shear $\overline{\gamma}_p$ and $\overline{\gamma}_n$, respectively. (b) SOE predictions for the lock-up limits $\overline{\gamma}_a^{lock}$, $\overline{\gamma}_p^{lock}$ and $\overline{\gamma}_n^{lock}$ of axisymmetric, in-plane and antiplane shear loadings, respectively—applied to composites with incompressible Gent constituents—as functions of the lock-up parameter of the fibers, $J_m^{(2)}$, for various values of c_0 and $J_m^{(1)} = 30$. 219

A.6 (a) Combined loading of the composite considered in Fig. A.3. The predictions of the SOE for the stresses $\sqrt{3}\,\overline{S}_a(\overline{\gamma}_a,\overline{\gamma}_p,\overline{\gamma}_n)$, $\sqrt{3}\,\overline{S}_p(\overline{\gamma}_a,\overline{\gamma}_p,\overline{\gamma}_n)$ and $\sqrt{3}\,\overline{S}_n(\overline{\gamma}_a,\overline{\gamma}_p,\overline{\gamma}_n)$, normalized by $\mu^{(1)}$, are plotted as functions of the loading parameter $\overline{\gamma}_e$. (b) Combined loading of a fiber-reinforced elastomer with incompressible Gent phases. The normalized stresses $\overline{S}_a(\overline{\gamma}_a,\overline{\gamma}_p,\overline{\gamma}_n)$, $\overline{S}_p(\overline{\gamma}_a,\overline{\gamma}_p,\overline{\gamma}_n)$ and $\overline{S}_n(\overline{\gamma}_a,\overline{\gamma}_p,\overline{\gamma}_n)$, as predicted by the SOE and the Voigt upper bound (distinguished by a superscript "V"), are shown as functions of the loading parameter $\overline{\gamma}_e$. 220

A.7 (a) The predictions of the SOE, BHS and GPM models for the effective in-plane shear response of an elastomer reinforced with *randomly* distributed, rigid fibers are compared with corresponding experimental (Exp) results for *periodically* distributed fibers. The SOE makes use of an OLP model for the matrix. (b) The OLP and Neo-Hookean models, used to characterize the matrix material in part (a), are compared with corresponding experimental data for *uniaxial tension* ($\ell = \lambda - 1$, with λ being the tensile stretch) and *simple shear* ($\ell = \gamma$, with γ denoting the amount of shear) tests. 221

B.1 (a) Schematic of a fiber-reinforced composite in the undeformed configuration Ω_0, where the initial fiber direction is given by the unit vector $\mathbf{N}$. (b) Corresponding schematic of a laminate with lamination direction $\mathbf{N}$. The characteristic lengths of the macroscopic specimen, L, and of the fibers (or layers), d, are assumed to be well separated in the sense that $L \gg d$. 233

B.2 (a) Schematic of a fiber-reinforced material subjected to aligned axisymmetric shear. (b) Illustration of the critical pair of orthogonal vectors, $\mathbf{v}_{cr}$ and $\mathbf{u}_{cr}$, for which the overall response of the material loses strong ellipticity. 242

B.3 Onset of macroscopic instabilities in fiber-reinforced materials with Neo-Hookean matrix and fiber phases subjected to *aligned axisymmetric shear* (AXS) and *pure shear* (PS) loading conditions. The critical stretch $\overline{\lambda}_{cr}$ (a) for fiber-to-matrix contrasts $t = \mu^{(2)}/\mu^{(1)} = 20$, as a function of the volume fraction of fibers c_0, and (b) for $c_0 = 0.3$, as a function of t. The critical stress $\overline{S}_{cr}$, normalized by $\mu^{(1)}$, corresponding to (a) and (b) are shown in (c) and (d), respectively. These results are compared with the *approximate* result of Rosen (1965), and the *exact* result of Triantafyllidis and Maker (1985) for laminates (Lam) under aligned pure shear. 245

B.4 Onset of macroscopic instabilities in fiber-reinforced materials with Gent phases subjected to *aligned axisymmetric shear* deformations (B.23), as given by expression (B.24). Results are shown for fiber-to-matrix contrasts $t = \mu^{(2)}/\mu^{(1)} = 2, 5, 20$, and volume fraction of the fibers $c_0 = 0.2$. (a) The critical stretch $\overline{\lambda}_{cr}$ for a fixed value of the lock-up parameter of the matrix, $J_m^{(1)} = 100$, as a function of $J_m^{(2)}$. (b) The critical stretch $\overline{\lambda}_{cr}$ for a fixed value of $J_m^{(2)} = 100$, as a function of $J_m^{(1)}$. 246

B.5 Onset of macroscopic instabilities in fiber-reinforced materials with Neo-Hookean matrix and fiber phases subjected to *non-aligned* loadings: (a) *axisymmetric shear*, and (b) *pure shear*. The critical stretch $\overline{\lambda}_{cr}$ is shown for fiber-to-matrix contrasts $t = \mu^{(2)}/\mu^{(1)} = 2, 5, 20$, volume fraction of fibers $c_0 = 0.3$, as a function of the angle of fiber misalignment Θ. . . 252

B.6 Onset of macroscopic instabilities in fiber-reinforced materials subjected to *non-aligned* loadings. (a) Comparison of *pure shear* failure surfaces for a Neo-Hookean fiber-reinforced composite with Gent fiber-reinforced composites (right) and with a Neo-Hookean laminate (left). All material systems have $c_0 = 0.3$ and $t = 20$, while for materials with Gent phases results are shown for several values of J_m (10, 20, 30, 50). (b) The critical stretch $\overline{\gamma}_{cr}$ for Neo-Hookean matrix and fiber phases under *simple shear* loading, as a function of the fiber misalignment angle Θ, for $t = \mu^{(2)}/\mu^{(1)} = 2, 5, 20$, and $c_0 = 0.3$. 254

B.7 Comparison of the predictions for macroscopic instabilities under transverse uniaxial tensile (UT) loading for fiber-reinforced (with both Gent and Neo-Hookean phases) and laminates (with Neo-Hookean phases). The critical stress $\overline{S}_{cr}$, normalized by the shear modulus of the matrix phase $\mu^{(1)}$, for (a) fiber-to-matrix contrasts $t = \mu^{(2)}/\mu^{(1)} = 10, 50$, as a function of the volume fraction of fibers c_0, and for (b) $c_0 = 0.1, 0.3$, as a function of t. 260

B.8 Comparison of the predictions for macroscopic instabilities under transverse uniaxial tension (UT) for fiber-reinforced (with both Gent and Neo-Hookean phases) with the general analytical formula (B.1). The critical stretch $\overline{\lambda}_n^{cr}$ along the fiber direction for (a) fiber-to-matrix contrasts $t = \mu^{(2)}/\mu^{(1)} = 10, 50$, as a function of the volume fraction of fibers c_0, and for (b) $c_0 = 0.1, 0.3$, as a function of t. 261

Chapter 1

Introduction

Polymeric molecules, such as polyethylene, polypropylene, Nylon-6, etc., tend to form regular crystal structures by folding along a well-defined direction, called the chain axis **c**, when cooled from the molten state to room temperature. Interestingly, the cooling process in these materials, unlike metals, does never result in 100% crystallization and the remaining part of the polymer is found in a disordered or amorphous state. Hence, these materials are called semi-crystalline polymers. The volume fraction of the crystalline phase, also called "crystallinity", ranges from 10% to 90%. For example, the crystallinity of high-density polyethylene (HDPE) is about 70% while that of Nylon-6 is 40%. At room temperature, the amorphous phase is "soft" and exhibits primarily a rubbery elastic behavior, while the crystalline phase is "stiff" and, similar to metal single crystals, may undergo large plastic deformations which are crystallographic in nature and responsible for the high ductility of semi-crystalline polymers. It is important to remark that the crystalline phase is practically inextensible along the chain axis **c** and, therefore, it possesses only four independent slip-systems. Upon formation, the crystalline and amorphous regions in a semi-crystalline polymer are in intimate contact with each other, forming alternating lamellar layers whose thickness is of the order of nanometers. Typically, but not always, these lamellar morphologies radiate out from various center-points in the composite and extend for lengths of the order of micrometer, leading in this way to a special type of morphological structures called spherulites (see Fig. 1.1(b)). In other cases, the lamellar stacks form grains that are randomly oriented in space (see Fig. 1.1(a)). Finally, at the length-scale of structural applications, a semi-crystalline polymer consists of a large number of spherulites or grains with a granular morphology similar to that of metal polycrystals. Therefore, in the undeformed configuration, semi-crystalline polymers are macroscopically isotropic and they exhibit heterogeneity at two well-separated length-scales: the nanometer "layer" scale and the micrometer "grain" or "spherulite" scale.

Semi-crystalline polymers constitute the largest class of polymers used in structural applications. Examples include thin films, coatings, fibers and ribbons. Upon processing, these materials

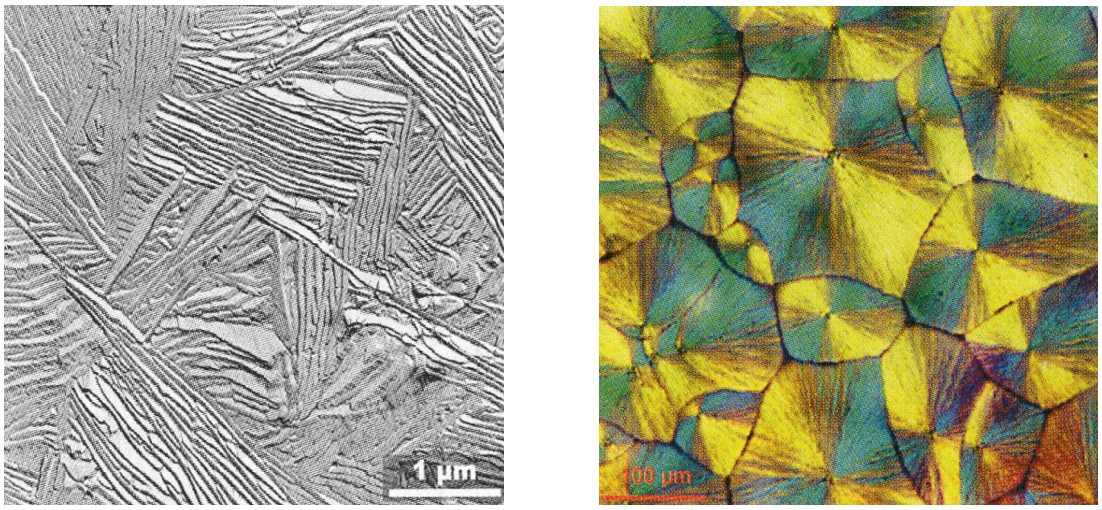

(a) (b)

Figure 1.1: (a) TEM micrograph of "granular" microstructure in polyethylene crystallized at 130 C for 27 days. (b) Optical micrograph of "spherulitic" microstructure in a typical semi-crystalline polymer (PPS). (Taken from Ref. [13].)

are often subjected to large plastic deformation leading to increasingly anisotropic mechanical properties. Over the past several decades, a large number of experimental studies has been conducted towards the understanding of the various deformation mechanisms involved, and the interplay between the evolution of the underlying sub-structure and the macroscopic response of semi-crystalline polymers (see, e.g., the review article by Lin and Argon [84]). Many of these studies focus on HDPE, primarily because of its relatively simple sub-structure and its high crystallinity (G'Sell and Jonas [46], Bartczak et al. [10], Galeski et al. [36], Bartczak et al. [9], Hiss et al. [54]). Based on these investigations, it has been well-established that the plastic deformation of semi-crystalline polymers involves, in general, three important types of texture (depending intrinsically on the applied loading conditions): (*i*) the crystallographic texture, resulting from the rotation of the lattice of the crystalline regions towards preferred orientations, (*ii*) the macromolecular texture, induced by the alignment of the polymer molecules in the amorphous regions along the direction of the local maximum stretch and (*iii*) the lamellar texture, due to the preferential orientation of the layered structures underlying the spherulites or grains. The evolution of the sub-structure at finite strains has, in turn, a crucial effect in the macroscopic response and overall stability of semi-crystalline polymers. In this regard, it worth mentioning that HDPE specimens have been reported (G'Sell and Jonas [46], Bartczak et al. [9], Hiss et al. [54]) to harden significantly when subjected to uniaxial tension but not under simple shear. Moreover, for the case of simple shear loadings on initially isotropic HDPE, Bartczak et al. [9] observed a gradual localization of plastic

deformation into shear bands (approximately) parallel to the shear direction, which eventually extends throughout the specimen leading to the complete destruction of the crystalline-amorphous lamellar morphology. As observed from texture evolution micrographs, this type of deformation is favored in lamellar stacks oriented perpendicular to the shear direction and occurs along the chain axis **c**. The development of macroscopic shear bands has been attributed to the rotation of the lamellar stacks towards a favorable orientation, as a result of the large applied plastic deformation. In more recent work, Krumova et al. [67] investigated the development of chevron morphologies in a variety of semi-crystalline polymers under tensile loadings and, based on additional results from the literature, they draw some interesting conclusions. Specifically, these authors observed that chevron folding is favorable for crystalline-amorphous lamellar stacks which are oriented perpendicular to the tensile loading direction and concluded that this deformation mechanism is very common in semi-crystalline polymers and quite similar to the chevron patterns observed in other material systems with lamellar morphologies, such as styrene-butadiene-styrene block copolymers (see, e.g., Cohen et al. [19]). Furthermore, based on the observation that chevron patterns are formed in some semi-crystalline polymers (e.g., high-density polyethylene) but not in others (e.g., low-density polyethylene), and similar observations for other material systems, Krumova et al. [67] concluded that the prerequisites for chevron patterns formation in composite materials, in general, are (*i*) the existence of stacks of parallel lamellar morphologies in the sub-structure of the composite and (*ii*) a sufficiently high heterogeneity contrast between the constituent phases.

Over the past few decades, several attempts—with increasing levels of sophistication—have been made to model the overall response and texture evolution in semi-crystalline polymers. Building on earlier work [10], Lee et al. [80] modeled the semi-crystalline polymer as a collection of a large number of randomly oriented lamellar "composite inclusions" consisting of a crystalline and an amorphous layer and, in order to deal with the lack of five independent slip-systems in the crystalline phase, they made use of a *hybrid* model combining Taylor and Sachs approximations—i.e., the uniform stress and uniform stain-rate model, respectively—to account for the distribution of the fields. In this work, it was further assumed that both phases exhibit a purely viscoplastic behavior, and a back-stress tensor (given by the Arruda-Boyce model [6]) was introduced in order to account for kinematic hardening in the amorphous phase. It should be emphasized that this later feature turns out to provide a somewhat artificial but efficient way to account for the elastic resistance of the amorphous phase, which is entropic in nature and it is due to the stretching of the macromolecules. Despite the fact that the Taylor and Sachs models are known to yield very stiff and very soft results, respectively, the Lee et al. [80] model managed to reproduce *qualitatively* the macroscopic stress-strain response of HDPE measured experimentally. An alternative approach, ignoring the contribution of the amorphous phase, has been proposed by Dahoun et al. [25], who modeled the crystalline layers as oblate ellipsoids and made use of the "tangent self-consistent"

[105, 77] approach. More recently, van Dommelen et al. [146] extended the "composite inclusion" model of Lee et al. [80] by incorporating finite elastic deformations for the amorphous and crystalline phase. This made it possible to account for the initial elastic modulus, yield stress and post-yield behavior, as well as to handle cyclic loadings. Furthermore, a numerical model was used by van Dommelen et al. [145] to investigate the mechanics of intra-spherulitic deformation of polyethylene. Recently, Nikolov et al. [110] proposed another constitutive model for semi-crystalline polymers assuming that the "spherulites" (or "grains") are made out of alternating layers of crystalline and amorphous viscoplastic materials, with the amorphous phase deforming only under shear strains parallel to the crystalline layer and characterized by a special form of the kinematic hardening model used by Lee et al. [80]. In the context of this model, the interactions among the "grains" are accounted for by means of a self-consistent approximation, which is known to be well-suited for granular systems. In general, the predictions of the Nikolov et al. [109] model for the overall response and texture evolution of HDPE were found to be more accurate than the corresponding predictions of the model of Lee et al. [80]. The most important disadvantage of these models is probably their failure to capture the qualitative features of the effective response of HDPE in certain cases, such as the dramatic softening observed under simple shear at large strains. It should be remarked that none of the above theoretical works dealt with the macroscopic stability of semi-crystalline polymers.

A common feature of all the aforementioned constitutive models is that they make use of approximate micromechanical models. A more proper treatment of the associated homogenization problem for the semi-crystalline polymer is expected to lead to improved estimates for its effective mechanical properties. This fact may be easily understood by noticing that the homogenization problem for the semi-crystalline polymer determines, in principle, the local stress and deformation fields developed in it under finite-strain loadings, which in turn determine completely the overall response, texture evolution and macroscopic stability of the material. Therefore, accounting properly for the distribution of these fields in the composite is of crucial importance.

In this thesis, we propose to model the viscoplastic response of semi-crystalline polymers, by accounting for the coupled effect of the crystalline and amorphous phases, as well as for fine substructural information at both the levels of the layered grains and of the grained polycrystal. Instead of making use of simplifying micromechanical approximations that are specific to these material systems, we carry out a more rigorous and complete homogenization analysis, which is able to better account for the internal stress and deformation fields and, consequently, for a more accurate representation of the sub-structure (in a suitable statistical sense) and its evolution. To this end, we propose a suitable generalization of the "generalized-secant second-order" (GSO) "linear comparison" method—introduced by Ponte Castañeda [118] and further developed by Ponte Castañeda and co-workers [64, 86] in the context of *single-scale* systems—to multi-scale viscoplastic

composites. This homogenization technique has been found to yield the most accurate estimates to date for single-scale viscoplastic composites [119, 65, 22] and polycrystals [86, 87], including texture evolution [88, 78]. In addition, we provide the corresponding generalizations of the earlier versions of this method—also proposed by Ponte Castañeda [114, 117]—known as the "secant" (SEC) and "tangent second-order" (TSO) method. At this point, it is relevant to remark that applications of the TSO method to two-scale thermoplastic elastomers with lamellar morphology have been already considered in the works of Lopez-Pamies et al. [98] and Racherla et al. [132], where it was shown that the TSO estimates are consistent with the development of macroscopic instabilities in these composites when such instabilities are expected to occur from physical experience.

Chapter 2 of this thesis provides a precise statement of the homogenization problem for the instantaneous effective behavior of a multi-scale viscoplastic composite and its (approximate) treatment by means of the SEC, TSO and GSO linear comparison procedures. Composites with arbitrary number of phases and general incompressible viscoplastic behavior of the constituents are considered. For convenience, the relevant analysis is presented for two-scale systems, but its generalization to n-scale composites is straightforward. More specifically, in this chapter we discuss in detail the sub-structural characterization of random two-scale composites of both granular and particulate type, and introduce the "separation of the length-scales hypothesis" characterizing the heterogeneity of the materials of interest at both the "micro-scale" and the "meso-scale" level. For example, in the case of the semi-crystalline polymer the micro-scale corresponds to the thickness of a typical crystalline or amorphous layer and the meso-scale corresponds to the diameter of a typical spherulite or grain. Based on these considerations, we present two equivalent variational formulations of the associated homogenization problem linking the effective constitutive behavior of a two-scale viscoplastic composite to the local material behavior of the phases and the underlying sub-structure. The first formulation, referred to as the "direct approach", is a one-step procedure—analogous to the corresponding variational problem for a single-scale system—requiring the determination of the local fields in the two-scale composite. The second formulation, referred to as the "sequential approach", is a two-step procedure which—by taking advantage of the separation of the length-scales hypothesis for the meso-scale heterogeneous-phases (e.g., the grains in the case of a semi-crystalline polymer)—"decomposes" the homogenization problem for a two-scale composite into a sequence of corresponding problems for single-scale composites. Finally, the homogenization problem, as characterized by means of the aforementioned variational statements, is treated approximately by means of the SEC, TSO and GSO procedures. These methods are first presented in full detail in the context of single-scale composites and then generalized to two-scale systems.

In chapter 3, with the objective of developing some insight on the general estimates proposed

in chapter 2, we apply the SEC, TSO and GSO methods to simple material systems. Two-scale composite systems of both the particulate and granular type are considered. Each material is taken to be made out of a viscoplastic isotropic phase and a rigid phase. The associated estimates for the corresponding single-scale composites are also discussed. The main objective of these applications is to compare the estimates based on the direct variational approach with the corresponding estimates based on the sequential variational approach, as well as to highlight the differences in the effective behavior of a two-scale composite and a corresponding single-scale composite. In this connection, it is remarked that although the direct and sequential variational formulations constitute two equivalent statements of the associated homogenization problem, the corresponding estimates obtained from these formulations—due to the approximations involved—may differ from each other. The direct and sequential estimates generated by means of the SEC method are found to be exactly identical. In addition, the results of this chapter indicate that, in general, both the TSO and the GSO estimates of the direct type are in very good agreement with the corresponding estimates of the sequential type for all values of the nonlinearity parameter and for any concentration of the rigid phase, as they should. In turn, this observation provides credence to these estimates and further encourages the application of the more general methods of chapter 2 to two-scale composites with more complicated sub-structures.

In chapter 4 of this thesis, by means of the variational procedures of chapter 2, we develop a constitutive model for the finite-strain macroscopic response and texture evolution in semi-crystalline polymers. Similar to the work of Lee et al. [80], both the amorphous and the crystalline phase in these composites are assumed to be viscoplastic materials, while the effect of finite elastic strains in the amorphous phase is also taken into account through a back-stress model. However, in our approach we account for fine sub-structural information at both levels of the layered grains and the grained polycrystal, as detailed above. Furthermore, making use of standard kinematical arguments, in this chapter we also develop constitutive equations for the evolution of the underlying sub-structure in the semi-crystalline polymer. This, in turn, allows consideration of finite-strain loading processes. The predictions of this model both for the macroscopic response and texture evolution in high-density polyethylene under uniaxial compression, simple shear and uniaxial tension loading histories are discussed in full detail. In each case, these estimates are compared with relevant experimental results and the corresponding predictions of the models of Lee et al. [80] and Nikolov et al. [110]. It is found that the predictions of the present model are in a good agreement with the experimental results for all types of loadings considered and that they improve over the predictions of the earlier models.

In chapter 5, the GSO method of chapter 2 is specialized to two-scale polycrystals with granular meso-structures and underlying lamellar micro-structures. This result is, in turn, used to study the macroscopic instantaneous response of a textured polycrystals with γ-TiAl-based polysynthetically

twinned grains. The lamellar grains in this material are modeled as stacks of matrix-twin pairs of crystals. Both the matrix and the twin phase are made out of the same γ-TiAl tetragonal lattice structure, oriented differently in the two phases (see Lebensohn et al. [79]). These materials are obtained by appropriate heat treatments or after casting, and are often highly anisotropic due to the preferential orientation of the lamellar structures underlying the grains. The predictions of this model are compared with available experimental data as well as with the corresponding predictions of the model of Lebensohn [73]. Furthermore, constitutive equations for the evolution of the sub-structure in the two-scale polycrystals of interest are also developed in this chapter. Making use of this framework, we compute the textures developed in an initially un-textured $(\alpha + \beta)$ Ti alloy under rolling conditions. Each grain in this material has a lamellar structure of alternating α and β phase, with phase α corresponding to an *hcp* single-crystal and phase β corresponding to a *bcc* single-crystal. The phases α and β are characterized by special crystallographic and morphological correlations (see Lebensohn and Canova [74]). It is remarked that *single-scale polycrystals* made out of single-crystal grains, each of which is constituted either by α or by β phase, may also be constructed. It has been experimentally observed (Dunst et al. [31]) that rolling of initially un-textured *two-scale* Ti alloy polycrystals at sufficiently large plastic strains results in the development of a bi-modal texture of the basal plane normals of the *hcp* phase, with one of its components located around the normal and the other pointing towards the transverse direction. The interesting point here is that, when specimens of initially un-textured *single-scale* Ti alloy polycrystals are subjected to the same rolling conditions only the texture component of the basal plane normals located around the normal direction is observed. Hence, these two problems constitute especially well-suited tests for the predictive capabilities of the general theory proposed in chapter 2. It is found that the predictions of the GSO method for both problems are consistent with the corresponding experimental results.

Finally, it is remarked that in the course of this dissertation the author has also been involved in a research project—conducted in collaboration with Dr. Oscar Lopez-Pamies and Dr. Pedro Ponte Castañeda—on the overall constitutive behavior and macroscopic failure of incompressible fiber-reinforced elastomer with general hyperelastic phases. This work resulted in two corresponding publications, which are attached in this thesis as appendixes A and B, respectively.

List of publications resulting from this dissertation work

1. Agoras, M., Lopez-Pamies, O., Pedro Castañeda, P., 2009. A general hyperelastic model for incompressible fiber-reinforced elastomers. *Journal of the Mechanics and Physics of Solids* 57, 268–286.

2. Agoras, M., Lopez-Pamies, O., Pedro Castañeda, P., 2009. Onset of macroscopic instabilities in fiber-reinforced elastomers at finite strain. *Journal of the Mechanics and Physics of Solids* 57, 1828–1850.

Chapter 2

Theory

In this chapter, we develop *general* variational procedures for the *approximate* determination of the effective constitutive behavior of *multi-scale* composites with *random* sub-structures. This work generalizes appropriately the "linear comparison composite" methods introduced by Ponte Castañeda [114, 117, 118] and further developed by Ponte Castañeda and co-workers ([64, 86]) in the context of corresponding *single-scale* composite systems. Bounds and estimates for multi-scale *granular* and *particulate* systems with *incompressible*, *viscoplastic* constituents and arbitrary number of phases are discussed in detail. The general results of this chapter are intended to provide the basis for the development of constitutive models for the instantaneous response of semi-crystalline polymers and metal polycrystals, which are of special interest in this work and are presented in subsequent chapters. For simplicity, the general methods of this chapter are presented in the context of *two-scale* composites. It is remarked, however, that the extension of these methods to n-scale composites is straightforward.

For the purposes of this work, a composite exhibiting heterogeneity at two well-separated length-scales is a "*two-scale*" composite. The smaller length-scale is referred to as the "*micro-scale*" and the larger as the "*meso-scale*". The term "*macro-scale*" is preserved for the length-scale of a "representative volume" (to be defined further below) of the two-scale composite, and it is assumed to be much larger than the meso-scale. A "*single-scale*" composite is similarly defined as a composite exhibiting heterogeneity at only one length-scale. For example, a polycrystal is a single-scale composite, while a granular system made out of grains which are themselves (different) polycrystals is a two-scale composite. At the micro-scale level a two-scale system is composed of "*homogeneous-phases*" or simply "*phases*", while at the meso-scale level it is made out of "*composite-phases*" (e.g., in the previous example, the polycrystals are composite-phases, while the single-crystals underlying a polycrystal are homogeneous-phases). A two-scale composite system is taken to be made out of an arbitrary number N of different composite-phases, and each composite-phase r, with $r = 1, ..., N$, is assumed to be made out of a number $N^{(r)}$ of different

homogeneous-phases. The representative volume of the two-scale composite is denoted by Ω, while the part of Ω occupied by composite-phase r is denoted by $\Omega^{(r)}$ and the part of Ω occupied by the homogeneous-phase (r,p), with $p = 1, ..., N^{(r)}$, is denoted by $\Omega^{(r,p)}$. The notation $\langle\cdot\rangle$, $\langle\cdot\rangle^{(r)}$ and $\langle\cdot\rangle^{(r,p)}$ is used to denote the volume-average of a field over Ω, $\Omega^{(r)}$ and $\Omega^{(r,p)}$, respectively.

The material of this chapter is organized as follows. Section 2.1 discusses in detail the sub-structural characterization of random single-scale and two-scale granular composites, while section 2.2 provides the corresponding discussion for random single-scale and two-scale particulate composites. Section 2.3 defines the viscoplastic behavior of the constituents for the composite materials of interest in this work. Based on the definitions introduced in the first three sections, section 2.4 presents two alternative variational formulations of the homogenization problem linking the effective constitutive behavior of a two-scale viscoplastic composite to the local material behavior and the sub-structure. Section 2.5 introduces in full detail the "secant", "tangent" and "generalized-secant" linear comparison composite methods in the context of single-scale composites. This facilitates the discussions of sections 2.6, 2.7 and 2.8, where the extension of the corresponding methods to two-scale composites is presented. Finally, section 2.9 provides some concluding remarks on the main results of this chapter.

2.1 Sub-structural characterization of granular composites

The homogenization problem for a heterogeneous body (e.g., a structural element) is defined over a region of the body called the "representative volume element" (RVE). Quite generally, the RVE can be any part of the body, provided that its characteristic length-scale is much smaller than the dimensions of the body and the scale of variation of the loading conditions to which the body may be subjected in a given application. These requirements reflect the practical purpose of homogenization, which consists in replacing the sharply varying properties of the body over small regions around points $\mathbf{x}$ with the smoothly varying average (or effective) properties over neighborhoods (RVEs) of $\mathbf{x}$ that are larger, but still small enough compared to the size of the body. In preparation for the precise statement of the associated homogenization problem, this section deals with the formal characterization of the random sub-structure underlying an RVE of a two-scale granular composite material. The corresponding discussion for the case of a two-scale particulate composite is provided in the following section. The discussion on the sub-structural characterization of a two-scale composite builds on the relevant discussion for a corresponding single-scale composite.

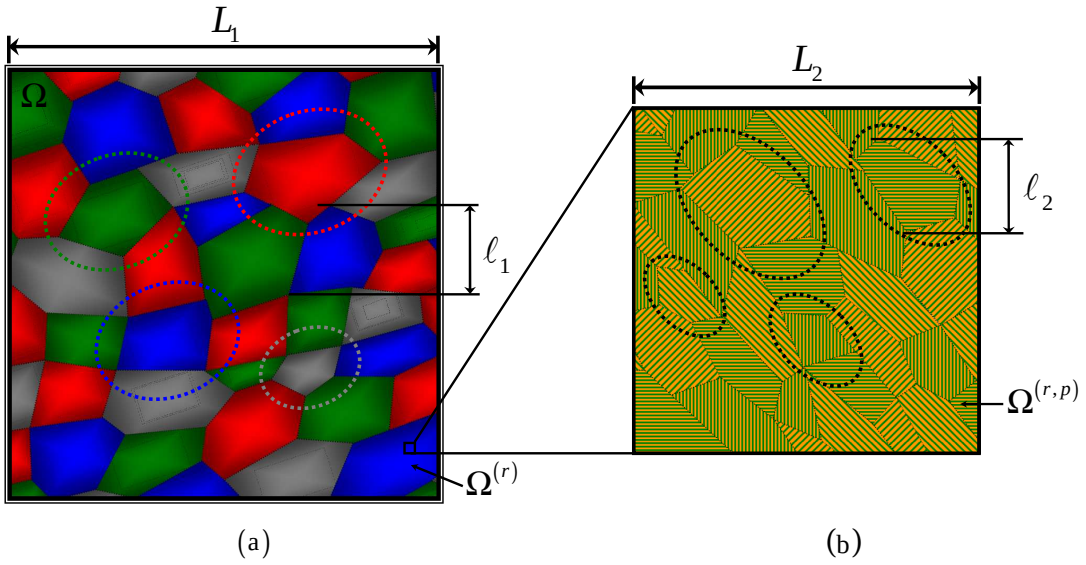

Figure 2.1: A two-scale granular composite with random distributions of ellipsoidal symmetry (dotted ellipses). (*a*) Macroscopic RVE Ω: composite-grain families (distinguished by color). (*b*) Mesoscopic RVE of the composite-grain family r: single-crystal orientations.

2.1.1 Single-scale systems

Following the works of Willis [150, 152], in this subsection we deal with the sub-structural characterization of a random, *single-scale*, *granular* composite. To this end, we consider the material system of Fig. 2.1(a), which is made out of different grains distributed randomly over the RVE Ω. For the purposes of the current discussion, each grain of Fig. 2.1(a) is assumed to be *homogeneous*, so that the local material properties vary from grain-to-grain but not within the individual grains (i.e., we ignore part (b) of this figure). The term *family* (or *phase*) is used here for the set of all grains exhibiting identical constitutive behavior (i.e., all grains shown in Fig. 2.1(a) with a specific color). For the purpose of generality, the RVE Ω of Fig. 2.1(a) is taken to be made out of an arbitrary number N of grain-families and each grain-family r ($r = 1, ..., N$) is assumed to occupy the subregion $\Omega^{(r)}$ of Ω. Formally, the sub-structure of the *specific* composite under consideration could be prescribed through the characteristic functions

$$\chi^{(r)}(\mathbf{x}) = \begin{cases} 1, & \text{if } \mathbf{x} \in \Omega^{(r)} \\ 0, & \text{otherwise} \end{cases} . \tag{2.1}$$

In practice, however, for a random composite it is neither possible nor useful to know the characteristic functions $\chi^{(r)}$, as defined by (2.1), exactly. This point will become more evident in the discussion that follows. We note in passing that in the case of a periodic composite it is conceivable

for such information to be available, since it would only require knowledge of these functions over appropriately defined unit cells.

The notion of a *random* composite refers to a member of a sample space S with a specific realization of the sub-structure (such as the granular system of Fig. 2.1(a)), labeled α for short, which is associated with a probability density $p(\alpha)$ defined over S. Therefore, the characteristic functions $\chi^{(r)}$, as defined by (2.1), for a random system depend also on α. The relevant sub-structural information for such systems is naturally available in terms of the associated n-point probability functions. The one-point probability $p^{(r)}(\mathbf{x})$ of finding a grain of type r at point $\mathbf{x}$ is defined as the ensemble average

$$p^{(r)}(\mathbf{x}) = \int_S \chi^{(r)}(\mathbf{x}, \alpha) p(\alpha) d\alpha. \tag{2.2}$$

The two-point probability $p^{(rs)}(\mathbf{x}, \mathbf{x}')$ of finding simultaneously a grain of type r at $\mathbf{x}$ and a grain of type s at $\mathbf{x}'$ is given by

$$p^{(rs)}(\mathbf{x}, \mathbf{x}') = \int_S \chi^{(r)}(\mathbf{x}, \alpha) \chi^{(s)}(\mathbf{x}', \alpha) p(\alpha) d\alpha. \tag{2.3}$$

Higher-point probabilities are defined similarly. We emphasize that the sub-structural characterization given by expressions such as (2.2) and (2.3) is valid for random single-scale composites of any type. For granular systems, in particular, such a description is well-suited since it allows consideration of multi-point statistical information for the positions of the grains and at the same time requires no specific grain-shape commitment.

At this point it is relevant to introduce the "*separation of the length-scales hypothesis*", which is of fundamental importance in homogenization theory. Referring to Fig. 2.1(a), there are two important length-scales that are associated with the RVE Ω: (i) the macro-scale L_1, which is characteristic of the size of Ω and (ii) the length-scale ℓ_1, characterizing the heterogeneity (i.e., the size of a typical grain). The separation of the length-scales hypothesis states that

$$\ell_1 << L_1. \tag{2.4}$$

The RVE Ω of Fig. 2.1(a) is assumed to be *statistically uniform*, i.e., the n-point probability functions are invariant under translations. This implies that the one-point probabilities $p^{(r)}(\mathbf{x})$ are constants, the two-point probabilities $p^{(rs)}(\mathbf{x}, \mathbf{x}')$ are functions of $(\mathbf{x} - \mathbf{x}')$, etc. Although, in general, it is easy to think of heterogeneous systems (e.g., a periodic composite) in which these conditions fail, under the separation of the length-scales hypothesis (2.4) it is reasonable to expect that the random system of Fig. 2.1(a) is statistically uniform, except in some "thin layer" along its boundary. Furthermore, we will make use of the *ergodic* assumption that the configurations in neighborhoods centered at a given point $\mathbf{x}$ in the sample occur with the same frequency as they occur in neighborhoods centered at various points in a single realization. This allows the

replacement of ensemble averages with the corresponding volume averages over the RVE Ω. For example, expressions (2.2) and (2.3) may be respectively replaced by

$$p^{(r)}(\mathbf{x}) = \frac{1}{|\Omega|}\int_{\Omega}\chi^{(r)}(\mathbf{x}'')d\mathbf{x}'' = \frac{|\Omega^{(r)}|}{|\Omega|} \equiv c^{(r)}, \tag{2.5}$$

where $c^{(r)}$ denotes the volume fraction of the grain-family r, and

$$p^{(rs)}(\mathbf{x}-\mathbf{x}') = \frac{1}{|\Omega|}\int_{\Omega}\chi^{(r)}(\mathbf{x}+\mathbf{x}'')\chi^{(s)}(\mathbf{x}'+\mathbf{x}'')d\mathbf{x}''. \tag{2.6}$$

In addition, it will be assumed that the granular composite under consideration possesses *no long-range order*, which implies that

$$p^{(rs)}(\mathbf{x}-\mathbf{x}') \sim p^{(r)}(\mathbf{x})p^{(s)}(\mathbf{x}'), \tag{2.7}$$

for large values of $|\mathbf{x}-\mathbf{x}'|$. The meaning of this assumption is that the expectations of finding a grain of the type r at point $\mathbf{x}$ and a grain of the type s at point $\mathbf{x}'$ are statistically independent when $\mathbf{x}$ and $\mathbf{x}'$ are far apart. Notice that the separation of the length-scales hypothesis (2.4) is of crucial importance for condition (2.7) as well.

For simplicity, in this work we will restrict attention to one- and two-point probability functions. Furthermore, we will make use of the "*ellipsoidal symmetry*" hypothesis for the two-point probabilities (due to Willis [150]), i.e., we will assume that $p^{(rs)}$ depend on $(\mathbf{x}-\mathbf{x}')$ only through the combination $|\mathbf{Z}_d^{(rs)}(\mathbf{x}-\mathbf{x}')|$, where $\mathbf{Z}_d^{(rs)}$ are constant, symmetric, positive definite, second-order tensors. Note that, due to the property $p^{(rs)}(\mathbf{z}) = p^{(sr)}(-\mathbf{z})$ deduced from (2.6), the tensors $\mathbf{Z}_d^{(rs)}$ posses the symmetry property $\mathbf{Z}_d^{(rs)} = \mathbf{Z}_d^{(sr)}$. The special case $\mathbf{Z}_d^{(rs)} = \mathbf{I}$ corresponds to the well-known "*statistical isotropy*" assumption, i.e., the two-point probabilities are orientation independent. More generally, the tensors $\mathbf{Z}_d^{(rs)}$ define the following ellipsoids centered at $\mathbf{x}_C$

$$\Omega_d^{(rs)} = \{\mathbf{x} | (\mathbf{x}-\mathbf{x}_C)\cdot\mathbf{Z}_d^{(rs)}(\mathbf{x}-\mathbf{x}_C) \leq 1\}, \tag{2.8}$$

which are characteristic for the distribution of the grains in the RVE Ω. Finally, it is remarked that in this work we will restrict consideration to granular systems such that $\mathbf{Z}_d^{(rs)} \equiv \mathbf{Z}$ for all pairs (rs), with $r, s = 1, ..., N$. This assumption is indicated in Fig. 2.1(a) by the doted ellipses (since only a cross section of the material is shown), which are shown to have the same shape and orientation for all grains.

2.1.2 Two-scale systems

Next, we turn our attention on the sub-structural characterization of the random, *two-scale*, *granular* composite of Fig. 2.1. Towards this end, we make use of the work of Smyshlyaev and Willis [136] on martensitic polycrystals along with the development of the previous subsection.

Recall that in the context of the discussion of the previous subsection for single-scale granular systems it was assumed that the grains of Fig. 2.1(a) are homogeneous. Here, we remove this restriction and each grain of Fig. 2.1(a) is taken to be a polycrystal, as shown in Fig. 2.1(b). Hence, in the present context, the grains of Fig. 2.1(a) are referred to as composite-grains and, similarly, the single-crystals of Fig. 2.1(b) are referred to as homogeneous-grains. In general, different composite-grains are assumed to be different polycrystals. The term *composite-grain-family* (or *composite-phase*) is used for the set of all composite-grains that are made out of the same polycrystal (i.e., all grains shown in Fig. 2.1(a) with a specific color). In analogy, the term *homogeneous-grain-family* (or *homogeneous-phase*) refers to the set of all single-crystals of a given orientation (Fig. 2.1(b)). The sub-structures of Figs. 2.1(a) and 2.1(b) are respectively referred to as the *meso-structure* and *micro-structure* of the two-scale composite. Similarly, the terms *meso-scale* ℓ_1 and *micro-scale* ℓ_2 are used respectively for the characteristic length-scale of the size of a typical composite-grain (Fig. 2.1(a)) and a typical homogeneous-grain (Fig. 2.1(b)), while the term *macro-scale* L_1 is used to characterize the size of the RVE Ω of the two-scale medium. The RVE Ω of Fig. 2.1 is taken to be made out of an arbitrary number N of composite-grain-families occupying subregions $\Omega^{(r)}$, with $r = 1, ..., N$, of Ω, and each composite-grain-family r is assumed to consist of a large number $N^{(r)}$ of single-crystal orientations occupying subregions $\Omega^{(r,p)}$, with $p = 1, ..., N^{(r)}$, of Ω.

Towards the definition of the sub-structure of the two-scale granular composite of Fig. 2.1, we consider the following characteristic functions associated with the homogeneous-phases (r, p), with $r = 1, ..., N$ and $p = 1, ..., N^{(r)}$,

$$\tilde{\chi}^{(r,p)}(\mathbf{x}) = \begin{cases} 1, & \text{if } \mathbf{x} \in \Omega^{(r,p)} \\ 0, & \text{otherwise} \end{cases} , \tag{2.9}$$

which are required to be compatible with the corresponding composite-phase functions $\chi^{(r)}$, given by (2.1), i.e.,

$$\sum_{p=1}^{N^{(r)}} \tilde{\chi}^{(r,p)}(\mathbf{x}) = \chi^{(r)}(\mathbf{x}). \tag{2.10}$$

The functions $\tilde{\chi}^{(r,p)}$, as defined by (2.9) along with the constraints (2.10), account both for the heterogeneity at the micro-scale ℓ_2, i.e., at the level of the homogeneous-grains (Fig. 2.1(b)), and the heterogeneity at the meso-scale ℓ_1, i.e., at the level of the composite-grains (Fig. 2.1(a)), and, therefore, fully characterize the sub-structure underlying the *specific* two-scale system of Fig. 2.1. As implicitly suggested from the discussion of the previous subsection, our intention in this work is to account for the functions $\chi^{(r)}$ and $\tilde{\chi}^{(r,p)}$ only through the associated one- and two-point probabilities. The one-point probability function $\tilde{p}^{(r,p)}(\mathbf{x})$ associated with $\tilde{\chi}^{(r,p)}$, i.e., the

expectation that $\tilde{\chi}^{(r,p)}(\mathbf{x},\alpha)=1$, is defined by

$$\tilde{p}^{(r,p)}(\mathbf{x})=\int_S \tilde{\chi}^{(r,p)}(\mathbf{x},\alpha)p(\alpha)d\alpha, \tag{2.11}$$

and the two-point probability $\tilde{p}^{(r,p;s,q)}(\mathbf{x},\mathbf{x}')$, i.e., the expectation that $\tilde{\chi}^{(r,p)}(\mathbf{x},\alpha)\tilde{\chi}^{(s,q)}(\mathbf{x}',\alpha)=1$, is similarly defined by

$$\tilde{p}^{(r,p;s,q)}(\mathbf{x},\mathbf{x}')=\int_S \tilde{\chi}^{(r,p)}(\mathbf{x},\alpha)\tilde{\chi}^{(s,q)}(\mathbf{x}',\alpha)p(\alpha)d\alpha. \tag{2.12}$$

The compatibility requirement (2.10) for the functions $\tilde{\chi}^{(r,p)}$ implies analogous restrictions on $\tilde{p}^{(r,p)}$ and $\tilde{p}^{(r,p;s,q)}$. For example, from (2.10) and (2.11) it follows that

$$\sum_{p=1}^{N^{(r)}} \tilde{p}^{(r,p)}(\mathbf{x})=p^{(r)}(\mathbf{x}), \tag{2.13}$$

while from (2.10) and (2.12) it can be seen that

$$\sum_{p=1}^{N^{(r)}}\sum_{q=1}^{N^{(s)}} \tilde{p}^{(r,p;s,q)}(\mathbf{x},\mathbf{x}')=p^{(rs)}(\mathbf{x},\mathbf{x}'), \tag{2.14}$$

where we recall that $p^{(r)}(\mathbf{x})$ and $p^{(rs)}(\mathbf{x},\mathbf{x}')$ denote respectively the one- and two-point correlation functions associated with $\chi^{(r)}(\mathbf{x})$, which have been already considered in the previous subsection. The two-point correlation functions $\tilde{p}^{(r,p;s,q)}$ defined in this way are very general to be of any practical use. Furthermore, given the constraints imposed to these functions because of (2.10), we do not see an obvious way in which simplifying assumptions, such as the ones used in the context of $p^{(rs)}$, could help in restricting the class of possible functions $\tilde{p}^{(r,p;s,q)}$. It is remarked that higher point statistics could be defined similarly.

In order to make further progress, we restrict our attention to composite systems that are consistent with the separation of the length-scales hypothesis (2.4), as well as with the corresponding hypothesis in the composite-grains

$$\ell_2 << L_2, \tag{2.15}$$

where we recall that the length-scale L_2 characterizes the size of the mesoscopic RVE in a typical composite-grain (see Fig. 2.1(b)), and we further assume that

$$L_2 << \ell_1. \tag{2.16}$$

In addition, we restrict our consideration to two-scale composites with micro-structures (Fig. 2.1(b)) that are *statistically independent* from the associated meso-structures (Fig. 2.1(a)). More specifically, we assume that the characteristic functions $\tilde{\chi}^{(r,p)}$ of a two-scale composite may be expressed in the form

$$\tilde{\chi}^{(r,p)}(\mathbf{x})=\chi^{(r)}(\mathbf{x})\chi^{(r,p)}(\mathbf{x}), \tag{2.17}$$

where, for a given $r = 1, ..., N$, we assume that the functions $\chi^{(r,p)}(\mathbf{x})$, defined over $\Omega^{(r)}$, exhibit *statistical uniformity*, *ergodicity* and *no long-range order* in the entire space, such that

$$\sum_{p=1}^{N^{(r)}} \chi^{(r,p)}(\mathbf{x}) = 1. \tag{2.18}$$

In other words, for any given composite-phase $r = 1, ..., N$, the set of functions $\chi^{(r,p)}$, with $p = 1, ..., N^{(r)}$, defines a single-scale composite material (i.e., the material of Fig. 2.1(b)) independently of the characteristic functions $\chi^{(r)}$ (defining the "single-scale" composite of Fig. 2.1(a)). Hence, relation (2.17) interprets the sub-structure $\tilde{\chi}^{(r,p)}$ of the two-scale composite of Fig. 2.1 as the "intersection" of the sub-structure $\chi^{(r)}$ of the "single-scale" composite of Fig. 2.1(a) with the sub-structures $\chi^{(r,p)}$ of the N different single-scale composites of Fig. 2.1(b).

Now, recalling that the characteristic functions $\chi^{(r,p)}$ have been assumed to be statistically uniform and ergodic, it makes sense to consider the *microscopic* probability functions $p^{(r,p)}(\mathbf{x})$ and $p^{(r,pq)}(\mathbf{x}, \mathbf{x}')$ defined as the expectations that $\chi^{(r,p)}(\mathbf{x}, \alpha) = 1$ and $\chi^{(r,p)}(\mathbf{x}, \alpha)\chi^{(r,q)}(\mathbf{x}', \alpha) = 1$, respectively. Note that, due to the ergodicity of $\chi^{(r,p)}$, the average of a quantity at a point $\mathbf{x}$ over the sample may be replaced by the corresponding average in a particular specimen over any neighborhood of $\mathbf{x}$ that is sufficiently large compared to the size of the heterogeneity (i.e., the size of a single-crystal). For the case of $\chi^{(r,p)}$, it is convenient to chose this neighborhood to be the entire volume $\Omega^{(r)}$ occupied by the composite-grain-phase r in the RVE Ω of the two-scale composite. Thus, the one-point probability functions $p^{(r,p)}$ reduce to

$$p^{(r,p)}(\mathbf{x}) = \frac{1}{|\Omega^{(r)}|}\int_{\Omega^{(r)}} \chi^{(r,p)}(\mathbf{x}')d\mathbf{x}' = \frac{|\Omega^{(r,p)}|}{|\Omega^{(r)}|} \equiv c^{(r,p)}, \tag{2.19}$$

where the single-crystal concentrations $c^{(r,p)}$ are such that $\sum_{p=1}^{N^{(r)}} c^{(r,p)} = 1$ for each $r = 1, ..., N$. The two-point probability functions $p^{(r,pq)}$ are given by

$$p^{(r,pq)}(\mathbf{x} - \mathbf{x}') = \frac{1}{|\Omega^{(r)}|}\int_{\Omega^{(r)}} \chi^{(r,p)}(\mathbf{x} + \mathbf{x}'')\chi^{(r,q)}(\mathbf{x} + \mathbf{x}'')d\mathbf{x}''. \tag{2.20}$$

For practical purposes, it is also important to assume that the two-point correlation functions $p^{(r,pq)}$ are characterized by ellipsoidal symmetry, so that $p^{(r,pq)}(\mathbf{x} - \mathbf{x}') = p^{(r,pq)}(|\mathbf{Z}_d^{(r,pq)}(\mathbf{x} - \mathbf{x}')|)$, where $\mathbf{Z}_d^{(r,pq)}$ are the associated shape tensors defining the following microscopic distributional ellipsoids (centered at $\mathbf{x}_C$)

$$\Omega_d^{(r,pq)} = \{\mathbf{x} | (\mathbf{x} - \mathbf{x}_C) \cdot \mathbf{Z}_d^{(r,pq)}(\mathbf{x} - \mathbf{x}_C) \leq 1\}. \tag{2.21}$$

Furthermore, in the applications of this work we will only consider composites for which $\mathbf{Z}_d^{(r,pq)} \equiv \mathbf{Z}_d^{(r)}$ for all pairs (pq), with $p, q = 1, ..., N^{(r)}$, but for different values of r the tensors $\mathbf{Z}_d^{(r)}$ will be taken to be different, in general.

Based on the preceding considerations, we are now in a position to simplify further the probability functions $\tilde{p}^{(r,p)}$ and $\tilde{p}^{(r,p;s,q)}$ associated with the two-scale characteristic functions $\tilde{\chi}^{(r,p)}$ defined by (2.9). The micro-meso-structural statistical independence assumed for $\tilde{\chi}^{(r,p)}$ in the context of (2.17) consists in the following two conditions: (i) for a fixed value of r, the functions $\chi^{(r)}$ and $\chi^{(r,p)}$ are mutually independent and (ii) for different values of r and s, the functions $\chi^{(r,p)}$ and $\chi^{(s,q)}$ are also mutually independent. Conditions (i) and (ii) imply that the probability functions $\tilde{p}^{(r,p)}$ and $\tilde{p}^{(r,p;s,q)}$ for these special types of sub-structures are respectively given by

$$\tilde{p}^{(r,p)} = p^{(r)} p^{(r,p)} \equiv c^{(r)} c^{(r,p)}, \tag{2.22}$$

and

$$\tilde{p}^{(r,p;s,q)}(\mathbf{z}) = p^{(rs)}(\mathbf{z}) \left[\delta_{rs} p^{(r,pq)}(\mathbf{z}) + (1 - \delta_{rs}) c^{(r,p)} c^{(s,q)} \right]. \tag{2.23}$$

The quantities $p^{(r)}$ and $p^{(rs)}$ in the above expressions correspond respectively to the one- and two-point correlation functions associated with $\chi^{(r)}$. Furthermore, the concentrations $p^{(r)} = c^{(r)}$ and $p^{(r,p)} = c^{(r,p)}$ are given by (2.5) and (2.19), respectively. In expression (2.23), $\delta_{rs} = 1$ if $r = s$ and 0 otherwise, and no summation is implied for the repeated indexes r and s.

In summary, the sub-structure of a random, two-scale granular composite—for the purposes of this work—is completely determined by means of the probability functions $\tilde{p}^{(r,p)}$ and $\tilde{p}^{(r,p;s,q)}$ given by (2.22) and (2.23), respectively. Expressions (2.22) and (2.23) relate the *two-scale* functions $\tilde{p}^{(r,p)}$ and $\tilde{p}^{(r,p;s,q)}$ with the corresponding *single-scale* microscopic, $p^{(r,p)}$ and $p^{(r,pq)}$, and mesoscopic, $p^{(r)}$ and $p^{(rs)}$, probability functions. The one-point probability functions $p^{(r,p)}$, given by (2.19), are identified with the volume fractions $c^{(r,p)}$ of the single-crystal orientations (r,p) in the polycrystal r, while the two-point probability functions $p^{(r,pq)}$ are given in terms of the associated shape tensor $\mathbf{Z}_d^{(r)}$, characterizing the distribution of the pairs of single-crystals (pq) in the polycrystal r. The corresponding mesoscopic probabilities $p^{(r)}$, $p^{(rs)}$ are obtained from the discussion of the previous subsection. In particular, assuming that the functions $\chi^{(r)}$ are statistically uniform, ergodic and with no long-range order, the one-point probabilities $p^{(r)}$ are given by (2.5) and correspond to the volume fractions $c^{(r)}$ of the composite-grains. Assuming, in addition, that the two-point probabilities $p^{(rs)}$ are characterized by ellipsoidal symmetry with the same features for all pairs of composite-grains, i.e., choosing the shape tensors $\mathbf{Z}_d^{(rs)} \equiv \mathbf{Z}_d$ for all pairs (rs), with $r, s = 1, ..., N$, in the definition (2.8) of the distributional ellipsoids $\Omega_d^{(rs)}$, the two-point correlations $p^{(rs)}$ reduce to a function of $|\mathbf{Z}_d(\mathbf{x} - \mathbf{x}')|$ only.

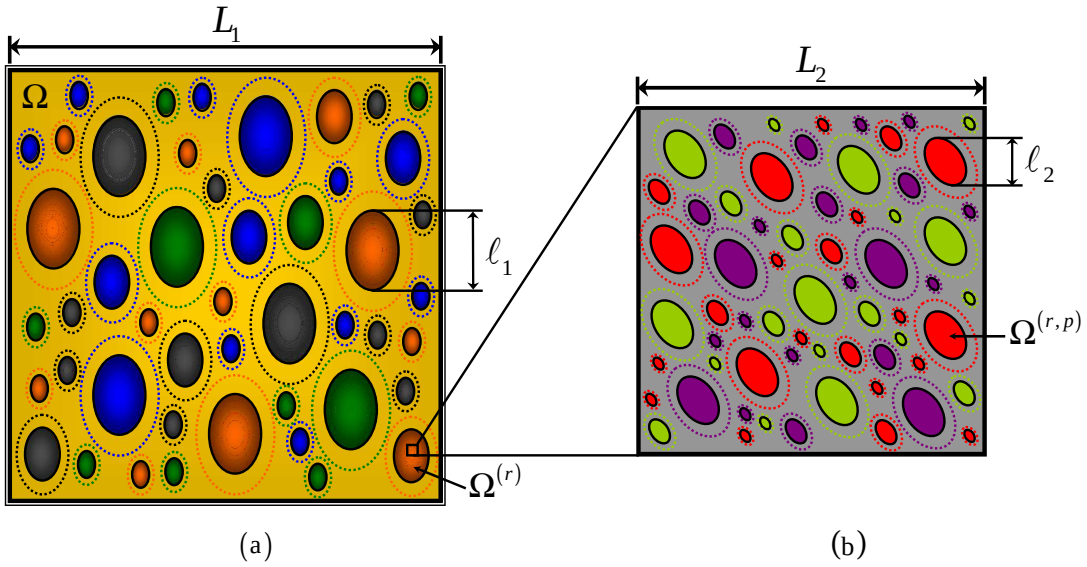

Figure 2.2: A two-scale particulate composite with random distributions of ellipsoidal symmetry (dotted ellipses). (*a*) Macroscopic RVE Ω: composite-inclusion families in a composite-matrix (distinguished by color). (*b*) Mesoscopic RVE of the composite-inclusion family r: homogeneous-inclusion families in a homogeneous-matrix.

2.2 Sub-structural characterization of particulate composites

2.2.1 Single-scale systems

In this subsection, following the work of Ponte Castañeda and Willis [126], we define the sub-structure underlying a random, *single-scale*, *particulate* composite. For definiteness, we consider the heterogeneous system of Fig. 2.2(a) consisting of particles distributed randomly in a well-defined matrix material. For the purposes of the present discussion, all constituents of Fig. 2.2(a) are taken to be *homogeneous* (i.e., we ignore part (b) of this figure). The term *family* (of particles) is used here for the set of all particles with a given constitutive behavior (i.e., particles shown in Fig. 2.2(a) with a specific color), while the term *phase* has a more general meaning in the sense that it may refer either to a family of inclusions or to the matrix material. For consistency with the notation used in the previous section for granular systems, the RVE of Fig. 2.2(a) is denoted by Ω and it is assumed to consist of N different phases. The label $r = 1$ is preserved for the matrix phase while the labels $r = 2, ..., N$ are used to indicate the inclusion phases, so that $\Omega^{(1)}$ denotes the subregion of Ω occupied by the matrix while $\Omega^{(r)}$, with $r = 2, ..., N$, is the subregion of Ω occupied by particles of the type r, with $r = 2, ..., N$, respectively. A convenient way to

fully characterize the sub-structure of the particulate composite of Fig. 2.2(a) is to prescribe the shape and orientation of the inclusions and, in addition, make use of the associated multi-point probability functions to account for the spatial arrangements of their centers. The precise manner in which this objective can be achieved is detailed next.

For the purpose of generality, inclusions belonging to different families are allowed to have different shapes and orientations. It is assumed, however, that family r, with $r = 2, ..., N$, consists of $n^{(r)}$ inclusions of the same shape, size and orientation, characterized by a reference domain $\Omega_i^{(r)}$, but they are taken to be centered at different points $\mathbf{x}_A$ $(A = 1, ..., n^{(r)})$ in each realization α in the sample space S. Thus, the characteristic function of the inclusion-phase r may be written as follows

$$\chi^{(r)}(\mathbf{x}, \alpha) = \sum_{A=1}^{n^{(r)}} \chi_i^{(r)}(\mathbf{x} - \mathbf{x}_A), \tag{2.24}$$

where the reference function $\chi_i^{(r)}$ is defined as $\chi_i^{(r)}(\mathbf{x}) = 1$ if $\mathbf{x} \in \Omega_i^{(r)}$ and $\chi_i^{(r)}(\mathbf{x}) = 0$ otherwise. Note that, although the points $\mathbf{x}_A$ depend on the specific realization α, the functions $\chi_i^{(r)}$ are completely determined once the reference volumes $\Omega_i^{(r)}$ are prescribed. Introducing the random density field $\varphi^{(r)}(\mathbf{z}, \alpha)$ associated with the random points $\mathbf{x}_A$ [137],

$$\varphi^{(r)}(\mathbf{z}, \alpha) = \sum_{A=1}^{n^{(r)}} \delta(\mathbf{z} - \mathbf{x}_A), \tag{2.25}$$

with δ denoting the delta function, the characteristic function of inclusion-phase r may be rewritten as

$$\chi^{(r)}(\mathbf{x}, \alpha) = \int_\Omega \left[\chi_i^{(r)}(\mathbf{x} - \mathbf{z})\varphi^{(r)}(\mathbf{z}, \alpha)\right] d\mathbf{z}. \tag{2.26}$$

The advantage in expressing $\chi^{(r)}$ by means of (2.26) instead of (2.24) is that the random density field $\varphi^{(r)}$ may be related to the associated multi-point probability functions through suitable ensemble averages, as follows

$$\int_S \varphi^{(r)}(\mathbf{x}, \alpha)p(\alpha)d\alpha = p^{(r)}(\mathbf{x}), \tag{2.27}$$

$$\int_S \varphi^{(r)}(\mathbf{x}, \alpha)\varphi^{(s)}(\mathbf{x}', \alpha)p(\alpha)d\alpha = \delta_{rs}p^{(r)}(\mathbf{x})\delta(\mathbf{x} - \mathbf{x}') + p^{(rs)}(\mathbf{x}, \mathbf{x}'), \tag{2.28}$$

etc., where $p^{(r)}$ and $p^{(rs)}$ denote respectively the one- and two-point probability functions for the centers of the particles, defined further below. Once again, it is remarked that in expression (2.28) $\delta_{rs} = 1$ if $r = s$ and 0 otherwise, and no summation is implied for the repeated index r in the first term of the right-hand-side of this relation. Finally, in the case of the particulate composite of Fig. 2.2(a) we will further assume that the associated reference domains $\Omega_i^{(r)}$ are ellipsoidal and they are characterized by means of the corresponding shape tensors $\mathbf{Z}_i^{(r)}$, so that

$$\Omega_i^{(r)} = \{\mathbf{x} | \mathbf{x} \cdot \mathbf{Z}_i^{(r)}\mathbf{x} \leq 1\}. \tag{2.29}$$

At this point, we emphasize that the random character of the composite material under consideration will be accounted for in this work only through the one- and two-point probability functions associated with the centers of the inclusions. In this regard, the discussion of subsection 2.1.1 on the sub-structural characterization of a single-scale granular composite applies here as well, with the only difference that quantities of subsection 2.1.1 referred to a grain-family r should be interpreted in the present context as quantities referred to an inclusion-family r. In particular, the separation of the length-scales hypothesis (2.4) is assumed to hold, where the macro-scale L_1 and the length-scale ℓ_1 characterize respectively the size of the RVE Ω and the size of a typical inclusion of Fig. 2.2(a). Furthermore, the sub-structure of the RVE of Fig. 2.2(a) is assumed to be statistically uniform, ergodic and to possess no-long-range order. Thus, for each $r = 2, ..., N$, the one-point probability $p^{(r)}(\mathbf{x})$, i.e., the expectation of finding an inclusion of type r centered at $\mathbf{x}$, is constant and equal to the volume fraction $c^{(r)}$ of the inclusion-phase r. Note that the concentration of the matrix phase is given by $c^{(1)} = 1 - \sum_{r=2}^{N} c^{(r)}$. Finally, for each pair (rs), with $r, s = 2, ..., N$, the two-point correlation function $p^{(rs)}(\mathbf{x} - \mathbf{x}')$, i.e., the expectation of finding an inclusion of type r centered at $\mathbf{x}$ and an inclusion of type s centered at $\mathbf{x}'$, is assumed to possess ellipsoidal symmetry, namely, $p^{(rs)}(\mathbf{x} - \mathbf{x}') = p^{(rs)}(|\mathbf{Z}_d^{(rs)}(\mathbf{x} - \mathbf{x}')|)$, where $\mathbf{Z}_d^{(rs)}$ are the relevant shape tensors defining by means of (2.8) the associated distributional ellipsoids $\Omega_d^{(rs)}$ for the centers of the inclusions.

Clearly, the tensors $\mathbf{Z}_i^{(r)}$, defining the shape and orientation of the inclusions, can be chosen independently for each inclusion-phase $r = 2, ..., N$. Moreover, the tensors $\mathbf{Z}_d^{(rs)}$, defining the two-point correlations $p^{(rs)}$ for the centers of pairs of inclusions (rs), may also be taken to be different for different pairs (rs), with $r, s = 2, ..., N$. In this work, however, we will only be interested in particulate composites such that $\mathbf{Z}_d^{(rs)} = \mathbf{Z}_i^{(r)} \equiv \mathbf{Z}$ for all inclusion-phases $r, s = 2, ..., N$.

2.2.2 Two-scale systems

The sub-structure underlying a random, *two-scale*, *particulate* composite can be easily characterized by a straightforward generalization of the discussion of the previous subsection for single-scale particulate systems, based on the development of subsection 2.1.2 for the definition of the sub-structure of a two-scale granular composite. For completeness, we present next the relevant discussion for the two-scale particulate system of Fig. 2.2.

The constituent phases of the RVE Ω of Fig. 2.2(a), which in the previous subsection were assumed to be homogeneous, are here taken to be single-scale particulate systems, as shown in Fig. 2.2(b). Hence, the matrix and inclusions of Fig. 2.2(a) are respectively referred to as composite-matrix and composite-inclusions. In general, each composite-inclusion of Fig. 2.2(a) is assumed to be made of a different single-scale particulate system, which is, in addition, different from the

single-scale particulate system constituting the material of the composite-matrix. A *composite-inclusion-family* is defined as the set of all composite-inclusions of Fig. 2.2(a) made out of the same single-scale system. The term *composite-phase* is used either for the composite-matrix material or for a composite-inclusion-family. The terms *homogeneous-inclusion-family* and *homogeneous-phase* refer to a single-scale particulate composite underlying a given composite-phase (Fig. 2.2(b)) and indicate the fact that the constituents of the family and phase, respectively, are homogeneous media. The RVE Ω is assumed to be made out of an arbitrary number N of composite-phases, with the composite-matrix, labeled by $r = 1$, occupying the subregion $\Omega^{(1)}$ of Ω and the composite-inclusion-family r, with $r = 2, ..., N$, occupying the subregion $\Omega^{(r)}$ of Ω. The composite-matrix consists of a number $(N^{(1)} - 1)$ of different homogeneous-inclusion-families, labeled by $(1, p)$ with $p = 2, ..., N^{(1)}$, which are embedded in a different homogeneous-matrix, labeled by $(1, 1)$, so that the homogeneous-inclusion-family $(1, p)$ occupies the subregion $\Omega^{(1,p)}$ of Ω and the homogeneous-matrix-phase $(1, 1)$ occupies the subregion $\Omega^{(1,1)}$ of Ω. In analogy, the composite-inclusion-family r, with $r = 2, ..., N$, is taken to be made out of a number $(N^{(r)} - 1)$ of different homogeneous-inclusion-families that are distributed in a different homogeneous-matrix material such that the homogeneous-inclusion-family (r, p), with $p = 2, ..., N^{(r)}$, occupies the subregion $\Omega^{(r,p)}$ of Ω and the homogeneous-matrix-phase $(r, 1)$ occupies the subregion $\Omega^{(r,1)}$ of Ω. For consistency with the terminology used in the case of the two-scale granular system of Fig. 2.1, the sub-structure of Figs. 2.2(a) and 2.2(b) are referred to respectively as the *meso-structure* and *micro-structure* of the two-scale particulate composite. Similarly, the *macro-scale* L_1, the *meso-scale* ℓ_1 and the *micro-scale* ℓ_2 denote the characteristic length-scales of the size of the RVE Ω, the size of a typical composite-inclusion (Fig. 2.2(a)) and the size of a typical homogeneous inclusion (Fig. 2.2(b)), respectively.

Following the formulation used in subsection 2.1.2 for the sub-structural characterization of a two-scale granular system, we assume that the characteristic function $\tilde{\chi}^{(r,p)}(\mathbf{x})$ of the two-scale particulate composite of Fig. 2.2 admits the decomposition (2.17) in terms of the associated mesoscopic $\chi^{(r)}(\mathbf{x})$ and microscopic $\chi^{(r,p)}(\mathbf{x})$ characteristic functions. More specifically, we assume that the length-scales ℓ_2, ℓ_1 and L_1 are well-separated, i.e., relations (2.4) and (2.15) hold, and that, for any fixed r, the function $\chi^{(r)}$ is statistically independent from the set of functions $\chi^{(r,p)}$ $(p = 1, ..., N^{(r)})$. Furthermore, the usual assumptions of statistical uniformity, ergodicity and no long-range order are being made for the macroscopic "single-scale" composite (Fig. 2.2(a)), defined by $\chi^{(r)}$, and each of the (N) mesoscopic single-scale composites (Fig. 2.2(b)), defined by $\chi^{(r,p)}$ (one for each $r = 1, ..., N$). These considerations, in turn, allow the independent treatment of the associated meso- and micro-structure, as outlined next.

As detailed in the context of the discussion for single-scale particulate systems (subsection

2.2.1), the meso-structure of the two-scale particulate composite of Fig. 2.2(a) may be conveniently prescribed in terms of the shape and orientation of the composite-inclusions along with the associated correlation functions for the spatial distribution of their centers. In particular, the characteristic function $\chi^{(r)}$ corresponding to the composite-inclusion-family r, with $r = 2, ..., N$, may be expressed in terms of an associated reference characteristic function $\chi_i^{(r)}$, defining the shape and orientation $\Omega_i^{(r)}$ of the composite-inclusions of type r, and a random density field $\varphi^{(r)}$, defining the random distribution of the centers of the composite-inclusions by means of the associated one- $p^{(r)}$ and two-point $p^{(rs)}$ $(r, s = 2, ..., N)$ probability functions (see relations (2.27) and (2.28)). The reference domains $\Omega_i^{(r)}$ will be taken in this work to have ellipsoidal shape, defined through the corresponding shape tensor $\mathbf{Z}_i^{(r)}$ by means of (2.29). The one-point probability $p^{(r)}$, with $r = 2, ..., N$, is given by (2.5) and corresponds to the volume fraction $c^{(r)}$ of the composite-inclusion-phase r. Recall, again, that the volume fraction of the composite-matrix is given by $c^{(1)} = 1 - \sum_{r=2}^{N} c^{(r)}$. We assume that the two-point probability $p^{(rs)}$, with $r, s = 2, ..., N$, is characterized by ellipsoidal symmetry which is prescribed through a corresponding shape tensor $\mathbf{Z}_d^{(rs)}$, defining a distributional ellipsoid $\Omega_d^{(rs)}$ by means of (2.8). The two-scale particulate composites to be considered in this work are such that $\mathbf{Z}_i^{(r)} = \mathbf{Z}_d^{(rs)} \equiv \mathbf{Z}$ for all $r, s = 2, ..., N$.

In a completely analogous manner—for each composite-phase $r = 1, ..., N$ (i.e., the composite-matrix or a given composite-inclusion)—the characteristic function $\chi^{(r,p)}$ corresponding to the homogeneous-inclusion-family (r, p), with $p = 2, ..., N^{(r)}$, may be expressed in terms of a reference characteristic function $\chi_i^{(r,p)}$, which defines a reference volume $\Omega_i^{(r,p)}$ characterizing the shape and the orientation of the homogeneous-inclusions of type (r, p), and a random density field $\varphi^{(r,p)}$, which is given in terms of the associated one- $p^{(r,p)}$ and two-point $p^{(r,pq)}$ $(p, q = 2, ..., N^{(r)})$ probability functions for the centers of the homogeneous-inclusions. The domain $\Omega_i^{(r,p)}$ is again assumed to be an ellipsoid defined by a shape tensor $\mathbf{Z}_i^{(r,p)}$. The function $p^{(r,p)}$, with $p = 2, ..., N^{(r)}$, is given by (2.19) and corresponds to the volume fraction $c^{(r,p)}$ of the homogeneous-inclusion-phase (r, p) in the composite-phase r. The volume fraction of the homogeneous-matrix in composite-phase r is given by $c^{(r,1)} = 1 - \sum_{p=2}^{N^{(r)}} c^{(r,p)}$. The two-point correlation functions $p^{(r,pq)}$ are assumed to possess ellipsoidal symmetry characterized by shape tensors $\mathbf{Z}_d^{(r,pq)}$. For any given $r = 1, ..., N$, these shape tensors will be taken in the sequel to be $\mathbf{Z}_i^{(r,p)} = \mathbf{Z}_d^{(r,pq)} \equiv \mathbf{Z}^{(r)}$ for all $p, q = 2, ..., N^{(r)}$.

Finally, the one- $\tilde{p}^{(r,p)}$ and two-point $\tilde{p}^{(r,p;s,q)}$ correlation functions of the two-scale particulate composite of Fig. 2.2 are given by the simple expressions (2.22) and (2.23), respectively, in terms of the corresponding mesoscopic, $p^{(r)}$ and $p^{(rs)}$, and microscopic , $p^{(r,p)}$ and $p^{(r,pq)}$, correlation functions, which are, in turn, obtained as discussed above. It should be remarked, however, that the two-point correlation functions $p^{(1s)}$, with $s = 1, ..., N$, which have not been specified in the above discussion but they enter the calculation of $\tilde{p}^{(r,p;s,q)}$ in expression (2.23), must be computed

from the following identities

$$\sum_{r=1}^{N} p^{(rs)}(\mathbf{x},\mathbf{x}') = p^{(s)}(\mathbf{x}) \Rightarrow p^{(1s)}(\mathbf{x},\mathbf{x}') = p^{(s)}(\mathbf{x}) - \sum_{r=2}^{N} p^{(rs)}(\mathbf{x},\mathbf{x}'). \tag{2.30}$$

2.3 Viscoplastic constitutive behavior

The two-scale composite materials of interest in this work consist of N distinct composite-phases (Figs. 2.1(a) and 2.2(a)), each of which is taken to be made out of $N^{(r)}$, with $r = 1, ..., N$, different homogeneous-phases (Figs. 2.1(b) and 2.2(b)). Each homogeneous-phase is assumed to exhibit viscoplastic constitutive behavior characterized by *convex* stress-potentials $u^{(r,p)}$, with $p = 1, ..., N^{(r)}$, such that the *local* constitutive relation between the deformation rate tensor $\mathbf{D}$ (the symmetric part of the velocity gradient) and Cauchy stress tensor $\boldsymbol{\sigma}$ of the two-scale composite is given by

$$\mathbf{D} = \frac{\partial u}{\partial \boldsymbol{\sigma}}(\mathbf{x},\boldsymbol{\sigma}), \quad u(\mathbf{x},\boldsymbol{\sigma}) = \sum_{r=1}^{N} \chi^{(r)}(\mathbf{x}) u^{(r)}(\mathbf{x},\boldsymbol{\sigma}), \quad u^{(r)}(\mathbf{x},\boldsymbol{\sigma}) = \sum_{p=1}^{N^{(r)}} \chi^{(r,p)}(\mathbf{x}) u^{(r,p)}(\boldsymbol{\sigma}). \tag{2.31}$$

Note that, the above constitutive relation can also be used to model deformation theory of plasticity, in which case $\mathbf{D}$ should be interpreted as the infinitesimal strain tensor. In this work, we will focus attention on composite systems with incompressible, isotropic and crystalline constituents.

In the case of composites with isotropic phases, the stress-potentials $u^{(r,p)}$ are taken to be of the form

$$u(\boldsymbol{\sigma}) = \psi(\sigma_e), \qquad \sigma_e = \sqrt{\frac{3}{2}\boldsymbol{\sigma}_d \cdot \boldsymbol{\sigma}_d}, \tag{2.32}$$

with σ_e denoting the equivalent stress, and $\boldsymbol{\sigma}_d$ is the deviatoric part of the stress tensor. An example of $(2.32)_1$ is the power-law potential

$$\psi(\sigma_e) = \frac{\epsilon_0 \sigma_0}{n+1} \left(\frac{\sigma_e}{\sigma_0}\right)^{n+1}, \tag{2.33}$$

where n is a nonlinearity exponent (the inverse of the strain rate sensitivity $m = 1/n$) and ϵ_0, σ_0 are reference strain rate and stress measures, respectively. The power-law relation (2.33) is commonly used to model high-temperature creep of metals. The limiting values $n = 1$ ($m = 1$) and $n \to \infty$ ($m \to 0$) correspond to linearly-viscous and ideally-plastic materials, respectively. Note that, in the ideally-plastic limit the stress-potential (2.33) is not differentiable. In this case, the derivatives in $(2.31)_1$ should be interpreted in the sense of subdifferentials of convex analysis [32].

For the case of composites with crystalline phases, the plastic deformation is assumed to occur only through crystallographic slip in the single crystals. Let $K^{(r,p)}$ be the number of physically

distinct slip systems in the single crystal (r,p). The symmetric Schmidt tensor associated with the $k-th$ slip system $(k=1,..,K^{(r,p)})$ is defined as

$$\boldsymbol{\mu}_k^{(r,p)} = \frac{1}{2}\left(\mathbf{s}_k^{(r,p)} \otimes \mathbf{m}_k^{(r,p)} + \mathbf{m}_k^{(r,p)} \otimes \mathbf{s}_k^{(r,p)}\right), \tag{2.34}$$

where $\mathbf{s}_k^{(r,p)}$ and $\mathbf{m}_k^{(r,p)}$ are the corresponding slip direction and slip plane normal, respectively. The phase-potentials $u^{(r,p)}$ in $(2.31)_3$ are taken in this case to be a superposition of slip potentials $\psi^{(r,p)}$

$$u^{(r,p)}(\boldsymbol{\sigma}) = \sum_{k=1}^{K^{(r,p)}} \psi_k^{(r,p)}(\tau_k^{(r,p)}), \qquad \tau_k^{(r,p)} = \boldsymbol{\sigma}\cdot\boldsymbol{\mu}_k^{(r,p)}. \tag{2.35}$$

A special form of the slip potentials $\psi^{(r,p)}$, which will be used in this work, is the following power-law relation

$$\psi_k^{(r,p)}(\tau_k^{(r,p)}) = \frac{\gamma_0 \tau_k^{(r,p)}}{n_k^{(r,p)}+1}\left(\frac{|\tau_k^{(r,p)}|}{\tau_{0k}^{(r,p)}}\right)^{n_k^{(r,p)}}, \tag{2.36}$$

where γ_0 is a reference strain rate measure, $\tau_{0k}^{(r,p)}$ denotes the shear resistance of the $k-th$ slip system in the single-crystal (r,p) and $n_k^{(r,p)}$ is the corresponding rate exponent. Note that, when each composite-phase is made out of only one single-crystal distributed at various orientations, the material parameters $\tau_{0k}^{(r,p)}$ and $n_k^{(r,p)}$ are independent of r and p.

2.4 Variational formulations of the homogenization problem

This section states the homogenization problem determining, in principle, the effective behavior of a two-scale composite in terms of the underlying sub-structure and the material properties of the constituents, as defined in the previous sections. To this end, it is helpful, and probably more instructive, to present first the corresponding discussion for a single-scale composite.

2.4.1 Single-scale composites

For definiteness and later reference, consider the single-scale material systems of Figs. 2.1(a) and 2.2(a), described in detail in subsections 2.1.1 and 2.2.1, respectively, and let $\tilde{u}^{(r)}(\boldsymbol{\sigma})$ denote the associated phase-potentials. Note that these composites may be viewed as the special cases of the corresponding two-scale composites of Figs. 2.1 and 2.2 in which each composite-phase r, with $r=1,...,N$, is made out of identical homogeneous-phases, i.e., $u^{(r,p)}(\boldsymbol{\sigma}) \equiv \tilde{u}^{(r)}(\boldsymbol{\sigma})$ for all $p=1,...,N^{(r)}$. The potentials $\tilde{u}^{(r)}$ are assumed to be some known, convex functions of the stress $\boldsymbol{\sigma}$, but their specific form is not important at this stage. Thus, the local stress-potential of the single-scale composite under consideration here is given by

$$u(\mathbf{x},\boldsymbol{\sigma}) = \sum_{r=1}^{N} \chi^{(r)}(\mathbf{x})\tilde{u}^{(r)}(\boldsymbol{\sigma}). \tag{2.37}$$

The effective constitutive relation of the composite material (2.37) is defined as the relation between the averages over the RVE Ω of the deformation rate and stress tensor fields, determined by means of the following static equilibrium problem.

Assuming that all phases are perfectly bonded and that there are no body forces, the problem over the RVE Ω consist of: (i) the constitutive relation $(2.31)_1$, with (2.37), associating the local deformation rate tensor $\mathbf{D}(\mathbf{x})$ with the stress tensor $\boldsymbol{\sigma}(\mathbf{x})$, (ii) the compatibility conditions

$$\mathbf{D}(\mathbf{x}) = \frac{1}{2}\left(\nabla\mathbf{v}(\mathbf{x}) + (\nabla\mathbf{v}(\mathbf{x}))^T\right), \tag{2.38}$$

for the deformation rate field $\mathbf{D}(\mathbf{x})$ in the bulk of the phases, where $\mathbf{v}(\mathbf{x})$ denotes the associated velocity field, (iii) the equilibrium equations

$$\mathrm{div}\boldsymbol{\sigma}(\mathbf{x}) = 0, \tag{2.39}$$

for the stress field $\boldsymbol{\sigma}(\mathbf{x})$ in the bulk, (iv) the appropriate jump conditions across interphase boundaries and (v) the following "uniform traction" boundary condition

$$\boldsymbol{\sigma}(\mathbf{x})\mathbf{n}(\mathbf{x}) = \overline{\boldsymbol{\sigma}}\mathbf{n}(\mathbf{x}) \qquad \text{for} \quad \text{all} \qquad \mathbf{x} \in \partial\Omega, \tag{2.40}$$

where $\overline{\boldsymbol{\sigma}}$ is an arbitrary constant, symmetric, second-order tensor, $\partial\Omega$ denotes the boundary of Ω and $\mathbf{n}(\mathbf{x})$ is the associated unit outward normal vector field. Note that, making use of Gauss' theorem along with (2.39) and (2.40), it may be easily shown that the average of the stress field over Ω is equal to $\overline{\boldsymbol{\sigma}}$. This result, in turn, implies that the boundary condition (2.40) is sufficiently general for our purposes here.

For composite materials whose local response is defined in terms of a scalar potential function, in this case by expression (2.37), the associated effective constitutive relation is more conveniently given by [52]

$$\overline{\mathbf{D}} = \frac{\partial\,\tilde{u}}{\partial\,\overline{\boldsymbol{\sigma}}}, \tag{2.41}$$

where $\overline{\mathbf{D}} \equiv \langle\mathbf{D}(\mathbf{x})\rangle$ and $\overline{\boldsymbol{\sigma}} \equiv \langle\boldsymbol{\sigma}(\mathbf{x})\rangle$ are respectively the averages of the deformation rate and stress fields over Ω. In the above expression, $\tilde{u}$ denotes the effective stress-potential of the single-scale composite and it is determined as a function of $\overline{\boldsymbol{\sigma}}$ by means of the "*principle of minimum complementary energy*"

$$\tilde{u}(\overline{\boldsymbol{\sigma}}) = \min_{\boldsymbol{\sigma}\in\mathcal{S}(\overline{\boldsymbol{\sigma}})} \langle u(\mathbf{x},\boldsymbol{\sigma})\rangle = \min_{\boldsymbol{\sigma}\in\mathcal{S}(\overline{\boldsymbol{\sigma}})} \sum_{r=1}^{N} \langle \chi^{(r)}(\mathbf{x})\tilde{u}^{(r)}(\boldsymbol{\sigma})\rangle, \tag{2.42}$$

where

$$\mathcal{S}(\overline{\boldsymbol{\sigma}}) = \{\boldsymbol{\sigma},\ \mathrm{div}\boldsymbol{\sigma} = 0 \,\mathrm{in}\,\Omega \,\mathrm{and}\, \boldsymbol{\sigma}\mathbf{n} = \overline{\boldsymbol{\sigma}}\mathbf{n} \,\mathrm{on}\,\partial\Omega\}, \tag{2.43}$$

is the set of admissible stress fields. The variational principle (2.42) states that the trial field $\boldsymbol{\sigma} \in \mathcal{S}(\overline{\boldsymbol{\sigma}})$ which renders the functional $\langle u(\mathbf{x},\boldsymbol{\sigma})\rangle$ minimum is the actual stress field in the composite. Therefore, statement (2.42) is equivalent to the boundary value problem for the single-scale

composite defined above. It can be shown [125] that (strict) convexity of the phase-potentials $\tilde{u}^{(r)}$ implies (strict) convexity of the effective potential $\tilde{u}$.

At this point, it should be emphasized that the variational principle (2.42) applies for any specific realization of the sub-structure of a random single-scale composite (such as the specific systems of Figs. 2.1(a) and 2.2(a)), defined through the associated characteristic functions $\chi^{(r)}$. However, as already discussed in subsections 2.1.1 and 2.2.1, the functions $\chi^{(r)}$ in these material systems cannot be known exactly. Instead, the associated sub-structural information is expected to be given in terms of the multi-point statistics associated with $\chi^{(r)}$. Furthermore, the relevant statistical information that is usually available in practice is restricted to the first few n-point probability functions. Therefore, for practical purposes, it makes sense to focus our interest on classes of random composites characterized by a finite set of n-point probability functions, such as the one-point $p^{(r)}$ and two-point $p^{(rs)}$ statistics defined respectively by (2.2) and (2.3). In this connection, we remark that the dependence of the associated effective stress-potential $\tilde{u}$ on the n-point probability functions is incorporated in expression (2.42) by employing the statistical uniformity, no long-range order and ergodicity assumptions for $\chi^{(r)}$, allowing the replacement of the associated ensemble averages with corresponding volume averages over the RVE Ω (see, e.g., Willis [152] and Ponte Castañeda and Willis [152] for a detailed discussion in the context of linear composites).

2.4.2 Two-scale composites

The effective behavior of the two-scale composites of Figs. 2.1 and 2.2 is defined in terms of the boundary value problem over the RVE Ω considered in the previous subsection for single-scale composites, with the only difference that, in the present context, the phases of Figs. 2.1(a) and 2.2(a) must be allowed to have the internal structure shown in Figs. 2.1(b) and 2.2(b), respectively, along with the appropriate definition of the local stress-potential $u(\mathbf{x}, \boldsymbol{\sigma})$ by means of $(2.31)_2$, with $(2.31)_3$. (The notation $\tilde{u}^{(r)}(\boldsymbol{\sigma})$ will be used in this case to denote the effective stress-potentials of the composite-phases, which can not be known in advance.) The effective constitutive relation for a two-scale composite is still given by (2.41), but the associated potential $\tilde{u}(\overline{\boldsymbol{\sigma}})$ is now determined by means of either of the following variational approaches.

Direct approach. Taking into account expression (2.17) for the definition of the two-scale characteristic functions $\tilde{\chi}^{(r,p)}(\mathbf{x})$, in analogy to the case of single-scale composites discussed above, the effective stress-potential $\tilde{u}$ of a two-scale composite characterized by the local stress-potential

$(2.31)_2$, with $(2.31)_3$, may be determined directly by means of the variational principle

$$\tilde{u}(\overline{\boldsymbol{\sigma}}) = \min_{\boldsymbol{\sigma}\in\mathcal{S}(\overline{\boldsymbol{\sigma}})} \langle u(\mathbf{x},\boldsymbol{\sigma})\rangle = \min_{\boldsymbol{\sigma}\in\mathcal{S}(\overline{\boldsymbol{\sigma}})} \sum_{r=1}^{N}\sum_{p=1}^{N^{(r)}} \langle \chi^{(r)}(\mathbf{x})\chi^{(r,p)}(\mathbf{x})u^{(r,p)}(\boldsymbol{\sigma})\rangle. \tag{2.44}$$

Similar to expression (2.42) for single-scale systems, the variational principle (2.44) determines the effective stress-potential $\tilde{u}$ of any specific composite material with prescribed two-scale functions $\tilde{\chi}^{(r,p)}$, such as the systems of Figs. 2.1 and 2.2. The use of expression (2.44) for a class of random two-scale composites characterized by the relevant n-point probability functions associated with $\tilde{\chi}^{(r,p)}$, such as the one-point $\tilde{p}^{(r,p)}$ and two-point probabilities $\tilde{p}^{(r,p;s,q)}$ defined respectively by (2.11) and (2.12), requires assuming that the functions $\tilde{\chi}^{(r,p)}$ are statistically uniform, ergodic and possess no long-range order. It should be emphasized that, since the direct variational principle (2.44) depends explicitly on $\tilde{\chi}^{(r,p)}$, the assumption that the associated meso-structure, defined by $\chi^{(r)}$, is statistically independent (see subsection 2.1.2) from the corresponding micro-structure, defined by $\chi^{(r,p)}$, is *not* strictly required in the context of this principle. In practical applications, however, this assumption turns out to be particularly useful, due to the implied simplifying expressions (2.22), (2.23), etc. for the corresponding two-scale probabilities $\tilde{p}^{(r,p)}$, $\tilde{p}^{(r,p;s,q)}$, etc. (Smyshlyaev and Willis [136]).

Sequential approach. The effective stress-potential $\tilde{u}$ of a two-scale composite characterized by the local stress-potential $(2.31)_2$, with $(2.31)_3$, may also be determined through a sequential homogenization procedure. Specifically, given the separation of the length scales hypothesis (2.15), the effective stress-potential $\tilde{u}^{(r)}(\boldsymbol{\sigma})$ for each composite-phase r, with $r = 1, ..., N$, may first be determined by means of a homogenization problem defined over the corresponding single-scale mesoscopic RVE (Figs. 2.1(b) and 2.2(b)), with $\boldsymbol{\sigma}$ denoting the associated applied (constant) uniform stress. Then, making use of the effective potentials $\tilde{u}^{(r)}(\boldsymbol{\sigma})$ to characterize the local constitutive behavior within the composite-phases, the two-scale composite of interest (Figs. 2.1 and 2.2) reduces to a corresponding single-scale composite (Figs. 2.1(a) and 2.2(a)), defined by (2.37), the effective stress-potential $\tilde{u}$ of which is given by (2.42). In this connection, it is remarked that, by definition, the average material response of the heterogeneous medium in the composite-phase r over regions of length-scale L_2 (or higher)—i.e., regions of the size of the mesoscopic RVE (Figs. 2.1(a) and 2.2(a))—is indistinguishable and, therefore, it may be replaced by the corresponding material response of the "homogeneous" medium with stress-potential $\tilde{u}^{(r)}(\boldsymbol{\sigma})$. In general, this is not true within a layer across the boundary of the composite-phases (Fig. 2.1(a) and Fig. 2.2(a)) whose thickness is of the order of the micro-scale ℓ_2. But, given the separation of the length scales hypothesis $\ell_2 << \ell_1$, implied by (2.15) and (2.16), it is reasonable to assume that the effect of this layer on the overall response of the two-scale composite is negligible. Thus,

the effective stress-potential $\tilde{u}$ of the two-scale composite may be determined by means of the sequential variational statement (2.42), along with

$$\tilde{u}^{(r)}(\boldsymbol{\sigma}) = \min_{\boldsymbol{\tau}\in\mathcal{S}^{(r)}(\boldsymbol{\sigma})} \langle u^{(r)}(\mathbf{x},\boldsymbol{\tau})\rangle^{(r)} = \min_{\boldsymbol{\tau}\in\mathcal{S}^{(r)}(\boldsymbol{\sigma})} \sum_{p=1}^{N^{(r)}} \langle \chi^{(r,p)}(\mathbf{x}) u^{(r,p)}(\boldsymbol{\tau})\rangle^{(r)}, \tag{2.45}$$

where $\boldsymbol{\tau}$ stands here for a trial stress field in the mesoscopic RVE $\Omega^{(r)}$ and the statically admissible set $\mathcal{S}^{(r)}(\boldsymbol{\sigma})$ is defined by

$$\mathcal{S}^{(r)}(\boldsymbol{\sigma}) = \{\boldsymbol{\tau},\ \mathrm{div}\boldsymbol{\tau} = 0 \,\mathrm{in}\, \Omega^{(r)} \,\mathrm{and}\, \boldsymbol{\tau}\mathbf{n} = \boldsymbol{\sigma}\mathbf{n} \,\mathrm{on}\, \partial\Omega^{(r)}\}, \tag{2.46}$$

where $\mathbf{n}$ is the unit outward normal vector field on the boundary $\partial\Omega^{(r)}$ of $\Omega^{(r)}$.

It should be emphasized that the sequential variational statement (2.42), with (2.45), decomposed the homogenization problem for a specific two-scale composite with prescribed meso- and micro-structures, defined respectively by the characteristic functions $\chi^{(r)}$ and $\chi^{(r,p)}$, into corresponding problems for single-scale systems. In particular, the variational principle (2.42) determines the effective stress-potential $\tilde{u}$ of the two-scale composite in terms of the mesoscopic single-scale functions $\chi^{(r)}$ and the homogenized potentials $\tilde{u}^{(r)}$ and, independently, the principle (2.45) determines $\tilde{u}^{(r)}$ for each $r = 1, ..., N$ in terms of the associated microscopic single-scale functions $\chi^{(r,p)}$ and the homogeneous phase-potentials $u^{(r,p)}$. The separation of the length-scales hypotheses $\ell_2 << L_2 << \ell_1 << L_1$ (see Figs. 2.1 and 2.2) guarantee the validity of the sequential variational statement (2.42), with (2.45), and further ensure its equivalence with the corresponding direct statement (2.44) (Avellaneda [7], Braides and Lukkassen [17]).

In order to preserve the validity of the sequential homogenization procedure (2.42), with (2.45), for random two-scale composites with prescribed n-point statistics associated with $\tilde{\chi}^{(r,p)}$, additional assumptions are required. Specifically, in addition to the hypotheses $\ell_2 << L_2 << \ell_1 << L_1$, both the meso-structure and the underlying micro-structure in the context of (2.42) and (2.45), respectively, must be assumed to be statistically uniform, ergodic and with no long-range order. Furthermore, the meso-structure must be assumed to be statistically independent from the associated micro-structure. These requirements ensure that the variational principle (2.42) determines the effective stress-potential $\tilde{u}$ of the two-scale composite in terms of the mesoscopic single-scale probability functions $p^{(r)}$, $p^{(rs)}$, etc. (associated with $\chi^{(r)}$) and the homogenized potentials $\tilde{u}^{(r)}$ of the composite-phases and, independently, the principle (2.45) determines $\tilde{u}^{(r)}$ for each $r = 1, ..., N$ in terms of the associated microscopic single-scale probabilities $p^{(r,p)}$, $p^{(r,pq)}$, etc. (associated with $\chi^{(r,p)}$) and the homogeneous phase-potentials $u^{(r,p)}$. To see this, it suffices to recall from the relevant discussion of subsection 2.1.2 that the micro-meso-structural statistical independence assumption consists in the following two conditions: (i) for any fixed value of r, the functions $\chi^{(r)}$ and $\chi^{(r,p)}$ are mutually (statistically) independent and (ii) for different values of r and s, the

functions $\chi^{(r,p)}$ and $\chi^{(s,q)}$ are also mutually (statistically) independent. To see why conditions (i) and (ii) are also necessary, note that if (i) does not hold then the potentials $\tilde{u}^{(r)}$ cannot be defined independently of the effective stress-potential $\tilde{u}$, while if (ii) does not hold then for different values of r and s the corresponding potentials $\tilde{u}^{(r)}$ and $\tilde{u}^{(s)}$ cannot be defined independently. Finally, it should be remarked that, for two-scale composite systems with meso-structures that are statistical independent from the associated micro-structures, the sequential homogenization procedure (2.42), with (2.45), is equivalent to the corresponding direct procedure (2.44). Furthermore, for this class of composites, the single-scale probability functions—such as $p^{(r)}$, $p^{(rs)}$ and $p^{(r,p)}$, $p^{(r,pq)}$—involved in the sequential statement (2.42), with (2.45), are linked to the corresponding two-scale probabilities—such as $\tilde{p}^{(r,p)}$ and $\tilde{p}^{(r,p;s,q)}$—involved in the direct statement (2.44) by means of simple expressions of the type (2.22) and (2.23).

In summary, the problem of determining the effective response of a random two-scale viscoplastic composite consists in solving the variational problem (2.44) or, alternatively, (2.42) together with (2.45). It is however important to realize that—due to the constitutive nonlinearities of the phases and the random character of the sub-structure—it is impossible to solve exactly either problem. Nevertheless, approximate results for the effective stress-potential $\tilde{u}(\overline{\boldsymbol{\sigma}})$ can be derived by the appropriate generalization of ideas that have been developed in the literature in the context of single-scale composites. Along these lines, our strategy in this work is to make use of the linear comparison composite methods of Ponte Castañeda [116, 117, 118], which deliver estimates for $\tilde{u}(\overline{\boldsymbol{\sigma}})$ that account explicitly not only for the material properties of the constituents but also for fine sub-structural information. The following section provides a review of the linear comparison composite methods in the context of the the variational problem (2.42) for single-scale systems, while sections 2.6, 2.7 and 2.8 deal with the extension of these methods to two-scale composites. It is relevant at this point to remark that the approximations involved in the implementation of these methods to the direct variational problem (2.44) and the equivalent sequential problem (2.42), with (2.45), are different, in general, and therefore the corresponding estimates obtained for $\tilde{u}(\overline{\boldsymbol{\sigma}})$ need *not* necessarily be identical. For this reason, it is of interest to investigate both possibilities.

2.5 Linear comparison composite methods for single-scale composites

In this section, we focus our attention on the single-scale composite material of subsection 2.4.1, with local stress-potential given by (2.37), and implement the methods of Ponte Castañeda [116], [117] and [118] to the associated variational problem (2.42) in order to generate corresponding

estimates for the effective stress-potential $\tilde{u}(\overline{\boldsymbol{\sigma}})$ of this material. These methods are based on the notion of the "linear comparison composite" (LCC), which is a fictitious medium serving as a means to deal with the inherent difficulties associated with the nonlinear character of the constituents in the actual composite material. The LCC methods consist in constructing an LCC with the same microstructure as the actual composite (i.e., same characteristic functions $\chi^{(r)}(\mathbf{x})$) and expressing the effective properties of the nonlinear medium in terms of the corresponding effective properties of the LCC and appropriately defined error functions. The local properties of the LCC are determined through suitably designed optimization procedures based on the variational structure of the nonlinear problem. In this way, the LCC methods allow the "translation" of any estimate that may be available for linear composites into a corresponding estimate for the nonlinear composite of interest. It should be remarked that the method proposed in the work [116] is capable of generating bounds for the effective behavior of nonlinear composites from corresponding bounds that may be available for the LCC. On the other hand, the methods in [117] and [118] have the merit of delivering estimates for nonlinear systems that are exact to second-order in the heterogeneity contrast for weakly inhomogeneous composites, provided that the corresponding estimates used for the LCC are also exact to second-order in the contrast. In the sequel, the LCC methods of Ponte Castañeda [116], [117] and [118] will be respectively referred to as the "secant" (SEC), "tangent second-order" (TSO) and "generalized-secant second-order" (GSO) methods.

2.5.1 Secant method

As shown by Ponte Castañeda [116] in the context of single-scale nonlinear systems with *isotropic* phases, the secant method—introduced in a separate development [114] by the same author—is derivable from alternative representations of the classical variational principles (i.e., the original principle (2.42) and its dual counterpart). It should be mentioned that this method was independently proposed by Suquet [138] for the special case of *power-law* phases. Later on, deBotton and Ponte Castañeda [30] extended the secant method to viscoplastic polycrystals, while Idiart and Ponte Castañeda [62, 63] provided a full extension of this method to material systems with generally anisotropic phases.

Next, we provide a review of the secant method of Ponte Castañeda [116] in the context of the variational problem (2.42) for the effective stress-potential of a single-scale viscoplastic composite with *isotropic* phases (for the treatment of more general composite systems, we refer to the work of Idiart and Ponte Castañeda [62]). To this end, the phase-potentials $\tilde{u}^{(r)}(\overline{\boldsymbol{\sigma}})$ in the definition of the local stress-potential (2.37) of the nonlinear composite of interest will be taken here to be of the form $(2.32)_1$, i.e.,

$$\tilde{u}^{(r)}(\boldsymbol{\sigma}) = \tilde{\psi}^{(r)}(\sigma_e) \equiv \tilde{f}^{(r)}(\sigma_e^2), \tag{2.47}$$

where we recall that $\sigma_e = \sqrt{3\boldsymbol{\sigma}_d \cdot \boldsymbol{\sigma}_d/2}$ and that $\boldsymbol{\sigma}_d$ denotes the deviatoric part of the stress tensor. The $\tilde{f}^{(r)}$ in $(2.47)_2$ are assumed to be non-negative, convex functions of σ_e^2, such that $\tilde{f}^{(r)} \to \infty$ as $\sigma_e^2 \to \infty$. Note that, an example of a phase potential for which these requirements for $\tilde{f}^{(r)}$ are met is the power-law relation (2.33).

Towards an alternative representation of the original variational principle (2.42), we introduce a single-scale LCC (Figs. 2.1(a) and 2.2(a)) defined in terms of the local stress-potential

$$u_L(\mathbf{x}, \boldsymbol{\sigma}; \lambda^{(r)}) = \sum_{r=1}^{N} \chi^{(r)}(\mathbf{x}) u_L^{(r)}(\boldsymbol{\sigma}; \lambda^{(r)}), \tag{2.48}$$

with $u_L^{(r)}$ denoting the associated linear elastic phase-potentials which are taken to be of the form

$$u_L^{(r)}(\boldsymbol{\sigma}; \lambda^{(r)}) = \frac{1}{2}\boldsymbol{\sigma} \cdot \mathbf{M}^{(r)}\boldsymbol{\sigma}, \qquad \mathbf{M}^{(r)} = \frac{1}{2\lambda^{(r)}}\mathbf{K}, \tag{2.49}$$

where $\mathbf{K}$ is the fourth-order identity tensor in the deviatoric space and $\lambda^{(r)}$ are unknown scalar moduli to be determined further bellow. In addition, we introduce the error function

$$V(\mathbf{x}; \lambda^{(r)}) = \sum_{r=1}^{N} \chi^{(r)}(\mathbf{x}) V^{(r)}(\lambda^{(r)}), \tag{2.50}$$

with

$$V^{(r)}\left(\lambda^{(r)}\right) = \sup_{\hat{\boldsymbol{\sigma}}^{(r)}} \left[u_L^{(r)}(\hat{\boldsymbol{\sigma}}^{(r)}; \lambda^{(r)}) - \tilde{u}^{(r)}(\hat{\boldsymbol{\sigma}}^{(r)})\right]. \tag{2.51}$$

Making use of the above definitions for the LCC and the error function it can be shown that the original variational principle (2.42) for $\tilde{u}(\overline{\boldsymbol{\sigma}})$ admits the following equivalent representation

$$\tilde{u}(\overline{\boldsymbol{\sigma}}) = \min_{\boldsymbol{\sigma} \in \mathcal{S}(\overline{\boldsymbol{\sigma}})} \langle \sup_{\substack{\lambda^{(s)} \\ s=1,..,N}} \left[u_L(\mathbf{x}, \boldsymbol{\sigma}; \lambda^{(r)}) - V(\mathbf{x}; \lambda^{(r)})\right] \rangle. \tag{2.52}$$

Interchanging the order of the optimality operations in the above expression, which is allowed by Prop. VI.2.3 of Ekeland and Temam [32], we obtain

$$\tilde{u}(\overline{\boldsymbol{\sigma}}) = \sup_{\substack{\lambda^{(s)}(\mathbf{x}) \\ s=1,..,N}} \left[\tilde{u}_L(\overline{\boldsymbol{\sigma}}; \lambda^{(r)}) - \sum_{r=1}^{N} c^{(r)} \langle V^{(r)}\left(\lambda^{(r)}\right)\rangle^{(r)}\right], \tag{2.53}$$

where it is emphasized that the phase moduli $\lambda^{(r)}$ $(r = 1, ..., N)$ depend on $\mathbf{x}$. In expression (2.53), $\tilde{u}_L$ denotes the effective stress-potential of the LCC, which is, in principle, determined by means of the variational statement (2.42) and it is given by an expression of the form

$$\tilde{u}_L(\overline{\boldsymbol{\sigma}}) = \frac{1}{2}\overline{\boldsymbol{\sigma}} \cdot \widetilde{\mathbf{M}}\overline{\boldsymbol{\sigma}}, \tag{2.54}$$

in terms of the associated effective modulus tensor $\widetilde{\mathbf{M}}$.

At this point, it should be remarked that the variational principle (2.53) is by no means simpler than the original principle (2.42), given that the associated LCC involved in (2.53) is point-wise heterogeneous, i.e., it is made out of an infinite number of phases. However, compared to the original statement (2.42), the variational statement (2.53) has the advantage that the associated optimization variables $\lambda^{(r)}$ are free of differential constraints, which in turn allows the construction of non-trivial trial fields for these variables that are optimal in suitably restricted subclasses of the general set of $\lambda^{(r)}$.

Next, restricting our consideration to constant constant-per-phase moduli $\lambda^{(r)}$ in (2.53), we obtain the following bound for the effective stress-potential $\tilde{u}$ of the nonlinear composite

$$\tilde{u}(\overline{\boldsymbol{\sigma}}) \geq \sup_{\substack{\lambda^{(s)} \\ s=1,..,N}} \left[\tilde{u}_L(\overline{\boldsymbol{\sigma}}; \lambda^{(r)}) - \sum_{r=1}^{N} c^{(r)} V^{(r)} \left(\lambda^{(r)} \right) \right]. \tag{2.55}$$

Then, the optimality conditions in (2.51) and (2.55) reduce to

$$\frac{1}{2\lambda^{(r)}} = \frac{3\tilde{\psi}^{(r)'}(\hat{\sigma}_e^{(r)})}{2\hat{\sigma}_e^{(r)}}, \tag{2.56}$$

and

$$\hat{\sigma}_e^{(r)} = \sqrt{\langle \sigma_e^2 \rangle^{(r)}} = \sqrt{\frac{3}{2c^{(r)}} \overline{\boldsymbol{\sigma}} \cdot \frac{\partial \widetilde{\mathbf{M}}}{\partial (2\lambda^{(r)})^{-1}} \overline{\boldsymbol{\sigma}}}, \tag{2.57}$$

respectively. Note that, conditions (2.56) and (2.57) identify the phase-moduli $\lambda^{(r)}$ of the LCC with the corresponding secant moduli of the nonlinear phases in the actual composite evaluated at the second-moments of the stress field over the phases of the LCC. Finally, taking into account expressions (2.57), the bound (2.55) may be rewritten as

$$\tilde{u}(\overline{\boldsymbol{\sigma}}) \geq \sum_{r=1}^{N} c^{(r)} \tilde{\psi}^{(r)} \left(\hat{\sigma}_e^{(r)} \right). \tag{2.58}$$

It should be emphasized that in the derivation of the above bound for $\tilde{u}$ it has been implicitly assumed that the exact value for the effective potential $\tilde{u}_L$ of the LCC is used in (2.55). In practice, however, the exact calculation of $\tilde{u}_L$ is not possible, in general. In this work, the function $\tilde{u}_L$ will be computed by means of the expression (2.54), along with the self-consistent estimate (2.93) for $\widetilde{\mathbf{M}}$ in the case of a granular system and along with the Willis estimate (2.95) for $\widetilde{\mathbf{M}}$ in the case of a particulate composite. It is well-known that, under certain conditions, the Willis estimate (2.95) may be used to generate both upper and lower bounds for $\tilde{u}_L$. Clearly, if a lower bound is used for $\tilde{u}_L$ expression (2.55) still provides a lower bound for $\tilde{u}$. On the other hand, if an upper bound or any other estimate is used for $\tilde{u}_L$ expression (2.55) provides a corresponding estimate for $\tilde{u}$, which is not necessarily a bound.

2.5.2 Tangent method

In contrast to the secant method of the previous subsection, the tangent method [117] makes use of a linear *thermoelastic* comparison composite (LCC) (Figs. 2.1(a) and 2.2(a)) characterized by a stress-potential u_T of the form

$$u_T(\mathbf{x},\boldsymbol{\sigma};\boldsymbol{\sigma}^{(r)},\mathbf{M}^{(r)}) = \sum_{r=1}^{N} \chi^{(r)}(\mathbf{x}) u_T^{(r)}(\boldsymbol{\sigma};\boldsymbol{\sigma}^{(r)},\mathbf{M}^{(r)}), \tag{2.59}$$

where the phase-potentials $u_T^{(r)}$ are given by the following second-order, Taylor-like expansions of the corresponding nonlinear potentials $\tilde{u}^{(r)}(\boldsymbol{\sigma})$

$$u_T^{(r)}(\boldsymbol{\sigma};\boldsymbol{\sigma}^{(r)},\mathbf{M}^{(r)}) = \tilde{u}^{(r)}(\boldsymbol{\sigma}^{(r)}) + \frac{\partial \tilde{u}^{(r)}}{\partial \boldsymbol{\sigma}}(\boldsymbol{\sigma}^{(r)}) \cdot (\boldsymbol{\sigma} - \boldsymbol{\sigma}^{(r)}) + \frac{1}{2}(\boldsymbol{\sigma} - \boldsymbol{\sigma}^{(r)}) \cdot \mathbf{M}^{(r)} (\boldsymbol{\sigma} - \boldsymbol{\sigma}^{(r)}). \tag{2.60}$$

In the above expression, the variables $\boldsymbol{\sigma}^{(r)}$ are reference stress tensors, assumed to be independent of $\boldsymbol{\sigma}$, and $\mathbf{M}^{(r)}$ are reference compliance tensors, also independent of $\boldsymbol{\sigma}$, that are *not* necessarily equal to the tangent moduli $\partial^2 \tilde{u}^{(r)}/\partial \boldsymbol{\sigma}^2(\boldsymbol{\sigma}^{(r)})$. The precise values of these quantities will be determined further below. In addition, the associated error function is in this case defined by

$$V(\mathbf{x};\boldsymbol{\sigma}^{(r)},\mathbf{M}^{(r)}) = \sum_{r=1}^{N} \chi^{(r)}(\mathbf{x}) V^{(r)}(\boldsymbol{\sigma}^{(r)},\mathbf{M}^{(r)}), \tag{2.61}$$

with

$$V^{(r)}\left(\boldsymbol{\sigma}^{(r)},\mathbf{M}^{(r)}\right) = \underset{\hat{\boldsymbol{\sigma}}^{(r)}}{\text{stat}} \left[\tilde{u}^{(r)}(\hat{\boldsymbol{\sigma}}^{(r)}) - u_T^{(r)}(\hat{\boldsymbol{\sigma}}^{(r)};\boldsymbol{\sigma}^{(r)},\mathbf{M}^{(r)}) \right]. \tag{2.62}$$

The stat(ionarity) operation in (2.62) amounts in setting the derivative of the quantity within the square bracket with respect to $\boldsymbol{\sigma}$ equal to zero, solving for $\boldsymbol{\sigma}$ and substituting the solution, denoted here by $\hat{\boldsymbol{\sigma}}^{(r)}$, back to the expression in the square bracket. Thus, the relevant stationarity condition in (2.62) reads as follows

$$\frac{\partial \tilde{u}^{(r)}}{\partial \boldsymbol{\sigma}}(\hat{\boldsymbol{\sigma}}^{(r)}) - \frac{\partial \tilde{u}^{(r)}}{\partial \boldsymbol{\sigma}}(\boldsymbol{\sigma}^{(r)}) = \mathbf{M}^{(r)}(\hat{\boldsymbol{\sigma}}^{(r)} - \boldsymbol{\sigma}^{(r)}). \tag{2.63}$$

Making use of the definitions (2.59) with (2.60), for the LCC, and (2.61) with (2.62), for the error function, it can be shown that the variational principle (2.42) for the effective stress-potential $\tilde{u}$ admits the following alternative representation

$$\tilde{u}(\overline{\boldsymbol{\sigma}}) = \min_{\boldsymbol{\sigma} \in \mathcal{S}(\overline{\boldsymbol{\sigma}})} \langle \underset{\substack{\boldsymbol{\sigma}^{(s)} \\ s=1,..,N}}{\text{stat}} \left[u_T(\mathbf{x},\boldsymbol{\sigma};\boldsymbol{\sigma}^{(r)},\mathbf{M}^{(r)}) + V(\mathbf{x};\boldsymbol{\sigma}^{(r)},\mathbf{M}^{(r)}) \right] \rangle. \tag{2.64}$$

After interchanging the order of the optimality operations, expression (2.64) reduces to

$$\tilde{u}(\overline{\boldsymbol{\sigma}}) = \underset{\substack{\boldsymbol{\sigma}^{(s)}(\mathbf{x}) \\ s=1,..,N}}{\text{stat}} \left[\tilde{u}_T(\overline{\boldsymbol{\sigma}};\boldsymbol{\sigma}^{(r)},\mathbf{M}^{(r)}) + \sum_{r=1}^{N} c^{(r)} \langle V^{(r)}\left(\boldsymbol{\sigma}^{(r)},\mathbf{M}^{(r)}\right) \rangle^{(r)} \right], \tag{2.65}$$

where the dependence of $\boldsymbol{\sigma}^{(r)}$ on $\mathbf{x}$ has been emphasized. The quantity $\tilde{u}_T$ in the above expression denotes the effective stress-potential of the LCC and it is determined through the principle of minimum complementary energy (2.42), i.e.,

$$\tilde{u}_T(\overline{\boldsymbol{\sigma}};\boldsymbol{\sigma}^{(r)},\mathbf{M}^{(r)}) = \min_{\boldsymbol{\sigma}\in\mathcal{S}(\overline{\boldsymbol{\sigma}})} \langle u_T(\mathbf{x},\boldsymbol{\sigma};\boldsymbol{\sigma}^{(r)},\mathbf{M}^{(r)})\rangle = \min_{\boldsymbol{\sigma}\in\mathcal{S}(\overline{\boldsymbol{\sigma}})} \sum_{r=1}^{N} c^{(r)}\ \langle u_T^{(r)}(\boldsymbol{\sigma};\boldsymbol{\sigma}^{(r)},\mathbf{M}^{(r)})\rangle^{(r)}. \tag{2.66}$$

At this point, it is important to realize that the variational principle (2.65) is by no means simpler than the original principle (2.42). In fact, given that the LCC consist of infinitely many different phases ($\boldsymbol{\sigma}^{(r)}$ and $\mathbf{M}^{(r)}$ depend on $\mathbf{x}$), computing the stress field $\boldsymbol{\sigma}(\mathbf{x}) \in \mathcal{S}(\overline{\boldsymbol{\sigma}})$ in the LCC from (2.66) is by itself at least as difficult as computing the actual stress field $\boldsymbol{\sigma}(\mathbf{x}) \in \mathcal{S}(\overline{\boldsymbol{\sigma}})$ in the nonlinear medium from (2.42). Expression (2.65), however, has the advantage over (2.42) that the corresponding optimization variable is free of constraints, which, in turn, allows the construction of simple trial fields that are optimal in suitably restricted subclasses of the full set of all possible LCCs.

Following Ponte Castañeda [117], in the context of (2.65) we make use of the approximation that the reference stress $\boldsymbol{\sigma}^{(r)}$ and compliance $\mathbf{M}^{(r)}$ tensors are constant in each phase $r = 1, ..., N$. In addition, we chose $\hat{\boldsymbol{\sigma}}^{(r)} = \boldsymbol{\sigma}^{(r)}$ as the solution to (2.63), which, in turn, renders the error functions $V^{(r)}$ in (2.62) identically equal to zero. Then, the stationarity condition in (2.65) yields the result $\boldsymbol{\sigma}^{(r)} = \langle\boldsymbol{\sigma}\rangle^{(r)} \equiv \overline{\boldsymbol{\sigma}}^{(r)}$, by means of which (2.65) can be shown [122] to reduce to

$$\tilde{u}(\overline{\boldsymbol{\sigma}}) = \sum_{r=1}^{N} c^{(r)} \left[\tilde{u}^{(r)}(\overline{\boldsymbol{\sigma}}^{(r)}) + \frac{1}{2}\frac{\partial\tilde{u}^{(r)}}{\partial\boldsymbol{\sigma}}(\overline{\boldsymbol{\sigma}}^{(r)}) \cdot (\overline{\boldsymbol{\sigma}} - \overline{\boldsymbol{\sigma}}^{(r)})\right], \tag{2.67}$$

where, it is recalled that $\overline{\boldsymbol{\sigma}}^{(r)}$ denotes the average of the stress field over phase r of the LCC.

Note that the phase modulus tensors $\mathbf{M}^{(r)}$ remain undetermined from this process. A possibility for resolving this indeterminacy would be to further optimize expression (2.65) for $\tilde{u}$ with respect to $\mathbf{M}^{(r)}$. Such an optimization, however, leads to the condition

$$\langle(\boldsymbol{\sigma} - \overline{\boldsymbol{\sigma}}^{(r)}) \otimes (\boldsymbol{\sigma} - \overline{\boldsymbol{\sigma}}^{(r)})\rangle^{(r)} = \mathbf{0}, \tag{2.68}$$

which is a very severe constraint, requiring the stress field in each phase of the LCC to be constant. Based on this observation, Ponte Castañeda [117] proposed instead the use of the tangent prescription

$$\mathbf{M}^{(r)} = \frac{\partial^2\tilde{u}^{(r)}}{\partial\boldsymbol{\sigma}^2}(\overline{\boldsymbol{\sigma}}^{(r)}), \tag{2.69}$$

which is consistent with (2.63) in the limit $\hat{\boldsymbol{\sigma}}^{(r)} \to \boldsymbol{\sigma}^{(r)}$. Furthermore, for this choice of $\mathbf{M}^{(r)}$, it can be shown (see, e.g., [122]) that the estimate (2.67) for $\tilde{u}$ agrees exactly to second-order in the heterogeneity contrast with the small-contrast perturbation expansion of Suquet and Ponte

Castañeda [140]. Hence, expression (2.67) is referred to as the "tangent second-order" (TSO) estimate.

In summary, the TSO estimate (2.67) provides an expression for the computation of the effective stress-potentials $\tilde{u}$ of any single-scale composite with given phase-potentials $\tilde{u}^{(r)}$. This estimate is completely determined in terms of the average stress tensors $\overline{\boldsymbol{\sigma}}^{(r)}$ in the phases of the associated LCC, and it is therefore fairly easy to compute. The phase-averages $\overline{\boldsymbol{\sigma}}^{(r)}$ in the LCC are given by expressions of the form

$$\overline{\boldsymbol{\sigma}}^{(r)} = \mathbf{B}^{(r)}\overline{\boldsymbol{\sigma}} + \mathbf{b}^{(r)}, \tag{2.70}$$

where $\mathbf{B}^{(r)}$ and $\mathbf{b}^{(r)}$ are the associated stress concentration tensors, which, in this work, are obtained by means of the estimates for the corresponding linear thermoelastic problem (2.66) discussed in subsection 2.5.4. It should be remarked, however, that despite its simplicity, the TSO estimate (2.67) has been found to violate the secant bound (2.58) in certain special cases (see [81] and also Fig. 3.11 in chapter 3), corresponding to large values of the heterogeneity contrast in highly nonlinear composites where the stress field fluctuations are expected to be significant. These findings have motivated the development of the more sophisticated GSO method [118], which delivers estimates that depend explicitly on the field fluctuations, are fully consistent with the secant bound (2.58), and, at the same time, they are also exact to second-order in the contrast.

2.5.3 Generalized-secant method

Considering an LCC with local stress-potential of the form (2.59) with (2.60), and an error function given by (2.61) with (2.62), it can be shown that the original variational principle (2.42) for the nonlinear, single-scale composite of interest may also be expressed as

$$\tilde{u}(\overline{\boldsymbol{\sigma}}) = \min_{\boldsymbol{\sigma}\in\mathcal{S}(\overline{\boldsymbol{\sigma}})} \langle \operatorname*{stat}_{\substack{\mathbf{M}^{(s)}\\ s=1,..,N}} \Big[u_T(\mathbf{x},\boldsymbol{\sigma};\boldsymbol{\sigma}^{(r)},\mathbf{M}^{(r)}) + V(\mathbf{x};\boldsymbol{\sigma}^{(r)},\mathbf{M}^{(r)}) \Big] \rangle, \tag{2.71}$$

for any reference stress tensors $\boldsymbol{\sigma}^{(r)}$, which by interchanging the order of the optimality operations reduces to

$$\tilde{u}(\overline{\boldsymbol{\sigma}}) = \operatorname*{stat}_{\substack{\mathbf{M}^{(s)}(\mathbf{x})\\ s=1,..,N}} \left[\tilde{u}_T(\overline{\boldsymbol{\sigma}};\boldsymbol{\sigma}^{(r)},\mathbf{M}^{(r)}) + \sum_{r=1}^{N} c^{(r)} \langle V^{(r)} \left(\boldsymbol{\sigma}^{(r)},\mathbf{M}^{(r)} \right) \rangle^{(r)} \right], \tag{2.72}$$

where the effective stress-potential $\tilde{u}_T$ of the LCC is given by (2.66). Note that, in contrast to the variational principle (2.65) utilized in the context of the tangent method which required stationarity with respect to the reference stress fields $\boldsymbol{\sigma}^{(r)}(\mathbf{x})$, the variational statement (2.72) is based on stationarity conditions with respect to the reference modulus tensor fields $\mathbf{M}^{(r)}(\mathbf{x})$. But similar to (2.65), although the variational principle (2.72) is not simpler than the original principle (2.42), it has the advantage of allowing the construction of simple trial fields for $\mathbf{M}^{(r)}$ and $\boldsymbol{\sigma}^{(r)}$.

Employing the approach of Ponte Castañeda [118] in the context of the variational statement (2.72), we assume that the fields $\boldsymbol{\sigma}^{(r)}$ and $\mathbf{M}^{(r)}$ are constant per phase and explore the possibility of solutions to (2.63) that are different from $\hat{\boldsymbol{\sigma}}^{(r)} = \boldsymbol{\sigma}^{(r)}$. In this case, stationarity of (2.72) with respect to the modulus tensors $\mathbf{M}^{(r)}$ requires

$$(\hat{\boldsymbol{\sigma}}^{(r)} - \boldsymbol{\sigma}^{(r)}) \otimes (\hat{\boldsymbol{\sigma}}^{(r)} - \boldsymbol{\sigma}^{(r)}) = \langle (\boldsymbol{\sigma} - \boldsymbol{\sigma}^{(r)}) \otimes (\boldsymbol{\sigma} - \boldsymbol{\sigma}^{(r)}) \rangle^{(r)}. \tag{2.73}$$

Using this result, it can be easily shown that expression (2.72) for $\tilde{u}$ reduces to

$$\tilde{u}(\overline{\boldsymbol{\sigma}}) = \sum_{r=1}^{N} c^{(r)} \left[\tilde{u}^{(r)}(\hat{\boldsymbol{\sigma}}^{(r)}) + \frac{\partial \tilde{u}^{(r)}}{\partial \boldsymbol{\sigma}}(\boldsymbol{\sigma}^{(r)}) \cdot (\overline{\boldsymbol{\sigma}}^{(r)} - \hat{\boldsymbol{\sigma}}^{(r)}) \right], \tag{2.74}$$

where we recall that the phase-averages $\overline{\boldsymbol{\sigma}}^{(r)} \equiv \langle \boldsymbol{\sigma} \rangle^{(r)}$ in the LCC are given by (2.70).

Clearly, the determination of the estimate (2.74) for $\tilde{u}$ requires additional conditions for the computation of the reference stress tensors $\boldsymbol{\sigma}^{(r)}$. This problem could be fully resolved [118] by requiring, in addition, stationarity of (2.74) with respect to $\boldsymbol{\sigma}^{(r)}$. The enforcement of such a requirement, however, is not straightforward, and it will not be pursued in this work. Instead, we will restrict attention on simple prescriptions for these variables, which have been found to yield quite accurate predictions for the effective behavior of single-scale viscoplastic composites (see, e.g., [119, 64, 21, 87, 88]). The explicit choices for the reference tensors $\boldsymbol{\sigma}^{(r)}$ will be discussed in the context of the specific applications to be considered in this and other chapters of this work. At this stage, it suffices to remark that when $\boldsymbol{\sigma}^{(r)}$ are such that to zeroth-order in the heterogeneity contrast they reduce to $\overline{\boldsymbol{\sigma}}$ (the prescriptions to be used in this work are consistent with this requirement), it can be shown [118] that the estimate (2.74) for $\tilde{u}$ is exact to second-order in the contrast.

It should also be remarked that condition (2.73) associates the variables $\hat{\boldsymbol{\sigma}}^{(r)}$ with the stress-field fluctuations over the phases of the LCC about the reference stress tensors $\boldsymbol{\sigma}^{(r)}$. Thus, in contrast to the TSO estimate (2.67), the estimate (2.74) incorporates direct dependence not only on the phase averages (first-moments) but also on the second-moments of the stress-field in the phases of the LCC. Making use of this fact, it can be shown [118] that the estimate (2.74) is always consistent with the secant bound (2.58). Furthermore, since $\hat{\boldsymbol{\sigma}}^{(r)} \neq \boldsymbol{\sigma}^{(r)}$, in general, the stationarity condition (2.63) suggests the interpretation of the phase modulus tensors $\mathbf{M}^{(r)}$ as "generalized-secant" moduli, i.e., linearization moduli whose values range between the secant ($\boldsymbol{\sigma}^{(r)} = 0$) and tangent ($\boldsymbol{\sigma}^{(r)} = \hat{\boldsymbol{\sigma}}^{(r)}$) approximations of the associated nonlinear constitutive relations. Hence, expression (2.74) is referred to as "generalized-secant second-order" (GSO) estimate.

As pointed out by Ponte Castañeda [118], condition (2.73), although less restrictive than the corresponding condition (2.68) in the context of the TSO estimate, is still too difficult to impose in its complete generality, since this would require constraining the fluctuations of the stress field

in each phase of the LCC (right-hand side of (2.73)), which are in general expected to be full rank forth-order tensors, to rank-one tensors (left-hand side of (2.73)). In order to avoid possible inconsistencies, it has been suggested [118], instead, to enforce only certain traces of these conditions. This idea has been implemented thus far in full detail for single-scale composites with isotropic constituents [118] and polycrystals [87], and its extension to systems with general anisotropic phases remains to be developed.

Composites with isotropic phases. Next, we specialize the GSO estimate (2.74) to single-scale composites with isotropic constituents that are characterized by phase-potentials $\tilde{u}^{(r)}$ of the form (2.32), i.e.,

$$\tilde{u}^{(r)}(\boldsymbol{\sigma}) = \widetilde{\psi}^{(r)}(\sigma_e), \tag{2.75}$$

where we recall that $\sigma_e = \sqrt{3\boldsymbol{\sigma}_d \cdot \boldsymbol{\sigma}_d/2}$ and the subscript d is used to indicate the deviatoric part of a tensor. Motivated by the form of the tangent modulus $\partial^2\tilde{u}^{(r)}/\partial\boldsymbol{\sigma}^2(\boldsymbol{\sigma}^{(r)})$, the phase modulus tensors $\mathbf{M}^{(r)}$ of the LCC are taken to be of the form [118]

$$\mathbf{M}^{(r)} = \frac{1}{2\lambda_{\mathbf{E}}^{(r)}}\mathbf{E}^{(r)} + \frac{1}{2\lambda_{\mathbf{F}}^{(r)}}\mathbf{F}^{(r)}, \qquad \mathbf{E}^{(r)} = \frac{3}{2}\frac{\boldsymbol{\sigma}_d^{(r)}}{\sigma_e^{(r)}} \otimes \frac{\boldsymbol{\sigma}_d^{(r)}}{\sigma_e^{(r)}}, \qquad \mathbf{F}^{(r)} = \mathbf{K} - \mathbf{E}^{(r)}, \tag{2.76}$$

where the quantities $\lambda_{\mathbf{E}}^{(r)}$ and $\lambda_{\mathbf{F}}^{(r)}$ are unknown scalar moduli, $\mathbf{K}$ is the fourth-order identity tensor in the deviatoric space and $\mathbf{E}^{(r)}$, $\mathbf{F}^{(r)}$ are projection tensors such that

$$\mathbf{E}^{(r)}\mathbf{F}^{(r)} = \mathbf{F}^{(r)}\mathbf{E}^{(r)} = \mathbf{0}, \qquad \mathbf{E}^{(r)}\mathbf{E}^{(r)} = \mathbf{E}^{(r)}, \qquad \mathbf{F}^{(r)}\mathbf{F}^{(r)} = \mathbf{F}^{(r)}, \qquad \mathbf{E}^{(r)} + \mathbf{F}^{(r)} = \mathbf{K}. \tag{2.77}$$

Introducing, in addition, the "parallel" $\hat{\sigma}_{\parallel}^{(r)}$ and "perpendicular" $\hat{\sigma}_{\perp}^{(r)}$ projections of the fluctuation variables $\hat{\boldsymbol{\sigma}}^{(r)}$

$$\hat{\sigma}_{\parallel}^{(r)} = \sqrt{\frac{3}{2}\hat{\boldsymbol{\sigma}}^{(r)} \cdot \mathbf{E}^{(r)}\hat{\boldsymbol{\sigma}}^{(r)}}, \qquad \hat{\sigma}_{\perp}^{(r)} = \sqrt{\frac{3}{2}\hat{\boldsymbol{\sigma}}^{(r)} \cdot \mathbf{F}^{(r)}\hat{\boldsymbol{\sigma}}^{(r)}}, \tag{2.78}$$

it can be shown that the generalized-secant (2.63) and fluctuation (2.73) equations reduce respectively to the following system of scalar equations

$$\frac{\hat{\sigma}_{||}^{(r)}\widetilde{\psi}^{(r)'}(\hat{\sigma}_e^{(r)})}{\hat{\sigma}_e^{(r)}} - \widetilde{\psi}^{(r)'}(\sigma_e^{(r)}) = \frac{1}{3\lambda_{\mathbf{E}}^{(r)}}(\hat{\sigma}_{||}^{(r)} - \sigma_e^{(r)}), \qquad \frac{\widetilde{\psi}^{(r)'}(\hat{\sigma}_e^{(r)})}{\hat{\sigma}_e^{(r)}} = \frac{1}{3\lambda_{\mathbf{F}}^{(r)}}, \tag{2.79}$$

where $\hat{\sigma}_e^{(r)} = \sqrt{(\hat{\sigma}_{\parallel}^{(r)})^2 + (\hat{\sigma}_{\perp}^{(r)})^2}$, and

$$\hat{\sigma}_{||}^{(r)} = \sigma_e^{(r)} \pm \sqrt{\frac{3}{c^{(r)}}\frac{\partial\tilde{u}_T}{\partial(2\lambda_{\mathbf{E}}^{(r)})^{-1}}}, \qquad \hat{\sigma}_{\perp}^{(r)} = \pm\sqrt{\frac{3}{c^{(r)}}\frac{\partial\tilde{u}_T}{\partial(2\lambda_{\mathbf{F}}^{(r)})^{-1}}}, \tag{2.80}$$

for the unknowns $\hat{\sigma}_{\parallel}^{(r)}$, $\hat{\sigma}_{\perp}^{(r)}$, $\lambda_{\mathbf{E}}^{(r)}$ and $\lambda_{\mathbf{F}}^{(r)}$. It should be remarked at this point that, for given values of the reference tensors $\boldsymbol{\sigma}^{(r)}$ and $\mathbf{M}^{(r)}$, the effective potential $\tilde{u}_T$ of the LCC, entering the

calculations in (2.80), is completely determined by means of the estimates for linear thermoelastic composites provided in subsection 2.5.4. Finally, it can be easily shown that the GSO estimate (2.74) for the composite material under consideration reduces to

$$\tilde{u}(\overline{\boldsymbol{\sigma}}) = \sum_{r=1}^{N} c^{(r)} \left[\widetilde{\psi}^{(r)}(\hat{\sigma}_e^{(r)}) + \widetilde{\psi}^{(r)'}(\sigma_e^{(r)})(\overline{\sigma}_{||}^{(r)} - \hat{\sigma}_{||}^{(r)}) \right], \tag{2.81}$$

where $\overline{\sigma}_{||}^{(r)} = 3\overline{\boldsymbol{\sigma}}^{(r)} \cdot \boldsymbol{\sigma}^{(r)}/(2\sigma_e^{(r)})$, with $\overline{\boldsymbol{\sigma}}^{(r)}$ determined by (2.70) along with the corresponding results for linear thermoelastic composites of subsection 2.5.4.

As already mentioned, the optimal choice for the reference stress-tensors $\boldsymbol{\sigma}^{(r)}$ in the context of the GSO estimate (2.81) is still an open problem. In the relevant applications of this work considered in chapter 3, following Idiart et. al [64], we will make use of the prescriptions $\boldsymbol{\sigma}^{(r)} = \overline{\boldsymbol{\sigma}}$ for all $r = 1, .., N$.

Polycrystals. We conclude this subsection by discussing the associated GSO method of Liu and Ponte Castañeda [86] for a polycrystal with single-crystal phase-potentials $\tilde{u}^{(r)}$ of the form

$$\tilde{u}^{(r)}(\boldsymbol{\sigma}) = \sum_{k=1}^{K^{(r)}} \tilde{\psi}_k^{(r)}(\tau_k^{(r)}), \tag{2.82}$$

where $K^{(r)}$ denotes the number of slip systems of the single-crystal r, $\tau_k^{(r)} = \boldsymbol{\sigma} \cdot \boldsymbol{\mu}_k^{(r)}$ is the resolved shear stress in the $k-th$ slip system of the single-crystal r and $\boldsymbol{\mu}_k^{(r)}$ (given by an expression analogous to (2.34)) is the associated symmetric Schmidt tensor. Following Liu and Ponte Castañeda [86], we chose the stress phase-averages as the reference stresses, i.e., $\boldsymbol{\sigma}^{(r)} = \overline{\boldsymbol{\sigma}}^{(r)}$, and consider a single-scale LCC (2.59) with phase-potentials $u_T^{(r)}$ of the form

$$u_T^{(r)}(\boldsymbol{\sigma}) = \frac{1}{2}\boldsymbol{\sigma} \cdot \mathbf{M}^{(r)}\boldsymbol{\sigma} + \boldsymbol{\alpha}^{(r)} \cdot \boldsymbol{\sigma}, \tag{2.83}$$

where

$$\mathbf{M}^{(r)} = \sum_{k=1}^{K^{(r)}} \alpha_k^{(r)} \boldsymbol{\mu}_k^{(r)} \otimes \boldsymbol{\mu}_k^{(r)}, \qquad \boldsymbol{\alpha}^{(r)} = \frac{\partial u^{(r)}}{\partial \boldsymbol{\sigma}}(\overline{\boldsymbol{\sigma}}^{(r)}) - \mathbf{M}^{(r)} \cdot \overline{\boldsymbol{\sigma}}^{(r)}. \tag{2.84}$$

In this case, the generalized-secant conditions and the fluctuation equations reduce to

$$\frac{d\,\tilde{\psi}_k^{(r)}}{d\,\tau_k^{(r)}}(\hat{\tau}_k^{(r)}) - \frac{d\,\tilde{\psi}_k^{(r)}}{d\,\tau_k^{(r)}}(\overline{\tau}_k^{(r)}) = \alpha_k^{(r)} \left(\hat{\tau}_k^{(r)} - \overline{\tau}_k^{(r)} \right), \tag{2.85}$$

and

$$\hat{\tau}_k^{(r)} = \overline{\tau}_k^{(r)} \pm \sqrt{\frac{2}{c^{(r)}} \frac{\partial \tilde{u}_T}{\partial \alpha_k^{(r)}}}, \tag{2.86}$$

respectively, where $\overline{\tau}_k^{(r)} = \overline{\boldsymbol{\sigma}}^{(r)} \cdot \boldsymbol{\mu}_k^{(r)}$ and the LCC phase-averages $\overline{\boldsymbol{\sigma}}^{(r)}$ are given by (2.70) together with the corresponding results of subsection 2.5.4. Given that $\tilde{u}_T$ may also be determined from the

estimates of subsection 2.5.4, expressions (2.85) and (2.86) provide a system of equations for the unknown scalar moduli $\alpha_k^{(r)}$ and the fluctuation variables $\hat{\tau}_k^{(r)}$. It should be emphasized however that $\hat{\tau}_k^{(r)} \neq \hat{\boldsymbol{\sigma}}^{(r)} \cdot \boldsymbol{\mu}_k^{(r)}$, in general.

Finally, taking into account the above results it can be shown that the GSO estimate for the polycrystal reads as follows

$$\tilde{u}(\overline{\boldsymbol{\sigma}}) = \sum_{r=1}^{N} c^{(r)} \left[\tilde{\psi}_k^{(r)}(\hat{\tau}_k^{(r)}) + \frac{d\,\tilde{\psi}_k^{(r)}}{d\,\tau_k^{(r)}}(\overline{\tau}_k^{(r)})(\overline{\tau}_k^{(r)} - \hat{\tau}_k^{(r)} \right]. \tag{2.87}$$

2.5.4 Estimates for single-scale linear thermoelastic composites

This subsection deals with the computation of the effective properties of the *linear thermoelastic* (comparison) composites (LCCs) entering the calculation of the estimates for the overall response of single-scale nonlinear composites, discussed in the previous subsections. Specifically, we review estimates from the literature for random, *single-scale* systems with granular (Fig. 2.1(a)) and particulate (Fig. 2.2(a)) sub-structures incorporating dependence on one- and two-point statistics (see subsections 2.1.1 and 2.2.1). The results presented here are equally useful in the context of the various estimates for two-scale nonlinear composites that are developed in subsequent parts of this work.

For convenience, we express the local stress-potential u_T of an *incompressible*, N-phase, single-scale linear thermoelastic composite as

$$u_T(\mathbf{x}, \boldsymbol{\sigma}) = \sum_{r=1}^{N} \chi^{(r)}(\mathbf{x}) u_T^{(r)}(\boldsymbol{\sigma}), \qquad u^{(r)}(\boldsymbol{\sigma}) = \frac{1}{2}\boldsymbol{\sigma} \cdot \mathbf{M}^{(r)}\boldsymbol{\sigma} + \boldsymbol{\alpha}^{(r)} \cdot \boldsymbol{\sigma} + \phi^{(r)}, \tag{2.88}$$

where the material constants $\mathbf{M}^{(r)}$, $\boldsymbol{\alpha}^{(r)}$ and $\phi^{(r)}$ are assumed to be known; they stand respectively for the compliance tensor, the thermal strain tensor and the specific heat of phase r. The effective stress-potential $\tilde{u}_T$ of this material may be written in the form

$$\tilde{u}_T(\overline{\boldsymbol{\sigma}}) = \frac{1}{2}\overline{\boldsymbol{\sigma}} \cdot \widetilde{\mathbf{M}}\overline{\boldsymbol{\sigma}} + \widetilde{\boldsymbol{\alpha}} \cdot \overline{\boldsymbol{\sigma}} + \tilde{\phi}, \tag{2.89}$$

where $\widetilde{\mathbf{M}}$, $\widetilde{\boldsymbol{\alpha}}$ and $\tilde{\phi}$ are respectively the effective modulus, thermal strain and specific heat of the composite. These later quantities may be expressed in terms of the stress concentration tensors $\mathbf{B}^{(r)}$ and $\mathbf{b}^{(r)}$ as follows

$$\widetilde{\mathbf{M}} = \sum_{r=1}^{N} c^{(r)} \mathbf{M}^{(r)} \mathbf{B}^{(r)}, \quad \widetilde{\boldsymbol{\alpha}} = \sum_{r=1}^{N} c^{(r)} \left(\mathbf{B}^{(r)}\right)^T \boldsymbol{\alpha}^{(r)}, \quad \tilde{\phi} = \sum_{r=1}^{N} c^{(r)} \phi^{(r)} + \frac{1}{2} \sum_{r=1}^{N} c^{(r)} \boldsymbol{\alpha}^{(r)} \cdot \mathbf{b}^{(r)}. \tag{2.90}$$

Note that the concentration tensors $\mathbf{B}^{(r)}$ and $\mathbf{b}^{(r)}$ satisfy the identities

$$\sum_{r=1}^{N} c^{(r)} \mathbf{B}^{(r)} = \mathbf{K}, \qquad \sum_{r=1}^{N} c^{(r)} \mathbf{b}^{(r)} = \mathbf{0}, \tag{2.91}$$

where $\mathbf{K}$ is the identity tensor in the deviatoric space of fully symmetric forth-order tensors, but they are otherwise unknown. The computation of these tensors requires the solution of the variational problem (2.66), which completely determines, in principle, the effective behavior of the material under consideration. Despite its linear character, this problem is very difficult to solve, and exact results can be found in the literature only for very special types of sub-structures and loading conditions. A more pragmatic approach to the variational problem (2.66) consists in employing the variational principle of Hashin and Shtrikman [47] and generalizations due to Willis [150, 152]. This approach has the merits of incorporating dependence on both one- and two-point statistical information and delivering bounds and estimates for the effective properties of linear thermoelastic media that are exact to second-order in the heterogeneity contrast. With the objective of making more clear the way in which the two-point statistics are accounted for, we briefly outlined this approach next, and refer to Willis [152] for details.

The variational problem (2.66) can be expressed, equivalently, by means of a variational principle of the Hashin-Shtrikman type, i.e., a statement in terms of a "strain-polarization" field $\boldsymbol{\eta}(\mathbf{x})$, which is defined as the difference of the infinitesimal strain tensor in the linear thermoelastic composite under consideration and the strain tensor in a reference linear thermoelastic *homogeneous* material. Let the compliance and stiffness modulus tensors of the reference material be $\mathbf{M}^{(0)} + \mathbf{J}/(3\kappa^{(0)})$ and $\mathbf{L}^{(0)} + (3\kappa^{(0)})\mathbf{J}$, respectively, where $\kappa^{(0)}$ denotes its bulk modulus, $\mathbf{M}^{(0)}$ and $\mathbf{L}^{(0)}$ being inverse deviatoric modulus tensors and $\mathbf{J}$ is the volumetric forth-order identity tensor, so that $\mathbf{M}^{(0)}\mathbf{L}^{(0)} = \mathbf{K}$ and $\mathbf{M}^{(0)}\mathbf{J} = \mathbf{J}\mathbf{M}^{(0)} = \mathbf{L}^{(0)}\mathbf{J} = \mathbf{J}\mathbf{L}^{(0)} = \mathbf{0}$. Incompressible behavior will be recovered later on by taking the limit $\kappa^{(0)} \to \infty$. Accordingly, the associated boundary value problem for the stress field in the composite is expressed as an integral (linear) equation for $\boldsymbol{\eta}(\mathbf{x})$ in terms of an integral operator depending on the infinite-body Green's function associated with the homogeneous reference medium. Restricting attention to constant per phase trial fields $\boldsymbol{\eta}(\mathbf{x}) = \sum_{r=1}^{N} \chi^{(r)}(\mathbf{x})\boldsymbol{\eta}^{(r)}$, the integral operator reduces to constant per phase, forth-order tensor operators depending on the associated two-point probability functions, and therefore the integral equation for $\boldsymbol{\eta}(\mathbf{x})$ reduces to a set of algebraic equations for $\boldsymbol{\eta}^{(r)}$. When ellipsoidal symmetry is assumed for the two-point probabilities (see subsection 2.1.1), these tensor operators take a fairly simple form. As already mentioned, in this work we focus attention on composites for which the distribution of all phases is characterized by the same shape tensor $\mathbf{Z}$, which in the case of a particulate system characterize the shape and orientation of the inclusions as well. For these special sub-structures, the aforementioned forth-order tensor operators for the phases reduce to a single

tensor $\mathbf{Q}$, given by

$$\mathbf{Q} = \mathbf{L}^{(0)} - \mathbf{L}^{(0)}\mathbf{P}\mathbf{L}^{(0)}, \qquad \mathbf{P} = \frac{1}{4\pi \det \mathbf{Z}} \int_{|\boldsymbol{\xi}|=1} \mathbf{H}\, |\mathbf{Z}^{-1}\boldsymbol{\xi}|^{-3} dS,$$
$$H_{ijkl} = \lim_{\kappa^{(0)} \to \infty} \left[(\mathbf{N}^{-1})_{ik}\right] \xi_j \xi_l|_{(ij)(kl)}, \qquad N_{ij} = \left[\mathbf{L}^{(0)} + (3\kappa^{(0)})\mathbf{J}\right]_{ipjq} \xi_p \xi_q, \tag{2.92}$$

The parentheses in the subscripts of $(2.92)_3$ indicate symmetrization with respect to these indexes. The above simplifying assumptions allow the determination of closed-form expressions for the polarizations $\boldsymbol{\eta}^{(r)}$ in terms of the modulus $\mathbf{M}^{(0)}$ of the reference medium, the phase modulus tensors $\mathbf{M}^{(r)}$ of the actual linear thermoelastic composite and the microstructural tensor $\mathbf{Q}$, which as already mentioned depends on the two-point probability functions. These results may be used to generate corresponding estimates for the phase averages of the stress field, which, in turn, completely determine the effective behavior of the composite. Note that this method does not provide any prescriptions for the modulus tensor $\mathbf{M}^{(0)}$ (or $\mathbf{L}^{(0)}$) of the reference medium, which should therefore be chosen based on physical arguments. Without further details, we provide next the final expressions obtained in this way for the effective modulus tensor $\widetilde{\mathbf{M}}$ and the stress concentration tensors $\mathbf{B}^{(r)}$, $\mathbf{b}^{(r)}$ of linear thermoelastic composites with granular and particulate sub-structures.

Granular composites. In the case of an *incompressible* composite with granular microstructure no distinction can be made in the roles of the phases, and therefore it seems more reasonable to chose the effective modulus tensor as the reference modulus, i.e., $\mathbf{M}^{(0)} = \widetilde{\mathbf{M}}$. This prescription leads to the following self-consistent estimate for $\widetilde{\mathbf{M}}$

$$\widetilde{\mathbf{M}} = \left\{ \sum_{r=1}^{N} c^{(r)} \left[\mathbf{M}^{(r)} + \widetilde{\mathbf{M}}^{*}\right]^{-1} \right\}^{-1} - \widetilde{\mathbf{M}}^{*}, \tag{2.93}$$

where $\widetilde{\mathbf{M}}^{*} = \mathbf{Q}^{-1} - \widetilde{\mathbf{M}}$ and $\mathbf{Q}$ is given by (2.92) with $\mathbf{L}^{(0)} = \widetilde{\mathbf{M}}^{-1}$. Note that equation (2.93) is implicit and, therefore, it should be solved iteratively. The estimate (2.93) has been derived independently by various authors (see, e.g., Willis [152]). Finally, the associated stress concentration tensors $\mathbf{B}^{(r)}$ and $\mathbf{b}^{(r)}$ are respectively given by (see, e.g., Laws [72])

$$\mathbf{B}^{(r)} = \left[\mathbf{M}^{(r)} + \widetilde{\mathbf{M}}^{*}\right]^{-1} \mathbf{Q}^{-1}, \qquad \mathbf{b}^{(r)} = \left[\mathbf{M}^{(r)} + \widetilde{\mathbf{M}}^{*}\right]^{-1} \left(\widetilde{\boldsymbol{\alpha}} - \boldsymbol{\alpha}^{(r)}\right). \tag{2.94}$$

Particulate composites. For an *incompressible*, random composite made out of a well-defined matrix phase ($r = 1$) in which are embedded inclusions ($r = 2, ..., N$) it is more natural to chose the matrix as the reference homogeneous medium, i.e., $\mathbf{M}^{(0)} = \mathbf{M}^{(1)}$, in which case, the following estimate is obtained (see Willis [153]) for the effective modulus tensor $\widetilde{\mathbf{M}}$ of the composite

$$\widetilde{\mathbf{M}} = \sum_{r=1}^{N} c^{(r)} \mathbf{M}^{(r)} \left[\mathbf{K} + \mathbf{Q}(\mathbf{M}^{(1)} - \mathbf{M}^{(r)})\right]^{-1} \left\{ \sum_{s=1}^{N} c^{(s)} \left[\mathbf{K} + \mathbf{Q}(\mathbf{M}^{(1)} - \mathbf{M}^{(s)})\right]^{-1} \right\}^{-1}, \tag{2.95}$$

where we recall that $\mathbf{K}$ denotes the forth-order identity tensor in the deviatoric space. The stress concentration tensors $\mathbf{B}^{(r)}$ and $\mathbf{b}^{(r)}$ are, in this case, respectively given by

$$\mathbf{B}^{(r)} = \left[\mathbf{K} + \mathbf{Q}(\mathbf{M}^{(1)} - \mathbf{M}^{(r)})\right]^{-1} \left\{ \sum_{s=1}^{N} c^{(s)} \left[\mathbf{K} + \mathbf{Q}(\mathbf{M}^{(1)} - \mathbf{M}^{(s)})\right]^{-1} \right\}^{-1},$$
$$\mathbf{b}^{(r)} = \left[\mathbf{Q}^{-1} + (\mathbf{M}^{(r)} - \mathbf{M}^{(1)})\right]^{-1} \left(\widetilde{\boldsymbol{\alpha}} - \boldsymbol{\alpha}^{(r)}\right), \tag{2.96}$$

where $\widetilde{\boldsymbol{\alpha}}$ is given by $(2.90)_2$. The forth-order tensor $\mathbf{Q}$ in the above expressions is given by (2.92) with $\mathbf{L}^{(0)} = (\mathbf{M}^{(1)})^{-1}$.

In acknowledgement of his significant contribution on the development of these results, the estimate (2.95) will be referred to in the sequel as the Willis estimate.

2.6 Secant method for two-scale composites

This section deals with the extension of the secant method [116] of subsection 2.5.1 to two-scale viscoplastic composites. In particular, subsections 2.6.1 and 2.6.2 discuss respectively the implementation of the secant linearization scheme to the direct (2.44) and sequential (2.42), with (2.45), variational problems for the determination of corresponding bounds and estimates for the effective stress-potential $\tilde{u}$ of two-scale systems with *isotropic* constituents. Although a more general discussion is beyond the objectives of this thesis, it should be remarked that corresponding bounds and estimates for two-scale systems with *anisotropic* phases may also be obtained through a suitable generalization of the results of this section along with the variational procedure of Idiart and Ponte Castañeda [62].

2.6.1 Direct linearization scheme

Consider a two-scale nonlinear composite with local stress-potential given by expressions $(2.31)_2$ and $(2.31)_3$, where the phase-potentials $u^{(r,p)}$ are taken to be isotropic and to depend on the stress tensor $\boldsymbol{\sigma}$ only through the equivalent stress $\sigma_e = \sqrt{3\boldsymbol{\sigma}_d \cdot \boldsymbol{\sigma}_d/2}$, i.e.,

$$u^{(r,p)}(\boldsymbol{\sigma}) = \psi^{(r,p)}(\sigma_e) \equiv f^{(r,p)}(\sigma_e^2), \tag{2.97}$$

In agreement with the discussion of subsection 2.5.1, we assume that $f^{(r,p)}$ in $(2.97)_2$ are non-negative, convex functions of σ_e^2, such that $f^{(r,p)} \to \infty$ as $\sigma_e^2 \to \infty$ (e.g., the power-law relation (2.33) satisfies these requirements).

Next, we introduce a two-scale linear elastic comparison composite (LCC) with the same substructure as the actual nonlinear medium, characterized by the stress-potential

$$u_L(\mathbf{x},\boldsymbol{\sigma};\lambda^{(r,p)}) = \sum_{r=1}^{N} \chi^{(r)}(\mathbf{x}) u_L^{(r)}(\mathbf{x},\boldsymbol{\sigma};\lambda^{(r,p)}), \quad u_L^{(r)}(\mathbf{x},\boldsymbol{\sigma};\lambda^{(r,p)}) = \sum_{p=1}^{N^{(r)}} \chi^{(r,p)}(\mathbf{x}) u_L^{(r,p)}(\boldsymbol{\sigma};\lambda^{(r,p)}), \tag{2.98}$$

with

$$u_L^{(r,p)}(\boldsymbol{\sigma};\lambda^{(r,p)}) = \frac{1}{2}\boldsymbol{\sigma}\cdot\mathbf{M}^{(r,p)}\boldsymbol{\sigma}, \qquad \mathbf{M}^{(r,p)} = \frac{1}{2\lambda^{(r,p)}}\mathbf{K}, \tag{2.99}$$

where we recall that $\mathbf{K}$ denotes the fourth-order identity tensor in the deviatoric space and $\lambda^{(r,p)}$ are scalar moduli, which at this stage are unknown. Furthermore, we introduce the error function

$$V(\mathbf{x};\lambda^{(r,p)}) = \sum_{r=1}^{N} \chi^{(r)}(\mathbf{x}) V^{(r,p)}(\mathbf{x};\lambda^{(r,p)}), \qquad V^{(r,p)}(\mathbf{x};\lambda^{(r,p)}) = \sum_{p=1}^{N^{(r)}} \chi^{(r,p)}(\mathbf{x}) V^{(r,p)}(\lambda^{(r,p)}) \tag{2.100}$$

where

$$V^{(r,p)}(\lambda^{(r,p)}) = \sup_{\hat{\boldsymbol{\sigma}}^{(r,p)}} \left[u_L^{(r,p)}(\hat{\boldsymbol{\sigma}}^{(r,p)};\lambda^{(r,p)}) - u^{(r,p)}(\hat{\boldsymbol{\sigma}}^{(r,p)}) \right]. \tag{2.101}$$

Taking into account these definitions, the direct variational principle (2.44) may be equivalently expressed as

$$\tilde{u}(\overline{\boldsymbol{\sigma}}) = \min_{\boldsymbol{\sigma}\in\mathcal{S}(\overline{\boldsymbol{\sigma}})} \langle \sup_{\substack{\lambda^{(s,q)} \\ s=1,..,N \\ q=1,..,N^{(s)}}} \left[u_L(\mathbf{x},\boldsymbol{\sigma};\lambda^{(r,p)}) - V(\mathbf{x};\lambda^{(r,p)}) \right] \rangle, \tag{2.102}$$

which after interchanging the order of the optimality operations [32] reduces to

$$\tilde{u}(\overline{\boldsymbol{\sigma}}) = \sup_{\substack{\lambda^{(s,q)}(\mathbf{x}) \\ s=1,..,N \\ q=1,..,N^{(s)}}} \left[\tilde{u}_L(\overline{\boldsymbol{\sigma}};\lambda^{(r,p)}) - \sum_{r=1}^{N} c^{(r)} \sum_{p=1}^{N^{(r)}} c^{(r,p)} \langle V^{(r,p)}\left(\lambda^{(r,p)}\right)\rangle^{(r,p)} \right], \tag{2.103}$$

where $\tilde{u}_L$ is the effective stress-potential of the two-scale LCC (2.98), with (2.99). Notice that, since the LCC under consideration may be regarded as a special case of the nonlinear two-scale composite, the function $\tilde{u}_L$ may be determined, in principle, either through the direct variational problem (2.44) or by the sequential problem (2.42), with (2.45).

Assuming that the scalar moduli $\lambda^{(r,p)}$ are constant-per-phase, the variational principle (2.103) yields the following bound for $\tilde{u}$

$$\tilde{u}(\overline{\boldsymbol{\sigma}}) \geq \sup_{\substack{\lambda^{(s,q)} \\ s=1,..,N \\ q=1,..,N^{(s)}}} \left[\tilde{u}_L(\overline{\boldsymbol{\sigma}};\lambda^{(r,p)}) - \sum_{r=1}^{N} c^{(r)} \sum_{p=1}^{N^{(r)}} c^{(r,p)} V^{(r,p)}\left(\lambda^{(r,p)}\right) \right], \tag{2.104}$$

while the optimality conditions in (2.101) and (2.104) reduce respectively to

$$\frac{1}{2\lambda^{(r,p)}} = \frac{3\psi^{(r,p)'}(\hat{\sigma}_e^{(r,p)})}{2\hat{\sigma}_e^{(r,p)}}, \tag{2.105}$$

and

$$\hat{\sigma}_e^{(r,p)} = \sqrt{\langle \sigma_e^2 \rangle^{(r,p)}} = \sqrt{\frac{3}{2c^{(r)}c^{(r,p)}}\overline{\boldsymbol{\sigma}} \cdot \frac{\partial \widetilde{\mathbf{M}}}{\partial (2\lambda^{(r,p)})^{-1}}\overline{\boldsymbol{\sigma}}}. \tag{2.106}$$

Thus, based on conditions (2.105) and (2.106), the homogeneous-phase-moduli $\lambda^{(r,p)}$ may be interpreted as the secant moduli of the corresponding nonlinear phases evaluated at the second-moments of the stress field in the homogeneous-phases of the LCC. Finally, making use of the result (2.106), the bound (2.104) may be rewritten as

$$\tilde{u}(\overline{\boldsymbol{\sigma}}) \geq \sum_{r=1}^{N} c^{(r)} \sum_{p=1}^{N^{(r)}} c^{(r,p)} \psi^{(r,p)} \left(\hat{\sigma}_e^{(r,p)} \right). \tag{2.107}$$

At this point it should be emphasized that, in general, the effective stress-potential $\tilde{u}_L$ of the two-scale LCC can not be computed exactly. If a lower bound is used for $\tilde{u}_L$ the bounding character of (2.107) is preserved, while if an upper bound or any other type of estimate is used for $\tilde{u}_L$ the right-hand-side of (2.107) provides simply an estimate for $\tilde{u}$. In any case, $\tilde{u}_L$ is given by an expression of the form (2.54) in terms of the associated effective modulus tensor $\widetilde{\mathbf{M}}$.

The effective modulus tensor $\widetilde{\mathbf{M}}$ of the two-scale LCC will be estimated in this work by means of the sequential approach (2.42), with (2.45), making use of the self-consistent estimate (2.93) for the case of a granular system and the Willis estimate (2.95) for the case of a particulate system. It should be remarked, however, that analogous estimates may be obtained based on the direct variational approach (2.44), but the relevant calculations turn out to be more involved. In particular, $\widetilde{\mathbf{M}}$ will be computed by means of expressions (2.93) and (2.95), as appropriate, where the quantities $\mathbf{M}^{(r)}$ correspond to the effective modulus tensors of the composite-phases of the LCC. In the case of a granular composite-phase r, $\mathbf{M}^{(r)}$ is determined by the relevant self-consistent estimate

$$\mathbf{M}^{(r)} = \left\{ \sum_{p=1}^{N^{(r)}} c^{(r,p)} \left[\mathbf{M}^{(r,p)} + \mathbf{M}^{(r)^*} \right]^{-1} \right\}^{-1} - \mathbf{M}^{(r)^*}, \tag{2.108}$$

where $\mathbf{M}^{(r)^*} = \mathbf{Q}^{-1} - \mathbf{M}^{(r)}$ and $\mathbf{Q}$ is given by (2.92) with $\mathbf{L}^{(0)} = (\mathbf{M}^{(r)})^{-1}$ and $\mathbf{Z} = \mathbf{Z}^{(r)}$. In the case of a particulate composite-phase r, $\mathbf{M}^{(r)}$ is computed by means of the associated Willis estimate

$$\mathbf{M}^{(r)} = \sum_{p=1}^{N^{(r)}} c^{(r,p)} \mathbf{M}^{(r,p)} \left[\mathbf{K} + \mathbf{Q}(\mathbf{M}^{(r,1)} - \mathbf{M}^{(r,p)}) \right]^{-1} \left\{ \sum_{q=1}^{N^{(r)}} c^{(r,q)} \left[\mathbf{K} + \mathbf{Q}(\mathbf{M}^{(r,1)} - \mathbf{M}^{(r,q)}) \right]^{-1} \right\}^{-1}, \tag{2.109}$$

where the sub-structural tensor $\mathbf{Q}$, given by (2.92), must be evaluated at $\mathbf{L}^{(0)} = (\mathbf{M}^{(r,1)})^{-1}$ and $\mathbf{Z} = \mathbf{Z}^{(r)}$. It is recalled that $\mathbf{M}^{(r,1)}$ in (2.109) corresponds to the modulus tensor of the homogeneous-matrix-phase within the composite-phase r of the LCC.

2.6.2 Sequential linearization scheme

The implementation of the secant method to the sequential variational problem (2.42), with (2.45), for a two-scale nonlinear composite consists in applying the secant procedure of subsection 2.5.1 for single-scale composites multiple times. In particular, given the *homogenized* potential functions $\tilde{u}^{(r)}$ for the composite-phases—assumed to be of the form (2.47)—the effective stress-potential $\tilde{u}$, defined by (2.42), of a two-scale composite is computed by means of the secant estimate (2.58), as discussed in subsection 2.5.1. Therefore, the computation of $\tilde{u}$ reduces to determining the potentials $\tilde{u}^{(r)}$, which are defined by means of the variational principle (2.45). The variational problem (2.45) is also a homogenization problem for a single-scale composite with phase-potentials $u^{(r,p)}$, defined by (2.97), and therefore the secant procedure of subsection 2.5.1 applies for this problem as well. Next, for completeness, we briefly outline the treatment of (2.45) by means of the secant method.

In the context of the single-scale variational problem (2.45) for the composite-phase r of the nonlinear medium, we consider a single-scale LCC (Figs. 2.1(b) and 2.2(b)) characterized by a local stress-potential

$$u_L^{(r)}(\mathbf{x},\boldsymbol{\tau};\lambda^{(r,p)}) = \sum_{p=1}^{N^{(r)}} \chi^{(r,p)}(\mathbf{x}) u_L^{(r,p)}(\boldsymbol{\tau};\lambda^{(r,p)}), \tag{2.110}$$

where the potential functions $u_L^{(r,p)}(\boldsymbol{\tau};\lambda^{(r,p)})$ are given by (2.99), and $\boldsymbol{\tau}$ stands here for the local stress field developed in the LCC under an average applied stress $\boldsymbol{\sigma}$. Furthermore, we consider the error function

$$V^{(r)}(\mathbf{x};\lambda^{(r,p)}) = \sum_{p=1}^{N^{(r)}} \chi^{(r,p)}(\mathbf{x}) V^{(r,p)}(\lambda^{(r,p)}), \tag{2.111}$$

where the functions $V^{(r,p)}$ are defined by (2.101). Under these considerations, the original variational principle (2.45) admits the following alternative representation

$$\tilde{u}^{(r)}(\boldsymbol{\sigma}) = \sup_{\substack{\lambda^{(r,q)}(\mathbf{x}) \\ q=1,..,N^{(r)}}} \left[\tilde{u}_L^{(r)}(\boldsymbol{\sigma};\lambda^{(r,p)}) - \sum_{p=1}^{N^{(r)}} c^{(r,p)} \langle V^{(r,p)} \left(\lambda^{(r,p)} \right) \rangle^{(r,p)} \right], \tag{2.112}$$

where $\tilde{u}_L^{(r)}$ denotes the effective stress-potential of the single-scale LCC (2.110), which is determined by means of the variational principle (2.45) and may be expressed in terms of the associated effective modulus tensor $\mathbf{M}^{(r)}$ as

$$\tilde{u}_L^{(r)}(\boldsymbol{\sigma}) = \frac{1}{2}\boldsymbol{\sigma} \cdot \mathbf{M}^{(r)} \boldsymbol{\sigma}. \tag{2.113}$$

Next, assuming that the LCC phase-moduli $\lambda^{(r,p)}$ in (2.112) are constant for each $p = 1, ..., N^{(r)}$,

we obtain the following bound for $\tilde{u}^{(r)}$

$$\tilde{u}^{(r)}(\boldsymbol{\sigma}) \geq \sup_{\substack{\lambda^{(r,q)} \\ q=1,..,N^{(r)}}} \left[\tilde{u}_L^{(r)}(\boldsymbol{\sigma};\lambda^{(r,p)}) - \sum_{p=1}^{N^{(r)}} c^{(r,p)} V^{(r,p)} \left(\lambda^{(r,p)} \right) \right]. \tag{2.114}$$

In addition, the optimality conditions in (2.101) read as (2.105), while the optimality conditions in (2.114) reduce to

$$\hat{\sigma}_e^{(r,p)} = \sqrt{\langle \tau_e^2 \rangle^{(r,p)}} = \sqrt{\frac{3}{2c^{(r,p)}} \boldsymbol{\sigma} \cdot \frac{\partial \mathbf{M}^{(r)}}{\partial (2\lambda^{(r,p)})^{-1}} \boldsymbol{\sigma}}. \tag{2.115}$$

Making use of the above result, the bound (2.114) may also be expressed in the form

$$\tilde{u}^{(r)}(\boldsymbol{\sigma}) \geq \sum_{p=1}^{N^{(r)}} c^{(r,p)} \psi^{(r,p)} \left(\hat{\sigma}_e^{(r,p)} \right), \tag{2.116}$$

in the context of which it is implicitly assumed that a lower bound is used for $\tilde{u}_L^{(r)}$, since the use of any other estimate for $\tilde{u}_L^{(r)}$ in the right-hand-side of (2.116) leads to a corresponding estimate for $\tilde{u}^{(r)}$, which is not necessarily a bound.

The effective modulus tensors $\mathbf{M}^{(r)}$ in (2.113) will be computed in this work by means of the estimates (2.108) and (2.109) for granular and particulate systems, respectively. Furthermore, in order to guaranty isotropy of the homogenized potentials $\tilde{u}^{(r)}(\boldsymbol{\sigma}) = \tilde{\psi}^{(r)}(\sigma_e)$ (required in the context of the secant estimate (2.58) for $\tilde{u}$) we have to restrict our attention to two-scale composites with microscopic two-point correlation functions characterized by statistical isotropy (see subsections 2.1.2 and 2.2.2), i.e., the shape tensors $\mathbf{Z}^{(r)}$ in the context of the estimates (2.108) and (2.109) must be taken to be such that $\mathbf{Z}^{(r)} = \mathbf{I}$. Under these considerations, it can be shown that the effective modulus tensor $\mathbf{M}^{(r)}$, obtained either from (2.108) or from (2.109), is of the form

$$\mathbf{M}^{(r)} = \frac{1}{2\tilde{\lambda}^{(r)}} \mathbf{K}, \tag{2.117}$$

where $\tilde{\lambda}^{(r)}$ denotes the associated effective scalar modulus. It is emphasized that the moduli $\tilde{\lambda}^{(r)}$ and $\lambda^{(r)}$ in expressions (2.117) and $(2.49)_2$, respectively, are equal. To see this, note that differentiation of the estimate (2.114) for the effective stress-potential $\tilde{\psi}^{(r)}(\sigma_e)$ of the composite-phase r with respect to the associated applied equivalent stress σ_e yields the result

$$\frac{1}{2\tilde{\lambda}^{(r)}} = \frac{3\tilde{\psi}^{(r)'}(\sigma_e)}{2\sigma_e}, \tag{2.118}$$

where use has been made of the fact that the right-hand-side of (2.114) is stationary with respect to both $\lambda^{(r,p)}$ and $\hat{\sigma}_e^{(r,p)}$. Now, in the context of the secant estimate (2.58) for the effective stress-potential $\tilde{u}$ of the two-scale composite of interest here, the right-hand-side of (2.118) must be evaluated at $\sigma_e = \hat{\sigma}_e^{(r)}$, with $\hat{\sigma}_e^{(r)}$ given by (2.57). This fact, in turn, implies that expressions (2.118) and (2.56) for $\tilde{\lambda}^{(r)}$ and $\lambda^{(r)}$, respectively, are identical.

On the equivalence of the direct and sequential secant estimates. We conclude this section by showing that the sequential secant estimate (2.58), with (2.116), is identical to the corresponding direct secant estimate (2.107). To this end, we first show that the sequential estimate (2.58), with (2.116), may be written in the form (2.107) and then we prove that the corresponding second-moment variables $\hat{\sigma}_e^{(r,p)}$ involved in these two expressions are equal.

Recall first that the estimate (2.116) provides an expression for the effective stress-potential $\tilde{\psi}^{(r)}$ of the composite-phase r, with $r = 1, ..., N$, as a function of the associated (arbitrary) applied equivalent stress σ_e. Furthermore, note that the dependence of the function $\tilde{\psi}^{(r)}$ on σ_e in expression (2.116) is exclusively induced thought the dependence of the phase-potentials $\psi^{(r,p)}$ on the associated second-moment variables $\hat{\sigma}_e^{(r,p)} = \hat{\sigma}_e^{(r,p)}(\sigma_e)$, given by (2.115). However, when expression (2.116) for $\tilde{\psi}^{(r)}$ is used in the context of the secant estimate (2.58) for the effective stress-potential $\tilde{u}$ of the two-scale composite, the functions $\tilde{\psi}^{(r)}$, and therefore the variables $\hat{\sigma}_e^{(r,p)}$, must be evaluated at $\sigma_e = \hat{\sigma}_e^{(r)}$, with $\hat{\sigma}_e^{(r)}$ given by (2.57). Hence, substituting expression (2.116) for $\tilde{\psi}^{(r)}(\hat{\sigma}_e^{(r)})$ into (2.58), the sequential secant estimate reduces to

$$\tilde{u}(\overline{\boldsymbol{\sigma}}) \geq \sum_{r=1}^{N} c^{(r)} \sum_{p=1}^{N^{(r)}} c^{(r,p)} \psi^{(r,p)} \left(\hat{\sigma}_e^{(r,p)}(\hat{\sigma}_e^{(r)}) \right), \tag{2.119}$$

where the fact that $\hat{\sigma}_e^{(r,p)}$ are evaluated at $\sigma_e = \hat{\sigma}_e^{(r)}$ has been emphasized. The above result shows that, in order to prove that the sequential and direct secant estimates are equivalent, it suffices to show that the corresponding arguments of the functions $\psi^{(r,p)}$ in expressions (2.119) and (2.107), i.e., the corresponding second-moment variables $\hat{\sigma}_e^{(r,p)}$, are equal.

The later statement may be shown as follows. In the context of the sequential estimate (2.119), substituting relation (2.117) for $\mathbf{M}^{(r)}$ into the expression (2.115) for the second-moment variables $\hat{\sigma}_e^{(r,p)}$, we find that

$$\hat{\sigma}_e^{(r,p)}(\sigma_e) = \sqrt{\frac{1}{c^{(r,p)}} \frac{\partial (2\tilde{\lambda}^{(r)})^{-1}}{\partial (2\lambda^{(r,p)})^{-1}} \sigma_e^2}, \tag{2.120}$$

which when evaluated at $\sigma_e = \hat{\sigma}_e^{(r)}$, with $\hat{\sigma}_e^{(r)}$ given by (2.57), yields the result

$$\hat{\sigma}_e^{(r,p)}(\hat{\sigma}_e^{(r)}) = \sqrt{\frac{3}{2c^{(r)}c^{(r,p)}} \overline{\boldsymbol{\sigma}} \cdot \frac{\partial \widetilde{\mathbf{M}}}{\partial (2\lambda^{(r)})^{-1}} \frac{\partial (2\tilde{\lambda}^{(r)})^{-1}}{\partial (2\lambda^{(r,p)})^{-1}} \overline{\boldsymbol{\sigma}}} = \sqrt{\frac{3}{2c^{(r)}c^{(r,p)}} \overline{\boldsymbol{\sigma}} \cdot \frac{\partial \widetilde{\mathbf{M}}}{\partial (2\lambda^{(r,p)})^{-1}} \overline{\boldsymbol{\sigma}}}, \tag{2.121}$$

where in $(2.121)_2$ use has been made of the fact that $\tilde{\lambda}^{(r)} = \lambda^{(r)}$. Thus, the second-moment equations (2.106) and (2.121), determining the variables $\hat{\sigma}_e^{(r,p)}$ in the context of the direct (2.107) and sequential (2.119) estimate, respectively, are identical, and this completes the proof that the direct and the sequential secant estimates are equivalent.

2.7 Tangent method for two-scale composites

In this section, we extend the *tangent* second-order (TSO) procedure [117] to two-scale composites. In analogy to the corresponding development of subsection 2.5.2 for the single-scale problem (2.42), in subsections 2.7.1 and 2.7.2 we discuss respectively the treatment of the direct (2.44) and sequential (2.42), along with (2.45), variational problems by means of suitable generalizations of the tangent linearization scheme in order to generate corresponding estimates for the effective stress-potential $\tilde{u}$ of the two-scale composite of interest in terms of the effective stress-potential $\tilde{u}_T$ of an LCC—with the same sub-structure as the actual nonlinear medium—and an associated error function. The effective properties of the LCCs involved in these procedures are determined by the appropriate generalization of the results of subsection 2.5.4.

2.7.1 Direct linearization scheme

Recalling from subsection 2.4.2 that the direct problem (2.44) refers to a two-scale nonlinear medium with local stress-potential defined by $(2.31)_2$, with $(2.31)_3$, towards an alternative representation of (2.44) we consider a two-scale LCC characterized by the stress-potential

$$\begin{aligned} u_T(\mathbf{x},\boldsymbol{\sigma};\boldsymbol{\sigma}^{(r,p)},\mathbf{M}^{(r,p)}) &= \sum_{r=1}^{N}\chi^{(r)}(\mathbf{x})u_T^{(r)}(\mathbf{x},\boldsymbol{\sigma};\boldsymbol{\sigma}^{(r,p)},\mathbf{M}^{(r,p)}),\\ u_T^{(r)}(\mathbf{x},\boldsymbol{\sigma};\boldsymbol{\sigma}^{(r,p)},\mathbf{M}^{(r,p)}) &= \sum_{p=1}^{N^{(r)}}\chi^{(r,p)}(\mathbf{x})u_T^{(r,p)}(\boldsymbol{\sigma};\boldsymbol{\sigma}^{(r,p)},\mathbf{M}^{(r,p)}), \end{aligned} \tag{2.122}$$

where the quadratic phase-potentials $u_T^{(r,p)}$ are taken to be of the form

$$\begin{aligned} u_T^{(r,p)}(\boldsymbol{\sigma};\boldsymbol{\sigma}^{(r,p)},\mathbf{M}^{(r,p)}) =& u^{(r,p)}(\boldsymbol{\sigma}^{(r,p)}) + \frac{\partial u^{(r,p)}}{\partial\boldsymbol{\sigma}}(\boldsymbol{\sigma}^{(r,p)})\cdot(\boldsymbol{\sigma}-\boldsymbol{\sigma}^{(r,p)})\\ &+\frac{1}{2}(\boldsymbol{\sigma}-\boldsymbol{\sigma}^{(r,p)})\cdot\mathbf{M}^{(r,p)}(\boldsymbol{\sigma}-\boldsymbol{\sigma}^{(r,p)}), \end{aligned} \tag{2.123}$$

The quantities $\boldsymbol{\sigma}^{(r,p)}$ and $\mathbf{M}^{(r,p)}$ in the above expression denote respectively reference stress and compliance tensors, assumed to be independent of the stress tensor $\boldsymbol{\sigma}$. In addition, we consider the error function

$$\begin{aligned} V(\mathbf{x};\boldsymbol{\sigma}^{(r,p)},\mathbf{M}^{(r,p)}) &= \sum_{r=1}^{N}\chi^{(r)}(\mathbf{x})V^{(r)}(\mathbf{x};\boldsymbol{\sigma}^{(r,p)},\mathbf{M}^{(r,p)}),\\ V^{(r)}(\mathbf{x};\boldsymbol{\sigma}^{(r,p)},\mathbf{M}^{(r,p)}) &= \sum_{p=1}^{N^{(r)}}\chi^{(r,p)}(\mathbf{x})V^{(r,p)}\left(\boldsymbol{\sigma}^{(r,p)},\mathbf{M}^{(r,p)}\right), \end{aligned} \tag{2.124}$$

with

$$V^{(r,p)}\left(\boldsymbol{\sigma}^{(r,p)},\mathbf{M}^{(r,p)}\right) = \underset{\hat{\boldsymbol{\sigma}}^{(r,p)}}{\text{stat}}\left[u^{(r,p)}(\hat{\boldsymbol{\sigma}}^{(r,p)}) - u_T^{(r,p)}(\hat{\boldsymbol{\sigma}}^{(r,p)};\boldsymbol{\sigma}^{(r,p)},\mathbf{M}^{(r,p)})\right], \tag{2.125}$$

where the variables $\hat{\boldsymbol{\sigma}}^{(r,p)}$ are determined by means of the associated stationarity conditions

$$\frac{\partial u^{(r,p)}}{\partial \boldsymbol{\sigma}}(\hat{\boldsymbol{\sigma}}^{(r,p)}) - \frac{\partial u^{(r,p)}}{\partial \boldsymbol{\sigma}}(\boldsymbol{\sigma}^{(r,p)}) = \mathbf{M}^{(r,p)}(\hat{\boldsymbol{\sigma}}^{(r,p)} - \boldsymbol{\sigma}^{(r,p)}). \tag{2.126}$$

Based on the two-scale LCC and the associated error function introduced above, the original variational principle (2.44) for the nonlinear composite of interest may be equivalently expressed as

$$\tilde{u}(\overline{\boldsymbol{\sigma}}) = \underset{\substack{\boldsymbol{\sigma}^{(s,q)}(\mathbf{x}) \\ s=1,..,N \\ q=1,..,N^{(s)}}}{\text{stat}} \left[\tilde{u}_T(\overline{\boldsymbol{\sigma}}; \boldsymbol{\sigma}^{(r,p)}, \mathbf{M}^{(r,p)}) + \sum_{r=1}^{N} c^{(r)} \sum_{p=1}^{N^{(r)}} c^{(r,p)} \langle V^{(r,p)} \left(\boldsymbol{\sigma}^{(r,p)}, \mathbf{M}^{(r,p)} \right) \rangle^{(r,p)} \right]. \tag{2.127}$$

The effective stress-potential $\tilde{u}_T$ of the two-scale LCC in (2.127) may be determined either through the one-step, direct variational problem (2.44) or by the two-step, sequential problem (2.42), with (2.45), since this LCC medium is a special case of a two-scale nonlinear composite. In this regard, it is relevant to remark that the (approximate) treatment of the direct linear thermoelastic problem (2.44) for $\tilde{u}_T$ leads to more complicated calculations and it will not be pursued in this work. Instead, we will focus on the corresponding sequential problem (2.42), with (2.45), which can be solved approximately through a straightforward generalization of the results for single-scale linear thermoelastic media as discussed further below.

In the context of the variational problem (2.127), we assume that the reference tensors $\boldsymbol{\sigma}^{(r,p)}$ and $\mathbf{M}^{(r,p)}$ are constant in each phase (r,p) and choose the solution $\hat{\boldsymbol{\sigma}}^{(r,p)} = \boldsymbol{\sigma}^{(r,p)}$ to (2.126), which implies that the error functions $V^{(r,p)}$ in (2.125) are identically zero. Then, the stationarity condition in (2.127) leads to $\boldsymbol{\sigma}^{(r,p)} = \langle \boldsymbol{\sigma} \rangle^{(r,p)} \equiv \overline{\boldsymbol{\sigma}}^{(r,p)}$. Making use of these results together with the argument used by Ponte Castañeda and Suquet [122] in the the context of the TSO method for single-scale composites, it can be shown that (2.127) reduces to the following estimate for $\tilde{u}$

$$\tilde{u}(\overline{\boldsymbol{\sigma}}) = \sum_{r=1}^{N} c^{(r)} \sum_{p=1}^{N^{(r)}} c^{(r,p)} \left[u^{(r,p)}(\overline{\boldsymbol{\sigma}}^{(r,p)}) + \frac{1}{2} \frac{\partial u^{(r,p)}}{\partial \boldsymbol{\sigma}}(\overline{\boldsymbol{\sigma}}^{(r,p)}) \cdot (\overline{\boldsymbol{\sigma}} - \overline{\boldsymbol{\sigma}}^{(r,p)}) \right], \tag{2.128}$$

where we recall that $\overline{\boldsymbol{\sigma}}^{(r,p)}$ denote the phase-averages of the stress field developed in the two-scale LCC when subjected to an average stress $\overline{\boldsymbol{\sigma}}$.

As in the case of the TSO estimate (2.67) for single-scale composites, we will not attempt to optimize (2.128) with respect to $\mathbf{M}^{(r,p)}$. Instead, we make use of the tangent prescriptions

$$\mathbf{M}^{(r,p)} = \frac{\partial^2 u^{(r,p)}}{\partial \boldsymbol{\sigma}^2}(\overline{\boldsymbol{\sigma}}^{(r,p)}), \tag{2.129}$$

which ensure that the estimate (2.128) for $\tilde{u}$ is exact to second-order in the heterogeneity contrast, and, therefore, it will be referred to as the "direct linearization scheme" (DLS), "tangent second-order" (TSO) estimate.

Estimates for the two-scale LCC. As already mentioned, for the purposes of this work the effective stress-potential $\tilde{u}_T$ of the two-scale LCC will be determined by means of the sequential approach (2.42), with (2.45), along with the estimates of subsection 2.5.4 for single-scale linear thermoelastic composites.

For convenience, we first rewrite the local stress-potentials $(2.122)_2$, with (2.123), in the composite-phases of the LCC as

$$u_T^{(r)}(\mathbf{x},\boldsymbol{\sigma}) = \sum_{p=1}^{N^{(r)}} \chi^{(r,p)}(\mathbf{x}) u_T^{(r,p)}(\boldsymbol{\sigma}), \qquad u_T^{(r,p)}(\boldsymbol{\sigma}) = \frac{1}{2}\boldsymbol{\sigma}\cdot\mathbf{M}^{(r,p)}\boldsymbol{\sigma} + \boldsymbol{\alpha}^{(r,p)}\cdot\boldsymbol{\sigma} + \phi^{(r,p)}, \tag{2.130}$$

where $\boldsymbol{\alpha}^{(r,p)}$ and $\phi^{(r,p)}$ denote respectively the thermal strain tensor and specific heat associated with the homogeneous-phase (r,p) of the LCC, which in the context of the DLS-TSO estimate (2.128) may be readily expressed as functions of $\overline{\boldsymbol{\sigma}}^{(r,p)}$ by taking into account (2.123), the fact that $\boldsymbol{\sigma}^{(r,p)} = \overline{\boldsymbol{\sigma}}^{(r,p)}$ and prescriptions (2.129). The corresponding effective stress-potential $\tilde{u}_T^{(r)}$ of the composite-phase r is determined, in principle, by means of the variational problem (2.45). When the associated mesoscopic RVE (Figs. 2.1(b) and 2.2(b)) is subjected to an average stress $\boldsymbol{\sigma}$, in analogy to (2.89), $\tilde{u}_T^{(r)}$ may be expressed as

$$\tilde{u}_T^{(r)}(\boldsymbol{\sigma}) = \frac{1}{2}\boldsymbol{\sigma}\cdot\mathbf{M}^{(r)}\boldsymbol{\sigma} + \boldsymbol{\alpha}^{(r)}\cdot\boldsymbol{\sigma} + \phi^{(r)}, \tag{2.131}$$

where the quantities $\mathbf{M}^{(r)}$, $\boldsymbol{\alpha}^{(r)}$ and $\phi^{(r)}$ denote respectively the effective compliance, thermal strain and specific heat of composite-phase r of the LCC. Similar to (2.90), these quantities are given in terms of the stress concentration tensors $\mathbf{B}^{(r,p)}$ and $\mathbf{b}^{(r,p)}$ in the homogeneous-phases of the LCC by means of the following relations

$$\begin{aligned} \mathbf{M}^{(r)} &= \sum_{p=1}^{N^{(r)}} c^{(r,p)}\mathbf{M}^{(r,p)}\mathbf{B}^{(r,p)}, \quad \boldsymbol{\alpha}^{(r)} = \sum_{p=1}^{N^{(r)}} c^{(r,p)}\left(\mathbf{B}^{(r,p)}\right)^T\boldsymbol{\alpha}^{(r,p)}, \\ \phi^{(r)} &= \sum_{p=1}^{N^{(r)}} c^{(r,p)}\phi^{(r,p)} + \frac{1}{2}\sum_{p=1}^{N^{(r)}} c^{(r,p)}\boldsymbol{\alpha}^{(r,p)}\cdot\mathbf{b}^{(r,p)}. \end{aligned} \tag{2.132}$$

Under the above considerations, the calculation of the effective properties of the two-scale LCC reduces to a straightforward application of the results of subsection 2.5.4. Specifically, the effective stress-potential of the two-scale LCC is given by (2.89), with (2.90), where the effective modulus tensor $\widetilde{\mathbf{M}}$ and the stress-concentration tensors $\mathbf{B}^{(r)}$ and $\mathbf{b}^{(r)}$ of composite-phase r are computed by means of the corresponding estimates of subsection 2.5.4 for particulate and granular systems, depending on the type of composite considered each time. The quantities $\mathbf{M}^{(r)}$, $\mathbf{B}^{(r,p)}$ and $\mathbf{b}^{(r,p)}$, involved in these calculations, are readily obtained by means of the relations determining $\widetilde{\mathbf{M}}$, $\mathbf{B}^{(r)}$ and $\mathbf{b}^{(r)}$, respectively, where $\mathbf{M}^{(r)}$, $\boldsymbol{\alpha}^{(r)}$, $\phi^{(r)}$, $c^{(r)}$ and $\mathbf{Z}$ must be replaced by $\mathbf{M}^{(r,p)}$, $\boldsymbol{\alpha}^{(r,p)}$, $\phi^{(r,p)}$,

$c^{(r,p)}$ and $\mathbf{Z}^{(r)}$, respectively. Finally, the averages $\overline{\boldsymbol{\sigma}}^{(r,p)}$ of the stress field over the homogeneous-phases of the LCC are obtained through the relations

$$\overline{\sigma}_{ij}^{(r,p)} = \frac{1}{c^{(r)}c^{(r,p)}}\frac{\partial \tilde{u}_T}{\partial \alpha_{ij}^{(r,p)}} = \frac{1}{c^{(r)}c^{(r,p)}}\left[\frac{\partial \tilde{u}_T}{\partial \alpha_{kl}^{(r)}}\frac{\partial \alpha_{kl}^{(r)}}{\partial \alpha_{ij}^{(r,p)}} + \frac{\partial \tilde{u}_T}{\partial \phi^{(r)}}\frac{\partial \phi^{(r)}}{\partial \alpha_{ij}^{(r,p)}}\right], \tag{2.133}$$

which by taking into account expressions (2.89), (2.90) and (2.132) reduce to

$$\overline{\boldsymbol{\sigma}}^{(r,p)} = \mathbf{B}^{(r,p)}\overline{\boldsymbol{\sigma}}^{(r)} + \mathbf{b}^{(r,p)}, \qquad \overline{\boldsymbol{\sigma}}^{(r)} = \mathbf{B}^{(r)}\overline{\boldsymbol{\sigma}} + \mathbf{b}^{(r)}. \tag{2.134}$$

2.7.2 Sequential linearization scheme

Next, we turn our attention on the sequential problem (2.42), with (2.45), for a two-scale nonlinear composite material. The variational principle (2.42), which in this case defines the effective stress-potential $\tilde{u}$ of a two-scale composite in terms of the homogenized stress-potentials $\tilde{u}^{(r)}$ of the composite-phases, constitutes essentially a homogenization problem for a single-scale composite. The treatment of this problem by means of the tangent method has been already discussed in subsection 2.5.2, where the TSO estimate (2.67) for $\tilde{u}$ has been derived. Therefore, in order to complete the computation of the TSO estimate (2.67) for the two-scale composite of interest we have to determine the corresponding TSO estimates for the effective stress-potentials $\tilde{u}^{(r)}$ of the composite-phases, which are defined by (2.45). Since each composite-phase is a single-scale system, the tangent procedure of subsection 2.5.2 applies to these materials as well. For completeness, the tangent method for $\tilde{u}^{(r)}$ is briefly outlined next.

The stress-potential of the single-scale mesoscopic LCC (Figs. 2.1(b) and 2.2(b)) associated with the nonlinear composite-phase r, with $r = 1, ..., N$, is defined by

$$u_T^{(r)}(\mathbf{x}, \boldsymbol{\tau}; \boldsymbol{\sigma}^{(r,p)}, \mathbf{M}^{(r,p)}) = \sum_{p=1}^{N^{(r)}} \chi^{(r,p)}(\mathbf{x}) u_T^{(r,p)}(\boldsymbol{\tau}; \boldsymbol{\sigma}^{(r,p)}, \mathbf{M}^{(r,p)}), \tag{2.135}$$

with

$$u_T^{(r,p)}(\boldsymbol{\tau}; \boldsymbol{\sigma}^{(r,p)}, \mathbf{M}^{(r,p)}) = u^{(r,p)}(\boldsymbol{\sigma}^{(r,p)}) + \frac{\partial u^{(r,p)}}{\partial \boldsymbol{\tau}}(\boldsymbol{\sigma}^{(r,p)})\cdot(\boldsymbol{\tau}-\boldsymbol{\sigma}^{(r,p)}) + \frac{1}{2}(\boldsymbol{\tau}-\boldsymbol{\sigma}^{(r,p)})\cdot\mathbf{M}^{(r,p)}(\boldsymbol{\tau}-\boldsymbol{\sigma}^{(r,p)}), \tag{2.136}$$

where it is recalled that $u^{(r,p)}$ denote the stress-potentials of the nonlinear homogeneous phases, which are known functions of the local stress field $\boldsymbol{\tau}$, and $\boldsymbol{\sigma}^{(r,p)}$, $\mathbf{M}^{(r,p)}$ are the associated reference stress and compliance tensors. The corresponding error function is defined by

$$V^{(r)}(\mathbf{x}; \boldsymbol{\sigma}^{(r,p)}, \mathbf{M}^{(r,p)}) = \sum_{p=1}^{N^{(r)}} \chi^{(r,p)}(\mathbf{x}) V^{(r,p)}\left(\boldsymbol{\sigma}^{(r,p)}, \mathbf{M}^{(r,p)}\right), \tag{2.137}$$

where

$$V^{(r,p)}\left(\boldsymbol{\sigma}^{(r,p)}, \mathbf{M}^{(r,p)}\right) = \underset{\hat{\boldsymbol{\sigma}}^{(r,p)}}{\text{stat}}\left[u^{(r,p)}(\hat{\boldsymbol{\sigma}}^{(r,p)}) - u_T^{(r,p)}(\hat{\boldsymbol{\sigma}}^{(r,p)}; \boldsymbol{\sigma}^{(r,p)}, \mathbf{M}^{(r,p)})\right], \tag{2.138}$$

with the associated stationarity condition for $\hat{\boldsymbol{\sigma}}^{(r,p)}$ being

$$\frac{\partial u^{(r,p)}}{\partial \boldsymbol{\tau}}(\hat{\boldsymbol{\sigma}}^{(r,p)}) - \frac{\partial u^{(r,p)}}{\partial \boldsymbol{\tau}}(\boldsymbol{\sigma}^{(r,p)}) = \mathbf{M}^{(r,p)}(\hat{\boldsymbol{\sigma}}^{(r,p)} - \boldsymbol{\sigma}^{(r,p)}). \tag{2.139}$$

With these definitions, the variational statement (2.45) may alternatively be expressed as

$$\tilde{u}^{(r)}(\boldsymbol{\sigma}) = \underset{\substack{\boldsymbol{\sigma}^{(r,q)}(\mathbf{x}) \\ q=1,..,N^{(r)}}}{\text{stat}} \left[\tilde{u}_T^{(r)}(\boldsymbol{\sigma}; \boldsymbol{\sigma}^{(r,p)}, \mathbf{M}^{(r,p)}) + \sum_{p=1}^{N^{(r)}} c^{(r,p)} \langle V^{(r,p)} \left(\boldsymbol{\sigma}^{(r,p)}, \mathbf{M}^{(r,p)} \right) \rangle^{(r,p)} \right], \tag{2.140}$$

where the effective stress-potential $\tilde{u}_T^{(r)}$ of the mesoscopic LCC r is given by

$$\begin{aligned} \tilde{u}_T^{(r)}(\boldsymbol{\sigma}; \boldsymbol{\sigma}^{(r,p)}, \mathbf{M}^{(r,p)}) &= \min_{\boldsymbol{\tau} \in \mathcal{S}^{(r)}(\boldsymbol{\sigma})} \langle u_T^{(r)}(\mathbf{x}, \boldsymbol{\tau}; \boldsymbol{\sigma}^{(r,p)}, \mathbf{M}^{(r,p)}) \rangle^{(r)} \\ &= \min_{\boldsymbol{\tau} \in \mathcal{S}^{(r)}(\boldsymbol{\sigma})} \sum_{p=1}^{N^{(r)}} c^{(r,p)} \langle u_T^{(r,p)}(\boldsymbol{\tau}; \boldsymbol{\sigma}^{(r,p)}, \mathbf{M}^{(r,p)}) \rangle^{(r,p)}. \end{aligned} \tag{2.141}$$

Finally, restricting the optimality condition in (2.140) to constant per phase reference stress $\boldsymbol{\sigma}^{(r,q)}$ and compliance $\mathbf{M}^{(r,p)}$ tensors, and using the solution $\hat{\boldsymbol{\sigma}}^{(r,p)} = \boldsymbol{\sigma}^{(r,p)}$ of (2.139), we arrive at the result $\boldsymbol{\sigma}^{(r,p)} = \overline{\boldsymbol{\tau}}^{(r,p)}$ and the following TSO estimate for $\tilde{u}^{(r)}$

$$\tilde{u}^{(r)}(\boldsymbol{\sigma}) = \sum_{p=1}^{N^{(r)}} c^{(r,p)} \left[u^{(r,p)}(\overline{\boldsymbol{\tau}}^{(r,p)}) + \frac{1}{2} \frac{\partial u^{(r,p)}}{\partial \boldsymbol{\tau}}(\overline{\boldsymbol{\tau}}^{(r,p)}) \cdot (\boldsymbol{\sigma} - \overline{\boldsymbol{\tau}}^{(r,p)}) \right], \tag{2.142}$$

where we recall that $\overline{\boldsymbol{\tau}}^{(r,p)}$ denote the phase averages of the stress field developed in the associated LCC when subjected to a uniform stress $\boldsymbol{\sigma}$. Stationarity of (2.142) with respect to $\mathbf{M}^{(r,p)}$, once again, amounts in enforcing the severe constraint

$$\langle (\boldsymbol{\tau} - \overline{\boldsymbol{\tau}}^{(r,p)}) \otimes (\boldsymbol{\tau} - \overline{\boldsymbol{\tau}}^{(r,p)}) \rangle^{(r,p)} = \mathbf{0}, \tag{2.143}$$

and, for this reason, the following tangent prescriptions are used for $\mathbf{M}^{(r,p)}$ instead

$$\mathbf{M}^{(r,p)} = \frac{\partial^2 u^{(r,p)}}{\partial \boldsymbol{\tau}^2}(\overline{\boldsymbol{\tau}}^{(r,p)}). \tag{2.144}$$

The estimate (2.67) for $\tilde{u}$, together with (2.142) for $\tilde{u}^{(r)}$, will be referred in this work as the "sequential linearization scheme" (SLS), "tangent second-order" (TSO) estimate. Similar to the DLS-TSO estimate (2.128), the SLS-TSO estimate (2.67), with (2.142), may also be used to completely characterize the effective response of a two-scale viscoplastic composite with given phase-potentials $u^{(r,p)}$ of any type, including the isotropic (2.32) and anisotropic (2.35) relations of section 2.3. In addition, this estimate depends only on the average stress tensors $\overline{\boldsymbol{\tau}}^{(r,p)}$ and $\overline{\boldsymbol{\sigma}}^{(r)}$ in the phases of the corresponding LCCs, which are determined by relations of the form

$$\overline{\boldsymbol{\tau}}^{(r,p)} = \mathbf{B}^{(r,p)}\boldsymbol{\sigma} + \mathbf{b}^{(r,p)} \qquad \text{and} \qquad \overline{\boldsymbol{\sigma}}^{(\mathrm{r})} = \mathbf{B}^{(\mathrm{r})}\overline{\boldsymbol{\sigma}} + \mathbf{b}^{(\mathrm{r})}, \tag{2.145}$$

Given that the LCCs involve in the computation of the SLS-TSO estimate are single-scale systems, the stress-concentration tensors $\mathbf{B}^{(r)}$, $\mathbf{b}^{(r)}$, $\mathbf{B}^{(r,p)}$ and $\mathbf{b}^{(r,p)}$ in (2.145) may be readily determined by means of the corresponding results of subsection 2.5.4 for linear thermoelastic composites.

2.8 Generalized-secant method for two-scale composites

In this section, in analogy to the discussion of the previous section, we present the extension of the *generalized-secant* second-order (GSO) method [118] to two-scale composites. The relevant GSO procedures based on the direct (2.44) and sequential (2.42), with (2.45), variational formulations are discussed in subsections 2.8.1 and 2.8.2, respectively. The LCCs and error functions involved in these procedures have the same form as the LCCs and error functions introduced in the context of the corresponding TSO procedures of the previous section.

2.8.1 Direct linearization scheme

Taking into account the two-scale LCC (2.122), with (2.123), and the error function (2.124), with (2.125), it can be shown that the original variational principle (2.44) for the effective stress-potential $\tilde{u}$ of the nonlinear composite of interest may be alternatively expressed as

$$\tilde{u}(\overline{\boldsymbol{\sigma}}) = \underset{\substack{\mathbf{M}^{(s,q)}(\mathbf{x}) \\ s=1,..,N \\ q=1,..,N^{(s)}}}{\text{stat}} \left[\tilde{u}_T(\overline{\boldsymbol{\sigma}}; \boldsymbol{\sigma}^{(r,p)}, \mathbf{M}^{(r,p)}) + \sum_{r=1}^{N} c^{(r)} \sum_{p=1}^{N^{(r)}} c^{(r,p)} \langle V^{(r,p)} \left(\boldsymbol{\sigma}^{(r,p)}, \mathbf{M}^{(r,p)} \right) \rangle^{(r,p)} \right], \quad (2.146)$$

where $\tilde{u}_T$ denotes the effective stress-potential of the two-scale LCC.

In analogy to the GSO method of subsection 2.5.3 for single-scale systems, we explore the possibility of constant per phase reference stress $\boldsymbol{\sigma}^{(r,p)}$ and compliance $\mathbf{M}^{(r,p)}$ tensors, along with solutions to (2.126) that are different than $\hat{\boldsymbol{\sigma}}^{(r,p)} = \boldsymbol{\sigma}^{(r,p)}$. Under these considerations, the stationarity requirement in the variational statement (2.146) reduces to the following conditions for the fluctuations of the stress field over the homogeneous-phases of the LCC

$$(\hat{\boldsymbol{\sigma}}^{(r,p)} - \boldsymbol{\sigma}^{(r,p)}) \otimes (\hat{\boldsymbol{\sigma}}^{(r,p)} - \boldsymbol{\sigma}^{(r,p)}) = \langle (\boldsymbol{\sigma} - \boldsymbol{\sigma}^{(r,p)}) \otimes (\boldsymbol{\sigma} - \boldsymbol{\sigma}^{(r,p)}) \rangle^{(r,p)}, \quad (2.147)$$

which together with conditions (2.126) provide, in principle, a system of equations for the variables $\hat{\boldsymbol{\sigma}}^{(r,p)}$ and $\mathbf{M}^{(r,p)}$. The reference stress tensors $\boldsymbol{\sigma}^{(r,p)}$, as in the case of the GSO method for single-scale composites, will be prescribed in the context of the specific applications considered in this work, such that for small contrast systems they all reduce to $\overline{\boldsymbol{\sigma}}$. Using the result (2.147) in (2.146), we obtain the following approximation for $\tilde{u}$

$$\tilde{u}(\overline{\boldsymbol{\sigma}}) = \sum_{r=1}^{N} c^{(r)} \sum_{p=1}^{N^{(r)}} c^{(r,p)} \left[u^{(r,p)}(\hat{\boldsymbol{\sigma}}^{(r,p)}) + \frac{\partial u^{(r,p)}}{\partial \boldsymbol{\sigma}}(\boldsymbol{\sigma}^{(r,p)}) \cdot (\overline{\boldsymbol{\sigma}}^{(r,p)} - \hat{\boldsymbol{\sigma}}^{(r,p)}) \right]. \quad (2.148)$$

The variables $\overline{\boldsymbol{\sigma}}^{(r,p)}$ in (2.148), denoting the averages of the stress field over the homogeneous-phases of the LCC, are computed by expressions (2.134), as discussed at the end of subsection 2.7.1. It should be emphasized, however, that these calculations must be carried out for the values of $\boldsymbol{\sigma}^{(r,p)}$ and $\mathbf{M}^{(r,p)}$ determined by the GSO procedure of this section.

Note that conditions (2.126) allow the interpretation of $\mathbf{M}^{(r,p)}$ as generalized-secant moduli, while conditions (2.147) associate the variables $\hat{\boldsymbol{\sigma}}^{(r,p)}$ with the stress-field fluctuations over the phases of the two-scale LCC with respect to the reference stress tensors $\boldsymbol{\sigma}^{(r,p)}$. Furthermore, to zeroth-order in the contrast, it can be shown that all $\hat{\boldsymbol{\sigma}}^{(r,p)}$, $\overline{\boldsymbol{\sigma}}^{(r,p)}$ and $\boldsymbol{\sigma}^{(r,p)}$ reduce to $\overline{\boldsymbol{\sigma}}$, and, as can be easily seen from (2.126), $\mathbf{M}^{(r,p)}$ reduce to the tangent modulus (2.129). In this way, it follows that (2.148) and the DLS-TSO estimate (2.128) are identical up to second-order in the heterogeneity contrast, and therefore (2.148) is also exact to second-order in the contrast. Hence, expression (2.148) will be referred to in this work as the "direct linearization scheme" (DLS) "generalized-secant second-order" (GSO) estimate.

As already remarked in the context of the GSO estimate (2.74), conditions of the type (2.147) are too difficult to enforce in their tensorial form and only certain traces of them shall be considered. In this connection, we present next more specific DLS-GSO estimates for two-scale composites with isotropic and crystalline homogeneous-phases, which provide the associated generalization of the corresponding GSO estimates for single scale systems of subsection 2.5.3.

Composites with isotropic homogeneous-phases. Consider a two-scale nonlinear composite with isotropic constituents, defined by (2.31), with homogeneous-phase-potentials $u^{(r,p)}$ of the form

$$u^{(r,p)}(\boldsymbol{\sigma}) = \psi^{(r,p)}(\sigma_e). \tag{2.149}$$

It is recalled that $\sigma_e = \sqrt{3\boldsymbol{\sigma}_d \cdot \boldsymbol{\sigma}_d/2}$ is the equivalent stress and the subscript d stands for the deviatoric part of the stress tensor $\boldsymbol{\sigma}$.

The reference modulus tensors $\mathbf{M}^{(r,p)}$ of the two-scale LCC are taken here to be of the form

$$\mathbf{M}^{(r,p)} = \frac{1}{2\lambda_{\mathbf{E}}^{(r,p)}}\mathbf{E}^{(r,p)} + \frac{1}{2\lambda_{\mathbf{F}}^{(r,p)}}\mathbf{F}^{(r,p)}, \qquad \mathbf{E}^{(r,p)} = \frac{3}{2}\frac{\boldsymbol{\sigma}_d^{(r,p)}}{\sigma_e^{(r,p)}} \otimes \frac{\boldsymbol{\sigma}_d^{(r,p)}}{\sigma_e^{(r,p)}}, \qquad \mathbf{F}^{(r,p)} = \mathbf{K} - \mathbf{E}^{(r,p)}, \tag{2.150}$$

where, $\lambda_{\mathbf{E}}^{(r,p)}$ and $\lambda_{\mathbf{F}}^{(r,p)}$ are unknown scalar moduli, $\mathbf{E}^{(r,p)}$, $\mathbf{F}^{(r,p)}$ are forth-order projection tensors satisfying identities analogous to (2.77) and $\mathbf{K}$ is the forth-order identity tensor in the deviatoric space. Defining, in addition, the projection variables

$$\hat{\sigma}_{\parallel}^{(r,p)} = \sqrt{\frac{3}{2}\hat{\boldsymbol{\sigma}}^{(r,p)} \cdot \mathbf{E}^{(r,p)}\hat{\boldsymbol{\sigma}}^{(r,p)}}, \qquad \hat{\sigma}_{\perp}^{(r,p)} = \sqrt{\frac{3}{2}\hat{\boldsymbol{\sigma}}^{(r,p)} \cdot \mathbf{F}^{(r,p)}\hat{\boldsymbol{\sigma}}^{(r,p)}}, \tag{2.151}$$

the generalized secant conditions (2.126) and the fluctuation equations (2.147) reduce respectively to the following system of scalar equations

$$\frac{\hat{\sigma}_{||}^{(r,p)}\psi^{(r,p)'}(\hat{\sigma}_e^{(r,p)})}{\hat{\sigma}_e^{(r,p)}} - \psi^{(r,p)'}(\sigma_e^{(r,p)}) = \frac{1}{3\lambda_{\mathbf{E}}^{(r,p)}}(\hat{\sigma}_{||}^{(r,p)} - \sigma_e^{(r,p)}), \qquad \frac{\psi^{(r,p)'}(\hat{\sigma}_e^{(r,p)})}{\hat{\sigma}_e^{(r,p)}} = \frac{1}{3\lambda_{\mathbf{F}}^{(r,p)}}, \tag{2.152}$$

where $\hat{\sigma}_e^{(r,p)} = \sqrt{(\hat{\sigma}_{\parallel}^{(r,p)})^2 + (\hat{\sigma}_{\perp}^{(r,p)})^2}$, and

$$\hat{\sigma}_{||}^{(r,p)} = \sigma_e^{(r,p)} \pm \sqrt{\frac{3}{c^{(r)}c^{(r,p)}} \frac{\partial \tilde{u}_T}{\partial (2\lambda_{\mathbf{E}}^{(r,p)})^{-1}}}, \qquad \hat{\sigma}_{\perp}^{(r,p)} = \pm \sqrt{\frac{3}{c^{(r)}c^{(r,p)}} \frac{\partial \tilde{u}_T}{\partial (2\lambda_{\mathbf{F}}^{(r,p)})^{-1}}}. \tag{2.153}$$

Recalling that for given values of the reference tensors $\mathbf{M}^{(r,p)}$ and $\boldsymbol{\sigma}^{(r,p)}$ the effective stress-potential $\tilde{u}_T$ of the two-scale LCC is completely determined as discussed at the end of subsection 2.7.1, expressions (2.152) and (2.153) constitute a system of equations which can be solved iteratively for the scalar moduli $\lambda_{\mathbf{E}}^{(r,p)}$, $\lambda_{\mathbf{F}}^{(r,p)}$ and the fluctuation variables $\hat{\sigma}_{\parallel}^{(r,p)}$, $\hat{\sigma}_{\perp}^{(r,p)}$.

Finally, it can be easily shown that the DLS-GSO estimate (2.148) for the effective stress potential $\tilde{u}$ of the two-scale composite under consideration reduces to

$$\tilde{u}(\overline{\boldsymbol{\sigma}}) = \sum_{r=1}^{N} c^{(r)} \sum_{p=1}^{N^{(r)}} c^{(r,p)} \left[\psi^{(r,p)}(\hat{\sigma}_e^{(r,p)}) + \psi^{(r,p)'}(\sigma_e^{(r,p)})(\overline{\sigma}_{||}^{(r,p)} - \hat{\sigma}_{||}^{(r,p)}) \right], \tag{2.154}$$

where $\overline{\sigma}_{||}^{(r,p)} = 3\boldsymbol{\sigma}^{(r,p)} \cdot \overline{\boldsymbol{\sigma}}^{(r,p)} / (2\sigma_e^{(r,p)})$ and $\overline{\boldsymbol{\sigma}}^{(r,p)}$ are given by (2.134).

At this point, it should be remarked once again that the optimal choice for the reference stress-tensors $\boldsymbol{\sigma}^{(r,p)}$, required for the computation of the DLS-GSO estimate (2.154), is not currently known. For this reason, in the specific applications for two-scale composites considered in chapter 3 of this thesis we will make use of the simple prescriptions $\boldsymbol{\sigma}^{(r,p)} = \overline{\boldsymbol{\sigma}}$ for all $r = 1, .., N$ and $p = 1, .., N^{(r)}$. This prescription has the merit that when a two-scale particulate composite reduces to the corresponding single-scale particulate composite, the DLS-GSO estimate (2.154) reduces accordingly to the GSO estimate (2.81), as it should (see Figs. 3.1 and 3.4 and the corresponding discussions of subsections 3.2.3 and 3.3.3, respectively).

Composites with crystalline homogeneous-phases. Next, we present the generalization of the GSO method of Liu and Ponte Castañeda [86] (see subsection 2.5.3) to two-scale composites with crystalline homogeneous-phases, characterized by stress-potentials $u^{(r,p)}$ of the form

$$u^{(r,p)}(\boldsymbol{\sigma}) = \sum_{k=1}^{K^{(r,p)}} \psi_k^{(r,p)}(\tau_k^{(r,p)}), \tag{2.155}$$

where we recall that $K^{(r,p)}$ denotes for the number of slip systems of the single-crystal (r,p), $\boldsymbol{\mu}_k^{(r,p)}$, given by (2.34), is the symmetric Schmidt tensor associated with the $k-th$ slip system, and $\tau_k^{(r,p)} = \boldsymbol{\sigma} \cdot \boldsymbol{\mu}_k^{(r,p)}$ is the corresponding resolved shear stress.

For consistency with the work of Liu and Ponte Castañeda [86], we chose the reference stress tensors to be $\boldsymbol{\sigma}^{(r,p)} = \overline{\boldsymbol{\sigma}}^{(r,p)}$ and consider a two-scale LCC given by (2.122), with phase-potentials $u_T^{(r,p)}$ of the form

$$u_T^{(r,p)}(\boldsymbol{\sigma}) = \frac{1}{2}\boldsymbol{\sigma} \cdot \mathbf{M}^{(r,p)}\boldsymbol{\sigma} + \boldsymbol{\alpha}^{(r,p)} \cdot \boldsymbol{\sigma}, \tag{2.156}$$

where

$$\mathbf{M}^{(r,p)} = \sum_{k=1}^{K^{(r,p)}} \alpha_k^{(r,p)} \boldsymbol{\mu}_k^{(r,p)} \otimes \boldsymbol{\mu}_k^{(r,p)}, \qquad \boldsymbol{\alpha}^{(r,p)} = \frac{\partial u^{(r,p)}}{\partial \boldsymbol{\sigma}}(\overline{\boldsymbol{\sigma}}^{(r,p)}) - \mathbf{M}^{(r,p)} \overline{\boldsymbol{\sigma}}^{(r,p)}. \tag{2.157}$$

Making use of these definitions, the generalized-secant conditions and the fluctuation equations reduce to

$$\frac{d\,\psi_k^{(r,p)}}{d\,\tau_k^{(r,p)}}(\hat{\tau}_k^{(r,p)}) - \frac{d\,\psi_k^{(r,p)}}{d\,\tau_k^{(r,p)}}(\overline{\tau}_k^{(r,p)}) = \alpha_k^{(r,p)} \left(\hat{\tau}_k^{(r,p)} - \overline{\tau}_k^{(r,p)} \right), \tag{2.158}$$

and

$$\hat{\tau}_k^{(r,p)} = \overline{\tau}_k^{(r,p)} \pm \sqrt{\frac{2}{c^{(r)} c^{(r,p)}} \frac{\partial \tilde{u}_T}{\partial \alpha_k^{(r,p)}}}, \tag{2.159}$$

respectively, where $\overline{\tau}_k^{(r,p)} = \overline{\boldsymbol{\sigma}}^{(r,p)} \cdot \boldsymbol{\mu}_k^{(r,p)}$ For given values of $\overline{\boldsymbol{\sigma}}^{(r,p)}$ and $\mathbf{M}^{(r,p)}$, $\tilde{u}_T$ may be readily determined from the estimates for two-scale linear thermoelastic composites of subsection 2.7.1. Thus, expressions (2.158), (2.159) and (2.134) provide a system of nonlinear equations for the unknown scalar moduli $\alpha_k^{(r,p)}$, the fluctuation variables $\hat{\tau}_k^{(r,p)}$ and the phase-averages $\overline{\boldsymbol{\sigma}}^{(r,p)}$. It should be emphasized however that $\hat{\tau}_k^{(r,p)} \neq \hat{\boldsymbol{\sigma}}^{(r,p)} \cdot \boldsymbol{\mu}_k^{(r,p)}$, in general.

Taking into account the above results it can be shown that the DLS-GSO estimate for the effective stress-potential $\tilde{u}$ of this two-scale composite is given by

$$\tilde{u}(\overline{\boldsymbol{\sigma}}) = \sum_{r=1}^{N} c^{(r)} \sum_{p=1}^{N^{(r)}} c^{(r,p)} \left\{ \sum_{k=1}^{K^{(r,p)}} \left[\psi_k^{(r,p)}(\hat{\tau}_k^{(r,p)}) + \frac{d\,\psi_k^{(r,p)}}{d\,\tau_k^{(r,p)}}(\overline{\tau}_k^{(r,p)})(\overline{\tau}_k^{(r,p)} - \hat{\tau}_k^{(r,p)}) \right] \right\}. \tag{2.160}$$

2.8.2 Sequential linearization scheme

The GSO procedure for the sequential problem (2.42), with (2.45), is more straightforward, since it consists in applying the GSO method [118] for single-scale composites (see subsection 2.5.3) multiple times. Specifically, the effective stress-potential $\tilde{u}$ of the two-scale composite of interest is in this case given by expression (2.74) in terms of the homogenized stress-potentials $\tilde{u}^{(r)}$ of the composite-phases, which are, in turn, determined by means of the GSO method for single-scale systems with local stress-potentials defined by (2.45). For completeness, we summarize next the GSO procedure for composite-phase r, with $r = 1, ..., N$.

Considering a single-scale mesoscopic LCC (Figs. 2.1(b) and 2.2(b)) defined by (2.135), with (2.136), and an error function given by (2.137), with (2.138), it can be shown that the variational statement (2.45) admits the alternative representation

$$\tilde{u}^{(r)}(\boldsymbol{\sigma}) = \underset{\substack{\mathbf{M}^{(r,p)}(\mathbf{x}) \\ p=1,..,N^{(r)}}}{\text{stat}} \left[\tilde{u}_T^{(r)}(\boldsymbol{\sigma}; \boldsymbol{\sigma}^{(r,p)}, \mathbf{M}^{(r,p)}) + \sum_{p=1}^{N^{(r)}} c^{(r,p)} \langle V^{(r,p)} \left(\boldsymbol{\sigma}^{(r,p)}, \mathbf{M}^{(r,p)} \right) \rangle^{(r,p)} \right], \tag{2.161}$$

where we recall that $\boldsymbol{\sigma}$ denotes here the average stress applied on the mesoscopic RVE and $\tilde{u}_T^{(r)}$ is the effective stress-potential of the mesoscopic LCC, given by (2.141). Assuming that the

reference quantities $\boldsymbol{\sigma}^{(r,p)}$ and $\mathbf{M}^{(r,p)}$ are constant per phase and seeking for solutions different than $\hat{\boldsymbol{\sigma}}^{(r,p)} = \boldsymbol{\sigma}^{(r,p)}$ in (2.139), the stationarity conditions in the variational principle (2.161) reduce to

$$(\hat{\boldsymbol{\sigma}}^{(r,p)} - \boldsymbol{\sigma}^{(r,p)}) \otimes (\hat{\boldsymbol{\sigma}}^{(r,p)} - \boldsymbol{\sigma}^{(r,p)}) = \langle (\boldsymbol{\tau} - \boldsymbol{\sigma}^{(r,p)}) \otimes (\boldsymbol{\tau} - \boldsymbol{\sigma}^{(r,p)}) \rangle^{(r,p)}, \tag{2.162}$$

by means of which, (2.161) simplifies to

$$\tilde{u}^{(r)}(\boldsymbol{\sigma}) = \sum_{p=1}^{N^{(r)}} c^{(r,p)} \left[u^{(r,p)}(\hat{\boldsymbol{\sigma}}^{(r,p)}) + \frac{\partial u^{(r)}}{\partial \boldsymbol{\tau}}(\boldsymbol{\sigma}^{(r,p)}) \cdot (\overline{\boldsymbol{\tau}}^{(r,p)} - \hat{\boldsymbol{\sigma}}^{(r,p)}) \right], \tag{2.163}$$

where $\overline{\boldsymbol{\tau}}^{(r,p)} \equiv \langle \boldsymbol{\tau} \rangle^{(r,p)}$ are the phase-averages of the stress field $\boldsymbol{\tau}$ in the mesoscopic LCC r, which are given by relations $(2.145)_1$ along with the estimates of subsection 2.5.4 for single-scale linear thermoelastic composites. The reference stress tensors $\boldsymbol{\sigma}^{(r,p)}$ are taken to be such that in the limit of small contrast systems they all reduce to the applied stress $\boldsymbol{\sigma}$. Under this condition, the estimate (2.163) can be shown to be exact to second-order in the heterogeneity contrast (see subsection 2.5.3). Furthermore, conditions (2.162) associate the variables $\hat{\boldsymbol{\sigma}}^{(r,p)}$ with the stress-field-fluctuations over the phases of the LCC r with respect to $\boldsymbol{\sigma}^{(r,p)}$, while conditions (2.139) imply the interpretation of $\mathbf{M}^{(r,p)}$ as generalized-secant modulus tensors. Hence, the estimate (2.163) will be referred to as the "sequential linearization scheme" (SLS) "generalized-secant second-order" (GSO) estimate.

In summary, just like the DLS-GSO estimate (2.148), the SLS-GSO estimate (2.74) for $\tilde{u}$ together with (2.163) for $\tilde{u}^{(r)}$ can, in principle, be used to fully characterize the effective behavior of a two-scale viscoplastic composite. In practice, however, the SLS-GSO estimate has the disadvantage that it can not be used to generalize the already available GSO methods for single-scale composites with isotropic and crystalline phases to two-scale systems with corresponding homogeneous-phases. This is of course due to the fact that these methods are intrinsically related to the material symmetries of the constituents combined with the fact that the effective stress-potentials $\tilde{u}^{(r)}$ of the composite phases in a two-scale medium are not expected to be of the type (2.32) or (2.35), in general. Nevertheless, it is of interest to compute the SLS-GSO estimate (2.74), with (2.163), for the specific type of two-scale composites with isotropic mesoscale effective stress-potentials $\tilde{u}^{(r)}$ of the form (2.32).

Composites with isotropic composite-phase effective behavior. Next, we specialize the SLS-GSO estimates (2.74) and (2.163) to two-scale systems made out of composite-phases exhibiting isotropic overall behavior. Although the effective response at the meso-scale level cannot be known in advance, it can be anticipated that composite-phases with isotropic effective behavior could result, for example, from isotropic particles of spherical shape distributed isotropically in an isotropic matrix (Fig. 2.2*b*) or from an untextured polycrystal (Fig. 2.1*b*). The following discussion

is concerned with the case when both the effective $\tilde{u}^{(r)}$ and local $u^{(r,p)}$ stress-potentials are of the form (2.32), i.e.,

$$\tilde{u}^{(r)}(\boldsymbol{\sigma}) = \widetilde{\psi}^{(r)}(\sigma_e), \qquad u^{(r,p)}(\boldsymbol{\tau}) = \psi^{(r,p)}(\tau_e), \tag{2.164}$$

for all $r = 1, ..., N$ and all $p = 1, ..., N^{(r)}$, where it is recalled that $\sigma_e = \sqrt{3\boldsymbol{\sigma}_d \cdot \boldsymbol{\sigma}_d/2}$ and $\tau_e = \sqrt{3\boldsymbol{\tau}_d \cdot \boldsymbol{\tau}_d/2}$, with the subscript d used to indicate the deviatoric part of a tensor. The SLS-GSO estimate for the effective stress-potential $\tilde{u}$ of this material is given by expression (2.81) in terms of $\tilde{u}^{(r)}$, as discussed in subsection 2.5.3, and, for this reason, we next focus on the computation of $\tilde{u}^{(r)}$.

Referring to the single-scale mesoscopic LCC r, we consider phase modulus tensors $\mathbf{M}^{(r,p)}$ given by expression (2.150) in terms of the scalar moduli $\lambda_{\mathbf{E}}^{(r,p)}$, $\lambda_{\mathbf{F}}^{(r,p)}$ and the associated projection tensors $\mathbf{E}^{(r,p)}$, $\mathbf{F}^{(r,p)}$. Correspondingly, we define the projection variables $\hat{\sigma}_{\parallel}^{(r,p)}$ and $\hat{\sigma}_{\perp}^{(r,p)}$ by means of (2.151), and recall that $\hat{\sigma}_e^{(r,p)} = \sqrt{(\hat{\sigma}_{\parallel}^{(r,p)})^2 + (\hat{\sigma}_{\perp}^{(r,p)})^2}$. Then, the generalized-secant conditions (2.139) and the fluctuation equations (2.162) reduce respectively to

$$\frac{\hat{\sigma}_{||}^{(r,p)} \psi^{(r,p)'}(\hat{\sigma}_e^{(r,p)})}{\hat{\sigma}_e^{(r,p)}} - \psi^{(r,p)'}(\sigma_e^{(r,p)}) = \frac{1}{3\lambda_{\mathbf{E}}^{(r,p)}}(\hat{\sigma}_{||}^{(r,p)} - \sigma_e^{(r,p)}), \qquad \frac{\psi^{(r,p)'}(\hat{\sigma}_e^{(r,p)})}{\hat{\sigma}_e^{(r,p)}} = \frac{1}{3\lambda_{\mathbf{F}}^{(r,p)}}, \tag{2.165}$$

and

$$\hat{\sigma}_{||}^{(r,p)} = \sigma_e^{(r,p)}) \pm \sqrt{\frac{3}{c^{(r,p)}} \frac{\partial \tilde{u}_T^{(r)}}{\partial (2\lambda_{\mathbf{E}}^{(r,p)})^{-1}}}, \qquad \hat{\sigma}_{\perp}^{(r,p)} = \pm \sqrt{\frac{3}{c^{(r,p)}} \frac{\partial \tilde{u}_T^{(r)}}{\partial (2\lambda_{\mathbf{F}}^{(r,p)})^{-1}}}, \tag{2.166}$$

which constitute a system of coupled equations for the variables $\lambda_{\mathbf{E}}^{(r,p)}$, $\lambda_{\mathbf{F}}^{(r,p)}$, $\hat{\sigma}_{\parallel}^{(r)}$ and $\hat{\sigma}_{\perp}^{(r)}$. The effective stress-potential $\tilde{u}_T^{(r)}$ of the mesoscopic LCC r in (2.166) may be readily computed from the results of subsection 2.5.4, for given values of $\boldsymbol{\tau}^{(r,p)}$ and $\mathbf{M}^{(r,p)}$. Finally, we find that the GSO estimate (2.163) for $\tilde{u}^{(r)}$ takes the form

$$\tilde{u}^{(r)}(\boldsymbol{\sigma}) = \sum_{p=1}^{N^{(r)}} c^{(r,p)} \left[\psi^{(r,p)}(\hat{\sigma}_e^{(r,p)}) + \psi^{(r,p)'}(\sigma_e^{(r,p)})(\overline{\tau}_{||}^{(r,p)} - \hat{\sigma}_{||}^{(r,p)}) \right], \tag{2.167}$$

where $\overline{\tau}_{||}^{(r,p)} = 3\boldsymbol{\sigma}^{(r,p)} \cdot \overline{\boldsymbol{\tau}}^{(r,p)}/(2\sigma_e^{(r,p)})$ and the phase-averages $\overline{\boldsymbol{\tau}}^{(r,p)}$ are given by $(2.145)_1$.

The determination of the GSO estimate (2.167) for the single-scale composite phases of the two-scale medium under consideration requires knowledge of the reference stress-tensors $\boldsymbol{\sigma}^{(r,p)}$, the optimal choice of which is not currently known. For consistency with the corresponding prescriptions $\boldsymbol{\sigma}^{(r)} = \overline{\boldsymbol{\sigma}}$ used in the context of the GSO estimate (2.81), in the relevant applications of chapter 3 the variables $\boldsymbol{\sigma}^{(r,p)}$ in the context of the GSO estimate (2.167) will be chosen to be equal to the associated applied stress tensors, i.e., $\boldsymbol{\sigma}^{(r,p)} = \boldsymbol{\sigma}$ for all $r = 1, .., N$ and $p = 1, .., N^{(r)}$. With these prescriptions, as in the case of the DLS-GSO estimate (2.154), it can be shown that when a two-scale particulate composite reduces to the corresponding single-scale particulate composite,

the SLS-GSO estimate (2.81), with (2.167), reduces to the GSO estimate (2.81), as it should (see Figs. 3.1 and 3.4 and the corresponding discussions of subsections 3.2.3 and 3.3.3, respectively).

2.9 Concluding remarks

In this chapter, we have developed variational procedures for the determination of the instantaneous effective response of *two-scale* composites with fairly general *viscoplastic* constituents and *random* sub-structures under arbitrary loading conditions. These procedures are based on two equivalent variational formulations of the associated homogenization problem for the two-scale composite, namely, the "direct" (2.44) and the "sequential" (2.42), together with (2.45), variational principles, and they constitute the generalized versions of the corresponding "linear comparison composite" (LCC) methods of Ponte Castañeda [114], [117], [118] for *single-scale* systems, referred to as the "secant", "tangent second-order" (TSO) and "generalized-secant second-order" (GSO) methods, respectively. The main idea behind the LCC methods is to construct an LCC with the same sub-structure as the nonlinear two-scale medium and express the effective stress-potential $\tilde{u}$ of the composite material of interest in terms of the effective stress-potential $\tilde{u}_T$ of the LCC and an appropriately defined error function. In this connection, it is relevant to remark that the terms "secant", "tangent" and "generalized-secant" are used here to indicate the type of linearization scheme utilized in each case. The secant method is capable of delivering bounds for $\tilde{u}$ that are exact to first-order in the heterogeneity contrast for small contrast systems, while both the TSO and GSO methods deliver estimates for $\tilde{u}$ that are exact to second-order in the heterogeneity contrast. Results based on the implementation of these schemes on the direct (2.44) and sequential (2.42), with (2.45), problems are termed "direct linearization scheme" (DLS) and "sequential linearization scheme" (SLS) estimates, respectively.

For completeness, in this chapter we have also reviewed estimates from the literature for the effective behavior of single-scale linear thermoelastic composites and we have discussed in detail the appropriate generalization of these estimates to the corresponding two-scale systems, which are being utilized in the context of the various estimates for the nonlinear composites of interest. Results were presented both for *particulate* and *granular* random systems. These estimates are fairly simple to compute and, at the same time, they incorporate fine sub-structural information (i.e., they depend both on one- and two-point statistics) which allow consideration of a wide range of composite materials of practical interest in a realistic manner. This later feature will prove particularly helpful in the applications considered in later parts of this thesis, where fairly complex sub-structures, such as semi-crystalline polymers, will be modeled by accounting for crucially important, fine morphological features of the underlying sub-structure at both the meso- and micro-scale level.

More specifically, by applying the secant method to the direct (2.44) and the sequential (2.42), with (2.45), problems for the class of two-scale composites with isotropic constituents, we developed the estimates (2.107) and (2.119), respectively, which have been shown to be identical, as they should. An important property of the secant estimates, which was used in proving the equivalence of (2.107) and (2.119), is that they are stationary with respect to all material parameters defining the local properties of the associated LCCs. In this connection, it is relevant to remark here that the corresponding TSO and GSO estimates are not fully stationary. Furthermore, it was shown that the secant estimate constitutes a rigorous lower bound for the two-scale nonlinear medium when a corresponding lower bound is used for the LCC.

By implementing the TSO method to the direct (2.44) and the sequential (2.42), with (2.45), problems, in this chapter we have generated the DLS-TSO estimate (2.128) and SLS-TSO estimate (2.67), with (2.142), respectively. These estimates are completely general in the sense that they are applicable to two-scale viscoplastic composites with anisotropic homogeneous-phases and random sub-structures of any type. They are completely determined in terms of the stress phase-averages in the associated LCCs and, therefore, they are fairly simple to compute. It should be remarked, however, that since the corresponding TSO estimate for single-scale systems, which is a special case of the more general estimates developed in this work, is known to be inconsistent with the rigorous secant bounds in certain special cases, the predictions of the DLS-TSO and SLS-TSO estimates, at least for these special cases, are *not* expected to be accurate.

By applying the GSO method to the direct (2.44) and the sequential (2.42), with (2.45), problems we generated the DLS-GSO estimate (2.148) and SLS-GSO estimate (2.74), with (2.163), respectively. These estimates are also applicable to random sub-structures of any type and, potentially, to general anisotropic homogeneous-phases. Given, however, the fact that these GSO procedures provide generalizations of the corresponding GSO procedure for single-scale systems, which thus far has been developed in full detail for composites with isotropic and crystalline phases, the DLS-GSO estimate can be practically computed for systems with isotropic and crystalline homogeneous-phases, which is a fairly general class of two-scale composites, while the SLS-GSO estimate can be calculated for systems which are further restricted to be made out of composite-phases with isotropic effective behavior. Thus, by further specializing the DLS-GSO estimate (2.148) to composites with isotropic and crystalline homogeneous-phases we obtained the DLS-GSO estimates (2.154) and (2.160), respectively. The SLS-GSO estimate (2.74), with (2.163), was computed explicitly for the case of combined isotropic homogeneous-phases and composite-phases with isotropic effective behavior, and it is given by (2.81), with (2.167). In any case, the GSO estimates depend explicitly both on the stress phase-averages and the stress phase-field-fluctuation in the associated LCCs, and they are superior to the corresponding TSO estimates in that they are always consistent with the bounds.

In conclusion, the most important results of this chapter are the DLS-GSO estimate (2.154) for two-scale composites with isotropic homogeneous-phases and the DLS-GSO estimate (2.160) for two-scale composites with crystalline phases, to which we will mainly focus our attention in subsequent chapters. In chapter 3, however, we provide a thorough investigation of the predictions of all estimates derived here for special types of 2-dimensional model problems.

Chapter 3

Applications to 2-D model problems

In this chapter, we consider specific applications of the "secant", "tangent second-order" (TSO) and "generalized-secant second-order" (GSO) methods for two-scale viscoplastic composites developed in chapter 2. The main objective of these applications is to compare the predictions of the corresponding "direct linearization scheme" (DLS) and "sequential linearization scheme" (SLS) second-order estimates for the instantaneous effective response of particulate and granular systems, as well as to highlight the differences in the effective behavior of a two-scale composite and a corresponding single-scale composite. To this end, we focus our attention on the effective in-plane response of several *rigidly-reinforced* systems with *transversely isotropic* sub-structures. Specifically, we consider the *two-scale particulate* composites of Figs. 3.1(b) and 3.4(b), which for convenience are labeled by P1 and P2, respectively, the *single-scale particulate* composite of Figs. 3.1(a), labeled by P0, the *two-scale granular* system of Fig. 3.8(b), labeled by G2, and the *single-scale granular* system of Fig. 3.8(a), labeled by G0.

The structure of this chapter is as follows. In section 3.1, we recall the basic features of the estimates developed in the previous chapter and introduce some definitions that facilitate the discussion in the subsequent sections. Sections 3.2, 3.3 and 3.4 deal with the effective in-plane response of the two-scale composites P1, P2 and G2, while the single-scale composites P0 and G0 are treated as special cases of the corresponding two-scale composites. In each of the later sections, we first specialize the relevant secant, TSO and GSO estimates to the corresponding two-scale composite and then, in the context of specific results, we investigate their predictions and highlight some of their important features. The effective properties of the "linear comparison composites" (LCCs) involved in the calculation of these estimates are computed by means of the results provided in appendix I for general two-phase single-scale linear thermoelastic composites. Finally, in section 3.5 we summarize the main findings and conclusions of this chapter.

3.1 Preliminaries

With a slight abuse in notation, in the applications of this chapter we make use of the notation $\overline{\boldsymbol{\sigma}}$ to denote both the macroscopic and the mesoscopic applied stress[1] and $\overline{\boldsymbol{\sigma}}^{(r,p)}$ to denote the LCC homogeneous-phase-average stress tensors for both the DLS- and SLS-based[2] second-order estimates of the previous chapter, and let their interpretation be inferred by the context. Furthermore, we make use of the notation $A^{(\cdot)}$, where the superscript $(\cdot)$ indicates the phase of the LCC to which the quantity A is referred to.

In this chapter, we focus our attention on the two-scale composite systems P1, P2 and G2 shown schematically in Figs. 3.1(b), 3.4(b) and 3.8(b), respectively. A common feature of these systems is that each of them is characterized by transversely isotropic micro- and meso-structure. In other words, making contact with the discussions of subsections 2.1.2 and 2.2.2, the relevant meso-structural shape tensor $\mathbf{Z}$ and micro-structural shape tensors $\mathbf{Z}^{(r)}$ for the composites of interest will be taken to be such that $\mathbf{Z}^{(r)} = \mathbf{Z}$, where

$$\mathbf{Z} = \mathbf{I} - (1-\epsilon)\mathbf{e}_3 \otimes \mathbf{e}_3, \qquad \text{as} \qquad \epsilon \to 0, \tag{3.1}$$

with $\mathbf{e}_3$ denoting the preferred direction of transverse isotropy and $\mathbf{I}$ being the second-order identity tensor. In addition, these composites are constituted by a rigid-material, with stress-potential equal to infinity, reinforcing a deformable isotropic homogeneous-material, which is characterized by the following viscoplastic power-law stress-potential

$$u(\boldsymbol{\sigma}) = \psi(\sigma_e) = \frac{\epsilon_0 \sigma_0}{n+1}\left(\frac{\sigma_e}{\sigma_0}\right)^{n+1}, \tag{3.2}$$

where $\sigma_e = \sqrt{3\boldsymbol{\sigma}_d \cdot \boldsymbol{\sigma}_d/2}$, the subscript d is used to indicate the deviatoric part of a tensor, n is the nonlinearity exponent (the inverse of the rate-sensitivity $m = 1/n$) and ϵ_0, σ_0 are reference strain-rate and stress measures, respectively. Furthermore, we will restrict our attention to plane-stress loading conditions, i.e., loadings normal to the direction of transverse isotropy $\mathbf{e}_3$. For these loading conditions, it turns out that the corresponding effective stress-potential $\tilde{u}$ of these composites is also power-law with the same exponent n and reference stain ϵ_0 as those of the deformable material in (3.2), i.e.,

$$\tilde{u}(\overline{\boldsymbol{\sigma}}) = \tilde{\psi}(\bar{\sigma}_e) = \frac{\epsilon_0 \tilde{\sigma}_0}{n+1}\left(\frac{\overline{\sigma}_e}{\tilde{\sigma}_0}\right)^{n+1}, \tag{3.3}$$

where $\overline{\boldsymbol{\sigma}}$ denotes the applied stress, $\overline{\sigma}_e = \sqrt{3\overline{\boldsymbol{\sigma}}_d \cdot \overline{\boldsymbol{\sigma}}_d/2}$ and $\tilde{\sigma}_0$ is the in-plane effective yield-stress of the composite. The effective quantity $\tilde{\sigma}_0$ for each of the composite systems P1, P2 and G2 is determined by means of the five different estimates of the previous chapter, namely, the secant

[1] The mesoscopic applied stress in the context of the SLS methods of chapter 2 is denoted by $\boldsymbol{\sigma}$.

[2] In the context of the the SLS methods of chapter 2, these variables are denoted by $\overline{\boldsymbol{\tau}}^{(r,p)}$.

estimate (2.107), the DLS-TSO estimate (2.128), the SLS-TSO estimate (2.67), with (2.142), the DLS-GSO estimate (2.154) and the SLS-GSO estimate (2.81), with (2.167). It is recalled that these estimates are given in terms of the local and effective properties of LCCs with the same substructure as the actual nonlinear composites and defined in terms of the associated phase reference stress $\boldsymbol{\sigma}^{(\cdot)}$ and compliance $\mathbf{M}^{(\cdot)}$ tensors.

In the context of the TSO methods, the reference stresses $\boldsymbol{\sigma}^{(\cdot)}$ are such that $\boldsymbol{\sigma}^{(\cdot)} = \overline{\boldsymbol{\sigma}}^{(\cdot)}$, where we recall that $\overline{\boldsymbol{\sigma}}^{(\cdot)}$ denotes the volume-average of the stress field over phase $(\cdot)$ of the LCC, while the reference compliances $\mathbf{M}^{(\cdot)}$ are set equal to the tangent modulus tensors associated with the corresponding phase $(\cdot)$ of the LCC, evaluated at $\overline{\boldsymbol{\sigma}}^{(\cdot)}$. Therefore, the TSO estimates are completely determined in terms of the average stress tensors $\overline{\boldsymbol{\sigma}}^{(\cdot)}$ in the phases of the associated LCCs, which for the applications of interest in this chapter can be shown [107] to be proportional to the applied stress $\overline{\boldsymbol{\sigma}}$, i.e.,

$$\overline{\boldsymbol{\sigma}}^{(\cdot)} = \omega^{(\cdot)} \overline{\boldsymbol{\sigma}}, \tag{3.4}$$

where $\omega^{(\cdot)}$ denotes the associated proportionality constants. Taking into account the above result, it can be easily shown that the tangent modulus tensors $\mathbf{M}^{(\cdot)}$ may be expressed in the form

$$\mathbf{M}^{(\cdot)} = \frac{1}{2\lambda_{\mathbf{E}}^{(\cdot)}} \mathbf{E} + \frac{1}{2\lambda_{\mathbf{F}}^{(\cdot)}} \mathbf{F}, \qquad \mathbf{E} = \frac{3}{2} \frac{\overline{\boldsymbol{\sigma}}_d}{\bar{\sigma}_e} \otimes \frac{\overline{\boldsymbol{\sigma}}_d}{\bar{\sigma}_e}, \qquad \mathbf{F} = \mathbf{K} - \mathbf{E}, \tag{3.5}$$

where $\mathbf{K}$ is the forth-order identity tensor in the deviatoric space and the scalar moduli $\lambda_{\mathbf{E}}^{(\cdot)}$ and $\lambda_{\mathbf{F}}^{(\cdot)}$ associated with $\mathbf{M}^{(\cdot)}$ are functions of $\omega^{(\cdot)}$ and $\bar{\sigma}_e = \sqrt{3\overline{\boldsymbol{\sigma}}_d \cdot \overline{\boldsymbol{\sigma}}_d / 2}$.

Following Idiart et. al [64], all reference stress tensors of the LCCs involved in the calculations of the GSO estimates are set equal to the applied stress, i.e., $\boldsymbol{\sigma}^{(\cdot)} = \overline{\boldsymbol{\sigma}}$. These prescriptions have the merit that, when any one of the two-scale composites considered here reduces to the associated single-scale composite, the corresponding DLS-GSO and SLS-GSO estimates for the two-scale system reduce accordingly to a unique GSO estimate for the single-scale system. In addition, with these prescriptions the associated reference compliances $\mathbf{M}^{(\cdot)}$ are given by a relation of the form (3.5) in terms of the associated scalar variables $\lambda_{\mathbf{E}}^{(\cdot)}$ and $\lambda_{\mathbf{F}}^{(\cdot)}$, corresponding to generalized-secant moduli that are *not* known in advance. Furthermore, the phase averages $\overline{\boldsymbol{\sigma}}^{(\cdot)}$ in these LCCs can also be shown [107] to be proportional to the applied stress $\overline{\boldsymbol{\sigma}}$, i.e., they are given by (3.4) in terms of the corresponding proportionality constants $\omega^{(\cdot)}$ (which are different from the corresponding variables in the context of the TSO estimates). In addition to the determination of the phase-average constants $\omega^{(\cdot)}$, the GSO estimates require the computation of the corresponding fluctuation variables $\hat{\sigma}_{\parallel}^{(\cdot)}$ and $\hat{\sigma}_{\perp}^{(\cdot)}$ in the phases of the associated LCC. Recall that, in the context of the DLS-GSO estimate (2.154) the variables $\hat{\sigma}_{\parallel}^{(\cdot)}$ and $\hat{\sigma}_{\perp}^{(\cdot)}$ are defined by (2.151) and determined by means of the corresponding fluctuation equations (2.153), while in the context of the SLS-GSO estimate (2.81), with (2.167), these variables are defined by (2.151) and computed by (2.80), (2.166), as

appropriate. For later reference, we introduce at this point the following normalized fluctuation variables $x_{\|}^{(\cdot)}$ and $x_{\perp}^{(\cdot)}$, and anisotropy ratios $k^{(\cdot)}$,

$$x_{\|}^{(\cdot)} = \frac{\hat{\sigma}_{\|}^{(\cdot)}}{\bar{\sigma}_e}, \qquad x_{\perp}^{(\cdot)} = \frac{\hat{\sigma}_{\perp}^{(\cdot)}}{\bar{\sigma}_e}, \qquad k^{(\cdot)} = \frac{\lambda_{\mathbf{F}}^{(\cdot)}}{\lambda_{\mathbf{E}}^{(\cdot)}}, \tag{3.6}$$

where, again, the superscript $(\cdot)$ indicates the phase of the LCC to which a quantity is referred to. With these definitions, taking the ratio of the generalized-secant conditions $(2.152)_1$ and $(2.152)_2$ we obtain the following equation

$$\mathcal{E}^{(\cdot)} \equiv (1-k^{(\cdot)})x_{\|}^{(\cdot)} + k^{(\cdot)} - \left((x_{\|}^{(\cdot)})^2 + (x_{\perp}^{(\cdot)})^2\right)^{\frac{1-n}{2}} = 0. \tag{3.7}$$

Finally, following Idiart et. al [64], the root in the fluctuation equations (2.153), (2.80) and (2.166) is chosen according to the sign of $(\omega^{(\cdot)} - 1)$. Note that this prescription has the advantage of recovering the exact result $x_{\|}^{(\cdot)} = \omega^{(\cdot)}$ and $x_{\perp}^{(\cdot)} = 0$ when it so happens that the stress field is constant in the given phase $(\cdot)$ of the LCC.

3.2 Application to particulate composites—I

The single-scale composite P0 of Fig. 3.1(a) is assumed to be made out of aligned rigid-fibers (phase (f)) of cylindrical shape and circular cross-section that are distributed randomly and isotropically in a matrix material (phase (m)). Making contact with the discussion of subsection 2.2.1, the shape, orientation and distribution symmetry of the fibers in P0 are characterized by a tensor $\mathbf{Z}$ defined by (3.1). The matrix material is taken to be homogeneous and isotropic, characterized by a viscoplastic power-law stress-potential $u^{(m)}(\boldsymbol{\sigma}) = u(\boldsymbol{\sigma})$ given by (3.2). The volume fractions of the constituent phases of P0 are given by $c^{(m)} = |\Omega^{(m)}|/|\Omega|$ and $c^{(f)} = |\Omega^{(f)}|/|\Omega| = 1 - c^{(m)}$, where Ω is the volume of P0, $\Omega^{(m)}$ is the subregion of Ω occupied by the matrix and $\Omega^{(f)} = \Omega - \Omega^{(m)}$ is the subregion of Ω occupied by fibers.

The two-scale particulate composite P1 of Fig. 3.1(b) consists of aligned meso-scale ℓ_1 composite-fibers (phase (2)) of cylindrical shape and circular cross-section that are distributed randomly and isotropically in a homogeneous-matrix material (phase (1)). Each composite-fiber is essentially a single-scale composite P0 (Fig. 3.1(a)), made out of micro-scale ℓ_2 rigid-fibers (phase (2,2)) distributed randomly and isotropically in a homogeneous-matrix (phase (2,1)). The rigid-fibers in all composite-fibers are taken to be aligned along the same direction. In connection with the discussion of subsection 2.2.2, it is remarked that the shape tensors $\mathbf{Z}^{(2)}$ and $\mathbf{Z}$—defining the shape, orientation and distribution symmetry of the rigid- and composite-fibers, respectively—are such that $\mathbf{Z}^{(2)} = \mathbf{Z}$, with $\mathbf{Z}$ given by (3.1). The homogeneous-matrix-phases, characterized by the corresponding phase-potentials $u^{(1)}(\boldsymbol{\sigma})$ and $u^{(2,1)}(\boldsymbol{\sigma})$, are assumed to be made out of the same

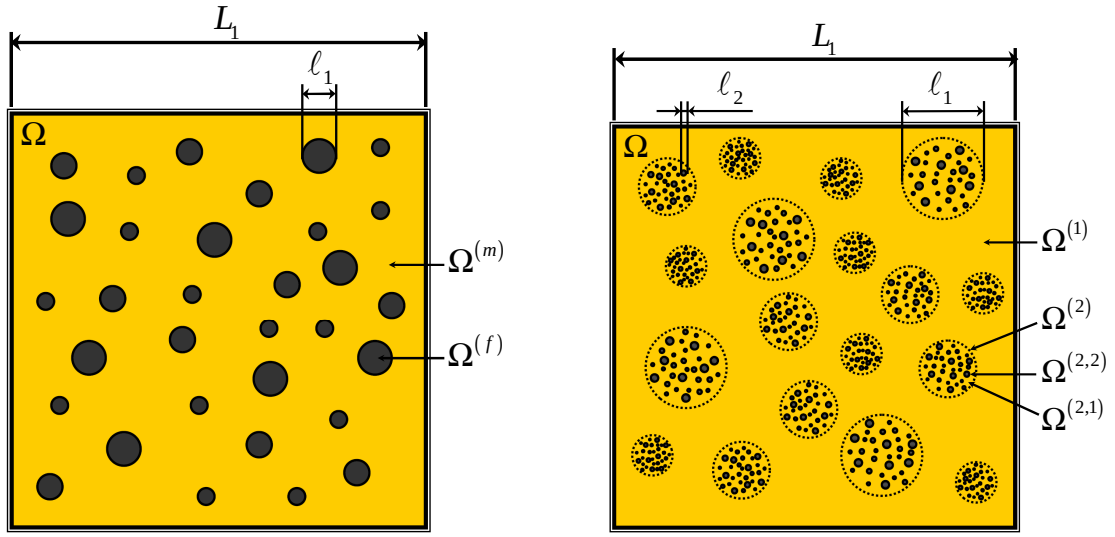

(a) (b)

Figure 3.1: Schematic of rigidly-reinforced *particulate* systems. (a) *Single-scale* composite P0 with rigid-fiber concentration $c^{(f)} = |\Omega^{(f)}|/|\Omega|$. (b) *Two-scale* composite P1 with (meso-scale ℓ_1) composite-fiber concentration $c^{(2)} = |\Omega^{(2)}|/|\Omega|$, (micro-scale ℓ_2) rigid-fiber concentration $c^{(2,2)} = |\Omega^{(2,2)}|/|\Omega^{(2)}|$ and overall rigid-fiber content $c^{(2)}c^{(2,2)} \equiv c^{(f)}$.

isotropic, viscoplastic material, i.e., $u^{(1)}(\boldsymbol{\sigma}) = u^{(2,1)}(\boldsymbol{\sigma}) = u(\boldsymbol{\sigma})$, with $u(\boldsymbol{\sigma})$ given by the power-law relation (3.2). Taking into account the fact that the stress-potential $u^{(2,2)}$ of the rigid-fiber-phase is equal to zero, the local stress-potential of the two-scale composite P1 is given by

$$u(\mathbf{x},\boldsymbol{\sigma}) = \chi^{(1)}(\mathbf{x})u(\boldsymbol{\sigma}) + \chi^{(2)}(\mathbf{x})u^{(2)}(\mathbf{x},\boldsymbol{\sigma}), \qquad u^{(2)}(\mathbf{x},\boldsymbol{\sigma}) = \chi^{(2,1)}(\mathbf{x})u(\boldsymbol{\sigma}), \tag{3.8}$$

with

$$\chi^{(1)}(\mathbf{x}) = \begin{cases} 1, & \text{if } \mathbf{x} \in \Omega^{(1)} \\ 0, & \text{otherwise} \end{cases}, \qquad \chi^{(2)}(\mathbf{x}) = \begin{cases} 1, & \text{if } \mathbf{x} \in \Omega^{(2)} \\ 0, & \text{otherwise} \end{cases},$$
$$\chi^{(2,1)}(\mathbf{x}) = \begin{cases} 1, & \text{if } \mathbf{x} \in \Omega^{(2,1)} \\ 0, & \text{otherwise} \end{cases}, \tag{3.9}$$

where $\Omega^{(1)}$ and $\Omega^{(2)} = \Omega - \Omega^{(1)}$ denote the parts of the volume Ω of P1 occupied by the matrix-phase (1) and the composite-fiber-phase (2), respectively, and $\Omega^{(2,1)}$ is the subregion of Ω occupied by the matrix-phase $(2,1)$ in the composite-fibers. For later reference, we introduce the volume fractions $c^{(1)} = |\Omega^{(1)}|/|\Omega|$, $c^{(2)} = |\Omega^{(2)}|/|\Omega| = 1 - c^{(1)}$, $c^{(2,1)} = |\Omega^{(2,1)}|/|\Omega^{(2)}|$ and $c^{(2,2)} = |\Omega^{(2,2)}|/|\Omega^{(2)}| = 1 - c^{(2,1)}$, where $\Omega^{(2,2)} = \Omega^{(2)} - \Omega^{(2,1)}$ is the part of Ω occupied by rigid-fibers, so that the total content of the rigid-fiber-phase in P1 is $c^{(2)}c^{(2,2)} \equiv c^{(f)}$. Note that in the special case $c^{(1)} = 0$ or, alternatively, $c^{(2,1)} = 0$, the two-scale composite P1 reduces to the single-scale composite P0.

3.2.1 Secant estimates for P1

First, we consider the specialization of the secant estimate (2.107) to the in-plane effective response of the two-scale particulate composite P1 of Fig. 3.1(b). In this connection, we recall that the direct secant estimate (2.107) is identical with the corresponding sequential secant estimate (2.58), with (2.116) (see subsection 2.6.2).

The relevant two-scale LCC under consideration here is characterized by a local stress-potential of the form

$$u_L(\mathbf{x},\boldsymbol{\sigma}) = \chi^{(1)}(\mathbf{x})u_L^{(1)}(\boldsymbol{\sigma}) + \chi^{(2)}(\mathbf{x})u_L^{(2)}(\mathbf{x},\boldsymbol{\sigma}), \qquad u_L^{(2)}(\mathbf{x},\boldsymbol{\sigma}) = \chi^{(2,1)}(\mathbf{x})u_L^{(2,1)}(\boldsymbol{\sigma}). \tag{3.10}$$

The phase-potentials $u_L^{(1)}$ and $u_L^{(2,1)}$ in the above expressions are respectively given by

$$u_L^{(1)}(\boldsymbol{\sigma}) = \frac{1}{2}\boldsymbol{\sigma}\cdot\mathbf{M}^{(1)}\boldsymbol{\sigma}, \qquad \mathbf{M}^{(1)} = \frac{1}{2\lambda^{(1)}}\mathbf{K}, \tag{3.11}$$

and

$$u_L^{(2,1)}(\boldsymbol{\sigma}) = \frac{1}{2}\boldsymbol{\sigma}\cdot\mathbf{M}^{(2,1)}\boldsymbol{\sigma}, \qquad \mathbf{M}^{(2,1)} = \frac{1}{2\lambda^{(2,1)}}\mathbf{K}, \tag{3.12}$$

where it is recalled that $\mathbf{K}$ is the forth order identity tensor in the deviatoric space and the scalar moduli $\lambda^{(1)}$ and $\lambda^{(2,1)}$ are unknown at this stage. The effective modulus tensor $\mathbf{M}^{(2)}$ of the composite-fiber-phase of the LCC is obtained as a special case of the more general estimate (3.29), provided in the following subsection, for $\lambda_{\mathbf{E}}^{(2,1)} = \lambda_{\mathbf{F}}^{(2,1)} = \lambda^{(2,1)}$. The corresponding effective modulus tensor $\widetilde{\mathbf{M}}$ of the two-scale LCC is computed by means of the Willis estimate (3.108), given in appendix I, and may be easily shown to reduce to

$$\widetilde{\mathbf{M}} = \frac{1}{2\tilde{\lambda}}\mathbf{K}, \qquad \frac{1}{2\tilde{\lambda}} = \frac{1}{2\lambda^{(1)}}\frac{c^{(2,1)}(1+c^{(2)})\lambda^{(1)} + c^{(1)}(1+c^{(2,2)})\lambda^{(2,1)}}{c^{(1)}c^{(2,1)}\lambda^{(1)} + (1+c^{(2)})(1+c^{(2,2)})\lambda^{(2,1)}}. \tag{3.13}$$

Note that the above estimate for $\widetilde{\mathbf{M}}$ corresponds to a lower bound for the effective stress-potential $\tilde{u}_L$ of the LCC, which, in turn, translates into a lower bound for the effective potential $\tilde{u}$ of P1, or, equivalently, into an upper bound for its in-plane effective yield-stress $\tilde{\sigma}_0$.

Next, for convenience, we introduce the normalized second-moment variables $x^{(1)} = \hat{\sigma}_e^{(1)}/\bar{\sigma}_e$, $x^{(2,1)} = \hat{\sigma}_e^{(2,1)}/\bar{\sigma}_e$, and the moduli ratio $k = \lambda^{(2,1)}/\lambda^{(1)}$. Then, making use of the result (3.13) in the second-moment equations (2.106), it can be readily shown that the variables $x^{(1)}$ and $x^{(2,1)}$ are respectively given by

$$x^{(1)} = \frac{2k^{\frac{n}{n-1}}\sqrt{1+c^{(2,2)}}}{c^{(1)}c^{(2,1)} + (1+c^{(2)})(1+c^{(2,2)})k}, \tag{3.14}$$

and

$$x^{(2,1)} = \frac{2k\sqrt{1+c^{(2,2)}}}{c^{(1)}c^{(2,1)} + (1+c^{(2)})(1+c^{(2,2)})k}, \tag{3.15}$$

where the unknown quantity k is determined as the solution to the following nonlinear equation

$$\left(c^{(2,1)}+(1+c^{(2,2)})k\right)^2+c^{(2)}\left(c^{(2,1)}-(1+c^{(2,2)})k\right)^2-4(1+c^{(2,2)})k^{\frac{2n}{n-1}}=0, \tag{3.16}$$

Finally, taking into account the results (3.14) and (3.15), it follows that the secant estimate (2.107) for the normalized effective yield-stress $\tilde{\sigma}_0/\sigma_0$ of P1 is given by

$$\frac{\tilde{\sigma}_0}{\sigma_0}=\left\{c^{(1)}\left(x^{(1)}\right)^{1+n}+c^{(2)}c^{(2,1)}\left(x^{(2,1)}\right)^{1+n}\right\}^{-\frac{1}{n}}, \tag{3.17}$$

which, as already mentioned, is an upper bound.

We remark that in the special case of a linearly elastic composite P1, i.e., $n=1$, expression (3.17) reduces to the corresponding Willis upper bound

$$\frac{\tilde{\sigma}_0}{\sigma_0}=\frac{1+c^{(2)}c^{(2,2)}}{1-c^{(2)}c^{(2,2)}}=\frac{1+c^{(f)}}{1-c^{(f)}}, \tag{3.18}$$

where use has been made of the notation $c^{(f)}=c^{(2)}c^{(2,2)}$ for the overall concentration of rigid-fibers in P1. Furthermore, in the ideally-plastic limit $n\to\infty$, the secant estimate (3.17) simplifies to

$$\frac{\tilde{\sigma}_0}{\sigma_0}=\frac{2c^{(1)}+(1+c^{(2)})\sqrt{(1+c^{(2,2)})(1-c^{(2)}c^{(2,2)})}}{\sqrt{4c^{(1)}\sqrt{(1+c^{(2,2)})(1-c^{(2)}c^{(2,2)})}+5(1-c^{(2)}c^{(2,2)})+c^{(2,2)}-c^{(2)}\left(1+c^{(1)}(1+c^{(2,2)})\right)}}. \tag{3.19}$$

In addition, for $c^{(1)}=0$ and $c^{(2,2)}\equiv c^{(f)}$ (or, equivalently, $c^{(2,1)}=0$ and $c^{(2)}\equiv c^{(f)}$), corresponding to the single-scale composite P0 (Fig. 3.1(a)) with rigid-fiber volume fraction $c^{(f)}$, the secant bound (3.17) reduces to

$$\frac{\tilde{\sigma}_0}{\sigma_0}=\left(1-c^{(f)}\right)^{-\frac{1}{n}}\left(1+c^{(f)}\right)^{\frac{n+1}{2n}}, \tag{3.20}$$

which has been derived by Ponte Castañeda and deBotton [121].

3.2.2 Tangent second-order estimates for P1

Direct linearization scheme estimate. Following the development of subsection 2.7.1 of chapter 2, the determination of the DLS-TSO estimate (2.128) for the two-scale nonlinear composite P1 of Fig. 3.1(b) requires the construction of a two-scale LCC with the sub-structure of P1 and a local stress-potential u_T given by

$$u_T(\mathbf{x},\boldsymbol{\sigma})=\chi^{(1)}(\mathbf{x})u_T^{(1)}(\boldsymbol{\sigma})+\chi^{(2)}(\mathbf{x})u_T^{(2)}(\mathbf{x},\boldsymbol{\sigma}),\qquad u_T^{(2)}(\mathbf{x},\boldsymbol{\sigma})=\chi^{(2,1)}(\mathbf{x})u_T^{(2,1)}(\boldsymbol{\sigma}), \tag{3.21}$$

where $u_T^{(1)}$ and $u_T^{(2,1)}$ denote respectively the stress-potentials of the homogeneous-phases (1) and $(2,1)$ of the LCC. The quadratic phase-potentials $u_T^{(1)}$ and $u_T^{(2,1)}$ have the functional form (2.123), which for convenience is expressed here as

$$u_T^{(\cdot)}(\boldsymbol{\sigma})=\frac{1}{2}\boldsymbol{\sigma}\cdot\mathbf{M}^{(\cdot)}\boldsymbol{\sigma}+\boldsymbol{\alpha}^{(\cdot)}\cdot\boldsymbol{\sigma}+\phi^{(\cdot)}, \tag{3.22}$$

where the superscript $(\cdot)$ indicates the phase of the LCC to which a quantity is referred to, and $\boldsymbol{\alpha}^{(\cdot)}$, $\phi^{(\cdot)}$ denote respectively the associated thermal strain tensor and specific heat, given by

$$\begin{aligned}\boldsymbol{\alpha}^{(\cdot)} &= \frac{\partial u}{\partial \boldsymbol{\sigma}}(\boldsymbol{\sigma}^{(\cdot)}) - \mathbf{M}^{(\cdot)}\boldsymbol{\sigma}^{(\cdot)},\\ \phi^{(\cdot)} &= u(\boldsymbol{\sigma}^{(\cdot)}) - \frac{\partial u}{\partial \boldsymbol{\sigma}}(\boldsymbol{\sigma}^{(\cdot)})\cdot\boldsymbol{\sigma}^{(\cdot)} + \frac{1}{2}\boldsymbol{\sigma}^{(\cdot)}\cdot\mathbf{M}^{(\cdot)}\boldsymbol{\sigma}^{(\cdot)}.\end{aligned} \tag{3.23}$$

In the above relations, $u(\boldsymbol{\sigma})$ denotes the stress-potential of the nonlinear homogeneous-matrix-phase, which is given by (3.2). Thus, $u_T^{(1)}$ and $u_T^{(2,1)}$ are defined by (3.22), with (3.23), in terms of the corresponding reference stress $\boldsymbol{\sigma}^{(1)}$, $\boldsymbol{\sigma}^{(2,1)}$ and compliance $\mathbf{M}^{(1)}$, $\mathbf{M}^{(2,1)}$ tensors, which in the context of the tangent method under consideration here are prescribed by $\boldsymbol{\sigma}^{(1)} = \overline{\boldsymbol{\sigma}}^{(1)}$, $\boldsymbol{\sigma}^{(2,1)} = \overline{\boldsymbol{\sigma}}^{(2,1)}$, $\mathbf{M}^{(1)} = \partial^2 u(\overline{\boldsymbol{\sigma}}^{(1)})/\partial\boldsymbol{\sigma}^2$ and $\mathbf{M}^{(2,1)} = \partial^2 u(\overline{\boldsymbol{\sigma}}^{(2,1)})/\partial\boldsymbol{\sigma}^2$. We recall that $\overline{\boldsymbol{\sigma}}^{(1)}$ and $\overline{\boldsymbol{\sigma}}^{(2,1)}$ denote the volume averages of the stress field over the phases (1) and $(2,1)$, respectively, of the LCC (3.21). For plane-stress loading conditions, these variables can be shown [107] to be proportional to the applied stress, i.e.,

$$\overline{\boldsymbol{\sigma}}^{(1)} = \omega^{(1)}\overline{\boldsymbol{\sigma}}, \qquad \overline{\boldsymbol{\sigma}}^{(2,1)} = \omega^{(2,1)}\overline{\boldsymbol{\sigma}}. \tag{3.24}$$

where $\omega^{(1)}$ and $\omega^{(2,1)}$ are constants to be determined further below. Making use of (3.24), it can be easily shown that the tangent modulus tensors $\mathbf{M}^{(1)}$ and $\mathbf{M}^{(2,1)}$ may be cast in the form (3.5) in terms of the corresponding moduli $\lambda_{\mathbf{E}}^{(1)}$, $\lambda_{\mathbf{F}}^{(1)}$ and $\lambda_{\mathbf{E}}^{(2,1)}$, $\lambda_{\mathbf{F}}^{(2,1)}$, respectively. The moduli $\lambda_{\mathbf{E}}^{(1)}$, $\lambda_{\mathbf{F}}^{(1)}$ are functions of $\omega^{(1)}$ and $\bar{\sigma}_e = \sqrt{3\overline{\boldsymbol{\sigma}}_d\cdot\overline{\boldsymbol{\sigma}}_d/2}$ only, while $\lambda_{\mathbf{E}}^{(2,1)}$ and $\lambda_{\mathbf{F}}^{(2,1)}$ are functions of $\omega^{(2,1)}$ and $\bar{\sigma}_e$ only. Note that, since $\overline{\boldsymbol{\sigma}}^{(1)}$ and $\overline{\boldsymbol{\sigma}}^{(2,1)}$ are different, in general, the potentials $u_T^{(1)}$ and $u_T^{(2,1)}$ are expected to be different, despite the fact that the corresponding nonlinear homogeneous-phases of P1 are essentially identical. Furthermore, it is remarked that the local material properties of the rigid-fiber-phase $(2,2)$ of the LCC are identically equal to zero, i.e.,

$$u_T^{(2,2)}(\boldsymbol{\sigma}) = 0, \qquad \mathbf{M}^{(2,2)} = \mathbf{0}, \qquad \boldsymbol{\alpha}^{(2,2)} = \mathbf{0}, \qquad \phi^{(2,2)} = 0, \tag{3.25}$$

where $u_T^{(2,2)}$, $\mathbf{M}^{(2,2)}$, $\boldsymbol{\alpha}^{(2,2)}$ and $\phi^{(2,2)}$ denote respectively the stress-potential, the compliance tensor, the thermal strain tensor and the specific heat associated with the rigid-fiber-phase of the LCC.

Making contact with the relevant discussion of subsection 2.7.1 of the previous chapter, the homogenization problem for the two-scale LCC (3.21) will be treated in this work by means of the sequential homogenization approach (see subsection 2.4.2). This approach allows the "decomposition" of the homogenization problem for the two-scale LCC (3.21) into a corresponding problem for a mesoscopic single-scale LCC (associated with the composite-fibers) with local stress-potential $u_T^{(2)}(\mathbf{x},\boldsymbol{\sigma})$ given by $(3.21)_2$, and a homogenization problem for a macroscopic single-scale LCC with local stress-potential of the form

$$u_T(\mathbf{x},\boldsymbol{\sigma}) = \chi^{(1)}(\mathbf{x})u_T^{(1)}(\boldsymbol{\sigma}) + \chi^{(2)}(\mathbf{x})\tilde{u}_T^{(2)}(\boldsymbol{\sigma}), \tag{3.26}$$

where $\tilde{u}_T^{(2)}$ denotes the effective stress-potential of the mesoscopic LCC. In this way, the determination of the effective properties of the two-scale LCC of interest reduces to a straightforward application of the results provided in appendix I, as detailed next.

The effective stress-potential $\tilde{u}_T^{(2)}$ of the mesoscopic LCC is of the form (3.22), where the associated effective quantities $\mathbf{M}^{(2)}$, $\boldsymbol{\alpha}^{(2)}$ and $\phi^{(2)}$ are obtained from the relevant expressions provided in appendix I for two-phase, single-scale linear thermoelastic composites, specialized in the present context. Thus, from $(3.103)_2$ and $(3.103)_3$ we obtain the results

$$\boldsymbol{\alpha}^{(2)} = c^{(2,1)} \left(\mathbf{B}^{(2,1)}\right)^T \boldsymbol{\alpha}^{(2,1)}, \qquad \phi^{(2)} = c^{(2,1)}\phi^{(2,1)} + \frac{1}{2} c^{(2,1)} \boldsymbol{\alpha}^{(2,1)} \cdot \mathbf{b}^{(2,1)}, \tag{3.27}$$

where the stress-concentration tensors $\mathbf{B}^{(2,1)}$ and $\mathbf{b}^{(2,1)}$ are given by (3.105), which for the LCC under consideration here reduce to

$$\mathbf{B}^{(2,1)} = \frac{1}{c^{(2,1)}} \left(\mathbf{M}^{(2,1)}\right)^{-1} \mathbf{M}^{(2)}, \qquad \mathbf{b}^{(2,1)} = \left(\mathbf{M}^{(2,1)}\right)^{-1} \left((\mathbf{B}^{(1)})^T - \mathbf{K}\right) \boldsymbol{\alpha}^{(2,1)}. \tag{3.28}$$

The effective modulus tensor $\mathbf{M}^{(2)}$ of the composite-fibers is determined by means of the Willis estimate (3.108) which, since $\mathbf{M}^{(2,2)} = \mathbf{0}$, simplifies to

$$\mathbf{M}^{(2)} = \mathbf{M}^{(2,1)} + c^{(2,2)} \left[c^{(2,1)}\mathbf{Q} - \left(\mathbf{M}^{(2,1)}\right)^{-1}\right]^{-1}, \tag{3.29}$$

where the micro-structural tensor $\mathbf{Q}$, given by (3.107), must be evaluated at the scalar moduli $\lambda_{\mathbf{E}}^{(0)} = \lambda_{\mathbf{E}}^{(2,1)}$ and $\lambda_{\mathbf{F}}^{(0)} = \lambda_{\mathbf{F}}^{(2,1)}$ associated with $\mathbf{M}^{(2,1)}$. Given the stress-potentials $u_T^{(1)}$ and $\tilde{u}_T^{(2)}$, as determined above, the macroscopic LCC defined by (3.26) is identical to the two-phase linear thermoelastic composite (3.100) considered in appendix I, and therefore the relevant discussion on the computation of its effective properties (provided in appendix I) applies without modifications.

Under the above considerations, the phase-average stress tensors $\overline{\boldsymbol{\sigma}}^{(1)}$ and $\overline{\boldsymbol{\sigma}}^{(2,1)}$ are given by

$$\overline{\boldsymbol{\sigma}}^{(1)} = \mathbf{B}^{(1)}\overline{\boldsymbol{\sigma}} + \mathbf{b}^{(1)}, \tag{3.30}$$

where $\mathbf{B}^{(1)}$, $\mathbf{b}^{(1)}$ are computed from (3.105), and

$$\overline{\boldsymbol{\sigma}}^{(2,1)} = \mathbf{B}^{(2,1)}\overline{\boldsymbol{\sigma}}^{(2)} + \mathbf{b}^{(2,1)}, \qquad \overline{\boldsymbol{\sigma}}^{(2)} = \mathbf{B}^{(2)}\overline{\boldsymbol{\sigma}} + \mathbf{b}^{(2)}. \tag{3.31}$$

where $\mathbf{B}^{(2,1)}$, $\mathbf{b}^{(2,1)}$ are given by (3.28), and $\mathbf{B}^{(2)}$, $\mathbf{b}^{(2)}$ are obtained from (3.104) along with (3.105). The above equations provide a system of two scalar equations for the constants $\omega^{(1)}$ and $\omega^{(2,1)}$. It can be shown that the scalar equation obtained from (3.31) leads to the result

$$\omega^{(2,1)} = \frac{1 - c^{(1)}\omega^{(1)}}{c^{(2)}(1 + c^{(2,2)}/\sqrt{n})}, \tag{3.32}$$

by means of which the scalar equation corresponding to (3.30) reduces to

$$\sqrt{n}\left(1 - \omega^{(1)}\right) + c^{(2)}\omega^{(1)} \left[(1 - c^{(2,2)}) \left(\frac{1 - c^{(1)}\omega^{(1)}}{c^{(2)}\omega^{(1)}(1 + c^{(2,2)}/\sqrt{n})}\right)^n - 1\right] = 0. \tag{3.33}$$

Finally, taking into account (3.24), it can be easily shown that the DLS-TSO estimate (2.128) for the effective in-plane reference stress $\tilde{\sigma}_0$ of P1, normalized by the reference stress σ_0 of the matrix, is given by

$$\frac{\tilde{\sigma}_0}{\sigma_0} = \left\{ c^{(1)} \left[(\omega^{(1)})^{1+n} + \frac{1+n}{2} (\omega^{(1)})^n \left(1 - \omega^{(1)}\right) \right] + c^{(2)} c^{(2,1)} \left[(\omega^{(2,1)})^{1+n} + \frac{1+n}{2} (\omega^{(2,1)})^n \left(1 - \omega^{(2,1)}\right) \right] \right\}^{-\frac{1}{n}}, \tag{3.34}$$

where $\omega^{(2,1)}$ is given by (3.32) in terms of $\omega^{(1)}$, which is, in turn, obtained as the solution to the nonlinear equation (3.33). Note that in the case of a linearly elastic matrix, i.e., $n = 1$, the DLS-TSO estimate (3.34) reduces to the Willis estimate (3.18), as it should. In the ideally-plastic limit $n \to \infty$, we find that $\omega^{(2,1)} = \omega^{(1)} = 1$ and (3.34) reduces to $\tilde{\sigma}_0 = \sigma_0$. Furthermore, in the special case $c^{(1)} = 0$ and $c^{(2,2)} \equiv c^{(f)}$ (or, equivalently, $c^{(2,1)} = 0$ and $c^{(2)} \equiv c^{(f)}$), corresponding to the single-scale composite P0 (Fig. 3.1(a)) with fiber and matrix concentrations $c^{(f)}$ and $c^{(m)} = 1 - c^{(f)}$, respectively, the TSO estimate (3.34) reduces to

$$\frac{\tilde{\sigma}_0}{\sigma_0} = \left\{ c^{(m)} \left[(1 + c^{(f)}/\sqrt{n})^{-(1+n)} + \frac{1+n}{2} (1 + c^{(f)}/\sqrt{n})^{-n} \left(1 - \frac{1}{1 + c^{(f)}/\sqrt{n}}\right) \right] \right\}^{-\frac{1}{n}}. \tag{3.35}$$

Sequential linearization scheme estimate. Next, we consider the application of the SLS-TSO estimate (2.67), with (2.142), to the effective in-plane response of the two-scale composite P1 (Fig. 3.1(b)). The estimate (2.142), specialized to P1, provides an expression for the effective in-plane yield-stress $\tilde{\sigma}_0^{(2)}$ of the composite fibers. This estimate requires the construction of a mescosopic single-scale LCC with the sub-structure of the composite fibers, depending on the average stress $\overline{\boldsymbol{\sigma}}^{(2,1)}$ in the underlying matrix-phase $(2,1)$. On the other hand, the estimate (2.67) treats the composite-fibers as a nonlinear homogenous material (phase (2)) and, therefore, it provides an expression for the determination of the overall effective in-plane yield-stress $\tilde{\sigma}_0$ of P1 in terms of σ_0 and $\tilde{\sigma}_0^{(2)}$. The later estimate requires the construction of a corresponding macroscopic single-scale LCC depending on the average stress tensors $\overline{\boldsymbol{\sigma}}^{(1)}$ and $\overline{\boldsymbol{\sigma}}^{(2)}$ over its constituent homogeneous-phases (1) and (2), respectively. Under plane-stress loadings, it can be shown [107] that $\overline{\boldsymbol{\sigma}}^{(1)}$, $\overline{\boldsymbol{\sigma}}^{(2)}$ and $\overline{\boldsymbol{\sigma}}^{(2,1)}$ are proportional to the corresponding applied stress, i.e.,

$$\overline{\boldsymbol{\sigma}}^{(1)} = \omega^{(1)} \overline{\boldsymbol{\sigma}}, \qquad \overline{\boldsymbol{\sigma}}^{(2)} = \omega^{(2)} \overline{\boldsymbol{\sigma}}, \qquad \overline{\boldsymbol{\sigma}}^{(2,1)} = \omega^{(2,1)} \overline{\boldsymbol{\sigma}}. \tag{3.36}$$

where $\omega^{(1)}$, $\omega^{(2)}$ and $\omega^{(2,1)}$ are constants that are determined further below. Note that, given the global average relation $c^{(1)} \overline{\boldsymbol{\sigma}}^{(1)} + c^{(2)} \overline{\boldsymbol{\sigma}}^{(2)} = \overline{\boldsymbol{\sigma}}$, the constants $\omega^{(1)}$ and $\omega^{(2)}$ are not independent, and, therefore, $\omega^{(2)}$ may be expressed in terms of $\omega^{(1)}$ as follows

$$\omega^{(2)} = \frac{1}{c^{(2)}} \left(1 - c^{(1)} \omega^{(1)}\right). \tag{3.37}$$

The local response of the mesoscopic LCC associated with the composite-fibers of P1 is defined by means of the stress-potential $u_T^{(2)}(\mathbf{x},\boldsymbol{\sigma})$ given by $(3.21)_2$. Hence, the associated effective stress-potential $\tilde{u}_T^{(2)}$ is determined as detailed above in the context of the DLS-TSO estimate for P1. Thus, the stress phase-average tensor $\overline{\boldsymbol{\sigma}}^{(2,1)}$ is given by $(3.31)_1$ and the stress-concentration tensors $\mathbf{B}^{(2,1)}$ and $\mathbf{b}^{(2,1)}$, involved in $(3.31)_1$, are given by (3.28). Given $(3.36)_3$, expression $(3.31)_1$ provides a scalar equation for $\omega^{(2,1)}$, which yields the result

$$\omega^{(2,1)} = \frac{1}{1+c^{(2,2)}/\sqrt{n}}. \tag{3.38}$$

Taking into account $(3.36)_3$, the TSO estimate (2.142) leads to the following expression for the normalized effective yield-stress $\tilde{\sigma}_0^{(2)}/\sigma_0$ of the composite-fibers

$$\frac{\tilde{\sigma}_0^{(2)}}{\sigma_0} = \left\{ c^{(2,1)} \left[\omega^{(2,1)})^{1+n} + \frac{1+n}{2} (\omega^{(2,1)})^n \left(1-\omega^{(2,1)}\right) \right] \right\}^{-\frac{1}{n}}, \tag{3.39}$$

where $\omega^{(2,1)}$ is given by (3.38). In other words, the effective stress-potential $\tilde{u}^{(2)}(\boldsymbol{\sigma})$ of the actual (nonlinear) composite-fiber-phase of P1 is given by the following power-law relation

$$\tilde{u}^{(2)}(\boldsymbol{\sigma}) = \tilde{\psi}^{(2)}(\sigma_e) = \frac{\epsilon_0 \tilde{\sigma}_0^{(2)}}{n+1} \left(\frac{\sigma_e}{\tilde{\sigma}_0^{(2)}} \right)^{n+1}, \tag{3.40}$$

where $\tilde{\sigma}_0^{(2)}$ is given by (3.39).

The macroscopic LCC involved in the calculations of the TSO estimate (2.67) for P1 is defined in terms of a local stress-potential of the form

$$u_T(\mathbf{x},\boldsymbol{\sigma}) = \chi^{(1)}(\mathbf{x}) u_T^{(1)}(\boldsymbol{\sigma}) + \chi^{(2)}(\mathbf{x}) \hat{u}_T^{(2)}(\boldsymbol{\sigma}), \tag{3.41}$$

where $u_T^{(1)}$ is defined by means of (3.22), with (3.23), in terms of $\boldsymbol{\sigma}^{(1)} = \overline{\boldsymbol{\sigma}}^{(1)}$ and $\mathbf{M}^{(1)} = \partial^2 u(\overline{\boldsymbol{\sigma}}^{(1)})/\partial\boldsymbol{\sigma}^2$, as discussed in the context of the DLS-TSO estimate for P1, while $\hat{u}_T^{(2)}$ is given by (3.22) in terms of the associated compliance $\mathbf{M}^{(2)}$, thermal strain $\boldsymbol{\alpha}^{(2)}$ and specific heat $\phi^{(2)}$. The quantities $\boldsymbol{\alpha}^{(2)}$ and $\phi^{(2)}$ are defined by

$$\begin{aligned} \boldsymbol{\alpha}^{(2)} &= \frac{\partial \tilde{u}^{(2)}}{\partial \boldsymbol{\sigma}}(\boldsymbol{\sigma}^{(2)}) - \mathbf{M}^{(2)}\boldsymbol{\sigma}^{(2)}, \\ \phi^{(2)} &= \tilde{u}^{(2)}(\boldsymbol{\sigma}^{(2)}) - \frac{\partial \tilde{u}^{(2)}}{\partial \boldsymbol{\sigma}}(\boldsymbol{\sigma}^{(2)}) \cdot \boldsymbol{\sigma}^{(2)} + \frac{1}{2}\boldsymbol{\sigma}^{(2)} \cdot \mathbf{M}^{(2)}\boldsymbol{\sigma}^{(2)}, \end{aligned} \tag{3.42}$$

where $\boldsymbol{\sigma}^{(2)} = \overline{\boldsymbol{\sigma}}^{(2)}$, $\mathbf{M}^{(2)} = \partial^2 \tilde{u}^{(2)}(\overline{\boldsymbol{\sigma}}^{(2)})/\partial\boldsymbol{\sigma}^2$, and we recall that $\tilde{u}^{(2)}(\boldsymbol{\sigma})$ is given by (3.39). Taking into account relation $(3.36)_2$, the modulus tensor $\mathbf{M}^{(2)}$ may be written in the form (3.5) in terms of the associated scalar moduli $\lambda_{\mathbf{E}}^{(2)}$ and $\lambda_{\mathbf{F}}^{(2)}$, which are functions of $\omega^{(2)}$ and $\bar{\sigma}_e = \sqrt{3\overline{\boldsymbol{\sigma}}_d \cdot \overline{\boldsymbol{\sigma}}_d/2}$. At this point it is important to emphasize that although the LCC defined by (3.41) and the LCC defined by $(3.21)_2$ appear to be identical, they are essentially different. In particular, although the

stress-potential $\hat{u}_T^{(2)}$ in (3.41) has the same form as the composite-fiber *effective* stress-potential $\tilde{u}_T^{(2)}$ in $(3.21)_2$, the material properties $\mathbf{M}^{(2)}$, $\boldsymbol{\alpha}^{(2)}$ and $\phi^{(2)}$ in the definition of $\hat{u}_T^{(2)}$ do *not* correspond to the associated composite-fiber effective properties, as they do in the case of $\tilde{u}_T^{(2)}$. Taking into account this important observation, the effective stress-potential $\tilde{u}_T$ of this single-scale macroscopic LCC (3.41) is given by expression (3.102) along with the relevant Willis estimates for $\widetilde{\mathbf{M}}$, $\widetilde{\boldsymbol{\alpha}}$ and $\tilde{\phi}$, as discussed in appendix I. The stress phase-average tensor $\overline{\boldsymbol{\sigma}}^{(1)}$ in the matrix of the macroscopic LCC is given by expression (3.30), where the associated stress-concentration tensors $\mathbf{B}^{(1)}$ and $\mathbf{b}^{(1)}$ are given by (3.105), together with the Willis estimate (3.108) for $\widetilde{\mathbf{M}}$. Expression (3.30) can be shown to reduce to the following nonlinear equation for $\omega^{(1)}$

$$c^{(2)}\omega^{(1)}\left(\omega^{(2)}\right)^n + \left(\sqrt{n} - (c^{(2)} + \sqrt{n})\omega^{(1)}\right)\left(\frac{\tilde{\sigma}_0^{(2)}}{\sigma_0}\omega^{(1)}\right)^n = 0, \tag{3.43}$$

where $\omega^{(2)}$ and $\tilde{\sigma}_0^{(2)}/\sigma_0$ are given by (3.37) and (3.39), respectively.

Finally, the SLS-TSO estimate (2.67) for the normalized effective yield-stress $\tilde{\sigma}_0/\sigma_0$ of the two-scale particulate composite P1 is given by

$$\begin{aligned}\frac{\tilde{\sigma}_0}{\sigma_0} = \Bigg\{ & c^{(1)}\left[(\omega^{(1)})^{1+n} + \frac{1+n}{2}(\omega^{(1)})^n\left(1-\omega^{(1)}\right)\right] \\ & + c^{(2)}\left(\frac{1}{\tilde{\sigma}_0^{(2)}/\sigma_0}\right)^n\left[(\omega^{(2)})^{1+n} + \frac{1+n}{2}(\omega^{(2)})^n\left(1-\omega^{(2)}\right)\right]\Bigg\}^{-\frac{1}{n}},\end{aligned} \tag{3.44}$$

where $\omega^{(2)}$ and $\tilde{\sigma}_0^{(2)}/\sigma_0$ are given by (3.37) and (3.39), respectively, and $\omega^{(1)}$ is obtained as the solution to the nonlinear equation (3.43). For the special case of a linearly elastic matrix, i.e., $n = 1$, the estimate (3.44) reduces to the Willis estimate (3.18), as it should. As in the case of the DLS-TSO estimate (3.34), in the limiting case $n \to \infty$ of an ideally-plastic matrix, the SLS-TSO estimate (3.44) reduces to $\tilde{\sigma}_0 = \sigma_0$. When $c^{(1)} = 0$ (or $c^{(2,1)} = 0$), the estimate (3.44) recovers the TSO estimate (3.35) for the single-scale composite P0 of Fig. 3.1(a), again, as it should.

3.2.3 Generalized-secant second-order estimates for P1

Direct linearization scheme estimate. The DLS-GSO estimate (2.154) for P1 involves a two-scale LCC with local stress-potential given by (3.21), where the phase-potentials $u_T^{(1)}$ and $u_T^{(2,1)}$ are defined as discussed in the previous subsection in terms of the associated reference stresses $\boldsymbol{\sigma}^{(1)}$, $\boldsymbol{\sigma}^{(2,1)}$ and reference compliances $\mathbf{M}^{(1)}$, $\mathbf{M}^{(2,1)}$. We emphasize, however, that in the present context the reference stresses are chosen such that $\boldsymbol{\sigma}^{(1)} = \boldsymbol{\sigma}^{(2,1)} = \overline{\boldsymbol{\sigma}}$, while the compliances $\mathbf{M}^{(1)}$ and $\mathbf{M}^{(2,1)}$ are given by (3.5) in terms of the scalars $\lambda_{\mathbf{E}}^{(1)}$, $\lambda_{\mathbf{F}}^{(1)}$ and $\lambda_{\mathbf{E}}^{(2,1)}$, $\lambda_{\mathbf{F}}^{(2,1)}$, respectively, which in this case are unknown generalized-secant moduli. Taking into account these remarks, the effective behavior of the LCC (3.21) under consideration is determined by means of the relevant procedure

described in the previous subsection. The computation of the DLS-GSO estimate (2.154) for P1 requires the determination of the proportionality constants $\omega^{(1)}$ and $\omega^{(2,1)}$, defined by (3.24), and the corresponding fluctuation variables $x_{\parallel}^{(1)}$, $x_{\perp}^{(1)}$, $x_{\parallel}^{(2,1)}$ and $x_{\perp}^{(2,1)}$, defined by $(3.6)_1$ and $(3.6)_2$, associated with the homogeneous-matrix-phases (1) and (2, 1) of the two-scale LCC.

The variables $\omega^{(1)}$ and $\omega^{(2,1)}$ may be determined from (3.30) and (3.31), respectively, in terms of the anisotropy ratios $k^{(1)}$, $k^{(2,1)}$, defined by $(3.6)_3$, and the variable $k = \lambda_{\mathbf{F}}^{(1)}/\lambda_{\mathbf{F}}^{(2,1)}$. Specifically, from (3.30) and (3.31) we obtain

$$\omega^{(1)} = \mathcal{W}^{(1)}\left(n, c^{(2)}, c^{(2,2)}, k^{(1)}, k^{(2,1)}, k\right), \quad \omega^{(2,1)} = \mathcal{W}^{(2,1)}\left(n, c^{(2)}, c^{(2,2)}, k^{(1)}, k^{(2,1)}, k\right) \tag{3.45}$$

respectively, where the functions $\mathcal{W}^{(1)}$ and $\mathcal{W}^{(2,1)}$ are given by the expressions (3.111) and (3.112) in appendix II. Next, from the fluctuation equations (2.153)—where we recall that the root is chosen according to the sign$(\omega^{(\cdot)} - 1)$—we obtain the following expressions

$$\begin{aligned} x_{\parallel}^{(1)} &= 1 + \frac{\text{sign}(\omega^{(1)} - 1)}{\bar{\sigma}_e}\sqrt{\frac{3}{c^{(1)}}\frac{\partial \tilde{u}_T}{\partial(2\lambda_{\mathbf{E}}^{(1)})^{-1}}} = \mathcal{X}_{\parallel}^{(1)}(n, c^{(2)}, c^{(2,2)}, \omega^{(1)}, k^{(1)}, k^{(2,1)}, k), \\ x_{\perp}^{(1)} &= \frac{1}{\bar{\sigma}_e}\sqrt{\frac{3}{c^{(1)}}\frac{\partial \tilde{u}_T}{\partial(2\lambda_{\mathbf{F}}^{(1)})^{-1}}} = \mathcal{X}_{\perp}^{(1)}(n, c^{(2)}, c^{(2,2)}, \omega^{(1)}, k^{(1)}, k^{(2,1)}, k), \end{aligned} \tag{3.46}$$

and

$$\begin{aligned} x_{\parallel}^{(2,1)} &= 1 + \frac{\text{sign}(\omega^{(2,1)} - 1)}{\bar{\sigma}_e}\sqrt{\frac{3}{c^{(2)}c^{(2,1)}}\frac{\partial \tilde{u}_T}{\partial(2\lambda_{\mathbf{E}}^{(2,1)})^{-1}}} = \mathcal{X}_{\parallel}^{(2,1)}(n, c^{(2)}, c^{(2,2)}, \omega^{(2,1)}, k^{(1)}, k^{(2,1)}, k), \\ x_{\perp}^{(2,1)} &= \frac{1}{\bar{\sigma}_e}\sqrt{\frac{3}{c^{(2)}c^{(2,1)}}\frac{\partial \tilde{u}_T}{\partial(2\lambda_{\mathbf{F}}^{(2,1)})^{-1}}} = \mathcal{X}_{\perp}^{(2,1)}(n, c^{(2)}, c^{(2,2)}, \omega^{(2,1)}, k^{(1)}, k^{(2,1)}, k), \end{aligned} \tag{3.47}$$

where the functions $\mathcal{X}_{\parallel}^{(1)}$, $\mathcal{X}_{\perp}^{(1)}$, $\mathcal{X}_{\parallel}^{(2,1)}$ and $\mathcal{X}_{\perp}^{(2,1)}$ are respectively given by (3.113), (3.114), (3.115) and (3.116). It is remarked that the variables $x_{\perp}^{(\cdot)}$ enter the calculations of the DLS-GSO estimate (2.154) for P1 only through their square value $(x_{\perp}^{(\cdot)})^2$, and therefore in the above expressions for $x_{\perp}^{(\cdot)}$ we have chosen the "+" root. Substitution of the above expressions for the variables $\omega^{(\cdot)}$, $x_{\parallel}^{(\cdot)}$ and $x_{\perp}^{(\cdot)}$ into (3.7) yields two corresponding equations $\mathcal{E}^{(1)}(n, c^{(2)}, c^{(2,2)}, \omega^{(1)}, k^{(1)}, k^{(2,1)}, k) = 0$ and $\mathcal{E}^{(2,1)}(n, c^{(2)}, c^{(2,2)}, \omega^{(2,1)}, k^{(1)}, k^{(2,1)}, k) = 0$ for the unknowns $k^{(1)}$, $k^{(2,1)}$ and k. To close the systems, we make use of the additional equation

$$\frac{(1 - k^{(1)})x_{\parallel}^{(1)} + k^{(1)}}{(1 - k^{(2,1)})x_{\parallel}^{(2,1)} + k^{(2,1)}} - k = 0, \tag{3.48}$$

obtained by taking the ratio of the equation $(2.152)_2$, applied for the phase (2, 1), with the equation $(2.152)_2$, applied for the phase (1), and taking advantage of (3.7) to express $((x_{\parallel}^{(\cdot)})^2 + (x_{\perp}^{(\cdot)})^2)^{\frac{1-n}{2}} = (1 - k^{(\cdot)})x_{\parallel}^{(\cdot)} + k^{(\cdot)}$.

Finally, taking into account the above considerations for the computation of the quantities $x_{\parallel}^{(1)}$, $x_{\perp}^{(1)}$, $x_{\parallel}^{(2,1)}$, $x_{\perp}^{(2,1)}$, $\omega^{(1)}$ and $\omega^{(2,1)}$, it is easy to show that the DLS-GSO estimate (2.154) for the normalized effective in-plane yield-stress of P1 is given by

$$\frac{\tilde{\sigma}_0}{\sigma_0} = \left\{ c^{(1)} \left[\left((x_{\parallel}^{(1)})^2 + (x_{\perp}^{(1)})^2 \right)^{\frac{1+n}{2}} + (1+n) \left(\omega^{(1)} - x_{\parallel}^{(1)} \right) \right] \right.$$
$$\left. + c^{(2)} c^{(2,1)} \left[\left((x_{\parallel}^{(2,1)})^2 + (x_{\perp}^{(2,1)})^2 \right)^{\frac{1+n}{2}} + (1+n) \left(\omega^{(2,1)} - x_{\parallel}^{(2,1)} \right) \right] \right\}^{-\frac{1}{n}}. \tag{3.49}$$

As the tangent estimates of the previous subsection, the DLS-GSO estimate (3.49) recovers the Willis estimate (3.18) for the special case of a linearly elastic matrix ($n = 1$) and in the ideally-plastic limit $n \to \infty$ it can be shown to reduce to $\tilde{\sigma}_0 = \sigma_0$. For $c^{(1)} = 0$ and $c^{(2,2)} \equiv c^{(f)}$ (or, equivalently, $c^{(2,1)} = 0$ and $c^{(2)} \equiv c^{(f)}$), corresponding to a single-scale composite P0 (Fig. 3.1(a)) with fiber and matrix concentrations $c^{(f)}$ and $c^{(m)} = 1 - c^{(f)}$, respectively, the DLS-GSO estimate (3.49) reduces to

$$\frac{\tilde{\sigma}_0}{\sigma_0} = \left\{ c^{(m)} \left[\left((x_{\parallel}^{(m)})^2 + (x_{\perp}^{(m)})^2 \right)^{\frac{1+n}{2}} + (1+n) \left(\omega^{(m)} - x_{\parallel}^{(m)} \right) \right] \right\}^{-\frac{1}{n}}, \tag{3.50}$$

where the variables $x_{\parallel}^{(m)}$, $x_{\perp}^{(m)}$ and $\omega^{(m)}$, associated with the matrix-phase, are accordingly obtained as special cases of the corresponding more general variables involved in the calculation of the estimate (3.49).

Sequential linearization scheme estimate. Next, following a procedure analogous to the one considered in the previous subsection for the derivation of the SLS-TSO estimate (3.44), with (3.39), we determine the SLS-GSO estimate (2.81), with (2.167), for the effective in-plane response of the two-scale composite P1 (Fig. 3.1(b)).

The GSO estimate (2.167) determines the effective in-plane yield-stress $\tilde{\sigma}_0^{(2)}$ of the composite-fiber-phase of P1 in terms of the local and effective properties of a mescosopic single-scale LCC with the micro-structure of the composite-fiber-phase of P1 and a local stress-potential $u_T^{(2)}(\mathbf{x}, \boldsymbol{\sigma})$ defined by $(3.21)_2$. The phase-potential $u_T^{(2,1)}$ in the definition $(3.21)_2$ of the mescosopic LCC is given by (3.22), with (3.23), in terms of the corresponding reference tensors $\boldsymbol{\sigma}^{(2,1)}$ and $\mathbf{M}^{(2,1)}$, where $\boldsymbol{\sigma}^{(2,1)} = \overline{\boldsymbol{\sigma}}$ and $\mathbf{M}^{(2,1)}$ is defined by (3.5) in terms of the associated generalized-secant moduli $\lambda_{\mathbf{E}}^{(2,1)}$ and $\lambda_{\mathbf{F}}^{(2,1)}$. Except of the later prescriptions for $\boldsymbol{\sigma}^{(2,1)}$ and $\mathbf{M}^{(2,1)}$, the mescosopic single-scale LCC under consideration here is identical to the corresponding mescosopic LCC involved in the context of the TSO estimate (3.39), and, for this reason, we refer to the relevant discussion of the previous subsection for the computation of its effective behavior. It can be easily shown that the GSO estimate (2.167) for the effective in-plane yield-stress $\tilde{\sigma}_0^{(2)}$ of the composite-fiber-phase of P1

is given by

$$\frac{\tilde{\sigma}_0^{(2)}}{\sigma_0} = \left\{ c^{(2,1)} \left[\left((x_{\|}^{(2,1)})^2 + (x_{\perp}^{(2,1)})^2 \right)^{\frac{1+n}{2}} + (1+n) \left(\omega^{(2,1)} - x_{\|}^{(2,1)} \right) \right] \right\}^{-\frac{1}{n}}, \tag{3.51}$$

where $\omega^{(2,1)}$, defined by $(3.36)_3$, is the stress phase-average constant associated with the homogeneous-matrix-phase $(2,1)$ of the mescosopic LCC, and $x_{\|}^{(2,1)}$, $x_{\perp}^{(2,1)}$ are the corresponding fluctuation variables, defined by $(3.6)_1$ and $(3.6)_2$, respectively. The constant $\omega^{(2,1)}$, obtained from equation $(3.31)_1$, is given in terms of the anisotropy ratio $\kappa^{(2,1)} = \lambda_{\mathbf{F}}^{(2,1)}/\lambda_{\mathbf{E}}^{(2,1)}$ by means of the expression (3.117), which is of the form

$$\omega^{(2,1)} = \mathcal{W}^{(2,1)} \left(n, c^{(2,2)}, k^{(2,1)} \right). \tag{3.52}$$

The fluctuation variables $x_{\|}^{(2,1)}$ and $x_{\perp}^{(2,1)}$, obtained from (2.166), are given by

$$\begin{aligned} x_{\|}^{(2,1)} &= 1 + \frac{\operatorname{sign}(\omega^{(2,1)} - 1)}{\bar{\sigma}_e} \sqrt{\frac{3}{c^{(2,1)}} \frac{\partial \tilde{u}_T^{(2)}}{\partial (2\lambda_{\mathbf{E}}^{(2,1)})^{-1}}} = \mathcal{X}_{\|}^{(2,1)}(n, c^{(2,2)}, \omega^{(2,1)}, k^{(2,1)}), \\ x_{\perp}^{(2,1)} &= \frac{1}{\bar{\sigma}_e} \sqrt{\frac{3}{c^{(2,1)}} \frac{\partial \tilde{u}_T^{(2)}}{\partial (2\lambda_{\mathbf{F}}^{(2,1)})^{-1}}} = \mathcal{X}_{\perp}^{(2,1)}(n, c^{(2,2)}, \omega^{(2,1)}, k^{(2,1)}), \end{aligned} \tag{3.53}$$

where $\tilde{u}_T^{(2)}$ is the effective stress-potential of the mescosopic LCC, obtained as discussed in the previous subsection in the context of the TSO estimate (3.39). It can be shown that the functions $\mathcal{X}_{\|}^{(2,1)}$ and $\mathcal{X}_{\perp}^{(2,1)}$ are given by (3.118) and (3.119). Substitution of the above expressions for $\omega^{(2,1)}$, $x_{\|}^{(2,1)}$ and $x_{\perp}^{(2,1)}$ into the corresponding generalized-secant condition (3.7) yields the equation $\mathcal{E}^{(2,1)}(n, c^{(2,2)}, \omega^{(2,1)}, k^{(2,1)}) = 0$ for the variable $\kappa^{(2,1)}$, which, in turn, completely determines the GSO estimate (3.51). Thus, expression (3.40), with $\tilde{\sigma}_0^{(2)}$ given by (3.51), provides an alternative estimate for the effective stress-potential $\tilde{u}^{(2)}(\boldsymbol{\sigma})$ of the composite-fibers of the two-scale composite P1. Note that—with the appropriate interpretation of the various quantities involved—the estimate (3.51) is identical to the corresponding GSO estimate (3.50) for the the single-scale composite P0 derived above.

The GSO estimate (2.81) for the overall in-plane yield-stress $\tilde{\sigma}_0$ of P1 is determined in terms of a macroscopic single-scale LCC with local stress-potential given by (3.41), where $u_T^{(1)}(\boldsymbol{\sigma})$ is defined by (3.22), with (3.23), in terms of the reference tensors $\boldsymbol{\sigma}^{(1)}$ and $\mathbf{M}^{(1)}$, and $\hat{u}_T^{(2)}(\boldsymbol{\sigma})$ is defined by the analogous expression (3.22), with (3.23), in terms of the reference tensors $\boldsymbol{\sigma}^{(2)}$ and $\mathbf{M}^{(2)}$. The reference variable $\boldsymbol{\sigma}^{(1)}$ is set equal to applied stress, i.e., $\boldsymbol{\sigma}^{(1)} = \overline{\boldsymbol{\sigma}}$, and the compliance $\mathbf{M}^{(1)}$ is prescribed by (3.5) in terms of the associated generalized-secant moduli $\lambda_{\mathbf{E}}^{(1)}$ and $\lambda_{\mathbf{F}}^{(1)}$, which are unknown at this stage. Although analogous definitions can be given for the reference tensors $\boldsymbol{\sigma}^{(2)}$ and $\mathbf{M}^{(2)}$, it turns out that the precise choice of these variables does not affect the estimate

(2.81) for the effective in-plane yield-stress $\tilde{\sigma}_0$ of P1. This is because in the context of the Willis estimate (3.108)—to be used for the determination of the effective behavior of the macroscopic LCC of interest here—it is assumed that the polarization field in the composite-fiber-phase of this LCC is constant (see subsection 2.5.4), which, in turn, implies that the stress field-fluctuations in this phase are equal to zero. Thus, for convenience, we make use of the prescriptions $\boldsymbol{\sigma}^{(2)} = \overline{\boldsymbol{\sigma}}^{(2)}$ and $\mathbf{M}^{(2)} = \partial^2 \tilde{u}^{(2)}(\overline{\boldsymbol{\sigma}}^{(2)})/\partial \boldsymbol{\sigma}^2$, and we recall that, under plane-stress loadings, the stress phase-averages $\overline{\boldsymbol{\sigma}}^{(1)}$ and $\overline{\boldsymbol{\sigma}}^{(2)}$ in the LCC are proportional to the applied stress tensor $\overline{\boldsymbol{\sigma}}$, i.e., $\overline{\boldsymbol{\sigma}}^{(1)} = \omega^{(1)}\overline{\boldsymbol{\sigma}}$ and $\overline{\boldsymbol{\sigma}}^{(2)} = \omega^{(2)}\overline{\boldsymbol{\sigma}}$, and that $\omega^{(2)}$ is given in terms of $\omega^{(1)}$ by means of (3.37). Note that, a direct consequence of the above prescriptions for $\boldsymbol{\sigma}^{(2)}$ and $\mathbf{M}^{(2)}$ is that the associated fluctuation equations for the variables $x_{\parallel}^{(2)}$ and $x_{\perp}^{(2)}$, defined respectively by $(3.6)_1$ and $(3.6)_2$ (i.e., equations (2.80) with $r = 2$), reduce to $x_{\parallel}^{(2)} = \omega^{(2)}$ and $x_{\perp}^{(2)} = 0$.

At this point, it should be remarked that the above prescriptions define completely the local material properties of the macroscopic single-scale LCC considered in the context of the GSO estimate (2.81) for P1, in terms of which its effective properties may be computed by means of the procedure discussed in appendix I. Under these considerations, it is straightforward to show that the GSO estimate (2.81) for the normalized effective yield-stress of the two-scale composite P1 simplifies to

$$\frac{\tilde{\sigma}_0}{\sigma_0} = \left\{ c^{(1)} \left[\left((x_{\parallel}^{(1)})^2 + (x_{\perp}^{(1)})^2 \right)^{\frac{1+n}{2}} + (1+n) \left(\omega^{(1)} - x_{\parallel}^{(1)} \right) \right] + c^{(2)} \omega^{(2)} \left(\frac{\omega^{(2)}}{\tilde{\sigma}_0^{(2)}/\sigma_0} \right)^n \right\}^{-\frac{1}{n}}, \quad (3.54)$$

where $\tilde{\sigma}_0^{(2)}$ is given by (3.51). The variables $\omega^{(1)}$, $\omega^{(2)}$ and $x_{\parallel}^{(1)}$, $x_{\perp}^{(1)}$—defined respectively by $(3.6)_1$, $(3.6)_2$—in the above expression are determined as follows. First, we make use of (3.37) to express $\omega^{(1)}$ in terms of $\omega^{(2)}$. Then, the fluctuation equations (2.80) for the homogeneous-matrix-phase (1) can be shown to reduce to

$$\begin{aligned} x_{\parallel}^{(1)} &= 1 + \frac{\operatorname{sign}(\omega^{(1)} - 1)}{\bar{\sigma}_e} \sqrt{\frac{3}{c^{(1)}} \frac{\partial \tilde{u}_T}{\partial (2\lambda_{\mathbf{E}}^{(1)})^{-1}}} = \mathcal{X}_{\parallel}^{(1)}(n, c^{(2)}, \omega^{(2)}, k^{(1)}), \\ x_{\perp}^{(1)} &= \frac{1}{\bar{\sigma}_e} \sqrt{\frac{3}{c^{(1)}} \frac{\partial \tilde{u}_T}{\partial (2\lambda_{\mathbf{F}}^{(1)})^{-1}}} = \mathcal{X}_{\perp}^{(1)}(n, c^{(2)}, \omega^{(2)}, k^{(1)}), \end{aligned} \quad (3.55)$$

where the functions $\mathcal{X}_{\parallel}^{(1)}$ and $\mathcal{X}_{\perp}^{(1)}$ are respectively given by relations (3.121) and (3.122) in appendix II. Making use of these relations in (3.30), we obtain the following equation for $\omega^{(2)}$ and the anisotropy ratio $k^{(1)} = \lambda_{\mathbf{F}}^{(1)}/\lambda_{\mathbf{E}}^{(1)}$

$$\mathcal{W}^{(2)} \left(n, c^{(2)}, \omega^{(2)}, k^{(1)} \right) = 0, \quad (3.56)$$

which is explicitly given by (3.123). Finally, substitution of expressions (3.55) and (3.56) in the corresponding generalized-secant condition (3.7) leads to the nonlinear equation $\mathcal{E}^{(1)}(n, c^{(2)}, \omega^{(2)}, k^{(1)}) =$

0, which along with (3.56) completely determine the GSO estimate (3.54). For the special cases of a linearly elastic matrix ($n = 1$), an ideally plastic matrix ($n \to \infty$) and in the limit of a single-scale composite P0 (Fig. 3.1(a)), the SLS-GSO estimate (3.54), with (3.51), becomes identical to the corresponding DLS-GSO estimate (3.49).

3.2.4 Results and discussion for P1

Figure 3.2 compares the secant (SEC) upper bound (3.20) for the normalized effective in-plane yield-stress $\tilde{\sigma}_0/\sigma_0$ of the single-scale particulate composite P0 (Fig. 3.1(a)) with the corresponding bound (3.17) for the two-scale composite P1 (Fig. 3.1(b)) with the same total rigid-fiber concentration $c^{(f)} = c^{(2)}c^{(2,2)}$. In particular, Fig. 3.2(a) shows results for $\tilde{\sigma}_0/\sigma_0$ as a function of the nonlinearity exponent $m = 1/n$ for fixed rigid-fiber contents $c^{(f)} = 0.1, 0.25, 0.4$, while Fig. 3.2(a) shows the same quantity as a function of $c^{(f)}$ for three different values of $m = 0.1, 0.25, 0.5$. From both Figs. 3.2(a) and 3.2(b), we observe that the corresponding secant estimates for P0 and P1 are in excellent agreement to each other, except of some minor differences which appear near the ideally-plastic limit ($m = 0$) for moderate values of $c^{(f)}$ (e.g., $c^{(f)} = 0.4$). This observation suggest that the effective in-plane response of P0 is very similar to that of P1 for the same overall rigid-fiber content $c^{(f)}$. This conclusion is further supported by the results of the following figure, showing the corresponding predictions of the second-order estimates.

Figure 3.3 provides a comparison of the SLS-based with the corresponding DLS-based second-order estimates derived in subsections 3.2.2 and 3.2.3 for the normalized effective in-plane yield-stress $\tilde{\sigma}_0/\sigma_0$ of the two-scale *particulate* composite P1 (Fig. 3.1(b)). Specifically, Fig. 3.3(a) shows the SLS-GSO estimate (3.54), with (3.51), and the DLS-GSO estimate (3.49) for $\tilde{\sigma}_0/\sigma_0$ as a function of the nonlinearity exponent $m = 1/n$ for three different values of the total rigid-fiber content in P1, $c^{(f)} = c^{(2)}c^{(2,2)} = 0.1, 0.25, 0.4$, while Fig. 3.3(c) presents the same estimates but as functions of $c^{(f)}$ for $m = 0.1, 0.25, 0.5$. Parts (b) and (d) of this figure show the corresponding results for $\tilde{\sigma}_0/\sigma_0$ as predicted by the SLS-TSO estimate (3.44), with (3.39), and the DLS-TSO estimate (3.34). All results shown in this figure have been obtained for $c^{(2)} = c^{(2,2)} = \sqrt{c^{(f)}}$. Furthermore, in each part of Fig. 3.3 the corresponding second-order estimates for the single-scale composite P0 (Fig. 3.1(a)) are also shown (recall that, material P0 is identical to P1 for $c^{(1)} = 0$ and $c^{(2,2)} \equiv c^{(f)}$ or, equivalently, for $c^{(2,1)} = 0$ and $c^{(2)} \equiv c^{(f)}$). The most important observation from this figure is the excellent agreement between the corresponding SLS and DLS estimates for composite P1 for all values of the nonlinearity exponent m and all total concentrations of rigid-fibers $c^{(f)}$. Furthermore, note that all second-order estimates of Fig. 3.3 are softer from the corresponding secant upper bounds of Fig. 3.2, as they should.

From Figs. 3.3, we also observe that the SLS and DLS estimates for P1 are in a very good

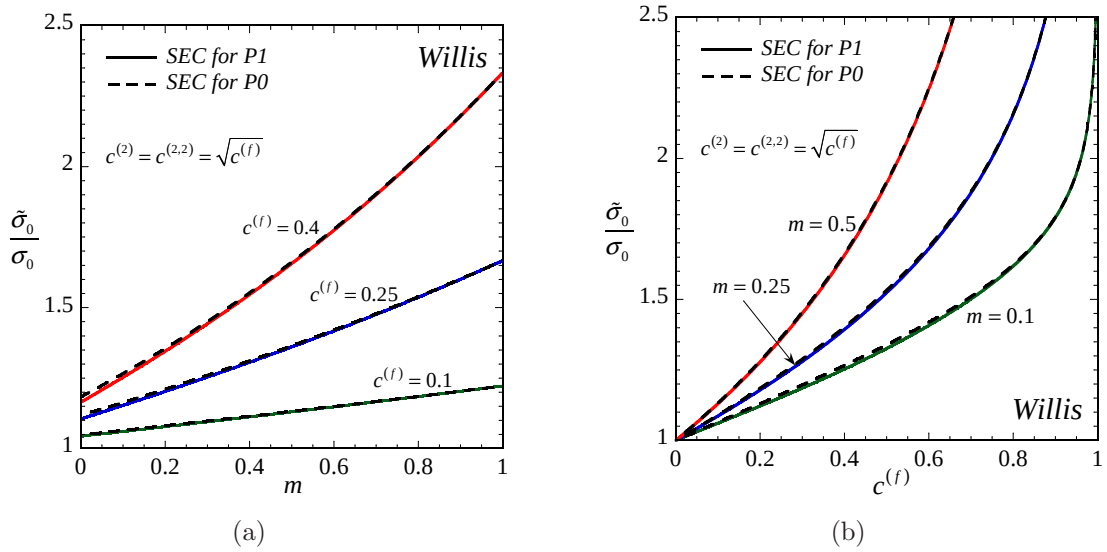

Figure 3.2: Comparison of the secant (SEC) bound (3.20) for a single-scale composite P0 (Fig. 3.1(a)), with rigid-fiber concentration $c^{(f)}$, and the secant (SEC) bound (3.17) for a two-scale composite P1 (Fig. 3.1(b)), with the same overall rigid-fiber content $c^{(f)} = c^{(2)}c^{(2,2)}$. The corresponding normalized effective in-plane yield-stresses $\tilde{\sigma}_0/\sigma_0$ are plotted (a) as a function of the nonlinearity exponent $m = 1/n$ for fixed values of $c^{(f)} = 0.1, 0.25, 0.4$ and (b) as a function of $c^{(f)}$ for fixed values of $m = 0.1, 0.25, 0.5$.

agreement with the corresponding estimates for P0, with the same overall content of rigid-fibers. Note that in the special case of a linearly elastic matrix ($m = 1$), the Willis estimate (3.18) for P1 depends only on the overall rigid-fiber content $c^{(f)} = c^{(2)}c^{(2,2)}$ in P1 and not on the specific values of $c^{(2)}$ and $c^{(2,2)}$. In this connection, it is relevant to remark that, from additional calculations performed for $c^{(2)} \neq c^{(2,2)}$ and $0 < m < 1$ it has been found that the second-order estimates for P1 are insensitive on the specific values of $c^{(2)}$ and $c^{(2,2)}$; they practically depend only on the total fiber concentration in P1. This, rather surprising, property of the estimates for P1 is probably related to the special sub-structure of this composite, since, as will be shown in the following sections, both the secant and the second-order estimates for the two-scale composites P2 (Fig. 3.4(b)) and G2 (Fig. 3.8(b)) depend explicitly on the meso-scale $c^{(2)}$ and micro-scale $c^{(1,2)}$ rigid-phase concentrations and not just on the corresponding overall rigid-phase content.

Another interesting observation from Figs. 3.3(a) and 3.3(b) is that in the ideally plastic limit $m \to 0$ all estimates shown reduce identically to 1, i.e., in this limit the effective yield-stress $\tilde{\sigma}_0$ of the composite materials P0 and P1 becomes equal to the yield-stress σ_0 of the matrix. Furthermore, from Figs. 3.3(c) and 3.3(d) we observe that the percolation limit—as predicted by the GSO and TSO estimates, respectively—for P0 and P1 is $c^{(f)} = 1$, i.e., these particulate composites can accommodate certain amount of deformation-rate even if they are *nearly* rigid. As

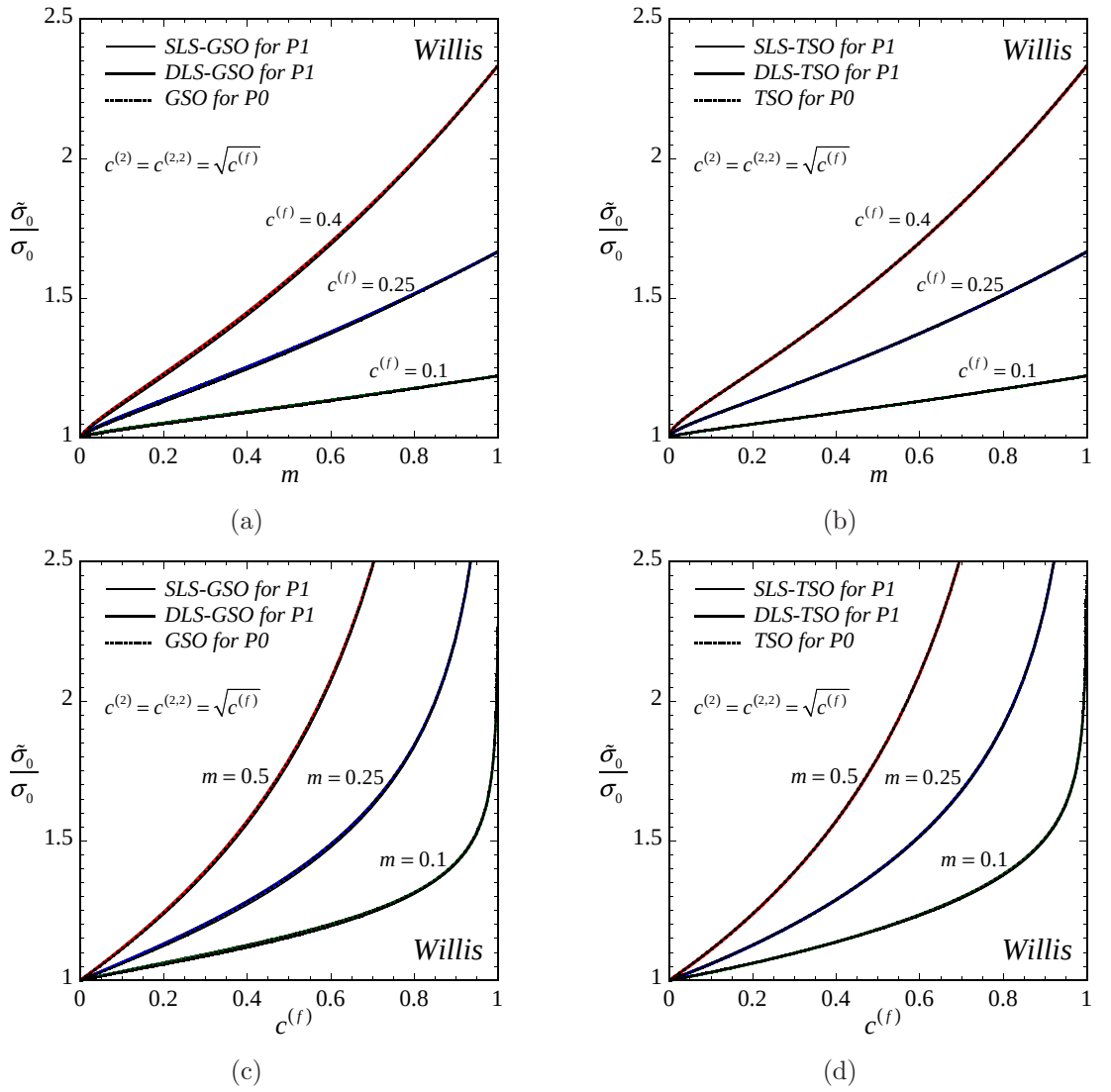

Figure 3.3: Comparison of SLS (continuous thin lines) and DLS (continuous thick lines) estimates for the two-scale *particulate* composite P1 (Fig. 3.1(b)). Part (a) shows the SLS-GSO estimate (3.54), with (3.51), and the DLS-GSO estimate (3.49) for the normalized effective in-plane yield-stress $\tilde{\sigma}_0/\sigma_0$ as a function of the rate-sensitivity exponent $m = 1/n$ for fixed values of the total rigid-fiber concentration $c^{(f)} = c^{(2)}c^{(2,2)} = 0.1, 0.25, 0.4$ in P1, with $c^{(2)} = c^{(2,2)} = \sqrt{c^{(f)}}$; part (c) shows the same estimates for $\tilde{\sigma}_0/\sigma_0$ as a function of $c^{(f)}$ for the cases $m = 0.1, 0.25, 0.5$. Parts (b) and (d) present the corresponding predictions of the SLS-TSO estimate (3.44), with (3.39), and the DLS-TSO estimate (3.34), respectively. GSO and TSO results corresponding to the special case $c^{(1)} = 0$ and $c^{(2,2)} = c^{(f)}$, i.e., the case of the single-scale *particulate* composite P0 (Fig. 3.1(a)), have been included in the relevant parts (dotted lines).

suggested by Ponte Castañeda [119], these results should be attributed to the use of the Willis estimate in computing the effective properties of the associated LCCs, since, as will be seen later, they hold for the particulate composite P2 as well, but not for the granular systems G0 and G2.

3.3 Application to particulate composites—II

The two-scale particulate composite P2 of Fig. 3.4(b) is assumed to made out of aligned meso-scale ℓ_1 rigid-fibers (phase (2)) of cylindrical shape and circular cross-section that are distributed randomly and isotropically in a composite-matrix material (phase (1)). The composite-matrix is actually a single-scale composite P0—which is depicted in Fig. 3.1(a) and for comparison purposes is also shown in Fig. 3.4(a)—consisting of micro-scale ℓ_2 rigid-fibers (phase (1,2)) of cylindrical shape and circular cross-section that are distributed randomly and isotropically in a homogeneous-matrix material (phase (1,1)). Both the meso-scale ℓ_1 and the micro-scale ℓ_2 rigid-fibers are aligned along the same direction. In connection with the discussion of subsection 2.2.2, it is remarked that the shape tensors $\mathbf{Z}^{(2)}$ and $\mathbf{Z}$—defining the shape, orientation and distribution symmetry of the micro- and meso-scale fibers, respectively—are such that $\mathbf{Z}^{(2)} = \mathbf{Z}$, with $\mathbf{Z}$ given by (3.1). The homogeneous-matrix-phase $(1,1)$ is assumed to be an isotropic material, characterized by a stress-potential $u^{(1,1)}(\boldsymbol{\sigma}) = u(\boldsymbol{\sigma})$ given by the power-law relation (3.2). Since the stress-potential $u^{(2)}$ and $u^{(1,2)}$ of the rigid-fiber-phases are identically equal to zero, the local stress-potential of the two-scale composite P2 is given by

$$u(\mathbf{x},\boldsymbol{\sigma}) = \chi^{(1)}(\mathbf{x})u^{(1)}(\mathbf{x},\boldsymbol{\sigma}), \qquad u^{(1)}(\mathbf{x},\boldsymbol{\sigma}) = \chi^{(1,1)}(\mathbf{x})u(\boldsymbol{\sigma}), \tag{3.57}$$

with

$$\chi^{(1)}(\mathbf{x}) = \begin{cases} 1, & \text{if } \mathbf{x} \in \Omega^{(1)} \\ 0, & \text{otherwise} \end{cases}, \quad \chi^{(1,1)}(\mathbf{x}) = \begin{cases} 1, & \text{if } \mathbf{x} \in \Omega^{(1,1)} \\ 0, & \text{otherwise} \end{cases}, \tag{3.58}$$

where $\Omega^{(1)}$ and $\Omega^{(1,1)}$ denote the subregions of the volume Ω of P2 occupied by the composite-matrix-phase (1) and the homogeneous-matrix-phase $(1,1)$, respectively. For later reference, we introduce the volume fractions $c^{(1)} = |\Omega^{(1)}|/|\Omega|$, $c^{(2)} = |\Omega^{(2)}|/|\Omega| = 1 - c^{(1)}$, with $\Omega^{(2)} = \Omega^{(1)} - \Omega$ being the part of Ω occupied by the meso-scale ℓ_1 rigid-fibers, $c^{(1,1)} = |\Omega^{(1,1)}|/|\Omega^{(1)}|$ and $c^{(1,2)} = |\Omega^{(1,2)}|/|\Omega^{(1)}| = 1 - c^{(1,1)}$, where $\Omega^{(1,2)} = \Omega^{(1)} - \Omega^{(1,1)}$ is the part of Ω occupied by the micro-scale ℓ_2 rigid-fibers, so that the overall content of rigid-fibers in P2 is $1-(1-c^{(2)})(1-c^{(1,2)}) \equiv c^{(f)}$. Note that in the special case $c^{(2)} = 0$ or, alternatively, $c^{(1,2)} = 0$, the two-scale composite P2 reduces to the single-scale composite P0.

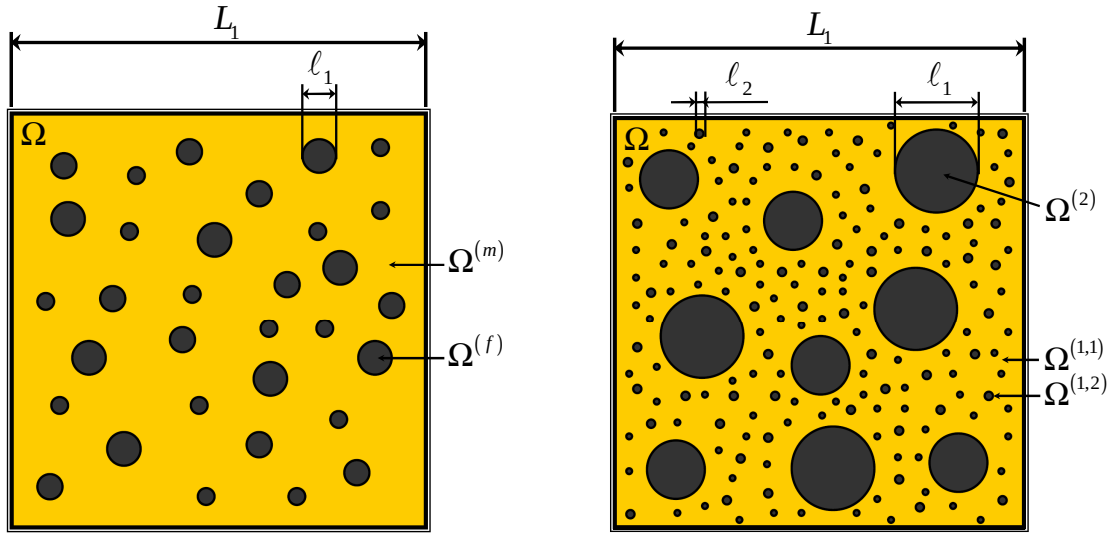

Figure 3.4: Schematic of rigidly-reinforced *particulate* systems. (a) *Single-scale* composite P0 with rigid-fiber concentration $c^{(f)} = |\Omega^{(f)}|/|\Omega|$. (b) *Two-scale* composite P2 with meso-scale ℓ_1 rigid-fiber concentration $c^{(2)} = |\Omega^{(2)}|/|\Omega|$, micro-scale ℓ_2 rigid-fiber concentration $c^{(1,2)} = |\Omega^{(1,2)}|/|\Omega^{(1)}|$ and overall rigid-fiber content $1 - (1 - c^{(2)})(1 - c^{(1,2)}) \equiv c^{(f)}$.

3.3.1 Secant estimates for P2

The direct secant estimate (2.107) or its equivalent sequential secant estimate (2.58), with (2.116), for the in-plane effective response of the two-scale composite P2 (Fig. 3.4(b)) may be determined by following an approach analogous to that developed in subsection 3.2.1 for P1. However, as discussed next, the in-plane effective yield-stress $\tilde{\sigma}_0$ of P2 is characterized by a special property which allows the computation of the associated secant estimate directly from the corresponding estimate (3.20) for the single-scale composite P0 (Fig. 3.4(a)), which has been already derived in subsection 3.2.1. It is important, however, to emphasize that the derivation of this property is based on the sequential homogenization approach (see subsection 2.4.2) along with some special features of the sub-structure of P2. Thus, the following property for the in-plane effective yield-stress $\tilde{\sigma}_0$ of P2 may also be utilized in the context of the second-order estimates of the sequential type, but not the direct ones. Furthermore, we note in passing, that the property of $\tilde{\sigma}_0$ discussed next is also valid for the two-scale granular system G2 of Fig. 3.8(b), which is discussed in section 3.4.

The in-plane effective yield-stress of the two-scale composites P2, normalized by the yield-stress

σ_0 of the homogeneous-matrix material, may be written as

$$\frac{\tilde{\sigma}_0}{\sigma_0} = \frac{\tilde{\sigma}_0}{\tilde{\sigma}_0^{(1)}} \frac{\tilde{\sigma}_0^{(1)}}{\sigma_0}. \tag{3.59}$$

where $\tilde{\sigma}_0^{(1)}$ denotes the in-plane effective yield-stress of the composite-matrix-phase of P2, which, as already mentioned, is essentially a single-scale composite P0 (Fig. 3.4(a)). Thus, the quantity $\tilde{\sigma}_0^{(1)}/\sigma_0$ corresponds to a (nonlinear) *mesocscopic* single-scale composite with the *micro-structure* of P2, while the quantity $\tilde{\sigma}_0/\tilde{\sigma}_0^{(1)}$ corresponds to a (nonlinear) *macroscopic* single-scale composite with the *meso-structure* of P2. Given the fact that the micro- and meso-structure of P2 are identical and that the heterogeneity contrast in the corresponding mesoscopic and macroscopic composites is the same (i.e., $\sigma_0^{(2)}/\tilde{\sigma}_0^{(1)} = \sigma_0^{(2)}/\sigma_0 = \infty$, with $\sigma_0^{(2)}$ denoting the yield-stress of the rigid-fibers), it follows that $\tilde{\sigma}_0^{(1)}/\sigma_0$ and $\tilde{\sigma}_0/\tilde{\sigma}_0^{(1)}$ must be identical functions of their arguments, and, in addition, they are identical to the corresponding function for the normalized in-plane effective yield-stress of the single-scale composite P0. Hence, $\tilde{\sigma}_0/\sigma_0$ may be obtained from the relation

$$\frac{\tilde{\sigma}_0}{\sigma_0}\left(n, c^{(2)}, c^{(1,2)}\right) = \frac{\hat{\sigma}_0}{\sigma_0}\left(n, c^{(2)}\right) \frac{\hat{\sigma}_0}{\sigma_0}\left(n, c^{(1,2)}\right), \tag{3.60}$$

where $\hat{\sigma}_0$ is used here to denote the in-plane effective yield-stress of P0, n denotes the nonlinearity exponent, $c^{(1,2)}$ is the volume fraction of the micro-scale ℓ_2 rigid-fibers in the composite matrix of P2 and $c^{(2)}$ is the concentration of the meso-scale ℓ_1 rigid-fibers in P2. It should be emphasized that the above relation is an *exact* result, i.e., it is independent of the estimate that may be used for $\hat{\sigma}_0$. Note that the property (3.60) imply the following symmetry relation

$$\frac{\tilde{\sigma}_0}{\sigma_0}(n, c^{(2)}, c^{(1,2)}) = \frac{\tilde{\sigma}_0}{\sigma_0}(n, c^{(1,2)}, c^{(2)}). \tag{3.61}$$

Making use of (3.60) together with the secant estimate (3.20) for the single-scale composite P0, it follows that the secant estimate (2.107) (which is identical to (2.58), with (2.116)), for the two-scale system P2 is given by

$$\frac{\tilde{\sigma}_0}{\sigma_0} = \left((1-c^{(2)})(1-c^{(1,2)})\right)^{-\frac{1}{n}} \left((1+c^{(2)})(1+c^{(1,2)})\right)^{\frac{1+n}{2n}}. \tag{3.62}$$

From the exact relation (3.60) and the fact that the secant estimate (3.20) is an upper bound for P0, it follows that the secant estimate (3.62) is an upper bound for P2.

3.3.2 Tangent second-order estimates for P2

Direct linearization scheme estimate. Towards the determination of the DLS-TSO estimate (2.128) for the two-scale particulate composite P2 (Fig. 3.4(b)), we consider a two-scale LCC with local stress potential of the form

$$u(\mathbf{x}, \boldsymbol{\sigma}) = \chi^{(1)}(\mathbf{x}) u_T^{(1)}(\mathbf{x}, \boldsymbol{\sigma}), \qquad u_T^{(1)}(\mathbf{x}, \boldsymbol{\sigma}) = \chi^{(1,1)}(\mathbf{x}) u_T^{(1,1)}(\boldsymbol{\sigma}), \tag{3.63}$$

where the phase-potential $u_T^{(1,1)}(\boldsymbol{\sigma})$, corresponding to the homogeneous-matrix material of the LCC, is defined by (3.22), with (3.23), in terms of the associated reference stress $\boldsymbol{\sigma}^{(1,1)}$ and compliance $\mathbf{M}^{(1,1)}$ tensors. Recall that, in the context of the DLS-TSO estimate (2.128), the reference tensors are prescribed by $\boldsymbol{\sigma}^{(1,1)} = \overline{\boldsymbol{\sigma}}^{(1,1)}$ and $\mathbf{M}^{(1,1)} = \partial^2 u(\overline{\boldsymbol{\sigma}}^{(1,1)})/\partial\boldsymbol{\sigma}^2$. Furthermore, under plane-stress loadings, the average stress tensor $\overline{\boldsymbol{\sigma}}^{(1,1)}$ in the homogeneous-matrix-phase of the LCC can be shown [107] to be proportional to the applied stress $\overline{\boldsymbol{\sigma}}$, i.e.,

$$\overline{\boldsymbol{\sigma}}^{(1,1)} = \omega^{(1,1)}\overline{\boldsymbol{\sigma}}, \tag{3.64}$$

and the tangent modulus $\mathbf{M}^{(1,1)}$ may be expressed in the form (3.5) in terms of the scalars $\lambda_{\mathbf{E}}^{(1,1)}$ and $\lambda_{\mathbf{F}}^{(1,1)}$, which are functions of $\omega^{(1,1)}$ and $\bar{\sigma}_e = \sqrt{3\overline{\boldsymbol{\sigma}}_d \cdot \overline{\boldsymbol{\sigma}}_d/2}$ only. In addition, it is remarked that in the definition (3.63) of the LCC we have taken into account the fact that the local material properties in both meso-scale ℓ_1 and micro-scale ℓ_2 rigid-fiber-phase are identically equal to zero, i.e.,

$$u_T^{(2)}(\boldsymbol{\sigma}) = 0, \qquad \mathbf{M}^{(2)} = \mathbf{0}, \qquad \boldsymbol{\alpha}^{(2)} = \mathbf{0}, \qquad \phi^{(2)} = 0, \tag{3.65}$$

and

$$u_T^{(1,2)}(\boldsymbol{\sigma}) = 0, \qquad \mathbf{M}^{(1,2)} = \mathbf{0}, \qquad \boldsymbol{\alpha}^{(1,2)} = \mathbf{0}, \qquad \phi^{(1,2)} = 0, \tag{3.66}$$

respectively, where $u_T^{(\cdot)}$, $\mathbf{M}^{(\cdot)}$, $\boldsymbol{\alpha}^{(\cdot)}$ and $\phi^{(\cdot)}$ denote the associated phase-potential, compliance tensor, thermal strain tensor and specific heat, respectively.

Following the relevant discussion of subsection 2.7.1, the effective behavior of the two-scale LCC (3.63) will be determined in this work by means of the sequential homogenization approach (see subsection 2.4.2). Specialized in the present context, this approach consists in determining first the effective behavior of the mesoscopic single-scale LCC—associated with the composite-matrix-phase of P2—with local stress potential $u_T^{(1)}(\mathbf{x}, \boldsymbol{\sigma})$ given by $(3.63)_2$, and then making use of this homogenized medium to characterize the local response in the composite-matrix-phase of the two-scale LCC, and thus reducing it to a single-scale macroscopic LCC defined by

$$u_T(\mathbf{x}, \boldsymbol{\sigma}) = \chi^{(1)}(\mathbf{x})\tilde{u}_T^{(1)}(\boldsymbol{\sigma}), \tag{3.67}$$

where $\tilde{u}_T^{(1)}$ denotes the effective stress-potential of the mesoscopic LCC. The effective properties of both the mesoscopic and macroscopic LCC may be easily estimated by appropriate specialization of the more general results provided in appendix I, as discussed next.

The effective stress-potential $\tilde{u}_T^{(1)}$ of the mesoscopic LCC $(3.63)_2$ is given by (3.22) in terms of the associated effective quantities $\mathbf{M}^{(1)}$, $\boldsymbol{\alpha}^{(1)}$ and $\phi^{(1)}$. Taking into account relations $(3.66)_2$, $(3.66)_3$ and $(3.66)_4$, from expressions $(3.103)_2$ and $(3.103)_3$ we find that

$$\boldsymbol{\alpha}^{(1)} = c^{(1,1)}\left(\mathbf{B}^{(1,1)}\right)^T\boldsymbol{\alpha}^{(1,1)}, \qquad \phi^{(1)} = c^{(1,1)}\phi^{(1,1)} + \frac{1}{2}c^{(1,1)}\boldsymbol{\alpha}^{(1,1)} \cdot \mathbf{b}^{(1,1)}, \tag{3.68}$$

while from (3.105) we obtain

$$\mathbf{B}^{(1,1)} = \frac{1}{c^{(1,1)}} \left(\mathbf{M}^{(1,1)}\right)^{-1} \mathbf{M}^{(1)}, \qquad \mathbf{b}^{(1,1)} = \left(\mathbf{M}^{(1,1)}\right)^{-1} \left((\mathbf{B}^{(1,1)})^T - \mathbf{K}\right) \boldsymbol{\alpha}^{(1,1)}. \tag{3.69}$$

The effective modulus tensor $\mathbf{M}^{(1)}$ in the above expressions is computed by means of the Willis estimate (3.108), which for the mesoscopic LCC $(3.63)_2$ is given by

$$\mathbf{M}^{(1)} = \mathbf{M}^{(1,1)} + c^{(1,2)} \left[c^{(1,1)}\mathbf{Q} - \left(\mathbf{M}^{(1,1)}\right)^{-1}\right]^{-1}, \tag{3.70}$$

where the micro-structural tensor $\mathbf{Q}$, given by (3.107), must be evaluated at the the scalar moduli $\lambda_{\mathbf{E}}^{(0)} = \lambda_{\mathbf{E}}^{(1,1)}$ and $\lambda_{\mathbf{F}}^{(0)} = \lambda_{\mathbf{F}}^{(1,1)}$ associated with $\mathbf{M}^{(1,1)}$.

The effective behavior of the macroscopic single-scale LCC (3.67) is determined in a completely analogous manner, by taking into account the above results for the effective properties of the mesoscopic LCC along with the relations $(3.65)_2$, $(3.65)_3$ and $(3.65)_4$. Specifically, the effective stress-potential $\tilde{u}_T$ macroscopic LCC is given by (3.102), with

$$\widetilde{\boldsymbol{\alpha}} = c^{(1)} \left(\mathbf{B}^{(1)}\right)^T \boldsymbol{\alpha}^{(1)}, \qquad \tilde{\phi} = c^{(1)}\phi^{(1)} + \frac{1}{2} c^{(1)} \boldsymbol{\alpha}^{(1)} \cdot \mathbf{b}^{(1)}, \tag{3.71}$$

where the stress concentration tensors $\mathbf{B}^{(1)}$ and $\mathbf{b}^{(1)}$ are given by

$$\mathbf{B}^{(1)} = \frac{1}{c^{(1)}} \left(\mathbf{M}^{(1)}\right)^{-1} \widetilde{\mathbf{M}}, \qquad \mathbf{b}^{(1)} = \left(\mathbf{M}^{(1)}\right)^{-1} \left((\mathbf{B}^{(1)})^T - \mathbf{K}\right) \boldsymbol{\alpha}^{(1)}, \tag{3.72}$$

and the effective modulus $\widetilde{\mathbf{M}}$ is computed by

$$\widetilde{\mathbf{M}} = \mathbf{M}^{(1)} + c^{(2)} \left[c^{(1)}\mathbf{Q} - \left(\mathbf{M}^{(1)}\right)^{-1}\right]^{-1}, \tag{3.73}$$

where the meso-structural tensor $\mathbf{Q}$, given by (3.107), must be evaluated at $\lambda_{\mathbf{E}}^{(0)} = \lambda_{\mathbf{E}}^{(1)}$ and $\lambda_{\mathbf{F}}^{(0)} = \lambda_{\mathbf{F}}^{(1)}$ associated with the effective modulus tensor $\mathbf{M}^{(1)}$ of the composite-matrix-phase, obtained from (3.70).

Finally, it can be shown that the DLS-TSO estimate (2.128) for the normalized in-plane effective yield-stress of the two-scale composites P2 reduces to

$$\frac{\tilde{\sigma}_0}{\sigma_0} = \left\{ c^{(1)} c^{(1,1)} \left[(\omega^{(1,1)})^{1+n} + \frac{1+n}{2} (\omega^{(1,1)})^n \left(1 - \omega^{(1,1)}\right) \right] \right\}^{-\frac{1}{n}}, \tag{3.74}$$

where the variable $\omega^{(1,1)}$, defined by (3.64), is computed by solving the scalar equation obtained from

$$\overline{\boldsymbol{\sigma}}^{(1,1)} = \mathbf{B}^{(1,1)} \overline{\boldsymbol{\sigma}}^{(1)} + \mathbf{b}^{(1,1)}, \qquad \overline{\boldsymbol{\sigma}}^{(1)} = \mathbf{B}^{(1)} \overline{\boldsymbol{\sigma}} + \mathbf{b}^{(1)}. \tag{3.75}$$

where we recall that $\mathbf{B}^{(1,1)}$ and $\mathbf{b}^{(1,1)}$ are given by (3.69), while $\mathbf{B}^{(1)}$ and $\mathbf{b}^{(1)}$ are given by (3.72). After some manipulations, it can be shown that (3.75) reduces to

$$\omega^{(1,1)} = \frac{n}{n + c^{(1,2)}\sqrt{n} + c^{(2)}\sqrt{(n + c^{(1,2)}\sqrt{n})(1 + c^{(1,2)}\sqrt{n})}}, \tag{3.76}$$

which, in turn, completely determines the DLS-TSO estimate (3.74).

Note that in the special case $c^{(2)} = 0$ and $c^{(1,2)} \equiv c^{(f)}$ (or, equivalently, $c^{(1,2)} = 0$ and $c^{(2)} \equiv c^{(f)}$), corresponding to a single-scale composite P0 (Fig. 3.4(a)), the DLS-TSO estimate (3.74) reduces to the corresponding TSO estimate (3.35), as it should, while in the limiting case $n \to \infty$ of an ideally-plastic matrix, the DLS-TSO estimate (3.74) reduces to $\tilde{\sigma}_0 = \sigma_0$. On the other hand, in the case of a linearly elastic matrix ($n = 1$), the DLS-TSO estimate (3.74) recovers the associated Willis estimate, which in the case of P2 is given by

$$\frac{\tilde{\sigma}_0}{\sigma_0} = \frac{(1+c^{(2)})(1+c^{(1,2)})}{(1-c^{(2)})(1-c^{(1,2)})} = \frac{1+c^{(f)}}{1-c^{(f)}} + 2\frac{c^{(2)}c^{(1,2)}}{1-c^{(f)}}, \tag{3.77}$$

where we recall that $c^{(f)} \equiv 1-(1-c^{(2)})(1-c^{(1,2)})$ in $(3.77)_2$ denotes the total volume fraction of the rigid-fibers in P2. It is remarked that the first term in $(3.77)_2$ corresponds to the Willis estimate for a linearly-elastic composite P0 with fiber concentration $c^{(f)}$. Thus, for linearly-elastic materials, the two-scale composite P2 is predicted to exhibit a stiffer behavior from the corresponding single-scale composite P0 for the same overall rigid-fiber content $c^{(f)}$ and all non-zero values of $c^{(2)}$ and $c^{(1,2)}$.

Sequential linearization scheme estimate. Taking into account relation (3.60) discussed in subsection 3.3.1, along with the TSO estimate (3.35) for the single-scale composite P0, it follows immediately that the SLS-TSO estimate (2.67), with (2.142), for P2 is given by

$$\frac{\tilde{\sigma}_0}{\sigma_0} = \frac{\tilde{\sigma}_0^{(1)}}{\sigma_0}\left\{c^{(1)}\left[(\omega^{(1)})^{1+n} + \frac{1+n}{2}(\omega^{(1)})^n\left(1-\omega^{(1)}\right)\right]\right\}^{-\frac{1}{n}}, \tag{3.78}$$

with

$$\frac{\tilde{\sigma}_0^{(1)}}{\sigma_0} = \left\{c^{(1,1)}\left[(\omega^{(1,1)})^{1+n} + \frac{1+n}{2}(\omega^{(1,1)})^n\left(1-\omega^{(1,1)}\right)\right]\right\}^{-\frac{1}{n}}, \tag{3.79}$$

where

$$\omega^{(1)} = \frac{1}{1+c^{(2)}/\sqrt{n}}, \qquad \omega^{(1,1)} = \frac{1}{1+c^{(1,2)}/\sqrt{n}}. \tag{3.80}$$

3.3.3 Generalized-secant second-order estimates for P2

Direct linearization scheme estimate. The DLS-GSO estimate (2.154) for the two-scale particulate composite P2 of Fig. 3.4(b) requires the computation of the effective properties of a two-scale LCC with a local stress-potential given by (3.63). This LCC differs from the two-scale LCC considered in the previous subsection in the context of the corresponding DLS-TSO estimate for P2 only in that the reference variables $\boldsymbol{\sigma}^{(1,1)}$ and $\mathbf{M}^{(1,1)}$ in the expression (3.22), with (3.23), defining the phase-potential $u_T^{(1,1)}(\boldsymbol{\sigma})$ of the homogeneous-matrix material of the LCC, are such

that $\boldsymbol{\sigma}^{(1,1)} = \overline{\boldsymbol{\sigma}}$ and $\mathbf{M}^{(1,1)}$ is prescribed by (3.5) in terms of the associated (unknown) generalized-secant moduli $\lambda_{\mathbf{E}}^{(1,1)}$ and $\lambda_{\mathbf{F}}^{(1,1)}$. Taking into account this remark, the effective properties of the LCC under consideration here are determined by following the procedure discussed in the previous subsection.

The DLS-GSO estimate (2.154) for the normalized in-plane effective yield-stress of P2 can be easily shown to reduce to

$$\frac{\tilde{\sigma}_0}{\sigma_0} = \left\{ c^{(1)} c^{(1,1)} \left[\left((x_{\parallel}^{(1,1)})^2 + (x_{\perp}^{(1,1)})^2 \right)^{\frac{1+n}{2}} + (1+n) \left(\omega^{(1,1)} - x_{\parallel}^{(1,1)} \right) \right] \right\}^{-\frac{1}{n}}, \tag{3.81}$$

where $\omega^{(1,1)}$ is the proportionality constant determining the phase-average stress tensor $\overline{\boldsymbol{\sigma}}^{(1,1)} = \omega^{(1,1)} \overline{\boldsymbol{\sigma}}$ in the homogeneous-matrix-phase of the LCC and $x_{\parallel}^{(1,1)}$, $x_{\perp}^{(1,1)}$ are the associated fluctuation variables, defined by $(3.6)_1$, $(3.6)_2$, respectively. Equation (3.75) determines $\omega^{(1,1)}$ in terms of the anisotropy ratio $\kappa^{(1,1)} = \lambda_{\mathbf{F}}^{(1,1)} / \lambda_{\mathbf{E}}^{(1,1)}$ by means of an expression of the form

$$\omega^{(1,1)} = \mathcal{W}^{(1,1)} \left(n, c^{(2)}, c^{(1,2)}, k^{(1,1)} \right), \tag{3.82}$$

which is given explicitly by (3.128) in appendix II. The variables $x_{\parallel}^{(1,1)}$, $x_{\perp}^{(1,1)}$ are obtained from the corresponding fluctuation equations (2.153), which by choosing the root according to the sign$(\omega^{(1,1)} - 1)$, reduce to

$$\begin{aligned} x_{\parallel}^{(1,1)} &= 1 + \frac{\text{sign}(\omega^{(1,1)} - 1)}{\bar{\sigma}_e} \sqrt{\frac{3}{c^{(1)} c^{(1,1)}} \frac{\partial \tilde{u}_T}{\partial (2\lambda_{\mathbf{E}}^{(1,1)})^{-1}}} = \mathcal{X}_{\parallel}^{(1,1)}(n, c^{(2)}, c^{(1,2)}, \omega^{(1,1)}, k^{(1,1)}), \\ x_{\perp}^{(1,1)} &= \frac{1}{\bar{\sigma}_e} \sqrt{\frac{3}{c^{(1)} c^{(1,1)}} \frac{\partial \tilde{u}_T}{\partial (2\lambda_{\mathbf{F}}^{(1,1)})^{-1}}} = \mathcal{X}_{\perp}^{(1,1)}(n, c^{(2)}, c^{(1,2)}, \omega^{(1,1)}, k^{(1,1)}), \end{aligned} \tag{3.83}$$

where the functions $\mathcal{X}_{\parallel}^{(1,1)}$ and $\mathcal{X}_{\perp}^{(1,1)}$ are provided in the appendix II by relations (3.126) and (3.127), respectively. Substitution of these results for $\omega^{(1,1)}$, $x_{\parallel}^{(1,1)}$ and $x_{\perp}^{(1,1)}$ into the associated generalized-secant condition yields the nonlinear equation $\mathcal{E}^{(1,1)}(n, c^{(2)}, c^{(1,2)}, \omega^{(1,1)}, k^{(1,1)}) = 0$ for the variable $\kappa^{(1,1)}$, the solution of which completely determines the DLS-GSO estimate (3.81) for P2.

In the case of a linearly elastic matrix ($n = 1$), the estimate (3.81) recovers the Willis estimate (3.77) for P2, as it should. In the ideally-plastic limit $n \to \infty$, (3.81) can be shown to reduce to $\tilde{\sigma}_0 = \sigma_0$. Finally, for $c^{(2)} = 0$ and $c^{(1,2)} \equiv c^{(f)}$ (or, equivalently, $c^{(1,2)} = 0$ and $c^{(2)} \equiv c^{(f)}$), the DLS-GSO estimate (3.81) recovers the corresponding GSO estimate (3.50) for the single-scale composite P0, again as it should.

Sequential linearization scheme estimate. Making use of relation (3.60) and the GSO estimate (3.50) for the single-scale composite P0, the SLS-GSO estimate (2.81), with (2.167), for the

normalized effective yield-stress of the two-scale composites P2 simplifies to

$$\frac{\tilde{\sigma}_0}{\sigma_0} = \frac{\tilde{\sigma}_0^{(1)}}{\sigma_0}\left\{c^{(1)}\left[\left((x_{\parallel}^{(1)})^2+(x_{\perp}^{(1)})^2\right)^{\frac{1+n}{2}}+(1+n)\left(\omega^{(1)}-x_{\parallel}^{(1)}\right)\right]\right\}^{-\frac{1}{n}}, \tag{3.84}$$

with

$$\frac{\tilde{\sigma}_0^{(1)}}{\sigma_0} = \left\{c^{(1,1)}\left[\left((x_{\parallel}^{(1,1)})^2+(x_{\perp}^{(1,1)})^2\right)^{\frac{1+n}{2}}+(1+n)\left(\omega^{(1,1)}-x_{\parallel}^{(1,1)}\right)\right]\right\}^{-\frac{1}{n}}, \tag{3.85}$$

where the variables in the above expressions are obtained from the following relations

$$\begin{aligned}
x_{\parallel}^{(1)} &= \mathcal{X}_{\parallel}^{(2,1)}\left(n,c^{(2)},\omega^{(1)},k^{(1)}\right), & x_{\parallel}^{(1,1)} &= \mathcal{X}_{\parallel}^{(2,1)}\left(n,c^{(1,2)},\omega^{(1,1)},k^{(1,1)}\right),\\
x_{\perp}^{(1)} &= \mathcal{X}_{\perp}^{(2,1)}\left(n,c^{(2)},\omega^{(1)},k^{(1)}\right), & x_{\perp}^{(1,1)} &= \mathcal{X}_{\perp}^{(2,1)}\left(n,c^{(1,2)},\omega^{(1,1)},k^{(1,1)}\right),\\
\omega^{(1)} &= \mathcal{W}^{(2,1)}\left(n,c^{(2)},k^{(1)}\right), & \omega^{(1,1)} &= \mathcal{W}^{(2,1)}\left(n,c^{(1,2)},k^{(1,1)}\right),
\end{aligned} \tag{3.86}$$

and

$$\mathcal{E}^{(2,1)}\left(n,c^{(2)},\omega^{(1)},k^{(1)}\right)=0, \qquad \mathcal{E}^{(2,1)}\left(n,c^{(1,2)},\omega^{(1,1)},k^{(1,1)}\right)=0. \tag{3.87}$$

For the determination of the functions $\mathcal{X}_{\parallel}^{(2,1)}$, $\mathcal{X}_{\perp}^{(2,1)}$, $\mathcal{W}^{(2,1)}$ and $\mathcal{E}^{(2,1)}$ we refer to the relevant discussion of subsection 3.2.3, in the context of the GSO estimate (3.51) for the composite fibers of P1, which as already discussed is identical to the GSO estimate (3.50) for P0.

3.3.4 Results and discussion for P2

In analogy to the results of Fig. 3.2 for P1 (Fig. 3.1(b)), Fig. 3.5 provides a comparison of the secant (SEC) upper bound (3.20) for the normalized effective in-plane yield-stress $\tilde{\sigma}_0/\sigma_0$ of the single-scale composite P0 (Fig. 3.4(a)) and the corresponding bound (3.62) for the two-scale particulate system P2 (Fig. 3.4(b)) with the same overall rigid-fiber concentration $c^{(f)} = 1-(1-c^{(2)})(1-c^{(1,2)})$. Thus, Fig. 3.5(a) presents $\tilde{\sigma}_0/\sigma_0$ as a function of the nonlinearity exponent $m = 1/n$ for fixed rigid-fiber concentrations $c^{(f)} = 0.1, 0.25, 0.4$, and Fig. 3.5(b) shows $\tilde{\sigma}_0/\sigma_0$ as a function of $c^{(f)}$ for $m = 0.1, 0.25, 0.5$. In contrast with the secant estimates for P1 (see Fig. 3.2), from Fig. 3.5 we observe that the secant estimates for P2 are stiffer than the corresponding estimates for P0 for all values of $c^{(f)}$ and m. In addition, it is observed that this difference increases with increasing $c^{(f)}$ and decreases slightly with decreasing m. Again, these predictions are qualitatively consistent with the results of the following figures showing the corresponding predictions of the second-order estimates.

Figs. 3.6(a) and 3.6(b) show the effect of the meso-scale ℓ_1 rigid-fiber concentration $c^{(2)}$ and the micro-scale ℓ_2 rigid-fiber concentration $c^{(1,2)}$ in the two-scale composite P2 (see Fig. 3.4(b)) on the normalized effective in-plane yield-stress $\tilde{\sigma}_0/\sigma_0$ of P2, as predicted by the associated DLS-GSO

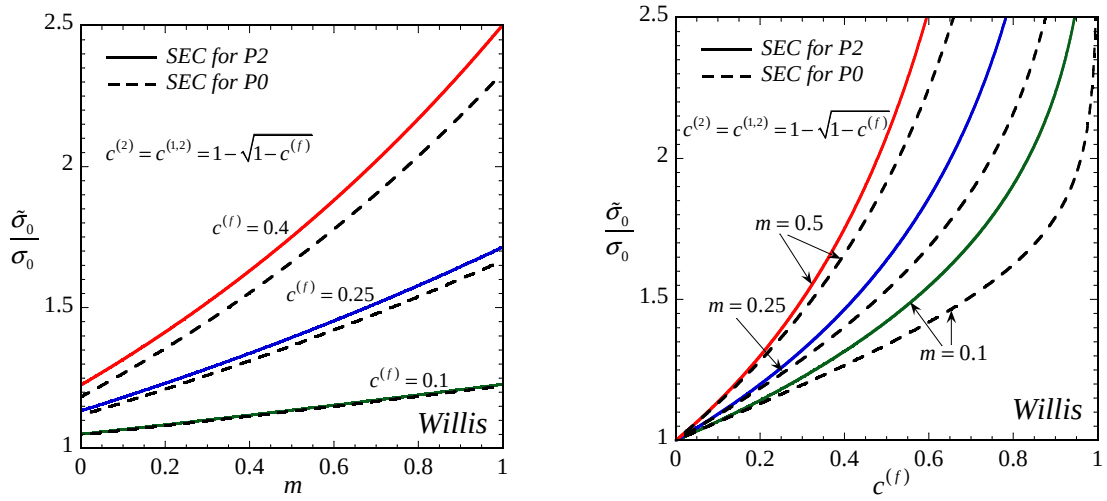

Figure 3.5: Comparison of the secant (SEC) bound (3.20) for a single-scale composite P0 (Fig. 3.1(a)), with rigid-fiber concentration $c^{(f)}$, and the secant (SEC) bound (3.62) for a two-scale composite P2 (Fig. 3.4(b)), with the same overall rigid-fiber content $c^{(f)} = 1 - (1 - c^{(2)})(1 - c^{(1,2)})$. The corresponding normalized effective in-plane yield-stresses $\tilde{\sigma}_0/\sigma_0$ are plotted (a) as a function of the nonlinearity exponent $m = 1/n$ for fixed values of $c^{(f)} = 0.1, 0.25, 0.4$ and (b) as a function of $c^{(f)}$ for fixed values of $m = 0.1, 0.25, 0.5$.

estimate (3.81) and DLS-TSO estimate (3.74), respectively. Results are shown for the fixed values $m = 0.1, 0.25$ of the rate-sensitivity exponent $m = 1/n$ and various values of the ratio $t \equiv c^{(2)}/c^{(1,2)}$ as functions of the overall rigid-fiber concentration $c^{(f)} = 1 - (1 - c^{(2)})(1 - c^{(1,2)})$ in P2. In both figures, it is observed that the curves corresponding to $t = 3$ and $t = 10$ coincide with the curves for $t = 1/3$ and $t = 1/10$, respectively, which suggests that both the DLS-GSO estimate (3.81) and the DLS-TSO (3.74) estimate satisfy the (exact) symmetry relation (3.61) for $\tilde{\sigma}_0/\sigma_0$ to an excellent degree of approximation. At this point, it is relevant to recall that the corresponding SLS-GSO (3.84), with (3.85), and SLS-TSO (3.78), with (3.79), estimates are by construction consistent with the symmetry relation (3.61) for $\tilde{\sigma}_0/\sigma_0$. Another interesting observation in the context of Fig. 3.6 is that both in the case of the GSO estimates of Fig. 3.6(a) and in the case of the TSO estimates of Fig. 3.6(b), the two-scale composite P2 is predicted to be stiffer than the single-scale composite P0 (dotted curves) in all cases considered. Specifically, the associated differences in the corresponding values of $\tilde{\sigma}_0/\sigma_0$ are small for small to moderate total fiber concentrations $c^{(f)}$, but become significant for higher values of $c^{(f)}$ and increase with increasing $c^{(f)}$. The maximum difference in the in-plane response of P0 and P2 corresponds to the case when $c^{(2)} = c^{(1,2)}$ in P2. In all cases considered in these plots, the TSO results are clearly stiffer than the corresponding

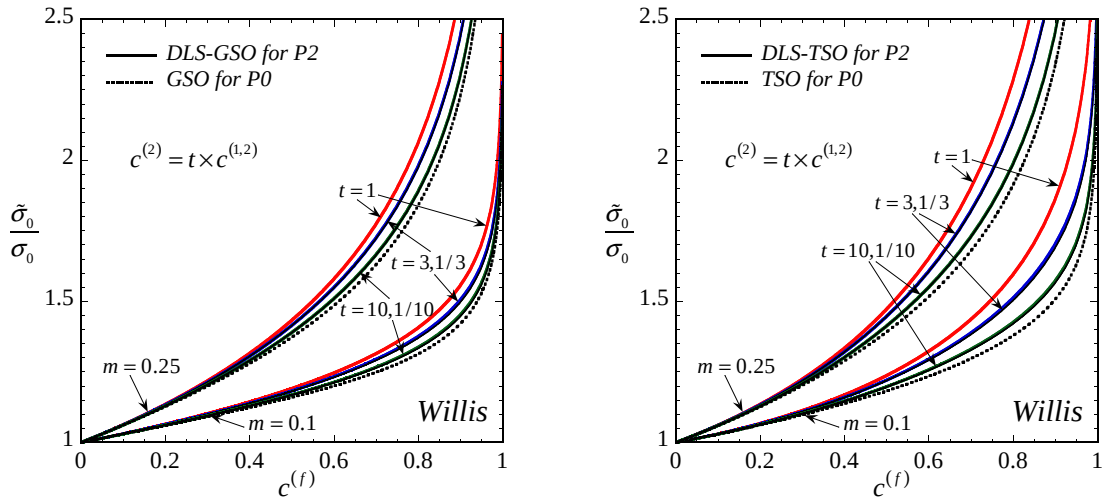

(a) (b)

Figure 3.6: The effect of the meso-scale ℓ_1 and micro-scale ℓ_2 rigid-fiber contents $c^{(2)}$ and $c^{(1,2)}$, respectively, on the overall response of the two-scale *particulate* composite P2 (Fig. 3.4(b)). Predictions of the (a) DLS-GSO estimate (3.81) and (b) DLS-TSO estimate (3.74) for the normalized effective in-plane yield-stress $\tilde{\sigma}_0/\sigma_0$ are plotted for the fixed values $m = 0.1, 0.25$ of the nonlinearity exponent $m = 1/n$ as functions of the total rigid-fiber concentration $c^{(f)} = 1 - (1 - c^{(2)})(1 - c^{(1,2)})$ for the combinations $c^{(2)} = c^{(1,2)}$, $c^{(2)} = 3c^{(1,2)}$, $c^{(2)} = 10c^{(1,2)}$ (continuous thick lines) and $c^{(1,2)} = 3c^{(2)}$, $c^{(1,2)} = 10c^{(2)}$ (continuous thin lines), as well as for the special case $c^{(2)} = 0$ or $c^{(1,2)} = 0$ (dotted lines), i.e., the case corresponding to the single-scale *particulate* composite P0 (Fig. 3.4(a)).

GSO results. Finally, it is remarked that the corresponding results for $\tilde{\sigma}_0/\sigma_0$ obtained by means of the SLS-GSO expression (3.84), with (3.85), and the SLS-TSO expression (3.78), with (3.79), are very similar to the DLS-GSO estimates of Fig. 3.6(a) and the DLS-TSO estimates of Fig. 3.6(b), respectively, and are therefore omitted.

The results presented in Figure 3.7 serve the same purpose as those of Figure 3.3, but for the two-scale particulate composite P2 (Fig. 3.4(b)). Specifically, Figs. 3.7(a) and 3.7(c) compare SLS-GSO (3.84), with (3.85), and DLS-GSO (3.81) estimates for $\tilde{\sigma}_0/\sigma_0$ of P2 as functions of the rate-sensitivity exponent $m = 1/n$ and the total rigid-fiber concentration $c^{(f)} = 1 - (1 - c^{(2)})(1 - c^{(1,2)})$ in P2, respectively, while Figs. 3.7(b) and 3.7(d) compare the corresponding SLS-TSO (3.78), with (3.79), and DLS-TSO (3.74) estimates. All calculations have been performed for the case $c^{(2)} = c^{(1,2)} = 1 - \sqrt{1 - c^{(f)}}$, which is expected to reveal the largest possible differences between the corresponding SLS- and DLS-based estimates, since, as already remarked in the context of Fig. 3.6, for $c^{(2)} \neq c^{(1,2)}$ both SLS- and DLS-based estimates for P2 are closer to the corresponding estimates for P0, and therefore to each other. From Figs. 3.7(a) and 3.7(c), it is observed that the

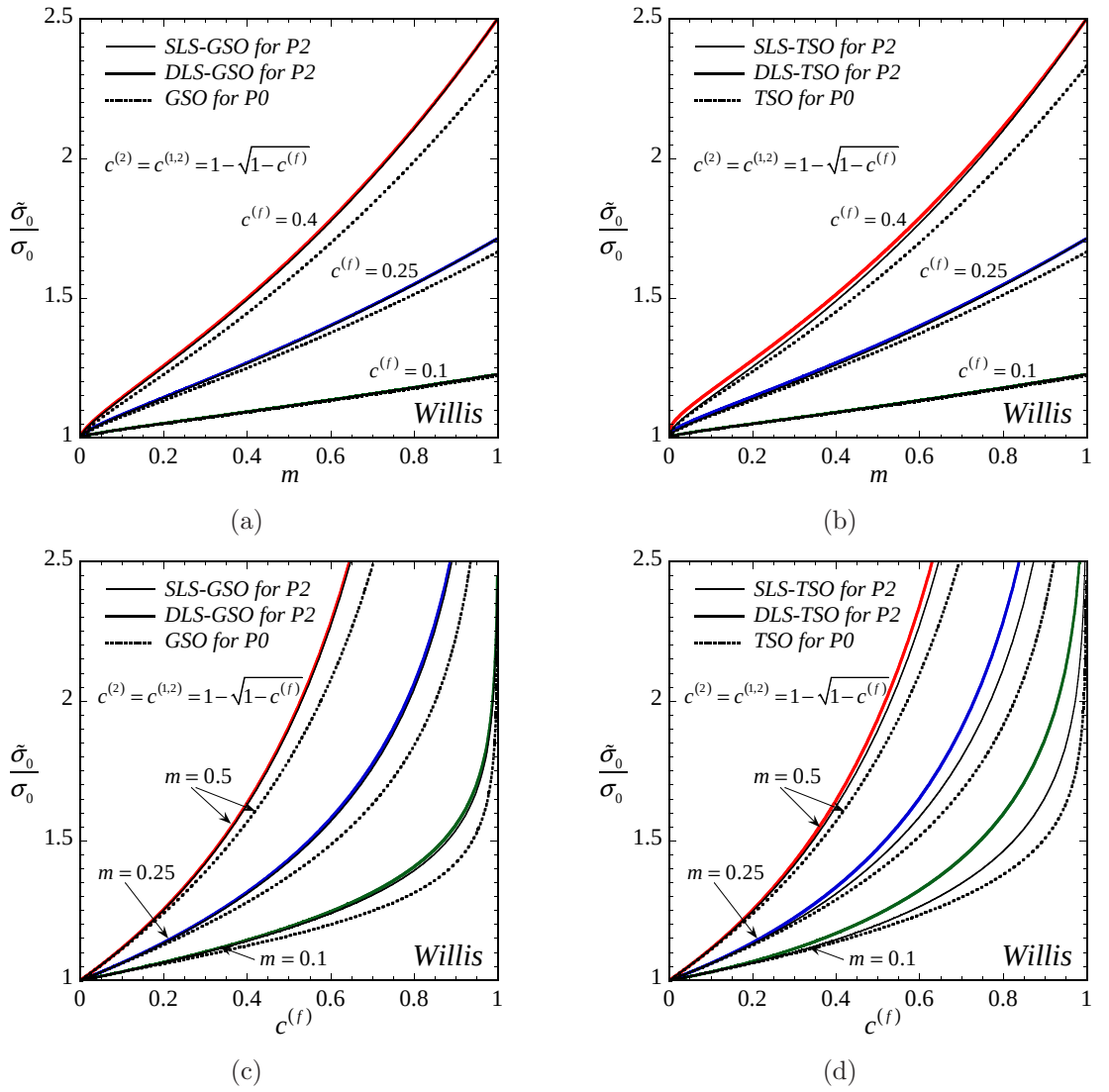

Figure 3.7: Comparison of SLS (continuous thin lines) and DLS (continuous thick lines) estimates for the two-scale *particulate* composite P2 (Fig. 3.4(b)). Part (a) shows the SLS-GSO estimate (3.84), with (3.85), and the DLS-GSO estimate (3.81) for the normalized effective in-plane yield-stress $\tilde{\sigma}_0/\sigma_0$ as a function of the rate-sensitivity exponent $m = 1/n$ for fixed values of the total rigid-fiber concentration $c^{(f)} = 0.1, 0.25, 0.4$ in P2, with $c^{(2)} = c^{(1,2)} = 1 - \sqrt{1 - c^{(f)}}$; part (c) shows the same estimates for $\tilde{\sigma}_0/\sigma_0$ as a function of $c^{(f)}$ for the cases $m = 0.1, 0.25, 0.5$. Parts (b) and (d) present the corresponding predictions of the SLS-TSO estimate (3.78), with (3.79), and the DLS-TSO estimate (3.74), respectively. GSO and TSO results corresponding to the special case $c^{(2)} = 0$ and $c^{(1,2)} = c^{(f)}$ (or $c^{(1,2)} = 0$ and $c^{(2)} = c^{(f)}$), i.e., the case of the single-scale *particulate* composite P0 (Fig. 3.4(a)), have been included in the relevant parts (dotted lines).

corresponding SLS-GSO and DLS-GSO estimates are practically indistinguishable for all values of m and $c^{(f)}$. From Figs. 3.7(b) and 3.7(d), on the other hand, we observe that the corresponding SLS-TSO and DLS-TSO estimates agree quite well for all values of m up to moderate volume fractions (see $c^{(f)} = 0.1$ and $c^{(f)} = 0.25$ in part (a)), while for higher values of $c^{(f)}$ (see $c^{(f)} > 0.3$ in Part (b)) the SLS-TSO and DLS-TSO estimates start to deviate and their difference increases with increasing $c^{(f)}$. In the ideally plastic limit $m = 0$, just like in the case of the corresponding results of Figs. 3.3(a) and 3.3(b) for P1, all second-order estimates of Figs. 3.7(a) and 3.7(b) for P2 reduce to 1. Finally, it is observed that all second-order estimates of Fig. 3.7 are fully consistent with the corresponding secant upper bounds of Fig. 3.5, as they should.

3.4 Application to granular composites

The single-scale granular composite G0 of Fig. 3.8(a) is constituted by two different types of "grains", one of which is assumed to be rigid (phase (f)) and the other one is taken to be a deformable material (phase (m)). Both phases are assumed to be aligned along a direction normal to the figure and distributed randomly and isotropically in the plane shown, so that the associated shape tensor $\mathbf{Z}$ (characterizing the distributional ellipsoids (2.8) of the phases) is again given by (3.1). The deformable-grains are assumed to be made out of a homogeneous and isotropic material, characterized by the viscoplastic power-law relation (3.2). The volume fractions of the phases of G0 are defined by $c^{(m)} = |\Omega^{(m)}|/|\Omega|$ and $c^{(f)} = |\Omega^{(f)}|/|\Omega| = 1 - c^{(m)}$, where Ω is the volume of G0 and $\Omega^{(m)}$, $\Omega^{(f)} = \Omega - \Omega^{(m)}$ are the complementary parts of Ω occupied by the deformable- and rigid-phase, respectively.

At the meso-scale level ℓ_1, the two-scale granular system G2 of Fig. 3.8(b) is constituted by rigid-grains (phase (2)) and deformable composite-grains (phase (1)). Each composite-grain is essentially a single-scale granular system G0, made out of micro-scale ℓ_2 rigid-grains (phase (1,2)) and micro-scale ℓ_2 deformable homogeneous-grains (phase (1,1)). All phases are assumed to be aligned along a direction normal to the figure and distributed randomly and isotropically in the plane shown, so that the associated shape tensors $\mathbf{Z}^{(1)}$ and $\mathbf{Z}$—defining respectively the mico-scale (2.21) and meso-scale (2.8) distributional ellipsoids—are such that $\mathbf{Z}^{(1)} = \mathbf{Z}$, with $\mathbf{Z}$ given by (3.1). The homogeneous-phase $(1,1)$ is assumed to be an isotropic material, characterized by a viscoplastic stress-potential $u^{(1,1)}(\boldsymbol{\sigma}) = u(\boldsymbol{\sigma})$ given by the power-law relation (3.2). Since the stress-potential $u^{(2)}$ and $u^{(1,2)}$ of the rigid-phases are identically equal to zero, the local stress-potential of the two-scale composite G2 is given by

$$u(\mathbf{x}, \boldsymbol{\sigma}) = \chi^{(1)}(\mathbf{x}) u^{(1)}(\mathbf{x}, \boldsymbol{\sigma}), \qquad u^{(1)}(\mathbf{x}, \boldsymbol{\sigma}) = \chi^{(1,1)}(\mathbf{x}) u(\boldsymbol{\sigma}), \tag{3.88}$$

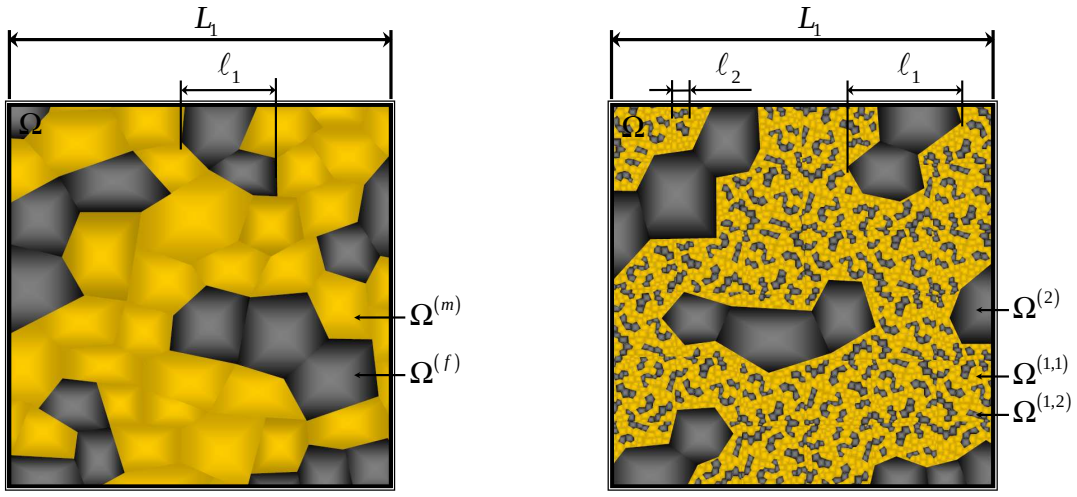

(a) (b)

Figure 3.8: Schematic of rigidly-reinforced *granular* systems. (a) *Single-scale* composite G0 with rigid-phase concentration $c^{(f)} = |\Omega^{(f)}|/|\Omega|$. (b) *Two-scale* composite G2 with meso-scale ℓ_1 rigid-phase concentration $c^{(2)} = |\Omega^{(2)}|/|\Omega|$, micro-scale ℓ_2 rigid-phase concentration $c^{(1,2)} = |\Omega^{(1,2)}|/|\Omega^{(1)}|$ and overall rigid-phase content $1-(1-c^{(2)})(1-c^{(1,2)}) \equiv c^{(f)}$.

with

$$\chi^{(1)}(\mathbf{x}) = \begin{cases} 1, & \text{if } \mathbf{x} \in \Omega^{(1)} \\ 0, & \text{otherwise} \end{cases}, \quad \chi^{(1,1)}(\mathbf{x}) = \begin{cases} 1, & \text{if } \mathbf{x} \in \Omega^{(1,1)} \\ 0, & \text{otherwise} \end{cases}, \tag{3.89}$$

where $\Omega^{(1)}$ and $\Omega^{(1,1)}$ denote the subregions of the volume Ω of G2 occupied by the deformable composite-phase (1) and homogeneous-phase $(1,1)$, respectively. For later reference, we introduce the volume fractions $c^{(1)} = |\Omega^{(1)}|/|\Omega|$, $c^{(2)} = |\Omega^{(2)}|/|\Omega| = 1 - c^{(1)}$, with $\Omega^{(2)} = \Omega^{(1)} - \Omega$ being the part of Ω occupied by the meso-scale ℓ_1 rigid-phase, $c^{(1,1)} = |\Omega^{(2,1)}|/|\Omega^{(1)}|$ and $c^{(1,2)} = |\Omega^{(1,2)}|/|\Omega^{(1)}| = 1-c^{(1,1)}$, where $\Omega^{(1,2)} = \Omega^{(1)} - \Omega^{(1,1)}$ is the part of Ω occupied by the micro-scale ℓ_2 rigid-phase, so that the overall content of the rigid material in G2 is $1-(1-c^{(2)})(1-c^{(1,2)}) \equiv c^{(f)}$. Note that in the special case $c^{(2)} = 0$ or, alternatively, $c^{(1,2)} = 0$, the two-scale composite G2 reduces to the single-scale composite G2.

At this point, it should be emphasized that, as opposed to the particulate system P2 of Fig. 3.4(b), the constituent phases of the granular system G2 of Fig. 3.8(b) may play a potentially equal role in its effective response. To allow for this possibility, the effective properties of the LCCs involved in the calculations of the various estimates for the granular composite G2 should be computed by means of the self-consistent estimate (3.109), given in appendix I. Taking into account this important remark, the procedures followed in the previous section for the derivation of the corresponding estimates for the particulate composite P2 apply in the present context without

modifications, except that the Willis estimates (3.70) and (3.73) for the effective modulus tensors $\mathbf{M}^{(1)}$ and $\widetilde{\mathbf{M}}$, respectively, must be replaced by the corresponding self-consistent estimates. For plane-stress loadings, the later estimates can be shown to be of the form

$$\mathbf{M}^{(1)} = \frac{1}{2\lambda_{\mathbf{E}}^{(1)}}\mathbf{E} + \frac{1}{2\lambda_{\mathbf{F}}^{(1)}}\mathbf{F}, \qquad \widetilde{\mathbf{M}} = \frac{1}{2\tilde{\lambda}_{\mathbf{E}}}\mathbf{E} + \frac{1}{2\tilde{\lambda}_{\mathbf{F}}}\mathbf{F}, \tag{3.90}$$

where the projection tensors $\mathbf{E}$ and $\mathbf{F}$ are defined by $(3.5)_2$ and $(3.5)_3$, respectively. The scalar moduli $\lambda_{\mathbf{E}}^{(1)}$ and $\lambda_{\mathbf{F}}^{(1)}$ in $(3.90)_1$ are implicitly determined by means of the following self-consistent estimate for $\mathbf{M}^{(1)}$

$$\mathbf{M}^{(1)} = \left\{ c^{(1,1)} \left[\mathbf{M}^{(1,1)} + \mathbf{M}^{*}\right]^{-1} + c^{(1,2)} \left(\mathbf{M}^{*}\right)^{-1} \right\}^{-1} - \mathbf{M}^{*}, \tag{3.91}$$

where $\mathbf{M}^{*} = \mathbf{Q}^{-1} - \mathbf{M}^{(1)}$ and the micro-structural tensor $\mathbf{Q}$, given by expression $(3.107)_2$, must be evaluated at $\lambda_{\mathbf{E}}^{(0)} = \lambda_{\mathbf{E}}^{(1)}$ and $\lambda_{\mathbf{F}}^{(0)} = \lambda_{\mathbf{F}}^{(1)}$. Similarly, the effective moduli $\tilde{\lambda}_{\mathbf{E}}$ and $\tilde{\lambda}_{\mathbf{F}}$ in $(3.90)_2$ are implicitly obtained in terms of the following self-consistent estimate for $\widetilde{\mathbf{M}}$

$$\widetilde{\mathbf{M}} = \left\{ c^{(1)} \left[\mathbf{M}^{(1)} + \widetilde{\mathbf{M}}^{*}\right]^{-1} + c^{(2)} \left(+\widetilde{\mathbf{M}}^{*}\right)^{-1} \right\}^{-1} - \widetilde{\mathbf{M}}^{*}, \tag{3.92}$$

where $\widetilde{\mathbf{M}}^{*} = \mathbf{Q}^{-1} - \widetilde{\mathbf{M}}$ and the meso-structural tensor $\mathbf{Q}$, given by $(3.107)_2$, must be evaluated at $\lambda_{\mathbf{E}}^{(0)} = \tilde{\lambda}_{\mathbf{E}}$ and $\lambda_{\mathbf{F}}^{(0)} = \tilde{\lambda}_{\mathbf{F}}$.

3.4.1 Secant estimates for G2

As already mentioned, the normalized in-plane effective yield-stress $\tilde{\sigma}_0/\sigma_0$ of the two-scale granular composite G2 (Fig. 3.8(b)) is given in terms of the corresponding quantity for the single-scale granular system G0 (Fig. 3.8(a)) by means of the relation (3.60). Therefore, taking into account (3.60), along with the secant estimate

$$\frac{\tilde{\sigma}_0}{\sigma_0} = \left(1 - c^{(f)}\right)^{\frac{n-1}{2n}} \left(1 - 2c^{(f)}\right)^{-\frac{n+1}{2n}}, \tag{3.93}$$

for a single-scale granular composite G0, derived by Ponte Castañeda [115], we conclude that the secant estimate for G2 is given by

$$\frac{\tilde{\sigma}_0}{\sigma_0} = \left((1 - c^{(2)})(1 - c^{(1,2)})\right)^{\frac{n-1}{2n}} \left((1 - 2c^{(2)})(1 - 2c^{(1,2)})\right)^{-\frac{n+1}{2n}}. \tag{3.94}$$

Note that in the linearly-elastic limit ($n = 1$), the secant estimate (3.94) reduces to the following self-consistent estimate

$$\frac{\tilde{\sigma}_0}{\sigma_0} = \frac{1}{(1 - 2c^{(2)})(1 - 2c^{(1,2)})} = \frac{1}{(1 - 2c^{(f)}) + 2c^{(2)}c^{(1,2)}}, \tag{3.95}$$

where $c^{(f)} = 1 - (1 - c^{(2)})(1 - c^{(1,2)})$ denotes the overall concentration of the rigid-phase in G2.

At this point, it is relevant to remark that although the estimate (3.94) is not a bound for the class of granular composites G2, it does provide a bound for any other nonlinear estimate that makes use of the same linear self-consistent estimates.

3.4.2 Tangent second-order estimates for G2

Direct linearization scheme estimate. The DLS-TSO estimate (2.128) for the normalized in-plane effective yield-stress $\tilde{\sigma}_0/\sigma_0$ of the two-scale granular composite G2 (Fig. 3.8(b)) is given by (3.74), where the variable $\omega^{(1,1)}$ is determined as discussed in subsection 3.3.2 in the context of the corresponding DLS-TSO estimate for the particulate system P2, by taking into account relations (3.91) and (3.92). It is remarked that $\omega^{(1,1)}$ may be computed in closed-form, but the relevant expression is too cumbersome to be included here.

It can be shown that, in the ideally-plastic limit $n \to \infty$, the DLS-TSO estimate (3.74) for G2 reduces to

$$\begin{aligned}\frac{\tilde{\sigma}_0}{\sigma_0} =& \frac{1}{2}\frac{1}{(1-2c^{(f)})+2c^{(2)}c^{(1,2)}} \\ & \Bigg\{ c^{(2)}\sqrt{\left(2c^{(1,2)}(1-c^{(1,2)})\right)^2(1-2c^{(2)})+\left(c^{(2)}-2c^{(2)}c^{(1,2)}(1-c^{(1,2)})\right)^2} \\ & + (c^{(2)})^2\left(1-2c^{(1,2)}(1-c^{(1,2)})\right)+2(1-2c^{(2)})\left(1-c^{(1,2)}\right)^2\Bigg\},\end{aligned} \tag{3.96}$$

while in the linearly-elastic limit ($n = 1$), the DLS-TSO estimate (3.74) for G2 reduces to the self-consistent estimate (3.95), as it should. Recalling that the case $c^{(2)} = 0$ or, alternatively, $c^{(1,2)} = 0$, corresponds to a single scale granular system G0 (Fig. 3.8(a)), we observe that for $c^{(2)} > 0$ and $c^{(1,2)} > 0$ the self-consistent estimate (3.95) for the two-scale system G2 is always softer than the corresponding estimate for the single-scale system G0. In the special case $c^{(2)} = 0$ and $c^{(1,2)} \equiv c^{(f)}$ (or, equivalently, $c^{(1,2)} = 0$ and $c^{(2)} \equiv c^{(f)}$), and general values of the nonlinearity exponent n, the DLS-TSO estimate (3.74) for G2 reduces to the following TSO estimate for the single-scale granular composite G0

$$\frac{\tilde{\sigma}_0}{\sigma_0} = \left\{(1-c^{(f)})\left[(\omega^{(m)})^{1+n}+\frac{1+n}{2}(\omega^{(m)})^n\left(1-\omega^{(m)}\right)\right]\right\}^{-\frac{1}{n}}, \tag{3.97}$$

where

$$\omega^{(m)} = \frac{2n(1-2c^{(f)})}{2n(1-2c^{(f)})+(c^{(f)})^2(1+n)+c^{(f)}\sqrt{4n(1-2c^{(f)})+(c^{(f)})^2(1+n)^2}}. \tag{3.98}$$

Sequential linearization scheme estimate. The SLS-TSO estimate (2.67), with (2.142), for the granular system G2 (Fig. 3.8(b)) is given by the expressions (3.78), with (3.79), where the variable $\omega^{(1,1)}$ is given by the right-hand-side of (3.98) with $c^{(f)}$ replaced by $c^{(1,2)}$ and, similarly, $\omega^{(1)}$ is given by the right-hand-side of (3.98) with $c^{(f)}$ replaced by $c^{(2)}$.

In the limit $n \to \infty$ of an ideally-plastic composite G2, the SLS-TSO estimate (3.78), with (3.79), takes the simple form

$$\frac{\tilde{\sigma}_0}{\sigma_0} = \frac{(1-c^{(2)})^2}{1-2c^{(2)}} \frac{(1-c^{(1,2)})^2}{1-2c^{(1,2)}}, \tag{3.99}$$

In the linearly-elastic limit ($n = 1$), the SLS-TSO estimate (3.78), with (3.79), for G2 recovers the self-consistent estimate (3.95), as it should, and in the special cases $c^{(2)} = 0$ or $c^{(1,2)} = 0$, the SLS-TSO estimate (3.78), with (3.79), for G2 reduces to the TSO estimate (3.97) for the single-scale system G0, again as it should.

3.4.3 Generalized-secant second-order estimates for G2

Direct linearization scheme estimate. The DLS-GSO estimate (2.154) for the two-scale granular composite G2 (Fig. 3.8(b)) is given by (3.81), where the variables $\omega^{(1,1)}$, $x_{\parallel}^{(1,1)}$ and $x_{\perp}^{(1,1)}$ are obtained as discussed in subsection 3.3.2 in the context of the corresponding DLS-GSO estimate for the composite system P2, by taking into account relations (3.91) and (3.92). The resulting equations for these variables are too complicated to be provided here. It is remarked, however, that in the linearly-elastic limit ($n = 1$), the DLS-GSO estimate (3.81) for G2 recovers the corresponding self-consistent estimate (3.95). Furthermore, quite interestingly, in the ideally-plastic limit $m \to 0$, the DLS-GSO estimate (3.81) for G2 can be shown to be exactly equal to the square-root of the corresponding DLS-TSO estimate (3.96). Finally, the GSO estimate for the single scale granular system G0 (Fig. 3.8(a)) may be obtained as the special case $c^{(2)} = 0$ or, equivalently, $c^{(1,2)} = 0$, of the DLS-GSO estimate (3.81) for G2.

Sequential linearization scheme estimate. Making use of the property (3.60) characterizing the normalized effective yield-stress $\tilde{\sigma}_0/\sigma_0$ of the two-scale granular composite G2, the SLS-GSO estimate (2.81), with (2.167), for G2 is determined by expressions (3.84), with (3.85), where the GSO estimates (3.84) and (3.85) are obtained as the special cases $c^{(2)} = 0$ and $c^{(1,2)} = 0$, respectively, of the DLS-GSO estimate (3.81) for G2 discussed above. We remark that in the linearly-elastic limit ($n = 1$), the SLS-GSO estimate (3.84) and (3.85) for G2 reduces to the self-consistent estimate (3.95), as it should. In addition, similar to the DLS-GSO estimate (3.81) for G2 discussed above, in the ideally-plastic limit $m \to 0$, the SLS-GSO estimate (3.84), with (3.85), for G2 can be shown to be exactly equal to the square-root of the corresponding SLS-TSO estimate (3.99).

3.4.4 Results and discussion for G2

Next, we consider the results of Fig. 3.9 for the two-scale granular composite G2 of Fig. 3.8(b), examining the effect of the meso-scale ℓ_1 and micro-scale ℓ_2 rigid-phase concentrations $c^{(2)}$ and $c^{(1,2)}$, respectively, on the normalized effective in-plane yield-stress $\tilde{\sigma}_0/\sigma_0$ of G2. In particular, Figs. 3.9(a) and 3.9(b) show respectively the DLS-GSO estimate (3.81) and the DLS-TSO estimate (3.74) for $\tilde{\sigma}_0/\sigma_0$ of G2 as a function of the total content of the rigid-phase $c^{(f)} = 1-(1-c^{(2)})(1-c^{(1,2)})$, for the fixed value $m = 0.25$ of the nonlinearity exponent $m = 1/n$ and various values of the concentration ratio $t \equiv c^{(2)}/c^{(1,2)}$. The corresponding GSO and TSO estimates for G0 are also included in Figs. 3.9(a) and 3.9(b), respectively. Recall that, for $c^{(2)} = 0$ or $c^{(1,2)} = 0$, the two-scale composite G2 reduces to G0. From both Figs. 3.9(a) and 3.9(b), we observe that the estimates for $t = 3$ and $t = 10$ are in a very good agreement with the corresponding results for $t = 1/3$ and $t = 1/10$, which in turn suggests that both DLS-GSO estimate (3.81) and DLS-TSO estimate (3.74) are consistent with the (exact) symmetry relation (3.61) for $\tilde{\sigma}_0/\sigma_0$ to a very good approximation. Furthermore, it is observed that the effective response of the two-scale composite G2 is softer than the effective response of the single-scale composite G0 for the same total rigid-phase concentration, and that the softest response of G2 corresponds to the case $c^{(2)} = c^{(1,2)}$. Note, in particular, that the percolation limit, which for G0 is given by the well-known value $c^{(f)} = 0.5$, for G2 is shifted to higher values of $c^{(f)}$, depending on the value of t. The maximum percolation limit for G2 corresponds to the case $t = 1$ and it is $c^{(f)} = 0.75$, as can be easily inferred from the self-consistent estimate (3.95) and the estimate (3.96) for ideally-plastic composites.

In analogy with the results of Fig. 3.3 for P1 and Fig. 3.7 for P2, Figure 3.10 compares the SLS-based second-order estimates with the corresponding DLS-based estimates for the normalized effective in-plane yield-stress $\tilde{\sigma}_0/\sigma_0$ of G2. Again, the results shown in this figure correspond to the case $c^{(2)} = c^{(1,2)} = 1-\sqrt{1-c^{(f)}}$, for which we expect to find the largest differences between the corresponding SLS- and DLS-based estimates. From Fig. 3.10(a) we observe that the agreement between the SLS-GSO and DLS-GSO estimates for G2 is excellent in the entire range of values of m for all values of $c^{(f)}$ considered, except for some small differences which appear near the ideally-plastic limit for $c^{(f)} = 0.4$. Similar conclusions can be drown from the results of Fig. 3.10(c), which further reveal that the class of granular composites G2 for which essential differences are observed between these SLS-GSO and DLS-GSO estimates is restricted to materials with nearly ideally plastic deformable-phase (e.g., $m = 0.1$) and a total rigid-phase concentration $c^{(f)}$ that is close to the associated percolation limit. From Figs. 3.10(b) and 3.10(d) it can be clearly seen that the agreement of corresponding SLS-TSO and DLS-TSO estimates is less satisfactory, especially near the percolation limit of nearly ideally-plastic composites. A more detailed examination of these estimates in the ideally plastic-limit $m = 0$ is considered next.

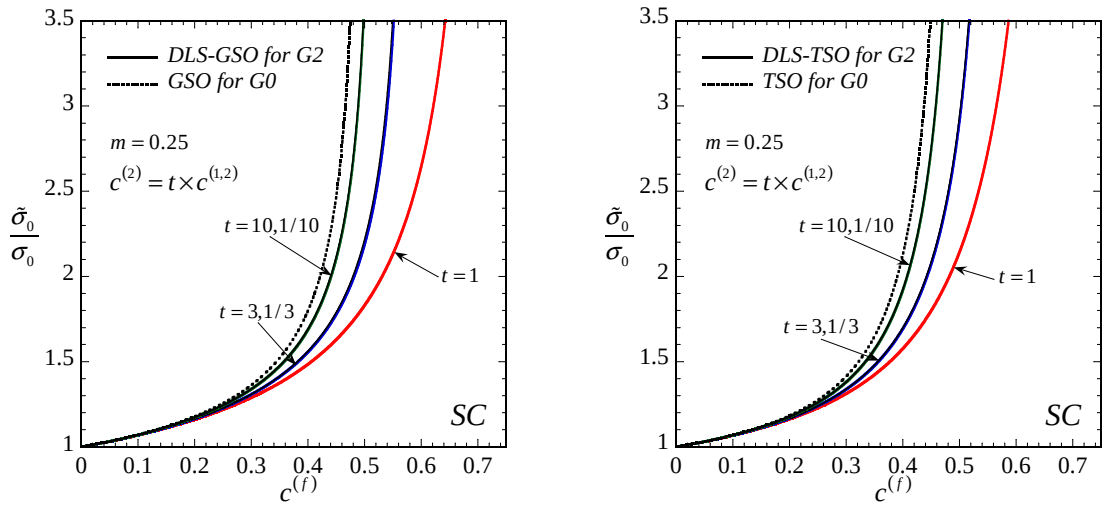

Figure 3.9: The effect of the meso-scale ℓ_1 and micro-scale ℓ_2 rigid-phase contents $c^{(2)}$ and $c^{(1,2)}$, respectively, on the overall in-plane response of the two-scale *granular* composite G2 (Fig. 3.8(b)). Predictions of the (a) DLS-GSO estimate (3.81) and (b) DLS-TSO estimate (3.74) for the normalized effective in-plane yield-stress $\tilde{\sigma}_0/\sigma_0$ are shown for the fixed value $m = 0.25$ of the nonlinearity exponent $m = 1/n$ as functions of the total rigid-phase concentration $c^{(f)} = 1-(1-c^{(2)})(1-c^{(1,2)})$ for the combinations $c^{(2)} = c^{(1,2)}$, $c^{(2)} = 3c^{(1,2)}$, $c^{(2)} = 10c^{(1,2)}$ (continuous thick lines) and $c^{(1,2)} = 3c^{(2)}$, $c^{(1,2)} = 10c^{(2)}$ (continuous thin lines), as well as for the special case $c^{(2)} = 0$ or $c^{(1,2)} = 0$ (dotted lines), i.e., the case corresponding to the single-scale *granular* composite G0 (Fig. 3.8(a)).

Fig. 3.11(a) compares the SLS-GSO and DLS-GSO estimates for the normalized in-plane effective yield-stress $\tilde{\sigma}_0/\sigma_0$ of ideally-plastic ($m = 0$) two-scale granular composites G2, plotted as a function of the overall rigid-phase content $c^{(f)}$ for $c^{(2)} = c^{(1,2)} = 1-\sqrt{1-c^{(f)}}$, while Fig. 3.11(b) provides the corresponding comparison for the associates SLS-TSO estimate (3.99) and DLS-TSO estimate (3.96). The corresponding GSO and TSO estimates for single-scale granular composites G0 are also shown in the relevant parts of this figure. Recall that the GSO estimates of Fig. 3.11(a) are exactly equal to the square-root of the corresponding TSO estimates of Fig. 3.11(b). (For a further comparison, Figs. 3.11(a) and 3.11(b) include also the corresponding secant (SEC) upper bounds (3.93) and (3.94) for G0 and G2, respectively.) As observed in the context of Fig. 3.10, these results are expected to reveal to maximum possible differences between the corresponding SLS- and DLS-based second-order estimates for G2. From Fig. 3.11(a), it is observed that the SLS-GSO and DLS-GSO estimates for G2 agree quite well up to a value of $c^{(f)} \approx 0.4$, after which their differences become evident and increase as $c^{(f)}$ approaches the percolation limit, with the

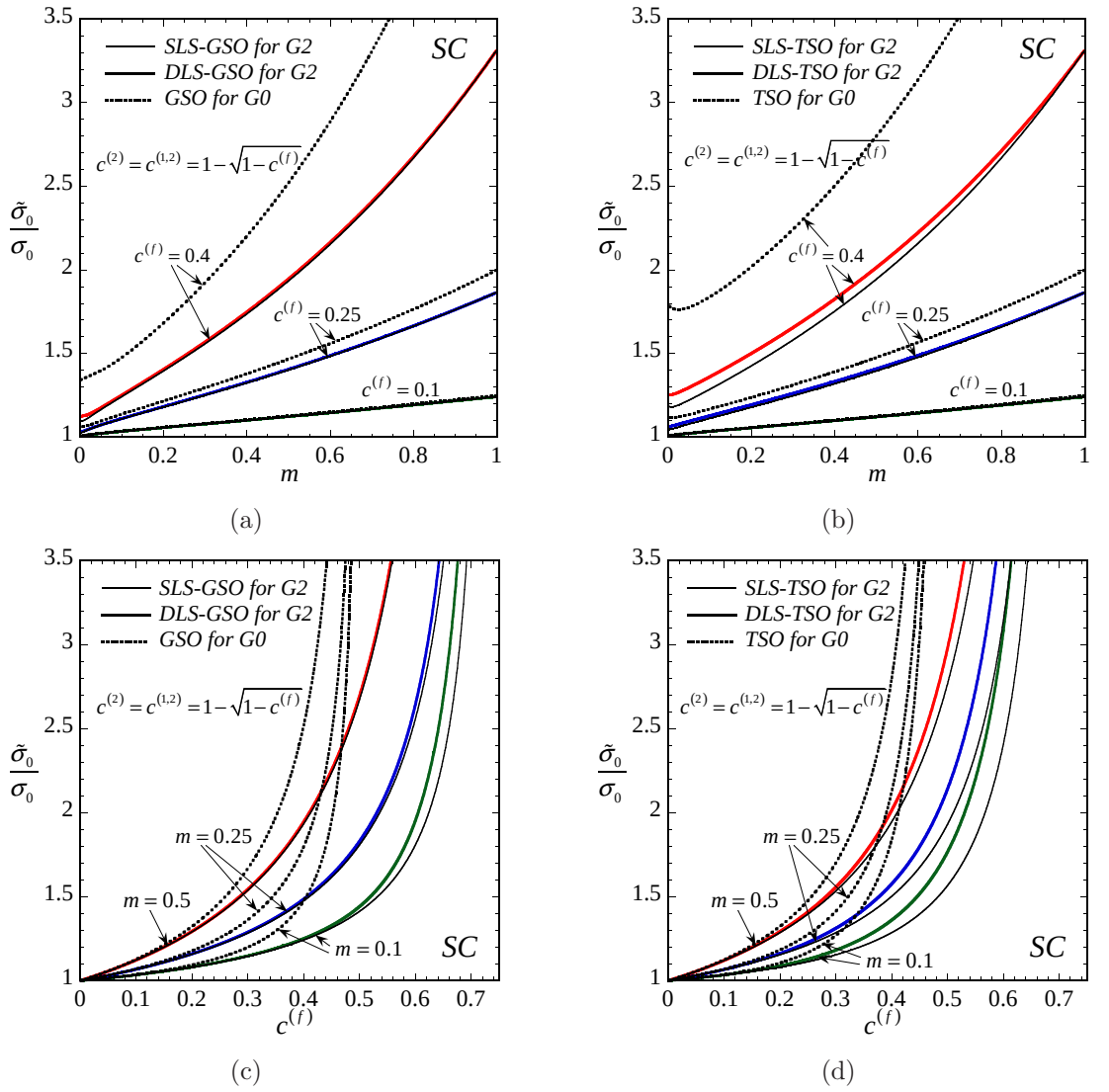

Figure 3.10: Comparison of SLS (continuous thin lines) and DLS (continuous thick lines) estimates for the two-scale *granular* composite G2 (Fig. 3.8(b)). Part (a) shows the SLS-GSO estimate (3.84), with (3.85), and the DLS-GSO estimate (3.81) for the normalized effective in-plane yield-stress $\tilde{\sigma}_0/\sigma_0$ as a function of the rate-sensitivity exponent $m = 1/n$ for fixed values of the total rigid-phase concentration $c^{(f)} = 0.1, 0.25, 0.4$ in G2, with $c^{(2)} = c^{(1,2)} = 1 - \sqrt{1 - c^{(f)}}$; part (c) shows the same estimates for $\tilde{\sigma}_0/\sigma_0$ as a function of $c^{(f)}$ for the cases $m = 0.1, 0.25, 0.5$. Parts (b) and (d) present the corresponding predictions of the SLS-TSO estimate (3.78), with (3.79), and the DLS-TSO estimate (3.74), respectively. GSO and TSO results corresponding to the special case $c^{(2)} = 0$ and $c^{(1,2)} = c^{(f)}$ (or $c^{(1,2)} = 0$ and $c^{(2)} = c^{(f)}$), i.e., the case of the single-scale *granular* composite G0 (Fig. 3.8(a)), have been included in the relevant parts (dotted lines).

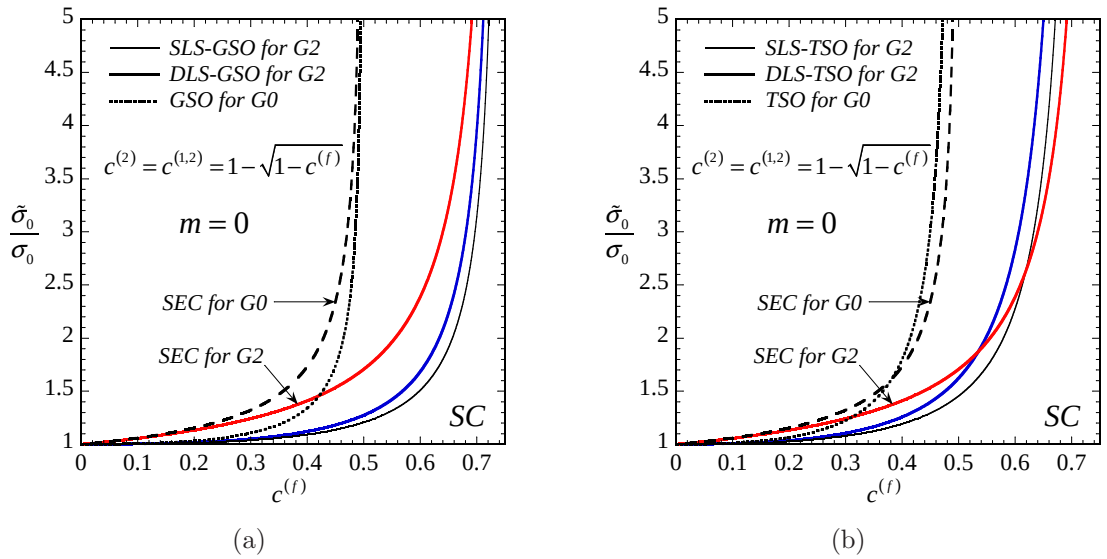

Figure 3.11: Comparison of SLS (continuous thin lines) and DLS (continuous thick lines) estimates for the two-scale *granular* composite G2 (Fig. 3.8(b)) in the ideally plastic limit $m = 0$. (a) SLS-GSO and DLS-GSO estimates for the normalized effective in-plane yield-stress $\tilde{\sigma}_0/\sigma_0$ as a function of the total rigid-phase concentration $c^{(f)}$, with $c^{(2)} = c^{(1,2)} = 1 - \sqrt{1 - c^{(f)}}$. (b) Corresponding SLS-TSO and DLS-TSO results. The associated results for the single-scale composite G0 of Fig. 3.8(a) are also shown (dotted lines). In addition, the corresponding secant (SEC) upper bounds for G2 and G0 are included.

SLS-GSO estimates being softer. Similar conclusions can be drawn for the TLS-GSO and DLS-TSO estimates of Fig. 3.11(b). Note, however, that the agreement between the SLS-GSO and DLS-GSO estimates is much better than that between the TLS-GSO and DLS-TSO results.

Another important observation that should be made in the context of the results of Fig. 3.11 is that the GSO estimates for both G0 and G2 are consistent with the bounding character of the associated secant estimates, while the corresponding TSO estimates are found to violate the secant upper bounds in both cases of G0 and G2 as the overall concentration of the rigid-phase approches the relevant percolation limit. These finding are consistent with the observation made by Ponte Castañeda [119] in the context of single-scale granular systems. Finally, similar to the GSO and TSO estimates, it is observed that the secant estimate for G0 is stiffer than the corresponding secant estimate for G2 with the same overall rigid-phase content.

3.5 Concluding remarks

Employing the general methods of chapter 2, in this chapter we have derived homogenization-based estimates for the effective response of viscoplastic rigidly-reinforced two-scale composites with

particulate and granular sub-structures. Specifically, following the general "direct linearization scheme" (DLS) and "sequential linearization scheme" (SLS) procedures based on the "secant", "tangent second-order" (TSO) and "generalized second-order" (GSO) methods of chapter 2, we generated the corresponding estimates for the effective in-plane response of the two-scale particulate systems P1 (Fig. 3.1(b)) and P2 (Fig. 3.4(b)), and the two-scale granular system G2 (Fig. 3.8(b)). For comparison, we also determined the relevant estimates for the corresponding single-scale particulate composite P0 (Fig. 3.1(a)) and the single-scale granular composite G0 (Fig. 3.8(a)). The estimates obtained in this chapter are fairly simple to compute, since they require at most the solution of a few nonlinear scalar equations, while in certain cases they are given in closed-form.

For each composite system, we investigated in detail the main features of the associated estimates by means of specific calculations for a wide range of values for the concentration of the rigid-phase and the nonlinearity parameter. An important conclusion implied from these results is that, for the case of the particulate systems P1 and P2, the DLS-based second-order estimates are in an excellent agreement with the corresponding SLS-based estimates for all values of the parameters considered. Furthermore, in the case of the granular system G2, the corresponding DLS- and SLS-based estimates are also in a very good agreement, in general, including the case of ideally-plastic composites G2 with small to moderate overall rigid-phase concentrations, compared to the associated percolation limit. For higher values of the total rigid-phase content in ideally-plastic systems G2, the differences between the corresponding DLS- and SLS-based estimates become increasingly more significant. It should be remarked, however, that the SLS-GSO and DLS-GSO estimates are in better agreement to each other than the corresponding SLS-TSO and DLS-TSO estimates. In addition, the GSO estimates were found to be consistent with the corresponding secant bounds for all composite systems considered in this chapter. On the other hand, the TSO estimates for the particulate composites P0, P1 and P2 were also found to be consistent with the corresponding secant bounds, but in the case of the granular composites G0 and G2 the TSO estimates were found to violate the secant bounds near the associated percolation limit. These observations provide credence to the GSO estimates, which, in turn, further encourages the application of the more general methods of chapter 2 to two-scale composites with more complicated sub-structures.

Another interesting conclusion implied by the results of this chapter is that, for the same overall rigid-phase content, the effective response of the two-scale particulate composite P1 is practically indistinguishable from that of the corresponding single-scale composite P0, while the two-scale particulate system P2 is always stiffer than P0 and the two-scale granular system G2 is always softer than the corresponding single-scale granular system G0. In the case of G2, in particular, we found that the presence of rigid-grains of two well-separated length-scales has the effect of

increasing the percolation limit of the composite. In contrast to the well-known percolation limit of 50% rigid-grain concentration for a single-scale system G0, the maximum percolation limit for a two-scale system G2 is 75% and corresponds to a composite with equal concentrations of micro- and meso-scale rigid-grains.

3.6 Appendix I. Two-phase single-scale linear thermoelastic composites

In this appendix, we specialize the estimates for the effective behavior of general N-phase single-scale linear thermoelastic composites discussed in subsection 2.5.4 to the corresponding two-phase ($N = 2$) systems of interest in this chapter.

Consider a two-phase linear thermoelastic composite with local stress-potential of the form

$$u_T(\mathbf{x}, \boldsymbol{\sigma}) = \chi^{(1)}(\mathbf{x}) u_T^{(1)}(\boldsymbol{\sigma}) + \chi^{(2)}(\mathbf{x}) u_T^{(2)}(\boldsymbol{\sigma}), \tag{3.100}$$

where the phase potentials $u_T^{(r)}$, with $r = 1, 2$ are given by

$$u_T^{(r)}(\boldsymbol{\sigma}) = \frac{1}{2}\boldsymbol{\sigma} \cdot \mathbf{M}^{(r)}\boldsymbol{\sigma} + \boldsymbol{\alpha}^{(r)} \cdot \boldsymbol{\sigma} + \phi^{(r)}, \tag{3.101}$$

with $\mathbf{M}^{(r)}$, $\boldsymbol{\alpha}^{(r)}$ and $\phi^{(r)}$ denoting respectively the compliance tensor, the thermal strain tensor and the specific heat of phase r. The effective stress-potential of this material is given by

$$\tilde{u}_T(\overline{\boldsymbol{\sigma}}) = \frac{1}{2}\overline{\boldsymbol{\sigma}} \cdot \widetilde{\mathbf{M}}\overline{\boldsymbol{\sigma}} + \widetilde{\boldsymbol{\alpha}} \cdot \overline{\boldsymbol{\sigma}} + \tilde{\phi}. \tag{3.102}$$

Recall that the effective modulus $\widetilde{\mathbf{M}}$, thermal strain tensor $\widetilde{\boldsymbol{\alpha}}$ and specific heat $\tilde{\phi}$ may be expressed in terms of the associated stress concentration tensors $\mathbf{B}^{(r)}$ and $\mathbf{b}^{(r)}$ of the phases by means of the following relations

$$\widetilde{\mathbf{M}} = \sum_{r=1}^{2} c^{(r)} \mathbf{M}^{(r)} \mathbf{B}^{(r)}, \quad \widetilde{\boldsymbol{\alpha}} = \sum_{r=1}^{2} c^{(r)} \left(\mathbf{B}^{(r)}\right)^T \boldsymbol{\alpha}^{(r)}, \quad \tilde{\phi} = \sum_{r=1}^{2} c^{(r)} \phi^{(r)} + \frac{1}{2} \sum_{r=1}^{2} c^{(r)} \boldsymbol{\alpha}^{(r)} \cdot \mathbf{b}^{(r)}, \tag{3.103}$$

where $c^{(r)}$ is the volume fraction of phase r, with $r = 1, 2$. Furthermore, we recall that the stress concentration tensors $\mathbf{B}^{(r)}$ and $\mathbf{b}^{(r)}$ satisfy the identities

$$c^{(1)}\mathbf{B}^{(1)} + c^{(2)}\mathbf{B}^{(2)} = \mathbf{K}, \qquad c^{(1)}\mathbf{b}^{(1)} + c^{(2)}\mathbf{b}^{(2)} = \mathbf{0}, \tag{3.104}$$

where $\mathbf{K}$ is the forth-order identity tensor in the deviatoric space.

Making use of expressions (3.103) and (3.104), as well as the relations $\overline{\mathbf{D}}^{(r)} = \mathbf{M}^{(r)}\overline{\boldsymbol{\sigma}}^{(r)} + \boldsymbol{\alpha}^{(r)}$, for $r = 1, 2$, it can be shown (Levin [82]) that the stress-concentration tensors $\mathbf{B}^{(1)}$ and $\mathbf{b}^{(1)}$ are

respectively given by

$$\mathbf{B}^{(1)} = \frac{1}{c^{(1)}}\left(\mathbf{M}^{(2)} - \mathbf{M}^{(1)}\right)^{-1}\left(\mathbf{M}^{(2)} - \widetilde{\mathbf{M}}\right),$$
$$\mathbf{b}^{(1)} = \left(\mathbf{M}^{(2)} - \mathbf{M}^{(1)}\right)^{-1}\left((\mathbf{B}^{(1)})^T - \mathbf{K}\right)(\boldsymbol{\alpha}^{(2)} - \boldsymbol{\alpha}^{(1)}), \tag{3.105}$$

while $\mathbf{B}^{(2)}$ and $\mathbf{b}^{(2)}$ are readily obtained from (3.104). Thus, the effective behavior of a two-phase linear thermoelastic composite is completely determined in terms of the associated effective modulus tensor $\widetilde{\mathbf{M}}$ only.

As discussed in the previous chapter, the effective modulus tensor $\widetilde{\mathbf{M}}$ for the composites of interest in this thesis will be computed by means of the Willis estimate (2.95) for the case of a particulate composite and by means of the self-consistent estimate (2.93) in the case of a granular system. Recall that the microstructural tensor $\mathbf{Q}$ entering the calculation of these estimates is given by expression (2.92) in terms of the reference tensor $\mathbf{M}^{(0)}$—taken to be the modulus of the matrix in the context of the Willis estimate (2.95) and the effective modulus tensor $\widetilde{\mathbf{M}}$ in the context of the self-consistent estimate (2.93)—and the shape tensor $\mathbf{Z}$. For the plane-stress loading conditions considered in the applications of this chapter, the reference tensor $\mathbf{M}^{(0)}$ in both cases has the form

$$\mathbf{M}^{(0)} = \frac{1}{2\lambda_{\mathbf{E}}^{(0)}}\mathbf{E} + \frac{1}{2\lambda_{\mathbf{F}}^{(0)}}\mathbf{F}, \qquad \mathbf{E} = \frac{3}{2}\frac{\overline{\boldsymbol{\sigma}}_d}{\bar{\sigma}_e} \otimes \frac{\overline{\boldsymbol{\sigma}}_d}{\bar{\sigma}_e}, \qquad \mathbf{F} = \mathbf{K} - \mathbf{E}, \tag{3.106}$$

where $\overline{\boldsymbol{\sigma}}$ denotes the stress tensor applied to the composite. Furthermore, in each case the tensor $\mathbf{P}$ in $(2.92)_2$ is evaluated at a shape tensor $\mathbf{Z} = \mathbf{I} - (1-\epsilon)\mathbf{e}_3 \otimes \mathbf{e}_3$ as $\epsilon \to 0$, with $\mathbf{e}_3$ denoting the preferred direction of transverse isotropy. Under plane-stress loadings, the tensors $\mathbf{P}^{(0)}$ and $\mathbf{Q}^{(0)}$, when evaluated at a reference modulus $\mathbf{M}^{(0)}$ of the form (3.106), can be shown [107] to reduce to

$$\mathbf{P} = \frac{k^{(0)}}{2(1+\sqrt{k^{(0)}})\lambda_{\mathbf{F}}^{(0)}}\mathbf{E} + \frac{\sqrt{k^{(0)}}}{2(1+\sqrt{k^{(0)}})\lambda_{\mathbf{F}}^{(0)}}\mathbf{F},$$
$$\mathbf{Q} = \left(2\lambda_{\mathbf{E}}^{(0)} - \frac{2\lambda_{\mathbf{E}}^{(0)}}{1+\sqrt{k^{(0)}}}\right)\mathbf{E} + \left(2\lambda_{\mathbf{F}}^{(0)} - \frac{2\lambda_{\mathbf{F}}^{(0)}\sqrt{k^{(0)}}}{1+\sqrt{k^{(0)}}}\right)\mathbf{F}, \tag{3.107}$$

where the notation $k^{(0)} = \lambda_{\mathbf{F}}^{(0)}/\lambda_{\mathbf{E}}^{(0)}$ has been introduced. Making use of the above result, the associated Willis and self-consistent estimates for $\widetilde{\mathbf{M}}$ are given by the following simple expressions.

Particulate composites. For the case of a two-phase composite ($N = 2$) consisting of aligned fibers (phase 2) embedded in a matrix material (phase 1), the general Willis estimate (2.95) simplifies to

$$\widetilde{\mathbf{M}} = \mathbf{M}^{(1)} + c^{(2)}\left[c^{(1)}\mathbf{Q} + \left(\mathbf{M}^{(2)} - \mathbf{M}^{(1)}\right)^{-1}\right]^{-1}, \tag{3.108}$$

where $\mathbf{Q}$ is given by $(3.107)_2$, where the reference modulus tensor is taken to be equal to the modulus of the matrix, i.e., $\mathbf{M}^{(0)} = \mathbf{M}^{(1)}$.

Granular composites. In the case of a two-phase ($N = 2$) granular composite the general self-consistent estimate (2.93) reduces to

$$\widetilde{\mathbf{M}} = \left\{ c^{(1)} \left[\mathbf{M}^{(1)} + \widetilde{\mathbf{M}}^* \right]^{-1} + c^{(2)} \left[\mathbf{M}^{(2)} + \widetilde{\mathbf{M}}^* \right]^{-1} \right\}^{-1} - \widetilde{\mathbf{M}}^*, \tag{3.109}$$

where $\widetilde{\mathbf{M}}^* = \mathbf{Q}^{-1} - \widetilde{\mathbf{M}}$ and $\mathbf{Q}$ is given by expression $(3.107)_2$, which must be evaluated at $\mathbf{M}^{(0)} = \widetilde{\mathbf{M}}$.

3.7 Appendix II. Some useful relations

In this appendix, we provide expressions for the variables entering the calculation of the various estimates of this chapter, which, for convenience, were not included in the main body of the text.

Variables involved in the computation of the DLS-GSO estimate for P1. Defining the quantity

$$\begin{aligned} A = & \Big\{ c^{(2,2)}(k^2(2c^{(2,2)} + \sqrt{k^{(2,1)}})(k^{(2,1)})^{3/2}(c^{(2)} - 1)^2 + 2k(2c^{(2,2)} - 1)\sqrt{k^{(1)}}k^{(2,1)}(c^{(2)} - 1) + \\ & (c^{(2)})^2(k^{(1)})^2(2\sqrt{k^{(2,1)}}c^{(2,2)} + 1) + 2(k^{(1)})^{3/2}(2c^{(2,2)}\sqrt{k^{(2,1)}}c^{(2)} + c^{(2)}) + \\ & k^{(1)}(-2kk^{(2,1)}(c^{(2)})^2 + 2kk^{(2,1)}c^{(2)} + 2c^{(2,2)}(2k(c^{(2)} - 1)c^{(2)}k^{(2,1)} + \sqrt{k^{(2,1)}}) + 1)) \Big\}^{1/2}, \end{aligned} \tag{3.110}$$

the phase-average variables $\omega^{(1)}$ and $\omega^{(2,1)}$ in the context of the DLS-GSO estimate (3.49) for P1 are given by

$$\begin{aligned} \omega^{(1)} = & \Big\{ 2\sqrt{(k^{(2,1)})^{3/2}}(c^{(2)}k^{(1)} + \sqrt{k^{(1)}} - k(c^{(2)} - 1)k^{(2,1)} + c^{(2,2)}(-kk^{(2,1)} + \sqrt{k^{(1)}}\sqrt{k^{(2,1)}} + \\ & c^{(2)}(\sqrt{k^{(2,1)}}k^{(1)} + k(k^{(2,1)} - \sqrt{k^{(2,1)}} - 1)))) + \sqrt{2}(k^{(2,1)} - 1)\mathrm{sign}(\omega^{(2,1)} - 1)A \Big\} \Big/ \\ & \Big\{ 2\sqrt{(k^{(2,1)})^{3/2}}(\sqrt{k^{(1)}}(\sqrt{k^{(2,1)}}c^{(2,2)} + 1) + k^{(1)}(c^{(2,2)}\sqrt{k^{(2,1)}}c^{(2)} + c^{(2)}) + \\ & k(c^{(2)} - 1)(c^{(2,2)} - 1)k^{(2,1)}) + \sqrt{2}(k^{(2,1)} - 1)\mathrm{sign}(\omega^{(2,1)} - 1)A \Big\}, \end{aligned} \tag{3.111}$$

and

$$\begin{aligned}\omega^{(2,1)} =&\Bigg\{2\sqrt{(k^{(2,1)})^{3/2}}(c^{(2,2)}(k\sqrt{k^{(2,1)}}(c^{(2)}-1)+c^{(2)}k^{(1)}+\sqrt{k^{(1)}})(k^{(2,1)}-1)+\\&\sqrt{k^{(2,1)}}(c^{(2)}k^{(1)}+\sqrt{k^{(1)}}-k(c^{(2)}-1)k^{(2,1)}))+\\&\sqrt{2}(k^{(2,1)}-1)\sqrt{k^{(2,1)}}\mathrm{sign}(\omega^{(2,1)}-1)A\Bigg\}\Bigg/\\&\Bigg\{\sqrt{k^{(2,1)}}(2\sqrt{(k^{(2,1)})^{3/2}}(\sqrt{k^{(1)}}(\sqrt{k^{(2,1)}}c^{(2,2)}+1)+k^{(1)}(c^{(2,2)}\sqrt{k^{(2,1)}}c^{(2)}+c^{(2)})+\\&k(c^{(2)}-1)(c^{(2,2)}-1)k^{(2,1)})+\sqrt{2}(k^{(2,1)}-1)\mathrm{sign}(\omega^{(2,1)}-1))A\Bigg\},\end{aligned}\tag{3.112}$$

respectively. The corresponding fluctuations variables $x_{\parallel}^{(1)}$, $x_{\perp}^{(1)}$, $x_{\parallel}^{(2,1)}$ and $x_{\perp}^{(2,1)}$ are respectively given by

$$\begin{aligned}x_{\parallel}^{(1)} =&\Bigg\{\sqrt{2}k\sqrt{c^{(2)}}c^{(2,2)}\sqrt{2\sqrt{k^{(1)}}c^{(2)}+1}(\sqrt{k^{(2,1)}}+1)\sqrt{(k^{(2,1)})^{3/2}}\mathrm{sign}(\omega^{(1)}-1)+\\&\sqrt[4]{k^{(1)}}(2\sqrt{(k^{(2,1)})^{3/2}}(\sqrt{k^{(1)}}(\sqrt{k^{(2,1)}}c^{(2,2)}+1)+k^{(1)}(c^{(2,2)}\sqrt{k^{(2,1)}}c^{(2)}+c^{(2)})+\\&k(c^{(2)}-1)(c^{(2,2)}-1)k^{(2,1)})+\sqrt{2}(k^{(2,1)}-1)\mathrm{sign}(\omega^{(2,1)}-1))A\Bigg\}\Bigg/\\&\Bigg\{\sqrt[4]{k^{(1)}}(2\sqrt{(k^{(2,1)})^{3/2}}(\sqrt{k^{(1)}}(\sqrt{k^{(2,1)}}c^{(2,2)}+1)+k^{(1)}(c^{(2,2)}\sqrt{k^{(2,1)}}c^{(2)}+c^{(2)})+\\&k(c^{(2)}-1)(c^{(2,2)}-1)k^{(2,1)})+\sqrt{2}(k^{(2,1)}-1)\mathrm{sign}(\omega^{(2,1)}-1))A\Bigg\},\end{aligned}\tag{3.113}$$

$$\begin{aligned}x_{\perp}^{(1)} =&\Bigg\{\sqrt{2}k\sqrt[4]{k^{(1)}}\sqrt{c^{(2)}}(\sqrt{k^{(2,1)}}+1)\sqrt{(k^{(2,1)})^{3/2}c^{(2,2)}}\Bigg\}\Bigg/\\&\Bigg\{2\sqrt{(k^{(2,1)})^{3/2}}(k^{(1)}(c^{(2)}\sqrt{k^{(2,1)}}c^{(2,2)}+c^{(2)})+\sqrt{k^{(1)}}(\sqrt{k^{(2,1)}}c^{(2,2)}+1)+\\&k(c^{(2)}-1)k^{(2,1)}(c^{(2,2)}-1))+\sqrt{2}(k^{(2,1)}-1)\mathrm{sgn}(\omega^{(2,1)}-1)A\Bigg\},\end{aligned}\tag{3.114}$$

$$x_{\parallel}^{(2,1)} = \Bigg\{ 2\sqrt{(k^{(2,1)})^{3/2}}(\sqrt{k^{(1)}}(\sqrt{k^{(2,1)}}c^{(2,2)}+1)+k^{(1)}(c^{(2,2)}\sqrt{k^{(2,1)}}c^{(2)}+c^{(2)})+ \\ k(c^{(2)}-1)(c^{(2,2)}-1)k^{(2,1)})+\sqrt{2}k^{(2,1)}A\text{sign}(\omega^{(2,1)}-1)\Bigg\} \Bigg/ \\ \Bigg\{ 2\sqrt{(k^{(2,1)})^{3/2}}(\sqrt{k^{(1)}}(\sqrt{k^{(2,1)}}c^{(2,2)}+1)+k^{(1)}(c^{(2,2)}\sqrt{k^{(2,1)}}c^{(2)}+c^{(2)})+ \\ k(c^{(2)}-1)(c^{(2,2)}-1)k^{(2,1)})+\sqrt{2}(k^{(2,1)}-1)A\text{sign}(\omega^{(2,1)}-1)\Bigg\}, \tag{3.115}$$

$$x_{\perp}^{(2,1)} = \Bigg\{ \sqrt{2}\sqrt{(k^{(2,1)})^{3/2}}\sqrt{c^{(2,2)}}(k^{(1)}c^{(2)}+\sqrt{k^{(1)}}-k(c^{(2)}-1)k^{(2,1)}) \Bigg\} \Bigg/ \\ \Bigg\{ \sqrt[4]{k^{(2,1)}}(2\sqrt{(k^{(2,1)})^{3/2}}(k^{(1)}(c^{(2)}\sqrt{k^{(2,1)}}c^{(2,2)}+c^{(2)})+\sqrt{k^{(1)}}(\sqrt{k^{(2,1)}}c^{(2,2)}+1)+ \\ k(c^{(2)}-1)k^{(2,1)}(c^{(2,2)}-1))+\sqrt{2}(k^{(2,1)}-1)\text{sign}(\omega^{(2,1)}-1)A)\Bigg\}, \tag{3.116}$$

where it is recalled that A is defined by (3.110).

Variables involved in the computation of the SLS-GSO estimate for P1. The variables $\omega^{(2,1)}$, $x_{\parallel}^{(2,1)}$ and $x_{\perp}^{(2,1)}$ in the context of the GSO estimate (3.51) for P1 are respectively given by

$$\omega^{(2,1)} = \Bigg\{ \sqrt{2}\left(k^{(2,1)}-1\right)\sqrt{k^{(2,1)}}\text{sgn}\left(\omega^{(2,1)}-1\right)\sqrt{c^{(2,2)}\left(2\sqrt{k^{(2,1)}}c^{(2,2)}+1\right)}+ \\ 2\sqrt{\left(k^{(2,1)}\right)^{3/2}}\left(\left(k^{(2,1)}-1\right)c^{(2,2)}+\sqrt{k^{(2,1)}}\right)\Bigg\} \Bigg/ \left\{\sqrt{k^{(2,1)}}B\right\}, \tag{3.117}$$

$$x_{\parallel}^{(2,1)} = \Bigg\{ \sqrt{2}k^{(2,1)}\text{sgn}\left(\omega^{(2,1)}-1\right)\sqrt{c^{(2,2)}\left(2\sqrt{k^{(2,1)}}c^{(2,2)}+1\right)}+ \\ 2\sqrt{\left(k^{(2,1)}\right)^{3/2}}\left(\sqrt{k^{(2,1)}}c^{(2,2)}+1\right)\Bigg\} \Bigg/ B, \tag{3.118}$$

$$x_{\perp}^{(2,1)} = \frac{\sqrt{2}\sqrt{k^{(2,1)}c^{(2,2)}}}{B}, \tag{3.119}$$

where the quantity B is defined by

$$B = \sqrt{2}\left(k^{(2,1)}-1\right)\text{sign}\left(\omega^{(2,1)}-1\right)\sqrt{c^{(2,2)}\left(2\sqrt{k^{(2,1)}}c^{(2,2)}+1\right)}+ \\ 2\sqrt{\left(k^{(2,1)}\right)^{3/2}}\left(\sqrt{k^{(2,1)}}c^{(2,2)}+1\right). \tag{3.120}$$

On the other hand, the fluctuation variables $x_{\|}^{(1)}$ and $x_{\perp}^{(1)}$ in the context of the GSO estimate (3.54) for P1 are expressed in terms of the unknowns $\omega^{(2)}$ and $k^{(1)}$ by means of the following relations

$$x_{\|}^{(1)} = \frac{\operatorname{sign}\left(\omega^{(1)}-1\right)\sqrt{c^{(2)}\left(\omega^{(2)}-1\right)^{2}\left(2\sqrt{k^{(1)}}c^{(2)}+1\right)}}{\sqrt{2}\sqrt[4]{k^{(1)}}\left(1-c^{(2)}\right)}+1, \tag{3.121}$$

$$x_{\perp}^{(1)} = \frac{\sqrt[4]{k^{(1)}}\sqrt{c^{(2)}\left(\omega^{(2)}-1\right)^{2}}}{\sqrt{2}\left(1-c^{(2)}\right)}, \tag{3.122}$$

by means of which the equation (3.56) reads as follows

$$\frac{k^{(1)}c^{(2)}+\sqrt{k^{(1)}}+C\left(c^{(2)}-1\right)\omega^{(2)}\left(-\left(\frac{\omega^{(2)}}{\tilde{\sigma}_0^{(2)}/\sigma_0}\right)^{-n}-n+1\right)}{k^{(1)}c^{(2)}+\sqrt{k^{(1)}}-Cn\left(c^{(2)}-1\right)}-\omega^{(2)}=0, \tag{3.123}$$

where $\tilde{\sigma}_0^{(2)}/\sigma_0$ is given by (3.51) and

$$C=\frac{\left(\frac{\omega^{(2)}}{\tilde{\sigma}_0^{(2)}/\sigma_0}\right)^{n}}{\omega^{(2)}}\left((x_{\|}^{(1)})^2+(x_{\perp}^{(1)})^2\right)^{(1-n)/2}. \tag{3.124}$$

Variables involved in the computation of the DLS-GSO estimate for P2. Letting

$$D=\sqrt{\frac{\sqrt{k^{(1,1)}}c^{(1,2)}+k^{(1,1)}}{\sqrt{k^{(1,1)}}c^{(1,2)}+1}}, \tag{3.125}$$

the fluctuation variable $x_{\|}^{(1,1)}$ in the context of the DLS-GSO estimate (3.81) for P2 is obtained in terms of $\omega^{(1,1)}$ and $k^{(1,1)}$ as the solution to the following linear equation

$$\begin{aligned} x_{\|}^{(1,1)} =& 1+\left\{(x_{\|}^{(1,1)}(-k^{(1,1)})+k^{(1,1)}+x_{\|}^{(1,1)})\operatorname{sign}(\omega^{(1,1)}-1)\left\{4k^{(1,1)}(c^{(1,2)})^3\times\right.\right.\\ &((c^{(2)})^2D+D+2c^{(2)})+2\sqrt{k^{(1,1)}}(c^{(1,2)})^2(2(k^{(1,1)}+2)(c^{(2)})^2D+3D+\\ &(4k^{(1,1)}+5)c^{(2)})+c^{(1,2)}(4(2k^{(1,1)}+1)(c^{(2)})^2D+\\ &\left.\left.2D+(9k^{(1,1)}+3)c^{(2)})+2\sqrt{k^{(1,1)}}c^{(2)}(2c^{(2)}D+1)\right\}^{1/2}\right\}\Big/\\ &\left\{4(k^{(1,1)})^{3/2}(\sqrt{k^{(1,1)}}c^{(1,2)}+1)^3D(c^{(2)}D+1)^2\right\}^{1/2}, \end{aligned} \tag{3.126}$$

by means of which, it can be shown that the variables $x_{\perp}^{(1,1)}$ and $\omega^{(1,1)}$, which also enter the calculation of the DLS-GSO estimate (3.81) for P2, are respectively given by

$$\begin{aligned} x_{\perp}^{(1,1)} =& \frac{1}{2}(x_{\parallel}^{(1,1)}(-k^{(1,1)}) + k^{(1,1)} + x_{\parallel}^{(1,1)})\times \\ & \left\{ \left\{ 2\sqrt{k^{(1,1)}}(c^{(1,2)})^2(D + c^{(2)}) + c^{(1,2)}(2D + 3k^{(1,1)}c^{(2)} + c^{(2)}) + 2\sqrt{k^{(1,1)}}c^{(2)} \right\} \Big/ \right. \\ & \left. \left\{ \sqrt{k^{(1,1)}}(\sqrt{k^{(1,1)}}c^{(1,2)} + 1)^3 D(c^{(2)}D + 1)^2 \right\} \right\}^{1/2}, \end{aligned} \tag{3.127}$$

and

$$\omega^{(1,1)} = \frac{\frac{x_{\parallel}^{(1,1)}(k^{(1,1)}-1)(c^{(2)}(\sqrt{k^{(1,1)}}c^{(1,2)}+1)D+\sqrt{k^{(1,1)}}c^{(1,2)})}{k^{(1,1)}} + 1}{(\sqrt{k^{(1,1)}}c^{(1,2)} + 1)(c^{(2)}D + 1)}. \tag{3.128}$$

Chapter 4

Applications to semi-crystalline polymers

In this chapter, we develop a constitutive model for the macroscopic response and texture evolution of semi-crystalline polymers at large plastic deformations. The semi-crystalline polymer is modeled as a two-scale composite, i.e., as a material system exhibiting heterogeneity at two well-separated length-scales. At the larger length-scale, the semi-crystalline polymer is assumed to be an aggregate of a large number of randomly distributed grains that, at the smaller length-scale, are made up of alternating layers of an amorphous and a crystalline phase. Both phases are taken to be viscoplastic materials, but the amorphous phase incorporates dependence also on elastic strains through a back-stress model. The lamellar grains are assumed to be oriented randomly and isotropically in the undeformed configuration, leading to an initially overall isotropic behavior for the composite system. The instantaneous effective response of the composite material is determined by means of the linear comparison composite (LCC) methods for nonlinear multi-scale systems developed in chapter 2. Recall that these methods consist in constructing an LCC with the same sub-structure as the actual nonlinear composite and local properties that are optimally chosen through suitably designed variational principles. The effective properties of the resulting two-scale LCC are in turn obtained though the sequential homogenization procedure (see subsection 2.4.2), involving the well-known exact solution for the effective behavior of the laminates in each grain and then making use of the self-consistent estimate for the granular system at the larger length-scale. With essentially no further computational expense, these results are also used to generate corresponding estimates for the grain- and phase-average deformation rate and spin tensors in the LCC, which along with standard kinematical arguments are used to establish evolution laws for the sub-structural variables of the semi-crystalline polymer. Thus, the present model accounts explicitly (on average) for the current state of the crystallographic, lamellar and morphological texture as well as for its evolution due to the finite changes in geometry at large applied strains. The general LCC model for semi-crystalline polymers is specialized to a high-density polyethylene (HDPE) composite material. The predictions of the model for the macroscopic stress-strain response and texture evolution in

HDPE under uniaxial compression, simple shear and uniaxial tension loadings are compared with corresponding experimental results as well as with the associated predictions of the models of Lee et al. [80] and Nikolov et al. [110]. For all three types of loading conditions considered here, the LCC estimates for the macroscopic response of HDPE are found to be in a very good agreement with the corresponding experimental results and they capture all the essential features of texture evolution. Furthermore, the LCC model is found to improve—in some cases significantly so—over the earlier models.

This chapter is organized as follows. In section 4.1 we deal with the formulation of the homogenization problem determining, in principle, the instantaneous effective response of the semi-crystalline polymer, including the relevant details on the modeling of the underlying sub-structure and the constitutive behavior of the phases. Making use of the LCC methods of chapter 2, in section 4.2 we derive an estimate for the instantaneous macroscopic response of the semi-crystalline polymer. In section 4.3 we derive corresponding estimates for the evolution of the sub-structure. Section 4.4 provides the relevant estimates for the effective behavior of the LCC entering the calculation of the corresponding results of the preceding two sections for the (nonlinear) semi-crystalline polymer material of interest in this work. In section 4.5 we discuss in detail applications of the LCC model to HDPE and compare the predictions of this model with the corresponding experimental results and the predictions of earlier models for uniaxial compression, simple shear and uniaxial tension loading conditions. In section 4.6 we provide some concluding remarks on the main results of this chapter. The numerical treatment of the LCC model for semi-crystalline polymers and its material frame indifference are discussed in appendices I and II, respectively.

4.1 Idealizations and instantaneous effective behavior

The effective behavior of a semi-crystalline polymer at a given instant t during a finite deformation process is, in principle, completely determined in terms of the underlying sub-structure and the constitutive properties of the phases. However, given the complexity of the sub-structure in an actual semi-crystalline polymer as well as its evolution as a function of the applied strain, it is practically impossible to keep a detailed track of all the associated sub-structural information. Furthermore, the constitutive behavior of both the amorphous and the crystalline phase is elasto-viscoplastic. Unfortunately, homogenization in the nonlinear elasto-viscoplastic context is a challenging problem, which is still largely unresolved, although some encouraging steps along these lines (in the context of single-scale composites) have been made recently by Lahellec and Suquet [70, 71]. For these reasons, our strategy in this work is to account (on average) for those sub-structural features and characteristics of the constitutive behavior of the phases that have an essential effect on the macroscopic response of the composite. This section provides the relevant

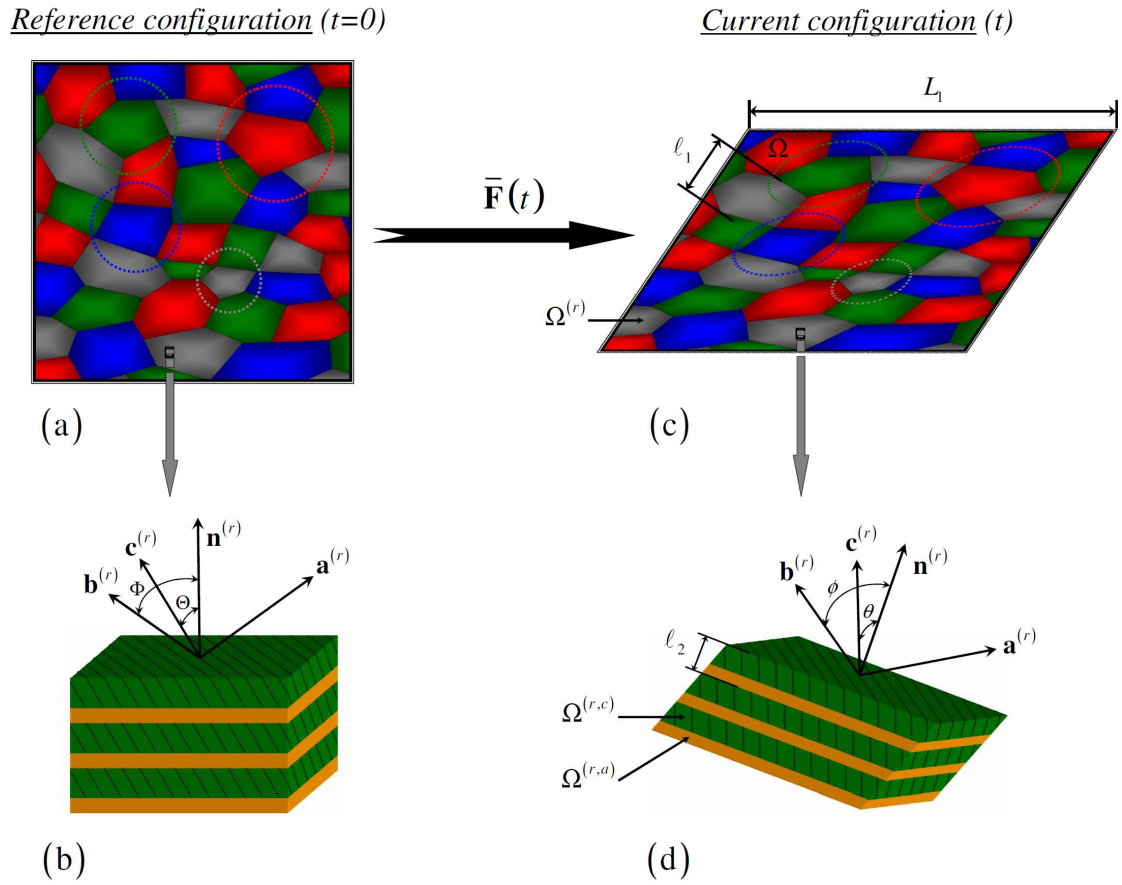

Figure 4.1: Schematic illustration of the mapping of a semi-crystalline polymer from the reference (Parts (a) and (b)) to the current (Parts (c) and (d)) configuration during an arbitrary finite deformation process prescribed through the macroscopic deformation gradient $\overline{\mathbf{F}}(t)$, with t standing for the time variable. At the meso-structural level (Parts (a) and (c)), the material consists of a large number N of grain-families distributed randomly with *isotropic* symmetry in the reference configuration (dotted circles in Part (a)) which evolves into *ellipsoidal* symmetry in the current configuration (dotted ellipses in Part (c)). At the micro-structural level (Parts (b) and (d)), the grains are taken to be lamellar composites consisting of alternating layers of an amorphous and a crystalline phase; both the orientation of the lamellar grains—defined by the vectors $\mathbf{n}^{(r)}$ normal to the layers—and the orientation of the crystals—defined by the associated lattice vectors $\mathbf{a}^{(r)}$, $\mathbf{b}^{(r)}$ and $\mathbf{c}^{(r)}$—evolve in time.

discussion on the idealization of the sub-structure and the material behavior of the constituent phases of a semi-crystalline polymer. To this end, Fig. 4.1 illustrates schematically the transformation of the (idealized) sub-structure in a semi-crystalline polymer from the reference (Parts (a) and (b)) to the current (Parts (c) and (d)) configuration due to an arbitrary macroscopic

deformation gradient $\overline{\mathbf{F}}(t)$ applied on its boundary. The determination of the macroscopic stress-strain response of a semi-crystalline polymer subjected to a finite-deformation loading history is regarded in this work as an incremental procedure from the initial (reference) to the final state. Each increment involves the computation of the instantaneous effective response of the composite at the beginning of the increment and the evolution of the sub-structure during the increment. The first problem, i.e., the determination of the instantaneous effective behavior, is defined in the present section and solved (approximately) in the following section. Hence, the physical quantities involved in the relevant discussions of these two sections refer to the instant t corresponding to the current configuration of the body, in which the sub-structure is assumed to be fixed and known. Note that this includes the reference configuration as the special case $t = 0$. The evolution of the sub-structure is discussed in section 4.3.

4.1.1 Sub-structural characterization

A semi-crystalline polymer is modeled in this work as a two-scale composite, the sub-structural characteristics of which in the current configuration are illustrated schematically in Parts (c) and (d) of Fig. 4.1. Part (c) of this figure shows a representative volume element (RVE) Ω of the material, made out of a large number N of randomly distributed and perfectly bonded grain-families. The term grain-family is used here to describe the set of all grains with identical underlying micro-structure and material properties. The grain-family r, with $r = 1, ..., N$, is assumed to occupy the subregion $\Omega^{(r)}$ of Ω. Fig. 4.1(d) shows the micro-structure within a grain of the type r, taken to be a perfect laminate with lamination orientation $\mathbf{n}^{(r)}$ and composed of perfectly bonded, alternating layers of an amorphous and a crystalline phase occupying respectively the sub-regions $\Omega^{(r,a)}$ and $\Omega^{(r,c)}$. Both the amorphous and the crystalline phase are assumed to be homogeneous materials, the constitutive behavior of which is described further below. The characteristic length-scales L_1, ℓ_1 and ℓ_2 in Fig. 4.1 stand respectively for the size of the RVE Ω, the size of a typical grain and the distance between two neighboring amorphous (or crystalline) layers. These quantities are assumed to be well-separated, i.e.,

$$\ell_2 << \ell_1 << L_1. \tag{4.1}$$

The sub-structure of the composite system of Fig. 4.1 is, in principle, completely characterized by means of the functions

$$\tilde{\chi}^{(r,p)}(\mathbf{x}) = \begin{cases} 1, & \text{if } \mathbf{x} \in \Omega^{(r,p)} \\ 0, & \text{otherwise} \end{cases}, \tag{4.2}$$

with the superscript $p = a, c$ standing for the amorphous and the crystalline phase, respectively. It is emphasized that the two-scale characteristic functions $\tilde{\chi}^{(r,p)}$ contain both meso-structural (Fig.

4.1(c)) and micro-structural (Fig. 4.1(d)) information. Next, we consider the decomposition (2.17) of the functions $\tilde{\chi}^{(r,p)}$ into the corresponding single-scale mesoscopic $\chi^{(r)}$ and microscopic $\chi^{(r,p)}$ characteristic functions, i.e.,

$$\tilde{\chi}^{(r,p)}(\mathbf{x}) = \chi^{(r)}(\mathbf{x})\chi^{(r,p)}(\mathbf{x}), \tag{4.3}$$

where $\chi^{(r)}$ and $\chi^{(r,p)}$ are defined by

$$\chi^{(r)}(\mathbf{x}) = \begin{cases} 1, & \text{if } \mathbf{x} \in \Omega^{(r)} \\ 0, & \text{otherwise} \end{cases}, \qquad \chi^{(r,p)}(\mathbf{x}) = \begin{cases} 1, & \text{if } \mathbf{x} \in \Omega^{(r,p)} \\ 0, & \text{otherwise} \end{cases}, \tag{4.4}$$

and satisfy the relations

$$\sum_{r=1}^{N} \chi^{(r)}(\mathbf{x}) = 1, \qquad \chi^{(r,a)}(\mathbf{x}) + \chi^{(r,c)}(\mathbf{x}) = 1. \tag{4.5}$$

Note that the spatial variation of the functions $\chi^{(r,a)}$ and $\chi^{(r,c)}$ is restricted along the lamination direction $\mathbf{n}^{(r)}$.

Since the composite material under consideration is random, the characteristic functions $\tilde{\chi}^{(r,p)}$ are expected to be known in terms of the associated multi-point probability functions. In this regard, following the discussion of subsection 2.1.2 (see also Smyshlyaev and Willis [136]), it is assumed that the meso-structure (defined by $\chi^{(r)}$) and the micro-structure (defined by $\chi^{(r,p)}$) of the two-scale composite of Fig. 4.1 are *statistically independent*. An important implication of this assumption is that the two-scale multi-point probability functions associated with $\tilde{\chi}^{(r,p)}$ may be explicitly expressed in terms of the corresponding single-scale multi-point probability functions associated with $\chi^{(r)}$ and $\chi^{(r,p)}$ (see, e.g., relations (2.22) and (2.23)). Furthermore, we assume that the characteristic functions $\chi^{(r)}$ and $\chi^{(r,p)}$ are *statistically uniform*, *ergodic* and possess *no long-range order*. From subsections 2.1.2 and 2.1.1, we recall that the later assumptions imply that the one-point probability functions $p^{(r)}$ $(r = 1, ..., N)$ and $p^{(r,p)}$ $(p = a, c)$, associated respectively with $\chi^{(r)}$ and $\chi^{(r,p)}$, reduce to

$$p^{(r)}(\mathbf{x}) = \frac{|\Omega^{(r)}|}{|\Omega|} \equiv c^{(r)}, \qquad p^{(r,p)}(\mathbf{x}) = \frac{|\Omega^{(r,p)}|}{|\Omega^{(r)}|} \equiv c^{(r,p)}, \tag{4.6}$$

where $c^{(r)}$ denotes the volume fraction of the grain-family r in the RVE Ω and $c^{(r,p)}$ is the volume fraction of phase p in the grain-family r. Furthermore, the corresponding two-point probability functions $p^{(rs)}$ $(r, s = 1, ..., N)$ and $p^{(r,pq)}$ $(p, q = a, c)$ depend on $\mathbf{x}$ and $\mathbf{x}'$ only through the vector $(\mathbf{x} - \mathbf{x}')$.

In this work, we also assume that the two-point probabilities $p^{(rs)}$ are characterized by ellipsoidal symmetry, i.e.,

$$p^{(rs)}(\mathbf{x} - \mathbf{x}') = p^{(rs)}(|\mathbf{Z}(\mathbf{x} - \mathbf{x}')|), \tag{4.7}$$

where the symmetric and positive definite second-order tensor $\mathbf{Z}$ is defined by

$$\mathbf{Z} = \overline{\lambda}_1 \mathbf{z}_1 \otimes \mathbf{z}_1 + \overline{\lambda}_2 \mathbf{z}_2 \otimes \mathbf{z}_2 + \overline{\lambda}_3 \mathbf{z}_3 \otimes \mathbf{z}_3, \tag{4.8}$$

with $\overline{\lambda}_i$ and $\mathbf{z}_i$ denoting respectively the principal values and the principal directions of $\mathbf{Z}$. As already discussed in subsection 2.1.1 (see also Willis [150]), the ellipsoidal symmetry assumption allows consideration of directionally-dependent spatial distributions for the grain-families—the specific features of which are defined through the shape tensor $\mathbf{Z}$—and it is a generalization of the statistical isotropy assumption, which corresponds to $\mathbf{Z} = \mathbf{I}$ and implies that the grains are equally distributed in all directions. For later reference, it is remarked at this point that the estimates for the effective behavior and texture evolution of semi-crystalline polymers to be developed in this chapter depend on $\overline{\lambda}_i$ only through the aspect ratios

$$w_1 = \frac{\overline{\lambda}_3}{\overline{\lambda}_1}, \qquad w_2 = \frac{\overline{\lambda}_3}{\overline{\lambda}_2}. \tag{4.9}$$

Finally, although the micro-structure within the lamellar grains is completely determined by means of the associated volume fractions of the phases $c^{(r,p)}$ and the lamination orientations $\mathbf{n}^{(r)}$, it is remarked here that the shape of the corresponding amorphous and crystalline layers may also be regarded as the limiting case of an ellipsoid with two of its principal values tending to infinity. This may in turn be defined through the shape tensors

$$\mathbf{Z}^{(r)} = \mathbf{n}^{(r)} \otimes \mathbf{n}^{(r)} + \epsilon \left(\mathbf{n}_1^{(r)\perp} \otimes \mathbf{n}_1^{(r)\perp} + \mathbf{n}_2^{(r)\perp} \otimes \mathbf{n}_2^{(r)\perp} \right), \tag{4.10}$$

in the limit as $\epsilon \to \infty$, where $\mathbf{n}_1^{(r)\perp}$ and $\mathbf{n}_2^{(r)\perp}$ are unit vectors orthogonal to $\mathbf{n}^{(r)}$ and to each other.

4.1.2 Amorphous phase

Following Lee et al. [80], the amorphous phase of the semi-crystalline polymer is assumed to be an isotropic and incompressible material, the constitutive behavior of which is characterized by a stress-potential $u^{(r,a)}$ $(r = 1, ..., N)$ of the form

$$u^{(r,a)}(\boldsymbol{\sigma}) = 2\psi^{(r,a)}(\tau^{(r,a)}), \qquad \tau^{(r,a)} = \sqrt{\frac{1}{2}\mathbf{S}^{(r)} \cdot \mathbf{S}^{(r)}}, \tag{4.11}$$

so that the local relation between the associated deformation rate tensor $\mathbf{D}^{(r,a)}$ and the deviatoric part $\boldsymbol{\sigma}_d$ of the Cauchy stress tensor is given by

$$\mathbf{D}^{(r,a)} \equiv \frac{\partial u^{(r,a)}}{\partial \boldsymbol{\sigma}} = \frac{\psi^{(r,a)'}(\tau^{(r,a)})}{\tau^{(r,a)}} \mathbf{S}^{(r)}. \tag{4.12}$$

In the above relation, $\mathbf{S}^{(r)}$ is the driving stress tensor for the plastic deformation of this phase, defined by

$$\mathbf{S}^{(r)} = \boldsymbol{\sigma}_d - \mathbf{T}_d^{(r)}. \tag{4.13}$$

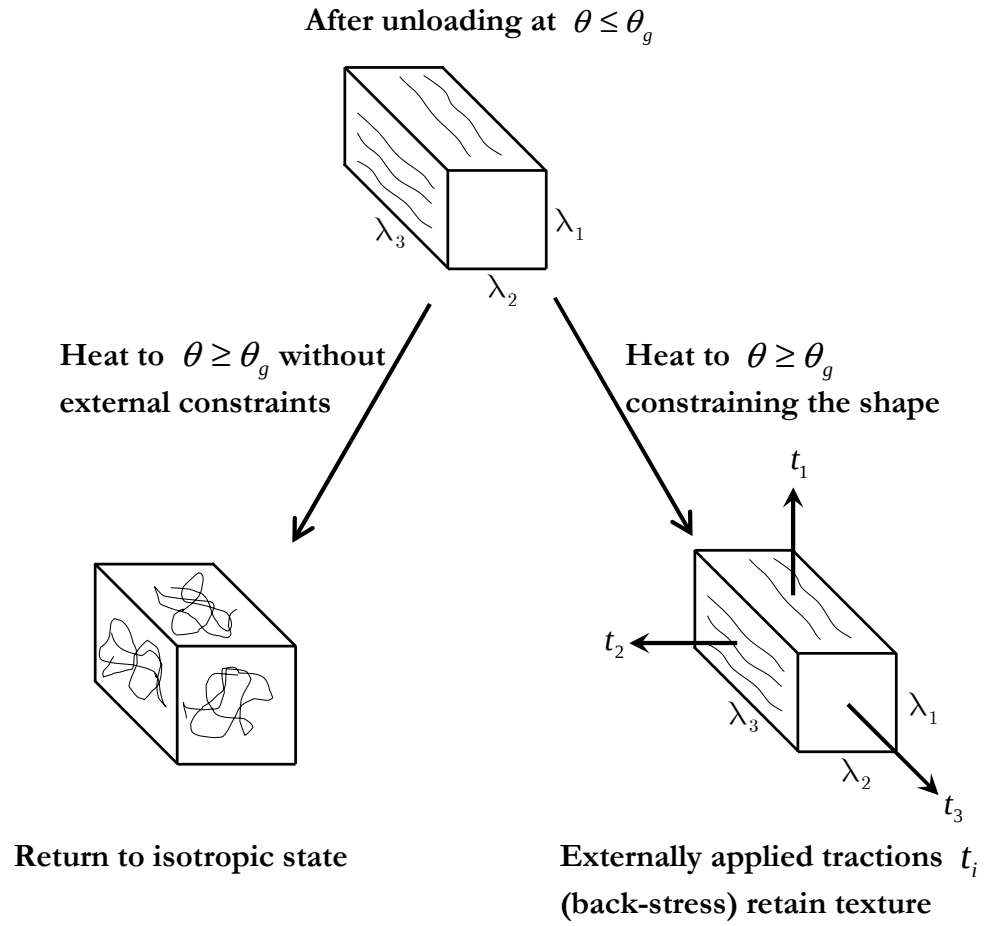

Figure 4.2: Physical description of the back-stress tensor $\mathbf{T}_d$ in principal stress space, where t_i and λ_i denote the principal values of $\mathbf{T}_d$ and the principal stretches, respectively, and θ_g denotes the glass transition temperature of the polymer. (reproduced from Boyce [14]).

where $\mathbf{T}_d^{(r)}$ denotes the deviatoric part of a back-stress tensor, which is discussed in detail further below. The potential function $\psi^{(r,a)}$ in $(4.11)_1$ is assumed to be of the power-law form

$$\psi^{(r,a)}(\tau^{(r,a)}) = \frac{\gamma_0 \tau^{(r,a)}}{n+1} \left(\frac{\tau^{(r,a)}}{\tau_0} \right)^n , \tag{4.14}$$

where n is the rate exponent, γ_0 is a reference strain rate and τ_0 is a reference stress. Note that the constants n, γ_0 and τ_0 have been taken to be identical in all grains.

In the context of the above model, the back-stress tensors $\mathbf{T}_d^{(r)}$ $(r = 1, ..., N)$ are treated as constant-per-phase, kinematic hardening variables accounting on average for the effect of the resistance to further deformation induced by the macromolecular texture developed in this phase at large deformations. The physical interpretation of the back-stress tensor is shown schematically in Fig. 4.2. Specifically, when an initially amorphous polymer is deformed at a temperature below its

glass transition limit θ_g it develops macromolecular texture which remains in the material after the removal of the loading stress. If, subsequently, the polymer is heated above θ_g without constraints it enters its rubbery regime and recovers completely its initially amorphous and isotropic state. In order to retain the shape of the polymer and the underlying macromolecular texture it had in the unloaded glassy state after heating it above θ_g, an external stress—i.e., the back-stress—must be applied to the material in the rubbery regime. Hence the back-stress tensor accounts for the entropic (elastic) hardening of the polymer at large strains. For this reason, we modeled the back-stress tensor $\mathbf{T}_d$ in the amorphous phase by means of the following incompressible hyperelastic constitutive relation

$$\mathbf{T}_d = 2g_I(I)\left(\mathbf{B} - \frac{1}{3}I\mathbf{I}\right), \tag{4.15}$$

where $\mathbf{B} = \mathbf{F}\mathbf{F}^T$ is the left Cauchy-Green tensor, $\mathbf{F}$ is the deformation gradient tensor and $I = \text{tr}\mathbf{B}$. In addition, the notation g_I in (4.15) is used for the the derivative of the stored energy function g with respect to the invariant I. The function g is modeled in this work by means of the expression

$$g(I) = \sum_{i=1}^{M} \frac{\mu_i}{2\alpha_i 3^{\alpha_i - 1}}\left(I^{\alpha_i} - 3^{\alpha_i}\right), \tag{4.16}$$

proposed recently by Lopez-Pamies [90], where μ_i and α_i are material constants and M is a finite integer.

At this point, it should be remarked that the use of the viscoplastic constitutive relation (4.12) in modeling the (primarily) rubbery behavior of the amorphous material—for which the use of the hyperelastic constitutive relation (4.15) alone would be more appropriate—has been motivated by the fact that the homogenization methods of chapter 2, to be used later on in determining the effective response of the semi-crystalline polymer, are restricted to viscoplastic constituents. However, it is important to realize that in the limit $\tau_0 \to 0$ relation (4.12) actually reduces to (4.15). This is because, in the limit $\tau_0 \to 0$, expression (4.12) implies that either the stress measure $\tau = \sqrt{\mathbf{S}\cdot\mathbf{S}/2}$ or the the driving stress tensor $\mathbf{S} = \boldsymbol{\sigma}_d - \mathbf{T}_d$ must equal to zero for the associated deformation rate tensor $\mathbf{D}$ in the amorphous material to have a finite value. But, the condition $\tau = \sqrt{\mathbf{S}\cdot\mathbf{S}/2} = 0$ implies that $|S_{ij}| = 0$ for all $i, j = 1, 2, 3$. Hence, in either case, as $\tau_0 \to 0$ the condition $\boldsymbol{\sigma}_d = \mathbf{T}_d$ must hold. Consider, for example, the case of pure shear loadings at a constant strain rate $D_{11} = -D_{22} \equiv c$, with $D_{ij} = 0$ otherwise, for which relation (4.12) implies that $(\boldsymbol{\sigma}_d)_{ij} = (\mathbf{T}_d)_{ij}$ for $i \neq j$ and $(\boldsymbol{\sigma}_d)_{33} = (\mathbf{T}_d)_{33}$. Furthermore, taking into account the fact that $(\boldsymbol{\sigma}_d - \mathbf{T}_d)_{22} = -(\boldsymbol{\sigma}_d - \mathbf{T}_d)_{11}$, implied by (4.12) and $D_{11} = -D_{22}$, from expression $(4.11)_2$ we find that $\tau = (\boldsymbol{\sigma}_d - \mathbf{T}_d)_{11}$, while from the conditions $\text{tr}\boldsymbol{\sigma}_d = \text{tr}\mathbf{T}_d = 0$ we obtain $(\boldsymbol{\sigma}_d)_{22} = -(\boldsymbol{\sigma}_d)_{11} - (\boldsymbol{\sigma}_d)_{33}$ and $(\mathbf{T}_d)_{22} = -(\mathbf{T}_d)_{11} - (\mathbf{T}_d)_{33}$. These results, in turn, imply that $\boldsymbol{\sigma}_d = \mathbf{T}_d$, provided that $(\boldsymbol{\sigma}_d)_{11} = (\mathbf{T}_d)_{11}$. Making use of the result $\tau = (\boldsymbol{\sigma}_d - \mathbf{T}_d)_{11}$ in relation (4.12), applied for $D_{11} \equiv c$, we find that $(\boldsymbol{\sigma}_d)_{11} = (\mathbf{T}_d)_{11} + \tau_0(c/\gamma_0)^{1/n}$, which for $\tau_0 \to 0$ reduces to

$(\boldsymbol{\sigma}_d)_{11} = (\mathbf{T}_d)_{11}$. Based on the above observation, we conclude that in practical applications, such the applications on high-density polyethylene considered in section 4.5, a small value for τ_0 should be used in the context of the viscoplastic constitute relation (4.12) for the amorphous material.

Given the viscoplastic formulation of the homogenization problem for the semi-crystalline polymer, in this work it is appropriate to make use of the hypoelastic form of the constitutive model (4.15). Next, referring to Truesdell and Noll [144] for a detailed discussion on hypo-elasticity, we derive the hypo-elastic form of expression (4.15). To this end, the inversion of (4.15) is required. First, we rewrite the constitutive relation (4.15) in the form

$$\mathbf{B} = \frac{1}{2g_I}\mathbf{T}_d + \frac{1}{3}I\mathbf{I}, \tag{4.17}$$

Note that (4.17) provides an expression for $\mathbf{B}$ in terms of $\mathbf{T}_d$ and I. Since the tensors $\mathbf{T}_d$ and $\mathbf{B}$ are co-axial (due to isotropy), the constitutive relation (4.15) may also be expressed in principal components, i.e.,

$$t_i = 2g_I\left(\lambda_i^2 - \frac{1}{3}I\right) \qquad \text{or} \qquad \lambda_i^2 = \frac{1}{2g_I}t_i + \frac{1}{3}I \tag{4.18}$$

where t_i and λ_i^2 denote respectively the principal values of $\mathbf{T}_d$ and $\mathbf{B}$. Then, substituting expressions $(4.18)_2$ into the incompressibility constraint $\det\mathbf{B} = \lambda_1^2\lambda_2^2\lambda_3^2 = 1$, we obtain the following nonlinear equation

$$\left(\frac{t_1}{2g_I} + \frac{1}{3}I\right)\left(\frac{t_2}{2g_I} + \frac{1}{3}I\right)\left(\frac{t_3}{2g_I} + \frac{1}{3}I\right) = 1, \tag{4.19}$$

which determines the invariant I in terms of t_i and completes the inversion of the hyper-elastic relation (4.15). Finally, the hypo-elastic constitutive relation for the back-stress tensor $\mathbf{T}_d$ is obtained by taking the time derivative of (4.15) and making use of relations (4.17) and (4.19) to express $\mathbf{B}$ and I as functions of $\mathbf{T}_d$. The result reads as follows

$$\dot{\mathbf{T}}_d = \frac{g_{II}\mathbf{T}_d\cdot\mathbf{D}}{g_I^2}\mathbf{T}_d + \frac{2}{3}\left[2Ig_I\mathbf{D} - (\mathbf{T}_d\cdot\mathbf{D})\,\mathbf{I}\right] + (\mathbf{D}\mathbf{T}_d + \mathbf{T}_d\mathbf{D}) + (\mathbf{W}\mathbf{T}_d - \mathbf{T}_d\mathbf{W})\,, \tag{4.20}$$

where $\mathbf{D}$ and $\mathbf{W}$ are respectively the deformation rate and spin tensors associated with the velocity gradient tensor $\mathbf{L} = \dot{\mathbf{F}}\mathbf{F}^{-1}$, and $g_{II} = d^2g(I)/d\,I^2$. Note that expression (4.20) may be rewritten in the invariant form

$$\overset{\triangledown}{\mathbf{T}}_d = \frac{g_{II}\mathbf{T}_d\cdot\mathbf{D}}{g_I^2}\mathbf{T}_d + \frac{2}{3}\left[(2Ig_I)\,\mathbf{D} - (\mathbf{T}_d\cdot\mathbf{D})\,\mathbf{I}\right] + (\mathbf{D}\mathbf{T}_d + \mathbf{T}_d\mathbf{D})\,, \tag{4.21}$$

where $\overset{\triangledown}{\mathbf{T}}_d$ denotes the Jaumann (co-rotational with $\mathbf{W}$) time derivative, defined by $\overset{\triangledown}{\mathbf{T}}_d = \dot{\mathbf{T}}_d + \mathbf{T}_d\mathbf{W} - \mathbf{W}\mathbf{T}_d$.

4.1.3 Crystalline phase

From extensive experimental research conducted over the past several decades (see, e.g., the review article of Lin and Argon [84] and references therein), it has been well established that the dominant

deformation mechanism for the plastic deformation of the crystalline phase in semi-crystalline polymers is crystallographic slip. Furthermore, the associated crystal lattice is orthorhombic and inextensible along the chain folding direction, which in turn implies that crystallographic slip in this phase is constrained on four independent slip-systems.

Hence, the crystalline phase in a grain of the type r is modeled as an incompressible, viscoplastic material, characterized by means of the stress-potential

$$u^{(r,c)}(\boldsymbol{\sigma}) = \sum_{k=1}^{K} \psi_k^{(r,c)}(\tau_k^{(r,c)}), \qquad \tau_k^{(r,c)} = \boldsymbol{\sigma} \cdot \boldsymbol{\mu}_k^{(r)}, \tag{4.22}$$

where $\psi_k^{(r,c)}$ is the slip-potential associated with the $k-th$ slip system, with $k = 1, ..., K$, and K stands for the total number of the physically distinct slip systems. In the above relation, it is recalled that $\tau_k^{(r,c)}$ denotes the resolved shear stress on the $k-th$ slip system and $\boldsymbol{\mu}_k^{(r)}$ are the associated symmetric Schmidt tensor, defined by

$$\boldsymbol{\mu}_k^{(r)} = \frac{1}{2}\left(\mathbf{s}_k^{(r)} \otimes \mathbf{m}_k^{(r)} + \mathbf{m}_k^{(r)} \otimes \mathbf{s}_k^{(r)}\right), \tag{4.23}$$

where $\mathbf{s}_k^{(r)}$ and $\mathbf{m}_k^{(r)}$ are the corresponding slip direction and slip plane normal vectors, respectively. The slip potentials $\psi_k^{(r,c)}$ in relation $(4.22)_1$ are taken to be of the form

$$\psi_k^{(r,c)}(\tau_k^{(r,c)}) = \frac{\gamma_0 \tau_k^{(r,c)}}{n+1}\left(\frac{|\tau_k^{(r,c)}|}{\tau_{0k}^{(r,c)}}\right)^n, \tag{4.24}$$

where γ_0 is a reference shear strain rate, n is the rate exponent and $\tau_{0k}^{(r,c)}$ is the critical resolved shear stress (CRSS) of the $k-th$ slip system. It is emphasized that, although γ_0 and n are chosen to be identical for all slip systems in all grains, the yield stresses $\tau_{0k}^{(r,c)}$ may be different for different slip systems in different grains, in general.

For the purpose of the specific applications of section 4.5 on high-density polyethylene, the CRSSs $\tau_{0k}^{(r,c)}$ will be prescribed in this work by means of the following strain-hardening law

$$\tau_{0k}^{(r,c)} = \tau_{0k} + \left(\tau_{1k} + \theta_{1k}(\Gamma^{(r,c)})^4\right)\left(1 - \mathrm{Exp}\left[-\Gamma^{(r,c)}\frac{\theta_{0k}}{\tau_{1k}}\right]\right), \tag{4.25}$$

where τ_{0k}, τ_{1k}, θ_{0k} and θ_{1k} are positive constants and $\Gamma^{(r,c)}$ is a measure of the deformation in the associated crystalline phase (r,c), given by

$$\Gamma^{(r,c)} = \sum_{k=1}^{K} \int_0^t \dot{\gamma}_k^{(r,c)} dt, \tag{4.26}$$

in terms of the corresponding shear rates $\dot{\gamma}_k^{(r,c)} = \psi_k^{(r,c)'}(\tau_k^{(r,c)})$ in the slip systems of this phase.

4.1.4 Effective behavior

Taking into account the above definitions, the local constitutive relation of the semi-crystalline polymer is given by

$$\mathbf{D} = \frac{\partial u}{\partial \boldsymbol{\sigma}}(\mathbf{x}, \boldsymbol{\sigma}), \quad u(\mathbf{x}, \boldsymbol{\sigma}) = \sum_{r=1}^{N} \chi^{(r)}(\mathbf{x}) \left[\chi^{(r,c)}(\mathbf{x}) u^{(r,c)}(\boldsymbol{\sigma}) + \chi^{(r,a)}(\mathbf{x}) u^{(r,a)}(\boldsymbol{\sigma}) \right], \tag{4.27}$$

where it is recalled that $\mathbf{D}$ denotes the deformation rate tensor, i.e., the symmetric part of the velocity gradient. Note that, taking into account relations (4.11) and (4.22), the stress potential $u(\mathbf{x}, \boldsymbol{\sigma})$ may be rewritten in the form

$$u(\mathbf{x}, \boldsymbol{\sigma}) = \sum_{r=1}^{N} \chi^{(r)}(\mathbf{x}) \left[\chi^{(r,c)}(\mathbf{x}) \sum_{k=1}^{K} \psi_k^{(r,c)}(\tau_k^{(r,c)}) + 2\chi^{(r,a)}(\mathbf{x}) \psi^{(r,a)}(\tau^{(r,a)}) \right]. \tag{4.28}$$

Following the analysis of subsection 2.4.2, the instantaneous effective response of the semi-crystalline polymer is given by

$$\overline{\mathbf{D}} = \frac{\partial\, \tilde{u}}{\partial\, \overline{\boldsymbol{\sigma}}}, \tag{4.29}$$

where we recall that $\overline{\mathbf{D}} \equiv \langle \mathbf{D}(\mathbf{x}) \rangle$ and $\overline{\boldsymbol{\sigma}} \equiv \langle \boldsymbol{\sigma}(\mathbf{x}) \rangle$ are respectively the averages of the deformation rate and stress fields over Ω. The effective stress-potential $\tilde{u}$ of the composite in (4.29) is defined by means of the following direct variational principle (see subsection 2.4.2)

$$\begin{aligned} \tilde{u}(\overline{\boldsymbol{\sigma}}) &= \min_{\boldsymbol{\sigma} \in \mathcal{S}(\overline{\boldsymbol{\sigma}})} \langle u(\mathbf{x}, \boldsymbol{\sigma}) \rangle = \\ &= \min_{\boldsymbol{\sigma} \in \mathcal{S}(\overline{\boldsymbol{\sigma}})} \sum_{r=1}^{N} c^{(r)} \left[c^{(r,c)} \sum_{k=1}^{K} \langle \psi_k^{(r,c)}(\tau_k^{(r,c)}) \rangle^{(r,c)} + 2c^{(r,a)} \langle \psi^{(r,a)}(\tau^{(r,a)}) \rangle^{(r,a)} \right], \end{aligned} \tag{4.30}$$

where $\langle \cdot \rangle^{(r,c)}$ and $\langle \cdot \rangle^{(r,a)}$ denote volume averages over $\Omega^{(r,c)}$ and $\Omega^{(r,a)}$, respectively, and

$$\mathcal{S}(\overline{\boldsymbol{\sigma}}) = \{ \boldsymbol{\sigma},\ \mathrm{div}\boldsymbol{\sigma} = 0 \,\mathrm{in}\, \Omega \,\mathrm{and}\, \boldsymbol{\sigma}\mathbf{n} = \overline{\boldsymbol{\sigma}}\mathbf{n} \,\mathrm{on}\, \partial\Omega \}, \tag{4.31}$$

is the set of admissible stress fields.

At this point it should be emphasized that the effective stress-potential $\tilde{u}$ in (4.30) depends not only on the applied stress $\overline{\boldsymbol{\sigma}}$ but also on the current state of the viscoplastic composite, which is in addition defined by the set of internal variables

$$\{ w_\alpha, \mathbf{z}_i, \mathbf{n}^{(r)}, \mathbf{a}^{(r)}, \mathbf{b}^{(r)}, \mathbf{c}^{(r)}, \mathbf{T}_d^{(r)}, \tau_{0k}^{(r,c)} \}, \tag{4.32}$$

where $\alpha = 1, 2$, $i = 1, 2, 3$, $r = 1, ..., N$ and $\mathbf{a}^{(r)}$, $\mathbf{b}^{(r)}$, $\mathbf{c}^{(r)}$ are the principal crystallographic axes of the crystalline phase in the grain-family r. Furthermore, it is important to realize that—due to the nonlinear nature of the composite material under consideration as well as the random character of the underlying sub-structure—the variational problem (4.30) can not be solved exactly.

4.2 Estimates for the instantaneous effective behavior

In this section, we implement the "direct linearization scheme", LCC methods of chapter 2 for nonlinear two-scale composites in order to generate an estimate for the effective stress-potential $\tilde{u}$ of the semi-crystalline polymer. In particular, we make use of a secant type of linearization for the amorphous phase and of a generalized-secant linearization for the crystalline phase. Note that the estimate for $\tilde{u}$ obtained in this way is not exact to second-order in the heterogeneity contrast. In this connection, it is remarked that the use of the generalized-secant linearization scheme for both phases, which would lead to an estimate for $\tilde{u}$ that is exact to second-order in the contrast, may be pursued as well. However, the determination of an estimate based on a secant linearization scheme for the amorphous phase has the advantage of being computationally simpler, which is of great importance for a material system with such a complex sub-structure as the semi-crystalline polymer. Furthermore, recall that the use of the generalized-secant linearization scheme for the amorphous phase requires the prescription of the associated reference stress tensors, the particular choice of which may be a source for additional computational difficulties, as discussed in the work of Idiart et. al [64]. Although these difficulties may be easily handled in the case of composite systems with simple sub-structures, in the case under consideration they constitute an additional technical challenge.

Consider a two-scale LCC with the same sub-structure as the nonlinear semi-crystalline polymer and local stress-potential defined by

$$u_T(\mathbf{x},\boldsymbol{\sigma}) = \sum_{r=1}^{N} \chi^{(r)}(\mathbf{x}) \left[\chi^{(r,c)}(\mathbf{x}) u_T^{(r,c)}(\boldsymbol{\sigma}) + \chi^{(r,a)}(\mathbf{x}) u_T^{(r,a)}(\boldsymbol{\sigma}) \right], \tag{4.33}$$

where the phase-potential $u_T^{(r,p)}$, with $p = c, a$ standing respectively for the crystalline and amorphous phase of the LCC, are quadratic functions of the Cauchy stress tensor $\boldsymbol{\sigma}$ which, for convenience, are expressed here as

$$u_T^{(r,p)}(\boldsymbol{\sigma}) = \frac{1}{2}\boldsymbol{\sigma}\cdot\mathbf{M}^{(r,p)}\boldsymbol{\sigma} + \boldsymbol{\alpha}^{(r,p)}\cdot\boldsymbol{\sigma} + \phi^{(r,p)}, \tag{4.34}$$

where $\mathbf{M}^{(r,p)}$, $\boldsymbol{\alpha}^{(r,p)}$ and $\phi^{(r,p)}$ correspond respectively to the modulus tensor, the thermal strain tensor and the specific heat associated with phase $p = c, a$ in the grain $r = 1, ..., N$ of the LCC. Following the work of Liu and Ponte Castañeda [86] the later quantities associated with the crystalline phase are taken to be of the form

$$\mathbf{M}^{(r,c)} = \sum_{k=1}^{K} \alpha_k^{(r)} \boldsymbol{\mu}_k^{(r)} \otimes \boldsymbol{\mu}_k^{(r)}, \qquad \boldsymbol{\alpha}^{(r,c)} = \frac{\partial u^{(r,c)}}{\partial \boldsymbol{\sigma}}(\overline{\boldsymbol{\sigma}}^{(r,c)}) - \mathbf{M}^{(r,c)}\overline{\boldsymbol{\sigma}}^{(r,c)}, \qquad \phi^{(r,c)} = 0, \tag{4.35}$$

where $\alpha_k^{(r)}$ are unknown scalar moduli to be determined further below. In order to avoid the use of more elaborate notation, the variables $\overline{\boldsymbol{\sigma}}^{(r,c)}$ in (4.35) denote at this stage some arbitrary reference

stress tensors which will be identified later on with the volume averages of the stress field over the corresponding crystalline phases of the LCC. The corresponding properties of the amorphous phase in the grain-family r of the LCC are assumed to be of the form

$$\mathbf{M}^{(r,a)} = \frac{1}{2\lambda^{(r)}}\mathbf{K}, \qquad \boldsymbol{\alpha}^{(r,a)} = -\mathbf{M}^{(r,a)}\mathbf{T}_d^{(r)}, \qquad \phi^{(r,a)} = \frac{1}{2}\mathbf{T}_d^{(r)} \cdot \mathbf{M}^{(r,a)}\mathbf{T}_d^{(r)}, \tag{4.36}$$

where $\lambda^{(r)}$ is the associated unknown scalar modulus and $\mathbf{T}_d^{(r)}$ is the corresponding back-stress tensor, assumed to be a (different) constant for each r. Making use of the definitions (4.35) and (4.36), expressions (4.33) and (4.34) may be respectively rewritten in the form

$$u_T(\mathbf{x}, \boldsymbol{\sigma}) = \sum_{r=1}^{N} \chi^{(r)}(\mathbf{x}) \left[\chi^{(r,c)}(\mathbf{x}) \sum_{k=1}^{K} \Psi_k^{(r,c)}(\tau_k^{(r,c)}) + \chi^{(r,a)}(\mathbf{x}) \Psi^{(r,a)}(\tau^{(r,a)}) \right], \tag{4.37}$$

and

$$u_T^{(r,c)}(\boldsymbol{\sigma}) = \sum_{k=1}^{K} \Psi_k^{(r,c)}(\tau_k^{(r,c)}), \qquad u_T^{(r,a)}(\boldsymbol{\sigma}) = \Psi^{(r,a)}(\tau^{(r,a)}), \tag{4.38}$$

where we recall that the local stress measures $\tau_k^{(r,c)}$ and $\tau^{(r,a)}$ are given by $(4.22)_2$ and $(4.11)_2$, respectively, and we have introduced the functions

$$\Psi_k^{(r,c)}(\tau_k^{(r,c)}) = \frac{1}{2}\alpha_k^{(r)} \left(\tau_k^{(r,c)} - \overline{\tau}_k^{(r,c)} \right)^2 + \psi_k^{(r,c)'}(\overline{\tau}_k^{(r,c)})\tau_k^{(r,c)} - \frac{1}{2}\alpha_k^{(r)}\overline{\tau}_k^{(r,c)}, \tag{4.39}$$

with $\overline{\tau}_k^{(r,c)} = \overline{\boldsymbol{\sigma}}^{(r,c)} \cdot \boldsymbol{\mu}_k^{(r)}$, and

$$\Psi^{(r,a)}(\tau^{(r,a)}) = \frac{1}{2\lambda^{(r)}}(\tau^{(r,a)})^2. \tag{4.40}$$

Next, we define the error function

$$V(\mathbf{x}; \lambda^{(s)}, \alpha_l^{(s)}) = \sum_{r=1}^{N} \chi^{(r)}(\mathbf{x}) \left[\chi^{(r,c)}(\mathbf{x}) \sum_{k=1}^{K} V_k^{(r,c)} \left(\alpha_k^{(r)} \right) + \chi^{(r,a)}(\mathbf{x}) V^{(r,a)} \left(\lambda^{(r)} \right) \right], \tag{4.41}$$

where

$$V_k^{(r,c)} \left(\alpha_k^{(r)} \right) = \underset{\hat{\tau}_k^{(r,c)}}{\text{stat}} \left[\psi_k^{(r,c)}(\hat{\tau}_k^{(r,c)}) - \Psi_k^{(r,c)}(\hat{\tau}_k^{(r,c)}) \right], \tag{4.42}$$

and

$$V^{(r,a)} \left(\lambda^{(r)} \right) = \underset{\hat{\tau}^{(r,a)}}{\text{stat}} \left[2\psi^{(r,a)}(\hat{\tau}^{(r,a)}) - \Psi^{(r,a)}(\hat{\tau}^{(r,a)}) \right]. \tag{4.43}$$

Note that the stationarity conditions in expressions (4.42) and (4.43), i.e.,

$$\psi_k^{(r,c)'}(\hat{\tau}_k^{(r,c)}) - \psi_k^{(r,c)'}(\overline{\tau}_k^{(r,c)}) = \alpha_k^{(r)}(\hat{\tau}_k^{(r,c)} - \overline{\tau}_k^{(r,c)}), \tag{4.44}$$

and

$$\frac{\psi^{(r,a)'}(\hat{\tau}^{(r,a)})}{\hat{\tau}^{(r,a)}} = \frac{1}{2\lambda^{(r)}}, \tag{4.45}$$

respectively, constitute a system of scalar equations for the determination of the scalar variables $\hat{\tau}^{(r,a)}$ and $\hat{\tau}_k^{(r,c)}$.

Taking into account the definition (4.37) for the LCC and (4.41) for the error function, it can be shown that the original variational principle (4.30) may be expressed in the alternative form

$$\tilde{u}(\overline{\boldsymbol{\sigma}}) = \min_{\boldsymbol{\sigma}\in\mathcal{S}(\overline{\boldsymbol{\sigma}})} \langle \operatorname*{stat}_{\substack{\lambda^{(s)},\alpha_l^{(s)} \\ s=1,..,N \\ l=1,..,K}} \left[u_T(\mathbf{x},\boldsymbol{\sigma}) + V(\mathbf{x};\lambda^{(r)},\alpha_k^{(r)}) \right] \rangle, \tag{4.46}$$

which after interchanging the order of the optimality operations reduces to

$$\tilde{u}(\overline{\boldsymbol{\sigma}}) = \operatorname*{stat}_{\substack{\lambda^{(s)}(\mathbf{x}),\alpha_l^{(s)}(\mathbf{x}) \\ s=1,..,N \\ l=1,..,K}} \left[\tilde{u}_T(\overline{\boldsymbol{\sigma}}) + \sum_{r=1}^{N} c^{(r)} \left[c^{(r,c)} \sum_{k=1}^{K} \langle V_k^{(r,c)}(\alpha_k^{(r)}) \rangle^{(r,c)} + c^{(r,a)} \langle V^{(r,a)}(\lambda^{(r)}) \rangle^{(r,a)} \right] \right], \tag{4.47}$$

where $\tilde{u}_T(\overline{\boldsymbol{\sigma}})$ is the effective stress-potential of the two-scale LCC under consideration. Assuming that the moduli fields $\lambda^{(r)}$ and $\alpha_k^{(r)}$ are constant in each phase, the optimality conditions in the above expression for $\tilde{u}$ read as follows

$$(\hat{\tau}_k^{(r,c)} - \overline{\tau}_k^{(r,c)})^2 = \langle (\tau_k^{(r,c)} - \overline{\tau}_k^{(r,c)})^2 \rangle^{(r,c)}, \tag{4.48}$$

and

$$(\hat{\tau}^{(r,a)})^2 = \langle (\tau^{(r,a)})^2 \rangle^{(r,a)}. \tag{4.49}$$

As already mentioned, the reference stress tensors $\overline{\boldsymbol{\sigma}}^{(r,c)}$ in the context of (4.47) are set equal to volume averages of the stress field over the corresponding crystalline phases of the LCC. Note that conditions (4.48) and (4.49) may be viewed as a system of equations for the phase-moduli $\lambda^{(r)}$ and $\alpha_k^{(r)}$. In addition, condition (4.48) imply the interpretation of the variables $\hat{\tau}_k^{(r,c)}$ as the fluctuations of the associated local resolved shear stresses $\tau_k^{(r,c)}$ in the crystalline phase of the LCC about the corresponding average resolved shear stresses $\overline{\tau}_k^{(r,c)}$. Similarly, condition (4.49) associates the variable $\hat{\tau}^{(r,a)}$ with the the stress field fluctuations in the amorphous phase of the LCC about the back-stress tensor. Furthermore, it should be emphasized that equations (4.48) and (4.49) have multiple solutions. In this work, following Liu and Ponte Castañeda [86], we chose the branch of (4.48) based on the sign of $\overline{\tau}_k^{(r,c)}$, i.e.,

$$\hat{\tau}_k^{(r,c)} = \overline{\tau}_k^{(r,c)} + \operatorname{sign}\left(\overline{\tau}_k^{(r,c)}\right) \sqrt{\langle (\tau_k^{(r,c)} - \overline{\tau}_k^{(r,c)})^2 \rangle^{(r,c)}}, \tag{4.50}$$

while in the case of (4.49), we always chose its positive branch, i.e.,

$$\hat{\tau}^{(r,a)} = \sqrt{\langle (\tau^{(r,a)})^2 \rangle^{(r,a)}}. \tag{4.51}$$

Making use of the results (4.48) and (4.49), it can be easily shown that the estimate (4.47) for $\tilde{u}$ reduces to

$$\tilde{u}(\overline{\boldsymbol{\sigma}}) = \sum_{r=1}^{N} c^{(r)} \left\{ c^{(r,c)} \sum_{k=1}^{K} \left[\psi_k^{(r,c)}(\hat{\tau}_k^{(r,c)}) + \psi_k^{(r,c)'}(\overline{\tau}_k^{(r,c)})(\overline{\tau}_k^{(r,c)} - \hat{\tau}_k^{(r,c)}) \right] + 2c^{(r,a)} \psi^{(r,a)}(\hat{\tau}^{(r,a)}) \right\}. \tag{4.52}$$

From the relevant discussion of subsection 2.7, it is recalled that the averages of the stress field over the phases of the two-scale LCC are given by (2.145), i.e.,

$$\overline{\boldsymbol{\sigma}}^{(r,p)} = \mathbf{B}^{(r,p)} \overline{\boldsymbol{\sigma}}^{(r)} + \mathbf{b}^{(r,p)}, \qquad \overline{\boldsymbol{\sigma}}^{(r)} = \mathbf{B}^{(r)} \overline{\boldsymbol{\sigma}} + \mathbf{b}^{(r)}, \tag{4.53}$$

where $p = a, c$, $\overline{\boldsymbol{\sigma}}^{(r)} \equiv \langle \boldsymbol{\sigma} \rangle^{(r)}$ are the grain-average stress tensors and $\mathbf{B}^{(r,p)}$, $\mathbf{b}^{(r,p)}$, $\mathbf{B}^{(r)}$, $\mathbf{b}^{(r)}$ are the associated stress concentration tensors. Furthermore, the fluctuations of the stress field in the phases of the LCC are determined by means of the relations

$$\langle (\tau_k^{(r,c)} - \overline{\tau}_k^{(r,c)})^2 \rangle^{(r,c)} = \boldsymbol{\mu}_k^{(r)} \cdot \mathbf{C}_{\boldsymbol{\sigma}}^{(r,c)} \boldsymbol{\mu}_k^{(r)}, \tag{4.54}$$

and

$$\langle (\tau^{(r,a)})^2 \rangle^{(r,a)} = \frac{1}{2} \mathbf{K} \cdot \mathbf{C}_{\boldsymbol{\sigma}}^{(r,a)}, \tag{4.55}$$

where the corresponding covariance tensors $\mathbf{C}_{\boldsymbol{\sigma}}^{(r,c)}$ and $\mathbf{C}_{\boldsymbol{\sigma}}^{(r,a)}$ are respectively defined by

$$\mathbf{C}_{\boldsymbol{\sigma}}^{(r,c)} = \langle (\boldsymbol{\sigma} - \overline{\boldsymbol{\sigma}}^{(r,c)}) \otimes (\boldsymbol{\sigma} - \overline{\boldsymbol{\sigma}}^{(r,c)}) \rangle^{(r,c)} = \langle \boldsymbol{\sigma} \otimes \boldsymbol{\sigma} \rangle^{(r,c)} - \overline{\boldsymbol{\sigma}}^{(r,c)} \otimes \overline{\boldsymbol{\sigma}}^{(r,c)}, \tag{4.56}$$

and

$$\mathbf{C}_{\boldsymbol{\sigma}}^{(r,a)} = \langle (\boldsymbol{\sigma} - \mathbf{T}_d^{(r)}) \otimes (\boldsymbol{\sigma} - \mathbf{T}_d^{(r)}) \rangle^{(r,a)} = \langle \boldsymbol{\sigma} \otimes \boldsymbol{\sigma} \rangle^{(r,a)} - \overline{\boldsymbol{\sigma}}^{(r,a)} \otimes \mathbf{T}_d^{(r)} - \mathbf{T}_d^{(r)} \otimes \overline{\boldsymbol{\sigma}}^{(r,a)} + \mathbf{T}_d^{(r)} \otimes \mathbf{T}_d^{(r)}, \tag{4.57}$$

where $\overline{\boldsymbol{\sigma}}^{(r,a)} \equiv \langle \boldsymbol{\sigma} \rangle^{(r,a)}$ are the amorphous phase average stress tensors in the LCC. The second-moments $\langle \boldsymbol{\sigma} \otimes \boldsymbol{\sigma} \rangle^{(r,p)}$, with $p = a, c$, in $(4.56)_2$ and $(4.57)_2$ are given by

$$\langle \boldsymbol{\sigma} \otimes \boldsymbol{\sigma} \rangle^{(r,p)} = \frac{2}{c^{(r)} c^{(r,p)}} \frac{\partial \tilde{u}_T}{\partial \mathbf{M}^{(r,p)}}, \tag{4.58}$$

where it is emphasized that the derivatives of $\tilde{u}_T$ must be taken by holding the thermal strain tensors $\boldsymbol{\alpha}^{(r,p)}$ and specific heats $\phi^{(r,p)}$ fixed. The pertinent discussion on the computation of the stress concentration tensors $\mathbf{B}^{(r,p)}$, $\mathbf{b}^{(r,p)}$, $\mathbf{B}^{(r)}$, $\mathbf{b}^{(r)}$ and the second-moment tensors $\langle \boldsymbol{\sigma} \otimes \boldsymbol{\sigma} \rangle^{(r,p)}$ is provided in section 4.4.

At this point, it is emphasized once again that the estimate (4.52) for the effective stress-potential $\tilde{u}$ of the semi-crystalline polymer depends also on the values of the internal variables (4.32) in the current configuration of the body. During a finite deformation process, these variables evolve as a result of the finite changes in the geometry of the body at large strains. The exact details of these changes are completely determined in terms of the local kinematics. However, as

already discussed, the computation of the local field in a nonlinear random composite is practically impossible. Therefore, the determination of the effective behavior of a semi-crystalline polymer for finite strain loadings requires the development of additional estimates for the evolution of the internal variables (4.32).

4.3 Estimates for the evolution of the internal variables

This section deals with the development of appropriate constitutive relations for the evolution of the internal variables (4.32). To this end, consider an arbitrary loading history prescribed through the average velocity gradient $\overline{\mathbf{L}}(t)$, with t being the time variable, which is decomposed into a symmetric and an anti-symmetric part,

$$\overline{\mathbf{L}}(t) = \overline{\mathbf{D}}(t) + \overline{\mathbf{W}}(t), \tag{4.59}$$

with $\overline{\mathbf{D}}(t)$ and $\overline{\mathbf{W}}(t)$ being the corresponding average (or applied) deformation rate and spin tensor, respectively. Note that, on any specific application, the prescribed loading conditions consist of the three components of the spin tensor $\overline{\mathbf{W}}(t)$ and any combination of five additional components of the deformation rate tensor $\overline{\mathbf{D}}(t)$ and the deviatoric stress tensor $\overline{\boldsymbol{\sigma}}_d(t)$; the remanning five unknown components are determined from the effective constitutive relation (4.29) of the composite. For the purposes of this section, it is assumed that both $\overline{\mathbf{D}}(t)$ and $\overline{\mathbf{W}}(t)$ are completely known. It can be easily shown that the average velocity gradient tensor $\overline{\mathbf{L}}(t)$ and the associated average deformation gradient tensor $\overline{\mathbf{F}}(t)$ are related by

$$\overline{\mathbf{L}}(t) = \dot{\overline{\mathbf{F}}}(t)\overline{\mathbf{F}}^{-1}(t), \tag{4.60}$$

which is a well-known result for the case of homogeneous deformations in homogeneous bodies. Thus, given $\overline{\mathbf{L}}(t)$, the applied deformation gradient $\overline{\mathbf{F}}(t)$ may be readily determined by integration of (4.60). It should be emphasized, however, that the corresponding grain- or phase-average quantities are *not* related by expressions of the type (4.60), in general. In other words, the grain- and phase-average deformation gradient tensors $\overline{\mathbf{F}}^{(r)}(t)$, $\overline{\mathbf{F}}^{(r,c)}(t)$ and $\overline{\mathbf{F}}^{(r,a)}(t)$ can not be computed from the corresponding velocity gradient tensors $\overline{\mathbf{L}}^{(r)}(t)$, $\overline{\mathbf{L}}^{(r,c)}(t)$ and $\overline{\mathbf{L}}^{(r,a)}(t)$, respectively.

4.3.1 Morphological texture evolution

The evolution of the shape tensor $\mathbf{Z}$—defined by (4.10) and characterizing the distribution symmetry of the grain-families—is assumed to be governed by the applied deformation. Specifically, the tensor $\mathbf{Z}$ is identified in this work with the left stretch tensor $\overline{\mathbf{V}}$ from the polar decomposition of the applied deformation gradient $\overline{\mathbf{F}} = \overline{\mathbf{V}}\,\overline{\mathbf{R}}$. Hence, the evolution equations for the aspect ratios w_α ($\alpha = 1, 2$), defined by (4.9), and the corresponding principal directions $\mathbf{z}_i$ ($i = 1, 2, 3$) of $\mathbf{Z}$ are

given by (see, e.g., Ogden [112])

$$\dot{w}_\alpha = w_\alpha(\mathbf{z}_3 \otimes \mathbf{z}_3 - \mathbf{z}_\alpha \otimes \mathbf{z}_\alpha) \cdot \overline{\mathbf{D}}, \tag{4.61}$$

where, in the right-hand-side, no sum is implied for the repeated index α, and

$$\dot{\mathbf{z}}_i = \overline{\omega}_{\mathbf{z}} \mathbf{z}_i, \tag{4.62}$$

where $\overline{\omega}_{\mathbf{z}}$ is the spin of the macroscopic Eulerian axes (i.e., the spin of the principal axes of $\overline{\mathbf{V}}$), which is given by

$$\overline{\omega}_{\mathbf{z}} = \overline{\mathbf{W}} + \overline{\mathbf{\Omega}}_{\mathbf{z}}, \qquad \overline{\mathbf{\Omega}}_{\mathbf{z}} = \sum_{\substack{i,j=1 \\ i \neq j, w_i \neq w_j}}^{3} \frac{w_i^2 + w_j^2}{w_i^2 - w_j^2} (\mathbf{z}_i \cdot \overline{\mathbf{D}} \mathbf{z}_j) \mathbf{z}_i \otimes \mathbf{z}_j, \tag{4.63}$$

with $w_3 \equiv 1$. It should be remarked that, if any two of the aspect ratios w_i and w_j for $i \neq j$ happen to be equal, the corresponding component of $\overline{\mathbf{\Omega}}_{\mathbf{z}}$ in (4.63) is set equal to zero, while in the case that $w_1 = w_2 = w_3$ we have $\overline{\mathbf{\Omega}}_{\mathbf{z}} = \mathbf{0}$ (see [4] and [23]). Clearly, the evolution equation (4.62) may be recast in the invariant form

$$\overset{\triangledown}{\mathbf{z}}_i = \overline{\mathbf{\Omega}}_{\mathbf{z}} \mathbf{z}_i, \tag{4.64}$$

where the superimposed inverted triangle denotes the Jaummann (co-rotational with $\overline{\mathbf{W}}$) time derivative, defined by $\overset{\triangledown}{\mathbf{z}}_i = \dot{\mathbf{z}}_i - \overline{\mathbf{W}} \mathbf{z}_i$.

4.3.2 Lamellar texture evolution

It can be easily shown (see, e.g., Lopez-Pamies [89]) that when a simple laminate composite is subjected to a constant (average) deformation gradient $\mathbf{F}$ the associated lamination orientation $\mathbf{N}$ in the reference configuration transforms into the corresponding orientation $\mathbf{n}$ in the current configuration according to Nanson's formula

$$\mathbf{n} = \mathbf{F}^{-T}\mathbf{N}/|\mathbf{F}^{-T}\mathbf{N}|. \tag{4.65}$$

It is remarked that the above result is purely kinematical and therefore independent of the material properties of the constituents. The rate form of the above equation may be readily obtained by taking its time derivative and using the kinematical relation (4.60) to express the time derivative of the applied deformation gradient $\mathbf{F}$ in terms of the corresponding velocity gradient $\mathbf{L}$. The result reads as follows

$$\dot{\mathbf{n}} = [\mathbf{W} - (\mathbf{D}\mathbf{n} \otimes \mathbf{n} - \mathbf{n} \otimes \mathbf{n}\mathbf{D})]\, \mathbf{n}, \tag{4.66}$$

where $\mathbf{D}$ and $\mathbf{W}$ are respectively the deformation rate and spin tensors associated with $\mathbf{L}$.

Making use of the result (4.66) and assuming that the evolution of the unit vector $\mathbf{n}^{(r)}$, defining on average the lamination orientation of the grain-family r, is governed by the associated grain-average velocity gradient $\overline{\mathbf{L}}^{(r)}$ in the LCC we obtain the following evolution law for $\mathbf{n}^{(r)}$

$$\dot{\mathbf{n}}^{(r)} = \overline{\omega}_{\mathbf{n}}^{(r)}\mathbf{n}^{(r)}, \qquad \overline{\omega}_{\mathbf{n}}^{(r)} = \overline{\mathbf{W}}^{(r)} - \left(\overline{\mathbf{D}}^{(r)}\mathbf{n}^{(r)} \otimes \mathbf{n}^{(r)} - \mathbf{n}^{(r)} \otimes \mathbf{n}^{(r)}\overline{\mathbf{D}}^{(r)}\right), \tag{4.67}$$

where $\overline{\mathbf{D}}^{(r)}$ and $\overline{\mathbf{W}}^{(r)}$ denote respectively the grain-average deformation rate and spin tensors associated with $\overline{\mathbf{L}}^{(r)}$. These later quantities are determined by means of the corresponding estimates provided in the following section. Note that, making use of the expression (4.91) for $\overline{\mathbf{W}}^{(r)}$, the evolution equation (4.67) may be rewritten in the invariant form

$$\overset{\triangledown}{\mathbf{n}}{}^{(r)} = \overline{\mathbf{\Omega}}_{\mathbf{n}}^{(r)}\mathbf{n}^{(r)}, \qquad \overline{\mathbf{\Omega}}_{\mathbf{n}}^{(r)} = -\left[\widetilde{\mathbf{R}}\widetilde{\mathbf{P}}^{-1}\left(\overline{\mathbf{D}} - \overline{\mathbf{D}}^{(r)}\right) + \left(\overline{\mathbf{D}}^{(r)}\mathbf{n}^{(r)} \otimes \mathbf{n}^{(r)} - \mathbf{n}^{(r)} \otimes \mathbf{n}^{(r)}\overline{\mathbf{D}}^{(r)}\right)\right], \tag{4.68}$$

where it is recalled that the Jaumann derivative of $\mathbf{n}^{(r)}$ is defined by $\overset{\triangledown}{\mathbf{n}}{}^{(r)} = \dot{\mathbf{n}}^{(r)} - \overline{\mathbf{W}}\mathbf{n}^{(r)}$.

4.3.3 Crystallographic texture evolution

The crystal lattice within grain-family r is assumed to rotate rigidly (on average) with a rate defined by the average lattice spin $\overline{\omega}_{\mathbf{c}}^{(r)}$ in the corresponding phase of the LCC. Thus, the evolution equations for the principal crystallographic axes $\mathbf{a}^{(r)}$, $\mathbf{b}^{(r)}$ and $\mathbf{c}^{(r)}$ are given by

$$\dot{\mathbf{a}}^{(r)} = \overline{\omega}_{\mathbf{c}}^{(r)}\mathbf{a}^{(r)}, \qquad \dot{\mathbf{b}}^{(r)} = \overline{\omega}_{\mathbf{c}}^{(r)}\mathbf{b}^{(r)}, \qquad \dot{\mathbf{c}}^{(r)} = \overline{\omega}_{\mathbf{c}}^{(r)}\mathbf{c}^{(r)}. \tag{4.69}$$

The lattice spin $\overline{\omega}_{\mathbf{c}}^{(r)}$ is defined as the difference between the average continuum spin tensor $\overline{\mathbf{W}}^{(r,c)}$ in the associated crystalline phase of the LCC and the corresponding average plastic spin tensor $\overline{\mathbf{W}}_{pl}^{(r,c)}$ (see Mandel [99])

$$\overline{\omega}_{\mathbf{c}}^{(r)} = \overline{\mathbf{W}}^{(r,c)} - \overline{\mathbf{W}}_{pl}^{(r,c)}, \tag{4.70}$$

The continuum spin $\overline{\mathbf{W}}^{(r,c)}$ is determined in this work by means of the estimate (4.100), while the plastic spin $\overline{\mathbf{W}}_{pl}^{(r,c)}$ is defined by

$$\overline{\mathbf{W}}_{pl}^{(r,c)} = \sum_{k=1}^{K} \dot{\overline{\gamma}}_k^{(r,c)} \frac{1}{2}\left(\mathbf{s}_k^{(r)} \otimes \mathbf{m}_k^{(r)} - \mathbf{m}_k^{(r)} \otimes \mathbf{s}_k^{(r)}\right), \qquad \dot{\overline{\gamma}}_k^{(r,c)} = \frac{\gamma_0 \overline{\tau}_k^{(r,c)}}{\tau_{0k}^{(r,c)}}\left(\frac{|\overline{\tau}_k^{(r,c)}|}{\tau_{0k}^{(r,c)}}\right)^{n-1}, \tag{4.71}$$

where we recall that $\overline{\tau}_k^{(r,c)} = \overline{\boldsymbol{\sigma}}^{(r,c)} \cdot \boldsymbol{\mu}_k^{(r)}$ and the average stress tensors $\overline{\boldsymbol{\sigma}}^{(r,c)}$ in the associated crystalline phases of the LCC are determined in subsection 4.4.2 further below. Taking into account expression (4.100) for $\overline{\mathbf{W}}^{(r,c)}$, the evolution laws (4.69) may be rewritten in the invariant form

$$\overset{\triangledown}{\mathbf{a}}{}^{(r)} = \overline{\mathbf{\Omega}}_{\mathbf{c}}^{(r)}\mathbf{a}^{(r)}, \qquad \overset{\triangledown}{\mathbf{b}}{}^{(r)} = \overline{\mathbf{\Omega}}_{\mathbf{c}}^{(r)}\mathbf{b}^{(r)}, \qquad \overset{\triangledown}{\mathbf{c}}{}^{(r)} = \overline{\mathbf{\Omega}}_{\mathbf{c}}^{(r)}\mathbf{c}^{(r)}, \tag{4.72}$$

where

$$\overline{\mathbf{\Omega}}_{\mathbf{c}}^{(r)} = -\left[\widetilde{\mathbf{R}}\widetilde{\mathbf{P}}^{-1}\left(\overline{\mathbf{D}} - \overline{\mathbf{D}}^{(r)}\right) + \frac{c^{(r,a)}}{2}\left(\mathbf{d}^{(r)} \otimes \mathbf{n}^{(r)} - \mathbf{n}^{(r)} \otimes \mathbf{d}^{(r)}\right) + \overline{\mathbf{W}}_{pl}^{(r,c)}\right]. \tag{4.73}$$

Here, it is recalled that $\mathbf{n}^{(r)}$ denotes the lamination orientation of the grain-family r and $\mathbf{d}^{(r)}$ is the velocity gradient jump vector at the corresponding lamellar interface, given by (4.98).

4.3.4 Macromolecular texture evolution: the back-stress tensor

Since the back-stress tensor $\mathbf{T}_d^{(r)}$ plays the role of an average measure of the kinematic hardening in the amorphous phase of the grain-family r, it is reasonable to assume that its evolution is governed by the corresponding deformation rate $\overline{\mathbf{D}}^{(r,a)}$ and spin $\overline{\mathbf{W}}^{(r,a)}$ tensors in the LCC. In particular, taking into account the hypo-elastic relation (4.20) for the back-stress model, we assume that the constitutive equation for the back-stress tensor $\mathbf{T}_d^{(r)}$, with $r = 1, ..., N$, is given by

$$\dot{\mathbf{T}}_d^{(r)} = \frac{g_{II}^{(r)}\mathbf{T}_d^{(r)} \cdot \overline{\mathbf{D}}^{(r,a)}}{(g_I^{(r)})^2}\mathbf{T}_d^{(r)} + \frac{2}{3}\left[\left(2I^{(r)}g_I^{(r)}\right)\overline{\mathbf{D}}^{(r,a)} - \left(\mathbf{T}_d^{(r)} \cdot \overline{\mathbf{D}}^{(r,a)}\right)\mathbf{I}\right] + \left(\overline{\mathbf{D}}^{(r,a)}\mathbf{T}_d^{(r)} + \mathbf{T}_d^{(r)}\overline{\mathbf{D}}^{(r,a)}\right) + \left(\overline{\mathbf{W}}^{(r,a)}\mathbf{T}_d^{(r)} - \mathbf{T}_d^{(r)}\overline{\mathbf{W}}^{(r,a)}\right), \tag{4.74}$$

where it is recalled that $g_I^{(r)} = dg(I^{(r)})/d\,I$ and $g_{II}^{(r)} = d^2g(I^{(r)})/d\,I^2$, with the stored-energy function $g(I)$ given by (4.16) and the invariant $I^{(r)}$ determined from the solution of (4.19) as a function of the corresponding principal values $t_i^{(r)}$ of $\mathbf{T}_d^{(r)}$. Taking account expression (4.99) for the spin tensors $\overline{\mathbf{W}}^{(r,a)}$, equation (4.74) may be rewritten in the invariant form

$$\overset{\triangledown}{\mathbf{T}}{}_d^{(r)} = \frac{g_{II}^{(r)}\mathbf{T}_d^{(r)} \cdot \overline{\mathbf{D}}^{(r,a)}}{(g_I^{(r)})^2}\mathbf{T}_d^{(r)} + \frac{2}{3}\left[\left(2I^{(r)}g_I^{(r)}\right)\overline{\mathbf{D}}^{(r,a)} - \left(\mathbf{T}_d^{(r)} \cdot \overline{\mathbf{D}}^{(r,a)}\right)\mathbf{I}\right] + \left(\overline{\mathbf{D}}^{(r,a)}\mathbf{T}_d^{(r)} + \mathbf{T}_d^{(r)}\overline{\mathbf{D}}^{(r,a)}\right) + \left(\overline{\mathbf{\Omega}}^{(r,a)}\mathbf{T}_d^{(r)} - \mathbf{T}_d^{(r)}\overline{\mathbf{\Omega}}^{(r,a)}\right), \tag{4.75}$$

where the Jaumann derivative of $\mathbf{T}_d^{(r)}$ is defined by $\overset{\triangledown}{\mathbf{T}}{}_d^{(r)} = \dot{\mathbf{T}}_d^{(r)} + \mathbf{T}_d^{(r)}\overline{\mathbf{W}} - \overline{\mathbf{W}}\mathbf{T}_d^{(r)}$, and

$$\overline{\mathbf{\Omega}}^{(r,a)} = \frac{c^{(r,c)}}{2}\left(\mathbf{d}^{(r)} \otimes \mathbf{n}^{(r)} - \mathbf{n}^{(r)} \otimes \mathbf{d}^{(r)}\right) - \widetilde{\mathbf{R}}\widetilde{\mathbf{P}}^{-1}\left(\overline{\mathbf{D}} - \overline{\mathbf{D}}^{(r)}\right), \tag{4.76}$$

where we recall that the vector $\mathbf{n}^{(r)}$ defines the orientation of the associated lamellar grain, the jump vector $\mathbf{d}^{(r)}$ is given by (4.98), the sub-structural tensors $\widetilde{\mathbf{R}}$ and $\widetilde{\mathbf{P}}$ are respectively obtained from (4.92) and $(4.88)_2$ and the grain-average deformation rate tensor $\overline{\mathbf{D}}^{(r)}$ is given by $(4.86)_2$. .

4.3.5 Evolution of the critical resolved shear stresses

In the context of the strain-hardening relation (4.25), with (4.26), we assume that the evolution of the critical resolved shear stresses (CRSSs) $\tau_{0k}^{(r,c)}$ of the crystalline phase within grain r are determined (on average) by the associated average shear rates $\dot{\overline{\gamma}}_k^{(r,c)}$ in the corresponding phase of the LCC, which are given by $(4.71)_2$. Specifically, the CRSSs $\tau_{0k}^{(r,c)}$ will be computed in this work by means of the following evolution law

$$\tau_{0k}^{(r,c)} = \tau_{0k} + \left(\tau_{1k} + \theta_{1k}(\overline{\Gamma}^{(r,c)})^4\right)\left(1 - \mathrm{Exp}\left[-\overline{\Gamma}^{(r,c)}\frac{\theta_{0k}}{\tau_{1k}}\right]\right), \tag{4.77}$$

where we recall that τ_{0k}, τ_{1k}, θ_{0k} and θ_{1k} are positive material constants, and

$$\overline{\Gamma}^{(r,c)} = \sum_{k=1}^{K} \int_0^t \dot{\overline{\gamma}}_k^{(r,c)} dt. \tag{4.78}$$

4.4 Estimates for the linear comparison composite

This section deals with the determination of the effective properties of the two-scale linear comparison composite (LCC) involved in the calculations of the corresponding estimates for the effective response and texture evolution in the semi-crystalline polymer developed in the previous sections. Following the sequential approach of subsection 2.4.2, the homogenization problem for the two-scale LCC is decomposed into a corresponding problem for each single-scale lamellar grain (Fig. 4.1(b)) and a problem for the single-scale granular composite (Fig. 4.1(a)) with homogenized grains. As detailed further below, the effective behavior of the laminates is determined exactly, while that of the single-scale granular composite is computed by means of the self-consistent estimate.

The effective stress-potential $\tilde{u}_T$ of the two-scale LCC, with local stress-potential defined by (4.33), is given by

$$\tilde{u}_T(\overline{\boldsymbol{\sigma}}) = \frac{1}{2}\overline{\boldsymbol{\sigma}} \cdot \widetilde{\mathbf{M}}\overline{\boldsymbol{\sigma}} + \widetilde{\boldsymbol{\alpha}} \cdot \overline{\boldsymbol{\sigma}} + \tilde{\phi}, \tag{4.79}$$

where $\widetilde{\mathbf{M}}$, $\widetilde{\boldsymbol{\alpha}}$ and $\tilde{\phi}$ are the associated effective modulus tensor, thermal strain tensor and specific heat, respectively. The corresponding macroscopic constitutive relation for the LCC is given by

$$\overline{\mathbf{D}} = \widetilde{\mathbf{M}}\overline{\boldsymbol{\sigma}} + \widetilde{\boldsymbol{\alpha}}. \tag{4.80}$$

The effective quantities $\widetilde{\boldsymbol{\alpha}}$ and $\tilde{\phi}$ in the above relations are obtained by

$$\widetilde{\boldsymbol{\alpha}} = \sum_{r=1}^{N} c^{(r)} \left(\mathbf{B}^{(r)}\right)^T \boldsymbol{\alpha}^{(r)}, \quad \tilde{\phi} = \sum_{r=1}^{N} c^{(r)}\phi^{(r)} + \frac{1}{2}\sum_{r=1}^{N} c^{(r)}\boldsymbol{\alpha}^{(r)} \cdot \mathbf{b}^{(r)}, \tag{4.81}$$

in terms of the corresponding effective properties $\boldsymbol{\alpha}^{(r)}$ and $\phi^{(r)}$ of the grains and the associated stress-concentration tensors $\mathbf{B}^{(r)}$ and $\mathbf{b}^{(r)}$. It is remarked that the quantities $\widetilde{\mathbf{M}}$, $\mathbf{B}^{(r)}$ and $\mathbf{b}^{(r)}$ are determined by means of the corresponding self-consistent estimates provided in subsection 4.4.1.

Similarly, the effective quantities $\boldsymbol{\alpha}^{(r)}$ and $\phi^{(r)}$ are respectively given by

$$\boldsymbol{\alpha}^{(r)} = c^{(r,a)} \left(\mathbf{B}^{(r,a)}\right)^T \boldsymbol{\alpha}^{(r,a)} + c^{(r,c)} \left(\mathbf{B}^{(r,c)}\right)^T \boldsymbol{\alpha}^{(r,c)}, \tag{4.82}$$

and

$$\phi^{(r)} = c^{(r,a)}\phi^{(r,a)} + \frac{1}{2}\left(c^{(r,a)}\boldsymbol{\alpha}^{(r,a)} \cdot \mathbf{b}^{(r,a)} + c^{(r,c)}\boldsymbol{\alpha}^{(r,c)} \cdot \mathbf{b}^{(r,c)}\right), \tag{4.83}$$

where the local properties of the phases $\boldsymbol{\alpha}^{(r,c)}$, $\boldsymbol{\alpha}^{(r,a)}$ and $\phi^{(r,a)}$ are defined by $(4.35)_2$, $(4.36)_3$ and $(4.36)_3$, respectively, and use has been made of the fact that $\phi^{(r,c)} = 0$. The variables $\mathbf{B}^{(r,p)}$

and $\mathbf{b}^{(r,p)}$, with $p = a, c$, in the the above expressions denote the stress-concentration tensors in the associated amorphous and crystalline phase of the LCC. The pertinent discussion on the computation of the quantities $\mathbf{B}^{(r,p)}$ and $\mathbf{b}^{(r,p)}$, as well as the computation of the effective modulus tensors $\mathbf{M}^{(r)}$ of the laminates, is given in subsection 4.4.2.

At this point, it is important to realize that once the quantities $\widetilde{\mathbf{M}}$, $\mathbf{B}^{(r)}$ $\mathbf{b}^{(r)}$, $\mathbf{M}^{(r)}$, $\mathbf{B}^{(r,p)}$ and $\mathbf{b}^{(r,p)}$ are known the computation of the averages (4.53) and the second-moments (4.58) of the stress field over the phases of the LCC is straightforward. Note, in particular, that the second-moment tensors may be readily obtained by using the chain rule in the right-hand-side of (4.58), i.e.,

$$\langle \boldsymbol{\sigma} \otimes \boldsymbol{\sigma} \rangle^{(r,p)} = \frac{2}{c^{(r)} c^{(r,p)}} \left[\frac{\partial \tilde{u}_T}{\partial \mathbf{M}^{(r)}} \frac{\partial \mathbf{M}^{(r)}}{\partial \mathbf{M}^{(r,p)}} + \frac{\partial \tilde{u}_T}{\partial \boldsymbol{\alpha}^{(r)}} \frac{\partial \boldsymbol{\alpha}^{(r)}}{\partial \mathbf{M}^{(r,p)}} + \frac{\partial \tilde{u}_T}{\partial \phi^{(r)}} \frac{\partial \phi^{(r)}}{\partial \mathbf{M}^{(r,p)}} \right], \tag{4.84}$$

where the partial derivatives of the effective grain properties $\mathbf{M}^{(r)}$, $\boldsymbol{\alpha}^{(r)}$ and $\phi^{(r)}$ with respect to $\mathbf{M}^{(r,p)}$ are given in subsection 4.4.2 further below and

$$\frac{\partial \tilde{u}_T}{\partial \mathbf{M}^{(r)}} = \frac{c^{(r)}}{2} \langle \boldsymbol{\sigma} \otimes \boldsymbol{\sigma} \rangle^{(r)}, \qquad \frac{\partial \tilde{u}_T}{\partial \boldsymbol{\alpha}^{(r)}} = c^{(r)} \overline{\boldsymbol{\sigma}}^{(r)} \qquad \frac{\partial \tilde{u}_T}{\partial \phi^{(r)}} = c^{(r)}. \tag{4.85}$$

For a detailed discussion on the computation of the second-moments $\langle \boldsymbol{\sigma} \otimes \boldsymbol{\sigma} \rangle^{(r)}$ in the grains we refer to the work of Liu [85] (Appendix 3). Futhermore, the average deformation rate tensors in the phases of the LCC involved in the computation of the evolution of the internal variables (4.32) (see section 4.3) are determined by

$$\overline{\mathbf{D}}^{(r,p)} = \mathbf{M}^{(r,p)} \overline{\boldsymbol{\sigma}}^{(r,p)} + \boldsymbol{\alpha}^{(r,p)}, \qquad \overline{\mathbf{D}}^{(r)} = \mathbf{M}^{(r)} \overline{\boldsymbol{\sigma}}^{(r)} + \boldsymbol{\alpha}^{(r)}. \tag{4.86}$$

The computation of the corresponding average spin tensors is discussed further below in the context of the self-consistent estimates of subsection 4.4.1 and the laminate solution of subsection 4.4.2.

4.4.1 Self-consistent estimates for the granular composite

Assuming, at this stage, that the effective modulus tensors $\mathbf{M}^{(r)}$ of the lamellar grains (Fig. 4.1(b)) are known, the self-consistent estimate for the effective modulus tensor $\widetilde{\mathbf{M}}$ of the single-scale granular composite of Fig. 4.1(a) is determined as the solution of the following implicit equation

$$\widetilde{\mathbf{M}} = \left\{ \sum_{r=1}^{N} c^{(r)} \left[\mathbf{M}^{(r)} + \widetilde{\mathbf{M}}^{*} \right]^{-1} \right\}^{-1} - \widetilde{\mathbf{M}}^{*}, \tag{4.87}$$

where $\widetilde{\mathbf{M}}^{*} = \widetilde{\mathbf{Q}}^{-1} - \widetilde{\mathbf{M}}$ and the sub-structural tensor $\widetilde{\mathbf{Q}}$ is defined by

$$\widetilde{\mathbf{Q}} = \widetilde{\mathbf{M}}^{-1} - \widetilde{\mathbf{M}}^{-1} \widetilde{\mathbf{P}} \widetilde{\mathbf{M}}^{-1}, \qquad \widetilde{\mathbf{P}} = \frac{1}{4\pi \det \mathbf{Z}} \int_{|\boldsymbol{\xi}|=1} \mathbf{H} \, |\mathbf{Z}^{-1} \boldsymbol{\xi}|^{-3} dS,$$

$$H_{ijkl} = \lim_{\widetilde{\kappa} \to \infty} \left[(\mathbf{N}^{-1})_{ik} \right] \xi_j \xi_l |_{(ij)(kl)}, \qquad N_{ij} = \left[\widetilde{\mathbf{M}}^{-1} + (3\widetilde{\kappa}) \mathbf{J} \right]_{ipjq} \xi_p \xi_q. \tag{4.88}$$

In the context of the (4.88), it is recalled that $\mathbf{Z}$, defined by (4.8), is the shape tensor characterizing the distributional symmetry of the grain-families, $\widetilde{\kappa}$ denotes the bulk modulus of the composite and the parentheses in the subscripts of $(4.9)_3$ indicate symmetrization with respect to these indexes, i.e.,

$$A_{ijkl}|_{(ij)(kl)} = \frac{1}{4}\left(A_{ijkl} + A_{ijlk} + A_{jikl} + A_{jilk}\right). \tag{4.89}$$

The stress concentration tensors $\mathbf{B}^{(r)}$ and $\mathbf{b}^{(r)}$ of the grains are respectively given by (see, e.g., Laws [72])

$$\mathbf{B}^{(r)} = \left[\mathbf{M}^{(r)} + \widetilde{\mathbf{M}}^{*}\right]^{-1}\widetilde{\mathbf{Q}}^{-1}, \qquad \mathbf{b}^{(r)} = \left[\mathbf{M}^{(r)} + \widetilde{\mathbf{M}}^{*}\right]^{-1}\left(\widetilde{\boldsymbol{\alpha}} - \boldsymbol{\alpha}^{(r)}\right), \tag{4.90}$$

where we recall that $\boldsymbol{\alpha}^{(r)}$ denote the effective thermal strain tensors of the grains, which are computed by means of the relations (4.82).

Finally, it can be shown (see, e.g., Liu [85]) that the self-consistent estimates for the grain-average spin tensors $\overline{\mathbf{W}}^{(r)}$ are given by

$$\overline{\mathbf{W}}^{(r)} = \overline{\mathbf{W}} - \widetilde{\mathbf{R}}\widetilde{\mathbf{P}}^{-1}\left(\overline{\mathbf{D}} - \overline{\mathbf{D}}^{(r)}\right), \tag{4.91}$$

where $\overline{\mathbf{W}}$ and $\overline{\mathbf{D}}$ are respectively the applied spin and deformation rate tensors, $\overline{\mathbf{D}}^{(r)}$ are the grain-average deformation rate tensors, given by $(4.86)_2$, and $\widetilde{\mathbf{R}}$ is a sub-structural tensor, defined by

$$\widetilde{\mathbf{R}} = \frac{1}{4\pi \det\mathbf{Z}}\int_{|\boldsymbol{\xi}|=1}\boldsymbol{\Gamma}\,|\mathbf{Z}^{-1}\boldsymbol{\xi}|^{-3}dS, \qquad \Gamma_{ijkl} = \lim_{\widetilde{\kappa}\to\infty}\left[(\mathbf{N}^{-1})_{ik}\right]\xi_j\xi_l|_{(ij)[kl]}, \tag{4.92}$$

where $\mathbf{N}$ is given by $(4.86)_4$ and the notation

$$A_{ijkl}|_{(ij)[kl]} = \frac{1}{4}\left(A_{ijkl} + A_{ijlk} - A_{jikl} - A_{jilk}\right), \tag{4.93}$$

has been introduced in $(4.92)_2$.

4.4.2 Exact estimates for the lamellar grains

Laminates constitute the only class of composite materials whose effective behavior may be computed exactly for arbitrary loading conditions and any type of constituent phases. This is due to the fact that when a laminate is subjected to an affine boundary condition (e.g., the uniform traction type of loading (2.40)) the fields developed in it are constant in each phase and may be completely determined from the associated average conditions along with the relevant traction and velocity (or displacement) continuity requirements at the lamellar interfaces.

Expression $(4.53)_1$ imply that the average stress tensors $\overline{\boldsymbol{\sigma}}^{(r,p)}$, with $p = a, c$, over the phases of the LCC correspond to the stress fields developed in the constituents of a lamellar grain of the type

r when subjected to an average stress $\overline{\boldsymbol{\sigma}}^{(r)}$. Hence, the stress-phase-averages $\overline{\boldsymbol{\sigma}}^{(r,p)}$ are determined by means of the stress-grain-average condition

$$c^{(r,a)}\overline{\boldsymbol{\sigma}}^{(r,a)} + c^{(r,c)}\overline{\boldsymbol{\sigma}}^{(r,c)} = \overline{\boldsymbol{\sigma}}^{(r)}, \tag{4.94}$$

the traction continuity requirement

$$\overline{\boldsymbol{\sigma}}^{(r,a)}\mathbf{n}^{(r)} = \overline{\boldsymbol{\sigma}}^{(r,c)}\mathbf{n}^{(r)} = \overline{\boldsymbol{\sigma}}^{(r)}\mathbf{n}^{(r)}, \tag{4.95}$$

and the compatibility condition

$$\mathbf{n}_{\alpha}^{(r)\perp} \cdot \overline{\mathbf{D}}^{(r,a)}\mathbf{n}_{\beta}^{(r)\perp} = \mathbf{n}_{\alpha}^{(r)\perp} \cdot \overline{\mathbf{D}}^{(r,c)}\mathbf{n}_{\beta}^{(r)\perp}, \qquad \alpha,\beta = 1,2, \tag{4.96}$$

where $\overline{\mathbf{D}}^{(r,a)}$ and $\overline{\mathbf{D}}^{(r,c)}$ are given by $(4.86)_1$, and $\mathbf{n}_1^{(r)\perp}$, $\mathbf{n}_2^{(r)\perp}$ are orthogonal unit vectors lying on the lamellar interface, i.e., they are also orthogonal to the associated lamination orientation $\mathbf{n}^{(r)}$. It should be remarked that although equations (4.94)-(4.96) determine both the deviatoric and the hydrostatic parts of $\overline{\boldsymbol{\sigma}}^{(r,a)}$ and $\overline{\boldsymbol{\sigma}}^{(r,c)}$ in terms of $\overline{\boldsymbol{\sigma}}^{(r)}$, the hydrostatic parts of these tensors do *not* enter the computation of the estimates for the effective behavior of the semi-crystalline polymer developed in the previous sections. The system of equations (4.94)-(4.96) may be treated as follows. First, we chose (any) three independent components of the stress-phase-average deviatoric tensors $\overline{\boldsymbol{\sigma}}_d^{(r,a)}$ and $\overline{\boldsymbol{\sigma}}_d^{(r,c)}$ as the principal unknowns. Then, making use of the linear equations (4.94) and (4.95), we express the remaining seven unknown components of $\overline{\boldsymbol{\sigma}}_d^{(r,a)}$ and $\overline{\boldsymbol{\sigma}}_d^{(r,c)}$, as well as the hydrostatic parts of $\overline{\boldsymbol{\sigma}}^{(r,a)}$ and $\overline{\boldsymbol{\sigma}}^{(r,c)}$, in terms of the principal unknowns. Finally, substituting the later expressions into (4.96) we obtain a system of three nonlinear equations for the three principal unknowns, which must be solved numerically.

From the velocity continuity requirement at the lamellar interface it follows that the jump of the velocity gradient field in the laminate is given by

$$\overline{\mathbf{L}}^{(r,a)} - \overline{\mathbf{L}}^{(r,c)} = \mathbf{d}^{(r)} \otimes \mathbf{n}^{(r)}, \tag{4.97}$$

where $\mathbf{d}^{(r)}$ denotes the associated jump vector. Taking the dot product of the symmetric part of (4.97) with $\mathbf{n}^{(r)}$, we obtain the following expression for $\mathbf{d}^{(r)}$

$$\mathbf{d}^{(r)} = 2(\overline{\mathbf{D}}^{(r,a)} - \overline{\mathbf{D}}^{(r,c)})\mathbf{n}^{(r)}, \tag{4.98}$$

where it is recalled that $\overline{\mathbf{D}}^{(r,a)}$ and $\overline{\mathbf{D}}^{(r,c)}$ are given by $(4.86)_1$. The spin tensors $\mathbf{W}^{(r,a)}$ and $\mathbf{W}^{(r,c)}$ in the corresponding amorphous and crystalline phase of the LCC are then given by the expressions

$$\overline{\mathbf{W}}^{(r,a)} = \overline{\mathbf{W}}^{(r)} + \frac{c^{(r,c)}}{2}(\mathbf{d}^{(r)} \otimes \mathbf{n}^{(r)} - \mathbf{n}^{(r)} \otimes \mathbf{d}^{(r)}), \tag{4.99}$$

and

$$\overline{\mathbf{W}}^{(r,c)} = \overline{\mathbf{W}}^{(r)} - \frac{c^{(r,a)}}{2}(\mathbf{d}^{(r)} \otimes \mathbf{n}^{(r)} - \mathbf{n}^{(r)} \otimes \mathbf{d}^{(r)}), \tag{4.100}$$

respectively, which are trivially obtained by solving the system of linear equations consisting of the anti-symmetric part of (4.97) and the relevant spin-grain-average condition $c^{(r,a)}\overline{\mathbf{W}}^{(r,a)} + c^{(r,c)}\overline{\mathbf{W}}^{(r,c)} = \overline{\mathbf{W}}^{(r)}$. We recall that $\overline{\mathbf{W}}^{(r)}$ denotes the associated grain-average spin tensor.

Making use of the solution of the laminate problem (4.94)-(4.96) for the average stress tensors $\overline{\boldsymbol{\sigma}}^{(r,a)}$ and $\overline{\boldsymbol{\sigma}}^{(r,c)}$ in the associated phases of the LCC, it can be easily shown (see, e.g., [120]) that the corresponding effective modulus tensor $\mathbf{M}^{(r)}$ of a lamellar grain of the type r is given by

$$\mathbf{M}^{(r)} = \mathbf{M}^{(r,a)} + c^{(r,c)}\left[c^{(r,a)}\mathbf{Q}^{(r)} + \left(\mathbf{M}^{(r,c)} - \mathbf{M}^{(r,a)}\right)^{-1}\right]^{-1}, \tag{4.101}$$

where $\mathbf{M}^{(r,a)}$ and $\mathbf{M}^{(r,c)}$ are the associated compliance tensors, defined respectively by $(4.36)_1$ and $(4.35)_1$, and the micro-structural tensor $\mathbf{Q}^{(r)}$ is given by

$$\mathbf{Q}^{(r)} = \mathbf{L}^{(r,a)} - \mathbf{L}^{(r,a)}\mathbf{H}^{(r)}\mathbf{L}^{(r,a)}, \qquad \mathbf{L}^{(r,a)} = (\mathbf{M}^{(r,a)})^{-1}. \tag{4.102}$$

The tensor $\mathbf{H}^{(r)}$ in the above expression is defined by

$$H^{(r)}_{ijkl} = \lim_{\kappa^{(r)}\to\infty}\left[\left(\mathbf{N}^{(r)}\right)^{-1}_{ik}\right] n^{(r)}_j n^{(r)}_l|_{(ij)(kl)}, \qquad N^{(r)}_{ij} = \left[\mathbf{L}^{(r,a)} + (3\kappa^{(r)})\mathbf{J}\right]_{ipjq} n^{(r)}_p n^{(r)}_q. \tag{4.103}$$

where $\kappa^{(r)}$ denotes the bulk modulus of the amorphous phase and the parentheses in the subscripts of $(4.103)_1$ indicate symmetrization with respect to the associated indexes (see (4.89)). Making use of the Caley-Hamilton theorem to compute the inverse of the second-order tensor $\mathbf{N}^{(r)}$, it can be shown that

$$\lim_{\kappa^{(r)}\to\infty}\left(\mathbf{N}^{(r)}\right)^{-1} = \frac{1}{I_3}\left[\mathbf{N}^{(r)}_0\mathbf{n}^{(r)}\otimes\mathbf{n}^{(r)} + \mathbf{n}^{(r)}\otimes\mathbf{n}^{(r)}\mathbf{N}^{(r)}_0 - \mathbf{N}^{(r)}_0 - I_1\mathbf{n}^{(r)}\otimes\mathbf{n}^{(r)} + I_2\mathbf{I}\right], \tag{4.104}$$

where

$$\left(\mathbf{N}^{(r)}_0\right)_{ij} = L^{(r,a)}_{ipjq} n^{(r)}_p n^{(r)}_q, \tag{4.105}$$

and

$$\begin{aligned} &I_1 = \mathrm{tr}\mathbf{N}^{(r)}_0, \qquad I_2 = \mathrm{tr}\mathbf{N}^{(r)}_0 - \mathbf{n}^{(r)}\cdot\mathbf{N}^{(r)}_0\mathbf{n}^{(r)}, \\ &I_3 = e_{ijk}\left[\left(\mathbf{N}^{(r)}_0\right)_{i1}\left(\mathbf{N}^{(r)}_0\right)_{j2} n^{(r)}_3 - \left(\mathbf{N}^{(r)}_0\right)_{i1}\left(\mathbf{N}^{(r)}_0\right)_{j3} n^{(r)}_2 - \left(\mathbf{N}^{(r)}_0\right)_{i3}\left(\mathbf{N}^{(r)}_0\right)_{j2} n^{(r)}_1\right] n^{(r)}_k, \end{aligned} \tag{4.106}$$

with e_{ijk} denoting the permutation tensor.

The stress concentration tensors $\mathbf{B}^{(r,p)}$ and $\mathbf{b}^{(r,p)}$, with $p = a, c$, are given by

$$\begin{aligned} &\mathbf{B}^{(r,a)} = \frac{1}{c^{(r,a)}}\left(\mathbf{K} - c^{(r,c)}\mathbf{B}^{(r,c)}\right), \qquad \mathbf{B}^{(r,c)} = \frac{1}{c^{(r,c)}}\left(\mathbf{M}^{(r,c)} - \mathbf{M}^{(r,a)}\right)^{-1}\left(\mathbf{M}^{(r)} - \mathbf{M}^{(r,a)}\right), \\ &\mathbf{b}^{(r,a)} = -\frac{c^{(r,c)}}{c^{(r,a)}}\mathbf{b}^{(r,c)}, \qquad \mathbf{b}^{(r,c)} = \left(\mathbf{B}^{(r,c)} - \mathbf{K}\right)\left(\mathbf{M}^{(r,c)} - \mathbf{M}^{(r,a)}\right)^{-1}(\boldsymbol{\alpha}^{(r,c)} - \boldsymbol{\alpha}^{(r,a)}), \end{aligned} \tag{4.107}$$

where $\mathbf{K}$ is the identity tensor in the deviatoric space of fully symmetric forth-order tensors.

Finally, taking into account expressions (4.101), (4.82), (4.83) and (4.107), determining the effective grain properties $\mathbf{M}^{(r)}$, $\boldsymbol{\alpha}^{(r)}$ and $\phi^{(r)}$ in the LCC, it is straightforward—although tedious—to show that

$$\begin{aligned}
\frac{\partial M^{(r)}_{stuv}}{\partial M^{(r,p)}_{ijkl}} &= c^{(r,p)} B^{(r,p)}_{ijst} B^{(r,p)}_{kluv}, \\
\frac{\partial \alpha^{(r)}_{st}}{\partial M^{(r,p)}_{ijkl}} &= \frac{c^{(r,p)}}{2} \left(B^{(r,p)}_{ijst} b^{(r,p)}_{kl} + b^{(r,p)}_{ij} B^{(r,p)}_{klst} \right), \\
\frac{\partial \phi^{(r)}}{\partial M^{(r,p)}_{ijkl}} &= \frac{c^{(r,p)}}{2} b^{(r,p)}_{ij} b^{(r,p)}_{kl},
\end{aligned} \tag{4.108}$$

where $p = a, c$. Making use of these results in (4.84), it can be easily shown that in the special case of a composite made out of only one lamellar grain ($N = 1$), the second-moments of the stress field in the phases reduce to $\langle \boldsymbol{\sigma} \otimes \boldsymbol{\sigma} \rangle^{(1,p)} = \overline{\boldsymbol{\sigma}}^{(1,p)} \otimes \overline{\boldsymbol{\sigma}}^{(1,p)}$, which is consistent with the fact that the stress field within each phase of a laminate is uniform.

4.5 Results and discussion

The purpose of this section is to investigate the predictive capabilities of the viscoplastic "linear comparison composite" (LCC) model for the macroscopic response and texture evolution in semi-crystalline polymers. To this end, the high-density polyethylene (HDPE) material investigated in a series of experimental works by Bartczak, Argon and Cohen [8, 10, 9] is chosen as a case study. In order to avoid the numerical evaluation of the derivatives of $\widetilde{u}$ with respect to $\overline{\boldsymbol{\sigma}}$ required in the context of the constitutive relation (4.29)—which would increase substantially the amount of the numerical calculations—the macroscopic response of the HDPE will be computed in this section by means of the constitutive relation (4.80) for the LCC. Based on experimental evidence for this material, subsection 4.5.1 provides the pertinent discussion on the choice of the parameters defining the sub-structure and the material properties of the constituents in the context of the LCC model. The predictions of the LCC model—both for the macroscopic response and texture evolution in this material—for uniaxial compression and simple shear loading conditions are discussed in detail in subsections 4.5.2 and 4.5.3, respectively. More specifically, the LCC estimates are confronted with the relevant experimental results of Bartczak et al. [10, 9] as well as with the corresponding predictions of the models of Lee et al. [80] and Nikolov et al. [110]. A corresponding discussion for the case of uniaxial tension is provided in subsection 4.5.4. The predictions of the models are in this case compared with the experimental measurements of G'Sell and Jonas [46] and Hiss et al. [54]. It should be emphasized, however, that the later experiments have been conducted for HDPE systems

with different properties (e.g., molecular weight) than the HDPE material used in the works of Bartczak et al. [8, 10, 9], for which the material parameters for the models were determined. For this reason, the comparison between the theoretical predictions and the experimental results for uniaxial tension are mainly qualitative.

4.5.1 On the choice of the model parameters

As reported by Bartczak et al. [10, 9], the undeformed samples of HDPE used in their experiments had no traces of crystallographic or lamellar orientation anisotropy. Hence, we consider a composite system which in the undeformed configuration consists of $N = 500$ randomly oriented grain-families with equal volume fractions, i.e., $c^{(r)} = 1/N$ for each $r = 1, ..., N$, and a spatial distribution characterized by isotropic symmetry, i.e., the associated shape tensor $\mathbf{Z}$ in (4.8) at $t = 0$ is taken to be $\mathbf{Z} = \mathbf{I}$. The initial crystallographic and lamellar texture of this system is represented in Fig. 4.3. Based on experimental [12] and theoretical [38] works on polyethylene, identifying the lamellar interfaces within the grains with the {201} planes of the associated crystal lattice, the initial angles Φ and Θ (see Fig. 4.1(b)) between the lamination orientation $\mathbf{n}^{(r)}$ and the corresponding crystallographic axes $\mathbf{b}^{(r)}$ and $\mathbf{c}^{(r)}$, respectively, in each grain r are set equal to $\Phi = 90^o$ and $\Theta = 35^o$. Following Lee et al. [80] and Nikolov et al. [110], the volume fraction of the crystalline phase (also referred to as crystallinity) in each grain r is chosen to be $c^{(r,c)} = 0.7$. The lattice parameters of the orthorhombic crystal of polyethylene are $|\mathbf{a}^{(r)}| = 7.4$ Å, $|\mathbf{b}^{(r)}| = 4.93$ Å and $|\mathbf{c}^{(r)}| = 2.54$ Å. The rate exponent n and the reference strain rate γ_0 for both the amorphous (4.14) and the crystalline (4.24) phase are taken to be $n = 9$ and $\gamma_0 = 10^{-3}s^{-1}$ (Lee et al. [80] and Nikolov et al. [110]), while the reference stress τ_0 of the amorphous phase is chosen to be $\tau_0 = 5.5$ MPa.

In the remaining part of this subsection we discuss the physical background underlying our prescriptions for the rest of the material parameters of the phases in the context of the LCC model (4.80). Before providing the relevant details, it is convenient at this point to spell out our final choices. The material parameters μ_i and α_i $(i = 1, ..., M)$—defining the kinematic hardening model (4.15) for the back-stress tensor $\mathbf{T}_d$ in the amorphous phase—are given in Table 4.2 by the set of values labeled (c), where we have restricted our consideration to the first three terms $(M = 3)$ in expression (4.16). Note that the ground-state shear modulus associated with this model is $\mu = \mu_1 + \mu_2 + \mu_3 = 14.696$ MPa. The values of the material parameters τ_{0k}, τ_{1k}, θ_{0k} and θ_{1k}—defining the strain-hardening relation (4.77), with (4.126), for the critical resolved shear stresses (CRSSs) $\tau_{0k}^{(r,c)}$ in the slip systems of the crystalline phase—are given in Table 4.1.

Ideally, the material properties of the phases in a homogenization-based constitutive model for HDPE should be determined experimentally. In an important contribution along these lines,

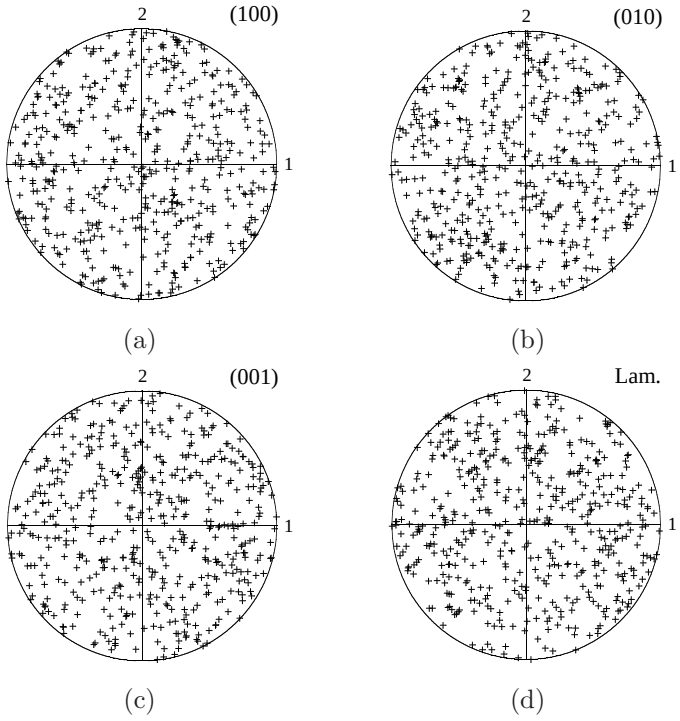

Figure 4.3: The initial crystallographic and lamellar texture in the 500-grain composite system used in the calculations of the LCC estimates of this section. Parts (a), (b) and (c) show respectively the equal area projections of the (100), (010) and (001) plane poles, i.e., the crystallographic axes $\mathbf{a}^{(r)}$, $\mathbf{b}^{(r)}$ and $\mathbf{c}^{(r)}$, respectively. Part (d) shows the corresponding representation of the lamination orientations $\mathbf{n}^{(r)}$.

Bartczak, Argon and Cohen [8] performed a series of experimental tests in quasi-single-crystal samples of HDPE with the objective of determining the associated CRSSs. These authors concluded that (to a good degree of approximation) the CRSSs $\tau^{cr}_{0(k)}$ obey the Coulomb yield criterion

$$\tau^{cr}_{0(k)} = \tau_{0(k)} - l_{(k)}\sigma_{n(k)}, \tag{4.109}$$

where $\tau_{0(k)}$ and $l_{(k)}$ are (positive) material constants and $\sigma_{n(k)}$ is the normal component of the traction vector on the associated slip plane. For our purposes here it suffices to recall that the values for the parameters $\tau_{0(k)}$ determined by Bartczak et al. [8] are: 7.2 MPa for (100)[001] chain slip, 15.6 MPa for (010)[001] chain slip, $>$ 13 MPa for {110}[001] chain slip and 12.2 MPa for (100)[010] transverse slip. As pointed out by these authors, the activation of competing deformation mechanisms did not allow the determination of the CRSSs in the remaining slip systems. An important implication of the yield criterion (4.109) is that the CRSSs $\tau^{cr}_{0(k)}$ increase with increasing compressive normal stresses $\sigma_{n(k)}$ and they decrease with increasing tensile normal stresses $\sigma_{n(k)}$. On the other hand, the behavior of the amorphous material—which is confined between two crystalline lamellae in HDPE—is fairly complex and the relevant experimental information from

	Slip system	τ_{0k} (MPa)	τ_{1k} (MPa)	θ_{0k} (MPa)	θ_{1k} (MPa)
Chain slip	(100)[001]	7.2*	–	0	–
	(010)[001]	15.6*	–	0	–
	{110}[001]	14	–	0	–
Transverse slip	(100)[010]	12.2*	1	0.01	3.5
	(010)[100]	20	1	0.01	5
	$\{110\}\langle 1\bar{1}0\rangle$	18	1	0.01	4.5

Table 4.1: The values of the material parameters in the strain-hardening relation (4.77) for the CRSSs $\tau_{0k}^{(r,c)}$ in the slip systems of the crystalline phase used in the calculations of the LCC estimates of this section. The superscript "$*$" indicates quantities determined experimentally by Bartczak et al. [8].

the literature is only qualitative in nature. The amorphous phase is an assembly of disordered macromolecules, which at room temperature is in a rubbery elastic state (see, e.g., Lin and Argon [84]).

In the absence of further quantitative information on the constitutive behavior of the phases, adopting the approach followed by Lee et al. [80] and Nikolov et al. [110], our strategy is to determine the unknown material parameters such that the associated macroscopic stress-strain curve predicted by the LCC model for uniaxial compression fits well the corresponding results of Bartczak et al. [10]. However, as discussed further below, there are two different sets of material parameters for which the LCC model predictions for uniaxial compression fit equally well the corresponding stress-strain results of Bartczak et al. [10]. The final choice between these two sets of values will be made by a further comparison of the associated LCC estimates for the macroscopic stress-strain response of HDPE under simple shear and uniaxial tension loadings with the corresponding experimental results of Bartczak et al. [9] and G'Sell and Jonas [46], respectively. The experimental measurements of Bartczak et al. [10] for the uniaxial compression test are shown in Fig. 4.5 with open squares, while the corresponding results of Bartczak et al. [9] for simple shear and G'Sell and Jonas [46] for uniaxial tension are presented in Fig. 4.6 with open squares and open circles, respectively. The continuous and dotted curves that are also shown in these figures are predictions of the LCC model (4.80) for different values of the material parameters of the phases, which have been selected as a representative sample of a larger number of calculations performed in order to obtain the best fit. Before we discuss these LCC estimates in more detail, it is important at this point to make a few comments on the experimental results for the uniaxial compression test.

Probably the most remarkable feature of the experimentally measured response of HDPE under uniaxial compression (open squares in Fig. 4.5) is the three different types of strain hardening

	μ_1 (MPa)	μ_2 (MPa)	μ_3 (MPa)	α_1	α_2	α_3
Set (a)	0.03167	7.33	7.33	5.842	−0.30145	−0.30145
Set (b)	0.00645	5.94296	8.71854	4.21778	−0.78498	0.07176
Set (c)	5.1176	0.00669	9.57171	0.36859	2.13754	−0.64543

Table 4.2: The values of material parameters defining the hyperelastic model (4.16) (with $M = 3$) for the back-stress tensor (4.15), used in the context of the various LCC estimates of Fig. 4.5. The LCC estimates discussed in subsections 4.5.2, 4.5.3 and 4.5.4 have been computed by using the set of values (c).

behavior exhibited in three corresponding ranges of the deformation process. These ranges are approximately the following: (*i*) the "small" deformation range $\overline{\varepsilon}_e \leq 0.35$, which is characterized by a monotonically decreasing hardening rate, (*ii*) the "moderate" deformation range $0.35 \leq \overline{\varepsilon}_e \leq 0.82$, which is a region of intense plastic deformation with small or no hardening and (*iii*) the "large" deformation range $\overline{\varepsilon}_e \geq 0.82$, which exhibits a monotonically increasing hardening rate. According to Bartczak et al. [10], the macroscopic hardening observed in the small deformation range is due to the non-linear elastic hardening of the amorphous phase, while the intense plasticity in the moderate deformation range should be primarily attributed to the plastic deformation of the crystals which, in this strain range, assume (on average) a particularly favorable orientation for crystallographic slip. As reported by Bartczak et al. [10], the elastic deformation of the amorphous phase saturates in the moderate deformation range and locks-up at a value $\overline{\varepsilon}_e \approx 0.5$. On the other hand, Bartczak et al. [10] did *not* provide a corresponding interpretation for the hardening behavior in the large deformation range. However, understanding the underlying mechanisms for the hardening of the material in this range is of crucial importance for the appropriate choice of the material parameters of the phases in the context of the LCC model. In this connection, we next provide a possible interpretation for the hardening response in the large strain range.

Note first that, as opposed to the other two deformation regimes, the strain range $\overline{\varepsilon}_e \geq 0.82$ is characterized by the development of a *strong* lamellar and crystallographic texture (see Bartczak et al. [10] and Figs. 4.9-4.12 in the following subsection). Specifically, in this range the lamellar grains are oriented with their normals $\mathbf{n}^{(r)}$ approximately aligned with the loading axis (Fig. 4.9). In this configuration, the laminates are subjected to an average loading—approximately, axisymmetric shear or pure shear compression—corresponding to a hard mode (Taylor-type) of deformation. Furthermore, it is well known that under this mode of deformation the stiffening of either of the constituent phases of a laminate leads to a corresponding stiffening of its macroscopic response. Therefore, a possible explanation for the macroscopic hardening of HDPE in the large deformation regime is the existence of some local hardening mechanism for either the amorphous or the crystalline phase (or both). In this regard, the possibility of the hardening of the amorphous

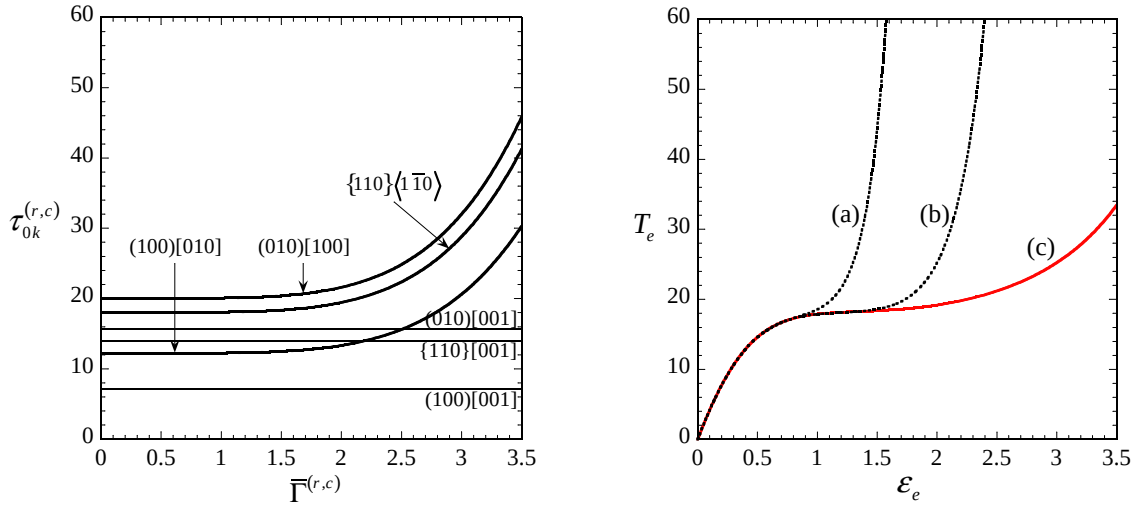

Figure 4.4: Left: Plots of the strain hardening relation (4.77) for the CRSSs $\tau_{0k}^{(r,c)}$ as functions of the deformation measure $\overline{\Gamma}^{(r,c)}$ for the values of the material parameters of Table 4.1. Right: Response of the homogeneous hyperelastic material (4.16) under axisymmetric shear compression—i.e., for $\mathbf{F} = \text{diag}\{\lambda^{-1/2}, \lambda^{-1/2}, \lambda\}$ with $\lambda < 1$—for the three different sets of material parameters (a), (b) and (c) of Table 4.2; the equivalent stress $T_e \equiv \sqrt{3\mathbf{T}_d \cdot \mathbf{T}_d/2}$ is plotted as a function of the equivalent strain $\overline{\varepsilon}_e \equiv \sqrt{2\varepsilon \cdot \varepsilon/3}$, with $\mathbf{T}_d$ and ε defined respectively by (4.15) and (4.110).

phase can be excluded, since this phase is already locked in the large deformation range (Bartczak et al. [10]). Therefore, there should be a mechanism causing an increasing hardening of the crystalline phase. A possible such mechanism is the Coulomb yield criterion (4.109), which, as already mentioned, has the effect of increasing the CRSS $\tau_{0(k)}^{(cr)}$ of a slip system with increasing the compressive stress component $\sigma_{n(k)}$ normal to the corresponding slip plane. This argument is supported by the crystallographic texture evolution in the strain range $\overline{\varepsilon}_e \geq 0.82$. For example, from Fig. 4.11 we observe that the (100) plane poles rotate monotonically towards the loading direction, and therefore the corresponding compressive normal stresses on these planes are expected to increase with increasing strain $\overline{\varepsilon}_e$.

At this point, it is important to realize that the use of the Coulomb criterion (4.109) requires consideration of a non-associative[1] flow model for the crystalline phase. Since the LCC model is by construction restricted to associative constituents, the Coulomb yield criterion cannot be incorporated explicitly in our model. In passing, it is interesting to note that constitutive models for semi-crystalline polymers proposed thus far in the literature (e.g., Dahoun et al. [25], Lee et al. [80], van Dommelen et al. [145], Nikolov et al. [110]) have neglected the Coulomb effect,

[1]It is recalled that a model is called associative if the flow direction, i.e., the deformation rate tensor, is parallel to the gradient of the yield function in the stress space, and it is called non-associative otherwise.

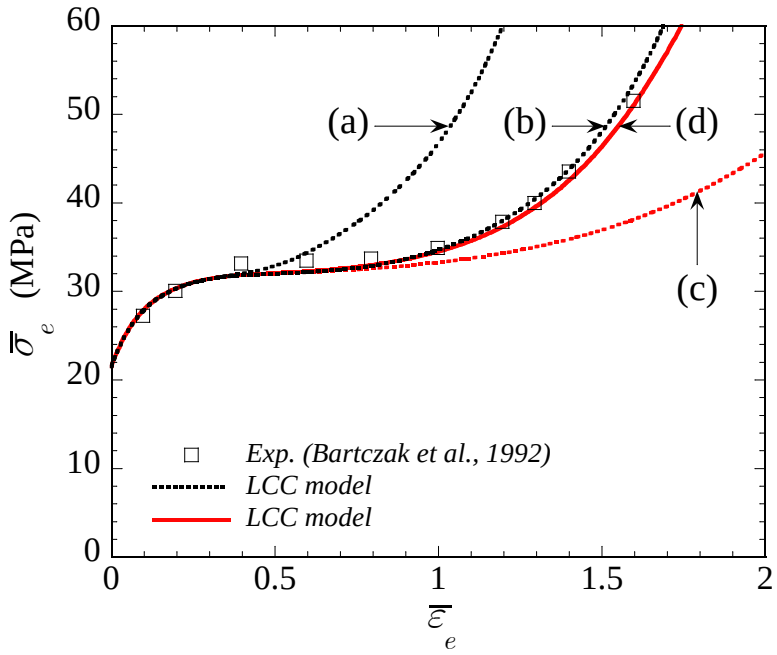

Figure 4.5: Fitting the LCC model to the experimental data of Bartczak et al. [10] for uniaxial compression of HDPE. The dotted curves correspond to constant CRSSs $\tau_{0k}^{(r,c)} = \tau_{0k}$ and the continuous curve corresponds to $\tau_{0k}^{(r,c)}$ given by (4.77), using the relevant material parameters of Table 4.1. The estimates (a), (b) and (c) make use of the respective sets of values (a), (b) and (c) of Table 4.2 for the elastic properties of the amorphous phase and the estimate (d) makes use of the set of values (c) of Table 4.2.

assuming that the CRSSs are constant. In an attempt to approximate the Coulomb effect at large deformations, in this work we consider the strain hardening law (4.77), with (4.126), for the CRSSs $\tau_{0k}^{(r,c)}$ of the crystalline phase. The values of the parameters τ_{0k}, τ_{1k}, θ_{0k} and θ_{1k} in (4.77) for both the chain and transverse slip systems are given in Table 4.1. For a better understanding of these prescriptions, the corresponding CRSSs $\tau_{0k}^{(r,c)}$ are plotted as functions of the associated deformation measure $\overline{\Gamma}^{(r,c)}$ in Fig. 4.4(Left). In passing, it is remarked that Fig. 4.4(Right) shows the stress-strain response of the *homogeneous* hyperelastic material (4.15) under axisymmetric shear compression. The curves labeled (a), (b) and (c) in Fig. 4.4(Right) correspond respectively to the sets of values (a), (b) and (c) in Table 4.2 for the parameters μ_i and α_i (i=1,2,3).

Next, we turn our attention to the LCC estimates for uniaxial compression of HDPE shown in Fig. 4.5. The dotted curves labeled (a), (b) and (c) correspond respectively to the sets of values (a), (b) and (c), given in Table 4.2, for the back-stress tensor (4.15) and have been computed for constant CRSSs $\tau_{0k}^{(r,c)} = \tau_{0k}$, with τ_{0k} given in Table 4.1. The continuous curve (d) has been computed by using the set of parameters (c), given in Table 4.2, for the back-stress tensor (4.15) along with the CRSSs $\tau_{0k}^{(r,c)}$ defined by (4.77), with the associated material parameters given in

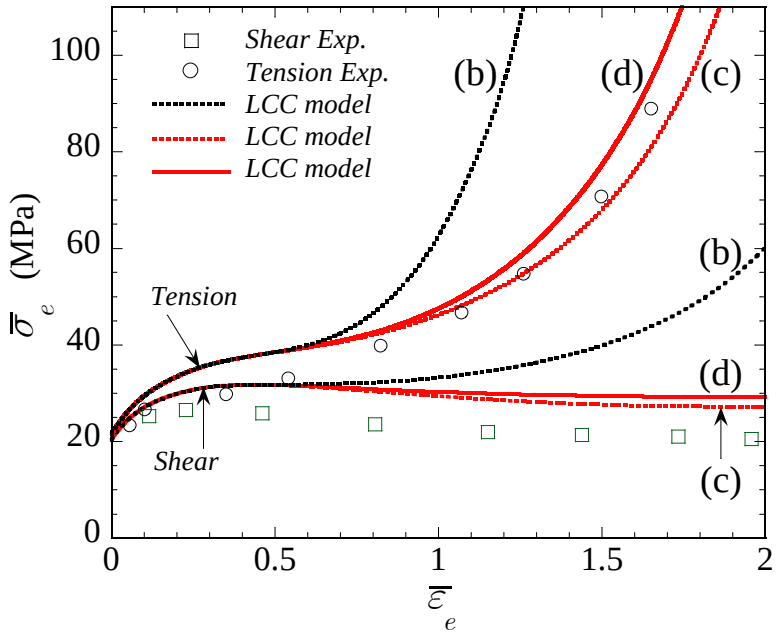

Figure 4.6: LCC estimates for the macroscopic stress-strain response of HDPE under simple shear and uniaxial tension loadings, corresponding to different values of the material parameters of the phases. The dotted curves correspond to constant CRSSs $\tau_{0k}^{(r,c)} = \tau_{0k}$ and the continuous curve corresponds to $\tau_{0k}^{(r,c)}$ given by (4.77), using the relevant material parameters of Table 4.1. The estimates (b) and (c) make use of the respective sets of values (b) and (c) of Table 4.2 for the elastic properties of the amorphous phase and the estimate (d) makes use of the set of values (c) of Table 4.2.

Table 4.1. From these results, it is observed that only the curves (b) and (d) capture accurately the hardening features of the experimentally measured stress-strain data in all three ranges of deformation. Note that the curves (b) and (d) are practically identical in the small and moderate deformation regimes. This is of course due to the fact that the corresponding material parameters used in these estimates are also practically identical for small and moderate strains (see Fig. 4.4). The hardening of the LCC estimate (b) in the large deformation regime is primarily due to the hardening of the amorphous phase, while the corresponding hardening of the LCC estimate (d) is mainly due to the hardening of the crystalline phase. This becomes immediately obvious by comparing the LCC estimates (b) and (d) with the LCC estimate (c), in the context of which the CRSSs $\tau_{0k}^{(r,c)}$ are constant and, in addition, the hardening of the amorphous phase at large strains is insignificant (compare curves (c) and (b) in Fig. 4.4(Right)).

The LCC estimate (a) of Fig. 4.5 corresponds to an attempt to model the locking of the amorphous phase (see curve (a) in Fig. 4.4(Right)) while the macroscopic deformation process is still in the moderate strain regime, as reported by Bartczak et al. [10]. This estimate predicts a

macroscopic stiffening in the moderate strain range which is inconsistent with the experimental results. For more insight on this unrealistically stiff prediction, consider the limit as the amorphous material within the grains locks-up. In the lock-up limit, the average deformation rate in the amorphous phase tends to $\overline{\mathbf{D}}^{(r,a)} = \mathbf{0}$, while the corresponding average stress becomes unbounded (see curve (a) in Fig. 4.4(Right)). In addition, the requirement $\overline{\mathbf{D}}^{(r,a)} = \mathbf{0}$ together with the compatibility condition (4.96), the incompressibility condition $\mathrm{tr}\overline{\mathbf{D}}^{(\mathrm{r,c})} = 0$ and the inextensibility condition $\mathbf{c}^{(r)} \cdot \overline{\mathbf{D}}^{(r,c)}\mathbf{c}^{(r)} = 0$, impose severe constrains on the corresponding deformation rate tensor $\overline{\mathbf{D}}^{(r,c)}$, which may end up having only one non-zero component. These results are, in turn, expected to lead to a significant macroscopic stiffening for the composite. At this point, it should be emphasized that the above (theoretical) argument is based on the assumption that the amorphous and the crystalline phase are perfectly bonded. This remark may be of crucial importance in explaining the apparent inconsistency between the theoretical estimate (a) and the experimental results. Indeed, in their uniaxial compression test of HDPE, Bartczak et al. [10] observed the formation of *local* kink bands leading to fragmentation of the corresponding lamellar structure at the microscopic level. More generally, the development of both microscopic and macroscopic instabilities have been extensively reported in experimental studies of HDPE materials and other semi-crystalline polymers (see, e.g., [46], [9], [54], [67]). For this reason, we think that the macroscopic hardening predicted by the LCC estimate (a) in the moderate strain range is unrealistic. For the same reason, we also regard the hardening predicted by the LCC estimate (b) in the large deformation regime as unrealistic.

Employing the same sets of material parameters that were used in the context of the LCC estimates of Fig. 4.5 for uniaxial compression, Fig. 4.6 shows the corresponding predictions (b), (c) and (d) of the LCC model for simple shear and uniaxial tension loading conditions. The LCC estimates for simple shear are here compared with the relevant experimental results of Bartczak et al. [9] (open squares), while those for uniaxial tension are compared with the corresponding experimental data of G'Sell and Jonas [46] (open circles). The results of Fig. 4.6 show that using the material parameters associated with the LCC estimate (b) for simple shear and uniaxial tension loading conditions leads to predictions that are inconsistent with the corresponding experimental results for large deformations. On the other hand, the LCC estimates labeled (d) in Fig. 4.6, just like in the case of uniaxial compression (Fig. 4.5), are in a reasonably good agreement with the experimental stress-strain curves both for simple shear and uniaxial tension loadings. A detailed discussion on the later estimates is provided in the relevant subsections 4.5.3 and 4.5.4.

In summary, in this work we model the HDPE used in the works of Bartczak et al. [8, 10, 9] by means of the material parameters corresponding to the LCC estimates (d) in Figs. 4.5 and 4.6. In particular, the back-stress tensor $\mathbf{T}_d$ of the amorphous phase is defined by (4.15), where the relevant material parameters are given by the set of values labeled (c) in Table 4.2. As argued above, we

find that this model for $\mathbf{T}_d$ (see curve (c) in Fig. 4.4(Right)) provides a better description for the elastic resistance of the actual amorphous material confined between two crystalline layers in HDPE than a corresponding model that would be more realistic for an unconstrained, homogeneous rubber (e.g., curve (a) in Fig. 4.4(Right)). The CRSSs $\tau_{0k}^{(r,c)}$ in the slip systems of the crystalline phase are defined by relation (4.77), where the associated material parameters are given in Table 4.1. The strain hardening relation (4.77) is motivated and it is meant to partially account for the Coulomb effect at large deformation. In this connection, it is remarked that no strain hardening has been assumed for the CRSSs associated with chain slip. Our motivation for this choice is that strain hardening of the chain slip systems is inconsistent with experimental evidence for simple shear tests. This point is discussed in more detail in subsection 4.5.3.

4.5.2 Uniaxial compression

In this subsection we discuss in detail the predictions of the LCC model for the macroscopic response and texture evolution in HDPE under uniaxial compression loading conditions. For definiteness, we consider a macroscopic cylindrical specimen of HDPE subjected to a constant deformation rate $\overline{D}_{33} < 0$ along its axis of symmetry $\mathbf{e}_3$, with its lateral surfaces being held stress-free. In addition, we prescribe the macroscopic continuum spin $\overline{\mathbf{W}} = \mathbf{0}$. The remaining unknown components of the macroscopic deformation rate tensor $\overline{\mathbf{D}}$ and the unknown component $\overline{\sigma}_{33}$ of the macroscopic Cauchy stress tensor $\overline{\boldsymbol{\sigma}}$ are determined by means of the LCC estimate (4.80) along with the incompressibility condition $\mathrm{tr}\overline{\mathbf{D}} = 0$. From these calculations, it turns out that the shear components of $\overline{\mathbf{D}}$ are practically equal to zero. Thus, for this type of loading, the macroscopic logarithmic strain tensor, defined by

$$\overline{\varepsilon} = \ln \overline{\mathbf{V}}, \tag{4.110}$$

is co-axial with $\overline{\mathbf{D}}$ and may be computed by

$$\overline{\varepsilon} = \int_0^t \overline{\mathbf{D}} dt. \tag{4.111}$$

It is recalled that the variable $\overline{\mathbf{V}}$ in (4.110) denotes the left stretch tensor from the polar decomposition of the macroscopic deformation gradient $\overline{\mathbf{F}} = \overline{\mathbf{V}}\,\overline{\mathbf{R}}$. For later reference, we introduce the von Misses equivalent stress $\overline{\sigma}_e$ and the equivalent strain measure $\overline{\varepsilon}_e$,

$$\overline{\sigma}_e = \sqrt{\frac{3}{2}\overline{\boldsymbol{\sigma}}_d \cdot \overline{\boldsymbol{\sigma}}_d}, \qquad \overline{\varepsilon}_e = \sqrt{\frac{2}{3}\overline{\varepsilon} \cdot \overline{\varepsilon}}, \tag{4.112}$$

where we recall that $\overline{\boldsymbol{\sigma}}_d$ denotes the deviatoric part of the stress tensor $\overline{\boldsymbol{\sigma}}$.

Figure 4.7 compares the LCC estimate (4.80), the estimate of Lee et al. [80] and the estimate of Nikolov et al. [110] with the corresponding experimental results of Bartczak et al. [10] for the macroscopic response of HDPE under uniaxial compression at a constant deformation rate

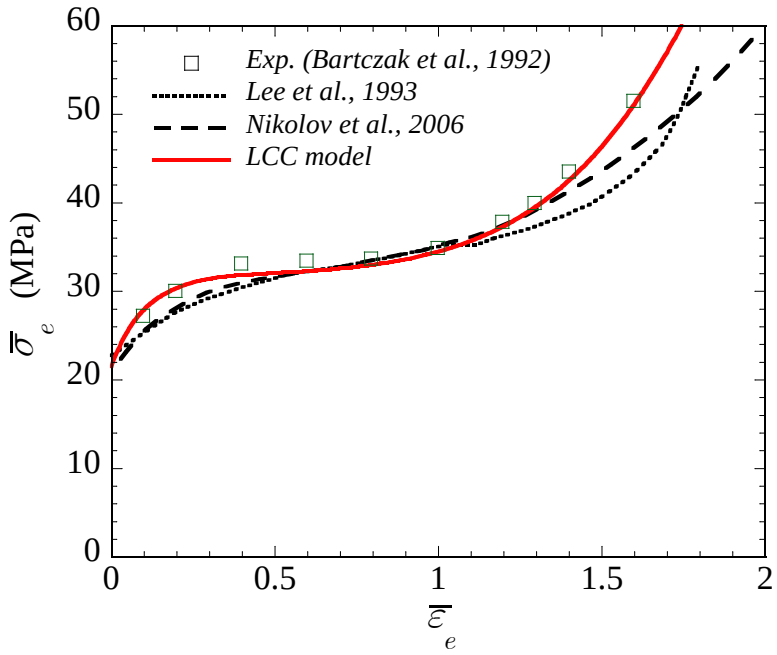

Figure 4.7: Macroscopic response of HDPE under uniaxial compression at a constant deformation rate $\overline{D}_{33} = -10^{-3}s^{-1}$. Comparison of the LCC estimate (4.80), the estimate of Lee et al. [80] and the estimate of Nikolov et al. [110] with the corresponding experimental results of Bartczak et al. [10]. The applied equivalent stress measure $\overline{\sigma}_e$ is plotted as a function of the applied equivalent strain measure $\overline{\varepsilon}_e$, with $\overline{\sigma}_e$ and $\overline{\varepsilon}_e$ defined by $(4.112)_1$ and $(4.112)_2$, respectively.

$\overline{D}_{33} = -10^{-3}s^{-1}$. In each case, the von Misses equivalent stress $\overline{\sigma}_e$, defined by $(4.112)_1$, is plotted as a function of the equivalent stain $\overline{\varepsilon}_e$, defined by $(4.112)_2$. We observe that the LCC estimate is in a very good agreement with the experimental results in the entire range of deformations considered. The most significant improvement of the LCC estimate over the earlier estimates is observed at large strains. This observation, in turn, suggest the importance of the Coulomb effect in the large deformation regime, which is not taken into account by the earlier models.

More generaly, the estimates of Lee et al. [80] and Nikolov et al. [110] are not as accurate as the LCC estimate. It should be remarked that, in general, the model of Nikolov et al. [110] delivers better predictions from that of Lee et al. [80], especially in the large strain range. As discussed in the work of Nikolov et al. [110], the improvement of their estimate over the earlier one is primarily due to the morphological texture evolution accounted for in their model but not in the model of Lee et al. [80] (see Fig. 12 in [110]). It should be pointed out, however, that the model of Lee et al. [80] accounts properly for general isochoric deformations in the amorphous phase as well as for the evolution of the lamellar normals $\mathbf{n}^{(r)}$. Both of these features are supported by experimental evidence (see [10], and in particular Fig. 7 in this reference). On the other hand,

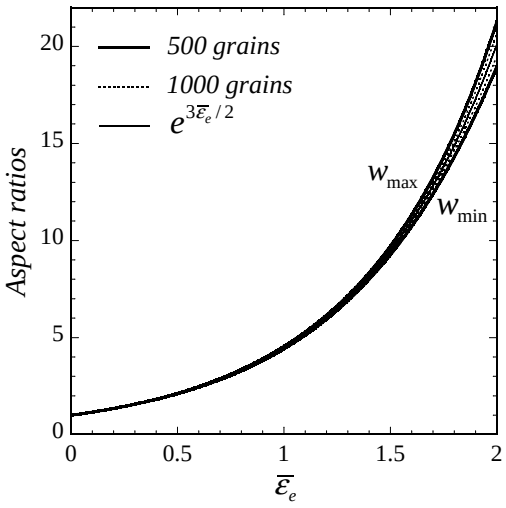

Figure 4.8: Morphological texture evolution in HDPE under uniaxial compression as predicted by the LCC model. The maximum $w_{\max}$ and minimum $w_{\min}$ aspect ratios of the distributional ellipsoid (4.8), defined respectively by $(4.113)_1$ and $(4.113)_2$, are plotted as functions of the applied equivalent strain $\overline{\varepsilon}_e$. Results are shown both for the 500-grain system of Fig. 4.3 and also for a refined 1000-grain system. For comparison, the aspect ratio $w_{\max} = w_{\min} = \text{Exp}[3\overline{\varepsilon}_e/2]$ corresponding to a perfectly transversely isotropic material is also shown.

Nikolov et al. [110] modeled the amorphous phase as an additional slip system attached to the crystalline phase, neglecting the compatibility conditions (4.96) and the evolution of the lamellar normals $\mathbf{n}^{(r)}$. As a result of these prescriptions, the influence of the material properties of the amorphous phase on the predicted macroscopic response is less significant in the case of the later model than in the former one. Note, in particular, that in order to capture the hardening features of the experimental stress-strain curve in the small deformation range, Nikolov et al. [110] made use of an initial shear modulus for the back-stress tensor that is significantly higher than the one used by Lee et al. [80]. Furthermore, the locking of the amorphous phase—used in both works as a mechanism for the macroscopic strain-hardening in the large deformation range—does not result in a corresponding significant hardening in the estimate of Nikolov et al. [110] as it does in the estimate of Lee et al. [80]. On the other hand, it should be emphasized that the LLC model is free of the above limitations of the earlier models. Specifically, the LLC model accounts properly for general deformations in the amorphous phase, for the evolution of the lamination orientations $\mathbf{n}^{(r)}$ and for the evolution of morphology.

Figure 4.8 shows the predictions of the LCC model for the evolution of the aspect ratios $w_{\max}$ and $w_{\min}$ of the ellipsoid (4.8), characterizing the spatial distribution of the grain-families in the

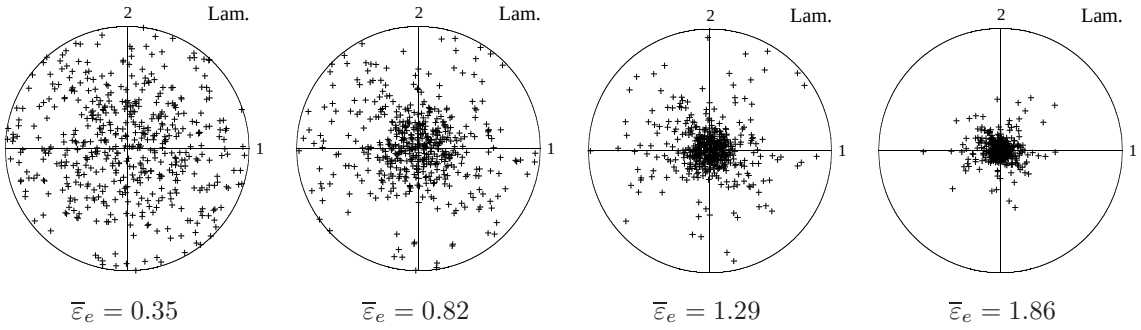

Figure 4.9: Lamellar texture evolution in HDPE under uniaxial compression as predicted by the LCC model. Equal area projection figures of the lamination orientations $\mathbf{n}^{(r)}$ are shown at various values of the applied equivalent strain $\overline{\varepsilon}_e$. The direction of compression is along the 3−axis.

HDPE material. The aspect ratios $w_{\max}$ and $w_{\min}$ are here defined by

$$w_{\max} = \frac{\overline{\lambda}_{\max}}{\overline{\lambda}_3}, \qquad w_{\min} = \frac{\overline{\lambda}_{\min}}{\overline{\lambda}_3}, \tag{4.113}$$

where $\overline{\lambda}_{\max}$ and $\overline{\lambda}_{\min}$ are respectively the maximum and minimum macroscopic stretches in the plane normal to the loading axis $\mathbf{e}_3$ and $\overline{\lambda}_3$ is the corresponding stretch along $\mathbf{e}_3$. Note that Fig. 4.8 includes results not only for the 500-grain system of Fig. 4.3 but also for a refined 1000-grain system, i.e., a system approximating better the initially isotropic response of the HDPE material. Recall that the distributional ellipsoid (4.8) has been identified in this work with the macroscopic Eulerian strain ellipsoid (see subsection 4.3.1), i.e., the ellipsoid defined by the left stretch tensor $\overline{\mathbf{V}}$. Therefore, the difference between $w_{\max}$ and $w_{\min}$ in Fig. 4.8 is a measure of deviation of the predicted macroscopic response from the ideally transversely isotropic behavior, corresponding to $w_{\max} = w_{\min} = \text{Exp}[3\overline{\varepsilon}_e/2]$ and represented in Fig. 4.8 with the continuous, thin line. These results show that the macroscopic response of the material, as predicted by the LCC model, is transversely isotropic to a very good degree of approximation. A small deviation from transverse isotropy is observed at large strains. The fact that the difference between $w_{\max}$ and $w_{\min}$ for the 1000-grain system (dotted, thin curve) is smaller than the corresponding difference for the case of 500-grains (continuous, thick curve) suggests that the aforementioned deviation from transverse isotropy at large strains is probably due to the corresponding small deviation of the behavior of the undeformed specimen from isotropy, which is expected to be enhanced with increasing strains as a result of the different strain hardening of the phases in different grains.

Figure 4.9 shows the equal area projection representations of the lamellar normals $\mathbf{n}^{(r)}$ at the applied strain values $\overline{\varepsilon}_e = 0.35$, $\overline{\varepsilon}_e = 0.82$, $\overline{\varepsilon}_e = 1.29$ and $\overline{\varepsilon}_e = 1.86$, as predicted by the LCC model. The main observation from these results is that the lamination orientations $\mathbf{n}^{(r)}$ rotate gradually towards the loading direction $\mathbf{e}_3$. This rotation is a result of interlamellar shear, i.e.,

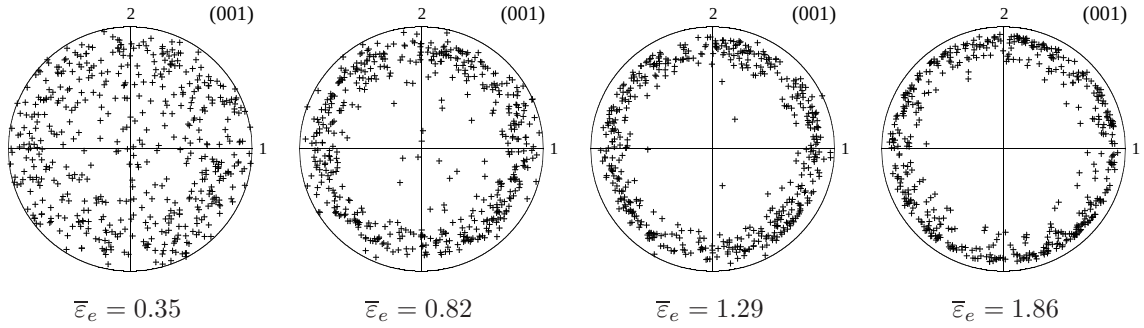

Figure 4.10: Crystallographic texture evolution in HDPE under uniaxial compression as predicted by the LCC model. Equal area projection figures of the (001) plane poles are shown at various values of the applied equivalent strain $\overline{\varepsilon}_e$. The direction of compression is along the 3−axis.

shear deformation parallel to the lamellar planes. At the strain level $\overline{\varepsilon}_e = 0.35$, we observe that only a relatively small portion of lamellar normals $\mathbf{n}^{(r)}$ have been rotated towards the loading axis $\mathbf{e}_3$ (compare with Fig. 4.3(d)), leading to a correspondingly weak lamellar texture. The rotation of the normals $\mathbf{n}^{(r)}$ is intensified in the moderate deformation range and a clear concentration of $\mathbf{n}^{(r)}$ close to the loading axis is observed at $\overline{\varepsilon}_e = 0.82$. At the strain level $\overline{\varepsilon}_e = 1.29$ the lamellar texture is well developed with a strong maximum at the loading axis, while at $\overline{\varepsilon}_e = 1.86$ the normals $\mathbf{n}^{(r)}$ are almost perfectly aligned with the loading axis. We note that these results are consistent with the corresponding experimental observations of Bartczak et al. [10].

Next, we turn our attention to the crystallographic texture evolution. Figures 4.10, 4.11 and 4.12 present the relevant equal area projections of the (001), (100), (010), {110} and {011} plane poles at the strain values $\overline{\varepsilon}_e = 0.35$, $\overline{\varepsilon}_e = 0.82$, $\overline{\varepsilon}_e = 1.29$ and $\overline{\varepsilon}_e = 1.86$, as predicted by the LCC model. Note that the (001), (100) and (010) plane poles correspond respectively to the $\mathbf{c}^{(r)}$, $\mathbf{a}^{(r)}$ and $\mathbf{b}^{(r)}$ crystallographic axes. For comparison purposes, in Figs. 4.11 and 4.12 we have also included the corresponding intensity plots—i.e., plots of the pole densities as a function of the angle they form with the loading axis $\mathbf{e}_3$—from the experimental work of Bartczak et al. [10]. In agreement with the experimental observations of Bartczak et al. [10], it is seen that the predicted pole figures are characterized by axial symmetry with respect to the loading axis $\mathbf{e}_3$, which is partially responsible for the predicted overall isotropic behavior of the material in the transverse plane.

From the LCC estimates of Figs. 4.10 and 4.11, we observe that both the $\mathbf{c}^{(r)}$- and $\mathbf{b}^{(r)}$-axes tend to migrate toward the radial direction with increasing strain, while the $\mathbf{a}^{(r)}$-axes rotate towards the loading direction $\mathbf{e}_3$. These rotations are primarily the result of the (100)[001] chain slip (rotations about the $\mathbf{b}^{(r)}$-axes) and (100)[010] transverse slip (rotations about the $\mathbf{c}^{(r)}$-axes), which correspond to the slip systems with the smallest CRSSs (see Table 4.1). Furthermore, we

observe that the $\mathbf{c}^{(r)}$-texture develops faster with a maximum closer to the radial direction than the corresponding $\mathbf{b}^{(r)}$-texture, which is consistent with the fact that the CRSS for (100)[001] chain slip is less than the CRSS for (100)[010] transverse slip. The evolution of the {110} and {011} plane poles, shown in Fig. 4.12, are of course completely determined from the evolution of the principal crystallographic axes $\mathbf{a}^{(r)}$, $\mathbf{b}^{(r)}$ and $\mathbf{c}^{(r)}$, since the crystals have been assumed to rotate rigidly (see subsection 4.3.3). Note, in particular, that the (110) and (011) plane poles, as predicted by the LCC model, migrate respectively towards the loading direction and away from it as a function of the applied strain $\overline{\varepsilon}_e$. In general, from Figs. 4.11 and Figs. 4.12 we observe that the crystallographic textures predicted by the LCC model are in a reasonably good agreement with the corresponding experimental results, although, as pointed out by Nikolov et al. [110], the specific form in which Bartczak et al. [10] chose to present their measurements makes a direct quantitative comparison somewhat difficult.

Similar to the lamellar textures, the crystallographic textures predicted by the LCC model are weakly developed at the strain level $\overline{\varepsilon}_e = 0.35$, while at $\overline{\varepsilon}_e = 0.82, 1.29, 1.86$ they exhibit sharp maxima and the concentration of the poles around the corresponding maxima is increased with increasing strain. We observe that the maxima of the (001) and (010) plane poles (Figs. 4.10 and 4.11) rotate towards the radial direction, while the maxima of the (100) and (110) plane poles (Figs. 4.11 and 4.12) rotates towards the loading direction $\mathbf{e}_3$. Note, in particular, that the predicted angles between the maximum of the $\mathbf{a}^{(r)}$-axes and the loading direction $\mathbf{e}_3$ at the strain values $\overline{\varepsilon}_e = 0.82, 1.29, 1.86$ are approximately 27^o, 25^o and 22^o, respectively. The corresponding experimentally determined angles of the $\mathbf{a}^{(r)}$-poles at $\overline{\varepsilon}_e = 0.82, 1.29, 1.86$ are respectively 28^o, 26^o and 22^o. These observations suggest that, in the large strain range $\overline{\varepsilon}_e \geq 0.82$, the Coulomb yield criterion (4.109) will have the effect of increasing the CRSSs associated with slip on the (100) and (110) planes with increasing strain, since these planes are subjected to substantial compressive normal stresses which increase as a function of the applied strain $\overline{\varepsilon}_e$. This is, in turn, expected to lead to an overall hardening of the crystals, independently of what the Coulomb effect on the remanning slip planes (010) and $(1\bar{1}0)$ is, since the orientation of the associated crystallographic systems is much less favorable for slip.

Finally, Fig. 4.13 shows the effect of the applied deformation rate $\overline{D}_{33}$ on the predictions of the LCC model for the effective behavior of HDPE under uniaxial compression. The corresponding macroscopic stress-strain curves are shown for the cases $\overline{D}_{33} = -10^{-4}s^{-1}$, $\overline{D}_{33} = -10^{-3}s^{-1}$ and $\overline{D}_{33} = -10^{-2}s^{-1}$. From these results we observe that the material exhibits a stiffer response with increasing deformation rate $|\overline{D}_{33}|$, as expected form physical experience.

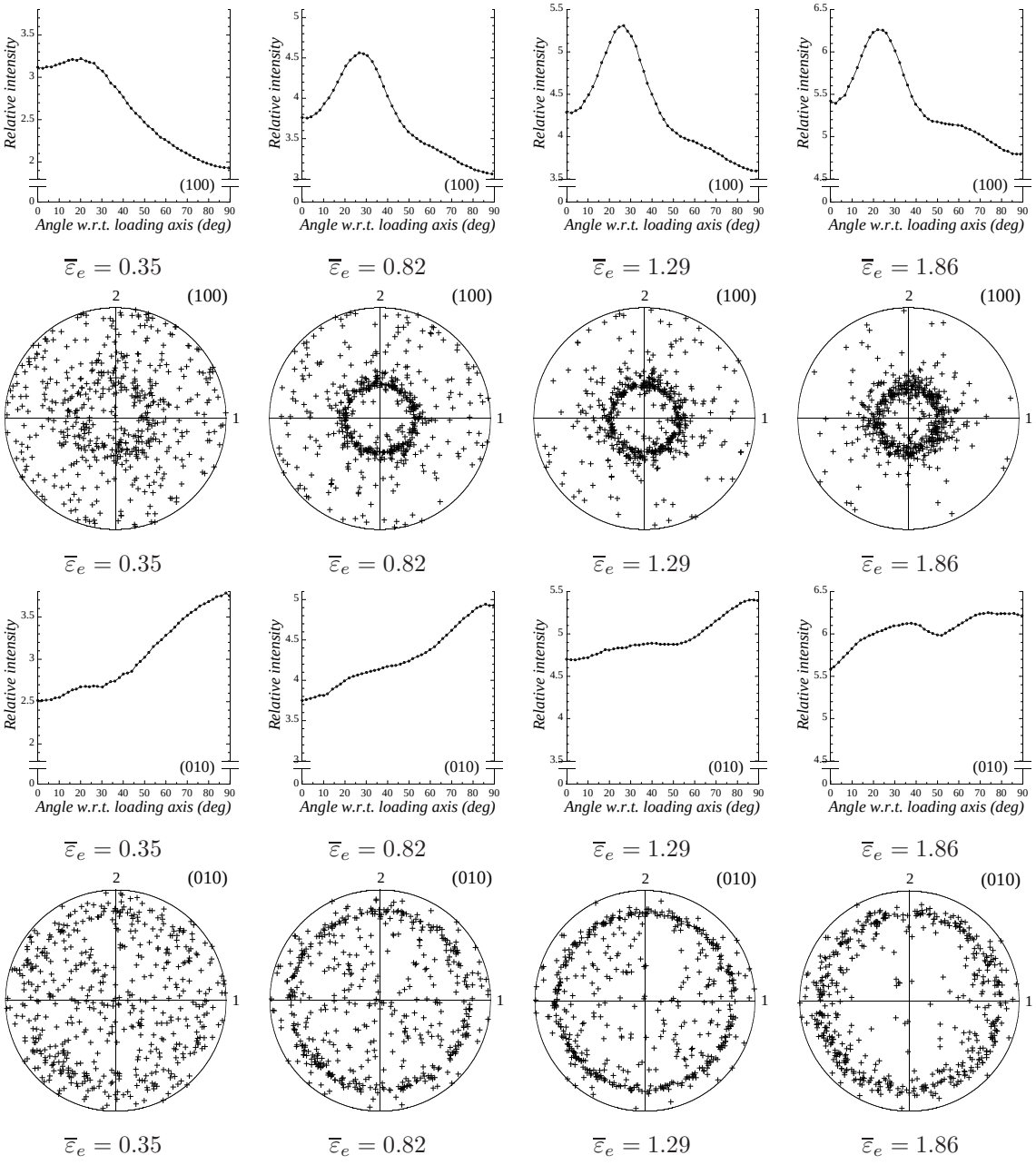

Figure 4.11: Crystallographic texture evolution in HDPE under uniaxial compression. The equal area projection figures of the (100) and (010) plane poles predicted by the LCC model are compared with the corresponding pole intensity plots measured experimentally by Bartczak et al. [10] at various values of the applied equivalent strain $\overline{\varepsilon}_e$. The direction of compression is along the 3−axis.

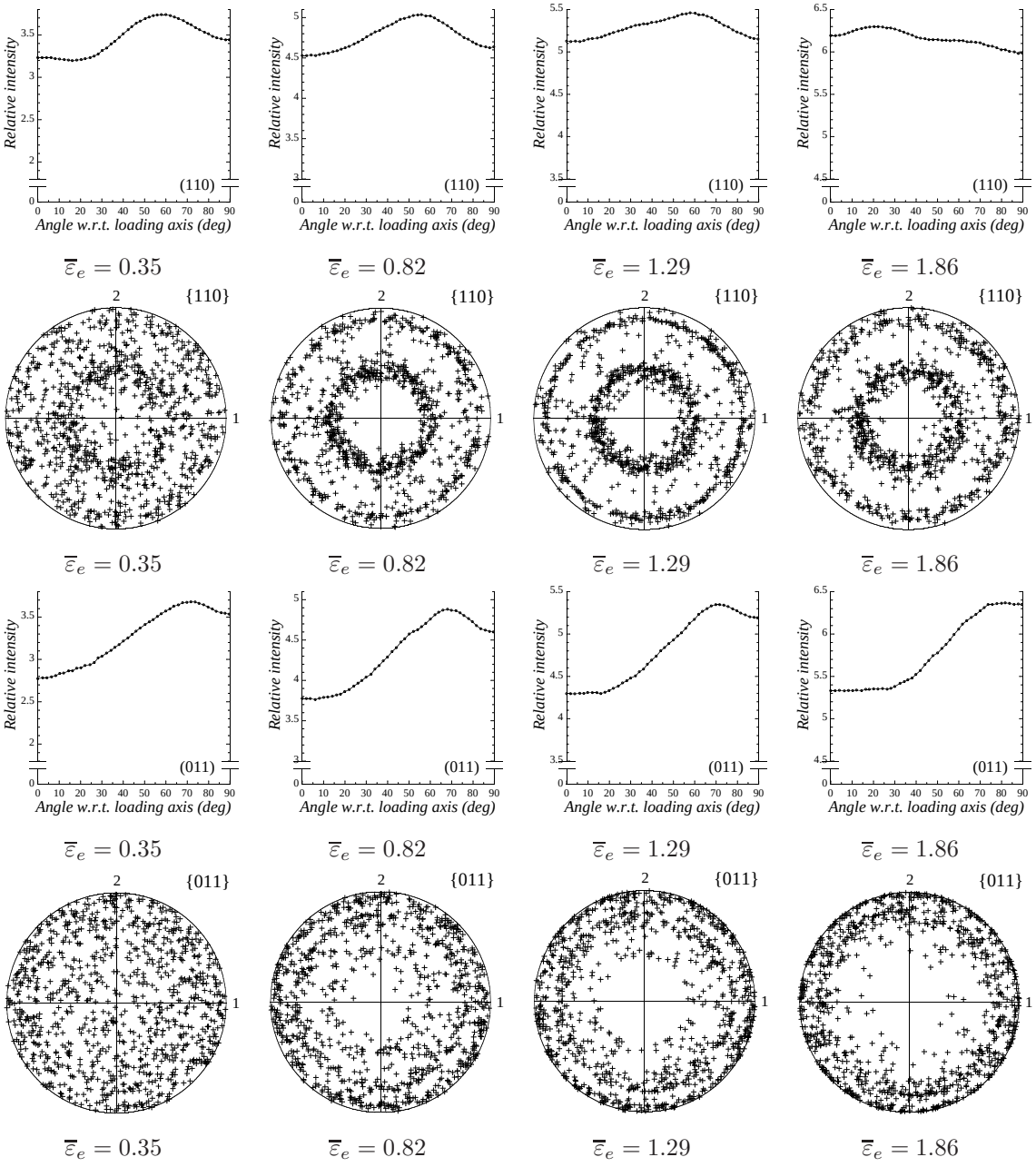

Figure 4.12: Crystallographic texture evolution in HDPE under uniaxial compression. The equal area projection figures of the {110} and {011} plane poles predicted by the LCC model are compared with the corresponding pole intensity plots measured experimentally by Bartczak et al. [10] at various values of the applied equivalent strain $\overline{\varepsilon}_e$. The direction of compression is along the 3−axis.

4.5.3 Simple shear

Next, following the structure of the previous subsection, we consider simple shear loading conditions. In particular, let a macroscopic cubic specimen of HDPE be subjected to a constant shear

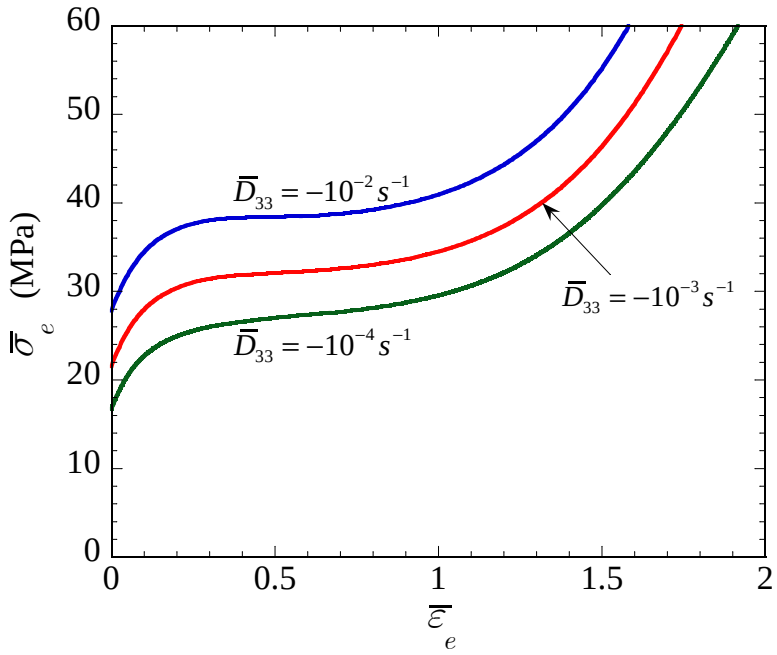

Figure 4.13: The effect of the deformation rate $\overline{D}_{33}$ on the LCC estimate (4.80) for the macroscopic response of HDPE under uniaxial compression. The applied equivalent stress $\overline{\sigma}_e$ is plotted as a function of the applied equivalent strain $\overline{\varepsilon}_e$ for $\overline{D}_{33} = -10^{-4} s^{-1}$, $\overline{D}_{33} = -10^{-3} s^{-1}$ and $\overline{D}_{33} = -10^{-2} s^{-1}$.

rate $\dot{\overline{\gamma}}$ along direction $\mathbf{e}_2$ on the plane normal to $\mathbf{e}_1$, so that the prescribed components of the macroscopic velocity gradient $\overline{\mathbf{L}}$ are given by $\overline{L}_{21} \equiv \dot{\overline{\gamma}}$ and $\overline{L}_{11} = \overline{L}_{22} = \overline{L}_{33} = \overline{L}_{12} = \overline{L}_{31} = \overline{L}_{32} = 0$, while those of the macroscopic Cauchy stress tensor $\overline{\boldsymbol{\sigma}}$ are $\overline{\sigma}_{13} = \overline{\sigma}_{31} = \overline{\sigma}_{23} = \overline{\sigma}_{32} = 0$. For consistency with the works of Lee et al. [80] and Nikolov et al. [110], in this subsection the variables $\overline{\sigma}_e$ and $\overline{\varepsilon}_e$ are defined by

$$\overline{\sigma}_e = \sqrt{3}\overline{\tau}, \qquad \overline{\varepsilon}_e = \frac{\overline{\gamma}}{\sqrt{3}}, \tag{4.114}$$

where $\overline{\gamma}$ is the amount of the applied shear deformation along direction $\mathbf{e}_2$ on the plane normal to $\mathbf{e}_1$ and $\overline{\sigma}_{21} \equiv \overline{\tau}$ is the corresponding shear stress. Note that, for the loading conditions under consideration, it can be easily shown that the shear stress component $\overline{\sigma}_{21}$ of the Cauchy stress tensor is equal to the corresponding component of the first Piola-Kirchhoff stress tensor. In other words, the applied shear stresses in the undeformed and deformed configuration are equal.

Figure 4.14 compares the LCC estimate (4.80), the estimate of Lee et al. [80] and the estimate of Nikolov et al. [110] with the corresponding experimental results of Bartczak et al. [9] and Dahoun [24] for the effective behavior of HDPE under simple shear at a constant shear rate $\dot{\overline{\gamma}} = 10^{-3} s^{-1}$. In each case, the stress measure $\overline{\sigma}_e = \sqrt{3}\overline{\tau}$ is plotted as a function of the stain measure $\overline{\varepsilon}_e = \overline{\gamma}/\sqrt{3}$. From the experimental data, it is observed that the material exhibits a hardening behavior up

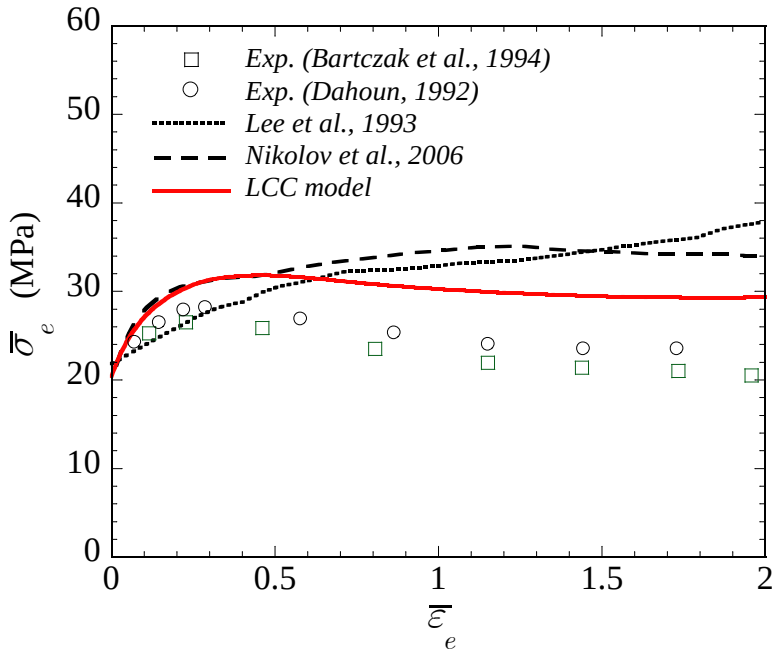

Figure 4.14: Macroscopic response of HDPE under simple shear at a constant shear rate $\dot{\overline{\gamma}} = 10^{-3}s^{-1}$. Comparison of the LCC estimate (4.80), the estimate of Lee et al. [80] and the estimate of Nikolov et al. [110] with the corresponding experimental results of Bartczak et al. [9] and Dahoun [24]. The applied equivalent stress measure $\overline{\sigma}_e$ is plotted as a function of the applied equivalent strain measure $\overline{\varepsilon}_e$, with $\overline{\sigma}_e$ and $\overline{\varepsilon}_e$ defined by $(4.114)_1$ and $(4.114)_2$, respectively.

to an applied strain $\overline{\varepsilon}_e \approx 0.25$, after which it undergoes softening up to the largest strain value shown. The rate of softening is initially high but it decreases with increasing strain. Note that this type of behavior is dramatically different from the one considered in the previous subsection for uniaxial compressive loading conditions. Among the theoretical results of Fig. 4.14, the LCC estimate is the only one which is in a good qualitative agreement with the experimental results in the entire range of deformations. Furthermore, although all three models overestimate the experimentally measured stress for the most part, in general, the LCC estimate is also in better quantitative agreement with the experimental results than the earlier estimates. Compared to the earlier models, it should be remarked that despite the considerably stiffer predictions of the LCC model for the large deformation response of the material under uniaxial compression (Fig. 4.7), in the case of simple shear (Fig. 4.14) the LCC model correctly predicts a much softer response at large strains.

The predictions of the Lee et al. [80] model in the strain range $\overline{\varepsilon}_e < 0.6$ are in a slightly better agreement with the experimental data compared to the corresponding predictions of the other two

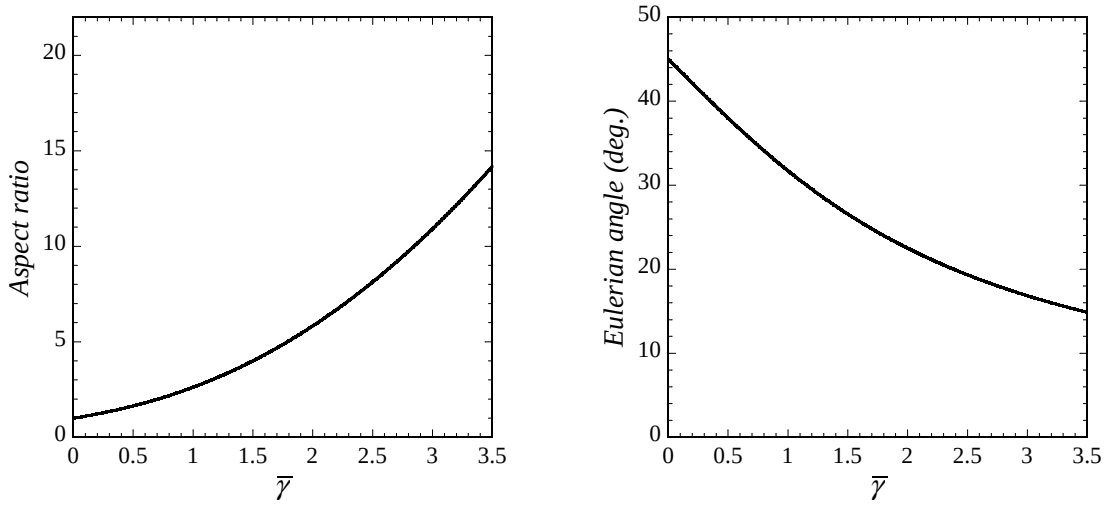

(a) (b)

Figure 4.15: Morphological texture evolution in HDPE under simple shear as predicted by the LCC model. (a) The aspect ratio $w = \overline{\lambda}_{\max}/\overline{\lambda}_{\min}$, with $\overline{\lambda}_{\max}$ and $\overline{\lambda}_{\max}$ being respectively the maximum and minimum applied stretches, is plotted as a function of the applied amount of shear $\overline{\gamma}$. (b) The angle $\overline{\theta}_E = \tan^{-1}(2/\overline{\gamma})/2$ between the major principal axis and the shear direction $\mathbf{e}_2$ is plotted as a function of the applied amount of shear $\overline{\gamma}$.

models. However, the model of Lee et al. [80] predicts a monotonically increasing stress as a function of the applied strain and, therefore, fails to capture the softening behavior at larger strains. On the other hand, the Nikolov et al. [110] model does predicts a slight strain softening beginning approximately at $\overline{\varepsilon}_e = 1.2$. Note, however, that this value is unrealistically high compared to the experimentally measured onset of softening ($\overline{\varepsilon}_e \approx 0.25$). The softening behavior predicted by the model of Nikolov et al. [110] at large strains is manly due to the corresponding (average) softening of the crystals with increasing strain (resulting from the crystallographic texture evolution discussed further below) in combination with the locking of the amorphous phase, which occurs also at about $\overline{\varepsilon}_e = 1.2$ (see Fig. 10 in [110]). In other words, in the context of the Nikolov et al. [110] estimate, the macroscopically applied strain in the range $\overline{\varepsilon}_e > 1.2$ is accommodated exclusively through crystallographic slip deformation of the crystalline phase, which is *not* constrained by the compatibility conditions (4.96), as it is in the context of the other two models. In this connection, it is emphasized once again that the locking of the amorphous phase in a model accounting explicitly for the compatibility of the deformation at the lamellar interfaces constrains severely the deformability of the crystalline phase which, in turn, inevitably leads to correspondingly stiff predictions for the macroscopic response.

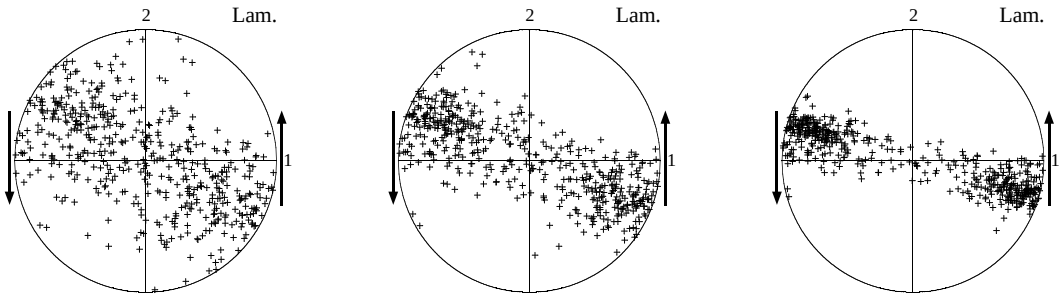

$\overline{\gamma} = 1$ $\overline{\gamma} = 1.8$ $\overline{\gamma} = 3$

Figure 4.16: Lamellar texture evolution in HDPE under simple shear as predicted by the LCC model. Stereographic projection figures of the lamination orientations $\mathbf{n}^{(r)}$ are shown at various values of the applied amount of shear $\overline{\gamma}$. The direction of shear is indicated by the arrows.

Figure 4.15 shows the predictions of the LCC model for the evolution of the distributional ellipsoid (4.8), which is identified in this work with the macroscopic Eulerian ellipsoid (see subsection 4.3.1). The aspect ratio of the ellipsoid shown in Fig. 4.15(a) is defined as $w \equiv \overline{\lambda}_{\max}/\overline{\lambda}_{\min}$, where $\overline{\lambda}_{\max}$ and $\overline{\lambda}_{\min}$ stand respectively for the maximum and minimum macroscopic stretches, while the Eulerian angle $\overline{\theta}_E$ shown in Fig. 4.15(b) is the angle between the direction of shear $\mathbf{e}_2$ and the major Eulerian axis (or, equivalently, the angle between $\mathbf{e}_1$ and the minor Eulerian axis). It is observed that the aspect ratio w and the Eulerian angle $\overline{\theta}_E$ predicted by the LCC model are practically identical with the corresponding well-known formula for simple shear deformation (see, e.g., Ogden [112]):

$$w = \frac{\left(\overline{\gamma} + \sqrt{4 + \overline{\gamma}^2}\right)^2}{4}, \qquad \overline{\theta}_E = \frac{1}{2}\tan^{-1}\left(\frac{2}{\overline{\gamma}}\right). \tag{4.115}$$

Note that, this observation is in agreement with the report of Bartczak et al. [9] that their experimental test was indeed a macroscopically homogeneous simple shear deformation.

Figure 4.16 presents the lamellar texture evolution in HDPE under simple shear, as predicted by the LCC model. The corresponding stereographic projections of the lamination orientations $\mathbf{n}^{(r)}$ are shown at the applied shear strains $\overline{\gamma} = 1$, $\overline{\gamma} = 1.8$ and $\overline{\gamma} = 3$. In agreement with the experimental observations of Bartczak et al. [9], it is seen that the lamellar normals $\mathbf{n}^{(r)}$ rotate gradually towards the minor axis of the macroscopic Eulerian strain ellipsoid, i.e., the axis of the minimum applied stretch. (Recall that this axis forms an angle $\overline{\theta}_E$ with the direction $\mathbf{e}_1$ on the plane $\mathbf{e}_1$-$\mathbf{e}_2$ which is shown as a function of $\overline{\gamma}$ in Fig. 4.15(b).) In particular, at the strain level $\overline{\gamma} = 1$ we observe that the normals $\mathbf{n}^{(r)}$ are confined within a relatively broad band which is approximately orthogonal to the major Eulerian axis. As the deformation is increased, this band becomes narrower, it follows the rotation of the Eulerian strain ellipsoid (the orientation of which is defined by the angle $\overline{\theta}_E$ in $(4.115)_2$) and, at the same time, the lamellar normals $\mathbf{n}^{(r)}$ within the

band migrate towards the equator. This leads to the strong lamellar texture observed at $\overline{\gamma} = 3$ having a maximum very close to the minor axis of the macroscopic Eulerian strain ellipsoid.

Next, it is relevant to discuss the effect of the lamellar texture evolution on the large deformation response of HDPE under simple shear (Fig. 4.14). In general, the deformation field in the lamellar grains is expected to be quite complicated. However, taking into account the above discussion on the lamellar texture evolution, it is safe to conclude that in the large strain regime the dominant deformation mechanism in the laminates is interlamellar shear, i.e., shear parallel to the lamellar planes, which is known to be the softest (Sachs-type) deformation mode of lamellar composites. This fact by itself is expected, in turn, to have a softening effect on the macroscopic response of the HDPE material at large strains. In contrast, we recall that in the case of uniaxial compression at large strains the laminates are subjected to a stiff mode of deformation (axisymmetric shear) which, in turn, contributes accordingly to the macroscopic hardening response of the material. These observations suggest that the lamellar texture evolution may have an important effect in determining the radically different types of behavior observed under uniaxial compression and simple shear at large strains.

Figures 4.17 and 4.18 compare the predictions of the LCC model for the crystallographic texture evolution with the corresponding experimental results of Bartczak et al. [9]. Specifically, Fig. 4.17 shows the relevant stereographic projections of the (001) and (100) plane poles at shear strains $\overline{\gamma} = 1$, $\overline{\gamma} = 1.8$ and $\overline{\gamma} = 3$, while Fig. 4.18 presents the corresponding results for the (010) and (110) plane poles. We recall that the (001), (100) and (010) plane poles correspond respectively to the $\mathbf{c}^{(r)}$, $\mathbf{a}^{(r)}$ and $\mathbf{b}^{(r)}$ crystallographic axes. According to the experimental results of Bartczak et al. [9], the evolution of the crystal lattices with increasing shear strain $\overline{\gamma}$ results gradually in the development of a bi-modal texture. The stronger component of this texture is formed by the rotation of the $\mathbf{c}^{(r)}$- and $\mathbf{a}^{(r)}$-axes towards orientations that are tilted a few degrees away from the $\mathbf{e}_2$- and $\mathbf{e}_1$-axis, respectively, and a corresponding rotation of the $\mathbf{b}^{(r)}$-axes towards $\mathbf{e}_3$. Interestingly, the maxima of these orientation distributions do not rotate as a function of the applied strain $\overline{\gamma}$. The weaker component of the bi-modal texture is formed by a rotation of the $\mathbf{c}^{(r)}$-axes towards the direction of maximum stretch, a rotation of the $\mathbf{a}^{(r)}$-axes towards the direction of minimum stretch and a corresponding rotation of the $\mathbf{b}^{(r)}$-axes towards $\mathbf{e}_3$. Thus, the later component of the texture rotates according to the rotation of the macroscopic Eulerian strain ellipsoid. As reported by Bartczak et al. [9], the strong overlapping of the two orientation clusters of the $\mathbf{a}^{(r)}$-axes is an experimental artefact. From Figs. 4.17 and 4.18, we observed that the textures predicted by the LCC model are in reasonably good agreement with the corresponding experimental results, except of the fact that the predicted pole figures exhibit an additional texture component, which is however much weaker than the other two. This third component is formed by a (001) plane pole texture oriented along the $\mathbf{e}_3$-direction and a $\{110\}$ plane pole texture oriented

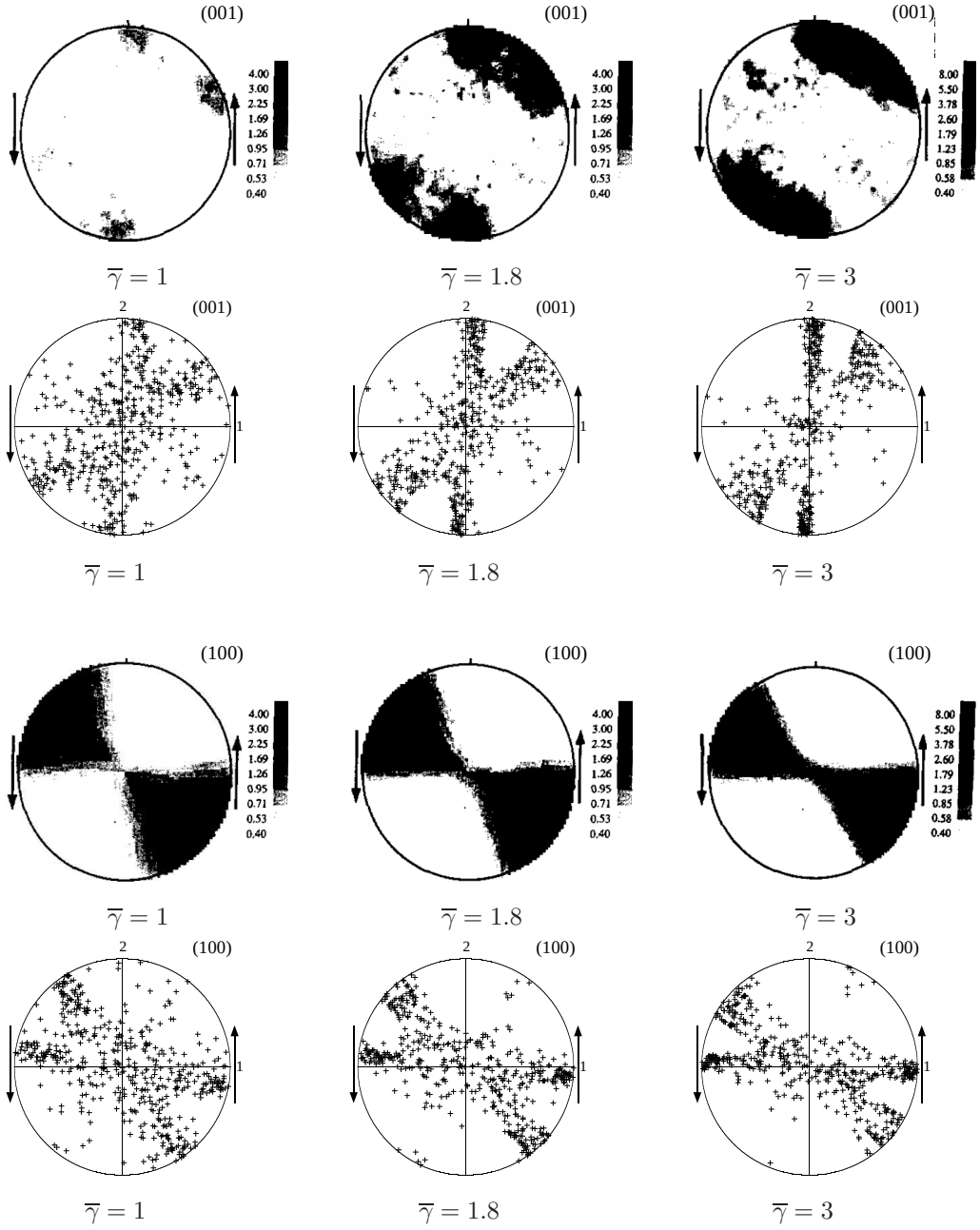

Figure 4.17: Crystallographic texture evolution in HDPE under simple shear. Stereographic projection figures of the (001) and (100) plane poles predicted by the LCC model are compared with corresponding experimental results by Bartczak et al. [9]. The theoretical predictions are presented below the corresponding experimental results. The direction of shear is indicated by the arrows.

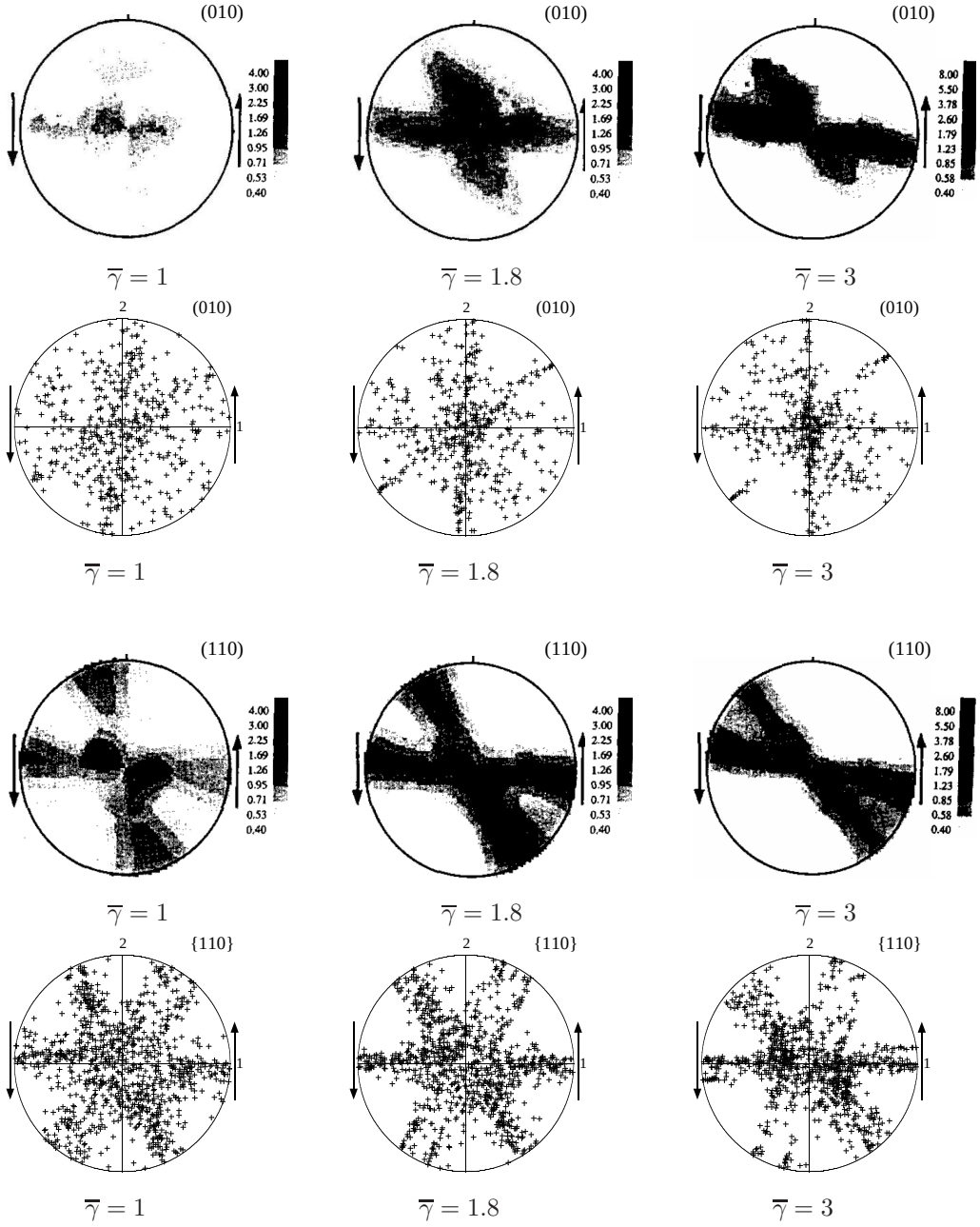

Figure 4.18: Crystallographic texture evolution in HDPE under simple shear. Stereographic projection figures of the (010) and {110} plane poles predicted by the LCC model are compared with corresponding experimental results by Bartczak et al. [9]. The theoretical predictions are presented below the corresponding experimental results. The direction of shear is indicated by the arrows.

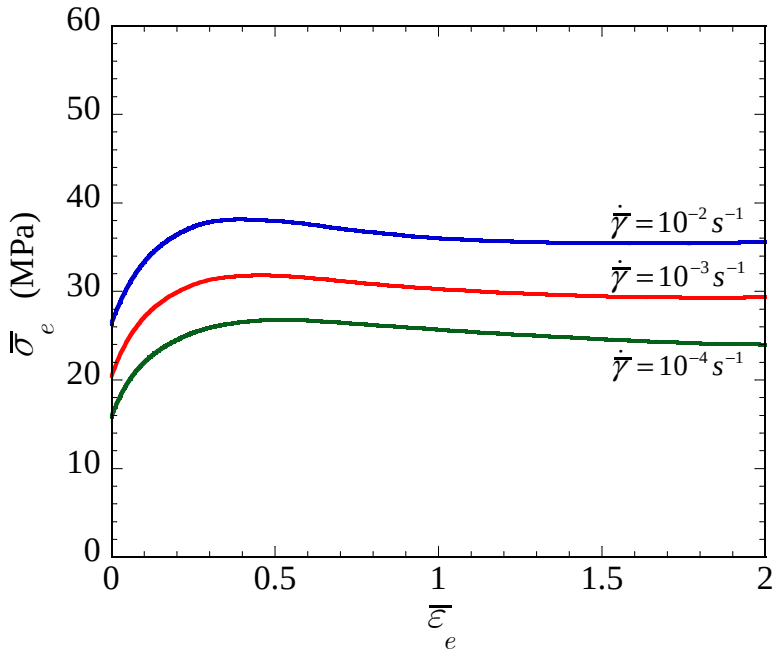

Figure 4.19: The effect of the shear rate $\dot{\bar{\gamma}}$ on the LCC estimate (4.80) for the macroscopic response of HDPE under simple shear. The applied equivalent stress $\overline{\sigma}_e$ is plotted as a function of the applied equivalent strain $\overline{\varepsilon}_e$ for $\dot{\bar{\gamma}} = 10^{-4} s^{-1}$, $\dot{\bar{\gamma}} = 10^{-3} s^{-1}$ and $\dot{\bar{\gamma}} = 10^{-2} s^{-1}$.

approximately along the direction of maximum stretch.

The cystallographic texture evolution has a crucial softening effect on the macroscopic response of the material. This effect is primarily due to a significant increase of the (100)[001] chain slip activity in the crystals with increasing strain, resulting from a corresponding increase of the associated resolved shear stress in this system. Recall that (100)[001] is the slip system with the lowest critical resolved shear stress (see Table 4.1). From both the predictions of the LCC model and the corresponding experimental results of Bartczak et al. [9] shown in Fig. 4.17 we observe that there are two possible mechanisms contributing in increasing the resolved shear stress on the (100)[001] slip system in the various crystals: (*i*) the rotation of the $\mathbf{a}^{(r)}$- and $\mathbf{c}^{(r)}$-axes of the crystals towards the equatorial region of either the stronger or the weaker texture component and (*ii*) the rotation of the weaker texture component such that the corresponding $\mathbf{c}^{(r)}$-axes are getting closer to the shear direction. The other three *chain* slip systems (see Table 4.1) are less favorable for crystallographic slip (see Figs. 4.17 and 4.18) and, therefore, their contribution on the overall softening of the material is expected to be less significant. Although Bartczak et al. [9] did not provide specific information about the macroscopic normal stress component applied on the shear plane of their specimen during the simple shear test, on the basis of the above argument we may conclude that any possible increase of the CRSSs of the chain slip systems in the various crystals

due to the Coulomb effect (4.109) should not be significant compared to the corresponding increase of the associated resolved shear stresses. This observation, as already mentioned, has motivated us to prescribe constant values for the CRSSs of the chain slip systems (see Table 4.1) in the context of the LCC model.

Fig. 4.13 examines the effect of the applied shear rate $\dot{\bar{\gamma}}$ on the LCC estimate (4.80) for the overall response of HDPE under simple shear. The corresponding macroscopic stress-strain curves are shown for the cases $\dot{\bar{\gamma}} = -10^{-4}s^{-1}$, $\dot{\bar{\gamma}} = -10^{-3}s^{-1}$ and $\dot{\bar{\gamma}} = -10^{-2}s^{-1}$. Similar to the corresponding results of Fig. 4.19 for uniaxial compression, the LCC model predicts that the material response under simple shear is stiffer for higher shear rates $\dot{\bar{\gamma}}$.

4.5.4 Uniaxial tension

We conclude this section with a discussion on the macroscopic response and texture evolution in HDPE under uniaxial tension. The loading conditions considered in this subsection differ from the uniaxial compression case of subsection 4.5.2 only in that the applied deformation rate along the axis of the cylinder is $\overline{D}_{33} > 0$. The associated von Misses equivalent stress $\overline{\sigma}_e$ and the equivalent strain measure $\overline{\varepsilon}_e$ are defined by $(4.112)_1$ and $(4.112)_2$, respectively.

Figure 4.20 compares the theoretical predictions of the LCC estimate (4.80), the Lee et al. [80] estimate and the Nikolov et al. [110] estimate for uniaxial tension of HDPE at a constant deformation rate $\overline{D}_{33} = 10^{-3}s^{-1}$. For further comparison, this figure includes also the corresponding experimental results from the works of G'Sell and Jonas [46] and Hiss et al. [54]. As already mentioned, these experiments have been performed for HDPE materials with a different molecular weight than the HDPE for which the material parameters of the models were chosen. Therefore, a quantitative comparison of the estimates with the experimental data is not entirely fair. It is observed that the estimate of Lee et al. [80] is softer and closer to the experimental results than the other two estimates up a strain near $\overline{\varepsilon}_e = 1$. However, shortly after this value the model of Lee et al. [80] predicts a strong macroscopic hardening, leading to a significant deviation from the experimental data. On the other hand, the LCC estimate and the estimate of Nikolov et al. [110] are in a good qualitative agreement with each other as well as with the experimental results in the entire range of deformations considered. The estimate of Nikolov et al. [110] is softer and in slightly better agreement with the experimental data than the LCC estimate. Comparing the results of Fig. 4.20 with the corresponding results of Fig. 4.7, we observe that the response of HDPE under tension is qualitatively similar to that under compression, but the material is significantly stiffer under tension than under compression.

In analogy with the results of Fig. 4.8 for the morphological texture evolution under uniaxial compression, Figure 4.21 shows the evolution of the aspect ratios of the distributional ellipsoid

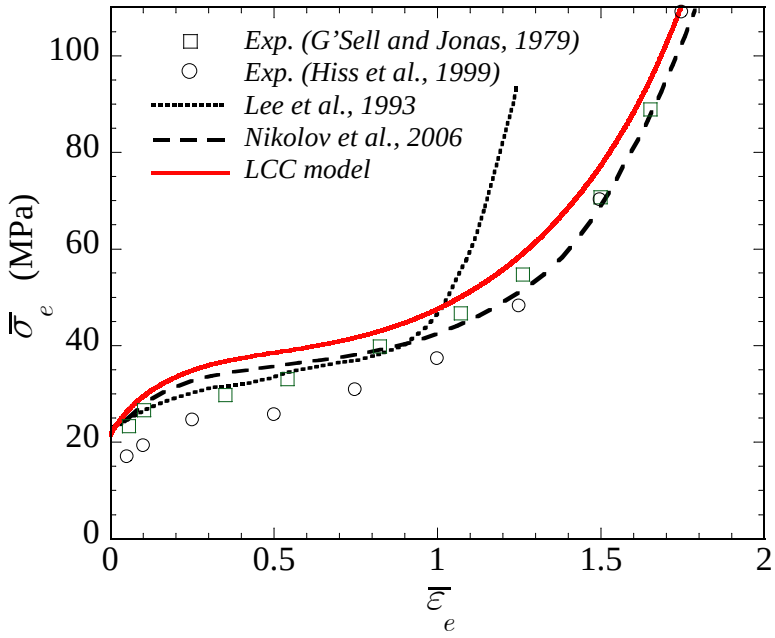

Figure 4.20: Macroscopic response of HDPE under uniaxial tension at a constant deformation rate $\overline{D}_{33} = 10^{-3}s^{-1}$. Comparison of the LCC estimate (4.80), the estimate of Lee et al. [80] and the estimate of Nikolov et al. [110] with the experimental results of G'Sell and Jonas [46] and Hiss et al. [54]. The applied equivalent stress measure $\overline{\sigma}_e$ is plotted as a function of the applied equivalent strain measure $\overline{\varepsilon}_e$, with $\overline{\sigma}_e$ and $\overline{\varepsilon}_e$ defined by $(4.112)_1$ and $(4.112)_2$, respectively.

(4.8) for uniaxial tension, as predicted by the LCC model. Once again, results are presented both for the 500-grain system of Fig. 4.3 and for a refined 1000-grain system. The aspect ratios $w_{\max}$ and $w_{\min}$ shown in Fig. 4.21 are in this case defined by

$$w_{\max} = \frac{\overline{\lambda}_3}{\overline{\lambda}_{\max}}, \qquad w_{\min} = \frac{\overline{\lambda}_3}{\overline{\lambda}_{\min}}, \tag{4.116}$$

where we recall that $\overline{\lambda}_{\max}$ and $\overline{\lambda}_{\min}$ are respectively the maximum and minimum macroscopic stretches in the plane normal to the loading axis $\mathbf{e}_3$ and $\overline{\lambda}_3$ is the corresponding stretch along $\mathbf{e}_3$. It is also recalled that the difference between $w_{\max}$ and $w_{\min}$ provides a measure for the deviation of the material response from perfectly transversely isotropic behavior corresponding to $w_{\max} = w_{\min} = \mathrm{Exp}[3\overline{\varepsilon}_e/2]$ and represented in Fig. 4.21 with the continuous, thin line. We observe that the difference between $w_{\max}$ and $w_{\min}$ is negligible up to a strain value $\overline{\varepsilon}_e = 1$, after which it becomes somewhat more evident and increases with increasing strain. Similar to the case of uniaxial compression, the difference between $w_{\max}$ and $w_{\min}$ for the 1000-grain system (dotted, thin curves) is smaller than the corresponding difference for the 500-grain system (continuous, thick curves), suggesting once again that the deviation of the material response from transverse isotropy

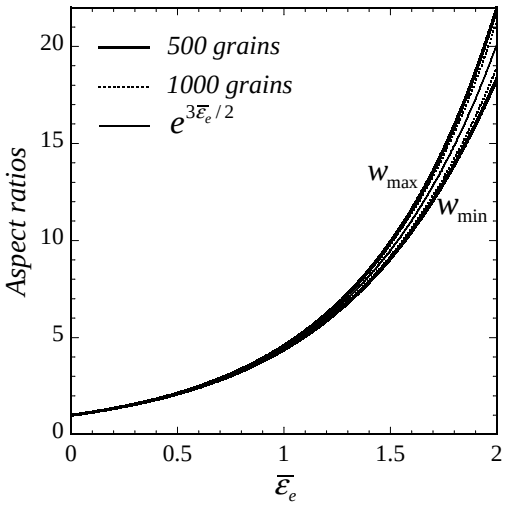

Figure 4.21: Morphological texture evolution in HDPE under uniaxial tension as predicted by the LCC model. The maximum $w_{\max}$ and minimum $w_{\min}$ aspect ratios of the distributional ellipsoid (4.8), defined respectively by $(4.116)_1$ and $(4.116)_2$, are plotted as functions of the applied equivalent strain $\overline{\varepsilon}_e$. Results are shown both for the 500-grain system of Fig. 4.3 and also for a refined 1000-grain system. For comparison, the aspect ratio $w_{\max} = w_{\min} = \text{Exp}[3\overline{\varepsilon}_e/2]$ corresponding to a perfectly transversely isotropic material is also shown.

at large strains is probably due to the corresponding deviation of the undeformed specimen from the isotropic behavior.

Figure 4.22 shows the stereographic projection representations of the lamellar normals $\mathbf{n}^{(r)}$ at the applied strain values $\overline{\varepsilon}_e = 0.4$, $\overline{\varepsilon}_e = 0.8$, $\overline{\varepsilon}_e = 1.3$ and $\overline{\varepsilon}_e = 2.1$, as predicted by the LCC model. In contrast with the uniaxial compression case, here we observe that the lamellar normals $\mathbf{n}^{(r)}$ rotate monotonically towards the radial direction with increasing strain $\overline{\varepsilon}_e$. This evolution of the normals $\mathbf{n}^{(r)}$ leads progressively to configurations corresponding to stiffer deformation modes for the laminates. Note, in particular, that at $\overline{\varepsilon}_e = 2.1$ the lamination orientations $\mathbf{n}^{(r)}$ are practically perpendicular to the tensile direction. In this configuration, the laminates are expected to exhibit their stiffest possible response (Taylor-type). Hence, similar to uniaxial compression, the lamellar texture evolution is expected to have a stiffening effect on the overall response of HDPE under uniaxial tension at large strains. Taking into account that the rotation of the laminates takes place through interlamellar shear, the predicted evolution of the normals $\mathbf{n}^{(r)}$ is consistent with physical experience.

Next, we consider the predictions of the LCC model for the crystallographic texture evolution. Figure 4.23 shows the stereographic projection representations of the (001), (100) and (010) plane poles—i.e., the $\mathbf{c}^{(r)}$, $\mathbf{a}^{(r)}$ and $\mathbf{b}^{(r)}$ crystallographic axes, respectively—as well as the {011} plane

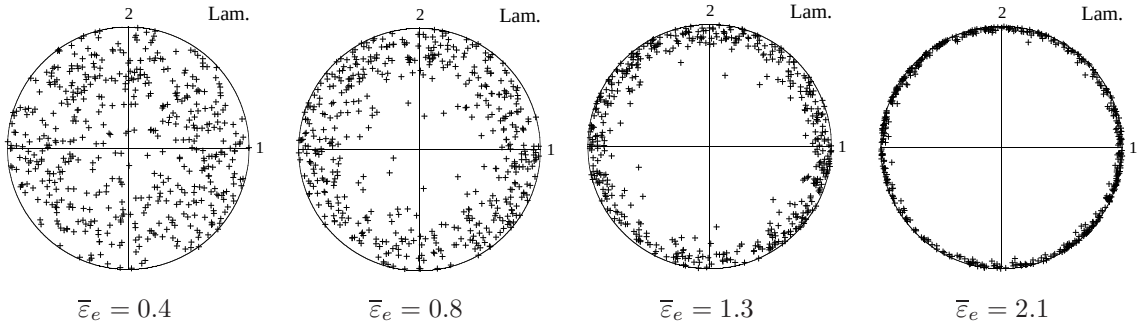

Figure 4.22: Lamellar texture evolution in HDPE under uniaxial tension as predicted by the LCC model. Stereographic projection figures of the lamination orientations $\mathbf{n}^{(r)}$ are shown at various values of the applied equivalent strain $\overline{\varepsilon}_e$. The direction of tension is along the 3−axis.

poles at the applied strain values $\overline{\varepsilon}_e = 0.4$, $\overline{\varepsilon}_e = 0.8$, $\overline{\varepsilon}_e = 1.3$ and $\overline{\varepsilon}_e = 2.1$. We observe the gradual development of a very strong texture component formed through an intense rotation of the $\mathbf{c}^{(r)}$ axes towards the loading direction $\mathbf{e}_3$ combined with a corresponding rotation of the $\mathbf{a}^{(r)}$ and $\mathbf{b}^{(r)}$ axes towards the radial direction. Note, in particular, that at $\overline{\varepsilon}_e = 2.1$ the $\mathbf{c}^{(r)}$ axes are almost perfectly aligned with the tensile axis $\mathbf{e}_3$. The formation of this texture suggests that the dominant deformation mechanism in the associated crystals is chain slip, since the rotation of the chain axes $\mathbf{c}^{(r)}$—in addition to any possible contribution from the rotation of the lamination orientations $\mathbf{n}^{(r)}$ (Fig. 4.22)—takes place through crystallographic chain slip. Another interesting observation from Fig. 4.23 is that the maximum of the strong texture component of the $\{011\}$ plane poles is aligned with the tensile axis $\mathbf{e}_3$ at $\overline{\varepsilon}_e = 0.4$ and $\overline{\varepsilon}_e = 0.8$, but it is tilted slightly away from it at $\overline{\varepsilon}_e = 1.3$ and at the strain level $\overline{\varepsilon}_e = 2.1$ it forms an angle approximately 20^o with $\mathbf{e}_3$.

From Fig. 4.23 we also observe the development of a second texture component, which is much weaker than the one discussed above. This texture consists of a small fraction of crystals whose chain axes $\mathbf{c}^{(r)}$ remain practically fixed throughout the deformation at an orientation nearly perpendicular to the loading axis $\mathbf{e}_3$, presumably because the associated resolved shear stresses are not sufficient to activate chain slip. The $\mathbf{b}^{(r)}$ and $\mathbf{a}^{(r)}$ axes of these crystals rotate respectively towards and away the loading axis, which in turn suggests that the dominant deformation mechanism in these crystals is (100)[010] transverse slip. In particular, at the strain level $\overline{\varepsilon}_e = 2.1$ we observe that the $\mathbf{b}^{(r)}$ and $\mathbf{a}^{(r)}$ axes are oriented at 25^o and 65^o, respectively, with respect to the loading direction $\mathbf{e}_3$.

Figure 4.24 reproduces the experimentally determined (Li et al. [83]) crystallographic texture in a specimen of HDPE subjected to uniaxial tension up to a strain value $\overline{\varepsilon}_e = 2.1$. The relevant stereographic projections of the (001), (100) and (010) plane poles in both the undeformed and deformed, after relaxation, sample are shown. It is emphasized that the undeformed specimen of

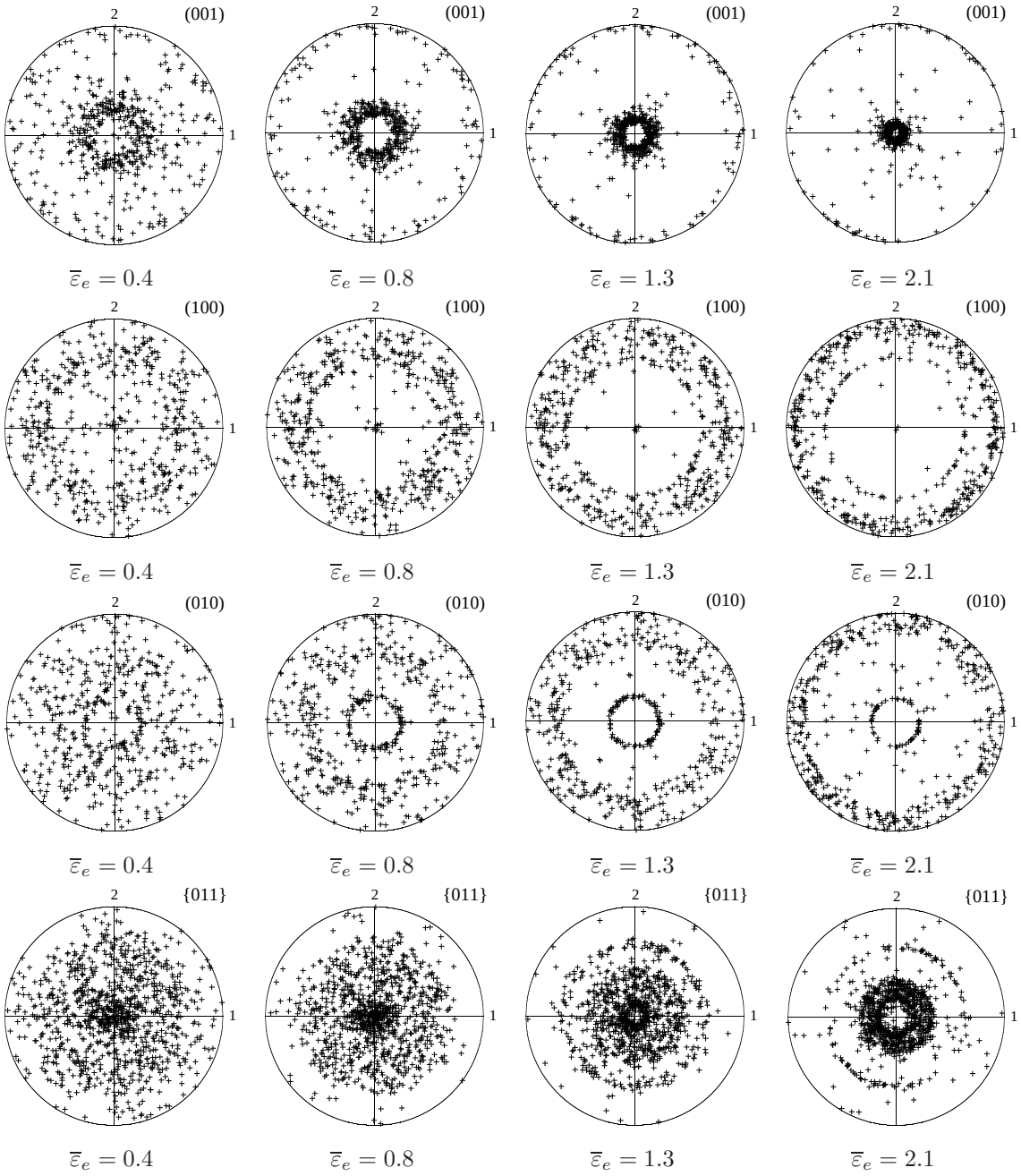

Figure 4.23: Crystallographic texture evolution in HDPE under uniaxial tension as predicted by the LCC model. Stereographic projection figures of the (001), (100), (010) and {011} plane poles are shown at various values of the applied equivalent strain $\overline{\varepsilon}_e$. The direction of tension is along the 3−axis.

Fig. 4.24 is strongly textured and, therefore, a quantitative comparison of these results with the corresponding LCC predictions of Fig. 4.23 is not entirely appropriate. The dominant feature of

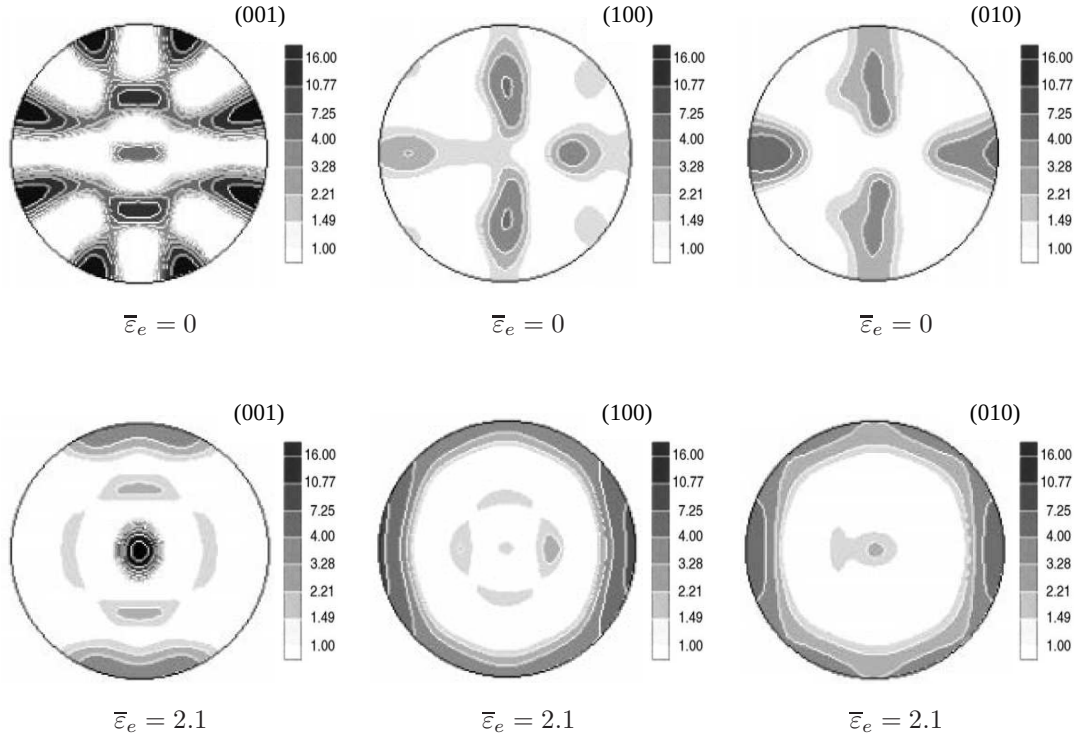

Figure 4.24: Crystallographic texture in the HDPE specimen used by Li et al. [83] in their uniaxial tension test. The corresponding stereographic projection figures of the (001), (100) and (010) plane poles are shown in the undeformed and deformed to $\overline{\varepsilon}_e = 2.1$ sample, after relaxation. The direction of tension is normal to the plane shown.

the results of Fig. 4.24 is the formation of a very strong texture component in which the $\mathbf{c}^{(r)}$-axes are almost perfectly aligned with the tensile axis (normal to the pole figures) and the $\mathbf{a}^{(r)}$- and $\mathbf{b}^{(r)}$-axes are oriented towards the radial direction. From Fig. 4.23, it is recalled that this texture component is also the dominant feature of the corresponding crystalographic texture evolution predicted be the LCC model. As reported by Li et al. [83], their results show, in addition, the formation of a weaker texture component—in which the axes $\mathbf{c}^{(r)}$, $\mathbf{a}^{(r)}$ and $\mathbf{b}^{(r)}$ are respective oriented at about 25^o, 90^o and 65^o with respect to the loading axis—as well as an even weaker component—in which the axes $\mathbf{b}^{(r)}$ are aligned and $\mathbf{c}^{(r)}$, $\mathbf{a}^{(r)}$ are normal to the tensile axis. The weaker texture components may be due to the initial texture of the material. These later textures are not predicted by the LCC estimate.

The evolution of the strong crystallographic texture component discussed above is expected to have a significant hardening effect on the overall response of the composite. This becomes

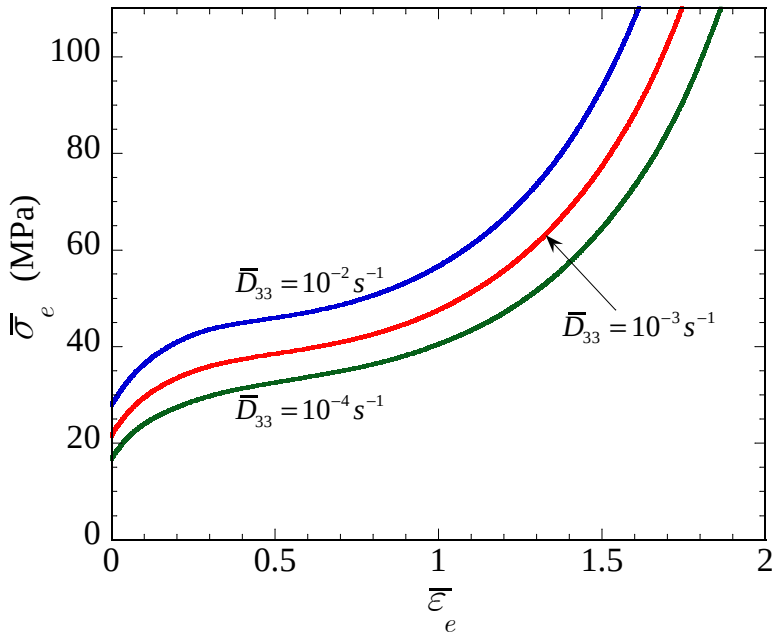

Figure 4.25: The effect of the deformation rate $\overline{D}_{33}$ on the LCC estimate (4.80) for the macroscopic response of HDPE under uniaxial tension. The applied equivalent stress $\overline{\sigma}_e$ is plotted as a function of the applied equivalent strain $\overline{\varepsilon}_e$ for $\overline{D}_{33} = 10^{-4} s^{-1}$, $\overline{D}_{33} = 10^{-3} s^{-1}$ and $\overline{D}_{33} = 10^{-2} s^{-1}$.

immediately obvious by taking into account the rotation of the chain axes $\mathbf{c}^{(r)}$ towards the tensile direction with increasing strain and recalling that the $\mathbf{c}^{(r)}$ axes correspond to an inextensible direction for the crystals. This observation is probably the main reason for which the macroscopic response of a HDPE material under tension is much stiffer than its response under compression (compare Figs. 4.20 and 4.7).

Finally, we consider the effect of the applied applied deformation rate $\overline{D}_{33}$ on the macroscopic response of HDPE under uniaxial tenstion, as predicted by the LCC model (4.80). Fig. 4.25 shows results for the cases $\overline{D}_{33} = 10^{-2} s^{-1}$, $\overline{D}_{33} = 10^{-3} s^{-1}$ and $\overline{D}_{33} = 10^{-4} s^{-1}$. Once again, we observe that increasing the deformation rate $\overline{D}_{33}$ results in a stiffer macroscopic response for the composite. This observation in consistent with corresponding experimental findings (see, e.g., G'Sell and Jonas [46], Hiss et al. [54]).

4.6 Concluding remarks

In this chapter we have developed a constitutive model for the macroscopic response and texture evolution of semi-crystalline polymers under general finite strain loading histories. In the context of this model, the semi-crystalline polymer is idealized as a two-scale composite with a granular

meso-structure and a lamellar micro-structure, incorporating fine sub-structural information at both length-scales. The constitutive behavior of both the crystalline and the amorphous phase is characterized by means of viscoplastic models. It is important to emphasize, however, that the effect elastic strains in the amorphous material is also accounted for by means of a back-stress model. The instantaneous effective behavior of this material has been determined by means of the "linear comparison composite" (LCC) methods, introduced in the context of more general two-scale viscoplastic systems in chapter 2. Specifically, the LCC estimate for the semi-crystalline polymer has been derived by employing a "secant" type of linearization for the amorphous phase (subsection 2.6.1) and a "generalized-secant" type of linearization (subsection 2.8.1) for the crystalline phase. The effective behavior of the associated two-scale LCC is determined sequentially by making combined use of the well-suited self-consistent estimate for the granular meso-structure and the well-known exact solution for the lamellar (grain) micro-structure. As a byproduct of these homogenization estimates for the LCC, we generated corresponding estimates for the associated grain- and phase-average deformation rate and spin tensors, which were in turn used to establish appropriate evolution laws for the internal variables of the semi-crystalline polymer.

Applications on "high-density polyethylene" (HDPE) materials were considered in great detail. Based on the experimental results of Bartczak et al. [10] for the uniaxial compression test of HDPE, we argued that the micro-mechanical mechanism responsible for the intense macroscopic hardening of the material at large strains is the hardening of the crystalline phase due to the Coulomb effect (Bartczak et al. [8]) on the critical resolve shear stresses (CRSSs) of the crystals. To the best of our knowledge, this interpretation is novel and of crucial importance in modeling the constitutive behavior of the crystalline phase. In passing, it is remarked, in the context of earlier theoretical works such as the models proposed by Lee et al. [80] and Nikolov et al. [110], that it has been implicitly assumed that the underlying mechanism for the macroscopic hardening of HDPE under compressive loadings is the hardening of the amorphous material. The use of the Coulomb yield criterion (4.109) for the CRSSs requires consideration of a non-associative constitutive relation for the crystalline phase. Unfortunately, the LCC model proposed here—and, more generally, the LCC methods of chapter 2—are restricted to associative constitutive models for the phases. These observations motivated our prescription of the strain-hardening relation (4.77) for the CRSSs in the context of the LCC model. This prescription is by no means equivalent to the Coulomb yield criterion (4.109), but it has the advantage of attributing the aforementioned hardening behavior at large strains to the corresponding hardening of the crystalline phase, which is an important difference between our model and the models of Lee et al. [80] and Nikolov et al. [110].

The predictions of the LCC model for the macroscopic response and texture evolution in HDPE were confronted with corresponding experimental results and compared with the associated predictions of the models of Lee et al. [80] and Nikolov et al. [110] for uniaxial compression, simple shear

and uniaxial tension loading conditions. The LCC estimates were found to be in a good agreement with the experimental results for all loadings and to improve, in some cases significantly, over the predictions of the earlier models.

4.7 Appendix I. Numerical aspects

In this appendix, we discuss the numerical algorithms used in computing the LCC model predictions of this chapter for the macroscopic response and texture evolution of semi-crystalline polymers. As already mentioned in the main body of the text, the computation of the LCC model for any given finite deformation loading process is performed incrementally from the initial to the final state of the body. Therefore, for the purpose of the present discussion it suffices to restrict our consideration to a generic time increment $[t_m, t_m + \Delta t]$, with m being a nonnegative integer, during an arbitrary finite strain loading history. The increment Δt may be chosen to be different for different values of m. Note that the special case $m = 0$ corresponds to the reference configuration of the body (Figs. 4.1(a) and 4.1(b)). Within the increment $[t_m, t_m + \Delta t]$, we consider the numerical treatment of two problems: (i) the computation of the instantaneous effective constitutive relation (4.80) at $t = t_m$ and (ii) the integration of the evolution laws of section 4.3 for the internal variables (4.32) over the increment $[t_m, t_m + \Delta t]$. The later problem allows updating the state of the underlying sub-structure at the end of the increment $(t = t_m + \Delta t)$, which is in turn used as input in the corresponding calculations at the beginning of the next increment, i.e., at time $t = t_{m+1}$. In this connection, it is remarked that the sub-structure at $t = t_0$, corresponding to the reference configuration (Figs. 4.1(a) and 4.1(b)), is assumed to be known (see subsection 4.5.1). Hence, the values of the internal variables (4.32) at $t = t_m$ are assumed to be known in the context of problem (i) and to provide the initial conditions in the context of problem (ii). At this point, it should be emphasized that both problems (i) and (ii) are highly nonlinear and, therefore, they must be treated numerically. In passing, it is remarked that the numerical procedures described below determine also the effective stress-potential (4.52) of the semi-crystalline polymer at time $t = t_m$. Furthermore, appropriately modified versions of these procedures have been used in the calculations of the LCC estimates of chapter 5 for two-scale polycrystalline metals.

Instantaneous effective response at time $t = t_m$. Recall that the LCC relation (4.80) determines any combination of five independent components of the macroscopic deformation rate tensor $\overline{\mathbf{D}}$ and the deviatoric stress tensor $\overline{\boldsymbol{\sigma}}_d$ of the semi-crystalline polymer in terms of the remanning five components of these tensors, which are prescribed through the boundary conditions. In turn, the use of the LCC relation (4.80) requires the computation of the local and effective properties of the associated two-scale LCC. Specifically, the quantities that have to be determined

in the context of the LCC model (4.80) are: (i) the scalar phase-moduli $\alpha_k^{(r)}$ and $\lambda^{(r)}$, (ii) the stress-phase-average tensors $\overline{\boldsymbol{\sigma}}^{(r,c)}$ and $\overline{\boldsymbol{\sigma}}^{(r,a)}$, (iii) the stress-phase-fluctuation variables $\hat{\tau}_k^{(r,c)}$ and $\hat{\tau}^{(r,a)}$, (iv) the stress-grain-average tensors $\overline{\boldsymbol{\sigma}}^{(r)}$, (v) the effective-grain properties $\mathbf{M}^{(r)}$, $\boldsymbol{\alpha}^{(r)}$ and $\phi^{(r)}$ and (vi) the overall properties $\widetilde{\mathbf{M}}$, $\widetilde{\boldsymbol{\alpha}}$ and $\tilde{\phi}$ of the two-scale LCC. The quantities $\hat{\tau}_k^{(r,c)}$, $\hat{\tau}^{(r,a)}$, $\mathbf{M}^{(r)}$, $\boldsymbol{\alpha}^{(r)}$, $\phi^{(r)}$, $\widetilde{\boldsymbol{\alpha}}$ and $\tilde{\phi}$ are given explicitly by means of the expressions (4.54), (4.55), (4.101), (4.82), (4.83), $(4.81)_1$ and $(4.81)_2$, respectively, in terms of the variables

$$\{\alpha_k^{(r)}, \lambda^{(r)}, \overline{\boldsymbol{\sigma}}^{(r,c)}, \overline{\boldsymbol{\sigma}}^{(r,a)}, \overline{\boldsymbol{\sigma}}^{(r)}, \widetilde{\mathbf{M}}\}, \tag{4.117}$$

which are, therefore, chosen as the principal unknowns of the problem. These variables are determined by means of the system of equations

$$\{(4.44), (4.45), (4.94), (4.95), (4.96), (4.53)_2, (4.87)\}, \tag{4.118}$$

which, as already mentioned, is nonlinear and must be treated numerically.

The system of equations (4.118) is solved in this work by means of an algorithm consisting of four nested iterative procedures. In these procedures, the values of the variables (4.117) at $t = t_{m-1}$, with $m \geq 1$—obtained by solving equations (4.118) for $t = t_{m-1}$ in the previous increment—is used as an initial guess for the calculations at $t = t_m$. The prescription of the initial guess for $t = t_0$, i.e., in the reference configuration, is discussed further below. In the innermost procedure, the moduli of the crystalline $\alpha_k^{(r)}$ and the amorphous $\lambda^{(r)}$ phase in each grain $r = 1, ..., N$ of the LCC are held fixed and the system of equations (4.94), (4.95) and (4.96) is solved for the corresponding stress-phase-average tensors $\overline{\boldsymbol{\sigma}}^{(r,c)}$ and $\overline{\boldsymbol{\sigma}}^{(r,a)}$. From the relevant discussion of subsection 4.4.2, it is recalled that the equations (4.94), (4.95) and (4.96) may be reduced to the system of three scalar equations (4.96) for any three independent components of the stress-phase-average tensors $\overline{\boldsymbol{\sigma}}_d^{(r,c)}$ and $\overline{\boldsymbol{\sigma}}_d^{(r,a)}$, with the equations (4.94) and (4.95) providing explicit expressions for the computation of the remanning unknown components of $\overline{\boldsymbol{\sigma}}^{(r,c)}$ and $\overline{\boldsymbol{\sigma}}^{(r,a)}$. The system of equations (4.96) is nonlinear, but it can be easily solved numerically by means of Newton's method.

The two intermediate iterative procedures compute successively the effective modulus tensor $\widetilde{\mathbf{M}}$ and the stress-grain-average tensors $\overline{\boldsymbol{\sigma}}^{(r)}$. These calculations are performed by means of the "viscoplastic self-consistent" (VPSC) software, which is a Fortran code developed by C.N. Tomé and R.A. Lebensohn at the "Los Alamos National Laboratory" and it has been provided to us by R.A. Lebensohn. The core component of the VPSC code is a quite efficient solver which, making use of the fixed-point method, computes iteratively the self-consistent estimate (4.87) for the effective modulus tensor $\widetilde{\mathbf{M}}$ of a granular composite with arbitrary but fixed values of the associated grain modulus tensors $\mathbf{M}^{(r)}$. For a given value of $\widetilde{\mathbf{M}}$, the VPSC code then employs the fixed-point method once again in computing iteratively the estimate $(4.53)_2$ for the stress-grain-average tensors $\overline{\boldsymbol{\sigma}}^{(r)}$.

Finally, the outermost iterative procedure applies the fixed-point method to the equations (4.44) and (4.45), and—using the results of the previous procedures—computes the phase-moduli variables $\alpha_k^{(r)}$ and $\lambda^{(r)}$. It should be remarked that this procedure involves the computation of the second-moment tensors $\langle \boldsymbol{\sigma} \otimes \boldsymbol{\sigma} \rangle^{(r,p)}$ in the amorphous ($p = a$) and crystalline ($p = c$) phases of the LCC, given by (4.84), which in turn requires the calculation of the second-moment tensors $\langle \boldsymbol{\sigma} \otimes \boldsymbol{\sigma} \rangle^{(r)}$ in the grains. The computation of the later quantities is quite involved and it is performed by employing an appropriate subroutine that is available in the VPSC package, following a procedure proposed by Liu and Ponte Castañeda [86].

As already mentioned, in the above algorithm the initial guess for the variables (4.117) at time $t = t_m$ for $m \geq 1$ is chosen to be the solution of the equations (4.118) at time $t = t_{m-1}$. However, in the case of the first increment ($t = t_0$), corresponding to the reference configuration, this option is not available. Given the fact that the system of equations (4.118) are highly nonlinear, it is very difficult to make a good initial guess for this case. In order to obtain the required initial estimate for the variables (4.117) in the reference configuration, we solve the system of equations (4.118), as discussed above, for increasing values of the nonlinearity exponent n from $n = 1$ to $n = 9$ with a step Δn. This approach has the advantage that the case $n = 1$ corresponds to a linear elastic composite for which an initial guess can be easily found, while for any higher value of $n = 1 + m\Delta n$, with m being a positive integer, the solution for $n = 1 + (m-1)\Delta n$ can be used as an initial guess. Specifically, for $n = 1$ the phase-moduli are given by $\alpha_k^{(r)} = \gamma_0/\tau_{0k}$ and $\lambda^{(r)} = \tau_0/(2\,\gamma_0)$ for all $r = 1, ..., N$, where γ_0 is the reference strain rate while τ_{0k} and τ_0 are the associated reference stresses, given in subsection 4.5.1. Hence, the corresponding phase modulus tensors $\mathbf{M}^{(r,c)}$ and $\mathbf{M}^{(r,a)}$ are constant and the associated effective-grain tensors $\mathbf{M}^{(r)}$ may be readily obtained from (4.101). The Taylor estimate $\widetilde{\mathbf{M}} = [\sum_{r=1}^{N} c^r (\mathbf{M}^{(r)})^{-1}]^{-1}$ turns out to be a good initial guess for the effective modulus tensor for $n = 1$. Making use of this estimate for $\widetilde{\mathbf{M}}$, corresponding estimates for the stress-grain-average tensors $\overline{\boldsymbol{\sigma}}^{(r)}$ and the stress-phase-average tensors $\overline{\boldsymbol{\sigma}}^{(r,p)}$ ($p = a, c$) may be readily obtained from the expressions $(4.53)_2$ and $(4.53)_1$, respectively.

Evolution of the internal variables (4.32) over the time increment $[t_m, t_m + \Delta t]$. It is recalled once again that the evolution laws of section 4.3 are highly nonlinear and, therefore, their integration over the time increment $[t_m, t_m + \Delta t]$ can only be performed numerically.

Direct integration of the evolution equations (4.61) for the aspect ratios w_α ($\alpha = 1, 2$) of the shape tensor $\mathbf{Z}$ by employing a forward Euler scheme yields the result

$$w_\alpha(t_{m+1}) = w_\alpha(t_m) + \left[w_\alpha \left(\mathbf{z}_3 \otimes \mathbf{z}_3 - \mathbf{z}_\alpha \otimes \mathbf{z}_\alpha \right) \cdot \overline{\mathbf{D}} \right]_{t=t_m} \Delta t, \tag{4.119}$$

where the notation $t_{m+1} = t_m + \Delta t$ has been introduced and it is recalled that $\mathbf{z}_i$ ($i = 1, 2, 3$) denote the principal vectors of $\mathbf{Z}$.

The forward Euler scheme may also be used in integrating the evolution laws (4.62) for the principal vectors $\mathbf{z}_i$ of $\mathbf{Z}$. However, such an approximation has the disadvantage that the resulting vector $\mathbf{z}_i(t_{m+1})$ does *not* have unit length (see, e.g., [5]). For this reason, following Aravas and Ponte Castañeda [5], we approximate the evolution equation (4.62) in the time interval $t_m \leq t \leq t_m + \Delta t$ by

$$\dot{\mathbf{z}}_i(t) = \overline{\omega}_{\mathbf{z}}(t_m)\mathbf{z}_i(t), \tag{4.120}$$

where the spin tensor $\overline{\omega}_{\mathbf{z}}(t_m)$ may be readily obtained from (4.63) by making use of the results for the effective instantaneous response of the composite at time $t = t_m$, discussed earlier. The above equation may be integrated exactly, yielding the result

$$\mathbf{z}_i(t_{m+1}) = \exp\left[\overline{\omega}_{\mathbf{z}}(t_m)\Delta t\right]\mathbf{z}_i(t_m), \tag{4.121}$$

where it should be recalled that the exponential of an anti-symmetric tensor $\mathbf{A}$ is given by

$$\exp\left[\mathbf{A}\right] = \mathbf{I} + \frac{\sin a}{a}\mathbf{A} + \frac{1-\cos a}{a^2}\mathbf{A}^2, \tag{4.122}$$

with $a = \sqrt{\mathbf{A}\cdot\mathbf{A}/2}$ standing for the magnitude of $\mathbf{A}$. Making use of (4.122), it can be easily shown that $\mathbf{z}_i(t_{m+1})$ given by (4.121) is indeed a unit vector.

The evolution laws $(4.67)_1$ and (4.69) for the lamellar normals $\mathbf{n}^{(r)}$ and the lattice vectors $\mathbf{a}^{(r)}$, $\mathbf{b}^{(r)}$, $\mathbf{c}^{(r)}$, respectively, are integrated by following the same approach as in the case of the vectors $\mathbf{z}_i$. The results read as follows

$$\mathbf{n}^{(r)}(t_{m+1}) = \exp\left[\overline{\omega}^{(r)}_{\mathbf{n}}(t_m)\Delta t\right]\mathbf{n}^{(r)}(t_m), \tag{4.123}$$

where the spin $\overline{\omega}^{(r)}_{\mathbf{n}}(t_m)$ of the lamellar grains is given by $(4.67)_2$, and

$$\begin{aligned}
\mathbf{a}^{(r)}(t_{m+1}) &= \exp\left[\overline{\omega}^{(r)}_{\mathbf{c}}(t_m)\Delta t\right]\mathbf{a}^{(r)}(t_m),\\
\mathbf{b}^{(r)}(t_{m+1}) &= \exp\left[\overline{\omega}^{(r)}_{\mathbf{c}}(t_m)\Delta t\right]\mathbf{b}^{(r)}(t_m),\\
\mathbf{c}^{(r)}(t_{m+1}) &= \exp\left[\overline{\omega}^{(r)}_{\mathbf{c}}(t_m)\Delta t\right]\mathbf{c}^{(r)}(t_m),
\end{aligned} \tag{4.124}$$

where the lattice spin $\overline{\omega}^{(r)}_{\mathbf{c}}(t_m)$ is obtained from (4.70).

The evolution equations (4.74) for the back-stress tensors $\mathbf{T}^{(r)}_d$ are integrated by means of the forward Euler scheme, leading to

$$\begin{aligned}
\mathbf{T}^{(r)}_d(t_{m+1}) =& \mathbf{T}^{(r)}_d(t_m) + \{\frac{g^{(r)}_{II}\mathbf{T}^{(r)}_d\cdot\overline{\mathbf{D}}^{(r,a)}}{(g^{(r)}_I)^2}\mathbf{T}^{(r)}_d + \frac{2}{3}\left[\left(2I^{(r)}g^{(r)}_I\right)\overline{\mathbf{D}}^{(r,a)} - \left(\mathbf{T}^{(r)}_d\cdot\overline{\mathbf{D}}^{(r,a)}\right)\mathbf{I}\right]\\
&+ \left(\overline{\mathbf{D}}^{(r,a)}\mathbf{T}^{(r)}_d + \mathbf{T}^{(r)}_d\overline{\mathbf{D}}^{(r,a)}\right) + \left(\overline{\mathbf{W}}^{(r,a)}\mathbf{T}^{(r)}_d - \mathbf{T}^{(r)}_d\overline{\mathbf{W}}^{(r,a)}\right)\}_{t=t_m}\Delta t,
\end{aligned} \tag{4.125}$$

where it is recalled that $g^{(r)}_I(t_m)$ and $g^{(r)}_{II}(t_m)$ denote respectively the first and second derivative of the stored-energy function (4.16) with respect to the invariant I, evaluated at $t = t_m$, and that the variable $I^{(r)}(t_m)$, $\overline{\mathbf{D}}^{(r,a)}$ and $\overline{\mathbf{W}}^{(r,a)}$ are obtained from (4.19), (4.86) and (4.99), respectively.

Finally, recall that the critical resolved shear stresses (CRSSs) $\tau_{0k}^{(r,c)}(t_{m+1})$ in the slip systems of the crystalline phase within grain r are completely determined in terms of the associated deformation measure $\overline{\Gamma}^{(r,c)}(t_{m+1})$ by means of the expression (4.77). In turn, given $\overline{\Gamma}^{(r,c)}(t_m)$, the computation of the quantity $\overline{\Gamma}^{(r,c)}(t_{m+1})$ requires the numerical evaluation of the integral (4.126). Assuming that the average shear rates $\dot{\overline{\gamma}}_k^{(r,c)}(t)$ in the corresponding phase of the LCC are constant during the time increment $t_m \leq t \leq t_m + \Delta t$ and equal to its value at $t = t_m$, equation (4.126) yields the result

$$\overline{\Gamma}^{(r,c)}(t_{m+1}) = \overline{\Gamma}^{(r,c)}(t_m) + \sum_{k=1}^{K} \dot{\overline{\gamma}}_k^{(r,c)}(t_m)\Delta t. \tag{4.126}$$

4.8 Appendix II. Material frame indifference

This appendix demonstrates that the constitutive relations developed in this work for the finite-strain effective response of semi-crystalline polymers are consistent with the principle of "material frame indifference" or "objectivity", i.e., the requirement that *constitutive equations must be invariant under changes of frame of reference*.

The present discussion refers to the *homogenized* material and employs the terminology used in the classical treatise of Truesdell and Noll [144]. The terms "frame of reference" and "observer" have the same meaning. Tensorial quantities referred to a "fixed" frame are distinguished from the corresponding quantities referred to another arbitrary frame by an asterisk (*) attached in the superscript of the later. A material point $\overline{\mathbf{x}}$ in the deformed configuration of the body and its image $\overline{\mathbf{x}}^*$ under a general change of observer are related by the rigid transformation

$$\overline{\mathbf{x}}^* = \overline{\mathbf{c}} + \overline{\mathbf{Q}}\overline{\mathbf{x}}, \tag{4.127}$$

where $\overline{\mathbf{c}}$ is a translation vector and $\overline{\mathbf{Q}}$ is a rotation tensor. In the above relation, for simplicity, the dependence of $\overline{\mathbf{x}}^*$, $\overline{\mathbf{x}}$, $\overline{\mathbf{c}}$ and $\overline{\mathbf{Q}}$ on time t has not been expressed explicitly, and the same is true for the dependence of the deformation fields $\overline{\mathbf{x}}^*$ and $\overline{\mathbf{x}}$ on the corresponding material points $\overline{\mathbf{X}}^*$ and $\overline{\mathbf{X}}$, respectively, in the undeformed configuration of the body. The term *frame-indifferent* or *objective* is used to characterize any quantity which transforms according to certain rules under a change of frame. In the case of a scalar $\overline{s}$, a vector $\overline{\mathbf{v}}$, a second-order tensor $\overline{\mathbf{T}}$ and a forth-order tensor $\overline{\mathbf{L}}$, these rules are

$$\overline{s}^* = \overline{s}, \qquad \overline{\mathbf{v}}^* = \overline{\mathbf{Q}}\overline{\mathbf{v}}, \qquad \overline{\mathbf{T}}^* = \overline{\mathbf{Q}}\,\overline{\mathbf{T}}\,\overline{\mathbf{Q}}^T, \qquad \overline{L}^*_{ijkl} = \overline{Q}_{ip}\overline{Q}_{jq}\overline{Q}_{kr}\overline{Q}_{ls}\overline{L}_{pqrs}, \tag{4.128}$$

where in the last expression it is understood that the components of all three tensors $\overline{\mathbf{L}}^*$, $\overline{\mathbf{L}}$ and $\overline{\mathbf{Q}}$ are expressed in the same coordinate system. Mathematical entities describing a physical quantity in the deformation process of the body, such as a material volume or a material line element, must

be objective and, therefore, relations of the type (4.128) serve as criteria in distinguishing objective quantities from variables whose values depend inherently on the specific frame of reference. For example, it can be easily shown that the velocity field $\dot{\overline{\mathbf{x}}}$ does *not* transform according to $(4.128)_2$. On the other hand, the deformation rate $\overline{\mathbf{D}}$ and the Cauchy stress $\overline{\boldsymbol{\sigma}}$ tensors are objective, i.e.,

$$\overline{\mathbf{D}}^* = \overline{\mathbf{Q}}\,\overline{\mathbf{D}}\,\overline{\mathbf{Q}}^T, \qquad \overline{\boldsymbol{\sigma}}^* = \overline{\mathbf{Q}}\,\overline{\boldsymbol{\sigma}}\,\overline{\mathbf{Q}}^T, \tag{4.129}$$

where $(4.129)_1$ follows from (4.127), while $(4.129)_2$ is obtained by assuming that the traction vector associated with $\overline{\boldsymbol{\sigma}}$ is objective. The left stretch tensor $\overline{\mathbf{V}}$ from the polar decomposition of the applied deformation gradient $\overline{\mathbf{F}} = \overline{\mathbf{V}}\,\overline{\mathbf{R}}$, associated with the deformation field $\overline{\mathbf{x}}$, is another example of an objective second-order tensor. It is recalled that, although material time derivatives of objective tensors (except of scalars) are not objective, the corresponding co-rotational derivatives are objective. For example, it can be easily shown that the Jaumann (co-rotational with the macroscopic spin $\overline{\mathbf{W}}$) time derivative of an objective vector $\overline{\mathbf{v}}$ and an objective second-order tensor $\overline{\mathbf{T}}$, defined respectively by

$$\overset{\triangledown}{\overline{\mathbf{v}}} = \dot{\overline{\mathbf{v}}} - \overline{\mathbf{W}}\overline{\mathbf{v}} \qquad \text{and} \qquad \overset{\triangledown}{\overline{\mathbf{T}}} = \dot{\overline{\mathbf{T}}} + \overline{\mathbf{T}}\,\overline{\mathbf{W}} - \overline{\mathbf{W}}\,\overline{\mathbf{T}}, \tag{4.130}$$

are an objective vector and an objective second-order tensor, respectively.

Making use of the above definitions in the present context, the principle of material frame indifference may be formally stated as follows: if the constitutive equation (4.29) for the semi-crystalline polymer is satisfied for a pair $\{\overline{\mathbf{D}}, \overline{\boldsymbol{\sigma}}\}$, then it must be satisfied also for any other pair $\{\overline{\mathbf{D}}^*, \overline{\boldsymbol{\sigma}}^*\}$ associated with $\{\overline{\mathbf{D}}, \overline{\boldsymbol{\sigma}}\}$ by means of (4.129), for all rotation tensors $\overline{\mathbf{Q}}$. To this end, it suffices to show that the estimate (4.52) for the effective stress potential $\tilde{u}$ of the semi-crystalline polymer is an objective scalar function of its arguments, i.e.,

$$\begin{aligned}
&\tilde{u}\left(\overline{\boldsymbol{\sigma}}; w_\alpha, \mathbf{z}_i, \mathbf{n}^{(r)}, \mathbf{a}^{(r)}, \mathbf{b}^{(r)}, \mathbf{c}^{(r)}, \mathbf{T}_d^{(r)}, \tau_{0k}^{(r,c)}\right) = \\
&\tilde{u}\left(\overline{\mathbf{Q}}\,\overline{\boldsymbol{\sigma}}\,\overline{\mathbf{Q}}^T; w_\alpha, \overline{\mathbf{Q}}\mathbf{z}_i, \overline{\mathbf{Q}}\mathbf{n}^{(r)}, \overline{\mathbf{Q}}\mathbf{a}^{(r)}, \overline{\mathbf{Q}}\mathbf{b}^{(r)}, \overline{\mathbf{Q}}\mathbf{c}^{(r)}, \overline{\mathbf{Q}}\,\mathbf{T}_d^{(r)}\,\overline{\mathbf{Q}}^T, \tau_{0k}^{(r,c)}\right),
\end{aligned} \tag{4.131}$$

where the dependence of $\tilde{u}$ on the internal variables (4.32) has been emphasized. In this connection, it is recalled that w_α and $\mathbf{z}_i$ denote respectively the aspect ratios and the principal directions of the shape tensor $\mathbf{Z}$, defining the distribution symmetry of the grain-families, $\mathbf{n}^{(r)}$ stand for the unit vectors normal to the layers of the lamellar grains, $\mathbf{a}^{(r)}$, $\mathbf{b}^{(r)}$ and $\mathbf{c}^{(r)}$ are the lattice vectors of the crystals in the grains, $\mathbf{T}_d^{(r)}$ are the back-stress tensors in the corresponding amorphous parts of the grains and $\tau_{0k}^{(r,c)}$ are the critical resolved shear stresses (CRSSs) in the crystalline parts of the grains. These variables define the internal state of the material and must be objective tensors at any time t during a finite strain loading history. At time $t = 0$, corresponding to the reference configuration, the internal variables (4.32) are objective by definition. For any other instant t,

the objectivity of these variables can be shown by showing the material frame indifference of the associated evolution laws of section 4.3, from which they are determined. In other words, in addition to (4.131), it has to be shown that if the evolution equations

$$\{(4.61),(4.64),(4.68)_1,(4.72),(4.75),(4.77)\}, \tag{4.132}$$

are satisfied for the set of variables

$$\{\overline{\mathbf{D}},\overline{\boldsymbol{\sigma}};w_\alpha,\mathbf{z}_i,\mathbf{n}^{(r)},\mathbf{a}^{(r)},\mathbf{b}^{(r)},\mathbf{c}^{(r)},\mathbf{T}_d^{(r)},\tau_{0k}^{(r,c)}\}, \tag{4.133}$$

then, they must also be satisfied by the set of variables

$$\{\overline{\mathbf{Q}}\,\overline{\mathbf{D}}\,\overline{\mathbf{Q}}^T,\overline{\mathbf{Q}}\,\overline{\boldsymbol{\sigma}}\,\overline{\mathbf{Q}}^T;w_\alpha,\overline{\mathbf{Q}}\mathbf{z}_i,\overline{\mathbf{Q}}\mathbf{n}^{(r)},\overline{\mathbf{Q}}\mathbf{a}^{(r)},\overline{\mathbf{Q}}\mathbf{b}^{(r)},\overline{\mathbf{Q}}\mathbf{c}^{(r)},\overline{\mathbf{Q}}\,\mathbf{T}_d^{(r)}\,\overline{\mathbf{Q}}^T,\tau_{0k}^{(r,c)}\}. \tag{4.134}$$

Notice that the objectivity of the evolution equations (4.61) and (4.64) for w_α and $\mathbf{z}_i$, respectively, follows immediately by substituting (4.134) in these expressions. Alternatively, the objectivity of the variables w_α and $\mathbf{z}_i$ may also be established from the objectivity of the associated shape tensor $\mathbf{Z}$, which in this work has been identified with $\overline{\mathbf{V}}$.

Given that the estimate (4.52) for $\tilde{u}$ depends on the internal variables (4.32) and the applied stress $\overline{\boldsymbol{\sigma}}$ only through its dependence on the phase-fluctuation variables $\hat{\tau}_k^{(r,c)}$ and $\hat{\tau}^{(r,a)}$ and the phase-average variables $\overline{\tau}_k^{(r,c)}$, in order to show that (4.131) holds it suffices to show that the later quantities are objective scalar functions of their arguments. This, in turn, requires showing that the local and effective properties of the associated LCC—in terms of which $\hat{\tau}_k^{(r,c)}$, $\hat{\tau}^{(r,a)}$ and $\overline{\tau}_k^{(r,c)}$ are completely determined—are objective quantities. To this end, it is recalled from the relevant discussion of the previous appendix that the quantities $\hat{\tau}_k^{(r,c)}$, $\hat{\tau}^{(r,a)}$ and $\overline{\tau}_k^{(r,c)}$ may be explicitly written in terms of the set of variables (4.117), which are in turn determined as the solution to the system of equations (4.118). In passing, it is remarked that the objectivity of the variables $\overline{\tau}_k^{(r,c)}$ guaranties the objectivity of the associated CRSSs $\tau_{0k}^{(r,c)}$, which are completely determined by (4.77), with (4.126), in terms of $\overline{\tau}_k^{(r,c)}$. Recall also that the set of variables (4.117) consists of the scalar phase-moduli $\alpha_k^{(r)}$ and $\lambda^{(r)}$, the stress-phase-average tensors $\overline{\boldsymbol{\sigma}}^{(r,c)}$ and $\overline{\boldsymbol{\sigma}}^{(r,a)}$, the stress-grain-average tensors $\overline{\boldsymbol{\sigma}}^{(r)}$ and the effective modulus tensor $\widetilde{\mathbf{M}}$ of the two-scale LCC. Thus, the prof of (4.131) reduces in showing that if the system of equations

$$\{(4.44),(4.45),(4.94),(4.95),(4.96),(4.53)_2,(4.87)\}, \tag{4.135}$$

is satisfied for the set of variables

$$\{\overline{\boldsymbol{\sigma}};w_\alpha,\mathbf{z}_i,\mathbf{n}^{(r)},\mathbf{a}^{(r)},\mathbf{b}^{(r)},\mathbf{c}^{(r)},\mathbf{T}_d^{(r)},\tau_{0k}^{(r,c)};\alpha_k^{(r)},\lambda^{(r)},\overline{\boldsymbol{\sigma}}^{(r,c)},\overline{\boldsymbol{\sigma}}^{(r,a)},\overline{\boldsymbol{\sigma}}^{(r)},\widetilde{\mathbf{M}}\}, \tag{4.136}$$

then, they must also be satisfied by the set of variables

$$\begin{aligned}&\{\overline{\mathbf{Q}}\,\overline{\boldsymbol{\sigma}}\,\overline{\mathbf{Q}}^T;w_\alpha,\overline{\mathbf{Q}}\mathbf{z}_i,\overline{\mathbf{Q}}\mathbf{n}^{(r)},\overline{\mathbf{Q}}\mathbf{a}^{(r)},\overline{\mathbf{Q}}\mathbf{b}^{(r)},\overline{\mathbf{Q}}\mathbf{c}^{(r)},\overline{\mathbf{Q}}\,\mathbf{T}_d^{(r)}\,\overline{\mathbf{Q}}^T,\tau_{0k}^{(r,c)};\\&\alpha_k^{(r)},\lambda^{(r)},\overline{\mathbf{Q}}\,\overline{\boldsymbol{\sigma}}^{(r,c)}\overline{\mathbf{Q}}^T,\overline{\mathbf{Q}}\,\overline{\boldsymbol{\sigma}}^{(r,a)}\overline{\mathbf{Q}}^T,\overline{\mathbf{Q}}\,\overline{\boldsymbol{\sigma}}^{(r)}\overline{\mathbf{Q}}^T,\widetilde{\mathbf{M}}^*\},\end{aligned} \tag{4.137}$$

where $\widetilde{\mathbf{M}}^*$ is related to $\widetilde{\mathbf{M}}$ by $(4.128)_4$. The later statement may be readily shown by substituting (4.137) into (4.135) and taking into account the following properties of objective vectors $\overline{\mathbf{u}}$ and $\overline{\mathbf{v}}$, second-order tensors $\overline{\mathbf{S}}$ and $\overline{\mathbf{T}}$ and forth-order tensor $\overline{\mathbf{L}}$ and $\overline{\mathbf{M}}$:

$$\begin{aligned}
&\overline{\mathbf{u}}^* + \overline{\mathbf{v}}^* = \overline{\mathbf{Q}}(\overline{\mathbf{u}} + \overline{\mathbf{v}}), \quad \overline{\mathbf{u}}^* \cdot \overline{\mathbf{v}}^* = \overline{\mathbf{u}} \cdot \overline{\mathbf{v}},\\
&\overline{\mathbf{S}}^* + \overline{\mathbf{T}}^* = \overline{\mathbf{Q}}(\overline{\mathbf{S}} + \overline{\mathbf{T}})\overline{\mathbf{Q}}^T, \quad \overline{\mathbf{S}}^*\overline{\mathbf{T}}^* = \overline{\mathbf{Q}}(\overline{\mathbf{S}}\,\overline{\mathbf{T}})\overline{\mathbf{Q}}^T, \quad \overline{\mathbf{T}}^{*-1} = \overline{\mathbf{Q}}(\overline{\mathbf{T}}^{-1})\overline{\mathbf{Q}}^T, \quad \overline{\mathbf{T}}^*\overline{\mathbf{v}}^* = \overline{\mathbf{Q}}(\overline{\mathbf{T}}\overline{\mathbf{v}}),\\
&\overline{L}^*_{ijkl} + \overline{M}^*_{ijkl} = \overline{Q}_{ip}\overline{Q}_{jq}\overline{Q}_{kr}\overline{Q}_{ls}(\overline{\mathbf{L}} + \overline{\mathbf{M}})_{pqrs}, \quad \overline{L}^*_{ijmn}\overline{M}^*_{mnkl} = \overline{Q}_{ip}\overline{Q}_{jq}\overline{Q}_{kr}\overline{Q}_{ls}(\overline{\mathbf{L}}\,\overline{\mathbf{M}})_{pqrs},\\
&\overline{L}^{*-1}_{ijkl} = \overline{Q}_{ip}\overline{Q}_{jq}\overline{Q}_{kr}\overline{Q}_{ls}\overline{L}^{-1}_{pqrs}, \quad \overline{\mathbf{L}}^*\overline{\mathbf{T}}^* = \overline{\mathbf{Q}}(\overline{\mathbf{L}}\overline{\mathbf{T}})\overline{\mathbf{Q}}^T,
\end{aligned} \tag{4.138}$$

which follow directly from the definitions (4.128). In this context, it is remarked that the objectivity of the tensors $\widetilde{\mathbf{M}}$ and $\mathbf{Z}$ imply that the sub-structural tensors $\widetilde{\mathbf{P}}$ and $\widetilde{\mathbf{R}}$, defined respectively by $(4.88)_2$ and (4.92), are objective forth-order tensors. It is emphasized that the invariance of the equations (4.135) under the transformations (4.137) implies that the quantities (4.117) are objective. Making use of this fact together with the properties (4.138) of objective tensors, it can be easily shown that the effective-grain properties $\mathbf{M}^{(r)}$, $\boldsymbol{\alpha}^{(r)}$, $\phi^{(r)}$, and the overall properties $\widetilde{\boldsymbol{\alpha}}$ and $\tilde{\phi}$ of the two-scale LCC—given respectively by (4.101), (4.82), (4.83), $(4.81)_1$ and $(4.81)_2$—are also objective tensors. Similarly, from equations $(4.86)_1$, $(4.86)_2$ and (4.98) it respectively follows that the phase-average deformation rate tensors $\overline{\mathbf{D}}^{(r,p)}$, the grain-average deformation rate tensors $\overline{\mathbf{D}}^{(r)}$ and the jump vectors $\mathbf{d}^{(r)}$ at the lamellar interfaces are objective quantities. Furthermore, since both the effective modulus tensor $\widetilde{\mathbf{M}}$ and the effective thermal strain tensor $\widetilde{\boldsymbol{\alpha}}$ are objective, it follows that the constitutive relation (4.80) for the LCC is objective.

Finally, given the above results, the objectivity of the evolution equations $(4.68)_1$, (4.72) and (4.75) may be easily established. Since the left-hand-sides in everyone of these expressions are objective tensors (as the Jaummann derivatives of objective tensors) it suffices to show that the corresponding right-hand-sides are also objective tensors (of the same order). The later requirement follows immediately by taking into account the objectivity of the tensors $\widetilde{\mathbf{P}}$, $\widetilde{\mathbf{R}}$ and $\overline{\mathbf{D}}^{(r)}$ in the context of $(4.68)_1$; $\widetilde{\mathbf{P}}$, $\widetilde{\mathbf{R}}$, $\overline{\mathbf{D}}^{(r)}$ and $\mathbf{d}^{(r)}$ in the context of (4.72); $\widetilde{\mathbf{P}}$, $\widetilde{\mathbf{R}}$, $\overline{\mathbf{D}}^{(r)}$, $\mathbf{d}^{(r)}$ and $\overline{\mathbf{D}}^{(r,a)}$ in the context of (4.75). In the case of (4.75) it should also be remarked that the scalar functions $g_I^{(r)}$, $g_{II}^{(r)}$ and $I^{(r)}$ are invariant, and therefore objective, under the transformation (4.134). This is because the variables $I^{(r)}$ are determined from the corresponding equations (4.19) as functions of the principal values $t_i^{(r)}$ of the associated back-stress tensors $\mathbf{T}_d^{(r)}$ only, which are the same for $\mathbf{T}_d^{(r)}$ and $\overline{\mathbf{Q}}\,\mathbf{T}_d^{(r)}\,\overline{\mathbf{Q}}^T$.

Chapter 5

Applications to two-scale polycrystals

In this chapter, we consider applications of the theory developed in chapter 2 to two-scale polycrystals. In particular, we focus our attention on two-scale composite systems which, at the meso-scale level, are aggregates of composite-grains that, at the micro-scale level, have an underlying lamellar structure consisting of alternating layers of two different viscoplastic single-crystal-grains. The instantaneous effective response of these polycrystals is determined by means of the "direct linearization scheme" (DLS) "generalized-secant second-order" (GSO) estimate (2.160), which, for simplicity, will be referred to in this chapter as the "second-order estimate" (SOE). Recall that the SOE (2.160) has been derived in subsection 2.8.1 for composite-grains with more general micro-morphologies and made out of an arbitrary number of single-crystal-grains. The effective properties of the two-scale "linear comparison composite" (LCC), entering the calculation of the SOE (2.160), are in turn obtained though the sequential homogenization procedure (see subsection 2.4.2), involving the well-known exact solution for the effective behavior of the laminates in each composite-grain and then making use of the self-consistent estimate for the granular system at the larger length-scale. In order to account for finite strain loading histories, evolution laws are established for the sub-structural variables in the two-scale polycrystal based on standard kinematical arguments and making use of appropriate estimates for the averages of the deformation rate and spin tensor fields over the composite-grains and the single-crystal-grains of the LCC. This framework is subsequently used to compute the *instantaneous plastic anisotropy* of a textured specimen of γ-TiAl-based polysynthetically twinned (PST) alloy (Lebensohn et al. [79], Lebensohn [73]) and the *crystallographic texture* developed in an initially un-textured $(\alpha+\beta)$ Ti alloy under rolling conditions. The predictions of the SOE for these two problems are found to be in a reasonably good agreement with corresponding experimental results available from the literature.

The material of this chapter is organized as follows. In section 5.1 we define the sub-structure and the local constitutive relations for the single-crystal-grains in the two-scale polycrystal. In section 5.2 we specialize the SOE (2.160) to the material system of interest here and recall some

of its basic features. In section 5.3 we develop constitutive equations for the evolution of the underlying sub-structure. The aforementioned applications to γ-TiAl-based PST alloys and $(\alpha+\beta)$ Ti alloys are presented in sections 5.4 and 5.5, respectively. Finally, in section 5.6 we provide some concluding remarks.

At this point, it should be remarked that the two-scale LCC involved in the estimates for the two-scale polycrystals of this chapter is characterized by the same sub-structure as the two-scale LCC used in the context of the corresponding estimates for semi-crystalline polymers considered in chapter 4. Therefore, the effective properties of these LCCs are determined from the same general expressions, with the understanding that the appropriate local properties have to be used in each case. Given the special interest of this thesis on semi-crystalline polymers, the relevant discussion on the computation of the effective properties of these LCCs has been provided in section 4.4 of chapter 4. Furthermore, the corresponding discussions on the numerical treatment and the material frame indifference of the associated nonlinear estimates for semi-crystalline polymers, provided respectively in appendixes I and II of chapter 4, can also be easily adapted in the present context.

5.1 Preliminary definitions

In this section, we define the sub-structure and the constitutive behavior of the single-crystals in the two-scale polycrystalline material, determining the associated SOE (2.160) for the instantaneous effective response of this composite. It is important to realize, however, that when a polycrystal is subjected to a finite strain loading history the underlying sub-structure evolves in time. Fig. 5.1 shows the transformation of the sub-structure in a two-scale polycrystal from the reference (Parts (a) and (b)) to the current (Parts (c) and (d)) configuration due to an arbitrary macroscopic deformation gradient $\overline{\mathbf{F}}(t)$ applied on its boundary. In the reference configuration the sub-structure of the polycrystal is assumed to be known. At any other instant t during a finite deformation process the sub-structure is determined through an incremental procedure (starting from the reference configuration), with each increment involving the integration of the associated sub-structural evolution laws developed in section 5.3. All physical quantities involved in the present discussion refer to the current configuration of the body (Parts (c) and (d) in Fig. 5.1). Note that this includes the reference configuration as the special case $t = 0$.

5.1.1 Sub-structural characterization

Consider the representative volume element (RVE) Ω of a two-scale polycrystal in the current configuration shown in Parts (c) and (d) of Fig. 5.1. Fig. 5.1(c) shows the meso-structure of

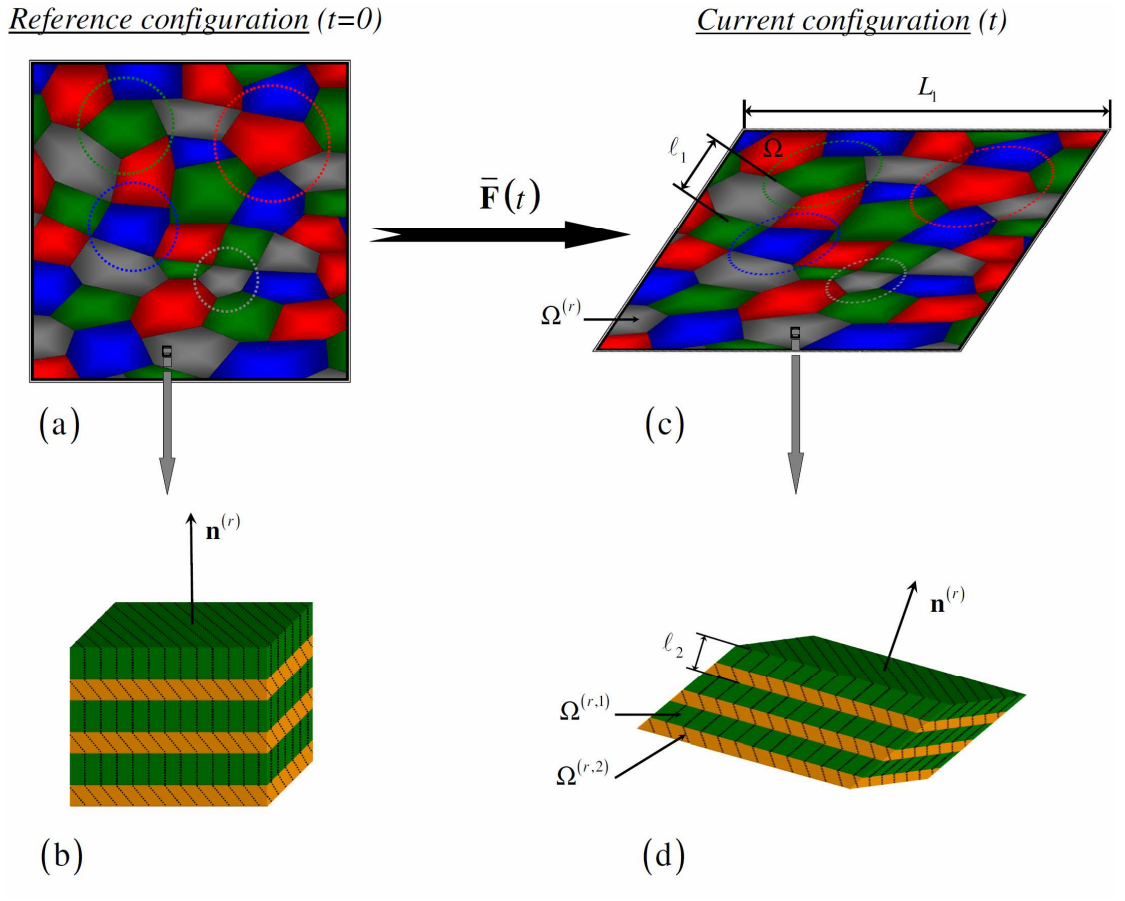

Figure 5.1: Schematic illustration of the mapping of a two-scale polycrystal from the reference (Parts (a) and (b)) to the current (Parts (c) and (d)) configuration during an arbitrary finite deformation process prescribed through the macroscopic deformation gradient $\overline{\mathbf{F}}(t)$, with t standing for the time variable. At the meso-structural level (Parts (a) and (c)), the material consists of a large number N of composite-grain-families distributed randomly with *ellipsoidal* symmetry (dotted ellipses in Parts (a) and (c)), the specific features of which change from the reference to the current configuration. At the micro-structural level (Parts (b) and (d)), the composite-grains have a lamellar structure consisting of alternating layers of two different single-crystal-grains; both the orientation of the lamellar grains—defined by the vectors $\mathbf{n}^{(r)}$ normal to the layers—and the orientation of the crystals evolve in time.

this material, consisting of a large number N of randomly distributed and perfectly bonded grain-families, with the grain-family r ($r = 1, ..., N$) occupying the subregion $\Omega^{(r)}$ of Ω. The term grain-family is used here to describe the set of all grains with identical underlying micro-structure and material properties. Fig. 5.1(d) shows the micro-structure within a grain of the type r, which is taken to be a perfect laminate with lamination orientation $\mathbf{n}^{(r)}$ and composed of perfectly

bonded, alternating layers of two different single-crystals occupying respectively the sub-regions $\Omega^{(r,p)}$, with $p = 1, 2$. The characteristic length-scales L_1, ℓ_1 and ℓ_2 in Fig. 5.1 stand respectively for the size of the RVE Ω, the size of a typical grain and the distance between two neighboring single-crystal layers of the same type. These quantities are assumed to be well-separated, i.e.,

$$\ell_2 << \ell_1 << L_1. \tag{5.1}$$

The sub-structure of the two-scale system of Figs. 5.1(c) and 5.1(d) is defined by means of the two-scale characteristic functions

$$\tilde{\chi}^{(r,p)}(\mathbf{x}) = \begin{cases} 1, & \text{if } \mathbf{x} \in \Omega^{(r,p)} \\ 0, & \text{otherwise} \end{cases}, \tag{5.2}$$

where it is emphasized that $\tilde{\chi}^{(r,p)}$ contain information both at the meso-structural (Fig. 5.1(c)) and at the micro-structural (Fig. 5.1(d)) level. Next, we consider the decomposition (2.17) of the functions $\tilde{\chi}^{(r,p)}$ into the corresponding single-scale mesoscopic $\chi^{(r)}$ and microscopic $\chi^{(r,p)}$ characteristic functions, i.e.,

$$\tilde{\chi}^{(r,p)}(\mathbf{x}) = \chi^{(r)}(\mathbf{x})\chi^{(r,p)}(\mathbf{x}), \tag{5.3}$$

where $\chi^{(r)}$ and $\chi^{(r,p)}$ are defined by

$$\chi^{(r)}(\mathbf{x}) = \begin{cases} 1, & \text{if } \mathbf{x} \in \Omega^{(r)} \\ 0, & \text{otherwise} \end{cases}, \qquad \chi^{(r,p)}(\mathbf{x}) = \begin{cases} 1, & \text{if } \mathbf{x} \in \Omega^{(r,p)} \\ 0, & \text{otherwise} \end{cases}, \tag{5.4}$$

and satisfy the relations

$$\sum_{r=1}^{N} \chi^{(r)}(\mathbf{x}) = 1, \qquad \chi^{(r,1)}(\mathbf{x}) + \chi^{(r,2)}(\mathbf{x}) = 1. \tag{5.5}$$

Note that the spatial variation of the functions $\chi^{(r,p)}$ for the single-crystals is restricted along the lamination direction $\mathbf{n}^{(r)}$.

Since the composite material under consideration is random, the characteristic functions $\tilde{\chi}^{(r,p)}$ are expected to be known in terms of the associated multi-point probability functions. In this regard, following the discussion of subsection 2.1.2 (see also Smyshlyaev and Willis [136]), it is assumed that the meso-structure (defined by $\chi^{(r)}$) and the micro-structure (defined by $\chi^{(r,p)}$) of the two-scale composite of Fig. 5.1 are *statistically independent*. An important implication of this assumption is that the two-scale multi-point probability functions associated with $\tilde{\chi}^{(r,p)}$ are completely determined in terms of the corresponding single-scale multi-point probability functions associated with $\chi^{(r)}$ and $\chi^{(r,p)}$ (e.g., see relations (2.22) and (2.23)). Furthermore, we assume that the characteristic functions $\chi^{(r)}$ and $\chi^{(r,p)}$ are *statistically uniform*, *ergodic* and possess *no long-range order*. From subsections 2.1.2 and 2.1.1, we recall that the later assumptions imply that

the one-point probability functions $p^{(r)}$ $(r = 1, ..., N)$ and $p^{(r,p)}$ $(p = a, c)$, associated respectively with $\chi^{(r)}$ and $\chi^{(r,p)}$, reduce to

$$p^{(r)}(\mathbf{x}) = \frac{|\Omega^{(r)}|}{|\Omega|} \equiv c^{(r)}, \qquad p^{(r,p)}(\mathbf{x}) = \frac{|\Omega^{(r,p)}|}{|\Omega^{(r)}|} \equiv c^{(r,p)}, \tag{5.6}$$

where $c^{(r)}$ denotes the volume fraction of the grain-family r in the RVE Ω and $c^{(r,p)}$ is the volume fraction of the single-crystal p $(p = 1, 2)$ in the grain-family r. Furthermore, the corresponding two-point probability functions $p^{(rs)}$ $(r, s = 1, ..., N)$ and $p^{(r,pq)}$ $(p, q = 1, 2)$ depend on $\mathbf{x}$ and $\mathbf{x}'$ only through the vector $(\mathbf{x} - \mathbf{x}')$.

In this work, we also assume that the two-point probabilities $p^{(rs)}$ are characterized by ellipsoidal symmetry, i.e.,

$$p^{(rs)}(\mathbf{x} - \mathbf{x}') = p^{(rs)}(|\mathbf{Z}(\mathbf{x} - \mathbf{x}')|), \tag{5.7}$$

where the shape tensor $\mathbf{Z}$ in (5.7) is defined by

$$\mathbf{Z} = \overline{\lambda}_1 \mathbf{z}_1 \otimes \mathbf{z}_1 + \overline{\lambda}_2 \mathbf{z}_2 \otimes \mathbf{z}_2 + \overline{\lambda}_3 \mathbf{z}_3 \otimes \mathbf{z}_3, \tag{5.8}$$

with $\overline{\lambda}_i$ and $\mathbf{z}_i$ denoting respectively the principal values and the principal directions of $\mathbf{Z}$. As already discussed in subsection 2.1.1 (see also Willis [150]), the ellipsoidal symmetry assumption (5.7)—indicated by the dotted ellipses in Fig. 5.1(c)—accounts for a possible bias in the spatial distribution of the grain-families. This assumption is a generalization of the statistical isotropy assumption (corresponding to $\mathbf{Z} = \mathbf{I}$) implying that the composite-grains are equally distributed in all directions. For later reference, we remark at this point that the estimates for the effective behavior and texture evolution of the polycrystal discussed further below depend on $\overline{\lambda}_i$ only through the aspect ratios

$$w_1 = \frac{\overline{\lambda}_3}{\overline{\lambda}_1}, \qquad w_2 = \frac{\overline{\lambda}_3}{\overline{\lambda}_2}. \tag{5.9}$$

Finally, although the micro-structure within the lamellar grains is completely determined by means of the associated volume fractions of the crystals $c^{(r,p)}$ and the lamination orientations $\mathbf{n}^{(r)}$, it is remarked here that the shape of the underlying crystalline layers may also be regarded as the limiting case of an ellipsoid with two of its principal values tending to infinity. This may, in turn, be defined through the shape tensors

$$\mathbf{Z}^{(r)} = \mathbf{n}^{(r)} \otimes \mathbf{n}^{(r)} + \epsilon \left(\mathbf{n}_1^{(r)\perp} \otimes \mathbf{n}_1^{(r)\perp} + \mathbf{n}_2^{(r)\perp} \otimes \mathbf{n}_2^{(r)\perp} \right), \tag{5.10}$$

in the limit as $\epsilon \to \infty$, where $\mathbf{n}_1^{(r)\perp}$ and $\mathbf{n}_2^{(r)\perp}$ are unit vectors orthogonal to $\mathbf{n}^{(r)}$ and to each other.

5.1.2 Constitutive relations for the single-crystals

Each single-crystal $p = 1, 2$ (Fig. 5.1(d)) is assumed to deform plastically through crystallographic slip on a number $K^{(p)}$ of available slip systems. At this stage, we impose no restrictions on the

material symmetries of the associated crystal lattices. The constitutive behavior of the crystals within a composite-grain of the type r is assumed to be characterized by means of the following incompressible, viscoplastic stress-potential

$$u^{(r,p)}(\boldsymbol{\sigma}) = \sum_{k=1}^{K^{(p)}} \psi_k^{(r,p)}(\tau_k^{(r,p)}), \qquad \tau_k^{(r,p)} = \boldsymbol{\sigma} \cdot \boldsymbol{\mu}_k^{(r,p)}, \tag{5.11}$$

where $\psi_k^{(r,p)}$ is the slip-potential associated with the $k-th$ slip system in a crystal of the type p within a composite-grain of the type r, $\tau_k^{(r,p)}$ denotes the corresponding resolved shear stress and $\boldsymbol{\mu}_k^{(r,p)}$ is the associated symmetric Schmidt tensor, defined by

$$\boldsymbol{\mu}_k^{(r,p)} = \frac{1}{2}\left(\mathbf{s}_k^{(r,p)} \otimes \mathbf{m}_k^{(r,p)} + \mathbf{m}_k^{(r,p)} \otimes \mathbf{s}_k^{(r,p)}\right), \tag{5.12}$$

with $\mathbf{s}_k^{(r,p)}$ and $\mathbf{m}_k^{(r,p)}$ denoting the corresponding slip direction and slip plane normal vector, respectively. The slip potentials $\psi_k^{(r,p)}$ in relation $(5.11)_1$ are taken to be of the power-law form

$$\psi_k^{(r,p)}(\tau_k^{(r,p)}) = \frac{\gamma_0 \tau_k^{(r,p)}}{n+1}\left(\frac{|\tau_k^{(r,p)}|}{\tau_{0k}^{(p)}}\right)^n, \tag{5.13}$$

where γ_0 is a reference shear strain rate, n is the rate exponent and $\tau_{0k}^{(p)}$ are the associated critical resolved shear stresses. For simplicity, γ_0 and n have been chosen to be identical for all slip systems and equal in both crystals, while no hardening is assumed for $\tau_{0k}^{(p)}$. In this connection, it is emphasized that these restrictions have been motivated from the applications considered in sections 5.4 and 5.5, and that they can be easily removed.

5.2 Estimates for the instantaneous effective behavior

Next, for completeness, we recall the main features of the "second-order estimate" (SOE) (2.160) for the effective stress-potential $\tilde{u}$ of the two-scale polycrystal under consideration, derived in subsection 2.8.1.

Based on the work of Liu and Ponte Castañeda [86], the two-scale "linear comparison composite" (LCC) used in the context of the SOE (2.160) is taken to have the same sub-structure as the nonlinear two-scale polycrystal (Figs. 5.1(c) and 5.1(d))—i.e., the same characteristic functions $\chi^{(r)}$ and $\chi^{(r,p)}$—and phase-potentials (single-crystal-potentials) $u_T^{(r,p)}$, with $p = 1, 2$, given by

$$u_T^{(r,p)}(\boldsymbol{\sigma}) = \frac{1}{2}\boldsymbol{\sigma} \cdot \mathbf{M}^{(r,p)}\boldsymbol{\sigma} + \boldsymbol{\alpha}^{(r,p)} \cdot \boldsymbol{\sigma}, \tag{5.14}$$

where $\mathbf{M}^{(r,p)}$ and $\boldsymbol{\alpha}^{(r,p)}$ denote respectively the corresponding modulus and thermal strain tensors, defined by

$$\mathbf{M}^{(r,p)} = \sum_{k=1}^{K^{(p)}} \alpha_k^{(r,p)} \boldsymbol{\mu}_k^{(r,p)} \otimes \boldsymbol{\mu}_k^{(r,p)}, \qquad \boldsymbol{\alpha}^{(r,p)} = \frac{\partial u^{(r,p)}}{\partial \boldsymbol{\sigma}}(\overline{\boldsymbol{\sigma}}^{(r,p)}) - \mathbf{M}^{(r,p)}\overline{\boldsymbol{\sigma}}^{(r,p)}. \tag{5.15}$$

In the above relations, $\alpha_k^{(r,p)}$ are scalar moduli, $\overline{\tau}_k^{(r,p)} = \overline{\boldsymbol{\sigma}}^{(r,p)} \cdot \boldsymbol{\mu}_k^{(r,p)}$ and $\overline{\boldsymbol{\sigma}}^{(r,p)} \equiv \langle \boldsymbol{\sigma} \rangle^{(r,p)}$ is the average of the stress field over the single-crystal p within the composite-grain r of the LCC. The moduli $\alpha_k^{(r,p)}$ along with the corresponding fluctuation variables $\hat{\tau}_k^{(r,p)}$ over the slip systems in the single-crystals of the LCC are obtained by means of the generalized-secant conditions

$$\psi_k^{(r,p)'}(\hat{\tau}_k^{(r,p)}) - \psi_k^{(r,p)'}(\overline{\tau}_k^{(r,p)}) = \alpha_k^{(r,p)}(\hat{\tau}_k^{(r,p)} - \overline{\tau}_k^{(r,p)}), \tag{5.16}$$

together with the fluctuation equations

$$(\hat{\tau}_k^{(r,p)} - \overline{\tau}_k^{(r,p)})^2 = \langle (\tau_k^{(r,p)} - \overline{\tau}_k^{(r,p)})^2 \rangle^{(r,p)}, \tag{5.17}$$

where it is recalled that $\tau_k^{(r,p)} = \boldsymbol{\sigma} \cdot \boldsymbol{\mu}_k^{(r,p)}$ and the notation $\langle \cdot \rangle^{(r,p)}$ is being used for the average of a quantity over the single-crystal p in the grain r. It should be emphasized that equations (5.17) have multiple solutions. In this work, following Liu and Ponte Castañeda [86], we chose the branch of (5.17) based on the sign of $\overline{\tau}_k^{(r,p)}$, i.e.,

$$\hat{\tau}_k^{(r,p)} = \overline{\tau}_k^{(r,p)} + \text{sign}\left(\overline{\tau}_k^{(r,p)}\right) \sqrt{\langle (\tau_k^{(r,p)} - \overline{\tau}_k^{(r,p)})^2 \rangle^{(r,p)}}. \tag{5.18}$$

In the above expression, we have

$$\langle (\tau_k^{(r,p)} - \overline{\tau}_p^{(r,c)})^2 \rangle^{(r,p)} = \boldsymbol{\mu}_k^{(r,p)} \cdot \mathbf{C}_{\boldsymbol{\sigma}}^{(r,p)} \boldsymbol{\mu}_k^{(r,p)}, \tag{5.19}$$

where $\mathbf{C}_{\boldsymbol{\sigma}}^{(r,p)}$ denote the associated covariance tensors, defined by

$$\mathbf{C}_{\boldsymbol{\sigma}}^{(r,p)} = \langle (\boldsymbol{\sigma} - \overline{\boldsymbol{\sigma}}^{(r,p)}) \otimes (\boldsymbol{\sigma} - \overline{\boldsymbol{\sigma}}^{(r,p)}) \rangle^{(r,p)} = \langle \boldsymbol{\sigma} \otimes \boldsymbol{\sigma} \rangle^{(r,p)} - \overline{\boldsymbol{\sigma}}^{(r,p)} \otimes \overline{\boldsymbol{\sigma}}^{(r,p)}. \tag{5.20}$$

The second-moments $\langle \boldsymbol{\sigma} \otimes \boldsymbol{\sigma} \rangle^{(r,p)}$, with $p = 1, 2$, in the above expression are given by

$$\langle \boldsymbol{\sigma} \otimes \boldsymbol{\sigma} \rangle^{(r,p)} = \frac{2}{c^{(r)} c^{(r,p)}} \frac{\partial \tilde{u}_T}{\partial \mathbf{M}^{(r,p)}}, \tag{5.21}$$

where it is emphasized that the derivatives of the effective stress-potential $\tilde{u}_T$ of the LCC must be taken by holding the thermal strain tensors $\boldsymbol{\alpha}^{(r,p)}$ fixed.

The effective properties of the two-scale LCC are determined though the sequential homogenization procedure (see subsection 2.4.2), by making use of the well-known exact solution for the effective behavior of the laminates in each composite-grain and then making use of the self-consistent estimate for the granular system at the larger length-scale. The relevant details for the computation of the effective behavior of this LCC are provided in section 4.4 of chapter 4 in the context of the corresponding LCC for a semi-crystalline polymer. Note that these two LCCs differ from each other only in terms of their local properties and, therefore, the general results of section 4.4 apply in the present context as well. From the results of section 4.4, we recall here that the single-crystal average stress tensors $\overline{\boldsymbol{\sigma}}^{(r,1)}$ and $\overline{\boldsymbol{\sigma}}^{(r,2)}$ in the LCC are computed by solving

the system of algebraic equations (4.94)-(4.96), while the corresponding second-moment tensors $\langle \boldsymbol{\sigma} \otimes \boldsymbol{\sigma} \rangle^{(r,p)}$ are given by (4.84).

Finally, the instantaneous effective constitutive relation of the viscoplastic two-scale polycrystal in the current configuration (Figs. 5.1(c) and 5.1(d)), i.e., the relation between the average deformation rate $\overline{\mathbf{D}} \equiv \langle \mathbf{D} \rangle$ and the average Cauchy stress $\overline{\boldsymbol{\sigma}} \equiv \langle \boldsymbol{\sigma} \rangle$ at time t, is given by

$$\overline{\mathbf{D}} = \frac{\partial\, \tilde{u}}{\partial\, \overline{\boldsymbol{\sigma}}}, \tag{5.22}$$

where $\tilde{u}$ denotes the associated effective stress-potential for the composite which, as already mentioned, will be determined in this work by means of the estimate (2.160), i.e.,

$$\tilde{u}(\overline{\boldsymbol{\sigma}}) = \sum_{r=1}^{N} c^{(r)} \sum_{p=1}^{2} c^{(r,p)} \left\{ \sum_{k=1}^{K^{(p)}} \left[\psi_k^{(r,p)}(\hat{\tau}_k^{(r,p)}) + \frac{d\, \psi_k^{(r,p)}}{d\, \tau_k^{(r,p)}} (\overline{\tau}_k^{(r,p)})(\overline{\tau}_k^{(r,p)} - \hat{\tau}_k^{(r,p)}) \right] \right\}. \tag{5.23}$$

It is recalled that the estimate (5.23) is exact to second-order in the heterogeneity contrast and, hence, it is referred to as the second-order estimate (SOE).

At this point, it should be emphasized that the SOE (5.23) for the effective stress-potential $\tilde{u}$ of the two-scale polycrystal depends also on the values of the underlying sub-structural variables in the current configuration of the body. During a finite deformation process, these variables evolve as a result of the finite changes in the geometry of the body at large strains. Therefore, in order to account for finite strain loading histories it is necessary to develop additional constitutive equations for the evolution of the sub-structure.

5.3 Estimates for the evolution of the sub-structure

Consider an arbitrary loading history prescribed through the average velocity gradient $\overline{\mathbf{L}}(t)$, with t being the time variable. Recall that the second-order tensor $\overline{\mathbf{L}}(t)$ may be decomposed into a symmetric and an anti-symmetric part,

$$\overline{\mathbf{L}}(t) = \overline{\mathbf{D}}(t) + \overline{\mathbf{W}}(t), \tag{5.24}$$

where $\overline{\mathbf{D}}(t)$ and $\overline{\mathbf{W}}(t)$ are the corresponding average (or applied) deformation rate and spin tensor, respectively. Furthermore, it can be easily shown that the average velocity gradient tensor $\overline{\mathbf{L}}(t)$ and the associated average deformation gradient tensor $\overline{\mathbf{F}}(t)$ are related by

$$\overline{\mathbf{L}}(t) = \dot{\overline{\mathbf{F}}}(t) \overline{\mathbf{F}}^{-1}(t), \tag{5.25}$$

which is a well-known result for the case of homogeneous deformations in homogeneous bodies. Thus, given $\overline{\mathbf{L}}(t)$, the applied deformation gradient $\overline{\mathbf{F}}(t)$ may be readily determined by integration of (5.25). It should be emphasized, however, that the corresponding grain-average or

single-crystal-average quantities are *not* related by expressions of the type (5.25), in general. In other words, the grain-average and single-crystal-average deformation gradient tensors $\overline{\mathbf{F}}^{(r)}(t)$ and $\overline{\mathbf{F}}^{(r,p)}(t)$ $(p=1,2)$ can not be computed from the corresponding velocity gradient tensors $\overline{\mathbf{L}}^{(r)}(t)$ and $\overline{\mathbf{L}}^{(r,p)}(t)$, respectively. The evolution laws for the sub-structural variables of the two-scale polycrystal discussed below make use of estimates for the symmetric and anti-symmetric parts of the tensors $\overline{\mathbf{L}}^{(r)}(t)$ and $\overline{\mathbf{L}}^{(r,p)}(t)$ associated with the corresponding two-scale LCC, which are discussed in detail in section 4.4 of chapter 4.

5.3.1 Morphological texture evolution

We assume that the evolution of the distribution symmetry of the composite-grain-families in the two-scale polycrystal is governed by the applied deformation. Specifically, the tensor $\mathbf{Z}$, defined by (5.8), is taken to be identical with the left stretch tensor $\overline{\mathbf{V}}$ from the polar decomposition of the applied deformation gradient $\overline{\mathbf{F}} = \overline{\mathbf{V}}\,\overline{\mathbf{R}}$. Hence, the evolution equations for the aspect ratios w_α $(\alpha=1,2)$, defined by (5.9), and the corresponding principal directions $\mathbf{z}_i$ $(i=1,2,3)$ of $\mathbf{Z}$ are given by (see, e.g., Ogden [112])

$$\dot{w}_\alpha = w_\alpha(\mathbf{z}_3\otimes\mathbf{z}_3 - \mathbf{z}_\alpha\otimes\mathbf{z}_\alpha)\overline{\mathbf{D}}, \tag{5.26}$$

where, in the right-hand-side, no sum is implied for the repeated index α, and

$$\dot{\mathbf{z}}_i = \overline{\omega}_{\mathbf{z}}\mathbf{z}_i, \tag{5.27}$$

where $\overline{\omega}_{\mathbf{z}}$ is the spin of the macroscopic Eulerian axes (i.e., the spin of the principal axes of $\overline{\mathbf{V}}$), which is given by

$$\overline{\omega}_{\mathbf{z}} = \overline{\mathbf{W}} + \overline{\mathbf{\Omega}}_{\mathbf{z}}, \qquad \overline{\mathbf{\Omega}}_{\mathbf{z}} = \sum_{\substack{i,j=1\\ i\neq j, w_i\neq w_j}}^{3} \frac{w_i^2+w_j^2}{w_i^2-w_j^2}(\mathbf{z}_i\cdot\overline{\mathbf{D}}\mathbf{z}_j)\mathbf{z}_i\otimes\mathbf{z}_j, \tag{5.28}$$

with $w_3\equiv 1$. It should be remarked that, if any two of the aspect ratios w_i and w_j for $i\neq j$ happen to be equal, the corresponding component of $\overline{\mathbf{\Omega}}_{\mathbf{z}}$ in (5.28) is set equal to zero, while in the case that $w_1=w_2=w_3$ we have $\overline{\mathbf{\Omega}}_{\mathbf{z}}=\mathbf{0}$ (see [4] and [23]). Clearly, the evolution equation (5.27) may be recast in the invariant form

$$\overset{\triangledown}{\mathbf{z}}_i = \overline{\mathbf{\Omega}}_{\mathbf{z}}\mathbf{z}_i, \tag{5.29}$$

where the superimposed inverted triangle denotes the Jaummann (co-rotational with $\overline{\mathbf{W}}$) time derivative, defined by $\overset{\triangledown}{\mathbf{z}}_i = \dot{\mathbf{z}}_i - \overline{\mathbf{W}}\mathbf{z}_i$.

5.3.2 Lamellar texture evolution

It can be easily shown (see, e.g., Lopez-Pamies [89]) that when a simple laminate composite is subjected to a constant (average) deformation gradient $\mathbf{F}$ the associated lamination orientation

$\mathbf{N}$ in the reference configuration transforms into the corresponding orientation $\mathbf{n}$ in the current configuration according to Nanson's formula

$$\mathbf{n} = \mathbf{F}^{-T}\mathbf{N}/|\mathbf{F}^{-T}\mathbf{N}|. \tag{5.30}$$

It is remarked that the above result is purely kinematical and therefore independent of the material properties of the constituents. The rate form of the above equation may be readily obtained by taking its time derivative and using the kinematical relation (5.25) to express the time derivative of the applied deformation gradient $\mathbf{F}$ in terms of the corresponding velocity gradient $\mathbf{L}$. The result reads as follows

$$\dot{\mathbf{n}} = [\mathbf{W} - (\mathbf{D}\mathbf{n} \otimes \mathbf{n} - \mathbf{n} \otimes \mathbf{n}\mathbf{D})]\,\mathbf{n}, \tag{5.31}$$

where $\mathbf{D}$ and $\mathbf{W}$ are respectively the deformation rate and spin tensors associated with $\mathbf{L}$.

Making use of the result (5.31) and assuming that the evolution of the unit vector $\mathbf{n}^{(r)}$, defining on average the lamination orientation of the grain-family r, is governed by the associated grain-average velocity gradient $\overline{\mathbf{L}}^{(r)}$ in the LCC we obtain the following evolution law for $\mathbf{n}^{(r)}$

$$\dot{\mathbf{n}}^{(r)} = \overline{\omega}_{\mathbf{n}}^{(r)}\mathbf{n}^{(r)}, \qquad \overline{\omega}_{\mathbf{n}}^{(r)} = \overline{\mathbf{W}}^{(r)} - \left(\overline{\mathbf{D}}^{(r)}\mathbf{n}^{(r)} \otimes \mathbf{n}^{(r)} - \mathbf{n}^{(r)} \otimes \mathbf{n}^{(r)}\overline{\mathbf{D}}^{(r)}\right), \tag{5.32}$$

where the associated composite-grain-average deformation rate $\overline{\mathbf{D}}^{(r)}$ and spin $\overline{\mathbf{W}}^{(r)}$ tensors are respectively given by expressions $(4.86)_2$ and (4.91) in chapter 4. Making use of the expression (4.91) for $\overline{\mathbf{W}}^{(r)}$, the evolution equation (5.32) may be rewritten in the invariant form

$$\overset{\triangledown}{\mathbf{n}}{}^{(r)} = \overline{\mathbf{\Omega}}_{\mathbf{n}}^{(r)}\mathbf{n}^{(r)}, \qquad \overline{\mathbf{\Omega}}_{\mathbf{n}}^{(r)} = -\left[\widetilde{\mathbf{R}}\widetilde{\mathbf{P}}^{-1}\left(\overline{\mathbf{D}} - \overline{\mathbf{D}}^{(r)}\right) + \left(\overline{\mathbf{D}}^{(r)}\mathbf{n}^{(r)} \otimes \mathbf{n}^{(r)} - \mathbf{n}^{(r)} \otimes \mathbf{n}^{(r)}\overline{\mathbf{D}}^{(r)}\right)\right], \tag{5.33}$$

where it is recalled that the Jaumann derivative of $\mathbf{n}^{(r)}$ is defined by $\overset{\triangledown}{\mathbf{n}}{}^{(r)} = \dot{\mathbf{n}}^{(r)} - \overline{\mathbf{W}}\mathbf{n}^{(r)}$. Furthermore, the sub-structural tensors $\widetilde{\mathbf{P}}$ and $\widetilde{\mathbf{R}}$ in the above expression are given by $(4.88)_2$ and $(4.92)_1$, respectively.

5.3.3 Crystallographic texture evolution

The crystal p, with $p = 1, 2$, within grain-family r is assumed to rotate rigidly (on average) with a rate defined by the corresponding average lattice spin $\overline{\omega}_{\mathbf{c}}^{(r,p)}$ in the corresponding phase of the LCC. Thus, letting $\mathbf{c}_i^{(r,p)}$ be the associated principal lattice vector defining the orientation of the crystal p in a grain of the type r, we have

$$\dot{\mathbf{c}}_i^{(r,p)} = \overline{\omega}_{\mathbf{c}}^{(r,p)}\mathbf{c}_i^{(r,p)}. \tag{5.34}$$

The lattice spin $\overline{\omega}_{\mathbf{c}}^{(r,p)}$ is defined by (see Mandel [99])

$$\overline{\omega}_{\mathbf{c}}^{(r,p)} = \overline{\mathbf{W}}^{(r,p)} - \overline{\mathbf{W}}_{pl}^{(r,p)}, \tag{5.35}$$

where $\overline{\mathbf{W}}^{(r,1)}$ and $\overline{\mathbf{W}}^{(r,2)}$ are the average continuum spin tensors of the associated crystalline phases of the LCC, obtained in this work by means of the (right-hand-sides) of (4.99) and (4.100), respectively, where the quantities $c^{(r,c)}$ and $c^{(r,a)}$ must be substituted by $c^{(r,2)}$ and $c^{(r,1)}$, as appropriate. Furthermore, the quantities $\overline{\mathbf{W}}_{pl}^{(r,p)}$ in (5.35) denote the corresponding plastic spin tensors, defined by

$$\overline{\mathbf{W}}_{pl}^{(r,p)} = \sum_{k=1}^{K} \dot{\overline{\gamma}}_k^{(r,p)} \frac{1}{2} \left(\mathbf{s}_k^{(r,p)} \otimes \mathbf{m}_k^{(r,p)} - \mathbf{m}_k^{(r,p)} \otimes \mathbf{s}_k^{(r,p)} \right), \qquad \dot{\overline{\gamma}}_k^{(r,p)} = \frac{\gamma_0 \overline{\tau}_k^{(r,p)}}{\tau_{0k}^{(r,p)}} \left(\frac{|\overline{\tau}_k^{(r,p)}|}{\tau_{0k}^{(r,p)}} \right)^{n-1}, \tag{5.36}$$

where we recall that $\overline{\tau}_k^{(r,p)} = \overline{\boldsymbol{\sigma}}^{(r,p)} \cdot \boldsymbol{\mu}_k^{(r,p)}$ and the phase average stress tensors $\overline{\boldsymbol{\sigma}}^{(r,p)}$ in the LCC are determined by solving the system of equations (4.94)-(4.96), as discussed in subsection 4.4.2 of chapter 4. Taking into account expressions (4.99) and (4.100) for $\overline{\mathbf{W}}^{(r,p)}$, the evolution laws (5.34) may be rewritten in the invariant form

$$\overset{\triangledown}{\mathbf{c}}{}_i^{(r,p)} = \overline{\boldsymbol{\Omega}}_{\mathbf{c}}^{(r,p)} \mathbf{c}_i^{(r,p)}, \tag{5.37}$$

where

$$\overline{\boldsymbol{\Omega}}_{\mathbf{c}}^{(r,1)} = -\left[\widetilde{\mathbf{R}} \widetilde{\mathbf{P}}^{-1} \left(\overline{\mathbf{D}} - \overline{\mathbf{D}}^{(r)} \right) - \frac{c^{(r,2)}}{2} \left(\mathbf{d}^{(r)} \otimes \mathbf{n}^{(r)} - \mathbf{n}^{(r)} \otimes \mathbf{d}^{(r)} \right) + \overline{\mathbf{W}}_{pl}^{(r,1)} \right], \tag{5.38}$$

and

$$\overline{\boldsymbol{\Omega}}_{\mathbf{c}}^{(r,2)} = -\left[\widetilde{\mathbf{R}} \widetilde{\mathbf{P}}^{-1} \left(\overline{\mathbf{D}} - \overline{\mathbf{D}}^{(r)} \right) + \frac{c^{(r,1)}}{2} \left(\mathbf{d}^{(r)} \otimes \mathbf{n}^{(r)} - \mathbf{n}^{(r)} \otimes \mathbf{d}^{(r)} \right) + \overline{\mathbf{W}}_{pl}^{(r,2)} \right]. \tag{5.39}$$

In the above relations, it is recalled that $\mathbf{n}^{(r)}$ denotes the lamination orientation of the grain-family r and $\mathbf{d}^{(r)}$ is the velocity gradient jump vector at the corresponding lamellar interface, given by (4.98).

5.4 Plastic anisotropy of γ-TiAl-based PST alloys

In this section, we investigate the predictions of the SOE (5.23) for the instantaneous plastic anisotropy of γ-TiAl-based polysynthetically twinned (PST) alloys. In passing, it is remarked that a variety of PST alloys with different sub-structures and properties can be obtained by appropriate thermomechanical treatments (see, e.g., Bartels et al. [11]). Materials with lamellar grains may be obtained after casting or rolling processes and have the advantage of exhibiting good creep resistance. In this work, we compute the SOE (5.23) for the plastic anisotropy of the as-cast sample studied both experimentally and theoretically by Lebensohn [73]. In his analysis, Lebensohn [73] made use of the tangent self-consistent scheme of Lebensohn and Tomé [77]. Just like Lebensohn [73], in the context of our calculations (i.e., in computing the SOE (5.23)), the material parameters

Slip mode	Slip system	τ_{0k}/τ_0^{long}
Longitudinal	$(\bar{1}\bar{1}1)[1\bar{1}0]$	1
	$(\bar{1}\bar{1}1)[011]$	1
	$(\bar{1}\bar{1}1)[101]$	1
	$(\bar{1}\bar{1}1)[\bar{1}\bar{1}\bar{2}]$	1
Mixed	$(111)[1\bar{1}0]$	2.72
	$(1\bar{1}1)[011]$	2.72
	$(\bar{1}11)[101]$	2.72
Transversal	$(1\bar{1}1)[110]$	3.33
	$(\bar{1}11)[110]$	3.33
	$(\bar{1}11)[0\bar{1}1]$	3.33
	$(1\bar{1}1)[\bar{1}01]$	3.33
	$(111)[0\bar{1}1]$	3.33
	$(111)[\bar{1}01]$	3.33
	$(\bar{1}11)[\bar{1}1\bar{2}]$	3.33
	$(1\bar{1}1)[1\bar{1}\bar{2}]$	3.33
	$(111)[11\bar{2}]$	3.33

Table 5.1: The critical resolved shear stresses τ_{0k} in the (matrix and tween) PST crystals, as determined by Lebensohn et al. [79].

and the crystallographic and lamellar textures are chosen based on the relevant experimental measurements of Lebensohn et al. [79] and Lebensohn [73].

The PST crystals underlying the composite-grains of the two-scale material under consideration are fairly complex. Specifically, these crystals consist of a γ-TiAl lamellar structure (tetragonal) and a few percent of α_2-Ti_3Al lamellae (hexagonal). The γ-phase is characterized by a "six-domain" structure of twin lamellae (see, e.g., Lebensohn et al. [79]). Following Lebensohn et al. [79], in this work we neglect the α_2-phase and model a PST crystal as a "two-domain" lamellar structure consisting of a "matrix" and a "twin" γ-TiAl crystal with equal volume fractions $c^{(r,1)} = c^{(r,2)} = 0.5$, as shown schematically in Fig. 5.2(a). Note that the common plane (lamellar plane) between the matrix and the twin is the $(\bar{1}\bar{1}1)$. The critical resolved shear stresses (CRSSs) of the matrix and twin crystals in the context of the laminate model of Fig. 5.2(a) were determined by Lebensohn et al. [79] such that the instantaneous effective behavior of the laminate fits well the corresponding experimentally measured behavior of the PST crystal. These authors classified the associated crystallographic slip-systems of the matrix and twin crystals in the context of the laminate model as: (*i*) *longitudinal slip-systems*, i.e., systems with their slip planes and slip

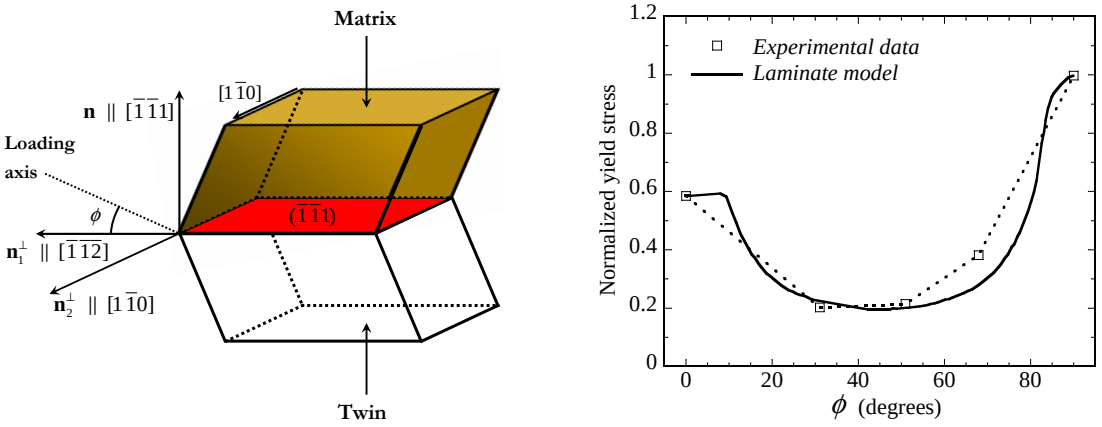

Figure 5.2: (a) The matrix-twin lamellar structure used to model a γ-TiAl PST crystal. (b) Comparison of the laminate model (Part (a)) predictions for the normalized yield stress $\widetilde{\tau}_{\phi}/\widetilde{\tau}_{90^o}$, given by 5.40, with the corresponding experimental results for a PST crystal subjected to uniaxial compression as a function of the loading angle ϕ, defined in Part (a). (Reproduced from Lebensohn et al. [79].)

directions parallel to the lamellar plane $(\bar{1}\bar{1}1)$, (*ii*) *mixed slip-systems*, i.e., systems with their slip directions parallel to the lamellar plane and their slip planes normal to it, and (*iii*) *transverse slip-systems*, i.e., systems having both their slip directions and planes normal to the lamellar plane. The CRSSs, normalized by the longitudinal CRSS τ_0^{long}, computed by Lebensohn et al. [79] are given in Table 5.1, while the comparison of the laminate model and the corresponding experimental results is shown in Fig. 5.2(b). Both the model and the actual PST material were subjected to uniaxial compressive loadings at various angles ϕ, with ϕ defined as the angle between the loading axis and the crystallographic direction $[\bar{1}\bar{1}\bar{2}]$ on the plane normal to $[1\bar{1}0]$ (see Fig. 5.2(a)), and the associated effective normalized yield stresses $\widetilde{\tau}_{\phi}/\widetilde{\tau}_{90^o}$ were measured. Given the viscoplastic constitutive behavior of the laminate model, Lebensohn et al. [79] estimated the associated normalized yield stresses by means of the (approximate) relation

$$\frac{\widetilde{\tau}_{\phi}}{\widetilde{\tau}_{90^o}} = \left(\frac{\widetilde{u}_{90^o}}{\widetilde{u}_{\phi}}\right)^{\frac{1}{n+1}}, \tag{5.40}$$

where n is the nonlinearity exponent in (5.13) and $\widetilde{u}_{\phi}$ denotes the effective stress-potential of the laminate evaluated at a uniaxial compressive stress $\overline{\sigma} = -4\tau_0^{long}$ applied along an axis defined by the angle ϕ (see Fig. 5.2(a)). The motivation behind the use of (5.40) is that in the ideally plastic limit $n \to \infty$, at least for isotropic materials, this expression is exact. For this reason, the value $n = 19$, corresponding to a relatively rate-insensitive material, has been prescribed in the power-law slip-potentials (5.13) for the matrix and twin crystals.

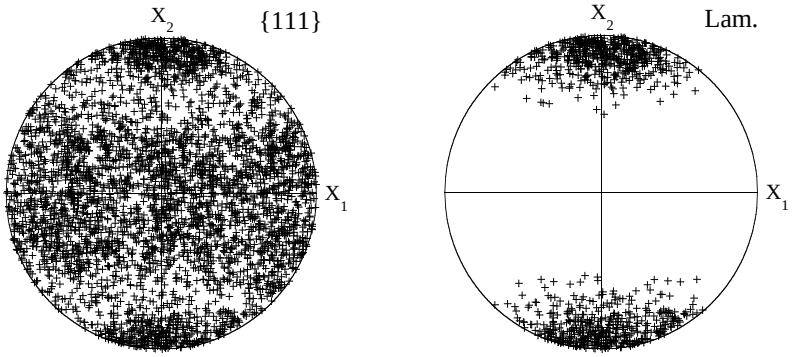

(a) (b)

Figure 5.3: Equal area projection figures of the crystallographic {111} plane poles (Part (a)) and of the lamination orientations $\mathbf{n}^{(r)}$ (Part (b)) in the as-cast sample of the PST polycrystal.

The experimentally measured crystallographic and lamellar texture (Lebensohn [73]) in the material of interest—which is also used in the context of the SOE (5.23)—is shown in Fig. 5.3. This system consists of 1000-grains. Note that this texture of Fig. 5.3 is approximately axisymmetric with symmetry axis X_2 and exhibits a strong lamellar anisotropy with the lamellar normals $\mathbf{n}^{(r)}$ concentrated near X_2. The grains are assumed to be equiaxed, i.e., the aspect ratios of the shape tensor $\mathbf{Z}$ are taken to be $w_1 = w_2 = w_3 = 1$, and the corresponding volume fractions are set equal, i.e., $c^{(r)} = 1/1000$ for all $r = 1, ..., 1000$.

Fig. 5.4 compares the predictions of the SOE (5.23) for the instantaneous plastic anisotropy of the two-scale PST composite material with the corresponding experimental results and the predictions of the model of Lebensohn [73]. Here, the material is subjected to uniaxial compression at various angles ϕ, with ϕ being the angle between the loading axis and the axis X_3 (see Fig. 5.3) on the plane $X_2 - X_3$. In the case of the models, a stress $\overline{\sigma} = -4\tau_0^{long}$ has been prescribed along the compressive axis and the associated normalized yield stresses $\widetilde{\tau}_\phi/\widetilde{\tau}_{90^o}$ have been estimated by means of (5.40), where now $\widetilde{u}_{90^o}$ and $\widetilde{u}_\phi$ stand respectively for the effective stress potential of the two-scale composite along direction X_2 (see Fig. 5.3) and at an angle ϕ, as defined above. Fig. 5.4(a) shows results for the effective normalized yield stresses $\widetilde{\tau}_\phi/\widetilde{\tau}_{90^o}$ as a function of the loading angle ϕ, while Fig. 5.4(b) presents the corresponding results for the ratios of the macroscopic deformation rate components $\overline{D}_{11}/\overline{D}_{33}$ and $\overline{D}_{22}/\overline{D}_{33}$. It is observed that the predictions of the SOE model (5.23) and those of the model of Lebensohn [73] are in a good agreement with each other and in a reasonably good agreement with the experimental results. The most remarkable observation from the results of Fig. 5.4(a) is that, despite the quantitative differences between the predictions of the two models and the experimental results for $\phi \approx 45^o$ and $\phi \approx 70^o$, they both capture the strong plastic anisotropy of the composite.

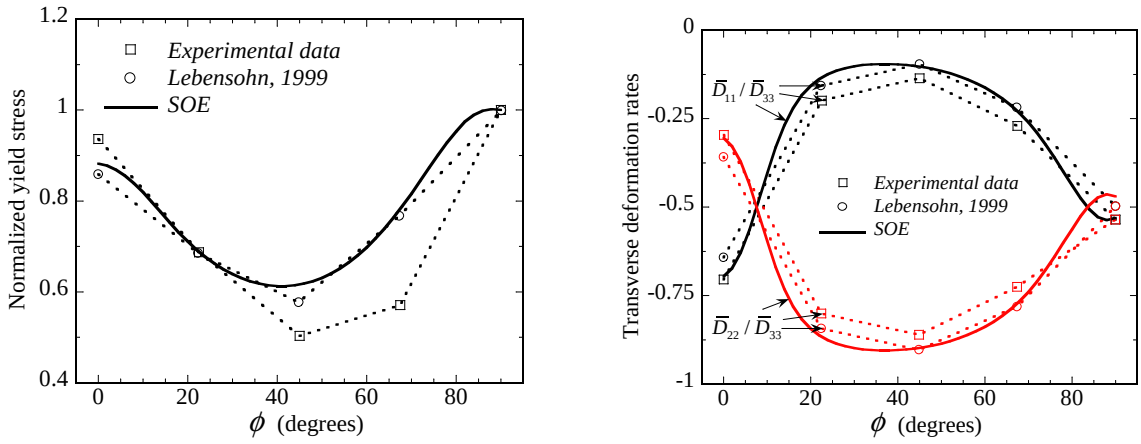

(a) (b)

Figure 5.4: Instantaneous plastic anisotropy of the textured PST polycrystal (see Fig. 5.3), subjected to compression along an axis forming an angle ϕ with the axis X_3 on the plane $X_2 - X_3$ (see Fig. 5.3). The predictions of the SOE model (5.23) and those of the model of Lebensohn [73] are compared with the corresponding experimental results (Lebensohn [73]). (a) The effective yield stress ratio $\widetilde{\tau}_{\phi}/\widetilde{\tau}_{90^o}$ is shown as a function of the loading angle ϕ. (b) The corresponding ratios of the macroscopic deformation rate components $\overline{D}_{11}/\overline{D}_{33}$ and $\overline{D}_{22}/\overline{D}_{33}$ are shown as a function of ϕ.

5.5 Texture evolution in $(\alpha + \beta)$ Ti alloys

In this section, we simulate the texture evolution in an initially isotropic $(\alpha + \beta)$ Ti alloy under rolling conditions by means of the finite-strain homogenization procedure for two-scale polycrystals developed in this chapter and referred to as the SOE model. Note that the α-phase corresponds to an *hcp* single-crystal, while the β-phase is a *bcc* single-crystal. Furthermore, it is relevant to remark that both the volume fraction of the phases and the underlying sub-structure in a $(\alpha + \beta)$ Ti alloy may vary significantly depending on the heat treatment (see, e.g., Dunst et al. [31]). In particular, by the appropriate heat treatment, it is possible to produce both single-scale and two-scale $(\alpha + \beta)$ Ti alloy polycrystals. The single-scale systems, called globular, consist of un-correlated single-crystal grains of either the α- or the β-phase, while the two-scale systems, called lamellar, exhibit a granular meso-structure and an underlying lamellar micro-structure. In this work, we focus our attention on the two-scale alloy studied experimentally by Dunst et al. [31]. This material is made out of 78% α-phase and 22% β-phase and lamellar composite-grains consisting of alternating layers of an α- and a β-single-crystal, whose relative orientation is defined by means of the Burgers relation $(10\bar{1}0)_{\alpha} \| (112)_{\beta}$; these two planes are in fact in intimate contact to each other and, therefore, they define the lamellar plane (Lebensohn and Canova [74]).

At this point, it should be remarked that the most significant feature of the orientation

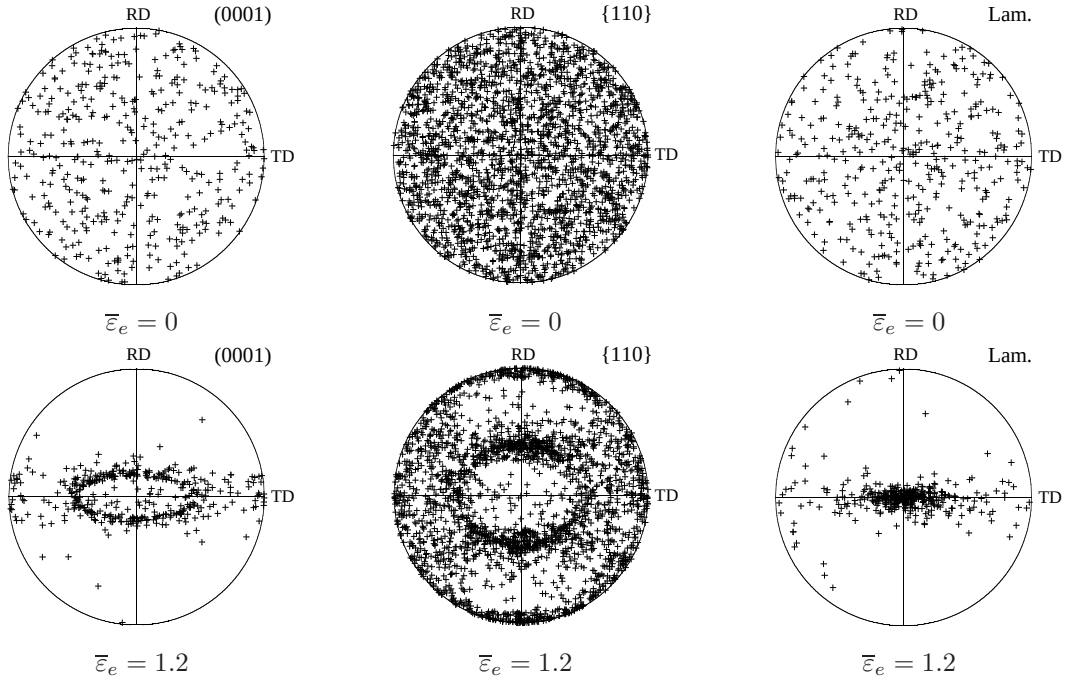

Figure 5.5: Texture development in the $(\alpha + \beta)$ Ti alloy under rolling, as predicted by the SOE model. Equal area projection figures are shown for the (0001) basal plane poles of the α-phase, the {110} plane poles of the β-phase and the lamination orientations $\mathbf{n}^{(r)}$. In these figures, RD and TD indicate the rolling and the transverse direction, respectively.

anisotropy developed in the two-scale systems under rolling conditions is the bi-modal character of the basal plane texture of the α-phase (Dunst et al. [31]). The stronger component of this texture consists of vectors normal to the basal planes of the *hcp* crystals oriented preferentially around the normal to the rolling direction, while the weaker component is made out of basal plane normals pointing towards the transverse rolling direction. Interestingly, the rolling textures of the single-scale systems exhibit only the former texture component, i.e., all basal plane normals are oriented around the normal to the rolling direction. This observation, in turn, suggests that the bi-modal character of the texture observed in the lamellar systems should be associated with the two-scale structure of these materials. Therefore, the rolling problem of a two-scale $(\alpha+\beta)$ Ti alloy constitutes a good challenge for the SOE model, which should be able to capture the bi-modal basal plane texture.

The various parameters defining the sub-structure and the material properties of the phases in the context of the present model will be prescribed to be identical to the corresponding parameters used by Lebensohn and Canova [74] in their model. Specifically, the volume fractions of the α- and β-crystals in each composite-grain r are respectively chosen to be $c^{(r,1)} = 0.78$ and $c^{(r,2)} = 0.22$,

and the lamellar plane normals $\mathbf{n}^{(r)}$ are prescribed according to the Burgers relation. The active slip modes in the β-phase are assumed to be $\{1\bar{1}0\}\langle 111\rangle$ and $\{11\bar{2}\}\langle 111\rangle$ slip with CRSSs equal to 0.25 (arbitrary units). The active slip modes in the α-phase are assumed to be the prismatic $\{10\bar{1}0\}\langle 1\bar{2}10\rangle$ slip and basal $(0001)\langle 1\bar{2}10\rangle$ slip, for both of which the CRSSs are taken to be equal to 1, as well as the pyramidal $\{10\bar{1}1\}\langle 1\bar{2}13\rangle$ slip with CRSSs equal to 8. The nonlinearity exponent n in the context of the power-law relations (5.13) is taken to be $n = 5$. The corresponding reference shear strain rate γ_0 is chosen to be $\gamma_0 = 1s^{-1}$. We consider a 400-grain system whose crystallographic and lamellar texture at zero strain ($\overline{\varepsilon}_e = 0$) is shown in Fig. 5.5. The grains are taken to be equiaxed and the corresponding volume fractions are assumed to be equal, i.e., $c^{(r)} = 1/400$ for all $r = 1, ..., 400$.

The $(\alpha + \beta)$ Ti alloy under consideration is subjected to rolling conditions (corresponding to pure shear deformation) at a constant deformation rate $1s^{-1}$ along the rolling direction (RD). Fig. 5.5 shows the predictions of the SOE model for the crystallographic and lamellar texture developed in this composite under rolling at the strain value $\overline{\varepsilon}_e = 1.2$. The most important observation from these results is that the SOE model indeed captures the bi-modal texture of the basal plane normals of the α-phase observed experimentally by Dunst et al. [31]. Specifically, the left part of Fig. 5.5 shows the development of both a strong and a weak basal pole texture components with their maxima located respectively around the normal (to the plane of the figure) and transverse (TD) rolling direction. It is remarked, however, that the transverse component of this texture is not as strong as the corresponding component measured experimentally by Dunst et al. [31]. In this connection, it should be emphasized that no effort has been made in this application to optimize the choice of the material parameters of the constituent phases in the context of the SOE model predictions of Fig. 5.5, and in particular the CRSSs, the values of which are *not* known experimentally and may have a significant effect on the predicted texture. Furthermore, the effect of these parameters in different models may be different. Recall that the various parameters in the context of the SOE model have been chosen here to be identical with the corresponding parameters used in the context of the model of Lebensohn and Canova [74]. Hence, given the possibility of further improvement of the predictions of the SOE model, the qualitative agreement of the predictions of Fig. 5.5 with the corresponding experimental results of Dunst et al. [31] should be regarded as encouraging.

5.6 Concluding remarks

In this chapter, we have considered applications of the "generalized-secant second-order" method developed in subsection 2.8.1 to two-scale polycrystals with lamellar grains. The instantaneous effective response in these systems is given in terms of the "second-order estimate" (SOE) (5.23)

for the associated effective stress-potential $\tilde{u}$ of the composite. This estimate incorporates fine sub-structural information on the current state of crystallographic, lamellar and morphological texture. The effective properties of the corresponding two-scale "linear comparison composite" (LCC) are determined through the sequential homogenization approach (see subsection 2.4.2) by employing the self-consistent estimate for the granular single-scale system at the larger length-scale and the well-known exact solution for the lamellar composites underlying the grains at the smaller length-scale. In this chapter, we also developed constitutive equations for the evolution of the sub-structure in these polycrystals which, along with the SOE (5.23), in turn allows the computation of both their macroscopic stress-strain response and texture evolution for finite deformation processes.

The SOE model has been employed in computing the instantaneous plastic anisotropy of a textured specimen of γ-TiAl-based polysynthetically twinned (PST) alloy and the crystallographic texture developed in an initially un-textured $(\alpha+\beta)$ Ti alloy under rolling conditions. In the former case, the material parameters in the context of the SOE model were chosen to be identical to those used in the corresponding calculations of Lebensohn [73], while in the later case they were set equal to the values used by Lebensohn and Canova [74] in the context of their model. The predictions of the SOE model were found to be in a good qualitative agreement with the corresponding experimental results. These predictions are encouraging and subject to possible improvements, which may be achieved though a better choice of the values of the material parameters involved in these SOE estimates since, as already mentioned, the relevant experimental information on these variables is very limited and the effect of these parameters in different models is expected to be different, in general.

Chapter 6

Closure

The determination of the macroscopic constitutive behavior of multi-scale viscoplastic composites with random sub-structures is a particularly challenging problem and, at the same time, a problem of great practical as well as theoretical interest. The main difficulties in dealing with this problem are the nonlinear character of the constitutive behavior of the phases and the complexity of the underlying sub-structure as well as its evolution resulting from the finite changes in the geometry of the body at large strains.

An efficient approach in dealing with the aforementioned difficulties is the so-called "linear comparison composite" (LCC) procedure, introduced by Ponte Castañeda [114, 117, 118] in the context of corresponding single-scale systems. These methods consist in constructing an LCC with the same micro-structure as the actual nonlinear medium and exploit the variational structure of the associated homogenization problem in order to obtain an expression for the effective properties of the nonlinear composite in terms of the corresponding effective properties of the LCC. The local properties of the LCC are optimally chosen through suitably designed variational procedures, while its effective properties may be easily determined from estimates that are available from the linear homogenization theory. Along these lines, three different linearization schemes have been proposed thus far, i.e., the "secant" (SEC) scheme, the "tangent second-order" (TSO) scheme and the "generalized-secant second-order" (GSO) scheme, due to Ponte Castañeda [114, 117, 118], respectively. The SEC method has the merit of generating bounds while the TSO and GSO methods have the advantage of delivering estimates that are exact to second-order in the heterogeneity contrast. The estimates provided by the GSO method are superior to those delivered by the TSO method. Furthermore, the estimates obtained by means of the GSO method, both for the macroscopic response of viscoplastic composites [119, 65, 22] and polycrystals [86, 87] as well as for the evolution of texture [78, 88], have been found to be the most accurate estimates to date. In the viscoplastic context, the GSO linearization scheme has been implemented thus far for single-scale composites with isotropic phases [118] and polycrystals with single-crystal-grains [86], while its

application to systems with more general constituents remains to be developed.

On theoretical grounds, the main contribution of this dissertation is the generalization of the LCC methods to multi-scale viscoplastic composites. In contrast to the case of single-scale systems, the homogenization problem for a multi-scale composite admits two equivalent variational formulations, i.e., the direct and the sequential (or iterative) approach. The direct approach is a one-step homogenization procedure requiring the computation of the local fields in terms of the properties of the homogeneous phases. The sequential approach is a multi-step homogenization procedure taking place hierarchically from the lowest to the highest heterogeneity length-scale, with each step requiring the solution of a homogenization problem for an associated single-scale composite, the effective properties of which are being used in the following step. Implementation of any of the LCC methods to either one of these two statements leads inevitably to two corresponding estimates, i.e., an estimate of the direct and an estimate of the sequential type. For n-scale systems with $n > 2$, it should be remarked that variational formulations of the mixed type are also possible and corresponding LCC estimates may be generated in a rather obvious way. For definiteness, the full extension of the available SEC, TSO and GSO methods to two-scale composites has been discussed in detail and corresponding estimates both of the direct and the sequential type have been derived. In this connection, it should be emphasized that the GSO estimates of the direct type are accessible for multi-scale viscoplastic composites with isotropic phases and single-crystal-grains, which cover a wide range of materials of practical interest. On the other hand, GSO estimates of the sequential type are currently available only for very special types of micro-structures and constitutive behavior of the phases. The extension of the GSO estimates of the sequential type to composite systems of practical interest requires further development of the GSO linearization scheme for systems with generally anisotropic phases, which is a separate research project well-beyond the scope of this thesis but, nevertheless, worth pursuing. In any case, for computational convenience, it has been proposed in this work to compute the effective properties of the multi-scale LCCs involved in these estimates by following the sequential variational approach.

Ideally, given the equivalence of the two formulations of the homogenization problem for multi-scale composites, it is desirable that the corresponding LCC estimates of the direct and sequential type to also be equivalent. As shown in chapter 2, the direct and sequential estimates obtained by employing the SEC linearization scheme are identical. The reason for this is probably because the SEC method is fully stationary with respect to the variables involved. The question of equivalence of the corresponding TSO and GSO estimates has been thoroughly investigated in chapter 3 in the context of application to 2-D model problems for both particulate and granular sub-structures. It has been found that the estimates of the direct type are in a very good agreement with the corresponding estimates of the sequential type, in general. Furthermore, similar to the case of single-scale systems, the TSO estimates for two-scale composites were found to violate the SEC

bounds in the special case of nearly ideally plastic granular systems close to the associated percolation limit, while the GSO estimates were shown to be entirely consistent with the SEC bounds, suggesting once again the superiority of the GSO method over the TSO method. Another interesting observation from the results of chapter 3 worth recalling here is that—comparing the estimates for the effective response of two-scale composites with the corresponding estimates for single-scale materials with the same overall rigid-phase concentration—the two-scale particulate systems are stiffer than the corresponding single-scale composites, while the two-scale granular systems are softer than the associated single-scale ones.

The general theoretical framework developed in chapter 2 is applicable to a wide range of two-scale composites of current interest. In chapters 4 and 5 we developed constitutive models for the effective behavior and texture evolution in semi-crystalline polymers and two-scale polycrystalline metals, respectively. A common feature of these two classes of composite materials is that they are both characterized by a granular meso-structure and a lamellar micro-structure. The effective properties of the associated two-scale LCCs in the context of these models are computed sequentially, by making use of the self-consistent estimate for the effective behavior of the granular system at the larger length-scale—which is particularly well-suited for this type of micro-structure—in combination with the well-known exact solution for the effective response of the lamellar grains at the smaller length-scale. At this point, it is relevant to recall that the theory of chapter 2 allows the computation of the instantaneous effective response of these composites in terms of the material properties of the phases and the underlying sub-structure in the current configuration. Hence, in order to account for finite strain loading processes, additional constitutive relations are required for the evolution of the sub-structure. In the context of a homogenization framework, these relations are ordinary differential equations—determining the evolution of appropriately defined sub-structural variables in an average sense—and were established in this work by making use of standard arguments along with corresponding estimates for the relevant kinematical variable in the associated LCC. Thus, the LCC models for semi-crystalline polymers and two-scale polycrystalline metals account explicitly for the current state of the corresponding crystallographic, lamellar and morphological texture as well as for its evolution due to the finite changes in the geometry of these materials at large strains. Furthermore, these models can be shown to be fully consistent with the "principle of material frame indifference".

In terms of applications, the main contribution of this work is the development of the LCC model for the large strain macroscopic response and texture evolution of semi-crystalline polymers. Motivated by the earlier works of Lee et al. [80] and Nikolov et al. [110], both the amorphous and the crystalline phase in the context of this model are assumed to be viscoplastic materials, while the effect of finite elastic strains in the amorphous phase is also taken into account by means of a back-stress model. However, unlike the earlier models, the present model has been

derived through a more rigorous and complete homogenization analysis, which employs the LCC procedures of chapter 2 and incorporates fine sub-structural information both at the level of the layered grains and the level of the grained "polycrystal". The predictions of the LCC model both for the macroscopic response and texture evolution in high-density polyethylene (HDPE) under uniaxial compression, simple shear and uniaxial tension were discussed in great detail. These results were compared with relevant experimental measurements as well as with the corresponding predictions of the models of Lee et al. [80] and Nikolov et al. [110]. It should be remarked that the material parameters defining the constitutive properties of the phases in the context of the LCC model were prescribed based on a detailed numerical analysis of the predictions of this model for uniaxial compression and special care has been placed in achieving the best possible consistency for the values of these parameters with available experimental evidence. Based on the results of Bartczak et al. [10, 8], we argued that the macroscopic strain hardening observed experimentally in HDPE under uniaxial compression at large strains is probably due to the hardening of the crystalline phase due to the Coulomb effect on the CRSSs in the slip systems of the crystals. Note that this interpretation, which to the best of our knowledge is new, is substantially different from the one implicitly assumed in the works of Lee et al. [80] and Nikolov et al. [110], i.e., that the macroscopic hardening is due to locking of the amorphous material. Given the fact that the Coulomb yield criterion (4.109) for the CRSSs cannot be explicitly incorporated in our LCC model—since this would require consideration of a non-associative flow model for the crystalline phase while the LCC theory is restricted to associative constituent—the strain hardening relation (4.77) for the CRSSs was used instead. Although this relation is by no means equivalent to the Coulomb yield criterion (4.109), it provides a mechanism for the hardening of the crystalline phase which ultimately leads to a macroscopic hardening for the composite at large strains under uniaxial compression. In general, the predictions of the LCC model were found to be in a much better agreement, both qualitatively and quantitatively, with the corresponding experimental result than the predictions of the earlier models.

The LCC model for two-scale polycrystals was employed in determining the instantaneous plastic anisotropy of a textured specimen of γ-TiAl-based polysynthetically twinned (PST) alloy as well as the crystallographic texture developed in an initially un-textured $(\alpha+\beta)$ Ti alloy under rolling conditions. These particular calculations were performed with the objective of testing the predictive capabilities of the LCC model through comparison with corresponding experimental results that are available from the literature. Note that, from the associated experimental studies, it is known that the plastic anisotropy of the PST alloy is primarily due to its strong lamellar texture [73], while the bi-modal rolling texture of the basal planes of the *hcp* crystals (α-phase) developed in the $(\alpha+\beta)$ Ti alloy at finite strains has been attributed to the two-scale character of its sub-structure [74]. The corresponding predictions of the LCC model were found to be consistent

with these experimental observations. It should be emphasized, however, that these calculations are preliminary in the sense that the material parameters of the constituent single-crystals (e.g., the associated critical resolved shear stresses) in the LCC model have been prescribed based on the values used in the context of other models from the literature. In this connection, it is remarked that the relevant experimental information for the values of these parameters is limited and that their choice may have a significant effect on the predictions of a theoretical model, such as the LCC model. In this regard, the predictions of the LCC model for these two problems are subject to improvements. Such an analysis, along with a more thorough investigation of the LCC estimates for γ-TiAl-based PST alloys and $(\alpha+\beta)$ Ti alloys, is expected to be relatively easy to pursue and it is proposed for a future work.

Several research directions may be proposed for future work, some of which have been already mentioned. A challenging research project would be the development of homogenization techniques for composite materials with non-associative constituent phases. To this end, the notion of the LCC could prove useful, but it should be emphasized that the applications of the LCC theory that have been considered thus far—for single-scale or multi-scale systems—are restricted to composites with associative phases. In any case, this problem is expected to be of great practical interest. For example, a homogenization framework for non-associative phases specialized to semi-crystalline polymers will allow consideration of the Coulomb yield criterion (4.109) for the CRSSs of the crystalline phase which, as already discussed, has a crucial effect on the macroscopic response of these materials under compression, at least for large strains. It is also interesting to investigate the effect of the Coulomb law for other loading conditions, which is, in general, expected to be different from the effect of the strain hardening relation (4.77) in the context of the corresponding LCC model proposed in this work. In this connection, note that studies on single-crystals (see, e.g., Qin and Bassani [127, 128] as well as Racherla and Bassani [131]) have shown that the non-associative character of the plastic flow leads to an asymmetric behavior for compression and tension, which persists in the strain hardening regime.

Another interesting problem that worth consideration is the implementation of the LCC methods, and in particular the GSO method, to multi-scale hyperelastic composites. In this connection, it is remarked that the hyperelastic version of the TSO method has been already employed by Lopez-Pamies et al. [44] and Racherla et al. [132] to study the macroscopic response and overall stability of two-scale hyperelastic elastomers with lamellar micro-structures. However, the TSO method has the disadvantage of being inconsistent with the incompressibility constraint for certain types of loadings in incompressible elastomers, which is particularly relevant in this case, given that elastomers are nearly incompressible materials. On the other hand, the GSO method for hyperelastic composites, proposed by Lopez-Pamies and Ponte Castañeda [92] for single-scale systems, is fully consistent with this constraint and has been used successfully to develop constitutive models

for the effective behavior of various hyperelastic composites and study their overall stability (see, e.g., [93, 95, 96, 2, 3]). Based on the direct variational formulation (see subsection 2.4.2) of the associated homogenization problem for composites with hyperelastic phases, the extension of the GSO method of Lopez-Pamies and Ponte Castañeda [92] to the corresponding multi-scale systems should not be very difficult. The resulting theory could then be used to generate constitutive models for two-scale hyperelastic composites of practical interest, such as triblock copolymers (see, e.g., Honeker et al. [58, 59]). Furthermore, these results can be used to study the overall stability of these materials. A quite interesting problem that could be studied in this context is the effect of fiber misalignment on the onset of macroscopic instabilities in fiber reinforced elastomers with a single family of fibers. This can be done by modeling the fiber composite as a two-scale system with granular structure at the larger length-scale and each grain, at the smaller length-scale, made out of perfectly aligned fibers embedded in a matrix; the fibers in different grains should then be taken to be slightly misaligned. In this connection, it should be remarked that, from extensive experimental and theoretical works on fiber-reinforced composites (see, e.g., Vogler et al. [148]), it has been found that the misalignment of the fibers in these material systems may have a significant destabilizing effect in their macroscopic response under compressive loadings along the fiber direction.

The ultimate goal is of course to develop a reasonably accurate method for multi-scale composites accounting both for finite elastic and plastic deformations, which would allow a more realistic modeling of the constitutive behavior of the phases. Although the development of such a method may sound a very ambitious plan at this stage, it should be remarked that encouraging steps along these lines (in the context of single-scale composites) have been taken recently by Lahellec and Suquet [70, 71].

Appendix A

A general hyperelastic model for incompressible fiber-reinforced elastomers

Abstract—This work presents a new constitutive model for the effective response of fiber-reinforced elastomers at finite strains. The matrix and fiber phases are assumed to be incompressible, isotropic, hyperelastic solids. Furthermore, the fibers are taken to be perfectly aligned and distributed randomly and isotropically in the transverse plane, leading to overall transversely isotropic behavior for the composite. The model is derived by means of the "second-order" homogenization theory, which makes use of suitably designed variational principles utilizing the idea of a "linear comparison composite." Compared to other constitutive models that have been proposed thus far for this class of materials, the present model has the distinguishing feature that it allows consideration of behaviors for the constituent phases that are more general than Neo-Hookean, while still being able to account directly for the shape, orientation, and distribution of the fibers. In addition, the proposed model has the merit that it recovers a known exact solution for the special case of incompressible Neo-Hookean phases, as well as some other known exact solutions for more general constituents under special loading conditions.

A.1 Introduction

Fiber-reinforced, elastomer-matrix composites constitute a broadly utilized class of materials in engineering applications. In addition, fiber-reinforced-type morphologies appear naturally in a number of other "soft" matter systems of current interest. Prominent examples include nanostructured thermoplastic elastomers (see, e.g., Honeker and Thomas [58] and Honeker et al. [59]) and soft biological tissues (see, e.g., Finlay et al. [34]; Quapp and Weiss [130]). It is often the

case that such fiber-reinforced "soft" materials are subjected to finite deformations, and it is therefore of practical interest to develop constitutive models for their mechanical behavior under such loading conditions. Beyond accounting for finite deformations, it is also desirable that these models incorporate full dependence on the constitutive behavior of the constituents (i.e., the matrix phase and the fibers), as well as on their spatial arrangement (i.e., the microstructure). In this paper, we will consider fiber-reinforced elastomers with *hyperelastic* matrix and fiber phases. In addition, we will restrict attention to microgeometries with a single family of aligned fibers which are taken to be initially circular in cross section and *randomly* and *isotropically* distributed in the undeformed configuration.

A variety of efforts have been pursued over the past few decades to model the effective behavior of fiber-reinforced hyperelastic materials. In terms of phenomenological approaches, there is the pioneering theory of Spencer [134], in the context of which the fibers are treated as inextensible material line elements. Other more sophisticated phenomenological models have been constructed by augmenting existing isotropic stored-energy functions with additional terms depending on the transversely isotropic invariants associated with the fiber direction [135]. Examples include the models proposed by Qiu and Pence [129], Merodio and Ogden [101], Horgan and Saccomandi [61], and Gasser et al. [37]. Although these models possess a number of desirable features, and in particular, they are simple and can be "calibrated" to become macroscopically unstable—via loss of strong ellipticity—for loading conditions where such instabilities are expected to occur from physical experience [141], their predictive capabilities for the general response of actual fiber-reinforced elastomers remain limited. In a separate effort—essentially making use of a micromechanics approach—Guo et al. [45] have proposed a hyperelastic model for fiber-reinforced elastomers with *incompressible Neo-Hookean* matrix phases.

On the other hand, homogenization approaches have also been used to obtain bounds and estimates for the constitutive response of these materials. In particular, there is the simple, microstructure-independent, Voigt-type bound [111], and the polyconvex Reuss-type lower bound [113], as well as an estimate put forward by deBotton et al. [26, 28] for fiber-reinforced elastomers with *incompressible Neo-Hookean* phases. One of the strengths of the later model [28] is that it predicts the exact effective response of composites with the "composite cylinder assemblage" microstructure, when subjected to axisymmetric and antiplane shear loadings. Based on the "second-order" homogenization procedure [117, 124], Lahellec et al. [69] proposed a constitutive model, for the transverse response of incompressible hyperelastic fiber-reinforced elastomers with *periodic* microstructures, and made successful comparisons with experimental and numerical results. In addition, by making use of the more recent "second-order" homogenization theory [118, 92], Lopez-Pamies and Ponte Castañeda [93] obtained closed-form estimates for the transverse in-plane response of incompressible elastomers reinforced with *randomly* distributed, *rigid*

fibers, while Brun et al. [18] provided more general estimates for fiber-reinforced elastomers with *compressible*, isotropic (matrix and fiber) phases and *periodic* microstructures.

In this paper, we will make use of the second-order homogenization theories [124, 92] to construct a complete three-dimensional constitutive model for the overall behavior of fiber-reinforced elastomers with *incompressible*, isotropic matrix and fiber phases and *random* microstructures. More specifically, the constitutive behaviors of the matrix and fibers are assumed to be characterized by *generalized Neo-Hookean* models. This class of materials is sufficiently general to model many types of real elastomers (see, e.g., Gent [40], Boyce and Arruda [15]) and, at the same time, is sufficiently simple to lead to analytical results. Furthermore, the fibers are assumed to be perfectly aligned and to be distributed randomly and isotropically in the transverse plane, leading to overall transversely isotropic behavior for the composite. The main result of this paper is given by expression (A.38), together with expressions (A.39)-(A.42), which provide estimates for the effective stored-energy function of the composite materials of interest.

It is relevant to mention that the two "second-order" homogenization methods [117, 118] were established on the common basis that available estimates for the effective behavior of (suitably constructed) linear composites can be converted into corresponding estimates for the effective behavior of nonlinear composites. They both have the capability to account for statistical information on the initial microstructure beyond the volume fraction, as well as for its evolution, resulting from the applied finite deformations. This point is crucial as the evolution of the microstructure may have a significant geometric softening or stiffening effect on the overall response of the material, which, in turn, may lead to the possible development of macroscopic instabilities. The first method, when it works, is simpler to use than the second. When the first method fails, the second method, using additional information about the field fluctuations, can deliver improved results at the expense of a somewhat heavier implementation. Finally, it is important to mention that in addition to the already-mentioned applications to fiber-reinforced elastomers, these homogenization methods can be employed more generally, and have already been used, for example, to construct constitutive models for the overall response of porous elastomers (Lopez-Pamies and Ponte Castañeda [91], Michel et al. [103]).

A.2 Problem formulation

Consider a specimen occupying a volume Ω_0 with boundary $\partial\Omega_0$ in the reference (undeformed) configuration, and made up of a single family of aligned, cylindrical fibers with circular cross section, distributed randomly and isotropically (in the transverse plane) in a matrix phase. The orientation of the fibers in the reference configuration is taken to be characterized by the unit vector $\mathbf{N}$. Furthermore, it is assumed that the average diameter of the fibers is much smaller than

the size of the specimen and the scale of variation of the applied load.

Both the matrix (phase 1) and the fibers (phase 2) are assumed to be made up of (different) homogeneous hyperelastic materials. Their constitutive behaviors are characterized by stored-energy functions $W^{(1)}$ and $W^{(2)}$, respectively, which are assumed to be *objective*, *isotropic*, strictly rank-one convex (strongly elliptic) functions of the deformation gradient tensor $\mathbf{F}$. Here, we will restrict our attention to stored-energy functions $W^{(r)}$ for the phases ($r = 1, 2$) of the form:

$$W^{(r)}(\mathbf{F}) = g^{(r)}(I) + h^{(r)}(J) + \frac{\kappa^{(r)}}{2}(J-1)^2, \tag{A.1}$$

where $I = \mathrm{tr}(\mathbf{F}^T\mathbf{F})$ and $J = \det \mathbf{F}$. In this expression, $g^{(r)}(I)$ and $h^{(r)}(J)$ are twice differentiable material functions that satisfy the "linearization" conditions: $g^{(r)}(3) = h^{(r)}(1) = 0$, $g^{(r)}_I(3) = \mu^{(r)}/2$, $h^{(r)}_J(1) = -\mu^{(r)}$, and $4g^{(r)}_{II}(3) + h^{(r)}_{JJ}(1) = \mu^{(r)}/3$, where the parameters $\mu^{(r)}$ and $\kappa^{(r)}$ denote the classical shear and bulk moduli. (Here and subsequently, the subscripts I and J denote differentiation with respect to these invariants, e.g., $g^{(r)}_I(\cdot) = \frac{dg^{(r)}}{dI}(\cdot)$, $g^{(r)}_{II}(\cdot) = \frac{d^2g^{(r)}}{dI^2}(\cdot)$.) Note that upon taking the limit $\kappa^{(r)} \to \infty$, the hyperelastic potentials (A.1) reduce to the (incompressible) *generalized Neo-Hookean* stored-energy functions $W^{(r)}(\mathbf{F}) = g^{(r)}(I)$, together with the incompressibility constraint $J = 1$.

An example of a model of the type (A.1), which captures the limited chain extensibility of elastomers, is the Gent model [40]:

$$W(\mathbf{F}) = -\frac{J_m\,\mu}{2}\ln\left[1 - \frac{I-3}{J_m}\right] - \mu \ln J + \left(\frac{\kappa}{2} - \frac{J_m+3}{3\,J_m}\mu\right)(J-1)^2, \tag{A.2}$$

where the parameter J_m corresponds to the limit of $I - 3$ for the lock-up of the elastomer. Note that, in the limit $J_m \to \infty$ the Gent model reduces to a compressible Neo-Hookean model.

It should be emphasized that the homogenization methods to be developed in this work could be applied for more general constitutive models for the phases, including dependence on the second invariant I_2. Indeed, generalizations of the above-mentioned constitutive models incorporating dependence on I_2 have been discussed by Horgan and Saccomandi [60]. However, one of the goals of this first application for *incompressible* fiber-reinforced materials is to obtain results that are as (analytically) explicit as possible, and in this respect the form (A.1) for the constitutive relation will greatly simplify the concomitant analyses.

The *local* stored-energy function of the fiber-reinforced elastomer may be conveniently written as

$$W(\mathbf{X};\mathbf{F}) = (1 - \chi_0(\mathbf{X}))W^{(1)}(\mathbf{F}) + \chi_0(\mathbf{X})W^{(2)}(\mathbf{F}), \tag{A.3}$$

where χ_0 denotes the characteristic function of the part of Ω_0 occupied by fibers (i.e., χ_0 is equal to one if the position vector $\mathbf{X}$ of a material point in the reference configuration is inside a fiber, and zero otherwise) and serves to characterize the microstructure of the material in the undeformed

configuration. Note that, in view of the assumed random distribution of the fibers, the dependence of χ_0 on $\mathbf{X}$ is not known precisely, and the microstructure is only partially defined in terms of its n-point statistics. (In this work, we will make use of one- and two-point statistics, as detailed further below.) The *local* constitutive relation for the composite is then given by:

$$\mathbf{S} = \frac{\partial W}{\partial \mathbf{F}}(\mathbf{X}; \mathbf{F}), \tag{A.4}$$

where $\mathbf{S}$ denotes the first Piola-Kirchhoff stress tensor.

Under the hypotheses of *statistical uniformity*, and the above-mentioned *separation of length scales*, the *effective* (or macroscopic) constitutive relation for the fiber-reinforced elastomer is defined [53] as follows:

$$\overline{\mathbf{S}} = \frac{\partial \widetilde{W}}{\partial \overline{\mathbf{F}}}, \tag{A.5}$$

where $\overline{\mathbf{S}} = \langle \mathbf{S} \rangle$, $\overline{\mathbf{F}} = \langle \mathbf{F} \rangle$ are the *average stress* and *average deformation gradient*, respectively, and

$$\begin{aligned} \widetilde{W}(\overline{\mathbf{F}}) &= \min_{\mathbf{F} \in \mathcal{K}(\overline{\mathbf{F}})} \langle W(\mathbf{X}; \mathbf{F}) \rangle \\ &= \min_{\mathbf{F} \in \mathcal{K}(\overline{\mathbf{F}})} \left[(1 - c_0) \, \langle W^{(1)}(\mathbf{F}) \rangle^{(1)} + c_0 \, \langle W^{(2)}(\mathbf{F}) \rangle^{(2)} \right] \end{aligned} \tag{A.6}$$

is the *effective stored-energy function* of the composite. In the above expressions, the triangular brackets $\langle \cdot \rangle$, $\langle \cdot \rangle^{(1)}$ and $\langle \cdot \rangle^{(2)}$ denote, respectively, volume averages over the specimen (Ω_0), the matrix ($\Omega_0^{(1)}$) and the fibers ($\Omega_0^{(2)}$), in the undeformed configuration. The scalar $c_0 = \langle \chi_0 \rangle$ stands for the volume fraction of the fibers in the undeformed configuration. Furthermore, $\mathcal{K}$ denotes the set of kinematically admissible deformation gradients:

$$\begin{aligned} \mathcal{K}(\overline{\mathbf{F}}) = \{ \mathbf{F} \, | \exists \, \mathbf{x} = \mathbf{x}(\mathbf{X}) \text{ with } \mathbf{F} = \operatorname{Grad} \mathbf{x} \text{ and } J > 0 \text{ in } \Omega_0, \\ \mathbf{x} = \overline{\mathbf{F}} \mathbf{X} \text{ on } \partial \Omega_0 \}. \end{aligned} \tag{A.7}$$

In passing, it is relevant to remark that $\widetilde{W}$ represents the average elastic energy stored in the composite when subjected to an affine deformation on its boundary. Note also that, by virtue of definition (A.6) together with the objectivity of $W^{(1)}$ and $W^{(2)}$, $\widetilde{W}$ is an objective scalar function of $\overline{\mathbf{F}}$.

Because of the non-convexity of W on $\mathbf{F}$, the solution (assuming that it exists) of the Euler-Lagrange equations associated with the variational problem (A.6) need not be unique. However, within a sufficiently small neighborhood of $\overline{\mathbf{F}} = \mathbf{I}$, the problem (A.6) is expected to lead to a well-posed linear elastic problem with a unique solution. As the deformation progresses beyond the linearly elastic neighborhood into the finite deformation regime, the composite may reach a point at which this "principal" solution bifurcates into different energy solutions. This point corresponds to the onset of an *instability*, beyond which the applicability of the "principal" solution becomes

questionable. Following the work of Triantafyllidis and collaborators (see, e.g., Geymonat et al. [41], Triantafyllidis et al. [143]), it is useful to make the distinction between "microscopic" instabilities, that is, instabilities with wavelengths that are small compared to the size of the specimen, and "macroscopic" instabilities, that is, instabilities with wavelengths comparable to the size of the specimen. The computation of "microscopic" instabilities is in general an extremely difficult task, especially for random systems. On the other hand, the computation of "macroscopic" instabilities is a much simpler endeavor, since it reduces to the detection of loss of strong ellipticity of the effective stored-energy function of the material evaluated at the above-described "principal" solution [41]. Based on these remarks, in this work, we will not attempt to solve the variational problem (A.6), but instead, we will estimate the overall behavior of fiber-reinforced elastomers by means of the effective stored-energy function:

$$\widehat{W}(\overline{\mathbf{F}}) = \underset{\mathbf{F}\in\mathcal{K}(\overline{\mathbf{F}})}{\text{stat}} [(1-c_0)\ \langle W^{(1)}(\mathbf{F})\rangle^{(1)} + c_0\ \langle W^{(2)}(\mathbf{F})\rangle^{(2)}], \tag{A.8}$$

where the stat(ionary) variational operation means evaluation at the above-described "principal" solution of the relevant Euler-Lagrange equations. Finally, it is relevant to mention that other definitions of macroscopic behavior for hyperelastic composites have been proposed in the literature, including the notion of a "globally equivalent homogeneous" material (Chen et al. [20]).

A.2.1 Transverse Isotropy

In view of the above-adopted constitutive and (micro)geometric assumptions, it follows that the effective stored-energy function (A.8) is a transversely isotropic scalar function of $\overline{\mathbf{F}}$ (with symmetry axis $\mathbf{N}$). Accordingly, the functional dependence of $\widehat{W}$ on $\overline{\mathbf{F}}$ may be conveniently expressed as

$$\widehat{W}(\overline{\mathbf{F}}) = \widehat{\phi}(\overline{\lambda}_p, \overline{\lambda}_n, \overline{\gamma}_p, \overline{\gamma}_n, \overline{\psi}_{\overline{\gamma}}), \tag{A.9}$$

where the scalars $\overline{\lambda}_p$, $\overline{\lambda}_n$, $\overline{\gamma}_p$, $\overline{\gamma}_n$, and $\overline{\psi}_{\overline{\gamma}}$ constitute a set of transversely isotropic invariant functions of $\overline{\mathbf{C}} = \overline{\mathbf{F}}^T\overline{\mathbf{F}}$, first introduced by Ericksen and Rivlin [33], and given by

$$\begin{aligned} &\overline{\lambda}_n = (\mathbf{N}\cdot\overline{\mathbf{C}}\,\mathbf{N})^{1/2}, \quad \overline{\lambda}_p = ((\det\overline{\mathbf{C}})^{1/2}/\overline{\lambda}_n)^{1/2}, \\ &\overline{\gamma}_n = (\mathbf{N}\cdot\overline{\mathbf{C}}\,\overline{\mathbf{C}}\,\mathbf{N} - \overline{\lambda}_n^4)^{1/2}/\overline{\lambda}_n, \quad \overline{\gamma}_p = (\mathrm{tr}\overline{\mathbf{C}} - \overline{\lambda}_n^2 - 2\overline{\lambda}_p^2 - \overline{\gamma}_n^2)^{1/2}. \end{aligned} \tag{A.10}$$

The invariant $\overline{\psi}_{\overline{\gamma}}$ is a more complicated function of $\overline{\mathbf{C}}$ and $\mathbf{N}$ and will not be spelled out here (see, e.g., deBotton et al. [28] for an explicit expression).

As discussed by deBotton et al. [28], a practical implication of the representation (A.9) is that, in order to determine $\widehat{W}$, it suffices to restrict attention to deformation gradient tensors $\overline{\mathbf{F}}$ of the

form

$$\overline{F}_{ij} = \begin{bmatrix} \overline{\lambda}_p & 0 & 0 \\ \overline{\gamma}_p & \overline{\lambda}_p & 0 \\ \overline{\gamma}_n \cos\overline{\psi}_{\overline{\gamma}} & \overline{\gamma}_n \sin\overline{\psi}_{\overline{\gamma}} & \overline{\lambda}_n \end{bmatrix} \tag{A.11}$$

in a coordinate system $\mathbf{e}_i$ $(i = 1, 2, 3)$ with $\mathbf{e}_3 = \mathbf{N}$. This particular type of applied deformation entails the following interpretation for the invariants in (A.10): $\overline{\lambda}_n$ is the stretch along the direction of the fibers $\mathbf{N}$, $\overline{\lambda}_p$ is a measure of the dilatation in the transverse plane, $\overline{\gamma}_n$ is the amount of antiplane shear, and $\overline{\gamma}_p$ is the amount of shear in the transverse plane (in-plane shear). The invariant $\overline{\psi}_{\overline{\gamma}}$ is a measure of the coupling among the other invariants and, like the orientation of $\mathbf{e}_1$ and $\mathbf{e}_2$ in the transverse plane, can be chosen arbitrarily whenever $\overline{\gamma}_p = 0$ or $\overline{\gamma}_n = 0$. (These two cases are of special interest in this work and will be considered in detail in Subsections A.3.2 and A.3.3.)

To conclude this section, it is appropriate to mention that the estimates to be derived next for the effective stored-energy function (A.8) of fiber-reinforced elastomers with matrix and fiber phases characterized by (A.1) will be shown in section 4 to depend weakly on the invariant $\overline{\psi}_{\overline{\gamma}}$. In addition, when the matrix and fibers are taken to be incompressible—which is precisely the case of interest in this work—the overall constraint

$$\det\overline{\mathbf{F}} = \overline{\lambda}_p^2\overline{\lambda}_n = 1 \tag{A.12}$$

must be satisfied. This means that in practice, the effective stored-energy function (A.8) of fiber-reinforced elastomers with incompressible generalized Neo-Hookean phases can be expediently approximated as a function solely of $\overline{\lambda}_n, \overline{\gamma}_p$, and $\overline{\gamma}_n$, namely:

$$\widehat{W}(\overline{\mathbf{F}}) \approx \widehat{\phi}(\overline{\lambda}_n^{-1/2}, \overline{\lambda}_n, \overline{\gamma}_p, \overline{\gamma}_n, 0) \doteq \widehat{\Phi}(\overline{\lambda}_n, \overline{\gamma}_p, \overline{\gamma}_n). \tag{A.13}$$

A.3 Second-order homogenization estimates

As already mentioned, we will make use the second-order variational procedures of Ponte Castañeda and Tiberio ([124]) and Lopez-Pamies and Ponte Castañeda ([92]) to estimate the effective stored-energy function (A.8) for the class of fiber-reinforced elastomers of interest in this work. The main concept behind these two methods is the construction of suitable variational principles making use of the idea of a "linear comparison composite" (LCC) with the same microstructure as the actual hyperelastic composite (see subsection A.3.1). Both methods have the distinguishing feature of delivering estimates that are exact to second order in the heterogeneity contrast, provided that the corresponding estimates used for the LCC are also exact to second order in the contrast (hence their names). However, the second method makes use of the deformation field fluctuations in the

linearization scheme, while the first method makes use only of the first moments, and is therefore easier to implement. For convenience, and reasons that will become more evident further below, we henceforth refer to the first procedure as the tangent second-order (TSO) method, and to the second as the generalized second-order (GSO) method.

The main objective of this work is to compute an estimate for the effective stored-energy function (A.8) of the class of fiber-reinforced elastomers defined in the previous section in the limit of incompressible behavior for the matrix and fiber phases (i.e., in the limit as $\kappa^{(1)} \to \infty$ and $\kappa^{(2)} \to \infty$ in expression (A.1)). To this end, we could in principle make use of the more accurate GSO method. However, in the limit of incompressibility, the use of this technique for general loading conditions leads to a fairly complex set of asymptotic equations that (although easy to solve numerically) are difficult to solve explicitly. On the other hand, it will be shown below that the simpler TSO method yields quite accurate results (relative to the generally more accurate GSO method) for the special case of *combined antiplane and axisymmetric shear deformations* (i.e., for $\overline{\gamma}_p = 0$ in (A.11)). For this reason, the GSO method will only be used to generate an estimate for *generalized plane-strain deformations* (i.e., for $\overline{\gamma}_n = 0$ in (A.11)), when the pertinent asymptotic analysis becomes more manageable (see below). The two estimates for the complementary sets of loading conditions will then be used in Section 4 to construct—via a nonlinear interpolation scheme—a complete constitutive model for general loading conditions.

A.3.1 Local and effective properties of the LCC

Consider a two-phase LCC with the same initial microstructure (i.e., the same χ_0) as the actual fiber-reinforced elastomer and with local stored-energy function

$$W_T(\mathbf{X};\mathbf{F}) = (1-\chi_0(\mathbf{X}))W_T^{(1)}(\mathbf{F}) + \chi_0(\mathbf{X})W_T^{(2)}(\mathbf{F}). \tag{A.14}$$

Here, $W_T^{(r)}$ $(r=1,2)$ are quadratic potentials in $\mathbf{F}$ given by the Taylor-like expressions

$$W_T^{(r)}(\mathbf{F}) = W^{(r)}(\mathbf{F}^{(r)}) + \mathbf{S}^{(r)}(\mathbf{F}^{(r)})\cdot(\mathbf{F}-\mathbf{F}^{(r)}) + \frac{1}{2}(\mathbf{F}-\mathbf{F}^{(r)})\cdot\mathbf{L}^{(r)}(\mathbf{F}-\mathbf{F}^{(r)}), \tag{A.15}$$

where the tensors $\mathbf{F}^{(r)}$ are constant reference deformation gradients, $\mathbf{S}^{(r)}(\cdot) = \partial W^{(r)}(\cdot)/\partial\mathbf{F}$, and $\mathbf{L}^{(r)}$ are constant fourth-order tensors with major symmetry. The specific choices for $\mathbf{F}^{(r)}$ and $\mathbf{L}^{(r)}$ are different in the contexts of the GSO and TSO methods, and therefore the pertinent discussions are postponed for now.

Having defined the local behavior, the corresponding effective stored-energy function of the LCC, $\widehat{W}_T$ say, can be readily determined in terms of the effective modulus tensor, $\widetilde{\mathbf{L}}$, of a *linear-elastic* composite with the same microstructure as the actual fiber-reinforced elastomer and phase moduli $\mathbf{L}^{(1)}$ and $\mathbf{L}^{(2)}$; an explicit expression for $\widehat{W}_T$ in terms of $\tilde{\mathbf{L}}$ is given by equation (28) in

Lopez-Pamies and Ponte Castañeda [92]. In this work, we will make use of the following Willis estimate [150]:

$$\widetilde{\mathbf{L}} = \mathbf{L}^{(1)} + c_0 \left[(1-c_0)\mathbf{P} - (\mathbf{L}^{(1)} - \mathbf{L}^{(2)})^{-1}\right]^{-1}, \tag{A.16}$$

which is known to be exact to second order in the heterogeneity contrast and to first order in c_0, and particularly well suited for the "particulate" microstructures of interest here. The Eshelby-type tensor $\mathbf{P}$ in (A.16) contains information about the shape (cylindrical and circular) and distribution (aligned and randomly and isotropically distributed in the transverse plane) of the fibers in the underformed configuration. The components of $\mathbf{P}$ in a coordinate system $\mathbf{e}_i$ $(i = 1, 2, 3)$ with $\mathbf{e}_3 = \mathbf{N}$ are given by

$$P_{ijkl} = \frac{1}{2\pi}\int_0^{2\pi} \left(L^{(1)}_{imkn}\xi_m\xi_n\right)^{-1} \xi_j\xi_l \, \mathrm{d}\theta, \tag{A.17}$$

where, $\xi_1 = \cos\theta$, $\xi_2 = \sin\theta$, and $\xi_3 = 0$. It should also be noted that $\mathbf{P}$ depends on the modulus tensor $\mathbf{L}^{(1)}$, but not on $\mathbf{L}^{(2)}$, has major symmetry, and

$$P_{i3kl} = P_{ijk3} = 0 \quad \text{for} \quad i, j, k, l = 1, 2, 3. \tag{A.18}$$

A.3.2 Tangent second-order estimates

Following Ponte Castañeda and Tiberio ([124]), the use of a LCC with the prescriptions $\mathbf{F}^{(r)} = \langle \mathbf{F} \rangle^{(r)} \equiv \overline{\mathbf{F}}^{(r)}$ and $\mathbf{L}^{(r)} = \partial^2 W^{(r)}(\overline{\mathbf{F}}^{(r)})/\partial \mathbf{F}^2$ $(r = 1, 2)$ leads to the following approximation for the effective stored-energy function (A.8):

$$\widehat{W}(\overline{\mathbf{F}}) = (1-c_0)[W^{(r)}(\overline{\mathbf{F}}^{(1)}) + \frac{1}{2}\mathbf{S}^{(1)}(\overline{\mathbf{F}}^{(1)}) \cdot (\overline{\mathbf{F}} - \overline{\mathbf{F}}^{(1)})] + c_0[W^{(2)}(\overline{\mathbf{F}}^{(2)}) + \frac{1}{2}\mathbf{S}^{(2)}(\overline{\mathbf{F}}^{(2)}) \cdot (\overline{\mathbf{F}} - \overline{\mathbf{F}}^{(2)})]. \tag{A.19}$$

In this context, the variables $\overline{\mathbf{F}}^{(1)}$ and $\overline{\mathbf{F}}^{(2)}$, denoting the phase averages of the deformation gradient field in the LCC, are determined by means of the system of equations:

$$\overline{\mathbf{F}} = (1-c_0)\overline{\mathbf{F}}^{(1)} + c_0\overline{\mathbf{F}}^{(2)} \tag{A.20}$$

and

$$\overline{\mathbf{F}} - \overline{\mathbf{F}}^{(1)} = \mathbf{P}\left(\mathbf{L}^{(1)}(\overline{\mathbf{F}} - \overline{\mathbf{F}}^{(1)}) + c_0(\mathbf{S}^{(1)}(\overline{\mathbf{F}}^{(1)}) - \mathbf{S}^{(2)}(\overline{\mathbf{F}}^{(2)}))\right). \tag{A.21}$$

Note that the estimate (A.19) is relatively simple to evaluate. This becomes more evident by first realizing—with the help of (A.18)—that $\overline{F}^{(1)}_{i3} = \overline{F}^{(2)}_{i3} = \overline{F}_{i3}$ for $i = 1, 2, 3$. Then, using (A.20) to express the unknown components of $\overline{\mathbf{F}}^{(2)}$ in terms of the unknown components of $\overline{\mathbf{F}}^{(1)}$, the problem essentially reduces to solving numerically the remaining six non-trivial scalar equations in (A.21) for the six remaining unknown components $\overline{F}^{(1)}_{i\beta}$ $(i = 1, 2, 3,$ and $\beta = 1, 2)$.

As opposed to the GSO estimate, the TSO estimate (A.19) has the disadvantage that it can become inconsistent with the overall kinematical constraint $\det \overline{\mathbf{F}} = 1$ resulting from the incompressibility limit $\kappa^{(1)} \to \infty$ and $\kappa^{(2)} \to \infty$ for *general loading conditions* (see Ponte Castañeda

[124], Lahellec et al. [69], Lopez-Pamies and Ponte Castañeda [91] for an in-depth discussion of this deficiency). However, for some special loading conditions, namely, for combined antiplane and axisymmetric shear deformations, the TSO estimate (A.19) can be shown to be fully consistent with the constraint $\det\overline{\mathbf{F}} = 1$ in the limit as the matrix and fibers are made incompressible. The explicit computation of (A.19) for these special conditions is spelled out in the next subsection.

Incompressible estimate for combined antiplane-axisymmetric shear

In this subsection, we outline the computation of the TSO estimate (A.19) for the effective stored-energy function of fiber-reinforced elastomers with *incompressible* generalized Neo-Hookean matrix and fiber phases under antiplane combined with axisymmetric shear deformations. To this end, we consider an $\overline{\mathbf{F}}$ of the form (A.11) with $\overline{\gamma}_p = \overline{\psi}_{\overline{\gamma}} = 0$ and set (without loss of generality) $\Delta = 1/\kappa^{(1)} = 1/\kappa^{(2)}$, where the parameter Δ will be taken to tend to zero in order to model incompressible behavior.

Then, guided by numerical results (not shown here) for finite values of $\kappa^{(1)}$ and $\kappa^{(2)}$, it is assumed that the asymptotic expansion for the 6 unknown components[1] $\overline{F}^{(1)}_{i\alpha}$ ($i = 1,2,3$, and $\alpha = 1,2$) in the limit as $\Delta \to 0$ is of the form:

$$\overline{F}^{(1)}_{i\alpha} = \overset{\circ}{\overline{F}}{}^{(1)}_{i\alpha} + \overset{\smile}{\overline{F}}{}^{(1)}_{i\alpha}\,\Delta + O(\Delta^2), \tag{A.22}$$

where $\overset{\circ}{\overline{F}}{}^{(1)}_{i\alpha}$ and $\overset{\smile}{\overline{F}}{}^{(1)}_{i\alpha}$ are unknown coefficients to be determined from the asymptotic expansion of equations (A.21) in the limit as $\Delta \to 0$. Indeed, substituting (A.22) in (A.21) and subsequently expanding in small values of Δ yields a system of hierarchical equations for the unknown coefficients in (A.22). The resulting equations of orders Δ^{-1} and Δ^0, which can be solved explicitly, are consistent with the *exact* overall incompressibility constraint (A.12), and lead to the following relations:

$$\overset{\circ}{\overline{F}}{}^{(1)}_{11} = \overset{\circ}{\overline{F}}{}^{(1)}_{22} = \overline{\lambda}_p, \quad \overset{\circ}{\overline{F}}{}^{(1)}_{12} = \overset{\circ}{\overline{F}}{}^{(1)}_{21} = \overset{\circ}{\overline{F}}{}^{(1)}_{32} = 0, \quad \overset{\circ}{\overline{F}}{}^{(1)}_{31} = \overline{\gamma}^{(1)}_n, \tag{A.23}$$

where the variable $\overline{\gamma}^{(1)}_n$ is determined as the solution of the non-linear algebraic equation

$$\sqrt{g^{(1)}_I(I^{(1)}_N)\left[g^{(1)}_I(I^{(1)}_N) + 2g^{(1)}_{II}(I^{(1)}_N)\left(\overline{\gamma}^{(1)}_n\right)^2\right]}\left(\overline{\gamma}_n - \overline{\gamma}^{(1)}_n\right) + c_0\left(g^{(2)}_I(I^{(2)}_N)\overline{\gamma}^{(2)}_n - g^{(1)}_I(I^{(1)}_N)\overline{\gamma}^{(1)}_n\right) = 0. \tag{A.24}$$

In this expression, the notations

$$\overline{\gamma}^{(2)}_n = \frac{\overline{\gamma}_n - (1-c_0)\overline{\gamma}^{(1)}_n}{c_0}, \tag{A.25}$$

$I^{(1)}_N = \overline{\mathbf{F}}^{(1)}\cdot\overline{\mathbf{F}}^{(1)} = 2/\overline{\lambda}_n + \overline{\lambda}^2_n + (\overline{\gamma}^{(1)}_n)^2$, and $I^{(2)}_N = \overline{\mathbf{F}}^{(2)}\cdot\overline{\mathbf{F}}^{(2)} = 2/\overline{\lambda}_n + \overline{\lambda}^2_n + (\overline{\gamma}^{(2)}_n)^2$ has been introduced for convenience. Physically, the variables $\overline{\gamma}^{(1)}_n$ and $\overline{\gamma}^{(2)}_n$ above denote the average amount of antiplane shear in the matrix and fibers, respectively, in the incompressibility limit.

[1] Recall that $\overline{F}^{(1)}_{i3} = \overline{F}_{i3}$ and $\overline{F}^{(2)}_{ij} = (\overline{F}_{ij} - (1-c_0)\overline{F}^{(1)}_{ij})/c_0$ $(i,j = 1,2,3)$.

With the help of relations (A.22)–(A.25), it is a simple matter to deduce that in the limit when the matrix and fibers are taken to be incompressible, the TSO estimate (A.19) reduces to:

$$\begin{aligned}\widehat{W}(\overline{\mathbf{F}}) = \widehat{\Phi}(\overline{\lambda}_n, 0, \overline{\gamma}_n) = (1-c_0)\left[g^{(1)}(I_N^{(1)}) + g_I^{(1)}(I_N^{(1)})\overline{\gamma}_n^{(1)}\left(\overline{\gamma}_n - \overline{\gamma}_n^{(1)}\right)\right] \\ + c_0\left[g^{(2)}(I_N^{(2)}) + g_I^{(2)}(I_N^{(2)})\overline{\gamma}_n^{(2)}\left(\overline{\gamma}_n - \overline{\gamma}_n^{(2)}\right)\right]\end{aligned} \tag{A.26}$$

for combined antiplane-axisymmetric shear deformations. Thus, the computation of this estimate is seen to amount to solving numerically only one non-linear equation. Moreover, for pure axisymmetric shear ($\overline{\gamma}_n = 0$), the TSO estimate (A.26) reduces identically to the Voigt bound, which is known to be an exact result for this mode of deformation (see Subsection 4.1). In addition, for Neo-Hookean phases (i.e., $g^{(1)}(I) = \mu^{(1)}(I-3)/2$ and $g^{(2)}(I) = \mu^{(2)}(I-3)/2$), (A.26) can be shown to be *exact* for fiber-reinforced elastomers with the "composite cylinder assemblage" microstructure of Hashin (see Subsection 4.1 below and Section 3 in deBotton et al. [28]).

A.3.3 Generalized second-order estimates

Following Lopez-Pamies and Ponte Castañeda [92], the alternative use of a LCC with prescriptions $\mathbf{F}^{(1)} = \overline{\mathbf{F}}$, $\mathbf{F}^{(2)} = \langle \mathbf{F} \rangle^{(2)} \equiv \overline{\mathbf{F}}^{(2)}$,

$$L_{ijkl}^{(1)} = \overline{Q}_{rm}\overline{Q}_{jn}\overline{Q}_{sp}\overline{Q}_{lq}\overline{R}_{ir}\overline{R}_{ks}L_{mnpq}^{*}, \tag{A.27}$$

and $\mathbf{L}^{(2)} = \partial^2 W^{(2)}(\overline{\mathbf{F}}^{(2)})/\partial \mathbf{F}^2$ leads to the following approximation for the effective stored-energy function (A.8):

$$\widehat{W}(\overline{\mathbf{F}}) = (1-c_0)[W^{(1)}(\hat{\mathbf{F}}^{(1)}) - \mathbf{S}^{(1)}(\overline{\mathbf{F}}) \cdot (\hat{\mathbf{F}}^{(1)} - \overline{\mathbf{F}}^{(1)})] + c_0 W^{(2)}(\overline{\mathbf{F}}^{(2)}). \tag{A.28}$$

In the above expressions, $\overline{\mathbf{R}}$ and $\overline{\mathbf{Q}}$ are the orthogonal tensors in the decompositions $\overline{\mathbf{F}} = \overline{\mathbf{R}}\,\overline{\mathbf{U}} = \overline{\mathbf{R}}\,\overline{\mathbf{Q}}\,\overline{\mathbf{D}}\,\overline{\mathbf{Q}}^T$, where $\overline{\mathbf{D}} \doteq \sum_{i=1}^{3} \overline{\lambda}_i \overline{\mathbf{v}}_i \otimes \overline{\mathbf{v}}_i$ and $\overline{\mathbf{Q}} = \overline{\mathbf{M}}_i \otimes \overline{\mathbf{v}}_i$, with $\overline{\mathbf{v}}_i$ denoting a Cartesian basis for the laboratory frame of reference and $\overline{\lambda}_i$, $\overline{\mathbf{M}}_i$ the principal values and the corresponding directions of the macroscopic right stretch tensor $\overline{\mathbf{U}}$. The tensor $\mathbf{L}^*$ is orthotropic relative to $\overline{\mathbf{v}}_i$ and is defined in terms of seven independent moduli, denoted by ℓ_α^* ($\alpha = 1, 2, ..., 7$) (see relation (A.51) in the Appendix). Moreover, $\overline{\mathbf{F}}^{(1)}$ and $\overline{\mathbf{F}}^{(2)}$ denote the phase averages of the deformation gradient field in the LCC which, together with the tensor $\hat{\mathbf{F}}^{(1)}$ and the seven unknown moduli ℓ_α^* in $\mathbf{L}^*$, are determined by the following system of coupled, non-linear, algebraic equations:

$$\overline{\mathbf{F}} = (1-c_0)\overline{\mathbf{F}}^{(1)} + c_0\overline{\mathbf{F}}^{(2)}, \tag{A.29}$$

$$\overline{\mathbf{F}} - \overline{\mathbf{F}}^{(2)} = (1-c_0)\mathbf{P}\left(\mathbf{L}^{(1)}(\overline{\mathbf{F}} - \overline{\mathbf{F}}^{(2)}) - \mathbf{S}^{(1)}(\overline{\mathbf{F}}) + \mathbf{S}^{(2)}(\overline{\mathbf{F}}^{(2)})\right), \tag{A.30}$$

$$\mathbf{S}^{(1)}(\hat{\mathbf{F}}^{(1)}) - \mathbf{S}^{(1)}(\overline{\mathbf{F}}) = \mathbf{L}^{(1)}(\hat{\mathbf{F}}^{(1)} - \overline{\mathbf{F}}), \tag{A.31}$$

$$(\hat{\mathbf{F}}^{(1)}-\overline{\mathbf{F}})\cdot\frac{\partial\mathbf{L}^{(1)}}{\partial\ell_\alpha^*}(\hat{\mathbf{F}}^{(1)}-\overline{\mathbf{F}})=\frac{2}{1-c_0}\frac{\partial\widehat{W}_T}{\partial\ell_\alpha^*}=k_\alpha, \tag{A.32}$$

where the variables k_α ($\alpha=1,2,...,7$) are given by

$$k_\alpha=-\frac{c_0}{1-c_0}(\overline{\mathbf{F}}-\overline{\mathbf{F}}^{(2)})\cdot\frac{\partial\mathbf{L}^{(1)}}{\partial\ell_\alpha^*}(\overline{\mathbf{F}}-\overline{\mathbf{F}}^{(2)})-\frac{c_0}{(1-c_0)^2}\mathbf{A}\cdot\frac{\partial\mathbf{P}}{\partial\ell_\alpha^*}\mathbf{A}. \tag{A.33}$$

with $\mathbf{A}\doteq\mathbf{P}^{-1}(\overline{\mathbf{F}}-\overline{\mathbf{F}}^{(2)})$. Note that equation (A.29)—which is nothing more than the overall average condition of the deformation gradient field—can be solved explicitly for $\overline{\mathbf{F}}^{(1)}$ in terms of $\overline{\mathbf{F}}^{(2)}$. Furthermore, with the help of (A.18), it is not difficult to show from (A.30) that $\overline{F}_{i3}^{(2)}=\overline{F}_{i3}$ ($i=1,2,3$). Thus, the computation of the GSO estimate (A.28) is seen to reduce ultimately to solving numerically a system of 22 coupled, non-linear, algebraic equations for the 22 scalar unknowns $\overline{F}_{i\beta}^{(2)}$ ($i=1,2,3;\beta=1,2$), $\hat{F}_{ij}^{(1)}$ ($i,j=1,2,3$), and ℓ_α^* ($\alpha=1,2,...,7$).

For general loading conditions of the form (A.11), the computation of the GSO estimate (A.28) in the incompressible limit leads to a complex set of asymptotic equations that are difficult to simplify analytically. However, for the special case of generalized plane-strain deformations (i.e., $\overline{\gamma}_n=0$), the resulting asymptotic analysis becomes manageable (see the Appendix). The specialization of (A.28) to these special conditions is the substance of the next subsection.

Incompressible estimate for generalized plane-strain deformations

To avoid loss of continuity, the pertinent (lengthy) derivations are given in the Appendix, and here we will only record the final result of the asymptotic analysis. Thus, in the limit as $\kappa^{(1)}\to\infty$ and $\kappa^{(2)}\to\infty$, the estimate (A.28) for the effective stored-energy function (A.8) simplifies to:

$$\widehat{W}(\overline{\mathbf{F}})=\widehat{\Phi}(\overline{\lambda}_n,\overline{\gamma}_p,0)=(1-c_0)g^{(1)}(\hat{I}_P^{(1)})+c_0g^{(2)}(I_P^{(2)}), \tag{A.34}$$

for generalized-plane strain deformations. In these expressions,

$$\begin{aligned}\hat{I}_P^{(1)}=&c_0\left(\frac{\overline{\lambda}_1-\overline{\lambda}_1^{(2)}}{(1-c_0)\,\overline{\lambda}_1^{(2)}\overline{\lambda}_1\overline{\lambda}_n}\right)^2\left[\left(\overline{\lambda}_1^{(2)}\overline{\lambda}_1\overline{\lambda}_n+1\right)^2+\left(\overline{\lambda}_1^2+\left(\overline{\lambda}_1^{(2)}\right)^2\right)\overline{\lambda}_n\right]\\&+\left(\frac{\overline{\lambda}_1-c_0\overline{\lambda}_1^{(2)}}{1-c_0}\right)^2+\left(\frac{\overline{\lambda}_2-c_0\overline{\lambda}_2^{(2)}}{1-c_0}\right)^2+\overline{\lambda}_n^2\end{aligned} \tag{A.35}$$

and

$$I_P^{(2)}=\left(\overline{\lambda}_1^{(2)}\right)^2+\left(\overline{\lambda}_2^{(2)}\right)^2+\overline{\lambda}_n^2, \tag{A.36}$$

where $\overline{\lambda}_1=\frac{\sqrt{\overline{\gamma}_p^2+4\overline{\lambda}_p^2}-\overline{\gamma}_p}{2}$, $\overline{\lambda}_2=\frac{\sqrt{\overline{\gamma}_p^2+4\overline{\lambda}_p^2}+\overline{\gamma}_p}{2}$, $\overline{\lambda}_2^{(2)}=1/\left(\overline{\lambda}_1^{(2)}\,\overline{\lambda}_n\right)$, with $\overline{\lambda}_p$ satisfying the exact incompressibility constraint (A.12), and the variable $\overline{\lambda}_1^{(2)}$ being the solution of the non-linear

algebraic equation

$$\Big[(1+c_0)g_I^{(1)}(\hat{I}_P^{(1)})+(1-c_0)g_I^{(2)}(I_P^{(2)})\Big]\left(\overline{\lambda}_n^{-2}-(\overline{\lambda}_1^{(2)})^4\right)- \\ g_I^{(1)}(\hat{I}_P^{(1)})\left[2\overline{\lambda}_1^{(2)}\overline{\lambda}_1(\overline{\lambda}_2^2-(\overline{\lambda}_1^{(2)})^2)-\frac{(\overline{\lambda}_1^4-(\overline{\lambda}_1^{(2)})^4)\overline{\lambda}_2}{\overline{\lambda}_1}\right]=0. \tag{A.37}$$

Thus, it is seen that the GSO estimate (A.34) is quite simple in form, as its computation amounts to solving numerically just one non-linear equation. Moreover, it is worth remarking that for pure axisymmetric shear ($\overline{\gamma}_p=0$), the estimate (A.34)—much like the TSO estimate (A.26)—reduces identically to the Voigt bound. In addition, for pure plane-strain deformations ($\overline{\lambda}_p=1$) and in the limit of rigid fibers, (A.34) recovers the estimate of Lopez-Pamies and Ponte Castañeda ([93]) for the effective behavior of elastomers reinforced by a random distribution of circular rigid particles (see relation (27) together with (33) in that reference).

A.4 A constitutive model for general loading conditions

The effective stored-energy function (A.8) of *incompressible* fiber-reinforced elastomers under *general loading conditions* can in principle be determined (approximately) by taking the limit $\kappa^{(1)}\to\infty$ and $\kappa^{(2)}\to\infty$ in the second-order estimate (A.28). However, as already pointed out in the preceding section, the asymptotic analysis required for the computation of this limit is quite complicated. Because of this, and keeping in mind our objective to construct an estimate for (A.8) that is as simple as possible, we do not attempt to carry out such an asymptotic analysis here, and instead we propose to combine in a consistent fashion the GSO result (A.34) for generalized plane-strain deformations with the TSO result (A.26) for antiplane-axisymmetric shear deformations into one estimate for general loading conditions.

Before proceeding with the details, it is helpful to make the following two remarks:

1. The GSO estimate (A.28) for the effective stored-energy function of fiber-reinforced elastomers, with generalized Neo-Hookean phases of the form (A.1), depends weakly on the invariant $\overline{\psi}_{\overline{\gamma}}$.

2. The TSO estimate (A.19) for the effective stored-energy function of *incompressible* fiber-reinforced elastomers is practically identical to the GSO estimate (A.28) for the special case of combined antiplane-axisymmetric deformations.

To illustrate the first remark, sample GSO results for the effective stored-energy function $\widehat{W}(\overline{\mathbf{F}})=\widehat{\phi}(1+\ell,(1+\ell)^{-2},\ell,\ell,\overline{\psi}_{\overline{\gamma}})$ of a specific fiber-reinforced composite with compressible Gent phases (A.2) are plotted in Fig. A.1 for $\overline{\psi}_{\overline{\gamma}}=0,\pi/4$ and $\pi/2$, as a function of the loading parameter ℓ.

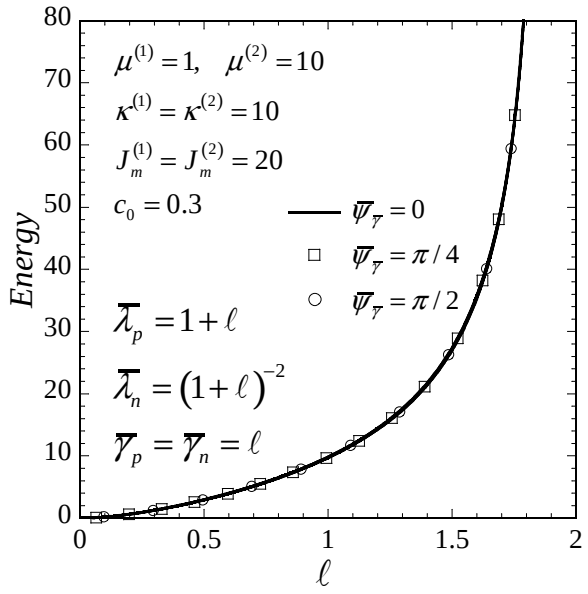

Figure A.1: The GSO estimate (A.28) for the effective stored-energy $\widehat{\phi}$ of a fiber-reinforced elastomer with compressible Gent phases subjected to an $\overline{\mathbf{F}}$ of the form (A.11), as a function of the loading parameter ℓ, for various values of the invariant $\overline{\psi}_{\overline{\gamma}}$.

The results clearly indicate that the GSO estimates are very much independent of the value of the invariant $\overline{\psi}_{\overline{\gamma}}$. To illustrate the second remark, on the other hand, sample GSO and TSO results for the effective stored-energy function $\widehat{W}(\overline{\mathbf{F}})=\widehat{\phi}(1+\ell,(1+\ell)^{-2},0,\ell,0)$ of fiber-reinforced elastomers with Gent phases are plotted in Fig. A.2 for various values of the bulk moduli $\kappa^{(1)}$ and $\kappa^{(2)}$, as a function of the loading parameter ℓ. The results in this figure clearly show that the GSO and TSO estimates are very close for large values of $\kappa^{(1)}$ and $\kappa^{(2)}$.

Guided by the above two remarks, we now proceed with the combination of the estimates (A.34) and (A.26) into one estimate for general loading conditions. We start out by considering a macroscopic deformation gradient of the form $\overline{\mathbf{F}}=\overline{\mathbf{D}}+\overline{\gamma}_n\mathbf{e}_3\otimes\mathbf{e}_1$, where $\overline{\mathbf{D}}$ is given by (A.49) in the Appendix, such that $\det\overline{\mathbf{F}}=\det\overline{\mathbf{D}}=\overline{\lambda}_1\overline{\lambda}_2\overline{\lambda}_n=\overline{\lambda}_p^2\overline{\lambda}_n=1$. Note that this form of $\overline{\mathbf{F}}$ is sufficiently general for our purposes, since it depends on all three invariants $\overline{\lambda}_n$, $\overline{\gamma}_p$ and $\overline{\gamma}_n$, but *not* on $\overline{\psi}_{\overline{\gamma}}$, and for the special cases $\overline{\gamma}_n=0$ and $\overline{\gamma}_p=0$, it reduces identically to the loading conditions associated with the estimates (A.34) and (A.26), respectively.

Then, for consistency with the above-proposed form of $\overline{\mathbf{F}}$, we generalize the values of the quantities $\mathbf{F}^{(1)}$, $\overline{\mathbf{F}}^{(1)}$, $\mathbf{F}^{(2)}$, $\overline{\mathbf{F}}^{(2)}$ and $\hat{\mathbf{F}}^{(1)}$, involved in the computation of the GSO and TSO estimates, in the following manner: $\mathbf{F}^{(1)}=\overline{\mathbf{D}}+\overline{\gamma}_n^{(1)}\mathbf{e}_3\otimes\mathbf{e}_1$, $\overline{\mathbf{F}}^{(1)}=\overline{\mathbf{D}}^{(1)}+\overline{\gamma}_n^{(1)}\mathbf{e}_3\otimes\mathbf{e}_1$, $\mathbf{F}^{(2)}=\overline{\mathbf{F}}^{(2)}=\overline{\mathbf{D}}^{(2)}+\overline{\gamma}_n^{(2)}\mathbf{e}_3\otimes\mathbf{e}_1$, where $\overline{\mathbf{D}}^{(1)}=\mathrm{diag}(\overline{\lambda}_1^{(1)},\overline{\lambda}_2^{(1)},\overline{\lambda}_\mathrm{n})$ and $\overline{\mathbf{D}}^{(2)}=\mathrm{diag}(\overline{\lambda}_1^{(2)},\overline{\lambda}_2^{(2)},\overline{\lambda}_\mathrm{n})$ are coaxial with $\overline{\mathbf{D}}$, and $\hat{\mathbf{F}}^{(1)}=\hat{F}_{\alpha\beta}^{(1)}\mathbf{e}_\alpha\otimes\mathbf{e}_\beta+\overline{\lambda}_n\mathbf{e}_3\otimes\mathbf{e}_3+\overline{\gamma}_n^{(1)}\mathbf{e}_3\otimes\mathbf{e}_1$ $(\alpha,\beta=1,2)$. In the same spirit,

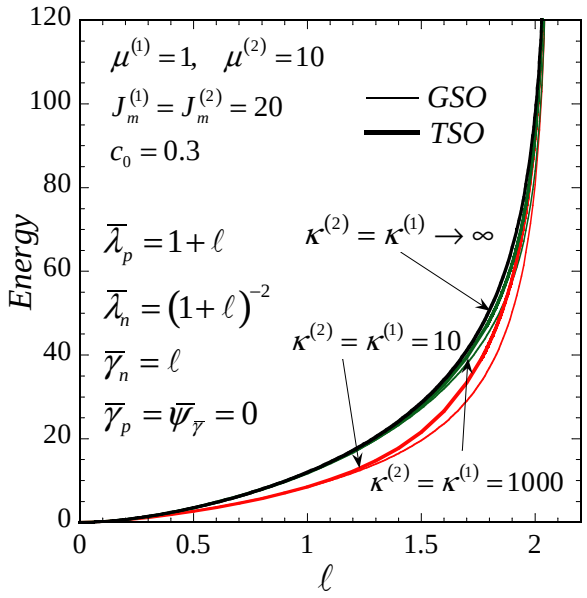

Figure A.2: The GSO (A.28) and TSO (A.19) estimates for the effective stored-energy $\widehat{\phi}$ of fiber-reinforced elastomers with compressible Gent phases subjected to antiplane combined with axisymmetric shear loadings, as a function of the loading parameter ℓ, for $\kappa^{(1)}=\kappa^{(2)}=10$ and $\kappa^{(1)}=\kappa^{(2)}=1000$. The corresponding incompressible TSO estimate (A.26) is also shown.

the associated invariants $I_N^{(1)}$, $I_N^{(2)}$, $I_P^{(2)}$ and $\hat{I}_P^{(1)}$ are generalized as follows: $I_N^{(1)}\doteq I^{(1)}=\mathbf{F}^{(1)}\cdot\mathbf{F}^{(1)}$, $I_N^{(2)}=I_P^{(2)}\doteq I^{(2)}=\overline{\mathbf{F}}^{(2)}\cdot\overline{\mathbf{F}}^{(2)}$, and $\hat{I}_P^{(1)}\doteq\hat{I}^{(1)}=\hat{\mathbf{F}}^{(1)}\cdot\hat{\mathbf{F}}^{(1)}$.

Next, we assume that the equation (A.37) for $\overline{\lambda}_1^{(2)}$ in the context of the GSO estimate (A.34) and the equation (A.24) for $\overline{\gamma}_n^{(1)}$ in the context of the TSO estimate (A.26), hold for the more general loading condition $\overline{\mathbf{F}}=\overline{\mathbf{D}}+\overline{\gamma}_n\mathbf{e}_3\otimes\mathbf{e}_1$, with the only difference that the invariants $I_N^{(1)}$, $I_N^{(2)}$, $I_P^{(2)}$, and $\hat{I}_P^{(1)}$ in the relevant expressions are replaced by their more general counterparts defined above, i.e., $I_N^{(1)}\to I^{(1)}=\mathbf{F}^{(1)}\cdot\mathbf{F}^{(1)}$, $\{I_N^{(2)},I_P^{(2)}\}\to I^{(2)}=\overline{\mathbf{F}}^{(2)}\cdot\overline{\mathbf{F}}^{(2)}$ and $\hat{I}_P^{(1)}\to\hat{I}^{(1)}=\hat{\mathbf{F}}^{(1)}\cdot\hat{\mathbf{F}}^{(1)}$.

Finally, making use of the above hypotheses, we obtain the following estimate for the effective stored-energy function (A.8) of fiber-reinforced elastomers, with incompressible generalized Neo-Hookean phases, subjected to general loading conditions:

$$\begin{aligned}\widehat{W}(\overline{\mathbf{F}})=\widehat{\Phi}(\overline{\lambda}_n,\overline{\gamma}_p,\overline{\gamma}_n)=&(1-c_0)\left[g^{(1)}(\hat{I}^{(1)})+g_I^{(1)}(I^{(1)})\overline{\gamma}_n^{(1)}\left(\overline{\gamma}_n-\overline{\gamma}_n^{(1)}\right)\right]\\&+c_0\left[g^{(2)}(I^{(2)})+g_I^{(2)}(I^{(2)})\overline{\gamma}_n^{(2)}\left(\overline{\gamma}_n-\overline{\gamma}_n^{(2)}\right)\right],\end{aligned}\tag{A.38}$$

referred in what follows as the second-order estimate (SOE). In this expression,

$$\begin{aligned}
\hat{I}^{(1)} = \hat{\mathbf{F}}^{(1)} \cdot \hat{\mathbf{F}}^{(1)} &= \left(\frac{\overline{\lambda}_1 - c_0 \overline{\lambda}_1^{(2)}}{1 - c_0} \right)^2 + \left(\frac{\overline{\lambda}_2 - c_0 \overline{\lambda}_2^{(2)}}{1 - c_0} \right)^2 + \overline{\lambda}_n^2 + \left(\overline{\gamma}_n^{(1)} \right)^2 + \\
&\quad + c_0 \left(\frac{\overline{\lambda}_1 - \overline{\lambda}_1^{(2)}}{(1 - c_0)\, \overline{\lambda}_1^{(2)} \overline{\lambda}_1 \overline{\lambda}_n} \right)^2 \left[\left(\overline{\lambda}_1^{(2)} \overline{\lambda}_1 \overline{\lambda}_n + 1 \right)^2 + \left(\overline{\lambda}_1^2 + \left(\overline{\lambda}_1^{(2)} \right)^2 \right) \overline{\lambda}_n \right], \\
I^{(1)} = \mathbf{F}^{(1)} \cdot \mathbf{F}^{(1)} &= \overline{\lambda}_1^2 + \overline{\lambda}_2^2 + \overline{\lambda}_n^2 + \left(\overline{\gamma}_n^{(1)} \right)^2, \\
I^{(2)} = \overline{\mathbf{F}}^{(2)} \cdot \overline{\mathbf{F}}^{(2)} &= \left(\overline{\lambda}_1^{(2)} \right)^2 + \left(\overline{\lambda}_2^{(2)} \right)^2 + \overline{\lambda}_n^2 + \left(\overline{\gamma}_n^{(2)} \right)^2,
\end{aligned} \tag{A.39}$$

where

$$\overline{\lambda}_1 = \frac{\sqrt{\overline{\gamma}_p^2 + 4/\overline{\lambda}_n} - \overline{\gamma}_p}{2}, \quad \overline{\lambda}_2 = \frac{\sqrt{\overline{\gamma}_p^2 + 4/\overline{\lambda}_n} + \overline{\gamma}_p}{2}, \quad \overline{\lambda}_2^{(2)} = \frac{1}{\overline{\lambda}_1^{(2)} \overline{\lambda}_n}, \quad \overline{\gamma}_n^{(2)} = \frac{\overline{\gamma}_n - (1 - c_0) \overline{\gamma}_n^{(1)}}{c_0}, \tag{A.40}$$

and the variables $\overline{\lambda}_1^{(2)}$ and $\overline{\gamma}_n^{(1)}$ are the solution of the system of *coupled*, non-linear equations:

$$\begin{aligned}
&\sqrt{g_I^{(1)}(I^{(1)}) [g_I^{(1)}(I^{(1)}) + 2 g_{II}^{(1)}(I^{(1)}) (\overline{\gamma}_n^{(1)})^2]} (\overline{\gamma}_n - \overline{\gamma}_n^{(1)}) \\
&+ c_0 \left(g_I^{(2)}(I^{(2)}) \overline{\gamma}_n^{(2)} - g_I^{(1)}(I^{(1)}) \overline{\gamma}_n^{(1)} \right) = 0,
\end{aligned} \tag{A.41}$$

and

$$\begin{aligned}
&\left[(1 + c_0) g_I^{(1)}(\hat{I}^{(1)}) + (1 - c_0) g_I^{(2)}(I^{(2)}) \right] \left(\overline{\lambda}_n^{-2} - (\overline{\lambda}_1^{(2)})^4 \right) \\
&- g_I^{(1)}(\hat{I}^{(1)}) \left[2 \overline{\lambda}_1^{(2)} \overline{\lambda}_1 (\overline{\lambda}_2^2 - (\overline{\lambda}_1^{(2)})^2) - \frac{(\overline{\lambda}_1^4 - (\overline{\lambda}_1^{(2)})^4) \overline{\lambda}_2}{\overline{\lambda}_1} \right] = 0.
\end{aligned} \tag{A.42}$$

In connection with the above estimate for fiber-reinforced elastomers, it is useful to make the following remarks:

- As opposed to other constitutive models that have thus far been proposed in the literature, the model (A.38) permits the consideration of constitutive behaviors for the matrix and fibers that are more general than Neo-Hookean.

- For generalized plane-strain deformations ($\overline{\gamma}_n = 0$), the stored-energy function (A.38) reduces identically to the GSO estimate (A.34). On the other hand, for antiplane-axisymmetric shear deformations ($\overline{\gamma}_p = 0$), (A.38) reduces to the TSO estimate (A.26). For more general loading conditions with $\overline{\gamma}_n \neq 0$ and $\overline{\gamma}_p \neq 0$, (A.38) can be thought of as a *non-linear interpolation* between (A.34) and (A.26).

- The computation of the constitutive model (A.38) amounts to solving a system of only two non-linear algebraic equations, (A.41) and (A.42), and thus it can be readily implemented into commercial numerical packages (e.g., ABAQUS) for solving structural problems of interest.

- In the limit of small deformations, (A.38) recovers the corresponding linear-elastic Willis estimate, which is known to be very accurate for small and moderate values of the volume fraction of fibers c_0.

A.4.1 Comparisons with bounds and other estimates

For the fairly general class of matrix and fiber behaviors of interest in this work, the only known (non-trivial) bound for the effective stored-energy function (A.8) is the Voigt upper bound [111]:

$$\widehat{\Phi}^V(\overline{\lambda}_n, \overline{\gamma}_p, \overline{\gamma}_n) = (1-c_0)g^{(1)}(\overline{I}) + c_0 g^{(2)}(\overline{I}), \tag{A.43}$$

where $\overline{I} = \overline{\mathbf{F}}\cdot\overline{\mathbf{F}} = 2/\overline{\lambda}_n + \overline{\lambda}_n^2 + \overline{\gamma}_p^2 + \overline{\gamma}_n^2$. It should be noted that (A.43) is isotropic and depends on the microstructure only through the volume fraction of the fibers c_0. In general, the result (A.43) is expected to be too stiff, in view of the fact that it is a rigorous upper bound. Note, for instance, that in the limit of rigid fibers (A.43) becomes unbounded for all $\overline{\mathbf{F}} \neq \mathbf{I}$, that is, the composite is undeformable, which is in contradiction with physical evidence (for transverse and longitudinal shear loading). Nevertheless, there exist certain special cases for which the Voigt bound is an *exact* result, as it will be discussed below (see He et al. [49] for a general discussion on uniform-field exact solutions in fiber-reinforced elastomers). At any rate, the proposed constitutive model (A.38) can be shown to satisfy the rigorous upper bound (A.43) for all deformations.

The Voigt bound (A.43) makes use of the trial field $\mathbf{F}(\mathbf{X}) = \overline{\mathbf{F}}$ for all $\mathbf{X}$ in Ω_0, which in general is consistent with the equilibrium requirement at all points $\mathbf{X}$ in $\Omega_0^{(1)}$ (but *not* on $\partial\Omega_0^{(1)}$) and all $\mathbf{X}$ in $\Omega_0^{(2)}$ (but *not* on $\partial\Omega_0^{(2)}$). Thus, this field is an exact solution to the problem (A.8) for all values of $\overline{\mathbf{F}}$ whenever the traction-continuity requirement across the matrix/fibers interfaces:

$$\mathbf{S}^{(1)}(\overline{\mathbf{F}})\mathbf{e} = \mathbf{S}^{(2)}(\overline{\mathbf{F}})\mathbf{e} \quad \text{for all} \quad \mathbf{e}\perp\mathbf{N} \quad \text{with} \quad \mathbf{e}\cdot\mathbf{e} = 1 \tag{A.44}$$

are satisfied. For axisymmetric shear deformations, conditions (A.44) reduce to the constraint $p^{(1)} - p^{(2)} = 2(g_I^{(1)}(\overline{I}) - g_I^{(2)}(\overline{I}))/\overline{\lambda}_n$— with $p^{(1)}$ and $p^{(2)}$ denoting respectively the constant pressures in the matrix and fibers—which can be satisfied for any value of $\overline{\lambda}_n$. In other words, the Voigt bound (A.43) is exact for axisymmetric shear deformations. For loading conditions other than axisymmetric shear, (A.44) is equivalent to $p^{(1)} = p^{(2)}$ and $g_I^{(1)}(\overline{I}) = g_I^{(2)}(\overline{I})$, which actually require equality of the stress tensors in the matrix and fibers. Although the first of these conditions can always be enforced, the second cannot be satisfied, in general. For example, in the case of composites with Neo-Hookean phases $g_I^{(1)}(\overline{I}) = \mu^{(1)}/2 \neq \mu^{(2)}/2 = g_I^{(2)}(\overline{I})$. However, there are materials for which the requirement $g_I^{(1)}(\overline{I}) = g_I^{(2)}(\overline{I})$ is met for certain values of $\overline{I}$. An example is that of composites with Gent constituents, for which the requirement specializes to:

$$\frac{\mu^{(1)} J_m^{(1)}}{J_m^{(1)} - (\overline{I}-3)} = \frac{\mu^{(2)} J_m^{(2)}}{J_m^{(2)} - (\overline{I}-3)}, \tag{A.45}$$

where $J_m^{(1)}$ and $J_m^{(2)}$ denote the lock-up parameters of the matrix and fibers, respectively. The above equation has a unique, physically plausible solution for $\overline{I}$ provided that $(J_m^{(1)}(3+J_m^{(2)})\mu^{(1)} - J_m^{(2)}(3+J_m^{(1)})\mu^{(2)})/(J_m^{(1)}\mu^{(1)} - J_m^{(2)}\mu^{(2)}) > 3$. It is not difficult to show that the proposed constitutive model (A.38) recovers such exact solutions of the Voigt-type. Indeed, note that the values $\overline{\lambda}_1^{(2)} = \overline{\lambda}_1$ and $\overline{\gamma}_n^{(1)} = \overline{\gamma}_n$, for which we have $\hat{I}^{(1)} = I^{(1)} = I^{(2)} = \overline{I}$, constitute a solution of the system of equations (A.41) and (A.42) whenever $g_I^{(1)}(\overline{I}) = g_I^{(2)}(\overline{I})$, and for these special cases, the stored-energy function (A.38) reduces to the Voigt bound (A.43).

For the special case when the underlying matrix and fibers are characterized by incompressible Neo-Hookean solids, deBotton et al. [28] derived the following estimate for the effective stored-energy function (A.8):

$$\widehat{\Phi}^{BHS}(\overline{\lambda}_n, \overline{\gamma}_p, \overline{\gamma}_n) = \frac{1}{2}\overline{\mu}\left(\overline{\lambda}_n^2 + \frac{2}{\overline{\lambda}_n} - 3\right) + \frac{\widetilde{\mu}}{2}(\overline{\gamma}_p^2 + \overline{\gamma}_n^2), \tag{A.46}$$

where $\overline{\mu} = (1-c_0)\mu^{(1)} + c_0\mu^{(2)}$ and

$$\widetilde{\mu} = \mu^{(1)}\frac{(1-c_0)\mu^{(1)} + (1+c_0)\mu^{(2)}}{(1+c_0)\mu^{(1)} + (1-c_0)\mu^{(2)}}. \tag{A.47}$$

A nice feature of this estimate—beyond its simplicity—is that it is *exact* for antiplane combined with axisymmetric shear deformations ($\overline{\gamma}_p = 0$) for fiber-reinforced Neo-Hookean elastomers with the "composite cylinder assemblage" microstructure of Hashin. Specializing now the constitutive model (A.38) to Neo-Hookean phases—namely, setting $g^{(1)} = \mu^{(1)}(I-3)/2$ and $g^{(2)} = \mu^{(2)}(I-3)/2$—leads to:

$$\widehat{\Phi}(\overline{\lambda}_n, \overline{\gamma}_p, \overline{\gamma}_n) = (1-c_0)\frac{\mu^{(1)}}{2}(\hat{I}_P^{(1)} - 3) + c_0\frac{\mu^{(2)}}{2}(I_P^{(2)} - 3) + \frac{\widetilde{\mu}}{2}\overline{\gamma}_n^2, \tag{A.48}$$

where it is recalled that $\hat{I}_P^{(1)}$ and $I_P^{(2)}$ are given by expressions (A.35) and (A.36), depending on the unknown $\overline{\lambda}_1^{(2)}$ to be computed as the solution to the forth-order polynomial equation resulting from (A.42) by substituting $g_I^{(1)}(\hat{I}^{(1)}) = \mu^{(1)}/2$ and $g_I^{(2)}(I^{(2)}) = \mu^{(2)}/2$. Clearly, expressions (A.48) and (A.46) are different for general loading conditions. However, for antiplane combined with axisymmetric shear deformations ($\overline{\gamma}_p = 0$), it is easy to verify that (A.48) reduces identically to (A.46), which, again, is exact for "composite cylinder assemblage" microstructures. For more general loading conditions, although not identical, the estimates (A.46) and (A.48) lead to fairly similar results.

A.5 Results and discussion

In this section, we examine in detail some important features of the predictions of the SOE (A.38) for the overall response of fiber-reinforced elastomers. For the purposes of the current discussion,

we consider specific applications to composites with incompressible Neo-Hookean and Gent constituents. Particular emphasis is placed on the specific features of the predicted anisotropy and the coupling among the three modes of shear. In addition, the predictions of the SOE (A.38) are compared with the corresponding predictions of the deBotton et al. (BHS) model (A.46) (for Neo-Hookean phases) and the Voigt upper bound (A.43).

For the purpose of comparing the axisymmetric mode with the in-plane and antiplane modes, it proves useful to introduce the axisymmetric shear variable: $\overline{\gamma}_a = \pm(\overline{\lambda}_n^2 + 2/\overline{\lambda}_n - 3)^{1/2}$, where the plus and minus signs correspond to $\overline{\lambda}_n > 1$ and $\overline{\lambda}_n < 1$, respectively. A path in loading space is defined by $\overline{\gamma}_a = \alpha_a \overline{\gamma}_e$, $\overline{\gamma}_p = \alpha_p \overline{\gamma}_e$ and $\overline{\gamma}_n = \alpha_n \overline{\gamma}_e$, where α_a, α_p and α_n are constants, such that $\overline{\gamma}_e \equiv (\overline{\gamma}_a^2 + \overline{\gamma}_p^2 + \overline{\gamma}_n^2)^{1/2} = (\overline{I} - 3)^{1/2}$. For our objectives here, it will be sufficient to confine our attention to loadings for which $\overline{\gamma}_a \geq 0$. Furthermore, we define the stored-energy function $\widehat{\Psi}$ such that $\widehat{\Psi}(\overline{\gamma}_a, \overline{\gamma}_p, \overline{\gamma}_n) = \widehat{\Phi}(\overline{\lambda}_n, \overline{\gamma}_p, \overline{\gamma}_n)$, and the stress measures $\overline{S}_a = \partial\widehat{\Psi}/\partial\overline{\gamma}_a$, $\overline{S}_p = \partial\widehat{\Psi}/\partial\overline{\gamma}_p$ and $\overline{S}_n = \partial\widehat{\Psi}/\partial\overline{\gamma}_n$, so that the effective response of a composite for a given loading path may be conveniently represented by $\widehat{\Psi}$ and/or $\overline{S}_a$, $\overline{S}_p$, $\overline{S}_n$ as functions of $\overline{\gamma}_e$.

Figure A.3 shows the SOE for the response of a fiber-reinforced elastomer with incompressible Neo-Hookean phases under axisymmetric, in-plane and antiplane shear loadings. The calculations have been performed for a contrast $\mu^{(2)}/\mu^{(1)} = 10$ and an initial volume fraction of the fibers $c_0 = 0.3$. Recall that the predictions of the Voigt model are identical for all three modes of shear and coincide with the predictions of the SOE and the BHS model for the axisymmetric mode, which correspond to exact solutions of the Voigt-type (see section A.4), while the predictions of the BHS model for the other two modes are the same as the SOE predictions for antiplane shear. It is observed that the response of the composite under axisymmetric shear is much stiffer than its responses under the other two modes (as predicted by the SOE and BHS models). This observation together with the fact that the predictions of the SOE and BHS models are exact for the antiplane mode and the composite cylinder assemblage microstructure illustrates how inaccurate the predictions of the Voigt model can be. In addition, according to the SOE, the in-plane mode is slightly stiffer than the antiplane mode. The difference between these predictions increases with increasing amount of shear, but it remains small even at very large deformations.

The results shown in Fig. A.3 are representative of the main features of the SOE (A.48), and for this reason we do not include here further applications for composites with incompressible Neo-Hookean constituents. It should be noticed, however, that the difference between the SOE predictions for the responses under in-plane and antiplane shear loadings increase with increasing $\mu^{(2)}/\mu^{(1)}$ and/or increasing c_0, although not significantly. In addition, calculations for combined loading conditions have shown that coupling effects are also insignificant. The above observations lead us to the conclusion that the predictions of the SOE and BHS models for composites with incompressible Neo-Hookean constituents are in good agreement.

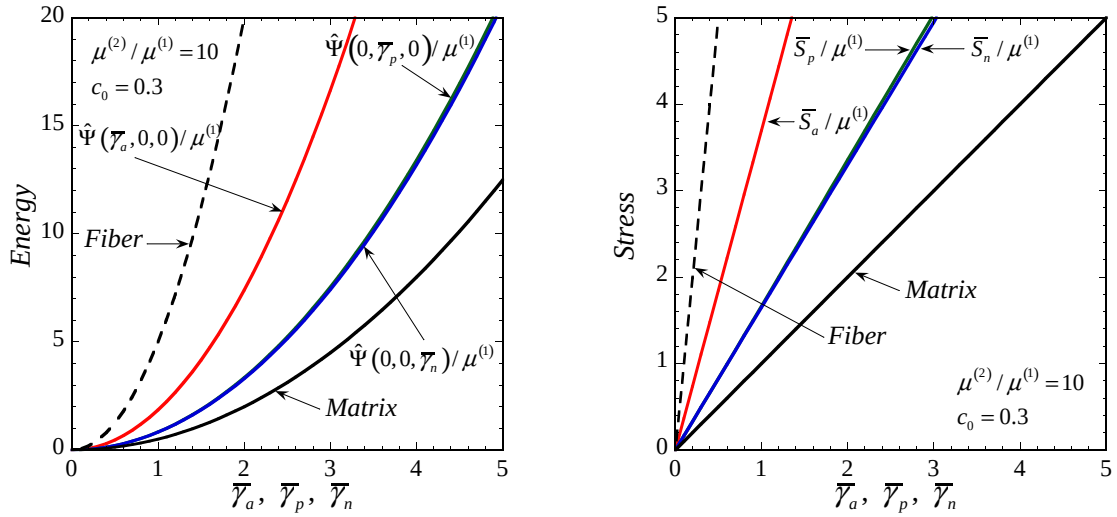

Figure A.3: Second-order estimates (SOE) for the effective response of a fiber-reinforced elastomer with incompressible Neo-Hookean phases under the three different modes of shear. The results are shown as a function of the corresponding amount of shear $\overline{\gamma}_a$,$\overline{\gamma}_p$ and $\overline{\gamma}_n$. (a) The energies $\widehat{\Psi}(\overline{\gamma}_a,0,0)$, $\widehat{\Psi}(0,\overline{\gamma}_p,0)$ and $\widehat{\Psi}(0,0,\overline{\gamma}_n)$, normalized by $\mu^{(1)}$. (b) The corresponding (non-zero) normalized stresses $\overline{S}_a(\overline{\gamma}_a,0,0)$, $\overline{S}_p(0,\overline{\gamma}_p,0)$ and $\overline{S}_n(0,0,\overline{\gamma}_n)$.

Figure A.4 shows the same results as Figure A.3, but for a composite made of incompressible Gent phases with $\mu^{(2)}/\mu^{(1)}=10$, $J_m^{(1)}=30$, $J_m^{(2)}=5$ and $c_0=0.3$. Recall again that the SOE for the axisymmetric mode is identical to the Voigt upper bound and therefore exact. It is observed that, in accordance with the behavior of a homogeneous Gent material, there exists a range of deformations for which the effective response of the composite under consideration can be approximated reasonably well by the corresponding response of the composite with incompressible Neo-Hookean phases shown in Fig. A.3. This is because, within this range of deformations, the contribution of the parameters $J_m^{(1)}$ and $J_m^{(2)}$ is insignificant. It is also observed that the predictions for the axisymmetric mode are significantly stiffer than the predictions for the other two modes, and that this difference increases with increasing deformation. Finally, as opposed to the case of the composite with Neo-Hookean phases (Fig. A.3), we observe that here the difference between the predicted responses under in-plane and antiplane shear is substantial at large deformations, with the predictions for the antiplane mode being stiffer.

Figure A.5(a) compares the SOE for the in-plane and antiplane shear responses of fiber-reinforced elastomers with an incompressible Gent matrix with $\mu^{(1)}=1$ and $J_m^{(1)}=30$ and incompressible Neo-Hookean fibers with $\mu^{(2)}=2,5,20,\infty$ and initial concentration $c_0=0.3$. It is observed that for all values of $\mu^{(2)}$ there exists a range of deformations, extending well beyond

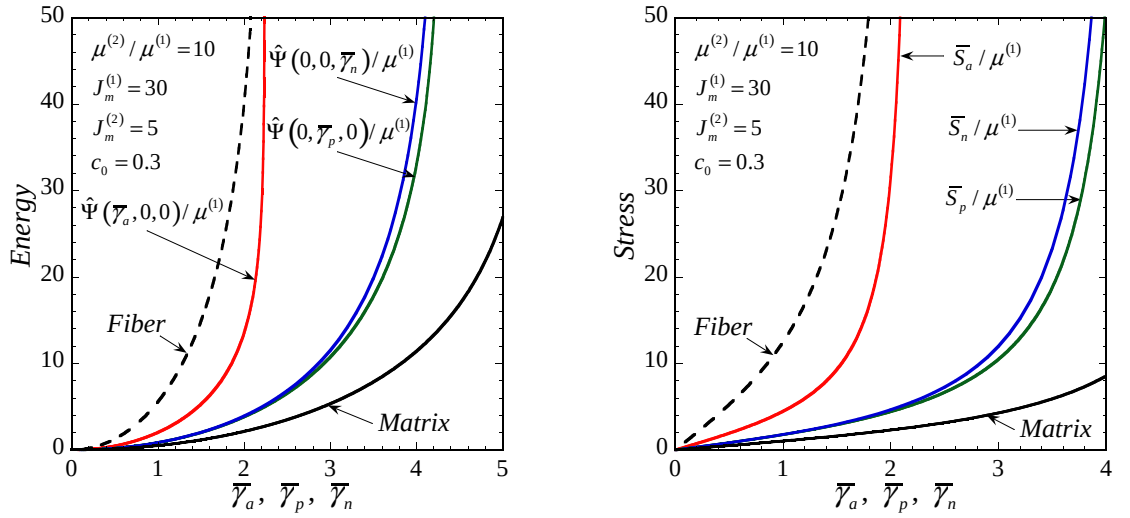

Figure A.4: Second-order estimates (SOE) for the effective response of a fiber-reinforced elastomer with incompressible Gent phases under the three different modes of shear. The results are shown as a function of the corresponding amount of shear $\overline{\gamma}_a$,$\overline{\gamma}_p$ and $\overline{\gamma}_n$. (a) The energies $\widehat{\Psi}(\overline{\gamma}_a,0,0)$, $\widehat{\Psi}(0,\overline{\gamma}_p,0)$ and $\widehat{\Psi}(0,0,\overline{\gamma}_n)$, normalized by $\mu^{(1)}$. (b) The corresponding (non-zero) normalized stresses $\overline{S}_a(\overline{\gamma}_a,0,0)$, $\overline{S}_p(0,\overline{\gamma}_p,0)$ and $\overline{S}_n(0,0,\overline{\gamma}_n)$.

the linear-elastic regime, for which the predictions for $\overline{S}_p$ and $\overline{S}_n$ are essentially the same. The size of this range increases with decreasing $\mu^{(2)}$. For larger values of the deformation, the predictions for $\overline{S}_p$ and $\overline{S}_n$ are different, in general. The fact that the matrix of the composites considered here is a Gent material imposes limits in the amount of the applied deformation. We observe that the stresses $\overline{S}_p$ and $\overline{S}_n$ increase rapidly near the corresponding lock-up limits of the composites, which turn out to be different for in-plane and antiplane shear loadings. Specifically, for the composite with rigid fibers ($\mu^{(2)} \to \infty$) it is found that $\overline{\gamma}_p^{lock} < \overline{\gamma}_n^{lock}$, while for the other three cases ($\mu^{(2)} = 2, 5, 20$) we have $\overline{\gamma}_n^{lock} < \overline{\gamma}_p^{lock}$ (see Fig. A.5(b)). Finally, note that the intersection points of the curves representing $\overline{S}_p$, $\overline{S}_n$ and the corresponding stress measure of the matrix material (subjected to simple shear) correspond to exact solutions of the Voigt-type.

Figure A.5(b) presents the SOE predictions for the limiting values of axisymmetric, $\overline{\gamma}_a^{lock}$, in-plane, $\overline{\gamma}_p^{lock}$, and antiplane, $\overline{\gamma}_n^{lock}$, shear loadings at which composites made out of incompressible Gent phases locks up. The results are shown as functions of $J_m^{(2)}$ for a fixed lock-up parameter of the matrix, $J_m^{(1)} = 30$, and volume fractions of the fibers $c_0 = 0.1, 0.3, 0.5$. It is easy to show that $\overline{\gamma}_a^{lock} = \min\{(J_m^{(1)})^{1/2}, (J_m^{(2)})^{1/2}\}$, which, once again, is an exact result, and may be interpreted as follows: for $J_m^{(2)} < J_m^{(1)}$ the composite locks-up because the fibers lock-up, for $J_m^{(2)} > J_m^{(1)}$ the overall lock-up is due to the lock-up of the matrix and for $J_m^{(1)} = J_m^{(2)}$ the composite locks-up because both

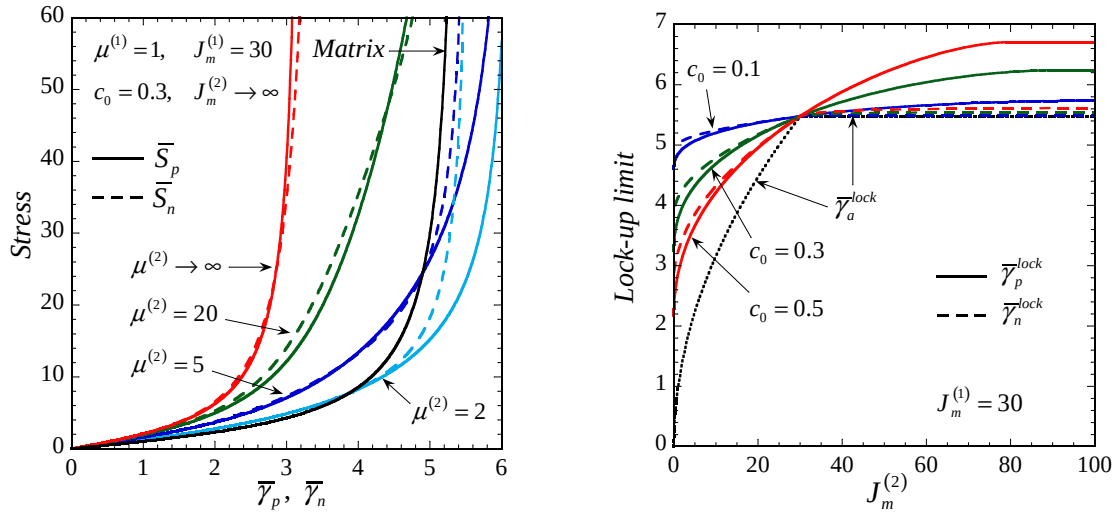

Figure A.5: (*a*) SOE predictions for the macroscopic stresses $\overline{S}_p(0,\overline{\gamma}_p,0)$ and $\overline{S}_n(0,0,\overline{\gamma}_n)$ of fiber-reinforced elastomers made out of an incompressible Gent matrix and Neo-Hookean fibers, with various values of $\mu^{(2)}$, as functions of the amounts of shear $\overline{\gamma}_p$ and $\overline{\gamma}_n$, respectively. (*b*) SOE predictions for the lock-up limits $\overline{\gamma}_a^{lock}$, $\overline{\gamma}_p^{lock}$ and $\overline{\gamma}_n^{lock}$ of axisymmetric, in-plane and antiplane shear loadings, respectively—applied to composites with incompressible Gent constituents—as functions of the lock-up parameter of the fibers, $J_m^{(2)}$, for various values of c_0 and $J_m^{(1)}=30$.

phases lock-up. The lock-up limit for in-plane shear loadings is the limiting value of $\overline{\gamma}_p$, which, along with the corresponding limiting value of $\overline{\lambda}_1^{(2)}$, satisfy at least one of the conditions $\hat{I}^{(1)}-3=J_m^{(1)}$ and $I^{(2)}-3=J_m^{(2)}$. It turns out that, for values of $J_m^{(2)}$ between zero and a "critical" value, depending on c_0, both conditions are met and they provide a system of two equations for the computation of the two unknowns, namely $\overline{\gamma}_p^{lock}$ and the corresponding limiting value of $\overline{\lambda}_1^{(2)}$. The aforementioned critical value of $J_m^{(2)}$ corresponds to the maximum $\overline{\gamma}_p^{lock}$ obtained in this way. For $J_m^{(2)}$ greater than this critical value, only the condition $\hat{I}^{(1)}-3=J_m^{(1)}$ is satisfied and $\overline{\gamma}_p^{lock}$ is independent of $J_m^{(2)}$. Note that $\overline{\gamma}_p^{lock}$ is independent of $\mu^{(2)}/\mu^{(1)}$ for all values of $J_m^{(2)}$. Similarly, the lock-up limit for antiplane shear loadings is the limiting value of $\overline{\gamma}_n$, which, along with the corresponding limiting value of $\overline{\gamma}_n^{(1)}$, satisfy at least one of the conditions $I^{(1)}-3=J_m^{(1)}$, or $I^{(2)}-3=J_m^{(2)}$. For $J_m^{(2)}\le J_m^{(1)}$ both conditions are satisfied, and $\overline{\gamma}_n^{lock}=(1-c_0)(J_m^{(1)})^{1/2}+c_0(J_m^{(2)})^{1/2}$. For $J_m^{(2)}>J_m^{(1)}$, only the first condition is met in the lock-up limit, which in this case depends weakly on $\mu^{(2)}/\mu^{(1)}$, and the corresponding results presented in this figure have been obtained numerically for $\mu^{(2)}/\mu^{(1)}=10$. It is observed that $\overline{\gamma}_a^{lock}$ is less than both $\overline{\gamma}_p^{lock}$ and $\overline{\gamma}_n^{lock}$ for all values of $J_m^{(2)}$. For $J_m^{(2)}<J_m^{(1)}$, we observe that $\overline{\gamma}_p^{lock}<\overline{\gamma}_n^{lock}$, while for $J_m^{(2)}>J_m^{(1)}$ it is found that $\overline{\gamma}_p^{lock}>\overline{\gamma}_n^{lock}$. In addition, the difference between $\overline{\gamma}_p^{lock}$ and $\overline{\gamma}_n^{lock}$ increases with increasing $|J_m^{(2)}-J_m^{(1)}|$, which is a measure of the

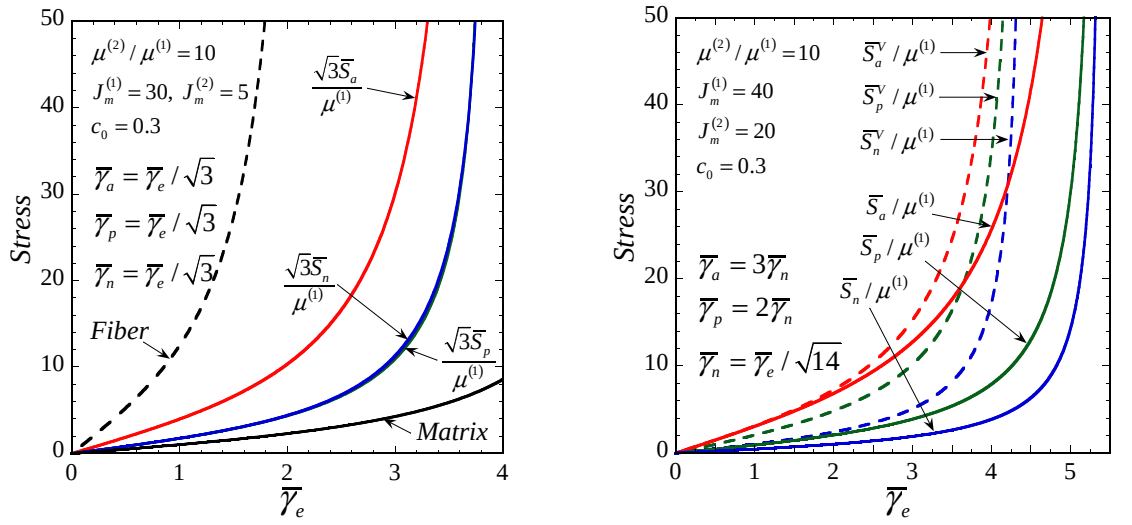

Figure A.6: (a) Combined loading of the composite considered in Fig. A.3. The predictions of the SOE for the stresses $\sqrt{3}\,\overline{S}_a(\overline{\gamma}_a,\overline{\gamma}_p,\overline{\gamma}_n)$, $\sqrt{3}\,\overline{S}_p(\overline{\gamma}_a,\overline{\gamma}_p,\overline{\gamma}_n)$ and $\sqrt{3}\,\overline{S}_n(\overline{\gamma}_a,\overline{\gamma}_p,\overline{\gamma}_n)$, normalized by $\mu^{(1)}$, are plotted as functions of the loading parameter $\overline{\gamma}_e$. (b) Combined loading of a fiber-reinforced elastomer with incompressible Gent phases. The normalized stresses $\overline{S}_a(\overline{\gamma}_a,\overline{\gamma}_p,\overline{\gamma}_n)$, $\overline{S}_p(\overline{\gamma}_a,\overline{\gamma}_p,\overline{\gamma}_n)$ and $\overline{S}_n(\overline{\gamma}_a,\overline{\gamma}_p,\overline{\gamma}_n)$, as predicted by the SOE and the Voigt upper bound (distinguished by a superscript "V"), are shown as functions of the loading parameter $\overline{\gamma}_e$.

heterogeneity contrast at large deformations, and/or increasing c_0. Finally, for $J_m^{(2)}=J_m^{(1)}$ and any value of c_0, it is found that $\overline{\gamma}_a^{lock}=\overline{\gamma}_p^{lock}=\overline{\gamma}_n^{lock}=(J_m^{(1)})^{1/2}$, which corresponds to an exact result of the Voigt type.

Figure A.6(a) illustrates the coupling in the SOE for the response of the composite considered in Fig. A.4. It is observed that, for the range of values of $\overline{\gamma}_e$ for which the overall response of this composite is essentially identical with the response of the corresponding composite with Neo-Hookean constituents (see discussion referred to Fig. A.3), the stresses associated with the combined loading are actually the same as the corresponding stresses for the individual modes (i.e., the three modes are uncoupled). For larger values of $\overline{\gamma}_e$, the overall response of the composite under the combined loading differs significantly from its responses under the pure loadings. Specifically, we observe that, although for combined loading the axisymmetric shear stress is substantially larger than the other two stress measures, the associated difference is much smaller than the corresponding difference observed for the case of the pure modes, and the same is true for the difference between the in-plane and antiplane shear stresses. Furthermore, for the limiting value of $\overline{\gamma}_e$ at which the composite locks-up, all stress measures become unbounded for the combined loading.

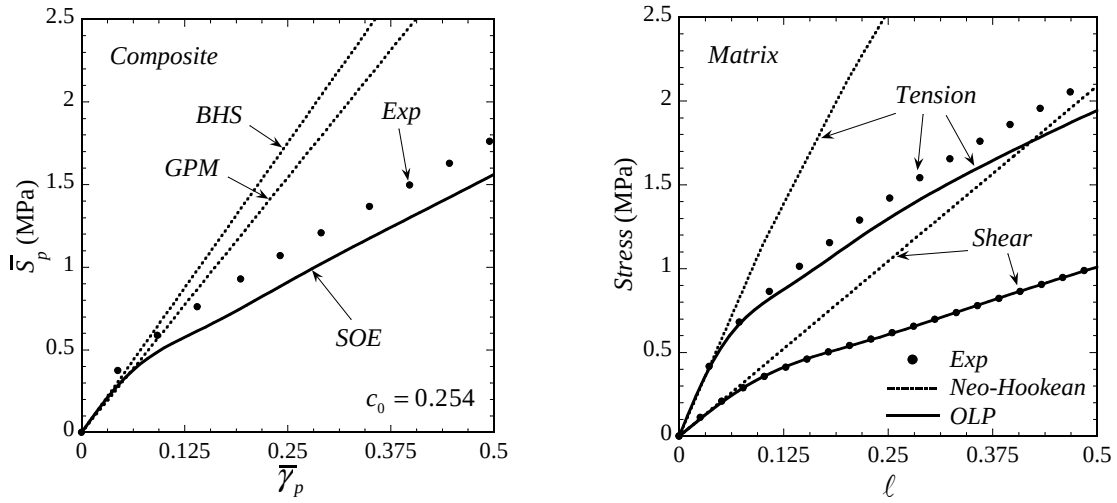

(a) (b)

Figure A.7: (*a*) The predictions of the SOE, BHS and GPM models for the effective in-plane shear response of an elastomer reinforced with *randomly* distributed, rigid fibers are compared with corresponding experimental (Exp) results for *periodically* distributed fibers. The SOE makes use of an OLP model for the matrix. (*b*) The OLP and Neo-Hookean models, used to characterize the matrix material in part (*a*), are compared with corresponding experimental data for *uniaxial tension* ($\ell = \lambda - 1$, with λ being the tensile stretch) and *simple shear* ($\ell = \gamma$, with γ denoting the amount of shear) tests.

Figure A.6(*b*) presents the SOE and the Voigt upper bound for the effective behavior of a fiber-reinforced elastomer made out of incompressible Gent constituents when subjected to combined loading conditions. It is observed that the predictions of the two models for the effective response differ significantly, and that the differences increase with increasing deformation. The Voigt model predicts that the limiting value of $\overline{\gamma}_e$ for which the composite locks-up is identical with the corresponding value of the material of the fibers (note that in this case $J_m^{(2)} < J_m^{(1)}$), while according to the SOE model, this value is in-between the corresponding values associated with the lock-up limits of the phase materials.

Finally, Fig. A.7(*a*) presents a comparison of the SOE with the experimental results of Lahellec et al. [69] for the transverse shear response of a fiber-reinforced elastomer with a *periodic* microstructure. While this comparison is not entirely fair since the SOE is for a random microstructure, and corresponds to the softest possible estimate for this type of microstructure (since it arises from the Willis estimates (A.16), which is a rigorous lower bound for the effective modulus tensor), the comparison shows that the method has the capability to incorporate more general constitutive behaviors (than neo-Hookean) for the matrix phase, leading to much better agreement with experimental results for actual rubbers. Thus, it can be seen that the SOE greatly improves

on the predictions of the model of deBotton et al. [28] (BHS) for reinforced Neo-Hookean solids, as well as the model of Guo et al. [45] (GPM), which appears to be inconsistent with the bounding character of the Willis estimate for infinitesimal deformations. In connection with these results, it should be mentioned that the matrix phase was fitted with the OLP model (Lopez-Pamies [90]; see also eqn. (33) in Lopez-Pamies et al [98]) for a simple shear test, as depicted in Fig. A.7(*b*). The material parameters for this (incompressible) matrix model were found to be: $\mu_1^{(1)} = 0.6$ MPa, $\mu_2^{(1)} = 1.664$ MPa, $\mu_3^{(1)} = 1.915$ MPa, $\alpha_1^{(1)} = -16.212$, $\alpha_2^{(1)} = -133.471$ and $\alpha_3^{(1)} = 0.696$. (Note that the shear modulus of the OLP model in the ground state is $\mu^{(1)} = \mu_1^{(1)} + \mu_2^{(1)} + \mu_3^{(1)} = 4.179$ MPa.) In this figure, a comparison is also provided with the experimental results for the matrix material in tension, which although not quite as good as for simple shear for the parameters chosen, is still much better than the Neo-Hookean model.

A.6 Concluding remarks

In this work, we have developed a homogenization-based constitutive model for *incompressible* fiber-reinforced elastomers with *random* microstructures. In particular, the model applies to composites with a single family of aligned, cylindrical fibers distributed randomly and isotropically in the matrix phase (in the undeformed configuration). The constitutive behavior of the phases is characterized by stored-energies that are *general* functions of the first invariant of the right Cauchy-Green deformation tensor (i.e., generalized Neo-Hookean materials). The model provides a generalization of the results of Lopez-Pamies and Ponte Castañeda [93] for plane strain (transverse in-plane) loading of fiber-reinforced elastomers (with rigid fibers), which it recovers in this limiting case. Compared to other constitutive models proposed thus far in the literature (e.g., Guo et al. [45], deBotton et al. [28]) for the materials of interest here, the present model has the unique feature that it is applicable to composites with more general matrix and fiber behaviors than Neo-Hookean while directly accounting in a rigorous manner for the microstructure. Given the well-known limitations of the Neo-Hookean model at large strains, the new model should prove useful in practical applications involving large elastic strains. Other important features of the model include the fact that it accounts for the coupling among the three possible modes of shear that are expected under general loading conditions, and that it recovers available exact solutions. More specifically, the model recovers any possible exact Voigt-type (i.e., uniform deformation field) solution, as well as the exact effective response of fiber-reinforced elastomers with Neo-Hookean phases and composite cylinder assemblage microstructures subjected to axisymmetric combined with antiplane shear deformations. A further strength of the model is that—in spite of incorporating fine microstructural information—it is still relatively simple to implement, requiring only the solution of a system of two non-linear, algebraic equations. Finally, it is important to emphasize

that one of the advantages of these homogenization-based models is that they can be generalized, at least in principle, to more general types of microstructures and material behaviors.

Acknowledgements

This work was begun with the support of NSF grant DMS-0204617 and completed with the support of NSF grant CMMI-0654063.

A.7 Appendix. Generalized second-order estimates for incompressible fiber-reinforced rubbers under generalized plane-strain conditions

In this appendix, we sketch the derivation for the incompressibility limit of the GSO estimate (A.28) under generalized plane-strain loading conditions. To this end, we first present the specialization of the general system of equations (A.29)–(A.32) associated with the compressible problem to generalized plane-strain deformations, and then discuss the corresponding asymptotic analysis in the limit as $\kappa^{(1)} = \kappa^{(2)} \to \infty$.

The generalized plane-strain problem corresponds to an $\overline{\mathbf{F}}$ with components (in the coordinate system $\mathbf{e}_i$) given by (A.11) with $\overline{\gamma}_n = 0$. Because of the objectivity and material symmetry (invariance under rotations about $\mathbf{N} = \mathbf{e}_3$) of the GSO estimate (A.28), there is no loss of generality in considering a diagonal $\overline{\mathbf{F}}$ of the form

$$\overline{\mathbf{F}} = \overline{\mathbf{D}} = \overline{\lambda}_1 \mathbf{e}_1 \otimes \mathbf{e}_1 + \overline{\lambda}_2 \mathbf{e}_2 \otimes \mathbf{e}_2 + \overline{\lambda}_n \mathbf{e}_3 \otimes \mathbf{e}_3, \tag{A.49}$$

where

$$\overline{\lambda}_1 = \frac{\sqrt{\overline{\gamma}_p^2 + 4\overline{\lambda}_p^2} - \overline{\gamma}_p}{2} \qquad \text{and} \qquad \overline{\lambda}_2 = \frac{\sqrt{\overline{\gamma}_p^2 + 4\overline{\lambda}_p^2} + \overline{\gamma}_p}{2}. \tag{A.50}$$

In this case, we have that $\overline{\mathbf{R}} = \overline{\mathbf{Q}} = \mathbf{I}$ and $\mathbf{L}^{(1)} = \mathbf{L}^*$ in (A.27). In addition, following Lopez-Pamies and Ponte Castañeda [93] and Brun et al. [18], the seven independent components of $\mathbf{L}^*$ are chosen to be $L^*_{1111} = \ell^*_1$, $L^*_{2222} = \ell^*_2$, $L^*_{3333} = \ell^*_3$, $L^*_{1122} = \ell^*_4$, $L^*_{1133} = \ell^*_5$, $L^*_{2233} = \ell^*_6$, $L^*_{1212} = \ell^*_7$, while the other non-zero components are defined as

$$\begin{aligned}
&L^*_{2121} = L^*_{1313} = L^*_{3131} = L^*_{2323} = L^*_{3232} = \ell^*_7,\\
&L^*_{1221} = \sqrt{(\ell^*_1 - \ell^*_7)(\ell^*_2 - \ell^*_7)} - \ell^*_4,\\
&L^*_{1331} = \sqrt{(\ell^*_1 - \ell^*_7)(\ell^*_3 - \ell^*_7)} - \ell^*_5,\\
&L^*_{2332} = \sqrt{(\ell^*_2 - \ell^*_7)(\ell^*_3 - \ell^*_7)} - \ell^*_6.
\end{aligned} \tag{A.51}$$

Making use of the above choice for $\mathbf{L}^{(1)}$, it follows that the non-zero components of the microstructural tensor $\mathbf{P}$, as defined by (A.17), specialize to:

$$
\begin{aligned}
&P_{1111} = \frac{\ell_2^* + \ell_7^*(1+2\sqrt{\ell_2^*/\ell_1^*})}{2\ell_7^*(\sqrt{\ell_1^*}+\sqrt{\ell_2^*})^2}, \quad P_{2222} = \frac{\ell_1^* + \ell_7^*(1+2\sqrt{\ell_1^*/\ell_2^*})}{2\ell_7^*(\sqrt{\ell_1^*}+\sqrt{\ell_2^*})^2},\\
&P_{1212} = \frac{\ell_2^* + \ell_7^* + 2\sqrt{\ell_1^*\ell_2^*}}{2\ell_7^*(\sqrt{\ell_1^*}+\sqrt{\ell_2^*})^2}, \qquad P_{2121} = \frac{\ell_1^* + \ell_7^* + 2\sqrt{\ell_1^*\ell_2^*}}{2\ell_7^*(\sqrt{\ell_1^*}+\sqrt{\ell_2^*})^2},\\
&P_{3131} = P_{3232} = \frac{1}{2\ell_7^*}, \quad P_{1122} = P_{1221} = -\frac{\sqrt{(\ell_1^*-\ell_7^*)(\ell_2^*-\ell_7^*)}}{2\ell_7^*(\sqrt{\ell_1^*}+\sqrt{\ell_2^*})^2},
\end{aligned}
\tag{A.52}
$$

$P_{2211} = P_{2112} = P_{1122}$, where it is noted that all of these components depend only on the moduli ℓ_1^*, ℓ_2^* and ℓ_7^*.

In the context of the diagonal form (A.49), together with the above choice of $\mathbf{L}^{(1)}$, it follows from (A.29) and (A.30) that the tensors $\overline{\mathbf{F}}^{(1)}$ and $\overline{\mathbf{F}}^{(2)}$ have the same diagonal form as $\overline{\mathbf{F}}$, and in particular, $\overline{\mathbf{F}}^{(1)} = \mathrm{diag}(\overline{\lambda}_1^{(1)}, \overline{\lambda}_2^{(1)}, \overline{\lambda}_\mathrm{n})$ and $\overline{\mathbf{F}}^{(2)} = \mathrm{diag}(\overline{\lambda}_1^{(2)}, \overline{\lambda}_2^{(2)}, \overline{\lambda}_\mathrm{n})$. In this connection, the relation (A.29) may be conveniently re-written as:

$$
\overline{\lambda}_1^{(1)} = \frac{\overline{\lambda}_1 - c_0\overline{\lambda}_1^{(2)}}{1-c_0} \quad \text{and} \quad \overline{\lambda}_2^{(1)} = \frac{\overline{\lambda}_2 - \mathrm{c}_0\overline{\lambda}_2^{(2)}}{1-\mathrm{c}_0}.
\tag{A.53}
$$

Furthermore, the two non-trivial scalar equations in (A.30) reduce to:

$$
\begin{aligned}
\overline{\lambda}_1 - \overline{\lambda}_1^{(2)} &= (1-c_0)\left[P_{1111}E_{11} + P_{1122}E_{22}\right],\\
\overline{\lambda}_2 - \overline{\lambda}_2^{(2)} &= (1-c_0)\left[P_{1122}E_{11} + P_{2222}E_{22}\right],
\end{aligned}
\tag{A.54}
$$

with

$$
\begin{aligned}
E_{11} =& \ell_1^*(\overline{\lambda}_1 - \overline{\lambda}_1^{(2)}) + \ell_4^*(\overline{\lambda}_2 - \overline{\lambda}_2^{(2)}) - 2(\overline{g}_I^{(1)}\overline{\lambda}_1 - \overline{g}_I^{(2)}\overline{\lambda}_1^{(2)}) -\\
& \overline{\lambda}_2\overline{\lambda}_n\left[\overline{h}_J^{(1)} + \kappa^{(1)}(\overline{J}-1)\right] + \overline{\lambda}_2^{(2)}\overline{\lambda}_n\left[\overline{h}_J^{(2)} + \kappa^{(2)}(\overline{J}^{(2)}-1)\right],\\
E_{22} =& \ell_4^*(\overline{\lambda}_1 - \overline{\lambda}_1^{(2)}) + \ell_2^*(\overline{\lambda}_2 - \overline{\lambda}_2^{(2)}) - 2(\overline{g}_I^{(1)}\overline{\lambda}_2 - \overline{g}_I^{(2)}\overline{\lambda}_2^{(2)}) -\\
& \overline{\lambda}_1\overline{\lambda}_n\left[\overline{h}_J^{(1)} + \kappa^{(1)}(\overline{J}-1)\right] + \overline{\lambda}_1^{(2)}\overline{\lambda}_n\left[\overline{h}_J^{(2)} + \kappa^{(2)}(\overline{J}^{(2)}-1)\right].
\end{aligned}
\tag{A.55}
$$

Here, $\overline{g}_I^{(1)} = g_I^{(1)}(\overline{I})$, $\overline{h}_J^{(1)} = h_J^{(1)}(\overline{J})$, $\overline{g}_I^{(2)} = g_I^{(2)}(\overline{I}^{(2)})$, $\overline{h}_J^{(2)} = h_J^{(2)}(\overline{J}^{(2)})$ have been introduced for ease of notation, where $\overline{I} = \overline{\mathbf{F}}\cdot\overline{\mathbf{F}} = 2\overline{\lambda}_p^2 + \overline{\lambda}_n^2 + \overline{\gamma}_p^2$, $\overline{J} = \det\overline{\mathbf{F}} = \overline{\lambda}_p^2\overline{\lambda}_n$, and

$$
\begin{aligned}
\overline{I}^{(2)} &= \overline{\mathbf{F}}^{(2)}\cdot\overline{\mathbf{F}}^{(2)} = (\overline{\lambda}_1^{(2)})^2 + (\overline{\lambda}_2^{(2)})^2 + \overline{\lambda}_n^2,\\
\overline{J}^{(2)} &= \det\overline{\mathbf{F}}^{(2)} = \overline{\lambda}_1^{(2)}\overline{\lambda}_2^{(2)}\overline{\lambda}_n.
\end{aligned}
\tag{A.56}
$$

The specialization of equations (A.31) and (A.32) to generalized plane-strain deformations has previously been worked out in detail by Brun et al. [18], but for completeness we recall it here. Thus,

for generalized plane-strain deformations of the form (A.49), the "generalized secant conditions" (A.31) can be shown to simplify to:

$$\begin{aligned}
\ell_1^* Y_{11} + \ell_4^* Y_{22} =& 2\hat{g}_I^{(1)}(Y_{11} + \overline{\lambda}_1) + \left[\hat{h}_J^{(1)} + \kappa^{(1)}(\hat{J}^{(1)} - 1)\right](Y_{22} + \overline{\lambda}_2)\overline{\lambda}_n \\
& - 2\overline{g}_I^{(1)}\overline{\lambda}_1 - \left[\overline{h}_J^{(1)} + \kappa^{(1)}(\overline{J} - 1)\right]\overline{\lambda}_2\overline{\lambda}_n, \\
\ell_4^* Y_{11} + \ell_2^* Y_{22} =& 2\hat{g}_I^{(1)}(Y_{22} + \overline{\lambda}_2) + \left[\hat{h}_J^{(1)} + \kappa^{(1)}(\hat{J}^{(1)} - 1)\right](Y_{11} + \overline{\lambda}_1)\overline{\lambda}_n \\
& - 2\overline{g}_I^{(1)}\overline{\lambda}_2 - \left[\overline{h}_J^{(1)} + \kappa^{(1)}(\overline{J} - 1)\right]\overline{\lambda}_1\overline{\lambda}_n, \\
L_{1221}^* =& -\left[\hat{h}_J^{(1)} + \kappa^{(1)}(\hat{J}^{(1)} - 1)\right]\overline{\lambda}_n, \\
\ell_7^* =& 2\hat{g}_I^{(1)},
\end{aligned} \tag{A.57}$$

and

$$\begin{aligned}
\ell_5^* Y_{11} + \ell_6^* Y_{22} =& 2\hat{g}_I^{(1)}\overline{\lambda}_n - 2\overline{g}_I^{(1)}\overline{\lambda}_n - \left[\overline{h}_J^{(1)} + \kappa^{(1)}(\overline{J} - 1)\right]\overline{\lambda}_1\overline{\lambda}_2 \\
& + \left[\hat{h}_J^{(1)} + \kappa^{(1)}(\hat{J}^{(1)} - 1)\right]\left[(Y_{11} + \overline{\lambda}_1)(Y_{22} + \overline{\lambda}_2) - p_1\right].
\end{aligned} \tag{A.58}$$

Here, $Y_{11} \doteq (\hat{F}_{11}^{(1)} - \overline{\lambda}_1)$, $Y_{22} \doteq (\hat{F}_{22}^{(1)} - \overline{\lambda}_2)$, $p_1 \doteq \hat{F}_{12}^{(1)}\hat{F}_{21}^{(1)}$, $\hat{g}_I^{(1)} = g_I^{(1)}(\hat{I}^{(1)})$, $\hat{h}_J^{(1)} = h_J^{(1)}(\hat{J}^{(1)})$, with

$$\begin{aligned}
\hat{I}^{(1)} &= \hat{\mathbf{F}}^{(1)} \cdot \hat{\mathbf{F}}^{(1)} = (Y_{11} + \overline{\lambda}_1)^2 + (Y_{22} + \overline{\lambda}_2)^2 + \overline{\lambda}_n^2 + s, \\
\hat{J}^{(1)} &= \det \hat{\mathbf{F}}^{(1)} = \overline{\lambda}_n^2\left((Y_{11} + \overline{\lambda}_1)(Y_{22} + \overline{\lambda}_2) - p_1\right),
\end{aligned} \tag{A.59}$$

and $s \doteq (\hat{F}_{12}^{(1)})^2 + (\hat{F}_{21}^{(1)})^2$. Furthermore, equations (A.32) can be shown to reduce to

$$Y_{11} = -\frac{k_1 + f_1\, k_4}{\sqrt{k_1 + 4f_1(f_1\, k_2 + k_4/2)}}, \quad Y_{22} = -\frac{k_4/2 + 2f_1\, k_2}{\sqrt{k_1 + 4f_1(f_1\, k_2 + k_4/2)}}, \tag{A.60}$$

and

$$p_1 = Y_{11}Y_{22} - k_4/2, \quad s = k_7 - 2f_4\, p_1, \tag{A.61}$$

where $f_1 = \partial L_{1221}^*/\partial \ell_1^*$ and $f_4 = \partial L_{1221}^*/\partial \ell_7^*$. In connection with the above expressions, it is recalled that the variables k_α are determined by relations (A.33) in the text, which after some algebraic manipulation, may be conveniently expressed as:

$$\begin{aligned}
k_1 =& -\frac{c_0(\overline{\lambda}_1 - \overline{\lambda}_1^{(2)})^2}{1 - c_0} - \frac{c_0}{(1 - c_0)^2}\left[A_{11}^2\frac{\partial P_{1111}}{\partial \ell_1^*} + 2A_{11}A_{22}\frac{\partial P_{1122}}{\partial \ell_1^*} + A_{22}^2\frac{\partial P_{2222}}{\partial \ell_1^*}\right], \\
k_2 =& -\frac{c_0(\overline{\lambda}_2 - \overline{\lambda}_2^{(2)})^2}{1 - c_0} - \frac{c_0}{(1 - c_0)^2}\left[A_{11}^2\frac{\partial P_{1111}}{\partial \ell_2^*} + 2A_{11}A_{22}\frac{\partial P_{1122}}{\partial \ell_2^*} + A_{22}^2\frac{\partial P_{2222}}{\partial \ell_2^*}\right], \\
k_4 =& -\frac{2c_0(\overline{\lambda}_1 - \overline{\lambda}_1^{(2)})(\overline{\lambda}_2 - \overline{\lambda}_2^{(2)})}{1 - c_0}, \\
k_7 =& -\frac{c_0}{(1 - c_0)^2}\left[A_{11}^2\frac{\partial P_{1111}}{\partial \ell_7^*} + 2A_{11}A_{22}\frac{\partial P_{1122}}{\partial \ell_7^*} + A_{22}^2\frac{\partial P_{2222}}{\partial \ell_7^*}\right],
\end{aligned} \tag{A.62}$$

and $k_3 = k_5 = k_6 = 0$, where A_{11} and A_{22} (the only non-zero components of the tensor $\mathbf{A}$) are simply given by

$$A_{11} = \frac{P_{1122}(\overline{\lambda}_2 - \overline{\lambda}_2^{(2)}) - P_{2222}(\overline{\lambda}_1 - \overline{\lambda}_1^{(2)})}{P_{1122}^2 - P_{1111}P_{2222}},$$
$$A_{22} = \frac{P_{1122}(\overline{\lambda}_1 - \overline{\lambda}_1^{(2)}) - P_{1111}(\overline{\lambda}_2 - \overline{\lambda}_2^{(2)})}{P_{1122}^2 - P_{1111}P_{2222}}. \tag{A.63}$$

In summary, for generalized plane-strain deformations, the general system of equations (A.29)–(A.32) essentially reduces to the system of 6 coupled, non-linear, algebraic equations formed by expressions (A.54) and (A.57), for the 6 unknowns $\overline{\lambda}_1^{(2)}$, $\overline{\lambda}_2^{(2)}$, ℓ_1^*, ℓ_2^*, ℓ_4^* and ℓ_7^*. (Note that equation (A.58), which establishes a connection between the moduli ℓ_5^*, ℓ_6^* and the other variables of the problem, does not intervene in the computation of the GSO estimate (A.34) for the effective stored-energy function $\widehat{W}$ under generalized plane-strain deformations.)

Next, we carry out the asymptotic analysis of the above equations associated with the limit $\kappa^{(1)} = \kappa^{(2)} \to \infty$. Making use of the *ansatz* proposed by Lopez-Pamies and Ponte Castañeda [93] (see Appendix A in that reference), it is assumed that the asymptotic expansion for the unknown variables in the limit $\kappa^{(1)} = \kappa^{(2)} \to \infty$ is of the form:

$$\begin{aligned}
\overline{\lambda}_1^{(2)} =& a_0 + a_1\Delta^{1/3} + a_2\Delta^{2/3} + a_3\Delta + a_4\Delta^{4/3} + O(\Delta^{5/3}),\\
\overline{\lambda}_2^{(2)} =& b_0 + b_1\Delta^{1/3} + b_2\Delta^{2/3} + b_3\Delta + b_4\Delta^{4/3} + O(\Delta^{5/3}),\\
\ell_1^* =& d_{-1}\Delta^{-1/3} + d_0 + d_1\Delta^{1/3} + d_2\Delta^{2/3} + d_3\Delta + O(\Delta^{4/3}),\\
\ell_2^* =& e_{-1}\Delta^{-1/3} + e_0 + d_1\Delta^{1/3} + e_2\Delta^{2/3} + e_3\Delta + O(\Delta^{4/3}),\\
\ell_4^* =& f_{-1}\Delta^{-1/3} + f_0 + f_1\Delta^{1/3} + f_2\Delta^{2/3} + f_3\Delta + O(\Delta^{4/3}),\\
\ell_7^* =& m_0 + m_1\Delta^{1/3} + m_2\Delta^{2/3} + m_3\Delta + O(\Delta^{4/3}),
\end{aligned} \tag{A.64}$$

where $\Delta \doteq 1/\kappa^{(1)} = /\kappa^{(2)}$ is a small parameter. The unknown coefficients in these expressions are to be determined from the asymptotic expansion of the system of equations (A.54) and (A.57) in the limit as $\Delta \to 0$. To simplify the presentation of the results, it proves helpful to introduce the following notation for the expansion of the intermediate quantities involved in (A.54) and (A.57):

$$
\begin{aligned}
Y_{11} =& x_0 + x_1\Delta^{1/3} + x_2\Delta^{2/3} + x_3\Delta + O(\Delta^{4/3}),\\
Y_{22} =& y_0 + y_1\Delta^{1/3} + y_2\Delta^{2/3} + y_3\Delta + O(\Delta^{4/3}),\\
p_1 =& z_0 + z_1\Delta^{1/3} + z_2\Delta^{2/3} + z_3\Delta + O(\Delta^{4/3}),\\
s =& t_0 + t_1\Delta^{1/3} + t_2\Delta^{2/3} + t_3\Delta + O(\Delta^{4/3}),\\
\overline{J}^{(2)} =& j_0 + j_1\Delta^{1/3} + j_2\Delta^{2/3} + j_3\Delta + j_4\Delta^{4/3} + O(\Delta^{5/3}),\\
\hat{J}^{(1)} =& \hat{j}_0 + \hat{j}_1\Delta^{1/3} + \hat{j}_2\Delta^{2/3} + \hat{j}_3\Delta + \hat{j}_4\Delta^{4/3} + O(\Delta^{5/3}),\\
\overline{g}_I^{(2)} =& \zeta_0 + \zeta_1\Delta^{1/3} + \zeta_2\Delta^{2/3} + \zeta_3\Delta + O(\Delta^{4/3}),\\
\hat{g}_I^{(1)} =& \hat{\zeta}_0 + \hat{\zeta}_1\Delta^{1/3} + \hat{\zeta}_2\Delta^{2/3} + \hat{\zeta}_3\Delta + O(\Delta^{4/3}),\\
\overline{h}_J^{(2)} =& \eta_0 + \eta_1\Delta^{1/3} + \eta_2\Delta^{2/3} + \eta_3\Delta + O(\Delta^{4/3}),\\
\hat{h}_J^{(1)} =& \hat{\eta}_0 + \hat{\eta}_1\Delta^{1/3} + \hat{\eta}_2\Delta^{2/3} + \hat{\eta}_3\Delta + O(\Delta^{4/3}),
\end{aligned}
\tag{A.65}
$$

where the coefficients in the above expressions are known functions of the coefficients in the right hand side of (A.64) too cumbersome to be included here.

Substituting expressions (A.64) and (A.65) in equations (A.54) and (A.57) and subsequently expanding in small values of Δ leads to a hierarchical system of equations for the unknown coefficients introduced in (A.64). After some algebraic manipulation, the equations of leading order $O(\Delta^{-1})$ can be shown to yield the following results:

$$
\overline{J} \doteq \overline{\lambda}_1\overline{\lambda}_2\overline{\lambda}_n \doteq \overline{\lambda}_p^2\overline{\lambda}_n = 1, \quad j_0 = 1, \quad \hat{j}_0 = 1. \tag{A.66}
$$

Note that condition $(A.66)_1$ is precisely the exact overall incompressibility constraint, and that $(A.66)_2$ may alternatively be written as $b_0 = 1/(a_0\overline{\lambda}_n)$. The equations of next order $O(\Delta^{-2/3})$ imply that $j_1 = 0$ and $\hat{j}_1 = 0$, which ultimately reduce to

$$
b_1 = -\frac{a_1}{a_0^2\overline{\lambda}_n} \quad \text{and} \quad e_{-1} = \overline{\lambda}_1^4\overline{\lambda}_n^2 d_{-1}, \tag{A.67}
$$

respectively.

At this point, in view of the results (A.66) and (A.67), it is useful to recognize that the coefficients x_0, y_0, z_0 and t_0 take the simple form:

$$
\begin{aligned}
x_0 =& \frac{c_0\left(\overline{\lambda}_1 - a_0\right)}{1 - c_0}, \quad y_0 = -\frac{c_0\left(\overline{\lambda}_1 - a_0\right)}{a_0\left(1 - c_0\right)\overline{\lambda}_1\overline{\lambda}_n}, \quad z_0 = -\frac{c_0\left(\overline{\lambda}_1 - a_0\right)^2}{a_0\left(1 - c_0\right)^2\overline{\lambda}_1\overline{\lambda}_n},\\
t_0 =& \frac{y_0^2}{c_0}\left[\left(a_0\overline{\lambda}_1\overline{\lambda}_n + 1\right)^2 + \left(\overline{\lambda}_1^2 + a_0^2\right)\overline{\lambda}_n\right],
\end{aligned}
\tag{A.68}
$$

which are seen to depend *only* on the coefficient a_0, i.e., the leading order term of $\overline{\lambda}_1^{(2)}$. In turn, making use of (A.68), it is not difficult to show that the leading order term of the GSO estimate

(A.28) does also depend *only* on the coefficient a_0. The resulting expression is given by relation (A.34)—together with (A.35) and (A.36)—in the text, where for clarity of notation a_0 was written as $\overline{\lambda}_1^{(2)}$.

Next, the equations of third order $O(\Delta^{-1/3})$ can be shown to lead to

$$j_2 = \hat{j}_2 = d_{-1}\overline{\lambda}_1\left(y_0\overline{\lambda}_1^2\overline{\lambda}_n + x_0\right), \quad f_{-1} = d_{-1}\overline{\lambda}_1\overline{\lambda}_n\left(y_0\overline{\lambda}_1^2\overline{\lambda}_n + \overline{\lambda}_1 + x_0\right), \tag{A.69}$$

while those of fourth order $O(\Delta^0)$ render expressions for j_3, $\hat{j}_3$ and f_0 in terms of a_0, a_1, d_{-1}, d_0 and e_0 too cumbersome to be included here, as well as the following useful result:

$$c_0\left(a_0-\overline{\lambda}_1\right)^2\left(e_0-d_0\overline{\lambda}_1^4\overline{\lambda}_N^2\right) = 2a_0\left(1-c_0\right)\left(\overline{\lambda}_1^4\overline{\lambda}_N^2-1\right)\left(2\overline{\lambda}_1\left(\hat{\zeta}_0-\overline{g}_I^{(1)}\right)+\left(x_0+\overline{\lambda}_1^2\overline{\lambda}_n y_0\right)\hat{\zeta}_0\right). \tag{A.70}$$

Finally, the equations of fifth order $O(\Delta^{1/3})$ are treated in the following manner. First, using the equations resulting from $(A.57)_1$ and $(A.57)_2$, we are able to write down an explicit expression for f_1 in terms of $\hat{j}_4$, a_0, a_1, a_2, b_2, d_{-1}, d_0, e_0, d_1 and e_1. Then, after substituting the obtained expression for f_1 in (the appropriate order equation resulting from) $(A.54)_1$, we generate an explicit expression for j_4 in terms of a_0, a_1, a_2, b_2, d_{-1}, d_0, e_0, d_1. Making use of these results for f_1 and j_4 in $(A.54)_2$ ultimately renders the following condition:

$$\begin{aligned}
&c_0\left(a_0-\overline{\lambda}_1\right)^2\left(e_0-d_0\overline{\lambda}_1^4\overline{\lambda}_n^2\right)a_0 = \\
&4a_0^4c_0\overline{\lambda}_1\overline{\lambda}_n\left(\hat{\zeta}_0+\overline{\lambda}_1^2\overline{\lambda}_n\left(\left(1-c_0\right)\zeta_0+\left(c_0+1\right)\hat{\zeta}_0\right)\right) \\
&+2a_0^3c_0\left(1-5\overline{\lambda}_1^4\overline{\lambda}_n^2\right)\hat{\zeta}_0+4a_0^2\overline{\lambda}_1\left(\overline{\lambda}_1^4\overline{\lambda}_n^2-1\right)\left(\hat{\zeta}_0-\overline{g}_I^{(1)}\left(1-c_0\right)\right) \\
&+2a_0c_0\overline{\lambda}_1^2\left(5-\overline{\lambda}_1^4\overline{\lambda}_n^2\right)\hat{\zeta}_0-4c_0\overline{\lambda}_1^3\left(\left(1-c_0\right)\zeta_0+\left(1+c_0+\overline{\lambda}_1^2\overline{\lambda}_n\right)\hat{\zeta}_0\right).
\end{aligned} \tag{A.71}$$

At this stage, it is recognized that relations (A.70) and (A.71) depend on unknowns other than a_0 only through the combination $e_0-d_0\overline{\lambda}_1^4\overline{\lambda}_n^2$, and so, after eliminating $e_0-d_0\overline{\lambda}_1^4\overline{\lambda}_n^2$ from these expressions, we obtain the following equation for a_0:

$$\left[(1+c_0)\hat{\zeta}_0+(1-c_0)\zeta_0\right]\left(\overline{\lambda}_n^{-2}-a_0^4\right)-\hat{\zeta}_0\left[2a_0\overline{\lambda}_1(\overline{\lambda}_2^2-a_0^2)-\frac{(\overline{\lambda}_1^4-a_0^4)\overline{\lambda}_2}{\overline{\lambda}_1}\right]=0. \tag{A.72}$$

Note that equation (A.72) is nothing more than equation (A.37) in the text with slightly different notation: $a_0\to\overline{\lambda}_1^{(2)}$, $\hat{\zeta}_0\to g_I^{(1)}(\hat{I}_P^{(1)})$, and $\zeta_0\to g_I^{(2)}(I_P^{(2)})$. As already emphasized, the solution of this equation serves to completely determines the incompressible GSO estimate (A.34).

Appendix B

Onset of macroscopic instabilities in fiber-reinforced elastomers at finite strain

Abstract—In this paper, we investigate theoretically the possible development of instabilities in fiber-reinforced elastomers (and other soft materials) when they are subjected to finite-strain loading conditions. We focus on the physically relevant class of "macroscopic" instabilities, i.e., instabilities with wavelengths that are much larger than the characteristic size of the underlying microstructure. To this end, we make use of recently developed homogenization estimates, together with a fundamental result of Geymonat, Müller and Triantafyllidis linking the development of these instabilities to the loss of strong ellipticity of the homogenized constitutive relations. For the important class of material systems with very stiff fibers and random microstructures, we derive a *closed-form* formula for the critical macroscopic deformation at which instabilities may develop under *general* loading conditions, and we show that this critical deformation is quite sensitive to the loading orientation relative to the fiber direction. The result is also confronted with classical estimates (including those of Rosen) for laminates, which have commonly been used as two-dimensional (2-D) approximations for actual fiber-reinforced composites. We find that while predictions based on laminate models are qualitatively correct for certain loadings, they can be significantly off for other more general 3-D loadings. Finally, we provide a parametric analysis of the effects of the matrix and fibers properties and of the fiber volume fraction on the onset of instabilities for various loading conditions.

B.1 Introduction

Many "soft" material systems of current interest exhibit an underlying fiber-reinforced structure. Prominent examples include a wide variety of soft biological tissues (see, e.g., Finlay et al. [34], Quapp and Weiss [130]) and nano-structured block copolymers (see, e.g., Honeker and Thomas [58],

Honeker et al. [59]). From the theoretical point of view, several efforts within the past few years have been devoted to construct constitutive models that accurately describe the macroscopic mechanical behavior—i.e., the stress-strain relation—of such classes of reinforced materials subjected to *finite deformations* (see, e.g., Qiu and Pence [129], Holzapfel et al. [57], Merodio and Ogden [101], deBotton [26], deBotton et al. [28], Guo et al. [45], Brun et al. [18], Agoras et al. [2]). By contrast, the study of instabilities in these systems—although of great practical importance—has received comparatively little attention, presumably because of the intrinsic technical difficulties. In fact, most of the work to date seems to have been restricted primarily to studying the loss of ellipticity of phenomenological constitutive relations from a qualitative standpoint (see, e.g., Triantafyllidis and Abeyaratne [141], Merodio and Pence [102], Merodio and Ogden [100]). It is appropriate to recall, however, that many researchers have utilized laminates as a two-dimensional (2-D) approximation of fiber-reinforced materials, starting with the pioneering work of Rosen [133]. Along these lines, a complete analysis of instabilities for hyperelastic laminates has been carried out by Triantafyllidis and co-workers by means of the Floquet theory for ODEs (see, e.g., Triantafyllidis and Maker [142], Nesterovic and Triantafyllidis [108]). Another approximate approach to microbuckling in fiber-reinforced composites consists in modeling the fibers as beams on an elastic foundation (see, e.g., Grandidier and Poitier-Ferry [43]).

The purpose of the present paper is to investigate the onset of "macroscopic" instabilities for a general class of fiber-reinforced *nonlinearly elastic* materials consisting of a soft matrix reinforced by a single family of stiff, aligned, cylindrical fibers that are distributed *randomly* and isotropically in the transverse plane, when subjected to arbitrary finite strains. To this end, we adopt a fundamental result of Geymonat et al. [41] which states that the onset of long-wavelength instabilities — i.e., wavelengths that are much larger than the characteristic size of the underlying microstructure — in (a rather general class of) heterogeneous hyperelastic materials may be expediently computed from the loss of strong ellipticity of the corresponding homogenized properties. Furthermore, these so-called "macroscopic" instabilities provide a rigorous upper bound for other types of instabilities with finite wavelengths, called "microscopic" instabilities. In this connection, we should mention the work of Abdelmoula et al. [1] which attempted a first study of microscopic and macroscopic instabilities in fiber-reinforced elastomers; however, the final results provided were also for a 2-D laminate model.

The approach discussed in the previous paragraph to determine the onset of macroscopic instabilities requires the knowledge of the homogenized behaviors of the materials of interest. But the problem of computing the homogenized properties of fiber-reinforced nonlinearly elastic materials, subjected to finite deformations—especially with random microstructures—is quite a difficult task in itself. Indeed, *exact* homogenization results are only accessible for particular loading conditions, special microstructures, and restricted local (matrix and fiber) constitutive behaviors (He

et al. [49]). *Approximate* results have also remained elusive until very recently. In addition to the elementary Voigt [111] and polyconvex (Ponte Castañeda [113]) bounds, there is the estimate of deBotton et al. [28] (see also Guo et al. [45]) for fiber–reinforced materials with incompressible Neo-Hookean matrix and fiber phases, and certain special types of microstructures.

In this work, we will make use of the "variational linear comparison" estimate recently developed by Agoras et al. [2] to model the homogenized properties of a large class of fiber-reinforced nonlinearly elastic materials. Specifically, the proposed estimate applies to materials with *random* transversely isotropic distribution of fibers and with matrix and fiber constituents that are characterized by a *general class* of incompressible, isotropic stored-energy functions. (A corresponding estimate for material systems with *compressible* generalized Neo-Hookean constituents and *periodic* microstructures has been given by Brun et al. [18].) The estimate of Agoras et al. [2] was derived by making combined use of the works of Ponte Castañeda and Tiberio [124] and Lopez-Pamies and Ponte Castañeda [92], which in turn provide generalizations of the "second-order" methods of Ponte Castañeda [117, 118], respectively, for hyperelastic composites. Besides its generality, the estimate of Agoras et al. [2] has the merit that it recovers known exact results for special loading conditions. Moreover, it accounts for fine statistical information about the *initial* microstructure beyond the volume fraction of fibers, as well as for its *evolution*, which results from the finite changes in geometry that are induced by the applied finite deformations. This feature is of the essence in the present context, as the evolution of microstructure can have a significant *geometric* softening (or stiffening) effect on the macroscopic response of the material, which may ultimately lead to the development of instabilities (see, e.g., the work of Lopez-Pamies and Ponte Castañeda [97]). In addition to the estimate of Agoras et al. [2], we will also consider the estimate of deBotton et al. [28]—which, as already stated, applies to the restricted but important case of materials with Neo-Hookean matrix and fiber constituents—to approximate the homogenized response of fiber-reinforced nonlinearly elastic materials.

The structure of the paper is as follows. First, in Section B.2 we describe in detail the (microgeometries and local constitutive behaviors of the) class of fiber-reinforced materials under study in this work. In addition, this section spells out the homogenized response of these materials under arbitrary finite deformations, as characterized by the estimates of Agoras et al. [2] and of deBotton et al. [28]. In Section B.3, the condition of strong ellipticity—used to determine the "macrocopic" instabilities—is recalled in general and then specialized to the constitutive relations of Agoras et al. [2] and deBotton et al. [28]. Making use of the relations put forward in Sections B.2 and B.3, results for the onset of instabilities in fiber-reinforced elastic materials subjected to finite deformations are then derived in Section B.4 and B.5 for aligned and non-aligned loading conditions, respectively. In Section B.6, we derive a closed-form formula (see also eqn. (B.1) below) for the possible development of instabilities under *general* loading conditions in Neo-Hookean composites,

and show that the result also applies, approximately, for more general material behavior, provided that the fiber-matrix heterogeneity contrast is sufficiently large. In sections B.4 to B.6, we also make comparisons with classical results from the literature, as well as with new results, for 2-D laminate models. These comparisons serve to elucidate the limitations of the use of the 2-D laminate approximation for general loading conditions. Finally, some concluding remarks will be drawn in Section B.7.

The main result of this paper can be summarized as follows: *along an arbitrary loading path with average deformation gradient* $\overline{\mathbf{F}}$*, macroscopic instabilities may develop in fiber-reinforced nonlinearly elastic materials whenever the stretch in the fiber direction reaches the critical value*

$$\overline{\lambda}_n = \left\|\overline{\mathbf{F}}\mathbf{N}\right\| = \left(1 - \frac{\widetilde{\mu}_n}{\widetilde{\mu}_a}\right)^{1/3}. \tag{B.1}$$

Here, the unit vector $\mathbf{N}$ characterizes the direction of the fibers in the undeformed configuration, while $\widetilde{\mu}_n$ and $\widetilde{\mu}_a$ denote, respectively, the effective longitudinal and axisymmetric shear moduli of the fiber-reinforced composite in the ground state.

B.2 Homogenization estimates for fiber-reinforced hyperelastic materials

The composites considered in this work consist of a matrix material (phase 1) reinforced by a single family of aligned, cylindrical fibers (phase 2) with initially circular cross section. For definiteness, the initial direction of fiber alignment is denoted by the unit vector $\mathbf{N}$ (see Fig. B.1(a)). The distribution of fibers in the transverse plane (i.e., perpendicular to $\mathbf{N}$) is taken to be random and isotropic in the undeformed configuration Ω_0. It is further assumed that the average diameter of the fibers is much smaller than the size of a typical macroscopic specimen; in other words, the macroscopic and microscopic length scales are well separated. Moreover, the constitutive behaviors of the phases are taken to be characterized by the general class of incompressible, isotropic stored-energy functions of the form

$$W^{(r)}(\mathbf{F}) = g^{(r)}(I) \qquad (r = 1, 2) \tag{B.2}$$

subject to the incompressibility constraint $\det \mathbf{F} = 1$ (i.e., $W^{(r)}(\mathbf{F}) = +\infty$ if $\det \mathbf{F} \neq 1$). Here, $\mathbf{F}$ denotes the deformation gradient tensor, $I = I_1 = \operatorname{tr} \mathbf{C}$ stands for the first principal invariant of the right Cauchy-Green deformation tensor $\mathbf{C} = \mathbf{F}^T\mathbf{F}$, and $g^{(r)}$ can be any differentiable material function satisfying the linearization conditions: $g^{(r)}(3) = 0$ and $g_I^{(r)}(3) = \mu^{(r)}/2$, where $\mu^{(r)}$ denotes the small-strain shear modulus of phase r, and the notation $g_I^{(r)}(\cdot) = dg^{(r)}(\cdot)/dI$ has been introduced for convenience.

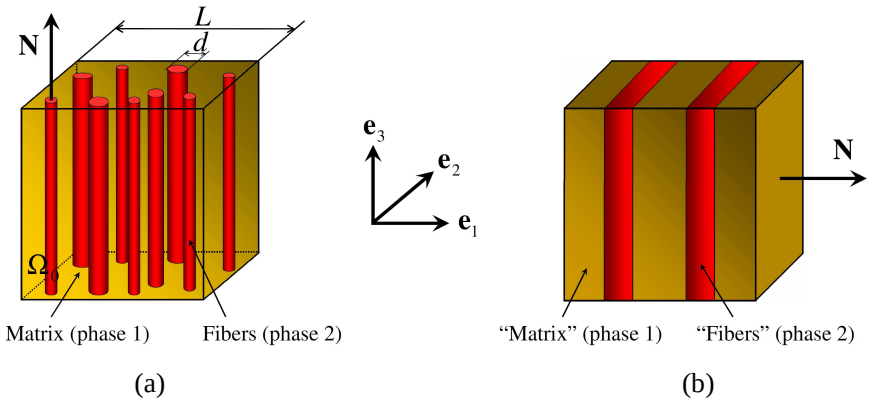

Figure B.1: (a) Schematic of a fiber-reinforced composite in the undeformed configuration Ω_0, where the initial fiber direction is given by the unit vector $\mathbf{N}$. (b) Corresponding schematic of a laminate with lamination direction $\mathbf{N}$. The characteristic lengths of the macroscopic specimen, L, and of the fibers (or layers), d, are assumed to be well separated in the sense that $L \gg d$.

A simple example of a stored-energy function of the form (B.2), which does capture the limiting chain extensibility of rubber-like solids, is the Gent material [40]

$$W(\mathbf{F}) = g(I) = -\frac{J_m\,\mu}{2}\ln\left[1-\frac{I-3}{J_m}\right]\,. \tag{B.3}$$

In this relation, the parameter J_m corresponds to the maximum deformation, as measured by $I-3$, that the material may undergo before it locks up. Note that, in the limit as $J_m \to \infty$, expression (B.3) reduces identically to the Neo-Hookean model

$$W(\mathbf{F}) = g(I) = \frac{\mu}{2}\,(I-3)\,. \tag{B.4}$$

The functional form of the homogenized (or macroscopic) response of the above-described fiber-reinforced nonlinearly elastic materials can be shown (Hill [53]) to be characterized by an *effective* hyperelastic potential, $\widehat{W}$, that is a transversely isotropic scalar function (with symmetry axis $\mathbf{N}$) of the macroscopic deformation gradient tensor $\overline{\mathbf{F}}$, subject to the macroscopic incompressibility constraint $\det\overline{\mathbf{F}} = 1$ (i.e., $\widehat{W}(\overline{\mathbf{F}}) = +\infty$ if $\det\overline{\mathbf{F}} \neq 1$). More specifically, $\widehat{W}$ depends on $\overline{\mathbf{F}}$ and $\mathbf{N}$ only through the 4 (canonical) transversely isotropic invariants: $\overline{I}_1 = \operatorname{tr}\overline{\mathbf{C}}$, $\overline{I}_2 = (1/2)((\operatorname{tr}\overline{\mathbf{C}})^2 - \operatorname{tr}\overline{\mathbf{C}}^2)$, $\overline{I}_4 = \mathbf{N}\cdot\overline{\mathbf{C}}\mathbf{N}$, $\overline{I}_5 = \mathbf{N}\cdot\overline{\mathbf{C}}^2\mathbf{N}$. In this work, we will make use of the equivalent set of invariants (see Ericksen and Rivlin [33], deBotton et al. [28]):

$$\begin{aligned}
\overline{\lambda}_n &= \left[(\overline{\mathbf{F}}\mathbf{N})\cdot(\overline{\mathbf{F}}\mathbf{N})\right]^{1/2}, \quad \overline{\gamma}_n = \left[\left(\overline{\mathbf{F}}^T\overline{\mathbf{F}}\mathbf{N}\right)\cdot\left(\overline{\mathbf{F}}^T\overline{\mathbf{F}}\mathbf{N}\right) - \overline{\lambda}_n^4\right]^{1/2}/\overline{\lambda}_n,\\
\overline{\gamma}_p &= \left(\overline{\mathbf{F}}\cdot\overline{\mathbf{F}} - \overline{\lambda}_n^2 - 2/\overline{\lambda}_n - \overline{\gamma}_n^2\right)^{1/2},
\end{aligned} \tag{B.5}$$

and $\overline{\psi}_\gamma$ (which depends on $\overline{I}_2$). These invariants, which can be easily written in the terms of the first set, have the advantage of a more direct physical interpretation: $\overline{\lambda}_n$ denotes the stretch along

the fiber direction $\mathbf{N}$, $\overline{\gamma}_n$ corresponds to the longitudinal (antiplane) shear, and $\overline{\gamma}_p$ stands for the shear in the transverse plane (in-plane shear).

The precise determination of $\widehat{W}$, however, is a difficult problem and, as a result, exact solutions are accessible only for very particular loading conditions and special local (matrix and fiber) constitutive behaviors (see, e.g., He et al. [49]). In the sequel, in order to approximate the homogenized behavior of the above-described general class of materials under arbitrary loading conditions, we will make use of the *variational linear comparison* estimate proposed recently by Agoras et al. [2]. We will also make use of the earlier estimate of deBotton et al. [28], which applies only to the special case of Neo-Hookean behavior for the matrix and fiber phases.

B.2.1 The estimate of Agoras et al. for generalized Neo-Hookean phases

By making use of the variational procedures of Lopez-Pamies and Ponte Castañeda [92] and Ponte Castañeda and Tiberio [124], Agoras et al. [2] have constructed an estimate for the effective stored-energy function $\widehat{W}$ of the fiber-reinforced materials described above, which was found to be rather insensitive to $\overline{\psi}_\gamma$, so that $\widehat{W}(\overline{\mathbf{F}}) = \widehat{\Phi}(\overline{\lambda}_n, \overline{\gamma}_p, \overline{\gamma}_n)$. The specific expression for $\widehat{\Phi}$ is given by

$$\begin{aligned}\widehat{\Phi}(\overline{\lambda}_n, \overline{\gamma}_p, \overline{\gamma}_n) &= (1-c_0)\left[g^{(1)}(\hat{I}^{(1)}) + g_I^{(1)}(I^{(1)})\overline{\gamma}_n^{(1)}\left(\overline{\gamma}_n - \overline{\gamma}_n^{(1)}\right)\right.\\ &+ \left. c_0\left[g^{(2)}(I^{(2)}) + g_I^{(2)}(I^{(2)})\overline{\gamma}_n^{(2)}\left(\overline{\gamma}_n - \overline{\gamma}_n^{(2)}\right)\right],\end{aligned} \tag{B.6}$$

where c_0 denotes the initial volume fraction of fibers, and

$$\begin{aligned}\hat{I}^{(1)} &= \left(\frac{\overline{\lambda}_1 - c_0\overline{\lambda}_1^{(2)}}{1-c_0}\right)^2 + \left(\frac{\overline{\lambda}_2 - c_0\overline{\lambda}_2^{(2)}}{1-c_0}\right)^2 + \overline{\lambda}_n^2 + \left(\overline{\gamma}_n^{(1)}\right)^2 +\\ &+ c_0\left(\frac{\overline{\lambda}_1 - \overline{\lambda}_1^{(2)}}{(1-c_0)\,\overline{\lambda}_1^{(2)}\overline{\lambda}_1\overline{\lambda}_n}\right)^2\left[\left(\overline{\lambda}_1^{(2)}\overline{\lambda}_1\overline{\lambda}_n + 1\right)^2 + \left(\overline{\lambda}_1^2 + \left(\overline{\lambda}_1^{(2)}\right)^2\right)\overline{\lambda}_n\right],\\ I^{(1)} &= \overline{\lambda}_1^2 + \overline{\lambda}_2^2 + \overline{\lambda}_n^2 + \left(\overline{\gamma}_n^{(1)}\right)^2,\\ I^{(2)} &= \left(\overline{\lambda}_1^{(2)}\right)^2 + \left(\overline{\lambda}_2^{(2)}\right)^2 + \overline{\lambda}_n^2 + \left(\overline{\gamma}_n^{(2)}\right)^2.\end{aligned} \tag{B.7}$$

In these expressions,

$$\begin{aligned}&\overline{\lambda}_1 = \frac{\sqrt{\overline{\gamma}_p^2 + 4/\overline{\lambda}_n} - \overline{\gamma}_p}{2}, \quad \overline{\lambda}_2 = \frac{\sqrt{\overline{\gamma}_p^2 + 4/\overline{\lambda}_n} + \overline{\gamma}_p}{2},\\ &\overline{\lambda}_2^{(2)} = \frac{1}{\overline{\lambda}_1^{(2)}\overline{\lambda}_n}, \quad \overline{\gamma}_n^{(2)} = \frac{\overline{\gamma}_n - (1-c_0)\overline{\gamma}_n^{(1)}}{c_0},\end{aligned} \tag{B.8}$$

and the variables $\overline{\lambda}_1^{(2)}$ and $\overline{\gamma}_n^{(1)}$ are the solution of the following system of two coupled, nonlinear, algebraic equations

$$\begin{aligned}\mathcal{E}_1\left(\overline{\lambda}_1^{(2)},\overline{\gamma}_n^{(1)}\right) \quad &= \sqrt{g_I^{(1)}(I^{(1)})\left[g_I^{(1)}(I^{(1)})+2g_{II}^{(1)}(I^{(1)})(\overline{\gamma}_n^{(1)})^2\right]}(\overline{\gamma}_n-\overline{\gamma}_n^{(1)})+\\ &\quad c_0\left(g_I^{(2)}(I^{(2)})\overline{\gamma}_n^{(2)}-g_I^{(1)}(I^{(1)})\overline{\gamma}_n^{(1)}\right)=0,\end{aligned} \tag{B.9}$$

$$\begin{aligned}\mathcal{E}_2\left(\overline{\lambda}_1^{(2)},\overline{\gamma}_n^{(1)}\right) \quad &= \left[(1+c_0)g_I^{(1)}(\hat{I}^{(1)})+(1-c_0)g_I^{(2)}(I^{(2)})\right]\left(\overline{\lambda}_n^{-2}-(\overline{\lambda}_1^{(2)})^4\right)-\\ &\quad g_I^{(1)}(\hat{I}^{(1)})\left[2\overline{\lambda}_1^{(2)}\overline{\lambda}_1(\overline{\lambda}_2^2-(\overline{\lambda}_1^{(2)})^2)-\frac{(\overline{\lambda}_1^4-(\overline{\lambda}_1^{(2)})^4)\overline{\lambda}_2}{\overline{\lambda}_1}\right]=0,\end{aligned} \tag{B.10}$$

where the notation $g_{II}^{(1)}(\cdot)=d^2g^{(1)}(\cdot)/dI^2$ has been employed in (B.9) for convenience. For a detailed description of the derivation and of the various quantities involved in the above estimate, we refer to Agoras et al. [2]. In the present context, it is appropriate to remark that the result (B.6) incorporates one-point (the volume fraction of fibers) and two-point (the cylindrical shape and random and transversely isotropic distribution of fibers) statistical information about the underlying *initial* microstructure. Furthermore, it also accounts for the *evolution* of such a microstructure, which results from the applied finite deformations. This feature is of critical importance since the evolution of microstructure can have significant softening (or stiffening) effect that may ultimately lead to the development of instabilities. In addition, the estimate (B.6) has the merit that it recovers known exact results for special loading conditions, including the case of aligned axisymmetric shear (He et al. [49]). Moreover, full numerical simulations (Moraleda et al. [106]) have also established that the estimate (B.6) leads to remarkably accurate predictions for in-plane loading conditions (i.e., $\overline{\lambda}_n=1$, $\overline{\gamma}_n=0$), at least for Neo-Hookean phases. Finally, it is relevant to remark that the stored-energy function (B.6) linearizes properly, as it reduces to the corresponding estimate of Walpole [149] in the limit as $\overline{\mathbf{F}}\to\mathbf{I}$, namely

$$\widehat{\Phi}(\overline{\lambda}_n,\overline{\gamma}_p,\overline{\gamma}_n)=\frac{\tilde{\mu}_a}{2}\overline{\varepsilon}_a^2+\frac{\tilde{\mu}_p}{2}\overline{\varepsilon}_p^2+\frac{\tilde{\mu}_n}{2}\overline{\varepsilon}_n^2+O\left(\left\|\overline{\mathbf{F}}-\mathbf{I}\right\|^3\right). \tag{B.11}$$

Here, $\overline{\varepsilon}_a,\overline{\varepsilon}_p$, and $\overline{\varepsilon}_n$ are the axisymmetric, transverse, and longitudinal shear invariants of the infinitesimal strain tensor $\overline{\boldsymbol{\varepsilon}}=(1/2)\left(\overline{\mathbf{F}}^T+\overline{\mathbf{F}}-2\mathbf{I}\right)$ (see, e.g., deBotton and Ponte Castañeda [29]), and $\tilde{\mu}_a$, $\tilde{\mu}_p$, and $\tilde{\mu}_p$ are the corresponding effective shear moduli in these three modes, which are given in terms of the shear moduli of the matrix and fibers, $\mu^{(1)}$ and $\mu^{(2)}$, and the volume fraction of fibers, c_0, by

$$\widetilde{\mu}_a=(1-c_0)\mu^{(1)}+c_0\mu^{(2)}\equiv\overline{\mu}, \tag{B.12}$$

and

$$\widetilde{\mu}_p=\widetilde{\mu}_n=\frac{(1-c_0)\mu^{(1)}+(1+c_0)\mu^{(2)}}{(1+c_0)\mu^{(1)}+(1-c_0)\mu^{(2)}}\mu^{(1)}\equiv\widetilde{\mu}. \tag{B.13}$$

Note that $\widetilde{\mu} \leq \overline{\mu}$, in general, and that $\widetilde{\mu} << \overline{\mu}$ in the limit of large heterogeneity contrast $t = \mu^{(2)}/\mu^{(1)} >> 1$, which has the physical interpretation that the axisymmetric shear mode is controlled by the stiffer fibers, while the transverse and longitudinal shear modes are controlled by the softer matrix behavior.

B.2.2 The estimate of Agoras et al. for Neo-Hookean phases

For later reference, we spell out next the specialization of the general estimate (B.6) to materials with Neo-Hookean behavior (B.4) for the matrix and fiber constituents. To this end, first it is helpful to recognize that equations (B.9) and (B.10) decouple into two independent equations for $\overline{\gamma}_n^{(1)}$ and $\overline{\lambda}_1^{(2)}$, respectively. The resulting equation (B.9) for $\overline{\gamma}_n^{(1)}$ can be solved in closed form rendering $\overline{\gamma}_n^{(1)} = (\mu^{(1)} + \mu^{(2)})\overline{\gamma}_n/((1+c_0)\mu^{(1)} + (1-c_0)\mu^{(2)})$, while (B.10) reduces to a nonlinear equation for $\overline{\lambda}_1^{(2)}$ shown below. After some algebraic manipulation, it is then straightforward to deduce that the stored-energy function (B.6) reduces to

$$\widehat{\Phi}(\overline{\lambda}_n, \overline{\gamma}_p, \overline{\gamma}_n) = (1-c_0)\frac{\mu^{(1)}}{2}(\hat{I}_P^{(1)} - 3) + c_0\frac{\mu^{(2)}}{2}(I_P^{(2)} - 3) + \frac{\widetilde{\mu}}{2}\overline{\gamma}_n^2, \tag{B.14}$$

where $\widetilde{\mu}$ is given by (B.13) and $\hat{I}_P^{(1)} = \hat{I}^{(1)} - \left(\overline{\gamma}_n^{(1)}\right)^2$, $I_P^{(2)} = I^{(2)} - \left(\overline{\gamma}_n^{(2)}\right)^2$ are ultimately functions of the unknown $\overline{\lambda}_1^{(2)}$, which is solution to the fourth-order polynomial equation

$$\begin{aligned}\mathcal{E}\left(\overline{\lambda}_1^{(2)}\right) = \quad & \left[(1+c_0)\mu^{(1)} + (1-c_0)\mu^{(2)}\right]\left(\overline{\lambda}_n^{-2} - (\overline{\lambda}_1^{(2)})^4\right) - \\ & \mu^{(1)}\left[2\overline{\lambda}_1^{(2)}\overline{\lambda}_1(\overline{\lambda}_2^2 - (\overline{\lambda}_1^{(2)})^2) - \frac{(\overline{\lambda}_1^4 - (\overline{\lambda}_1^{(2)})^4)\overline{\lambda}_2}{\overline{\lambda}_1}\right] = 0.\end{aligned} \tag{B.15}$$

B.2.3 The estimate of deBotton et al. for Neo-Hookean phases

As already mentioned, the effective stored-energy function (B.6) is the only available homogenization estimate for nonlinearly elastic fiber-reinforced composites allowing consideration of general constitutive behaviors (B.2) for the underlying matrix and fiber phases. However, in the simpler context of Neo-Hookean constituents with stored-energy functions of the form (B.4), deBotton et al. [28] have derived the following estimate

$$\widehat{\Phi}(\overline{\lambda}_n, \overline{\gamma}_p, \overline{\gamma}_n) = \frac{\overline{\mu}}{2}\left(\overline{\lambda}_n^2 + \frac{2}{\overline{\lambda}_n} - 3\right) + \frac{\widetilde{\mu}}{2}(\overline{\gamma}_p^2 + \overline{\gamma}_n^2), \tag{B.16}$$

where $\overline{\mu}$ and $\widetilde{\mu}$ have been defined by (B.12) and (B.13), respectively. It is worth remarking that $\overline{\gamma}_p$ and $\overline{\gamma}_n$ enter the above expression only as the sum $\overline{\gamma}_p^2 + \overline{\gamma}_n^2$, so that the model of deBotton et al. (B.16) actually depends *not* on 3 but only on 2 ($\overline{I}_1$ and $\overline{I}_4$) out of 4 ($\overline{I}_1, \overline{I}_2, \overline{I}_4, \overline{I}_5$) possible transversely isotropic invariants.

In spite of their different appearance, expressions (B.14) and (B.16) generally lead to similar overall stress-strain predictions. In particular, the stored-energy function (B.16) also linearizes according to relation (B.11). Moreover, expressions (B.14) and (B.16) can be shown to be identical for the case of antiplane combined with axisymmetric shear deformations (i.e., $\overline{\gamma}_p = 0$), which, incidentally, corresponds to an *exact* result for materials with the special "composite cylinder assemblage" microstructure of Hashin and Rosen (deBotton et al. [28]). The main difference between (B.14) and (B.16) appears for large values of the in-plane shear $\overline{\gamma}_p$ when—in agreement with full field simulations (Moraleda et al. [106])—(B.14) leads to a noticeably stiffer response.

B.3 Onset of macroscopic instabilities

In a remarkable contribution, Geymonat, Müller, and Triantafyllidis [41] demonstrated rigorously that (i) the onset of "macroscopic" instabilities (or instabilities with wavelengths that are much larger than the characteristic size of the underlying microstructure) for a general class of heterogeneous hyperelastic materials can be determined from the *loss of strong ellipticity of the homogenized response*, and (ii) the onset of such long-wavelength instabilities constitutes a rigorous upper bound to the onset of any other type of instabilities with finite wavelength (i.e., "microscopic" instabilities). From a practical point of view, the importance of these theoretical results derives from the fact that the "macroscopic" instabilities are much easier to compute (assuming that the homogenized response is available) than the "microscopic" ones. In fact, there is no feasible procedure for computing "microscopic" instabilities for composites with random microstructures, such as the ones of interest in this work. Moreover, it is often the case that first instabilities are of the long-wavelength type. For example, for the laminated materials considered by Triantafyllidis and Maker [142] and by Nesterovic and Triantafyllidis [108] under plane-strain loading conditions, the first instabilities are always of long wavelength, at least for sufficiently large concentrations of the reinforcing phase. Furthermore, recent work by Michel et al. [104] in the context of particulate reinforced elastomers has demonstrated that at least the microscopic instabilities that are related to the periodicity of the microstructure tend to disappear as the microstructure is perturbed (randomly) away from a purely periodic state, which suggests that the "macroscopic" instabilities may in some sense be the most relevant ones for random composites anyway.

For the type of fiber-reinforced materials of interest here, the first instabilities to be encountered along arbitrary loading paths are expected to be of the long-wavelength type, at least for fiber concentrations that are not too small. Thus, for materials with *sufficiently large* volume fraction of fibers, the loss of strong ellipticity of the homogenized behavior, at appropriate critical strains, would be expected to indicate accurately the development of first instabilities. For materials with very *small* volume fractions of fibers, on the other hand, the loss of strong ellipticity of

the homogenized response may *not* signal the onset of the first instabilities (something else may happen), but this condition is expected to provide, however, a useful upper bound for them.

We recall next the condition of strong ellipticity and spell out its specialization to the *estimates* (B.6), (B.14), and (B.16) for the homogenized behavior of fiber-reinforced nonlinearly elastic materials; these conditions will then be used in the next sections to estimate the onset of macroscopic instabilities in these materials under arbitrary loading conditions. Quite generally, strong ellipticity of a given constitutive relation corresponds to positive definiteness of the associated acoustic tensor. In particular, for a hyperelastic constitutive relation characterized by an *incompressible* stored-energy function $\widehat{W}(\overline{\mathbf{F}})$—such as the one of interest in this work—the condition of strong ellipticity may be written as

$$\widehat{\mathcal{L}}^c_{ijkl}(\overline{\mathbf{F}})v_j v_l u_i u_k > 0 \tag{B.17}$$

for all unit vectors $\mathbf{v}$ and $\mathbf{u}$ that satisfy the *incompressibility constraint* $\mathbf{v}\cdot\mathbf{u}=0$. In the above expression, $\widehat{\mathcal{L}}^c_{ijkl}(\overline{\mathbf{F}}) = \overline{F}_{jp}\overline{F}_{lq}\,\partial^2\widehat{W}(\overline{\mathbf{F}})/\partial\overline{F}_{ip}\partial\overline{F}_{kq}$ stands for the incremental tangent modulus in the current (deformed) configuration, hence the superscript c (see, e.g., Chapter 6.2.7 in the monograph by Ogden [112]).

As already noted above, the stored-energy function $\widehat{W}$ for the fiber-reinforced materials of interest in this work should linearize according to relation (B.11). Given that $\tilde{\mu}_a$, $\tilde{\mu}_p$, and $\tilde{\mu}_n$, as defined by expressions (B.12) and (B.13) are all positive, it follows that $\widehat{W}$ is strictly convex in the infinitesimal strain $\overline{\boldsymbol{\varepsilon}}$ for sufficiently small deformations. As a result, condition (B.17) is expected to hold true in some small neighborhood of $\overline{\mathbf{F}}=\mathbf{I}$, except possibly in the case of rigid fibers, when condition (B.17) may be violated at exactly $\overline{\mathbf{F}}=\mathbf{I}$. Along arbitrary loading paths, however, as the deformation progresses beyond $\overline{\mathbf{F}}=\mathbf{I}$ into the finite-deformation regime, a point may be reached at which condition (B.17) ceases to hold true for some critical $\overline{\mathbf{F}}_{cr}$ and pair of critical vectors $\mathbf{v}_{cr}$ and $\mathbf{u}_{cr}$. The set of all such critical values $\overline{\mathbf{F}}_{cr}$ defines a hypersurface in deformation space delimiting strongly elliptic from non-strongly-elliptic regions for the material response. In addition, the associated critical pairs of orthogonal vectors $\mathbf{v}_{cr}$ and $\mathbf{u}_{cr}$ describe the manner in which the material loses strong ellipticity. In particular, $\mathbf{v}_{cr}$ denotes the normal (in the deformed configuration) to a band (or bands) within which the material softens drastically and the deformation is thus prone to localize. On the other hand, the vector $\mathbf{u}_{cr}$ denotes the direction (also in the deformed configuration) along which the material softens within the band (or bands).

The estimate of Agoras et al. The general condition (B.17) simplifies considerably when specialized to a stored-energy function $\widehat{W}$ depending on $\overline{\mathbf{F}}$ (and $\mathbf{N}$) only through the invariants $\overline{\lambda}_n$, $\overline{\gamma}_p$ and $\overline{\gamma}_n$, which is the case for all estimates considered in this work. Indeed, using (B.5) to express $\overline{\lambda}_n$, $\overline{\gamma}_p$ and $\overline{\gamma}_n$ as functions of $\overline{\mathbf{F}}$ and $\mathbf{N}$, together with the chain rule, the condition of strong ellipticity for a stored-energy function of the form $\widehat{W}(\overline{\mathbf{F}}) = \widehat{\Phi}(\overline{\lambda}_n, \overline{\gamma}_p, \overline{\gamma}_n)$ can be shown to

reduce to

$$\sum_{i=1}^{3}(\alpha_i E_i + \beta_{ii} G_{ii}) + \beta_{12} G_{12} + \beta_{13} G_{13} + \beta_{23} G_{23} > 0. \tag{B.18}$$

In this relation,

$$\begin{aligned}
E_1 &= \mathbf{v}\cdot\overline{\mathbf{B}}\mathbf{v}, \qquad E_2 = \overline{\lambda}_n^2(\mathbf{n}\cdot\mathbf{v})^2,\\
E_3 &= \overline{\lambda}_n^2\left[((\mathbf{n}\cdot\mathbf{v})\mathbf{u}+(\mathbf{n}\cdot\mathbf{u})\mathbf{v})\cdot\overline{\mathbf{B}}\,((\mathbf{n}\cdot\mathbf{v})\mathbf{u}+(\mathbf{n}\cdot\mathbf{u})\mathbf{v}) + 2(\mathbf{n}\cdot\mathbf{v})(\mathbf{n}\cdot\overline{\mathbf{B}}\mathbf{v})\right],\\
G_{11} &= (\mathbf{v}\cdot\overline{\mathbf{B}}\mathbf{u})^2, \quad G_{22} = \overline{\lambda}_n^4(\mathbf{n}\cdot\mathbf{v})^2(\mathbf{n}\cdot\mathbf{u})^2,\\
G_{33} &= \overline{\lambda}_n^4\left[(\mathbf{n}\cdot\mathbf{v})(\mathbf{n}\cdot\overline{\mathbf{B}}\mathbf{u}) + (\mathbf{n}\cdot\mathbf{u})(\mathbf{n}\cdot\overline{\mathbf{B}}\mathbf{v})\right]^2,\\
G_{12} &= 2\overline{\lambda}_n^2(\mathbf{n}\cdot\mathbf{v})(\mathbf{n}\cdot\mathbf{u})(\mathbf{v}\cdot\overline{\mathbf{B}}\mathbf{u}),\\
G_{13} &= 2\overline{\lambda}_n^2(\mathbf{v}\cdot\overline{\mathbf{B}}\mathbf{u})\left[(\mathbf{n}\cdot\mathbf{v})(\mathbf{n}\cdot\overline{\mathbf{B}}\mathbf{u}) + (\mathbf{n}\cdot\mathbf{u})(\mathbf{n}\cdot\overline{\mathbf{B}}\mathbf{v})\right],\\
G_{23} &= 2\overline{\lambda}_n^4(\mathbf{n}\cdot\mathbf{v})(\mathbf{n}\cdot\mathbf{u})\left[(\mathbf{n}\cdot\mathbf{v})(\mathbf{n}\cdot\overline{\mathbf{B}}\mathbf{u}) + (\mathbf{n}\cdot\mathbf{u})(\mathbf{n}\cdot\overline{\mathbf{B}}\mathbf{v})\right],
\end{aligned} \tag{B.19}$$

where $\overline{\mathbf{B}} = \overline{\mathbf{F}}\,\overline{\mathbf{F}}^T$ is the left Cauchy-Green deformation tensor and $\mathbf{n} = \overline{\lambda}_n^{-1}\overline{\mathbf{F}}\mathbf{N}$ denotes the direction of the fibers in the deformed configuration. The rest of the quantities in expression (B.18) depend inherently on the derivatives of $\widehat{\Phi}$ with respect to its arguments $\overline{\lambda}_n$, $\overline{\gamma}_p$, $\overline{\gamma}_n$, and they are given by

$$\begin{aligned}
\alpha_1 &= \frac{1}{\overline{\gamma}_p}\frac{\partial\widehat{\Phi}}{\partial\overline{\gamma}_p}, \qquad \alpha_3 = \frac{1}{\overline{\lambda}_n^2}\left(\frac{1}{\overline{\gamma}_n}\frac{\partial\widehat{\Phi}}{\partial\overline{\gamma}_n} - \frac{1}{\overline{\gamma}_p}\frac{\partial\widehat{\Phi}}{\partial\overline{\gamma}_p}\right),\\
\alpha_2 &= \frac{1}{\overline{\lambda}_n}\frac{\partial\widehat{\Phi}}{\partial\overline{\lambda}_n} + \frac{1}{\overline{\gamma}_p}\frac{\partial\widehat{\Phi}}{\partial\overline{\gamma}_p}\left(\frac{\overline{\gamma}_n^2}{\overline{\lambda}_n^2} + \frac{1}{\overline{\lambda}_n^3} + 1\right) - \frac{1}{\overline{\gamma}_n}\frac{\partial\widehat{\Phi}}{\partial\overline{\gamma}_n}\left(\frac{\overline{\gamma}_n^2}{\overline{\lambda}_n^2} + 2\right),\\
\beta_{1i} &= \frac{1}{\overline{\gamma}_p}\frac{\partial\alpha_i}{\partial\overline{\gamma}_p}, \qquad \beta_{3i} = \frac{1}{\overline{\lambda}_n^2}\left(\frac{1}{\overline{\gamma}_n}\frac{\partial\alpha_i}{\partial\overline{\gamma}_n} - \frac{1}{\overline{\gamma}_p}\frac{\partial\alpha_i}{\partial\overline{\gamma}_p}\right),\\
\beta_{2i} &= \frac{1}{\overline{\lambda}_n}\frac{\partial\alpha_i}{\partial\overline{\lambda}_n} + \frac{1}{\overline{\gamma}_p}\frac{\partial\alpha_i}{\partial\overline{\gamma}_p}\left(\frac{\overline{\gamma}_n^2}{\overline{\lambda}_n^2} + \frac{1}{\overline{\lambda}_n^3} + 1\right) - \frac{1}{\overline{\gamma}_n}\frac{\partial\alpha_i}{\partial\overline{\gamma}_n}\left(\frac{\overline{\gamma}_n^2}{\overline{\lambda}_n^2} + 2\right)
\end{aligned} \tag{B.20}$$

with $i = 1, 2, 3$. Note that the above choice for the variables β_{ij} leads to the symmetry $\beta_{ij} = \beta_{ji}$.

For the special case of the estimate (B.6) of Agoras et al. [2] the explicit expressions for $\partial\widehat{\Phi}/\partial\overline{\lambda}_n$, $\partial\widehat{\Phi}/\partial\overline{\gamma}_p$, $\partial\widehat{\Phi}/\partial\overline{\gamma}_n$ and higher order derivatives of $\widehat{\Phi}$ in (B.20) are too cumbersome to be included here. For our purposes, in any case, it suffices to point out that they are known *closed-form* functions of the macroscopic loading parameters $\overline{\lambda}_n$, $\overline{\gamma}_p$, $\overline{\gamma}_n$, as well as of $\overline{\lambda}_1^{(2)}$, $\overline{\gamma}_n^{(1)}$, which are the solution of the system of equations (B.9) and (B.10).

The estimate of Agoras et al. for Neo-Hookean phases. The general strong ellipticity

condition (B.18), together with (B.19) and (B.20), when specialized to estimate (B.14) for Neo-Hookean phases, simplifies to

$$\begin{aligned}
&\frac{1}{\overline{\gamma}_p^2}\left(\frac{\partial^2\widehat{\Phi}}{\partial\overline{\gamma}_p^2}-\frac{1}{\overline{\gamma}_p}\frac{\partial\widehat{\Phi}}{\partial\overline{\gamma}_p}\right)\left[G_{11}-\frac{G_{13}}{\overline{\lambda}_n^2}+\frac{G_{33}}{\overline{\lambda}_n^4}+\right.\\
&\left.\left(\frac{\overline{\gamma}_n^2}{\overline{\lambda}_n^2}+\frac{1}{\overline{\lambda}_n^3}+1\right)\left(G_{12}-\frac{G_{23}}{\overline{\lambda}_n^2}+G_{22}\left(\frac{\overline{\gamma}_n^2}{\overline{\lambda}_n^2}+\frac{1}{\overline{\lambda}_n^3}+1\right)\right)\right]+\\
&\frac{1}{\overline{\lambda}_n\overline{\gamma}_p}\frac{\partial^2\widehat{\Phi}}{\partial\overline{\lambda}_n\partial\overline{\gamma}_p}\left[G_{12}-\frac{G_{23}}{\overline{\lambda}_n^2}+2G_{22}\left(\frac{\overline{\gamma}_n^2}{\overline{\lambda}_n^2}+\frac{1}{\overline{\lambda}_n^3}+1\right)\right]+\\
&\frac{G_{22}}{\overline{\lambda}_n^2}\left(\frac{\partial^2\widehat{\Phi}}{\partial\overline{\lambda}_n^2}-\frac{1}{\overline{\lambda}_n}\frac{\partial\widehat{\Phi}}{\partial\overline{\lambda}_n}\right)+\frac{E_2}{\overline{\lambda}_n}\frac{\partial\widehat{\Phi}}{\partial\overline{\lambda}_n}+\\
&\frac{1}{\overline{\gamma}_p}\frac{\partial\widehat{\Phi}}{\partial\overline{\gamma}_p}\left[E_1-\frac{E_3}{\overline{\lambda}_n^2}+2\frac{G_{23}}{\overline{\lambda}_n^4}+\frac{G_{22}}{\overline{\lambda}_n^5}+\left(E_2-4\frac{G_{22}}{\overline{\lambda}_n^2}\right)\left(\frac{\overline{\gamma}_n^2}{\overline{\lambda}_n^2}+\frac{1}{\overline{\lambda}_n^3}+1\right)\right]+\\
&\widetilde{\mu}\left[\frac{E_3}{\overline{\lambda}_n^2}-E_2\left(\frac{\overline{\gamma}_n^2}{\overline{\lambda}_n^2}+2\right)+\frac{2(2G_{22}(\overline{\gamma}_n^2+\overline{\lambda}_n^2)-G_{23})}{\overline{\lambda}_n^4}\right]>0,
\end{aligned}\tag{B.21}$$

where it is recalled that the variables E_i, G_{1i}, G_{2i} and G_{3i} $(i=1,2,3)$ are given by (B.19), and the partial derivatives of $\widehat{\Phi}$ with respect to $\overline{\lambda}_n$ and $\overline{\gamma}_p$ are known functions of $\overline{\lambda}_n$, $\overline{\gamma}_p$ and $\overline{\lambda}_1^{(2)}$, which, although much simpler than the corresponding derivatives of the more general estimate (B.6), are still too cumbersome to be included here.

The estimate of deBotton et al. for Neo-Hookean phases. Since the effective potentials (B.14) and (B.16) for composites with Neo-Hookean constituents differ only in their functional dependence on $\overline{\lambda}_n$ and $\overline{\gamma}_p$, the strong ellipticity condition for the deBotton et al. [28] model may be readily obtained from (B.21) by explicit computation of the partial derivatives of expression (B.16) for $\widehat{\Phi}$ with respect to $\overline{\lambda}_n$ and $\overline{\gamma}_p$. The result can be shown to reduce to

$$\widetilde{\mu}\mathbf{v}\cdot\overline{\mathbf{B}}\mathbf{v}+\frac{\overline{\mu}-\widetilde{\mu}}{\overline{\lambda}_n}\left[(\overline{\lambda}_n^3-1)(\mathbf{n}\cdot\mathbf{v})^2+3(\mathbf{n}\cdot\mathbf{v})^2(\mathbf{n}\cdot\mathbf{u})^2\right]>0,\tag{B.22}$$

where it is recalled again that $\overline{\mu}$ and $\widetilde{\mu}$ are given explicitly by relations (B.12) and (B.13), respectively. It should be emphasized that the simplicity of condition (B.22), compared to (B.21), is due to the fact that for the deBotton et al. [28] model (B.16) the three modes of shear are completely decoupled and the in-plane and antiplane responses are identical, while for the estimate (B.14) of Agoras et al. [2] this is *not* true. The significance of these features on the development of macroscopic instabilities will be examined in Section B.6 for uniaxial tension perpendicular to the fiber direction.

B.4 Aligned loadings

We are now in a position to examine the above-described conditions of strong ellipticity and determine subsequently the onset of macroscopic instabilities for the class of fiber-reinforced nonlinearly elastic materials described in Section 2, when subjected to *arbitrary, three-dimensional, finite deformations*. As already remarked in the preceding section, conditions (B.18), (B.21), and (B.22) are expected to hold true in small neighborhoods of $\overline{\mathbf{F}} = \mathbf{I}$ (i.e., for small enough deformations). But as the deformation progresses beyond $\overline{\mathbf{F}} = \mathbf{I}$ into the finite-deformation regime, a point may be reached at which their LHS vanish for some critical $\overline{\mathbf{F}}_{cr}$ and pair of critical vectors $\mathbf{v}_{cr}$ and $\mathbf{u}_{cr}$. The objective of this and of the next section is to compute the set of all such critical deformations ($\overline{\mathbf{F}}_{cr}$), and associated critical vectors ($\mathbf{v}_{cr}$ and $\mathbf{u}_{cr}$), in order to map out the complete onset of macroscopic instabilities in fiber-reinforced nonlinearly elastic materials under arbitrary finite deformations. In general, the computation of deformations $\overline{\mathbf{F}}_{cr}$ and vectors $\mathbf{v}_{cr}$ and $\mathbf{u}_{cr}$ for which the LHS of (B.18) and (B.21) vanish requires a tedious, but straightforward, numerical treatment. There are special loading paths, however, for which it is possible to compute $\overline{\mathbf{F}}_{cr}$, $\mathbf{v}_{cr}$, and $\mathbf{u}_{cr}$ in closed form. On the other hand, because of its simpler structure, the computation of critical deformations $\overline{\mathbf{F}}_{cr}$ and critical vectors $\mathbf{v}_{cr}$ and $\mathbf{u}_{cr}$ for which the LHS of condition (B.22) ceases to be positive can be carried out analytically for arbitrary loading conditions.

In this section, we provide closed-form expressions for the critical deformations and critical stresses at which the estimates (B.6), (B.14), and (B.16) lose strong ellipticity under *aligned* axisymmetric and pure shear loading conditions. The results will be compared with the results of Rosen [133] and Triantafyllidis and Maker [142] for 2-D laminates. Corresponding results for more general loadings will be given in Section B.5 and B.6.

For definiteness and without loss of generality, in this and the remaining sections, we will consider the initial direction of the fibers to be given by $\mathbf{N} = \mathbf{e}_3$, where $\{\mathbf{e}_i\}$ stands for the Cartesian basis utilized for the laboratory frame of reference (see Fig. B.1(a)).

B.4.1 Axisymmetric shear

In this subsection, we generate explicit results for the onset of macroscopic instabilities in fiber-reinforced nonlinearly elastic materials—as characterized by failure of the strong ellipticity conditions (B.18), (B.21), and (B.22)—subjected to axisymmetric macroscopic deformation gradients of the form

$$\overline{\mathbf{F}} = \overline{\lambda}^{-1/2}\mathbf{e}_1 \otimes \mathbf{e}_1 + \overline{\lambda}^{-1/2}\mathbf{e}_2 \otimes \mathbf{e}_2 + \overline{\lambda}\,\mathbf{e}_3 \otimes \mathbf{e}_3. \tag{B.23}$$

After recognizing from (B.23) that $\overline{\lambda}_n = \overline{\lambda}$ and $\overline{\gamma}_n = \overline{\gamma}_p = 0$ and some algebraic manipulation, it follows that the critical stretch, $\overline{\lambda}_{cr}$, at which the strong ellipticity condition (B.18) is violated

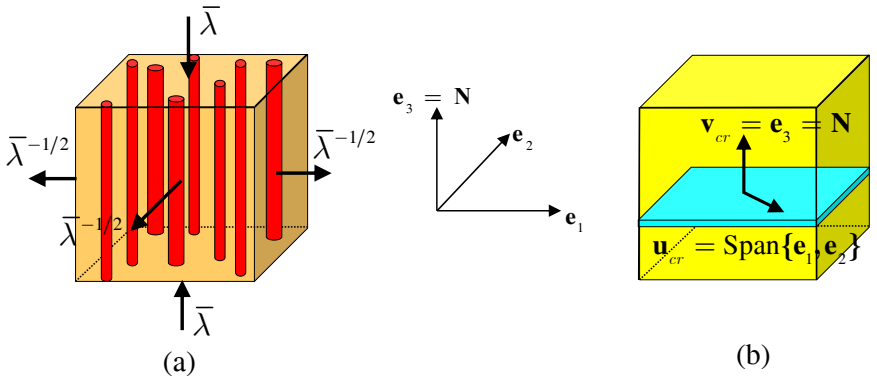

Figure B.2: (*a*) Schematic of a fiber-reinforced material subjected to aligned axisymmetric shear. (*b*) Illustration of the critical pair of orthogonal vectors, $\mathbf{v}_{cr}$ and $\mathbf{u}_{cr}$, for which the overall response of the material loses strong ellipticity.

under deformations of the form (B.23) is simply given by

$$\overline{\lambda}_{cr} = \left[\frac{(1-c_0)c_0 \left(g^{(1)}_{\overline{I}_{cr}} - g^{(2)}_{\overline{I}_{cr}} \right)^2}{\left((1-c_0) g^{(1)}_{\overline{I}_{cr}} + c_0 g^{(2)}_{\overline{I}_{cr}} \right) \left((1+c_0) g^{(1)}_{\overline{I}_{cr}} + (1-c_0) g^{(2)}_{\overline{I}_{cr}} \right)} \right]^{1/3}, \tag{B.24}$$

where $g^{(r)}_{\overline{I}_{cr}} = dg^{(r)}(\overline{I}_{cr})/dI$ with $\overline{I}_{cr} = \overline{\lambda}^2_{cr} + 2\overline{\lambda}^{-1}_{cr}$. In the physically relevant context when $g^{(1)}$ and $g^{(2)}$ are convex functions of their argument, it is easy to verify that the RHS of (B.24) is positive and less than one so that necessarily $\overline{\lambda}_{cr} < 1$. That is, under axisymmetric shear deformations, macroscopic instabilities may occur only for *compressive* loadings in the fiber direction and *not* for tensile ones, which is in agreement with physical experience. Note further that (B.24) constitutes a nonlinear algebraic equation for $\overline{\lambda}_{cr}$ which—although trivially solvable by numerical means—may or may not be solvable in closed form depending on the functional character of $g^{(1)}$ and $g^{(2)}$. In particular, for Neo-Hookean phases (B.4)—and more generally for Gent phases (B.3) with $J^{(1)}_m = J^{(2)}_m$—equation (B.24) can be readily solved in closed form rendering

$$\overline{\lambda}_{cr} = \left[\frac{(1-c_0)c_0 \left(\mu^{(1)} - \mu^{(2)} \right)^2}{\left((1-c_0)\mu^{(1)} + c_0 \mu^{(2)} \right) \left((1+c_0)\mu^{(1)} + (1-c_0)\mu^{(2)} \right)} \right]^{1/3}. \tag{B.25}$$

It is useful to note that this last expression may be rewritten more compactly as follows

$$\overline{\lambda}_{cr} = \left(1 - \frac{\widetilde{\mu}}{\overline{\mu}} \right)^{1/3}, \tag{B.26}$$

where it is recalled that $\widetilde{\mu}$ and $\overline{\mu}$ are respectively the longitudinal and axisymmetric shear moduli of the composite (in the linearized regime), and are given by relations (B.13) and (B.12). Thus, $\widetilde{\mu}$ characterizes the effective response of the fiber-reinforced material in *antiplane shear*, corresponding

to a *soft* mode of deformation, while $\overline{\mu}$ characterizes the effective response in *axisymmetric shear*, corresponding to a *hard* mode. It is evident from this expression that a heterogeneity contrast $t = \mu^{(2)}/\mu^{(1)} \neq 1$ (e.g., stiffer fibers) is required for $\overline{\lambda}_{cr}$ to be finite (different from zero), and that $\overline{\lambda}_{cr}$ tends to 1 (i.e., the instability tends to happen earlier) as the fibers become stiffer.

The associated pair of critical vectors for which loss of strong ellipticity occurs at the critical stretch (B.24) are $\mathbf{v}_{cr} = \mathbf{e}_3$ and $\mathbf{u}_{cr} = \text{Span}\{\mathbf{e}_1, \mathbf{e}_2\}$ (see Fig. B.2(b)). In other words, under axisymmetric *compressive* deformations of the form (B.23) with $\overline{\lambda} < 1$, fiber-reinforced materials become unstable because their overall shear response in *all* directions within the transverse plane to the fibers vanish identically. This result is consistent with the experimental results of Jelf and Fleck [66] for reinforced elastomers (see also Fleck [35], Kyriakides and Ruff [68] for other materials capable of undergoing plastic deformation), which have revealed that the failure mode in fiber-reinforced composites subjected to *compressive* deformation in the fiber direction leads to kink band instabilities.

For completeness, the instability results presented above in *deformation space* are presented next in *stress space*. With a suitable choice of the arbitrary pressure associated with the macroscopic incompressibility constraint ($\det \overline{\mathbf{F}} = 1$), the axisymmetric shear deformation (B.23) can equivalently be identified with a uniaxial stress condition (aligned with the direction of the fibers) of the form

$$\overline{\mathbf{S}} = \frac{\partial \widehat{W}}{\partial \overline{\mathbf{F}}} - p\, \overline{\mathbf{F}}^{-T} = \overline{S}_{33}(\overline{\lambda})\, \mathbf{e}_3 \otimes \mathbf{e}_3. \tag{B.27}$$

Here, $\overline{\mathbf{S}}$ denotes the first Piola-Kirchhoff stress tensor and p stands for the Lagrange multiplier associated with the incompressibility constraint. In this context, it then follows that the critical (first Piola-Kirchhoff) stress in the fiber direction at which the estimate (B.6) loses strong ellipticity under uniaxial stress is given by

$$\overline{S}_{cr} = \overline{S}_{33}(\overline{\lambda}_{cr}) = \frac{\mathrm{d}\widehat{\Psi}}{\mathrm{d}\overline{\lambda}}(\overline{\lambda}_{cr}) = 2\left(\overline{\lambda}_{cr} - \overline{\lambda}_{cr}^{-2}\right)\left[(1-c_0)g^{(1)}_{I_{cr}} + c_0 g^{(2)}_{I_{cr}}\right], \tag{B.28}$$

where $\widehat{\Psi}(\overline{\lambda}) \doteq \widehat{\Phi}(\overline{\lambda}, 0, 0)$ and $\overline{\lambda}_{cr}$ is the critical stretch defined by (B.24). For the special case of Neo-Hookean phases, (B.28) can be shown to simplify to the compact form

$$\overline{S}_{cr} = -\widetilde{\mu}\left(\frac{\overline{\mu}}{\overline{\mu} - \widetilde{\mu}}\right)^{2/3}. \tag{B.29}$$

The physical significance of the expressions (B.26) and (B.29) will be discussed further in subsection B.4.4, where comparisons will also be made with the commonly used laminate (2-D) idealization for fiber-reinforced composites.

Having examined the condition (B.18) associated with the general estimate (B.6), we now turn attention to the strong ellipticity condition (B.22) associated with the Neo-Hookean estimate (B.16) of deBotton et al. [28]. In this connection, it is a simple matter to deduce that—under

axisymmetric shear loadings of the form (B.23) with (B.27)—the LHS of (B.22) vanishes at the critical stretch (B.25) and critical vectors $\mathbf{v}_{cr} = \mathbf{e}_3$ and $\mathbf{u}_{cr} = \text{Span}\{\mathbf{e}_1, \mathbf{e}_2\}$, precisely as the LHS of (B.18) when specialized to Neo-Hookean phases.[1] Moreover, it is straightforward to show that the corresponding critical stress at which estimate (B.16) loses strong ellipticity is given by expression (B.29). That is, both homogenization estimates, (B.14) and (B.16), predict *exactly the same* critical deformation and the same critical stress for the onset of macroscopic instabilities in Neo-Hookean fiber-reinforced materials subjected to aligned axisymmetric shear.

With the objective of gaining more physical insight into the above-presented criteria for the onset of macroscopic instabilities, we develop further the above results for fiber-reinforced materials with Neo-Hookean (B.4) and Gent (B.3) matrix and fiber phases as functions of the (fiber-to-matrix) heterogeneity contrast $t = \mu^{(2)}/\mu^{(1)}$, volume fraction of fibers c_0, and lock-up parameters $J_m^{(1)}$ and $J_m^{(2)}$.

Figure B.3 presents results (labeled AXS) for the critical stretch (B.25) and stress (B.29) at which a fiber-reinforced material with Neo-Hookean matrix and fiber phases becomes macroscopically unstable when subjected to aligned axisymmetric shear loading (B.27) with (B.23). (Other results are shown in this figure for comparison and will be discussed in later sections.) Figure B.3(a) depicts the critical stretch $\overline{\lambda}_{cr}$ for a value of the fiber-to-matrix contrast $t = 20$, as a function of the volume fraction of fibers c_0. The main observation in this figure is that $\overline{\lambda}_{cr} \to 0$ as $c_0 \to 0$ and 1. This is consistent with the fact that both the pure matrix and fiber phases have been assumed to be strongly elliptic, so that in the absence of fibers ($c_0 = 0$) or matrix ($c_0 = 1$) the overall response remains stable for all deformations. As the initial volume fraction of fibers c_0 is increased from zero, $\overline{\lambda}_{cr}$ increases monotonically up to a certain $c_0 \leq 0.5$ at which it reaches a maximum. After this point, further increase in c_0 results in a monotonic decrease of $\overline{\lambda}_{cr}$. For fixed volume fraction of fibers (e.g., $c_0 = 0.3$), it can be seen from Figure B.3(b) that the critical stretch $\overline{\lambda}_{cr}$ increases monotonically with increasing fiber-to-matrix contrast t. In other words, the stiffer the behavior of the fibers (when compared to that of the matrix), the smaller the critical compressive deformation at which the fiber-reinforced material becomes unstable. In this regard, it is relevant to note that $\overline{\lambda}_{cr} \to 1$ as $t \to \infty$, irrespectively of the volume fraction of fibers (see expression (B.35) in subsection B.4.3). That is, in the limiting case of rigid fibers, the composite becomes unstable at zero strain (but not at zero stress of course). Similar observations can be made from Fig. B.3(c) and (d) for the critical stress $\overline{S}_{cr}$. However, the maximum (i.e., smallest compressive value) for $\overline{S}_{cr}$ is skewed towards smaller fiber concentrations c_0, although $\overline{S}_{cr} \to -\infty$ as $c_0 \to 0$ and as $c_0 \to 1$, in line with the behavior observed in Fig. B.3(a) for the critical stretch. In addition, in the limit as the fibers are taken to be rigid (i.e., $t \to \infty$), the critical stress tends

[1] The form (B.25) of the result was first presented by Lopez-Pamies and Ponte Castañeda [94], while the form (B.26) was first given by deBotton [27].

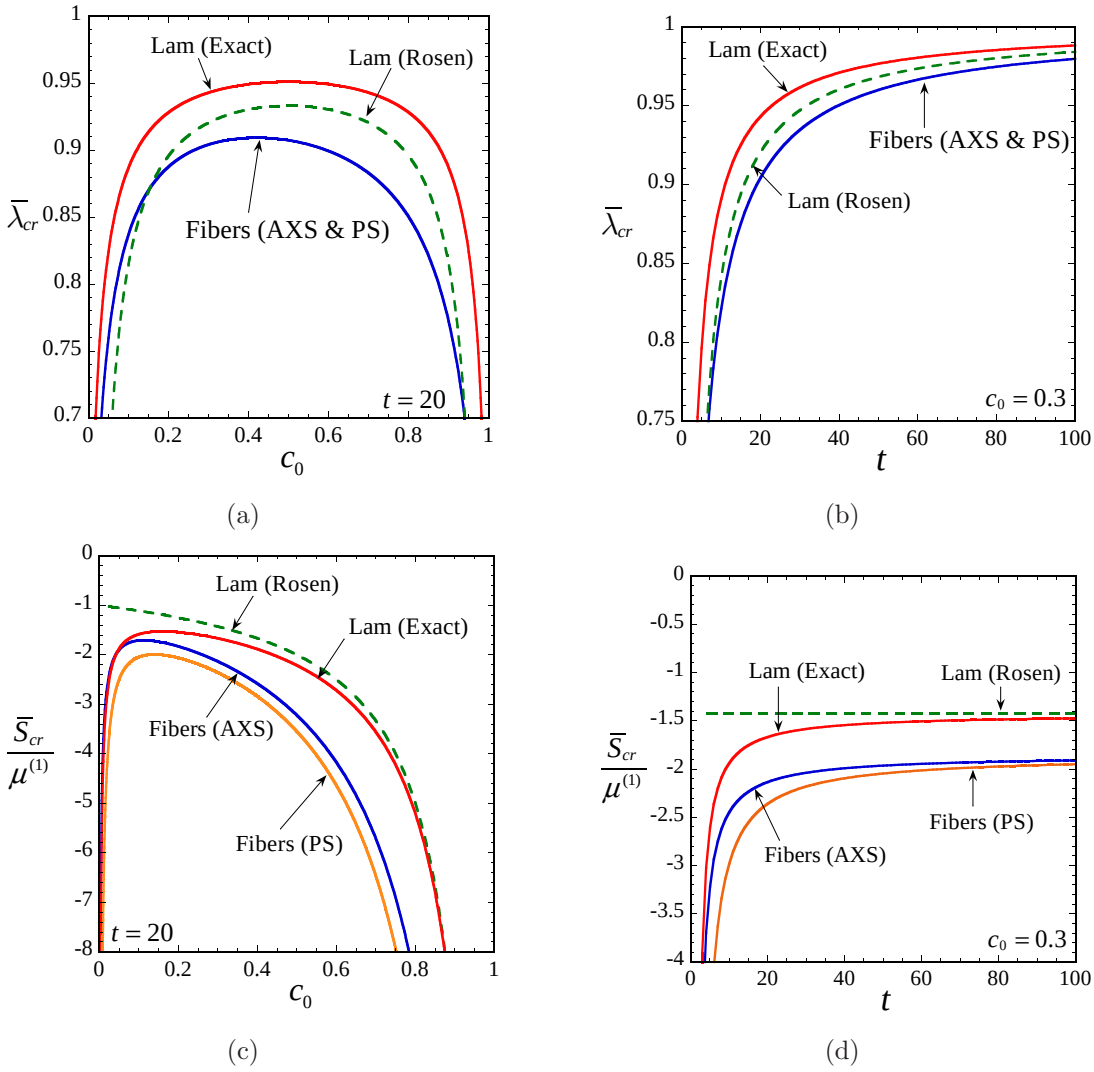

Figure B.3: Onset of macroscopic instabilities in fiber-reinforced materials with Neo-Hookean matrix and fiber phases subjected to *aligned axisymmetric shear* (AXS) and *pure shear* (PS) loading conditions. The critical stretch $\overline{\lambda}_{cr}$ (a) for fiber-to-matrix contrasts $t = \mu^{(2)}/\mu^{(1)} = 20$, as a function of the volume fraction of fibers c_0, and (b) for $c_0 = 0.3$, as a function of t. The critical stress $\overline{S}_{cr}$, normalized by $\mu^{(1)}$, corresponding to (a) and (b) are shown in (c) and (d), respectively. These results are compared with the *approximate* result of Rosen (1965), and the *exact* result of Triantafyllidis and Maker (1985) for laminates (Lam) under aligned pure shear.

to a *non-zero* value, which for this volume fraction ($c_0 = 0.3$) is about twice the shear modulus of the matrix phase.

Figure B.4 illustrates the influence of the lock-up parameters of the matrix ($J_m^{(1)}$) and fibers ($J_m^{(2)}$) on the critical stretch (B.24) for fiber-reinforced materials with Gent phases, when subjected

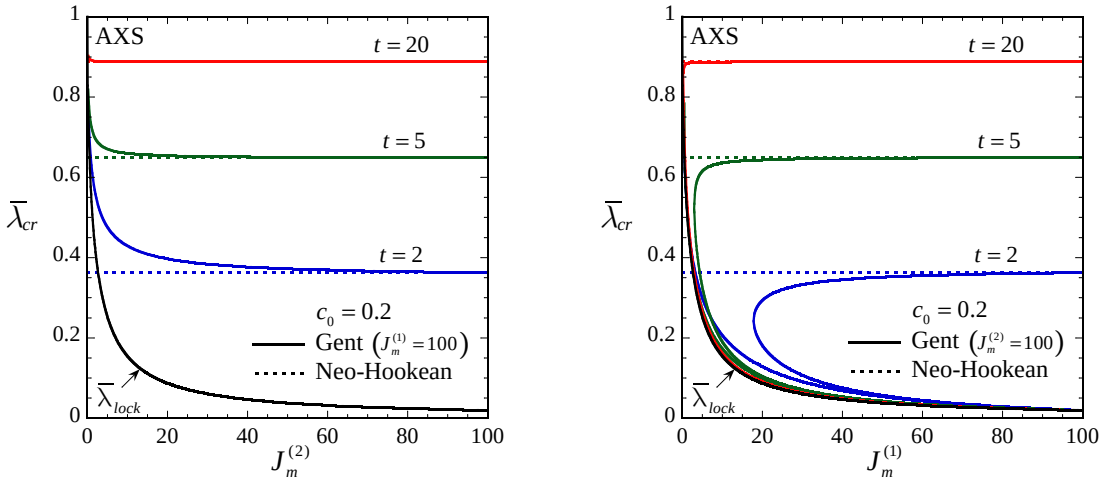

Figure B.4: Onset of macroscopic instabilities in fiber-reinforced materials with Gent phases subjected to *aligned axisymmetric shear* deformations (B.23), as given by expression (B.24). Results are shown for fiber-to-matrix contrasts $t = \mu^{(2)}/\mu^{(1)} = 2, 5, 20$, and volume fraction of the fibers $c_0 = 0.2$. (a) The critical stretch $\overline{\lambda}_{cr}$ for a fixed value of the lock-up parameter of the matrix, $J_m^{(1)} = 100$, as a function of $J_m^{(2)}$. (b) The critical stretch $\overline{\lambda}_{cr}$ for a fixed value of $J_m^{(2)} = 100$, as a function of $J_m^{(1)}$.

to aligned axisymmetric shear loadings (B.23). Results are shown for three values of the "initial" fiber-to-matrix contrast, $t = 2, 5, 20$, and volume fraction of the fibers $c_0 = 0.2$. Part (a) presents the critical stretch $\overline{\lambda}_{cr}$ for $J_m^{(1)} = 100$ as a function of $J_m^{(2)}$, and part (b) shows $\overline{\lambda}_{cr}$ for $J_m^{(2)} = 100$ as a function of $J_m^{(1)}$. The associated lock-up limit $\overline{\lambda}_{lock}$ for these materials, given by $\overline{\lambda}_{lock}^2 + 2/\overline{\lambda}_{lock} - 3 = \min\{J_m^{(1)}, J_m^{(2)}\}$ (see Section 5 in Agoras et al. [2] for details), as well as the critical stretches for the corresponding composites with Neo-Hookean phases (i.e., $J_m^{(1)} = J_m^{(2)} = \infty$) have been included in this figure for comparison purposes. Note that the different branches of the curves shown in Fig. B.4(b) correspond to distinct solutions of the *nonlinear* equation (B.24) for $\overline{\lambda}_{cr}$. It should be emphasized, however, that starting from the undeformed configuration and following the given axisymmetric loading path, the critical stretch at which a certain material becomes unstable corresponds to the highest among these values of $\overline{\lambda}_{cr}$. It is observed that for sufficiently large values of $J_m^{(2)}$ in part (a) and $J_m^{(1)}$ in part (b), these parameters have no essential effect on the stability of the composite and the associated critical stretch $\overline{\lambda}_{cr}$ is practically determined by the value of the contrast t. This observation is consistent with the fact that Gent materials behave like Neo-Hookean materials for deformations away from the lock-up limit $\overline{\lambda}_{lock}$. On the other hand, from part (a), we see that for small values of $J_m^{(2)}$ composites with Gent phases are more unstable than the corresponding composites with Neo-Hookean phases, while from part (b) we observe that for small values of $J_m^{(1)}$ the opposite is true. Recalling that for aligned axisymmetric shear (B.23)

the deformation gradient field is uniform in the matrix and fibers (see He et al. [49] and Section 4.1 in Agoras et al. [2]), these results may be understood as follows. For the case when $J_m^{(2)} < J_m^{(1)}$ (part (a)), as the applied stretch $\overline{\lambda}$ approaches the lock-up limit $\overline{\lambda}_{lock}$, the fibers tend to stiffen faster than the matrix with the consequence of effectively increasing the heterogeneity contrast (from its initial value $t = \mu^{(2)}/\mu^{(1)} > 1$) and thus accelerating the instability, while the opposite is true for $J_m^{(1)} < J_m^{(2)}$ (part (b)) (at least for not too small values of $J_m^{(1)}$, after which the behavior is controlled by the lock-up phenomenon).

B.4.2 Pure shear

Next, we consider the development of macroscopic instabilities for pure shear loadings of the form

$$\overline{\mathbf{F}} = \overline{\lambda}^{-1}\mathbf{e}_1 \otimes \mathbf{e}_1 + \mathbf{e}_2 \otimes \mathbf{e}_2 + \overline{\lambda}\,\mathbf{e}_3 \otimes \mathbf{e}_3, \tag{B.30}$$

where, similar to the preceding axisymmetric case, $\overline{\lambda}$ is a positive loading parameter, and it is recalled that the fibers are aligned in the $\mathbf{e}_3$ direction.

For the Neo-Hookean estimate (B.16) of deBotton et al. [28], it is not difficult to show that when specialized to loading conditions of the form (B.30), the LHS of relation (B.22) vanishes at the critical stretch (B.26) and critical vectors $\mathbf{v}_{cr} = \mathbf{e}_3$ and $\mathbf{u}_{cr} = \text{Span}\{\mathbf{e}_1, \mathbf{e}_2\}$ (see Fig. B.2(b)). Thus, under *compressive* pure shear deformations of the form (B.30) with $\overline{\lambda} < 1$, fiber-reinforced materials become unstable because their overall shear response in *all* directions within the transverse plane to the fibers vanish identically. This is essentially the same "failure" mechanism that was observed in the preceding subsection for axisymmetric shear conditions.

Next, by suitably selecting the arbitrary hydrostatic pressure associated with the macroscopic incompressibility constraint, we can identify the pure shear deformation (B.30) with the following biaxial stress state

$$\overline{\mathbf{S}} = \overline{S}_{22}(\overline{\lambda})\,\mathbf{e}_2 \otimes \mathbf{e}_2 + \overline{S}_{33}(\overline{\lambda})\,\mathbf{e}_3 \otimes \mathbf{e}_3. \tag{B.31}$$

It follows that the critical stress along the fiber direction at which the estimate (B.16) loses strong ellipticity is given by

$$\overline{S}_{cr} = \overline{S}_{33}(\overline{\lambda}_{cr}) = -\widetilde{\mu}\,\frac{\overline{\mu}}{\overline{\mu} - \widetilde{\mu}}\,, \tag{B.32}$$

which is very similar (but not identical) to the corresponding result (B.29) for axisymmetric loading conditions.

It should also be noted that the corresponding estimates for the critical stretch and stress using the model of Agoras et al. [2] may be easily computed for general behaviors for the phases. However, when specialized to the particular case of Neo-Hookean matrix and fiber phases (*cf.* (B.14)), the resulting estimates for the critical stretch and stress are very well approximated by expressions (B.26) and (B.32), respectively. Thus—as for axisymmetric shear—both homogenization

estimates (B.14) and (B.16) predict *essentially the same* critical deformations and stresses for the onset of macroscopic instabilities for Neo-Hookean fiber-reinforced materials subjected to aligned pure shear. Sample results, labeled PS, for the case of Neo-Hookean constituents are shown in Fig. B.3 as functions of the fiber volume fraction c_0 and contrast t. Comparing the results for $\overline{S}_{cr}$ for pure shear loading with the corresponding results for axisymmetric shear, it can be seen that the general trends are very similar. There are noticeable differences only for low values of the contrast t, but the differences tend to disappear as the contrast increases.

B.4.3 Asymptotic results in the limit of rigid fibers

The above-presented results correspond to general heterogeneity contrast between the matrix and the fibers. In practice, however, actual fibers in reinforced soft materials are usually several orders of magnitude stiffer than the matrix phase. In this regard, it is convenient to spell out the specialization of the above results in the limit as the fibers are taken to be rigid. To this end, it is first helpful to recognize that the assumed smoothness and proper linearization of $g^{(1)}$ imply that

$$g^{(1)}(I) = \frac{\mu^{(1)}}{2}\,(I-3) + \frac{1}{2}\,g^{(1)}_{II}(3)\,(I-3)^2 + O\left((I-3)^3\right). \tag{B.33}$$

Then, by setting (without loss of generality)

$$g^{(2)}(I) = \frac{\mu^{(2)}}{2}(I-3) \tag{B.34}$$

and subsequently defining the fiber-to-matrix heterogeneity contrast $t = \mu^{(2)}/\mu^{(1)}$, it follows that expression (B.24) for the critical stretch at which instabilities develop for the case of *aligned axisymmetric shear loading conditions* reduces to

$$\overline{\lambda}_{cr} = 1 - \frac{1+c_0}{3(1-c_0)c_0}\,t^{-1} + O(t^{-2}), \tag{B.35}$$

in the limit as $t \to \infty$, namely, in the limit as the fibers are taken to be rigid. Expression (B.28) for the corresponding critical stress can be shown to specialize to

$$\overline{S}_{cr} = -\frac{1+c_0}{1-c_0}\mu^{(1)} + O(t^{-1}). \tag{B.36}$$

Interestingly, the critical stretch and stress at which instabilities develop for the case of *pure shear loading conditions* can also be shown to reduce to expressions (B.35) and (B.36), respectively, in the limit as $t \to \infty$. That is, in the limit of rigid fibers, the critical stretch $\overline{\lambda}_{cr}$ and critical stress $\overline{S}_{cr}$ for aligned axisymmetric shear deformations agree identically with the critical stretch $\overline{\lambda}_{cr}$ and critical stress $\overline{S}_{cr}$ for aligned pure shear deformations.

Moreover, it should be emphasized that the critical relations (B.35) and (B.36) are valid for materials with arbitrary generalized Neo-Hookean matrix behavior $g^{(1)}$, but because of the rigidity

of the fibers, only the shear modulus in the ground state, $2\,g_I^{(1)}(3) = \mu^{(1)}$, enters these expressions. A practical implication of this result is that when considering the compressive failure in fiber-reinforced nonlinearly elastic materials with very stiff fibers, it suffices to model the matrix phase as Neo-Hookean. However, it should also be emphasized that the above asymptotic results tacitly assume that material parameters other than t are held fixed. As we have already seen, for instance, in the context of Fig. B.4 for composites with Gent phases, how stiff the fibers need to be may depend on the values of the lock-up parameters of the matrix and fiber phases.

B.4.4 Comparisons with earlier results for laminates under pure shear loading

A popular strategy in the literature to estimate the compressive failure of fiber-reinforced composites has been to idealize these materials as laminates. The motivation for this simplifying approach stems from the fact that—under plane-strain loading conditions—laminates resemble 2-D fiber-reinforced morphologies (see Fig. B.1(b)) and, at the same time, they permit an *exact* analytical treatment (see Appendix I for exact results for laminates with Neo-Hookean phases). In this section, we investigate the validity of such an approximation in light of the new results developed above for pure shear loading.

In one of the very first works proposing the use of laminates as 2-D approximations for fiber-reinforced composites, Rosen [133] considered a perfect laminate made up of alternating layers of different *linear elastic* isotropic materials that is subjected to *plane-strain* compressive load along the layers. By means of an energy method, he solved the problem *approximately* and concluded that the critical stretch $\overline{\lambda}_{cr}^{Ros}$ and associated critical stress $\overline{S}_{cr}^{Ros}$ at which long-wavelength instabilities develop in these material systems are given by

$$\overline{\lambda}_{cr}^{Ros} = 1 - \frac{\mu^{(1)}}{3\,c_0(1-c_0)\mu^{(2)}} \quad \text{and} \quad \overline{S}_{cr}^{Ros} = -\frac{\mu^{(1)}}{1-c_0}\,. \tag{B.37}$$

Later, Triantafyllidis and Maker [142] re-examined the laminate problem within the more general framework of finite elasticity. Specifically, these authors considered a perfect laminate, made up of alternating incompressible Neo-Hookean layers, under aligned pure shear loading conditions (B.30). By making use of Floquet theory for ODEs, they showed that the critical stretch $\overline{\lambda}_{cr}^{L}$ and associated critical stress $\overline{S}_{cr}^{L}$ at which long-wavelength instabilities develop in this case are given *exactly* by

$$\overline{\lambda}_{cr}^{L} = \left(1 - \frac{\widetilde{\mu}^{L}}{\overline{\mu}}\right)^{1/4} \quad \text{and} \quad \overline{S}_{cr}^{L} = -\widetilde{\mu}^{L}\left(\frac{\overline{\mu}}{\overline{\mu}-\widetilde{\mu}^{L}}\right)^{3/4}, \tag{B.38}$$

where $\overline{\mu}$ and $\widetilde{\mu}^{L}$ are defined by expressions (B.12) and $(B.62)_2$, respectively, and physically correspond to the "hard" axisymmetric (and transverse) shear mode and the "soft" longitudinal mode

for small strains (see Appendix I). Note that the *exact* results (B.38) of Triantafyllidis and Maker are generally different from the *approximate* results (B.37) of Rosen; in particular, $\overline{\lambda}_{cr}^{Ros} \leq \overline{\lambda}_{cr}^{L}$ and $\overline{S}_{cr}^{Ros} \geq \overline{S}_{cr}^{L}$. However, both sets of results share the same physically expected qualitative features. Namely, they predict that long-wavelength instabilities occur only for compressive deformations (i.e., $\overline{\lambda}_{cr}^{Ros}, \overline{\lambda}_{cr}^{L} \leq 1$ and $\overline{S}_{cr}^{Ros}, \overline{S}_{cr}^{L} \leq 0$). Moreover, both critical stretches, $\overline{\lambda}_{cr}^{Ros}$ and $\overline{\lambda}_{cr}^{L}$, are symmetric functions of the volume fractions of the matrix $1 - c_0$ and of the fibers c_0, as a result of the symmetric role that the matrix and fiber constituents play in laminates (see Fig. B.3 and the relevant discussion further below).

In connection with the above results for laminates, it is interesting to remark that the expressions (B.26), (B.29), and (B.32) for Neo-Hookean fiber-reinforced materials exhibit the same structure as the expressions (B.38) for Neo-Hookean laminates. In particular, both sets of results establish that long-wavelength instabilities may develop under aligned loadings whenever the compressive stretch in the fiber or layer direction reaches a critical value depending on the ratio of the "soft" effective longitudinal shear modulus to the "hard" axisymmetric shear modulus. (The differences in the exponents in these expressions are due to the different loadings and microstructures involved, since the relations between the stress and stretch variables are different for different loading conditions, e.g., pure shear vs. axisymmetric shear, while the response of layered and fiber-reinforced microstructures are also different.) More specific comparisons are given in Fig. B.3, showing plots of $\overline{\lambda}_{cr}$ and $\overline{S}_{cr}$, as functions of the volume fraction of fibers c_0 and the fiber-to-matrix contrast $t = \mu^{(2)}/\mu^{(1)}$. Thus, it is observed from Fig. B.3(a) and (b) that the critical stretch (B.26) for the axisymmetric and pure shear loading conditions (which, as already discussed, are identical to each other) indeed exhibit the same *qualitative* behavior as the exact critical stretch $(B.38)_1$ for laminates, both in terms of the dependence on volume fraction c_0, as well as contrast t. It is worth remarking, however, that unlike $(B.38)_1$, (B.26) is not symmetric about $c_0 = 0.5$. This feature is consistent with the fact that, unlike in laminates, the fibers and matrix phases in fiber-reinforced materials do *not* play a symmetric role. From a *quantitative* point of view, it is also observed that laminates are more unstable than fiber-reinforced materials, since they may develop long-wavelength instabilities at smaller compressive deformations (i.e., larger $\overline{\lambda}_{cr}$). Figures B.3(c) and (d) show that the critical stresses (B.29) and (B.32) for axisymmetric and pure shear loading conditions (which, as opposed to the associated stretches (B.26) are different from each other) are also in relatively good *qualitative* agreement with the corresponding exact result $(B.38)_2$ for laminates. Moreover, as in stretch-space, laminates are seen to be more unstable in stress-space than fiber-reinforced materials. It is also interesting to point out that for all results $\overline{\lambda}_{cr} \to 1$ in the limit of rigid fibers ($t \to \infty$). On the other hand, as $t \to \infty$, the stresses for laminates are seen to asymptotically approach a non-zero compressive value that is significantly smaller than that for fiber-reinforced materials.

B.5 Non-aligned loadings

Section B.4 has provided some insight into the development of macroscopic instabilities in fiber-reinforced nonlinearly elastic materials subjected to *aligned* (axisymmetric and pure shear) loading conditions. In this section, we consider more general applied deformations in which the principal axes of loading are *not* aligned with the fiber direction. These include axisymmetric, pure, and simple shear at an angle relative to the fiber orientation $\mathbf{N}$, as well as completely arbitrary loading conditions. Motivated by the fact that in realistic fiber-reinforced materials the underlying fibers are several orders of magnitude stiffer than the elastomeric matrix phase, we will primarily focus (see Section B.4.3) on material systems with Neo-Hookean constituents, and take advantage of the model of deBotton et al. [28] allowing for a full analytical treatment. However, some representative numerical results will also be presented using the model of Agoras et al. [2] for materials with Gent phases in order to illustrate the differences that may arise for materials with *non-Neo-Hookean* matrix and fiber behaviors, especially when the critical deformations happen to be relatively large.

B.5.1 Axisymmetric shear at an angle

We start out by considering the case in which a fiber-reinforced nonlinearly elastic material is subjected to axisymmetric shear deformations of the form

$$\overline{\mathbf{F}} = \overline{\mathbf{Q}}\,\overline{\mathbf{D}}\,\overline{\mathbf{Q}}^{T} \tag{B.39}$$

with

$$\overline{\mathbf{D}} = \overline{\lambda}^{-1/2}\mathbf{e}_1 \otimes \mathbf{e}_1 + \overline{\lambda}^{-1/2}\mathbf{e}_2 \otimes \mathbf{e}_2 + \overline{\lambda}\,\mathbf{e}_3 \otimes \mathbf{e}_3 \tag{B.40}$$

and

$$\overline{\mathbf{Q}} = \cos\Theta(\mathbf{e}_1 \otimes \mathbf{e}_1 + \mathbf{e}_3 \otimes \mathbf{e}_3) + \sin\Theta(\mathbf{e}_1 \otimes \mathbf{e}_3 - \mathbf{e}_3 \otimes \mathbf{e}_1) + \mathbf{e}_2 \otimes \mathbf{e}_2. \tag{B.41}$$

Here, we recall that the fibers are initially aligned in the $\mathbf{e}_3$ direction and remark that the scalars $\overline{\lambda} > 0$ and Θ play the role of two independent loading parameters. Note that $\Theta = n\pi$ ($n \in \mathbb{Z}$) corresponds to the aligned case presented in Section B.4.1.

After substituting expression (B.39), with (B.40) and (B.41), in condition (B.22), it is a simple matter to deduce that the critical stretch at which macroscopic instabilities may first develop along axisymmetric shear loading paths at an angle satisfy

$$\overline{\lambda}_{cr}^{3}\cos^2\Theta - \overline{\lambda}_{cr}\left(1 - \frac{\widetilde{\mu}}{\overline{\mu}}\right)^{2/3} + \sin^2\Theta = 0, \tag{B.42}$$

while the associated critical vectors are given by $\mathbf{v}_{cr} = \cos\alpha_{cr}\,\mathbf{e}_1 + \sin\alpha_{cr}\,\mathbf{e}_3$ and $\mathbf{u}_{cr} = \mathbf{e}_2$, with $\tan\alpha_{cr} = (\cot\Theta)/(1-\overline{\lambda}_{cr}^{3/2}) + \overline{\lambda}_{cr}^{3/2}(\tan\Theta)/(1-\overline{\lambda}_{cr}^{3/2})$. As expected, equation (B.42) is periodic in Θ with period π. For the limiting values $\Theta = 0, \pi$ expression (B.42) reduces, of course, to (B.26).

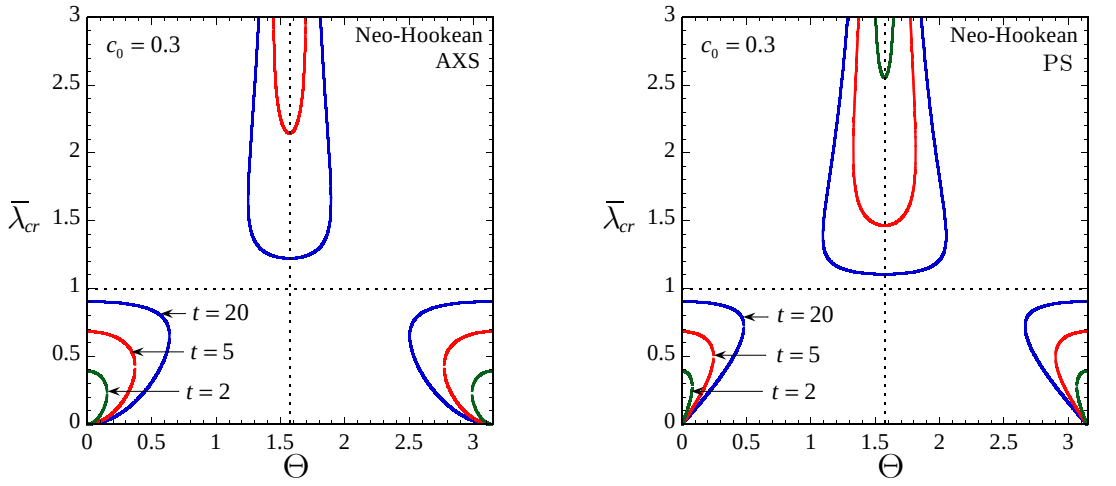

Figure B.5: Onset of macroscopic instabilities in fiber-reinforced materials with Neo-Hookean matrix and fiber phases subjected to *non-aligned* loadings: (a) *axisymmetric shear*, and (b) *pure shear*. The critical stretch $\overline{\lambda}_{cr}$ is shown for fiber-to-matrix contrasts $t = \mu^{(2)}/\mu^{(1)} = 2, 5, 20$, volume fraction of fibers $c_0 = 0.3$, as a function of the angle of fiber misalignment Θ.

To help examine the more general situation of intermediate values $\Theta \in (0, \pi)$, Fig. B.5(a) provides plots for $\overline{\lambda}_{cr}$ as a function of Θ, for fiber-to-matrix contrasts $t = \mu^{(2)}/\mu^{(1)} = 2, 5, 20$ and volume fraction of fibers $c_0 = 0.3$. (Part (b) of this figure will be discussed in the context of the next subsection.) A key observation from Fig. B.5(a) is that $\overline{\lambda}_{cr} < 1$ for angles near $\Theta = 0$ and $\Theta = \pi$, whereas $\overline{\lambda}_{cr} > 1$ for angles near $\Theta = \pi/2$. By contrast, there is a finite range of angles neighboring $\Theta = \pi/4$ and $\Theta = 3\pi/4$ for which macroscopic instabilities do not occur. Physically, these results entail that fiber-reinforced materials may develop macroscopic instabilities only when the deformation along the direction of the fibers is compressive and of a sufficiently large magnitude. Indeed, under loading conditions of the form (B.39) with $\overline{\lambda} < 1$, $\Theta = 0$ and $\Theta = \pi$ correspond to the cases at which maximum compression is applied along the fibers. Likewise, for $\overline{\lambda} > 1$ in (B.39), $\Theta = \pi/2$ corresponds to the case at which maximum compression is applied along the fibers. Deviating the value of Θ away from 0 and π when $\overline{\lambda} < 1$, and away from $\pi/2$ when $\overline{\lambda} > 1$, effectively decreases the amount of compression in the fiber direction, with the angles $\Theta = \pi/4$ and $\Theta = 3\pi/4$ corresponding to the cases in which the applied compressive deformation along the fibers is the smallest. In line with the findings of Section B.4.1 for aligned axisymmetric loading conditions, Fig. B.5(a) shows that increasing the heterogeneity contrast t results in macroscopic instabilities developing at smaller (tensile or compressive) deformations. In other words, the larger the contrast between the fibers and the matrix, the more unstable the behavior of fiber-reinforced

materials becomes. Given the loading path independence proper of hyperelastic materials, it is seen from Fig. B.5 that macroscopic instabilities may be possible at larger deformations for "non-radial" loading paths (i.e., when Θ is a function of $\overline{\lambda}$). In this case, the curves shown in Figs. B.5 should be interpreted as macroscopic "failure surfaces" in the sense of Triantafyllidis et al. [143].

B.5.2 Pure shear at an angle

We consider now the case in which a fiber-reinforced nonlinearly elastic material is subjected to pure shear deformations of the form (B.39) with $\overline{\mathbf{Q}}$ given by (B.41) and

$$\overline{\mathbf{D}} = \overline{\lambda}^{-1}\mathbf{e}_1 \otimes \mathbf{e}_1 + \mathbf{e}_2 \otimes \mathbf{e}_2 + \overline{\lambda}\,\mathbf{e}_3 \otimes \mathbf{e}_3. \tag{B.43}$$

Here, similar to the axisymmetric case, the scalars $\overline{\lambda} > 0$ and Θ are loading parameters. Note that $\Theta = n\,\pi$ $(n \in \mathbb{Z})$ corresponds to the aligned case presented in Section B.4.2. Note further that the shifts $\overline{\lambda} \to \overline{\lambda}^{-1}$ and $\Theta \to \Theta + \pi/2$ lead to the same loading.

By making explicit use of expression (B.39), with (B.43) and (B.41), in the strong ellipticity condition (B.22), it follows that the critical stretch at which macroscopic instabilities may develop in this case is solution to the following quartic equation

$$\overline{\lambda}_{cr}^4 \cos^2\Theta - \overline{\lambda}_{cr}^2 \left(1 - \frac{\widetilde{\mu}}{\overline{\mu}}\right)^{2/3} + \sin^2\Theta = 0. \tag{B.44}$$

Moreover, the corresponding critical vectors can be shown to be given by $\mathbf{v}_{cr} = \cos\alpha_{cr}\ \mathbf{e}_1 + \sin\alpha_{cr}\ \mathbf{e}_3$ and $\mathbf{u}_{cr} = \mathbf{e}_2$, where the angle α_{cr} is defined by $\tan\alpha_{cr} = (\cot\Theta)/(1-\overline{\lambda}_{cr}^2) + \overline{\lambda}_{cr}^2(\tan\Theta)/(1-\overline{\lambda}_{cr}^2)$. Note that equation (B.44) is periodic in Θ with period π, and hence it is sufficient to examine values $\Theta \in [0,\pi]$. Note further that for $\Theta = 0, \pi$ expression (B.44) reduces, of course, to (B.26).

Figure B.5(b) presents macroscopic failure surfaces for fiber-to-matrix contrasts $t = \mu^{(2)}/\mu^{(1)} = 2, 5, 20$ and volume fraction of fibers $c_0 = 0.3$, and shows that the onset of macroscopic instabilities along non-aligned pure shear loading paths is similar in character to the onset of macroscopic instabilities for non-aligned axisymmetric shear deformations (*cf.* Fig. B.5(a)). Indeed, it is observed that $\overline{\lambda}_{cr} < 1$ around $\Theta = 0$ and $\Theta = \pi$, $\overline{\lambda}_{cr} > 1$ around $\Theta = \pi/2$, and macroscopic instabilities do not occur near $\Theta = \pi/4$ and $\Theta = 3\pi/4$. Again, these results imply that fiber-reinforced materials may develop macroscopic instabilities only when the deformation along the direction of the fibers is of a sufficiently large compressive magnitude. Moreover, increasing the contrast t (and the volume fraction of fibers c_0, although not shown) is seen to render fiber-reinforced materials more unstable, irrespectively of the angle of fiber misalignment Θ.

The right side of Fig. B.6(a) shows a comparison of the failure surfaces for fiber-reinforced materials with Gent phases, with lock-up values $J_m^{(1)} = J_m^{(2)} = J_m = 10, 20, 30$ and 50, with

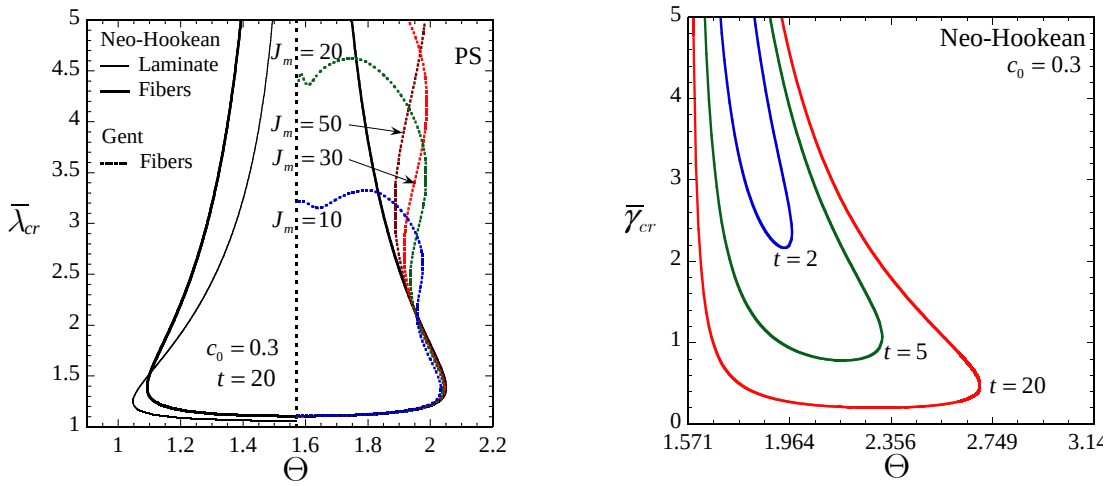

(a) (b)

Figure B.6: Onset of macroscopic instabilities in fiber-reinforced materials subjected to *non-aligned* loadings. (a) Comparison of *pure shear* failure surfaces for a Neo-Hookean fiber-reinforced composite with Gent fiber-reinforced composites (right) and with a Neo-Hookean laminate (left). All material systems have $c_0 = 0.3$ and $t = 20$, while for materials with Gent phases results are shown for several values of J_m (10, 20, 30, 50). (b) The critical stretch $\overline{\gamma}_{cr}$ for Neo-Hookean matrix and fiber phases under *simple shear* loading, as a function of the fiber misalignment angle Θ, for $t = \mu^{(2)}/\mu^{(1)} = 2, 5, 20$, and $c_0 = 0.3$.

the corresponding surfaces for fiber-reinforced materials with Neo-Hookean phases ($J_m \to \infty$) for $t = 20$ and $c_0 = 0.3$. In the context of Fig. B.6(a), it should be noted that the lower branches displayed in Fig. B.5(b) are exactly equivalent to the upper branch, when account is made of the invariance of the equations under the transformations $\overline{\lambda} \to \overline{\lambda}^{-1}$ and $\Theta \to \Theta + \pi/2$. For this reason, in Fig. B.6(a) only the upper branch is shown (magnified). In addition, only the right half of the Gent failure surfaces are shown, given their symmetry about the vertical axis. It can be seen from this figure that while the Neo-Hookean failure surfaces close up at infinity, the Gent surfaces close at a finite value of the stretch $\overline{\lambda}$, depending on the lock-up parameter J_m. However, for "radial" loading paths (i.e., for constant Θ) these differences are not relevant since the Gent and Neo-Hookean fiber composites are seen to fail at similar values of $\overline{\lambda}$, thus giving credence to the explicit formula (B.44) for materials other than Neo-Hookean.

For *non-aligned*, but still plane-strain, loading conditions, it is also possible to compute (in closed form) the exact critical deformations at which macroscopic instabilities may develop in Neo-Hookean laminates; the result is given by expression (B.65) in Appendix I. The predictions are qualitatively very similar (although quantitatively different) to the predictions for fiber-reinforced materials discussed earlier. An illustration of this is provided in Fig. B.6(a) for pure shear at

an angle (refer to the left side of the graph). There, it can be seen that the exact results for a laminate with Neo-Hookean phases—as given by expression (B.66) in Appendix I—are quite similar to the predictions for the fiber-reinforced material also with Neo-Hookean phases—as given by expression (B.44). Thus, these results indicate that modeling the behavior of fiber-reinforced nonlinearly elastic materials as laminates is certainly appropriate—in *qualitative* terms—when restricting attention to the special case of *plane-strain* loading conditions. As elaborated in Section B.6, however, this is not true when considering more general three-dimensional (3-D) loading conditions.

B.5.3 Simple shear at an angle

Next, we consider applied simple shear deformations of the form (B.39), where now

$$\overline{\mathbf{D}} = \mathbf{I} - \overline{\gamma}\, \mathbf{e}_1 \otimes \mathbf{e}_3, \tag{B.45}$$

with $\overline{\gamma} \geq 0$ and Θ being two independent loading parameters. Under this type of loading conditions, the critical amount of shear, $\overline{\gamma}_{cr}$, at which condition (B.22) first fails can be shown to be solution to the following quadratic equation

$$\overline{\gamma}_{cr}^2\, \frac{1+\cos 2\Theta}{2} + \overline{\gamma}_{cr} \sin 2\Theta - \left(1 - \frac{\widetilde{\mu}}{\overline{\mu}}\right)^{2/3} + 1 = 0, \tag{B.46}$$

while the associated critical vectors can be shown to be given by $\mathbf{v}_{cr} = \cos\alpha_{cr}\, \mathbf{e}_1 + \sin\alpha_{cr}\, \mathbf{e}_3$ and $\mathbf{u}_{cr} = \mathbf{e}_2$ with $\tan\alpha_{cr} = \cot\Theta - (\csc\Theta)^2/\overline{\gamma}_{cr}$. Again, as expected, equation (B.46) is periodic in Θ with period π, and therefore we restrict attention to the domain $\Theta \in [0, \pi]$. After recalling the inequality $\overline{\mu} \geq \widetilde{\mu}$, it is straightforward to check that within the range $\Theta \in [0, \pi/2]$, there is no real positive $\overline{\gamma}_{cr}$ that satisfies (B.46). On the contrary, for $\Theta \in (\pi/2, \pi)$, there are finite positive values of $\overline{\gamma}_{cr}$ for which equation (B.46) is satisfied.

Fig. B.6(b) shows a few of these results for $\overline{\gamma}_{cr}$, as a function of Θ, for $t = 2, 5, 20$ and $c_0 = 0.3$. It is noted that these failure surfaces look like shifted and distorted versions of the corresponding surfaces in Fig. B.6(a), the reason for this being that the loading (B.45) actually corresponds to the pure shear loading (B.43), together with a superposed rotation (which also depends on $\overline{\gamma}$). It is interesting that this applied rotation now makes "accessible" the previously unaccessible left side of the failure surface for pure shear (for a radial path). Similar to all previous cases, Fig. B.6(b) shows that for all values of fiber misalignment Θ, increasing the fiber-to-matrix contrast t and volume fraction of fibers c_0 (in the range of values considered) also render fiber-reinforced materials more unstable when subjected to non-aligned simple shear deformations. In addition, although not explicitly illustrated in the plots, Fig. B.6(b) does show that $\overline{\gamma}_{cr}$ is smaller for angles Θ for which more compressive deformation is applied along the direction of the fibers.

B.6 General loading conditions

By means of specific cases, Section B.4 and B.5 above have revealed that fiber-reinforced nonlinearly elastic materials can develop long-wavelength instabilities when subjected to loading conditions enforcing a sufficiently large compressive deformation along the fiber direction. In subsection B.6.1, we consider completely general loading conditions and cast the generic conclusions of the previous subsections for materials with Neo-Hookean constituents in general form using, for simplicity, the model of deBotton et al. [28]. The relevance of this explicit result for more general material behavior will be explored in subsection B.6.2 in the context of transverse uniaxial tension loading, where comparisons will also be made with the 2-D laminate approximation, showing the inappropriateness of this approximation for general loading conditions.

B.6.1 A closed-form analytical result for general loadings

As demonstrated in Appendix II, given an arbitrary loading path with starting point $\overline{\mathbf{F}} = \mathbf{I}$, the critical deformation gradient, $\overline{\mathbf{F}}_{cr}$, at which condition (B.22) first ceases to hold true is determined by the *invariant* expression

$$\left(\overline{\mathbf{F}}_{cr}\mathbf{N}\right)\cdot\left(\overline{\mathbf{F}}_{cr}\mathbf{N}\right) = \left\|\overline{\mathbf{F}}_{cr}\mathbf{N}\right\|^2 = \left(1-\frac{\widetilde{\mu}}{\overline{\mu}}\right)^{2/3}. \tag{B.47}$$

This relation states quite simply that fiber-reinforced hyperelastic materials may develop long-wavelength instabilities whenever the stretch in the fiber direction $\overline{\lambda}_n = \left\|\overline{\mathbf{F}}\mathbf{N}\right\|$ reaches a certain critical value depending on the antiplane-to-axisymmetric ratio of the ground shear moduli $\widetilde{\mu}/\overline{\mu}$.

The corresponding critical vectors $\mathbf{v}_{cr}$ and $\mathbf{u}_{cr}$ for which condition (B.22) fails are given by

$$\mathbf{v}_{cr} = \left\|\overline{\mathbf{F}}_{cr}^{-T}\mathbf{N}\right\|^{-1}\overline{\mathbf{F}}_{cr}^{-T}\mathbf{N} \tag{B.48}$$

and

$$\mathbf{u}_{cr} = \left\|\left(\overline{\mathbf{F}}_{cr}\mathbf{N}\right)\times\left(\overline{\mathbf{F}}_{cr}^{-T}\mathbf{N}\right)\right\|^{-1}\left(\overline{\mathbf{F}}_{cr}\mathbf{N}\right)\times\left(\overline{\mathbf{F}}_{cr}^{-T}\mathbf{N}\right), \tag{B.49}$$

respectively. Interestingly, the vector (B.48) is seen to correspond to the image (in the deformed configuration) of $\mathbf{N}$ when treated not as a material line element, but as the normal to a material surface element. Furthermore, note that the vector (B.49) is perpendicular to the direction of the fibers in the deformed configuration, $\mathbf{n} = \|\overline{\mathbf{F}}_{cr}\mathbf{N}\|^{-1}\overline{\mathbf{F}}_{cr}\mathbf{N}$, and, of course, also perpendicular to (B.48), as a result of the macroscopic incompressibility constraint.

It is also of interest to note here that the corresponding critical stress at which condition (B.22) fails is given by

$$\overline{\mathbf{S}}_{cr} = \widetilde{\mu}\,\overline{\mathbf{F}}_{cr}\left(\mathbf{I}-\mathbf{N}\otimes\mathbf{N}\right) + \left[\overline{\mu}\left(1-\frac{\widetilde{\mu}}{\overline{\mu}}\right)^{2/3} - p\right]\overline{\mathbf{F}}_{cr}^{-T} \tag{B.50}$$

where p is the Lagrange multiplier associated with the incompressibility constraint, and $\overline{\mathbf{F}}_{cr}$ is (partially) determined by condition (B.47).

It should be emphasized that these results are rigorously valid for the model of deBotton et al. [28] for fiber-reinforced composites with Neo-Hookean phases. However, as we have seen in the preceding sections (see in particular Section B.4.3), the result (B.47) for the critical deformation should also provide a good approximation not just for fiber-reinforced materials with Neo-Hookean phases, but more generally for fiber-reinforced materials with any incompressible, isotropic, non-linearly elastic constituents, provided that the fibers are sufficiently stiffer than the matrix phase (and therefore the resulting critical deformations are not too large). On the other hand, as it will be seen in the next subsection, the result (B.50) for the corresponding critical stress $\overline{\mathbf{S}}_{cr}$ is not expected to hold for general constitutive behavior for the phases, since it is clear from the derivation that this result will be highly dependent on the assumed behavior of the matrix and fibers.

B.6.2 Transverse uniaxial tension

We conclude this section with one final example involving general 3-D loading conditions. Referring to Fig. B.1(a), we consider *transverse uniaxial tension* (perpendicular to the fiber direction) of the form

$$\overline{\mathbf{S}} = \frac{\partial \widehat{W}}{\partial \overline{\mathbf{F}}} - p\,\overline{\mathbf{F}}^{-T} = \overline{S}(\overline{\lambda})\,\mathbf{e}_1 \otimes \mathbf{e}_1. \tag{B.51}$$

Given the transverse isotropy of the fiber-reinforced material, this type of stress loading condition leads to a triaxial deformation with macroscopic gradient

$$\overline{\mathbf{F}} = \overline{\lambda}\,\mathbf{e}_1 \otimes \mathbf{e}_1 + (\overline{\lambda}\,\overline{\lambda}_n)^{-1}\,\mathbf{e}_2 \otimes \mathbf{e}_2 + \overline{\lambda}_n\,\mathbf{e}_3 \otimes \mathbf{e}_3, \tag{B.52}$$

where the loading parameter $\overline{\lambda}$ corresponds to the stretch in the loading direction ($\mathbf{e}_1$) and $\overline{\lambda}_n$ denotes the stretch along the fiber direction ($\mathbf{e}_3$). For constitutive relations of the form $\widehat{W}(\overline{\mathbf{F}}) = \widehat{\Phi}(\overline{\lambda}_n, \overline{\gamma}_p, \overline{\gamma}_n)$, it is a simple matter to deduce that $\overline{\lambda}_n$ in (B.52) must satisfy the relation

$$\frac{\partial \widehat{\Phi}}{\partial \overline{\lambda}_n}\left(\overline{\lambda}_n, \overline{\lambda} - (\overline{\lambda}\,\overline{\lambda}_n)^{-1}, 0\right) + \frac{1}{\overline{\lambda}\,\overline{\lambda}_n^2}\frac{\partial \widehat{\Phi}}{\partial \overline{\gamma}_p}\left(\overline{\lambda}_n, \overline{\lambda} - (\overline{\lambda}\,\overline{\lambda}_n)^{-1}, 0\right) = 0. \tag{B.53}$$

Moreover, the tensile stress $\overline{S}$ in (B.51) satisfies the following identity

$$\overline{S}(\overline{\lambda}) = \left(1 + \frac{1}{\overline{\lambda}^2\,\overline{\lambda}_n}\right)\frac{\partial \widehat{\Phi}}{\partial \overline{\gamma}_p}\left(\overline{\lambda}_n, \overline{\lambda} - (\overline{\lambda}\,\overline{\lambda}_n)^{-1}, 0\right). \tag{B.54}$$

Under the transverse tension loading (B.51), the strong ellipticity condition (B.18) associated with the model of Agoras et al. [2] can be shown to first fail whenever $\overline{\lambda}$ and $\overline{\lambda}_n$ reach critical

values, $1 < \overline{\lambda}_{cr} < \infty$, and $0 < \overline{\lambda}_n^{cr} \leq 1$, that satisfy the nonlinear equation

$$\overline{\lambda}_{cr}^2 \frac{\partial^2 \widehat{\Phi}}{\partial \overline{\gamma}_n^2}\left(\overline{\lambda}_n^{cr}, \overline{\lambda}_{cr} - (\overline{\lambda}_{cr}\,\overline{\lambda}_n^{cr})^{-1}, 0\right) - \left[\overline{\lambda}_{cr} + (\overline{\lambda}_{cr}\,\overline{\lambda}_n^{cr})^{-1}\right] \frac{\partial \widehat{\Phi}}{\partial \overline{\gamma}_p}\left(\overline{\lambda}_n^{cr}, \overline{\lambda}_{cr} - (\overline{\lambda}_{cr}\,\overline{\lambda}_n^{cr})^{-1}, 0\right) = 0, \tag{B.55}$$

where it is emphasized that $\overline{\lambda}$ and $\overline{\lambda}_n$ are related by relation (B.53); the associated critical vectors are given by $\mathbf{v}_{cr} = \mathbf{e}_3$ and $\mathbf{u}_{cr} = \mathbf{e}_1$. Moreover, the corresponding critical stress is simply given by relation (B.54) evaluated at $\overline{\lambda}_{cr}$, namely $\overline{S}_{cr} = \overline{S}(\overline{\lambda}_{cr})$.

Unfortunately, the nonlinear, algebraic, coupled equations (B.53) and (B.55) for $\overline{\lambda}_{cr}$ and $\overline{\lambda}_n^{cr}$ do not admit significant simplification and, in general, must be treated numerically. However, for the special case of a Neo-Hookean matrix reinforced with rigid fibers, we have that $\overline{\lambda}_n = 1$, and the above critical conditions reduce to the following equation for $\overline{\lambda}_{cr}$:

$$\overline{\lambda}_{cr}^4 - 2\left(\overline{\lambda}_{cr}^3 - \overline{\lambda}_{cr} + 1\right) = c_0^{-1}, \tag{B.56}$$

which may be shown to have a *finite* root such that $1 < \overline{\lambda}_{cr} < \infty$, implying, in turn, a finite (positive) value for $\overline{S}_{cr}$. In this connection, it is interesting to note that when the fibers are rigid, the deformation is essentially plane-strain (transverse) shear. This case has already been discussed by Lopez-Pamies and Ponte Castañeda [93] as a 2-D plane-strain problem, and no (in-plane) macroscopic instabilities were found (for fibers with circular cross-sections). The above result is not inconsistent with the earlier finding, because in the present analysis, we are considering the possibility of more general 3-D bifurcations (that are not consistent with the plane-strain assumption).

The conditions (B.52) through (B.55), of course, also hold for the model of deBotton et al. [28]. In this case, the expression (B.16) for the effective stored-energy function $\widehat{\Phi}$ is completely explicit, so that its derivatives can be computed explicitly. It can then be readily seen that the first and second terms in expression (B.55) cancel out, so that the expression for the loss of ellipticity under transverse uniaxial loading conditions (B.51) reduces to

$$(\overline{\lambda}_{cr}\,\overline{\lambda}_n^{cr})^{-2}\widetilde{\mu} = 0, \tag{B.57}$$

which can only be achieved (asymptotically) in the limit as $\overline{\lambda} \to \infty$. This implies that the critical condition (B.47) for $\overline{\lambda}_n$ is only reached asymptotically for infinite $\overline{\lambda}$, and therefore from expression (B.54) that the corresponding critical stress $\overline{S}_{cr}$ is unbounded. Thus, the model of deBotton et al. [28] gives the prediction that *no* macroscopic instability is expected for this type of stress loading condition, in stark contradiction with the corresponding predictions arising from the model of Agoras et al. [2]. The fundamental reason for this difference can be traced to the different predictions of the two models for the transverse shear response. As already noted, the model of deBotton

et al. [28] exhibits the same response for longitudinal and transverse shear, while the model of Agoras et al. [2] exhibits a different response for these two modes, with the transverse shear mode being stiffer. Although the differences are small, recent numerical results by Moraleda et al. [106] do appear to confirm the stiffer predictions of the model of Agoras et al. [2] for transverse shear, strongly suggesting the possible development of macroscopic instabilities in transverse tension. Of course, only experiments can ultimately determine whether macroscopic instabilities can occur for this type of loading condition, but regardless of the outcome this example demonstrates just how sensitive these instabilities can be to the accuracy of the constitutive model on which they are based.

Next, for comparison purposes, we consider the predictions for the laminate model (B.60) for Neo-Hookean phases (see Appendix A), when subjected to the uniaxial loading condition (B.51). Referring to Fig. B.1(b), we note that this loading condition corresponds to uniaxial tension perpendicular to the layers. In this case, the resulting deformation is transversely isotropic of the form $\overline{\mathbf{F}} = \overline{\lambda}\,\mathbf{e}_1 \otimes \mathbf{e}_1 + \overline{\lambda}^{-1/2}\,\mathbf{e}_2 \otimes \mathbf{e}_2 + \overline{\lambda}^{-1/2}\,\mathbf{e}_3 \otimes \mathbf{e}_3$, where the tensile stretch $\overline{\lambda}$ is related to the applied stress via

$$\overline{S}(\overline{\lambda}) = \left(\overline{\lambda} - \overline{\lambda}^{-2}\right)\overline{\mu}. \tag{B.58}$$

The corresponding critical stretch and stress for the onset of macroscopic instabilities is determined via expression (B.64) (see Appendix I), which leads to the results

$$\overline{\lambda}^{\,L}_{cr} = \left(1 - \frac{\widetilde{\mu}^{\,L}}{\overline{\mu}}\right)^{-1/3} \quad \text{and} \quad \overline{S}^{\,L}_{cr} = \widetilde{\mu}^{\,L}\left(\frac{\overline{\mu}}{\overline{\mu} - \widetilde{\mu}^{\,L}}\right)^{1/3}, \tag{B.59}$$

respectively. Here, it is recalled that the moduli $\widetilde{\mu}^{\,L}$ and $\overline{\mu}$ have been defined in (B.62). In addition, it is noted that the critical vectors are given by $\mathbf{v}_{cr} = \text{Span}\{\mathbf{e}_2, \mathbf{e}_3\}$ and $\mathbf{u}_{cr} = \mathbf{e}_1$.

Figure B.7 presents a detailed comparison of the predictions for the critical stress $\overline{S}_{cr}$ of the laminate model (with Neo-Hookean phases) with the model of Agoras et al. [2] for fiber-reinforced composites (with both Neo-Hookean and Gent phases), when subjected to transverse uniaxial loading. (Recall that the model of deBotton et al. [28] predicts no instabilities for this loading.) The results for the laminate were obtained by means of expression $(B.59)_2$, while the results for the fiber-reinforced composites were obtained using expressions (B.54), along with (B.53) and (B.55). Part (a) shows plots of $\overline{S}_{cr}$, normalized by $\mu^{(1)}$, for fiber-to-matrix contrasts $t = \mu^{(2)}/\mu^{(1)} = 10, 50$, as a function of the fiber concentration c_0, while part (b) presents corresponding results for $c_0 = 0.1, 0.3$, as a function of t. In all plots, the value $J_m^{(1)} = J_m^{(2)} = 50$ has been used for the fiber composite with Gent constituents. The main observation from these results is that fiber-reinforced materials are substantially more stable than laminates for this loading. This result may be understood as follows. For the laminate, as discussed earlier, the deformation is transversely isotropic, and the applied stress leads to an equal amount of compressive stretch (i.e., hydrostatic deformation) in the

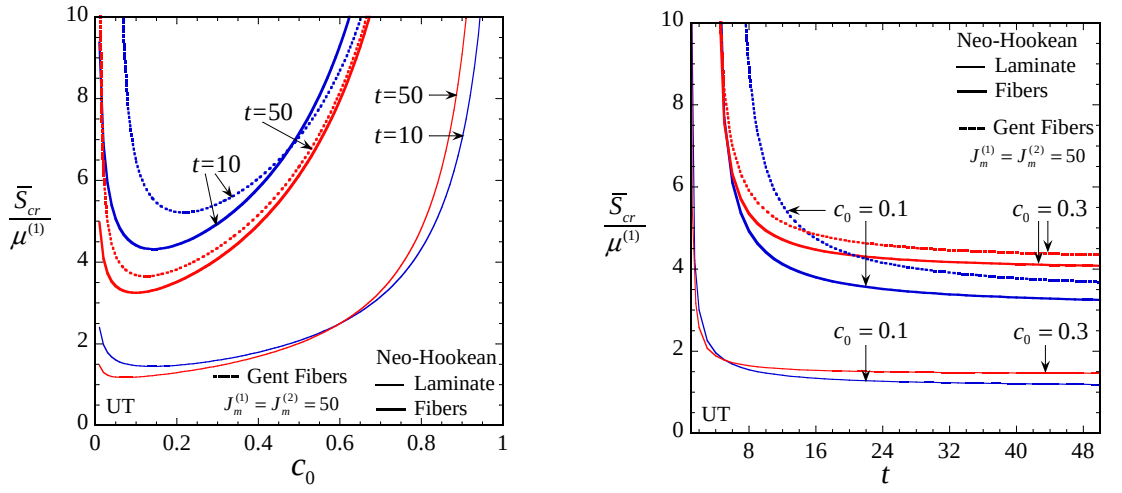

Figure B.7: Comparison of the predictions for macroscopic instabilities under transverse uniaxial tensile (UT) loading for fiber-reinforced (with both Gent and Neo-Hookean phases) and laminates (with Neo-Hookean phases). The critical stress $\overline{S}_{cr}$, normalized by the shear modulus of the matrix phase $\mu^{(1)}$, for (a) fiber-to-matrix contrasts $t = \mu^{(2)}/\mu^{(1)} = 10, 50$, as a function of the volume fraction of fibers c_0, and for (b) $c_0 = 0.1, 0.3$, as a function of t.

plane of the stiff layers ($\mathbf{e}_2$-$\mathbf{e}_3$), while for the fiber-reinforced composite, the applied tensile stress (perpendicular to the fibers) can be accommodated to a large extent by compressive deformation along the other direction ($\mathbf{e}_2$) perpendicular to the fibers, resulting in a proportionally smaller compressive stretch along the fiber direction ($\mathbf{e}_3$). It is also interesting to note that in the limit of infinite contrast $t \to \infty$ the laminate becomes macroscopically unstable at $\overline{\lambda}_{cr} = 1$, while for the fiber composite $\overline{\lambda}_{cr} > 1$ (compare (B.56) and $(B.59)_1$). In other words, a material reinforced with rigid fibers may accommodate some transverse deformation before failure, while the corresponding rigidly reinforced laminate cannot. Put together, these observations demonstrate that the laminate model does not provide reliable estimates for the onset of macroscopic instabilities in fiber-reinforced materials for general loading conditions.

In Section B.6.1, use was made of the model of deBotton et al. [28] to derive the expression (B.47) describing the onset of macroscopic instabilities in fiber-reinforced composites with Neo-Hookean phases. In addition, it was argued that this expression should also apply for fiber-reinforced composites with more general constitutive behaviors for the constituent phases, provided that the critical deformation $\overline{\mathbf{F}}_{cr}$ is not too large. However, we have found in this section that the model of deBotton et al. [28] can lead to potentially inconsistent predictions for certain types of loading conditions. This raises the question as to the validity of the above proposal. To shed some

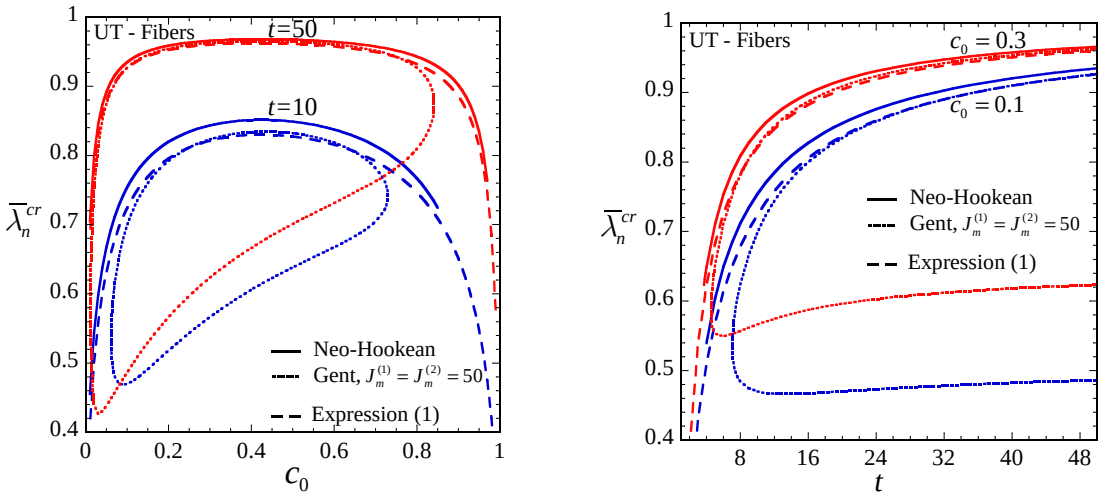

Figure B.8: Comparison of the predictions for macroscopic instabilities under transverse uniaxial tension (UT) for fiber-reinforced (with both Gent and Neo-Hookean phases) with the general analytical formula (B.1). The critical stretch $\overline{\lambda}_n^{cr}$ along the fiber direction for (a) fiber-to-matrix contrasts $t = \mu^{(2)}/\mu^{(1)} = 10, 50$, as a function of the volume fraction of fibers c_0, and for (b) $c_0 = 0.1, 0.3$, as a function of t.

light on this point, Fig. B.8 presents a comparison of the instability predictions of the model of Agoras et al. [2] for two different composites (one with Neo-Hookean phases and the other with Gent phases) with the analytical formula (B.47) for the critical value of the stretch $\overline{\lambda}_n^{cr}$ along the fiber direction under the uniaxial tensile loading (B.51). Parts (a) and (b) provide results for the same values of the parameters used in parts (a) and (b) of Fig. B.7 for the corresponding critical stress $\overline{S}_{cr}$. (Results are not shown for the laminates, as we have already seen that these results are fundamentally inconsistent with the results for actual fiber-reinforced composites in this case.) The main observation is that the predictions of the Agoras et al. model, as described by expressions (B.53) and (B.55) for $\overline{\lambda}_{cr}$ and $\overline{\lambda}_n^{cr}$, are in relatively good agreement with the analytical formula (B.47) for $\overline{\lambda}_n^{cr}$, even though the agreement is actually quite poor for $\overline{\lambda}_{cr}$ (not shown). The main differences occur for the larger fiber concentrations, when the Gent composite tends to lock up at stretches that are smaller than the critical stretches predicted by the formula (B.47), due to the strain concentration in the matrix at these higher concentrations. However, as can be seen from Fig. B.8(b), these differences in $\overline{\lambda}_n^{cr}$ improve with increasing fiber-to-matrix contrast $t = \mu^{(2)}/\mu^{(1)}$, and they practically disappear for sufficiently large values of t. On the other hand, it can be seen in Fig. B.7(b) that the differences in the corresponding critical stresses for Neo-Hookean and Gent fiber composites are more significant and they tend to persist even at large contrast. Therefore, we conclude that the formula (B.47) for the critical value of the stretch $\overline{\lambda}_n^{cr}$ along the fiber direction

can be safely used for general loading conditions and general material behavior, provided that the fibers are sufficiently stiffer than the matrix phase.

B.7 Concluding remarks

In this work, we presented a detailed study of the macroscopic failure of fiber-reinforced hyperelastic composites with random microstructures under general 3-D, finite-strain loading conditions. Based on the fundamental work of Geymonat et al. [41], the onset of failure in these materials was identified with the development of long-wavelength instabilities, corresponding to the loss of strong ellipticity of their homogenized behavior. For the characterization of the effective response of these materials we utilized the recently developed model of Agoras et al. [2], which applies to composites with a fairly general class of hyperelastic behavior for their constituent phases, as well as the model of deBotton et al. [28], which is applicable only to composites with Neo-Hookean constituents. The influence of the local properties of the matrix and fibers and of the volume fraction of fibers on the development of macroscopic instabilities was discussed in detail for several loadings (both aligned and non-aligned with the microstructure), where such instabilities would be expected to occur from physical experience. These results show that the main parameters controlling the possible onset of macroscopic instabilities are the fiber-to-matrix heterogeneity contrast and the fiber volume fraction. On the other hand, the specific features of the constitutive behavior of the phases (e.g., the lock-up parameter J_m for a Gent material) are less important, but may have a significant effect for small-contrast systems. For the practically important class of materials in which the fibers are much stiffer than the matrix, it was found that expression (B.47) provides a very good approximation for the corresponding critical deformation gradient under general loading conditions. This formula is insensitive to the specific constitutive models used for the phases, and shows that macroscopic instabilities may develop in fiber-reinforced elastic composites when the stretch along fibers direction reaches a critical value determined only by the ratio of the longitudinal-to-axisymmetric effective shear moduli of the composite for infinitesimal strains. Furthermore, it was found that, by properly accounting for the differences between the transverse and longitudinal modes at large strain (Moraleda et al. [106]), the model of Agoras et al. [2] appears to give more realistic predictions for the possible onset of instabilities than the corresponding model of deBotton et al. [28]. In particular, for the special case of uniaxial tensile stress transverse to the fiber direction, the model of Agoras et al. [2] gives a prediction consistent with the development of instabilities at a finite stress by virtue of the Poisson effect which leads to the activation of the critical condition (B.47) in the stretch along the fibers, while the model of deBotton et al. [28] results in the prediction of no instability, as the critical condition (B.47) is only achieved asymptotically for an infinite tensile stress in the transverse direction. In this connection,

it is important to note that while the model of Agoras et al. [2] made use of a Walpole-type estimate for the pertinent "linear comparison composite," the "second-order" procedure on which it is based can be used to obtain more specific estimates for special classes of fiber-reinforced composites. Such estimates may exhibit different responses for the transverse and longitudinal modes, even in the range of infinitesimal deformations. For this reason, we propose here the generalization (B.1) of the analytical estimate (B.47) for composites with more general linearized behavior exhibiting different effective ground shear moduli for the transverse and longitudinal modes.

In this work, we also investigated the validity of 2-D laminate models that have been used extensively in the literature to study approximately the stability of fiber-reinforced composites. For plane-strain loadings, for which the laminates do resemble fiber-reinforced composites, fairly good qualitative (but less good quantitative) agreement was observed for the corresponding instability predictions for the two classes of composites. On the other hand, for more general 3-D loadings, including transverse uniaxial tension, the estimates based on the laminate model for the onset of macroscopic instabilities were found to deviate significantly from the corresponding estimates for real fiber-reinforced systems, showing that the use of laminate models for general 3-D loadings is not appropriate. We propose instead the use of the analytical formula (B.1) for the critical stretch along the fiber direction, along with the model of Agoras et al. [2] for the macroscopic constitutive relation of the fiber-reinforced composites under general loading (including prescribed traction) conditions.

Finally, as revealed by an extensive body of literature on the compressive failure of fiber composites (see, e.g., Kyriakides and Ruff [68], Fleck [35]), the presence of imperfections, in general, and of plasticity for many materials, can have a significant effect on the onset of macroscopic instabilities in fiber-reinforced composites. While the specific results developed in this work are limited to systems with perfectly elastic behavior for the phases and perfectly aligned fibers, the general methods from which they have been derived can be generalized to incorporate the effect of imperfections in the microstructure (see Lopez-Pamies et al. [98] for an example in the context of oriented thermoplastic elastomers), as well as the effect of plasticity. The advantage of these potential extensions lies in the generality of the underlying framework, which is not restricted to specific loading conditions, or other simplifying hypotheses. Such generalizations will be pursued in future work.

Acknowledgements

This material is based upon work supported by the National Science Foundation under grants CMMI–0654063 and DMS–0708271.

B.8 Appendix I. Exact results for the macroscopic behavior of Neo-Hookean laminates

As stated in the main body of the text, numerous works have proposed the use of laminates as 2-D approximations for fiber-reinforced composites because: (i) they resemble fiber-reinforced morphologies (compare Fig. B.1(b) with Fig. B.1(a)) and, (ii) they permit, at the same time, an exact analytical treatment. With the objective of aiding the discussion of Section 6 about the validity of using laminates as approximations for fiber-reinforced nonlinearly elastic materials, in this appendix we summarize some *exact closed-form results* for laminates with (incompressible) Neo-Hookean phases of the form (B.4). Specifically, we provide results for the effective stored-energy function and the associated condition of strong ellipticity for *arbitrary 3-D finite deformations*. The pertinent derivations are a straightforward application of the framework given by Lopez-Pamies and Ponte Castañeda [97] and thus will not be detailed here. Instead, we proceed directly with the presentation of the final relevant results.

The effective stored-energy function for a laminate with Neo-Hookean phases (B.4) and direction of lamination $\mathbf{N}$ (see Fig. B.1(b)), subjected to a macroscopic deformation gradient $\overline{\mathbf{F}}$, can be shown to be given by

$$\widehat{W}(\overline{\mathbf{F}}) = \frac{\overline{\mu}}{2}\left(\overline{\mathbf{F}}\cdot\overline{\mathbf{F}}-3\right) - \frac{\overline{\mu}-\left(\overline{\mu^{-1}}\right)^{-1}}{2}\left[\left(\overline{\mathbf{F}}\mathbf{N}\right)\cdot\left(\overline{\mathbf{F}}\mathbf{N}\right) - \left[\left(\overline{\mathbf{F}}^{-T}\mathbf{N}\right)\cdot\left(\overline{\mathbf{F}}^{-T}\mathbf{N}\right)\right]^{-1}\right]. \tag{B.60}$$

where $\overline{\mu}$ and $\left(\overline{\mu^{-1}}\right)^{-1}$ denote the arithmetic and harmonic averages of $\mu^{(1)}$ and $\mu^{(2)}$ (see also deBotton [26] for a 2-D version of the result). This expression linearizes properly, as it reduces to the corresponding estimate in the limit as $\overline{\mathbf{F}}\to\mathbf{I}$, namely

$$\widehat{W}(\overline{\mathbf{F}}) = \frac{\widetilde{\mu}_a^L}{2}\overline{\varepsilon}_a^2 + \frac{\widetilde{\mu}_p^L}{2}\overline{\varepsilon}_p^2 + \frac{\widetilde{\mu}_n^L}{2}\overline{\varepsilon}_n^2 + O\left(\left\|\overline{\mathbf{F}}-\mathbf{I}\right\|^3\right), \tag{B.61}$$

where $\overline{\varepsilon}_a, \overline{\varepsilon}_p$, and $\overline{\varepsilon}_n$ are the axisymmetric, transverse, and longitudinal shear invariants of the infinitesimal strain tensor, which were introduced in the context of expression (B.11), and

$$\widetilde{\mu}_a^L = \widetilde{\mu}_p^L = \overline{\mu} \quad \text{and} \quad \widetilde{\mu}_n^L = \left(\overline{\mu^{-1}}\right)^{-1} = \left(\frac{1-c_0}{\mu^{(1)}} + \frac{c_0}{\mu^{(2)}}\right)^{-1} \equiv \widetilde{\mu}^L. \tag{B.62}$$

Note that, as expected, relation (B.60) is a transversely isotropic scalar function of $\overline{\mathbf{F}}$ with symmetry axis $\mathbf{N}$. In terms of the canonical basis of transversely isotropic invariants $\overline{I}_1, \overline{I}_2, \overline{I}_4$, and $\overline{I}_5$, (B.60) can be rewritten as $\widehat{W}(\overline{\mathbf{F}}) = \widehat{\Psi}(\overline{I}_1, \overline{I}_2, \overline{I}_4, \overline{I}_5)$, where

$$\widehat{\Psi}(\overline{I}_1, \overline{I}_2, \overline{I}_4, \overline{I}_5) = \frac{\overline{\mu}}{2}\left(\overline{I}_1 - 3\right) - \frac{\overline{\mu}-\widetilde{\mu}^L}{2}\left[\overline{I}_4 - \left(\overline{I}_2 - \overline{I}_1\overline{I}_4 + \overline{I}_5\right)^{-1}\right]. \tag{B.63}$$

In connection with this expression, it is worth remarking that in spite of the fact that the underlying *local* Neo-Hookean behavior (B.4) does not depend on the second invariant I_2, the *macroscopic* behavior (B.63) does depend on $\overline{I}_2$. Moreover, it is interesting to note that the *exact* relation (B.63) is *not* of the simple separable form $W = W_{iso}(I_1, I_2) + W_{ani}(I_4, I_5)$, which has often been assumed in the literature (see, e.g., Horgan and Saccomandi [61] and references therein) on a purely phenomenological basis.

Next, we write down the condition of strong ellipticity (B.17), as specialized to the constitutive relation (B.60):

$$\begin{aligned}&\overline{\mu}\left(\overline{\mathbf{F}}^{T}\mathbf{v}\right)\cdot\left(\overline{\mathbf{F}}^{T}\mathbf{v}\right)-(\overline{\mu}-\widetilde{\mu}^{L})\left[(\overline{\mathbf{F}}\mathbf{N})\cdot\mathbf{v}\right]^{2}-\\&(\overline{\mu}-\widetilde{\mu}^{L})\left[\left(\overline{\mathbf{F}}^{-T}\mathbf{N}\right)\cdot\left(\overline{\mathbf{F}}^{-T}\mathbf{N}\right)\right]^{-2}\left[\left(\overline{\mathbf{F}}^{-T}\mathbf{N}\right)\cdot\mathbf{u}\right)^{2}\times[1-\\&4\left[\left(\overline{\mathbf{F}}^{-T}\mathbf{N}\right)\cdot\left(\overline{\mathbf{F}}^{-T}\mathbf{N}\right)\right]^{-1}\left[\left(\overline{\mathbf{F}}^{-T}\mathbf{N}\right)\cdot\mathbf{v}\right]^{2}\Big]>0.\end{aligned}\tag{B.64}$$

Here, it is recalled that the unit vectors $\mathbf{v}$ and $\mathbf{u}$ satisfy the incompressibility constraint $\mathbf{v}\cdot\mathbf{u}=0$. For *plane-strain* loading conditions under which laminates resemble fiber-reinforced materials (i.e., in the context of Fig. B.1(b), deformations in the $\mathbf{e}_1$-$\mathbf{e}_3$–plane), the critical deformation gradient $\overline{\mathbf{F}}_{cr}$ and corresponding critical vectors $\mathbf{v}_{cr}$ and $\mathbf{u}_{cr}$ at which condition (B.64) is first violated can be computed in closed form. The result for $\overline{\mathbf{F}}_{cr}$ reads as follows

$$\frac{1-\left[\left(\overline{\mathbf{F}}_{cr}^{-T}\mathbf{N}\right)\cdot\left(\overline{\mathbf{F}}_{cr}^{-T}\mathbf{N}\right)\right]^{2}}{\left[\left(\overline{\mathbf{F}}_{cr}^{-T}\mathbf{N}\right)\cdot\left(\overline{\mathbf{F}}_{cr}^{-T}\mathbf{N}\right)\right]\left[(\overline{\mathbf{F}}_{cr}\mathbf{N})\cdot(\overline{\mathbf{F}}_{cr}\mathbf{N})\right]}=\frac{\widetilde{\mu}^{L}}{\overline{\mu}}.\tag{B.65}$$

It is relevant to remark that expression (B.65) generalizes the classical result $(B.38)_1$ of Triantafyllidis and Maker [142] for *aligned* loading conditions, to general loading conditions. When the applied macroscopic deformation is parameterized (without loss of generality) as a pure shear at an angle $\overline{\mathbf{F}}=\overline{\mathbf{Q}}\,\overline{\mathbf{D}}\,\overline{\mathbf{Q}}^{T}$, with $\mathbf{N}=\mathbf{e}_3$ and $\overline{\mathbf{Q}}$ and $\overline{\mathbf{D}}$ given by (B.41) and (B.43), expression (B.65) takes the more explicit form

$$\begin{aligned}&\overline{\lambda}_{cr}^{8}\left[\overline{\mu}+\widetilde{\mu}^{L}+(\overline{\mu}-\widetilde{\mu}^{L})\cos 2\Theta\right]\cos^{2}\Theta-\\&\overline{\lambda}_{cr}^{4}\frac{\overline{\mu}-\widetilde{\mu}^{L}}{2}(3+\cos 4\Theta)+\left[\overline{\mu}+\widetilde{\mu}^{L}-(\overline{\mu}-\widetilde{\mu}^{L})\cos 2\Theta\right]\sin^{2}\Theta=0.\end{aligned}\tag{B.66}$$

Note that for the particular case when $\Theta=0$, relation (B.66) does indeed reduce to the classical result $(B.38)_1$ of Triantafyllidis and Maker [142]. Sample results for more general non-aligned loading conditions are shown in Fig. B.6(a).

B.9 Appendix II. Demonstration of the criticality expressions (B.47), (B.48), and (B.49)

In this appendix, we provide a demonstration of the criticality conditions (B.47), (B.48), and (B.49) for the *first* loss of ellipticity in the expression (B.22) associated with the model of deBotton et al. [28]. To this end, we first show that the LHS of (B.22) does indeed vanish when evaluated at the values $\overline{\mathbf{F}}_{cr}$, $\mathbf{v}_{cr}$, and $\mathbf{u}_{cr}$ given by (B.47), (B.48), and (B.49). Then, we show that there are no macroscopic deformations smaller than those defined by (B.47) at which the LHS of (B.22) vanishes.

We start out by noticing that upon direct implementation of expressions (B.48) and (B.49),

$$\begin{aligned}
&\mathbf{v}_{cr}\cdot\overline{\mathbf{B}}\mathbf{v}_{cr}=\frac{1}{\left\|\overline{\mathbf{F}}_{cr}^{-T}\mathbf{N}\right\|^2}\left(\overline{\mathbf{F}}_{cr}^{-T}\mathbf{N}\right)\cdot\left(\overline{\mathbf{F}}_{cr}\,\overline{\mathbf{F}}_{cr}^{T}\,\overline{\mathbf{F}}_{cr}^{-T}\mathbf{N}\right)=\frac{1}{\left\|\overline{\mathbf{F}}_{cr}^{-T}\mathbf{N}\right\|^2}\,,\\
&\mathbf{n}\cdot\mathbf{v}_{cr}=\frac{1}{\overline{\lambda}_n\left\|\overline{\mathbf{F}}_{cr}^{-T}\mathbf{N}\right\|}\left(\overline{\mathbf{F}}_{cr}\mathbf{N}\right)\cdot\left(\overline{\mathbf{F}}_{cr}^{-T}\mathbf{N}\right)=\frac{1}{\overline{\lambda}_n\left\|\overline{\mathbf{F}}_{cr}^{-T}\mathbf{N}\right\|}\,,\\
&\mathbf{n}\cdot\mathbf{u}_{cr}=0\,,
\end{aligned}\tag{B.67}$$

where it is recalled that the unit vector $\mathbf{N}$ characterizes the direction of the fibers in the undeformed configuration, and $\overline{\lambda}_n=\left\|\overline{\mathbf{F}}_{cr}\mathbf{N}\right\|$. Making explicit use of these results in condition (B.22) leads to

$$\left\|\overline{\mathbf{F}}_{cr}^{-T}\mathbf{N}\right\|^{-2}\left(\widetilde{\mu}+\frac{\overline{\mu}-\widetilde{\mu}}{\overline{\lambda}_n^3}\left[(\overline{\lambda}_n^3-1)\right]\right)>0,\tag{B.68}$$

which is seen to be violated at the critical deformations defined by (B.47), when $\overline{\lambda}_n=(1-\widetilde{\mu}/\overline{\mu})^{1/3}$.

Next, to show that condition (B.22) first fails at deformations defined by (B.47)—and *not* before—it proves helpful to define $\mathbf{v}^*=\overline{\mathbf{F}}^{T}\mathbf{v}$, $\mathbf{u}^*=\overline{\mathbf{F}}^{T}\mathbf{u}$, and to introduce the parametrization

$$\overline{\lambda}_n=\delta\left(1-\frac{\widetilde{\mu}}{\overline{\mu}}\right)^{1/3},\tag{B.69}$$

where δ is a positive parameter, such that $\overline{\lambda}_n>(1-\widetilde{\mu}/\overline{\mu})^{1/3}$ whenever $\delta>1$ (i.e., loss of ellipticity *earlier* than that given by condition (B.47) would correspond to a value of $\delta>1$). Then, after some algebraic manipulation, the strong ellipticity condition (B.22) may be rewritten in the form

$$Q\equiv\widetilde{\mu}\left[\mathbf{v}^*\cdot\mathbf{v}^*-(\mathbf{N}\cdot\mathbf{v}^*)^2\right]+\overline{\mu}\,(\mathbf{N}\cdot\mathbf{v}^*)^2\left[1-\delta^{-3}+3\,\delta^{-5}\left(1-\frac{\widetilde{\mu}}{\overline{\mu}}\right)^{-2/3}(\mathbf{N}\cdot\mathbf{u}^*)^2\right]>0.\tag{B.70}$$

Note that $\overline{\mu}\geq\widetilde{\mu}>0$, $(\mathbf{N}\cdot\mathbf{u}^*)^2\geq 0$, $\mathbf{v}^*\cdot\mathbf{v}^*>0$, $(\mathbf{N}\cdot\mathbf{v}^*)^2\geq 0$, and $\mathbf{v}^*\cdot\mathbf{v}^*-(\mathbf{N}\cdot\mathbf{v}^*)^2\geq 0$. Clearly, these conditions ensure that $Q\geq 0$ when $\delta>1$ (since $1-\delta^{-3}>0$ in this case). To show that $Q>0$ whenever $\delta>1$, we consider two mutually exclusive cases: (i) $\mathbf{v}^*$ is not aligned with $\mathbf{N}$ in which case the first term is strictly positive and the second is non-negative, so that $Q>0$.

(ii) $\mathbf{v}^*$ is parallel to $\mathbf{N}$ in which case the first term vanishes identically and the smallest value of the second term occurs when $\mathbf{u}^*$ is perpendicular to $\mathbf{N}$ so that $Q = \overline{\mu}\left(\mathbf{N}\cdot\mathbf{v}^*\right)^2\left(1-\delta^{-3}\right) > 0$. Of course, when $\delta = 1$, case (ii) is exactly equivalent to the criticality conditions (B.47), (B.48), and (B.49).

Bibliography

[1] Abdelmoula, R., Krasucki, F. & Marigo, J.J. (1993). Microbuckling analysis of unidirectional fibred composites. In: Mecamat 93 – International Seminar on Micromechanics of Materials. Collection de la Direction des Etudes et Recherches d'Electricité de France, Eyrolles, pp. 303–314.

[2] Agoras, M., Lopez-Pamies, O. & Ponte Castañeda, P. (2009). A general hyperelastic model for incompressible fiber-reinforced elastomers. *J. Mech. Phys. Solids* **57**, 268–286.

[3] Agoras, M., Lopez-Pamies, O. & Ponte Castañeda, P. (2009). Onset of macroscopic instabilities in fiber-reinforced elastomers at finite strain. *J. Mech. Phys. Solids* **57**, 1828–1850.

[4] Aravas, N. (1992). Finite elastoplastic transformations of transversely isotropic metals. *Int. J. Solids Struct.* **29**, 2137–2157.

[5] Aravas, N. & Ponte Castañeda, P. (2004). Numerical methods for porous metals with deformation-induced anisotropy. *Comput. Methods Appl. Mech. Engrg.* **193**, 3767–3805.

[6] Arruda, E. M. & Boyce, M. C. (1993). A 3-dimensional constitutive model for the large stretch behavior of rubber elastic materials. *J. Mech. Phys. Solids* **41**, 389–412.

[7] Avellaneda, M. (1987). Iterated homogenization, differential effective theory and applications. *Communications on Pure and Applied Mathematics* **XL**, 527–554.

[8] Bartczak, Z., Argon, A.S. & Cohen, R.E. (1992). Deformation mechanisms and plastic resistance in single-crystal-textured high density polyethylene. *Macromolecules* **25**, 5036–5053.

[9] Bartczak, Z., Argon, A.S. & Cohen, R.E. (1994). Texture evolution in large strain simple shear deformation of high density polyethylene. *Polymer* **35**, 3427–3441.

[10] Bartczak, Z., Cohen, R.E. & Argon, A.S. (1992). Evolution of the crystalline texture of HDPE during uniaxial compression. *Macromolecules* **25**, 4692–4704.

[11] Bartels, A., Koeppe, C. & Mecking, H. (1995). Microstructure and properties of Ti-48Al-2Cr after thermomechanical treatment. *Mater. Sci. Engng A* **192/193**, 226–232.

[12] Bassett, D.C. & Hodge, A.M. (1981). On the morphology of melt-crystallized polyethylene I. Lamellar profiles. *Proc. R. Soc. Lond. A*, **377**, 25–37.

[13] Boudet, A., (2003). *Voyage au Coeur de la Matière Plastique.* CNRS Editions, Paris.

[14] Boyce, M. C. (1986). Large inelastic deformation of glassy polymers. Ph.D. thesis, Massachusetts Institute of Technology.

[15] Boyce, M. C. & Arruda, E. M. (2000). Constitutive models of rubber elasticity: A review. *Rubb. Chem. Technol.* **73**, 504–523.

[16] Boyce, M. C., Parks, D. M. & Argon, A.S. (1988). Large inelastyic deformation of glassy polymers. 1. Rate-depedent constitutive model. *Mech. Mater.* **7**, 15–33.

[17] Braides, A. & Lukkassen, D. (2000). Reiterated homogenization of integral functionals. *Mathematical Models and Methods in Applied Sciences* **10**, 47–71.

[18] Brun, M., Lopez-Pamies, O. & Ponte Castañeda, P. (2007). Homogenization estimates for fiber-reiforced elastomers with periodic microstructures. *Int. J. Solids Structures* **44**, 5953–5979.

[19] Cohen, Y., Brinkmann, M. & Thomas, E.L. (2001). Undulation, dilation, and folding of a layered block copolymer. *J. Chem. Phys.* **114**, 984–992.

[20] Chen, Y.-C., Rajagopal, K.R. & Wheeler, L. (2006). Homogenization and global responses of inhomogeneous spherical nonlinear elastic shells. *Journal of Elasticity* **82**, 193–214.

[21] Danas, K., Idiart, M.I. & Ponte Castañeda, P. (2008). A homogenization-based constitutive model for two-dimensional viscoplastic porous media. *C. R. Mecanique* **336**, 79-90

[22] Danas, K., Idiart, M.I. & Ponte Castañeda, P. (2008). A homogenization-based constitutive model for isotropic viscoplastic porous media. *Int. J. Solids Struct.* **45**, 3392–3409

[23] Dafalias, Y.F. (1985). The plastic spin. *J. Appl. Mech.* **52**, 865–871.

[24] Dahoun, A. (1991). Comportement plastique et textures de deformation des polyme‘res semicristallins en traction uniaxiale et cisaillement simple. Ph.D. Thesis, Institut national polytechnique de Lorraine.

[25] Dahoun, D., Canova, G.R., Molinari, A., Philippe, M.J. & Gsell, C. (1991) The modeling of large strain textures and stress-strain relations of polyethylene. *Macromolecules* **14**, 347–354

[26] deBotton, G. (2005). Transversely isotropic sequentially laminated composites in finite elasticity. *J. Mech. Phys. Solids* **53**, 1334–1361

[27] deBotton, G. (2008). Composites with one and two families of fibers. Presented at the Composites and Polycrystals Mini-Symposium at the 2008 SIAM Conference on Mathematical Aspects of Materials Science. Philadelphia.

[28] deBotton, G., Hariton, I. & Socolsky, E.A. (2006). Neo-Hookean fiber-reinforced composites in finite elasticity. *J. Mech. Phys. Solids* **54**, 533–559.

[29] deBotton, G. & Ponte Castañeda, P. (1993). Elastoplastic constitutive relations for fiber-reinforced solids. *Int. J. Solids Struct.* **30**, 1865-1890.

[30] deBotton, G. & Ponte Castañeda, P. (1995). Variational estimates for the creep behavior of polycrystals. *Proc. R. Soc. Lond. A* **448**, 121-142.

[31] Dunst, D., Dendievel, R. & Mecking, H. (1994). The development of deformation textures as a function of the phase fractions in two-phase titaniun-based alloys. *Materials Science Forum* **157-162**, 665–672.

[32] Ekeland, I. & Temam, R. (1999). Convex analysis and variational problems. *SIAM*, Philadelphia.

[33] Ericksen, J.L. & Rivlin, R.S. (1954). Large elastic deformations of homogeneous anisotropic materials. *Arch. Rat. Mech. Anal.* **3**, 281–301.

[34] Finlay, H.M., Whittaker, P. & Canham, P.B. (1998). Collagen organization in branching region of human brain arteries. *Stroke* **29**, 1595–1601.

[35] Fleck, N. (1997). Compressive failure of fiber composites. *Advances in Applied Mechanics* **33**, 43–117.

[36] Galeski, A., Bartczak, Z., Argon, A.S. & Cohen, R.E. (1992). Morphological alterations during texture-producing plastic plane strain compression of high-density polyethylene. *Macromolecules* **25**, 5705–5718.

[37] Gasser, T.C., Ogden, R.W. & Holzapfel, G.A. (2006). Hyperelastic modelling of arterial layers with distributed collagen fibre orientations. *Journal of the Royal Society Interface* **3**, 15–35.

[38] Gautam, S., Balijepalli, S., & Rutledge, G.C. (2000). Molecular simulations of the interlamellar phase in polymers. Effect of chain tilt. *Macromolecules* **33**, 9136–9145.

[39] Gel'fand, I. M.& Shilov, G.E. (1964). Generalized functions, Vol. I, *Properties and Operations*, Academic Press, New York.

[40] Gent, A. N., (1996). A new constitutive relation for rubber. *Rubb. Chem. Technol.* **69**, 59–61.

[41] Geymonat, G., Müller, S. & Triantafyllidis, N. (1993). Homogenization of nonlinearly elastic materials, macroscopic bifurcation and macroscopic loss of rank-one convexity. *Arch. Rat. Mech. Anal.* **122**, 231–290.

[42] Gilormini, P., Nebozhyn M. & Ponte Castañeda, P. (2001). Accurate estimates the creep behavior of hexagonal polycrystals. *Acta Mater.* **49**, 329-337.

[43] Grandidier, J. C. & Poitier-Ferry, M. (1990). Fiber microbuckling in a long fiber composite material. *Comptes Rendus de l'Academie des Sciences, Serie II* **310**, 1–6.

[44] Lopez-Pamies, O., Garcia, R., Chabert, E., Cavaillé, J.-Y. & Ponte Castañeda, P. (2008). Homogenization estimates for thermoplastic elastomers with lamellar morphology. *J. Mech. Phys. Solids* **56**, 3206–3223.

[45] Guo, Z.Y., Peng, X.Q. & Moran, B. (2006). A composites-based hyperelastic constitutive model for soft tissue with application to the human annulus fibrosus. *J. Mech. Phys. Solids* **54**, 1952–1971.

[46] G'Sell, C., & Jonas, J. J. (1979). Determination of the plastic behavior of solid polymers at constant true strain rate. *J. Mater. Sci.* **14**, 583–591.

[47] Hashin, Z. & Shtrikman, S. (1962). On some variational principles in anisotropic and nonhomogeneous elasticity. *J. Mech. Phys. Solids* **10**, 335–342.

[48] Hashin, Z. & Shtrikman, S. (1963). A variational approach to the theory of the elastic behavior of multiphase materials. *J. Mech. Phys. Solids* **11**, 127–140.

[49] He, Q.C., Le Quang, H. & Feng, Z.Q. (2006). Exact results for the homogenization of elastic fiber-reinforced solids at finite strain. *Journal of Elasticity* **83**, 153–177.

[50] Hill, R. (1965). Continuum micro-mechanics of elastoplastic polycrystals. *J. Mech. Phys. Solids* **13**, 89–101.

[51] Hill, R. (1965). A self-consistent mechanics of composite materials. *J. Mech. Phys. Solids* **13**, 213–222.

[52] Hill, R. (1967). The essensial structure of constitutive laws for metal composites and polycrystals. *J. Mech. Phys. Solids* **15**, 79–95.

[53] Hill, R. (1972). On constitutive macro-variables for heterogeneous solids at finite strain. *Proc. R. Soc. Lond.* **A 326**, 131–147.

[54] Hiss, R., Hobeika, S., Lynn, C., Strobl, G. (1999). Network stretching, slip processes, and fragmentation of crystallites during uniaxial drawing of polyethylene and related copolymers. A comparative study. *J. Appl. Polym. Sci.* **32 (13)**, 4390–4403.

[55] Holt, R.A. & Pingshun Zhao (2004). Micro-texture of extruded Zr2.5Nb tubes. *J. Nuclear Materials* **335**, 520–528.

[56] Holt, R. A. & Aldridge, S.A. (1985). Effect of extrusion variables on crystallographic texture of Zr2.5 wt% Nb. *J. Nuclear Materials* **135**, 246–259.

[57] Holzapfel, G.A., Gasser, T.C. & Ogden, R.W. (1985). A new constitutive framework for arterial wall mechanics and a comparative study of material models. *Journal of Elasticity* **61**, 1–48.

[58] Honeker, C.C. & Thomas, E.L. (1996). Impact of morphological orientation in determining mechanical properties in triblock copolymers. *Chemistry of Materials* **8**, 1702–1714.

[59] Honeker, C.C., Thomas, E.L., Albalak, R.J., Hadjuk, D.A., Gruner, S.M. & Capel, M.C. (2000). Perpendicular deformation of a near–single crystal triblock copolymer with a cylindrical morphology. 1. Synchroton SAXS. *Macromolecules* **33**, 9395–9406.

[60] Horgan, C.O. & Saccomandi, G. (1999). Simple torsion of isotropic, hyperelastic, incompressible materials with limiting chain extensibility. *Journal of Elasticity* **56**, 159-170.

[61] Horgan, C.O. & Saccomandi, G. (2005). A new constitutive theory for fiber-reinforced incompressible nonlinearly elastic solids. *J. Mech. Phys. Solids* **53**, 1985–2015.

[62] Idiart, I. & Ponte Castañeda, P. (2009). Variational linear comparison bounds for nonlinear composites with anisotropic phases. I. General Results. *Proc. R. Soc. Lond. A*, **463**, 907–924.

[63] Idiart, I. & Ponte Castañeda, P. (2009). Variational linear comparison bounds for nonlinear composites with anisotropic phases. II. Crystalline materials *Proc. R. Soc. Lond. A*, **463**, 925–943.

[64] Idiart, I., Danas, K. & Ponte Castañeda, P. (2006). Second-order theory for two-phase nonlinear composites and applications to isotropic constituents. *C. R. Mécanique*, **334**, 575–581.

[65] Idiart, I. Moulinec, H., Ponte Castañeda, P., & Suquet, P. (2006). Macroscopic behavior and field fluctuations for viscoplastic composites: Second-order estimates versus full-field simulations. *J. Mech. Phys. Solids* **54**, 1029–1063.

[66] Jelf, P.M. & Fleck, N. (1992). Compression failure mechanisms in unidirectional composites. *Journal of Composite Materials* **26**, 2706–2726.

[67] Krumova, M., Henning, S. & Michlel, G.H. (2005). Shevron morphology in deformed semicrystalline polymers. *Philosophical Magazine* **86**, 1689–1712.

[68] Kyriakides, S. & Ruff, A.E. (1997). Aspects of the failure and postfailure of fiber composites in compression. *Journal of Composite Materials* **31**, 1633–1670.

[69] Lahellec, N., Mazerolle, F. & Michel, J.C. (2004). Second-order estimate of the macroscopic behavior of periodic hyperelastic composites: theory and experimental validation. *J. Mech. Phys. Solids* **52**, 27–49.

[70] Lahellec, N. & Suquet, P. (2007). On the effective behavior of nonlinear inelastic composites: I. Incremental variational principles. *J. Mech. Phys. Solids* **55**, 1932–1963.

[71] Lahellec, N. & Suquet, P. (2007). On the effective behavior of nonlinear inelastic composites: II: A second-order procedure. *J. Mech. Phys. Solids* **55**, 1964–1992.

[72] Laws, N. (1973). On the thermostatics of composite materials. *J. Mech. Phys. Solids* **21**, 9–17.

[73] Lebensohn, R. A. (1999). Modelling the role of local correlations in polycrystal plasticity using viscoplastic self-consistent schemes. *Modelling Simul. Mater. Sci. Eng.* **7**, 739–746.

[74] Lebensohn, R. A. & Canova, G.R. (1997). A self-consistent approach for modeling texture development of two-phase polycrystals: applications to titanium alloys. *Acta Mater.* **45**, 3687–3694.

[75] Lebensohn, R. A., Liu, Y. & Ponte Castañeda, P. (2004). Macroscopic properties and field fluctuations in model power-law polycrystals: full-field solutions versus second-order estimates. *Proc. R. Soc. Lond. A* **460**, 1381-1405.

[76] Lebensohn, R. A., Liu, Y. & Ponte Castañeda, P. (2004). On the accuracy of the self-consistent approximation for polycrystals: comparison with numerical simulations. *Acta Mater.* **52**, 5347-5361.

[77] Lebensohn, R. A. & Tomé, C. N. (1993). A self-consistent anisotropic approach for the simulation of plastic deformation and texture development of polycrystals: application to zirconium alloys. *Acta. Metall. Mater.* **41**, 2611–2624.

[78] Lebensohn, R. A., Tomé, C. N. & Ponte Castañeda, P. (2005). Improving the self-consistent predictions of texture development of polycrystals incorporating intragranular field fluctuations. *Materials Science Forum* **495-497**, 955-963.

[79] Lebensohn, R. A., Uhlenhut, H., Hartig, C. & Mecking, H. (1998). Plastic flow of γ-TiAl-based polysynthetically twinned crystals: micromechanical modeling and experimental validation. *Acta. Metall. Mater.* **46**, 4701–4709.

[80] Lee, B.J., Parks, D. M. & Ahzi, S. (1993). Micromechanical modeling of large plastic deformations and texture evolution in semi-crystalline polymers. *J. Mech. Phys. Solids* **41** , 1651–1687.

[81] Leroy, Y. & Ponte Castañeda, P. (2001). Bounds on the self-consistent approximation for nonlinear media and implications for the second-order method. *C.R. Acad. Sci. Paris IIB* **329 (8)**, 571577.

[82] Levin, V.M. (1967). Thermal expansion coefficients of heterogeneous materials. *Mekh. Tverd. Tela.* **2**, 83–94.

[83] Li, D., Garmestani, H., Kalidindi, S.R. & Alamo, R. (2001). Crystallographic texture evolution in high-density polyethylene during uniaxial tension. *Polymer* **42**, 4903–4913.

[84] Lin, L. & Argon, A. S. (1994). Structure and plastic deformation of polyethylene. *J. Mater. Sci.* **29**, 294–323.

[85] Liu, Y. (2003). Macroscopic behavior, field fluctuations and texture evolution in viscoplastic polycrystals. Ph.D. thesis, University of Pennsylvania.

[86] Liu, Y., & Ponte Castañeda, P. (2004). Second-order theory for the effective behavior and field fluctuations in viscoplastic polycrystals. *J. Mech. Phys. Solids* **52**, 467–495.

[87] Liu, Y. & Ponte Castañeda, P. (2004). Homogenization estimates for the average behavior and field fluctuations in cubic and hexagonal viscoplastic polycrystals. *J. Mech. Phys. Solids* **52**, 1175–1211.

[88] Liu, Y., Gilormini, P. & Ponte Castañeda, P. (2005). Second-order estimates for texture evolution in halite. *Tectonophysics* **406**, 179-195.

[89] Lopez-Pamies, O. (2006). On the effective behavior, microstructure evolution, and macroscopic stability of elastomeric composites. Ph.D. thesis, University of Pennsylvania.

[90] Lopez-Pamies, O. (2010). A new I_1-based hyperelastic model for rubber elastic materials. *Comptes Rendus Mecanique* **338**, 3–11.

[91] Lopez-Pamies, O. & Ponte Castañeda, P. (2004). Second-order estimates for the macroscopic response and loss of ellipticity in porous rubbers at large deformations. *J. Elasticity* **76**, 247-287.

[92] Lopez-Pamies, O. & Ponte Castañeda, P. (2006). On the overall behavior, microstructure evolution and macroscopic stability in reinforced rubbers at large deformations: I—Theory. *J. Mech. Phys. Solids* **54**, 807–830.

[93] Lopez-Pamies, O. & Ponte Castañeda, P. (2006). On the overall behavior, microstructure evolution and macroscopic stability in reinforced rubbers at large deformations: II—Application to cylindrical fibers. *J. Mech. Phys. Solids* **54**, 831–863.

[94] Lopez-Pamies, O. & Ponte Castañeda, P. (2006). Effective behavior, microstructure evolution and macroscopic instabilities in reinforced elastomers. Presented at the Instabilities in Solids, Structures and Materials Mini-Symposium at the 15th U.S. National Congress of Theoretical and Applied Mechanics, Boulder.

[95] Lopez-Pamies, O. & Ponte Castañeda, P. (2007). Homogenization-based constitutive models for porous elastomers and implications for macroscopic instabilities: I—Analysis. *J. Mech. Phys. Solids* **55**, 1677–1701.

[96] Lopez-Pamies, O. & Ponte Castañeda, P. (2007). Homogenization-based constitutive models for porous elastomers and implications for macroscopic instabilities: I—Results. *J. Mech. Phys. Solids* **55**, 1702–1728.

[97] Lopez-Pamies, O. & Ponte Castañeda, P. (2009). Microstructure evolution in hyperelastic laminates and implications for overall behavior and macroscopic stability. *J. Mech. Phys. Solids* **41**, 364–374.

[98] Lopez-Pamies, O., Garcia, R., Chabert, E., Cavaille , J.-Y. & Ponte Castañeda, P. (2008). Multiscale modeling of oriented thermoplastic elastomers with lamellar morphology. *J. Mech. Phys. Solids* **56**, 3206–3223.

[99] Mandel, J. (1972). Plasticité et viscoplasticité. CISM Udine Courses and Lectures. No **97**, New York, Springer-Verlag.

[100] Merodio, J. & Ogden, R.W. (2003). Instabilities and loss of ellipticity in fiber-reinforced nonlinearly elastic solids under plane deformation. *Int. J. Solids Struct.*, **40**, 4707–4727.

[101] Merodio, J. & Ogden, R.W. (2005). Mechanical response of fiber-reinforced incompressible nonlinear elastic solids. *Int. J. Nonlinear Mech.*, **40**, 213–227.

[102] Merodio, J. & Pence (2003). Kink surfaces in a directionally reinforced Neo-Hookean material under plane deformation: I. Mechanical equilibrium. *Journal of Elasticity*, **62**, 119–144.

[103] Michel, J.-C., Lopez-Pamies, O., Ponte Castañeda, P. & Triantafyllidis, N. (2007). Microscopic and macroscopic instabilities in finitely strained porous elastomers. *J. Mech. Phys. Solids*, **55**, 900–938.

[104] Michel, J.-C., Lopez-Pamies, O., Ponte Castañeda, P. & Triantafyllidis, N. (2009). Microscopic and macroscopic instabilities in finitely strained reinforced elastomers. In preparation.

[105] Molinari, A., Canova, G. R. & Ahzi, S. (1987). A self-consistent approach of the large deformation polycrystal viscoplasticity. *Acta Metall. Mater.* **35**, 2983–2994.

[106] Moraleda, J., Segurado, J. & Llorca, J. (2009). Computational micromechanics of fiber-reinforced elastomers. *J. Mech. Phys. Solids* **57**, 1596–1613.

[107] Nebozhyn, M. & Ponte Castañeda, P. (1999). The second-order procedure: exact vs approximate results for isotropic, two-phase composites. *J. Mech. Phys. Solids* **47**, 2171-2185.

[108] Nesterovic, N. & Triantafyllidis, N. (2004). Onset of failure in finitely strained layered composites subjected to combined normal and shear loading. *J. Mech. Phys. Solids* **52**, 941–974.

[109] Nikolov, S., Doghri, I., Pierard, O., Zealouk, L., Goldberg, A. (2002). Multi-scale constitutive modeling of the small deformations of semi-cristalline polymers. *J. Mech. Phys. Solids* **50**, 2275–2302.

[110] Nikolov, S., Lebensohn, R.A. & Raabe, D. (2006). Self-consistent modeling of large plastic deformation, texture and morphology evolution in semi-crystalline polymers. *J. Mech. Phys. Solids* **54**, 1350–1375.

[111] Ogden, R. (1978). Extremum principles in non-linear elasticity and their application to composites—I Theory. *Int. J. Solids Struct.*, **14**, 265–282.

[112] Ogden, R. (1984). *Nonlinear elastic deformations.* Dover Publications, New York.

[113] Ponte Castañeda, P. (1989). The overall constitutive behaviour of nonlinearly elastic composites. *Proc. R. Soc. Lond.* **A 422**, 147–171.

[114] Ponte Castañeda, P. (1991). The effective mechanical properties of nonlinear isotropic composites. *J. Mech. Phys. Solids* **39**, 45–71.

[115] Ponte Castañeda, P. (1992). Bounds and estimates for the properties of nonlinear heterogeneous systems. *Phil. Trans. R. Soc. Lond. A* **340**, 531-567.

[116] Ponte Castañeda, P. (1992). New variational principles in plasticity and their application to composite materials. *J. Mech. Phys. Solids* **40**, 1757–1788.

[117] Ponte Castañeda, P. (1996). Exact second-order estimates for the effective mechanical properties of nonlinear composite materials. *J. Mech. Phys. Solids* **44**, 827–862.

[118] Ponte Castañeda, P. (2002). Second-order homogenization estimates for nonlinear composites incorporating field fluctuations. I – Theory. *J. Mech. Phys. Solids* **50**, 737–757.

[119] Ponte Castañeda, P. (2002). Second-order homogenization estimates for nonlinear composites incorporating field fluctuations. II. Applications. *J. Mech. Phys. Solids* **50**, 759–782.

[120] Ponte Castañeda, P. (2005). *Heterogeneous Materials.* Lecture Notes, Department of Mechanics, Ecole Polytechnique, 191 pages (ISBN 2-7302-1267-1).

[121] Ponte Castañeda, P. & deBotton, G. (1992). On the homogenized yield strength of two-phase composites. *Proc. R. Soc. Lond. A* **438**, 419–431.

[122] Ponte Castañeda, P. & Suquet, P. (1998). Nonlinear composites. *Adv. Appl. Mech.* **34**, 171–302.

[123] Ponte Castañeda, P. & Suquet, P. (2001). Nonlinear composites and microstructure evolution. In *Mechanics for a New Millennium* (H. Aref and J.W. Phillips, eds.), pp 253–273. Dordrecht: Kluwer.

[124] Ponte Castañeda, P. & Tiberio, E. (2000). A second-order homogenization procedure in finite elasticity and applications to black-filled elastomers. *J. Mech. Phys. Solids* **48**, 1389–1411.

[125] Ponte Castañeda, P. & Willis, J. R. (1988). On the overall properties of nonlinearly viscous composites. *Proc. R. Soc. Lond. A* **416**, 217–244.

[126] Ponte Castañeda, P. & Willis, J. R. (1995). The effect of spatial distribution on the effective behavior of composite materials and cracked media. *J. Mech. Phys. Solids* **43**, 1919–1951.

[127] Qin, Q. & Bassani, J.L. (1992). Non-Schmid yield behavior in single crystals. *J. Mech. Phys. Solids* **40**, 813–833.

[128] Qin, Q. & Bassani, J.L. (1992). Non-associated plastic flow in single crystals. *J. Mech. Phys. Solids* **40**, 835–862.

[129] Qiu, G.Y. & Pence, T.J. (1997). Remarks on the behavior of simple directionally reinforced incompressible nonlinearly elastic solids. *Journal of Elasticity* **49**, 1–30.

[130] Quapp, M.K. & Weiss, J.A. (1998). Material characterization of human medial collateral ligament. *Journal of Biomechanical Enginnering* **120**, 757–763.

[131] Racherla, V. & Bassani, J.L. (2007). Strain burst phenomena in the necking of a sheet that deforms by non-associated plastic flow. *Modelling Simul. Mater. Sci. Eng.* **15**, S297.

[132] Racherla, V., Lopez-Pamies, O. & Ponte Castaeda, P. (2010). Macroscopic response and onset of instabilities in lamellar nanostructured elastomers with "oriented" and "unoriented" polydomain microstructures. *Mechanics of Materials* **42**, 451–468.

[133] Rosen, B.W. (1965). Mechanics of Composite Strengthening. In: Fiber Composite Materials. American Society for Metals, pp. 37–75.

[134] Spencer, A.J.M. (1972). Deformations of Fibre-reinforced Materials. Oxford University Press, Oxford.

[135] Spencer, A.J.M. (1984). Deformations of Fibre-reinforced Materials. Continuum Theory of the Mechanics of Fibre-reinforced Composites. Springer, Wein, New York.

[136] Smyshlyaev, V. & Willis, J.R. (1998). A non-local variational approach to the elastic energy minimization of martensitic polycrystals. *Proc. R. Soc. Lond. A* **454**, 1573–1613.

[137] Stratonovich, R. L. (1963). Topics in Theory of Random Noise, Vol. 1. Gordon and Breach, New York.

[138] Suquet, P. (1993). Overall potentials and extremal surfaces of power law or ideally plastic materials. *J. Mech. Phys. Solids* **41**, 981–1002.

[139] Suquet, P. (1995). Overall properties of nonlinear composites : a modified secant moduli theory and its link with Ponte Castañeda's nonlinear variational procedure. *C. R. Acad. Sc. Paris II* **320**, 563–571.

[140] Suquet, P., & Ponte Castañeda, P. (1993). Small-contrast perturbation expansions for the effective properties of nonlinear composites. *C.R. Acad. Sc. Paris II* **317**, 1515–1522.

[141] Triantafyllidis, N. & Abeyaratne, R.C. (1983). Instability of a finitely deformed fiber-reinforced elastic material. *Journal of Applied Mechanics* **50**, 149–156.

[142] Triantafyllidis, N. & Maker, B.N. (1985). On the comparison between microscopic and macroscopic instability mechanisms in a class of fiber-reinforced composites. *Journal of Applied Mechanics* **52**, 794–800.

[143] Triantafyllidis, N., Nestorović, M.D. & Schraad, M.W. (2006). Failure surfaces for finitely strained two-phase periodic solids under general in-plane loading. *Journal of Applied Mechanics* **73**, 505–515.

[144] Truesdell, C. & Noll, W. (2004). *Nonlinear field theories.* Springer-Verlag, Berlin Heidelberg, Germany.

[145] van Dommelen, J. A. W., Parks, D. M., Boyce, M. C., Brekelmans, W; A., Baaijens, F. P. T. (2003). Micromechanical modeling of intraspherulitic deformation of semicrystalline polymers. *Polymer* **44** 6089–6101.

[146] van Dommelen, J. A. W., Parks, D. M., Boyce, M. C., Brekelmans, W; A., Baaijens, F. P. T. (2003). Micromechanical modeling of the elasto-viscoplastic behavior of semi-crystalline polymers. *J. Mech. Phys. Solids* **51**, 519–541.

[147] Vincent, P.G., Monerie, Y., Suquet, P. (2008). Ductile damage of porous materials with two populations of voids. *C. R. Mecanique* **336**, 245–259.

[148] Vogler, T.J., Hsu, S.-Y., Kyriakides, S. (2000). Composite failure under combined compression and shear. *Int. J. Solids Struct.* **37**, 1765–1791.

[149] Walpole, L. J. (1969). On the overall elastic moduli of composite materials. *J. Mech. Phys. Solids* **17**, 235–251.

[150] Willis, J. R. (1977). Bounds and self-consistent estimates for the overall moduli of anisotropic composites. *J. Mech. Phys. Solids* **25**, 185–202.

[151] Willis, J. R. (1978). Variational principles and bounds for the overall properties of composites. In Continuum Models for Discrete Systems (ed. J. W. Provan). *University of Waterloo Press, Waterloo.* 185–215.

[152] Willis, J. R. (1981). Variational and related methods for the overall properties of composites. *Adv. Appl. Mech.* **21**, 1–78.

[153] Willis, J. R. (1982). Elasticity theory of composites. *Mechanics of Solids, The Rodney Hill 60th aniversary* Pergamon Press, Oxford, 653–686.